

# **Nuclear Structure From A Simple Perspective**

*R. F. Casten*

**OXFORD UNIVERSITY PRESS**

**NUCLEAR STRUCTURE FROM  
A SIMPLE PERSPECTIVE**

## OXFORD STUDIES IN NUCLEAR PHYSICS

General Editor: P.E. Hodgson

1. J. McL. Emmerson: *Symmetry principles in particle physics* (1972)
2. J. M. Irvine: *Heavy nuclei, superheavy nuclei, and neutron stars* (1975)
3. I. S. Towner: *A shell-model description of light nuclei* (1977)
4. P. E. Hodgson: *Nuclear heavy-ion reactions* (1978)
5. R. D. Lawson: *Theory of the nuclear shell model* (1980)
6. W. E. Frahn: *Diffractive processes in nuclear physics* (1985)
7. S. S. M. Wong: *Nuclear statistical spectroscopy* (1986)
8. N. Ullah: *Matrix ensembles in the many-nucleon problem* (1987)
9. A. N. Antonov, P. E. Hodgson, and I. Zh. Petkov: *Nucleon momentum and density distributions in nuclei* (1988)
10. D. Bonatsos: *Interacting boson models of nuclear structure* (1988)
11. H. Ejiri and M. J. A. de Voigt: *Gamma-ray and electron spectroscopy in nuclear physics* (1989)
12. B. Castel and I. S. Towner: *Modern theories of nuclear moments* (1990)
13. R. F. Casten: *Nuclear structure from a simple perspective* (1990)

# NUCLEAR STRUCTURE FROM A SIMPLE PERSPECTIVE

R. F. Casten

*Brookhaven National Laboratory  
Institut für Kernphysik, University of Köln*

New York      Oxford  
OXFORD UNIVERSITY PRESS  
1990

Oxford University Press

Oxford New York Toronto  
Delhi Bombay Calcutta Madras Karachi  
Petaling Jaya Singapore Hong Kong Tokyo  
Nairobi Dar es Salaam Cape Town  
Melbourne Auckland  
and associated companies in  
Berlin Ibadan

Copyright © 1990 by Oxford University Press, Inc.

Published by Oxford University Press, Inc.,  
200 Madison Avenue, New York, New York 10016

Oxford is a registered trademark of Oxford University Press

All rights reserved. No part of this publication may be reproduced,  
stored in a retrieval system, or transmitted, in any form or by any means,  
electronic, mechanical, photocopying, recording, or otherwise,  
without the prior permission of Oxford University Press.

Library of Congress Cataloging-in-Publication Data  
Casten, R.

Nuclear structure from a simple perspective/R.F. Casten/  
p. cm.—(Oxford studies in nuclear physics)

ISBN 0-19-504599-8

1. Nuclear structure. 2. Nuclear excitation.
3. Collective excitations. I. Title. II. Series.

QC793.3.S8C37 1990

539.7'4—dc20 89-23064 CIP

2 4 6 8 9 7 5 3 1

Printed in the United States of America  
on acid-free paper

## P R E F A C E

This is a very personal book, reflecting the way I see and understand nuclear physics and my belief that if something cannot be explained simply it is not really understood, nor will it be a fertile inspiration for new ideas. It is quite different from existing texts. It is in no way intended to replace them, but aims instead to complement the standard approaches to nuclear structure.

The idea for the book and much of its approach arose gradually out of both formal and informal courses in nuclear structure I have given at the Institute Laue-Langevin in Grenoble, France, the Institut für Kernphysik in Köln, Germany, and at Drexel University, Philadelphia, as well as from a series of very informal tutorial-like sessions with several of my graduate students. The book represents an attempt to cut through the often heavy mathematical formalism of nuclear structure and to present the underlying physics of some pivotal models in a simple way that frequently emphasizes semi-classical pictures of nuclear and nucleonic motion and repeatedly exploits a few fundamental ideas. Such an approach has worked for me. I can only hope others will find it useful.

The emphasis in this book always centers on seeking the essence of the physics: rigor is therefore often sacrificed. Of course, rigor is absolutely essential to a proper development of nuclear models and to precise calculations. Yet it can also be terrifying with page upon page of complex formalism, Racah algebra, tensor expansions, and the like. Necessary as this is, especially to those who will become practitioners of particular models, many readers can become either discouraged or buried in the formalism. Unfortunately, in either case, the beauty, elegance, and conceptual economy of nuclear structure theory is often missed. The complexity necessary in formal treatments at times obscures rather than illuminates the simple physics at work. Moreover, rigor can be found elsewhere, in many excellent texts: there is no need for another book to repeat it. (Several of the best of these texts, such as those by de Shalit and Talmi, Bohr and Mottelson, Brussaard and Glaudemans, deShalit and Feshbach, or the recent work by Heyde, are cited in the reference list at the end. They are indispensable.) What cannot be found so easily, though most individual parts of it probably exist scattered throughout the literature, is a systematic attempt to convey a more physically intuitive way of thinking about nuclear structure and of extracting the essential physics behind the derivations and models.

I honestly do not know whether this attempt will work. I feel it is worth a try since it is, in fact, a way of thinking used every day by practicing scientists but that is seldom presented in formal texts. If successful, it can deepen real understanding. As T. D. Lee once said (BNL Colloquium, May 1983): “That a thing is elementary does not mean it cannot be deep.” Moreover, since physics research is fundamentally a creative act depending on insight and imagination (backed, of course, by hard science—experimental or theoretical) an intuitive sense of nuclear structure can foster new inspirations and remove much of the mystery surrounding formal or calculational complexity. Finally, an approach of this type can be of considerable practical use. My hope in fact is that the reader will come to appreciate how far one can go in obtaining many results of detailed calculations almost instantly, essentially “by inspection.” It can help, for example, in anticipating the potential usefulness of a given model, in spotting errors in calculations, or in estimating the effects of particular parameter changes. One of the best examples is the famous Nilsson diagram: nearly all its features, and even the semiquantitative structure of Nilsson wave functions, can be deduced without calculation. The same applies to much of the study of residual interactions in the shell model, to collective models, to the structure of RPA vibrational wave functions, Coriolis coupling, or the IBA. To facilitate the development of this “sense” of the physics, and to provide contact between models and real data, concrete examples are almost always discussed in some detail and compared to exact calculations.

The book is in no way intended as a complete treatise on nuclear structure, either in overall coverage or within each topic. Other texts are more comprehensive. For example, many active areas of modern nuclear physics (e.g., relativistic heavy ion physics and quark-gluon plasmas, mesonic and quark degrees of freedom, or baryon excitations such as delta resonances) are totally ignored. Nevertheless, the book relates to all of them in that it discusses the basic models of nuclear structure, which successfully describe virtually all low energy nuclear phenomena, and which subnucleonic approaches must eventually reproduce. Just as it is difficult to discuss relativistic effects in nuclei without first knowing how far a non-relativistic theory can go, it is necessary to understand how far traditional nuclear structure theory can go if one is to isolate the effects of quarks, mesons, nucleonic excitations, and the like.

Even within traditional nuclear structure, many areas are bypassed. One reason for this selectivity is that it allows deeper and more detailed discussions of the subjects that are treated, discussions that would normally be found only in specialized monographs. A more practical and honest reason is that the book reflects that small part of the subject with which I am somewhat familiar and where I felt I could attempt something that was more than just parroting existing texts.

Finally, in addition to selectivity in topics there is a selectivity in treatment of each subject. For many areas, there exist several equivalent approaches. For example, there are works on residual interactions in the shell model that barely mention the concept of seniority and others that stress it throughout. Likewise, high spin phenomena in deformed nuclei can be discussed in terms

of the Nilsson model with Coriolis coupling or with the formalism of the cranked shell model. In each case, I have used the approach (in these examples, seniority and the Nilsson-Coriolis concepts, respectively) that makes the essential physics clearest to me (and, I hope, to the reader) and with which I feel most comfortable.

*Upton, New York*

R. C.

*This page intentionally left blank*

## ACKNOWLEDGMENTS

This book, while my responsibility, owes much to many people, both to those who molded my own education or who were important in the development of the approach I use here, and to those who played specific roles in the book itself. I cannot mention all but would particularly like to single out, for special thanks and gratitude, the following:

Above all, my father, Daniel F. Casten, for everything.

Ed Kennedy, who gave me my initiation into the excitement of nuclear physics.

D. A. Bromley, who more than fulfilled those early expectations and who has continually encouraged me since.

D. D. Warner, who never lets me get away with anything, for his creativity and insight, and for years of exciting work together at a perfect time. The section of Chapter 6 on the IBA is only slightly modified from portions of a review article co-authored with him. A particular piece of Chapter 7 (so noted at the appropriate point) is also largely due to him.

F. Iachello and A. Arima whose work and inspiration forever altered the course of my own work.

Igal Talmi, for innumerable discussions and for making occasional friendly disagreements so interesting, and enlightening.

J. A. Cizewski, who started the whole business of this book by asking and caring deeply about nuclear structure and who seemed to enjoy my efforts to answer.

A. Aprahamian, whose excitement at learning and discovery is an inspiration, for our collaborations, friendship, and discussions.

Jolie and Ani were my principal “guinea pigs” in all this and I am very grateful for their enthusiasm, which inspired my own, both for research and for trying to understand what nuclear structure is all about. Without them, this book would not exist.

K. Heyde, for many clarifications of my muddled thinking and collaborations that taught me much. Part of Section 4.4 is based largely on discussions with him, and Figures 4.14 a and b are based on ones in his book.

O. Hansen, S. Pittel, A. (“Aleee”) Frank, D. S. Brenner, and Zhang, Jing-ye for many productive and enlightening collaborations and discussions that broadened my horizons.

J. Weneser, M. Goldhaber, W. R. Kane, and H. Feshbach for discussions, encouragement, and moral support.

H. Börner and K. Schreckenbach for a series of productive collaborations, for demonstrating to me the power of precision, and for their efforts to create such an attractive ambiance for nuclear physics at the ILL.

The students at the ILL in 1975–1976, those (particularly K. Schiffer) in Köln in 1984–1985, and those at Drexel University in 1987 who also bore the burden of listening to these ideas in embryonic form.

P. von Brentano and A. Gelberg for countless thought-provoking discussions and for creating the stimulating atmosphere in Köln where much of this book was written.

Gritti's Café, Dürrenerstrasse, Köln, and its staff, where most of that writing actually took place, for its atmosphere, its music (by Achille), and its cappuccino conducive to physics and physics poetry.

The mountains near Wengen, Switzerland, for much of the same, at an especially crucial stage.

My wife, Jo Ann, for her patience during thousands of hours when I was trying to write this book and for submerging her feelings that nuclei are, after all, a silly sort of thing to get all excited about.

Bob and Marian Haight and Don, Jo Ann and Kim Reisler, and Tom and Ahng Suarez for years of friendship, talk, hiking, skiing, tennis, and general support.

Jackie Hartt, whose patience is outdone only by her tennis.

Judy Otto, Irma Reilly, Walter Palais, and Whitey Caiazza of the Illustration group at Brookhaven National Laboratory for their very professional, and enthusiastic, help with the figures. I am also grateful to the Photography Group for their excellent work and for putting up with so many “emergencies.”

Jackie Mooney, whose skills, including cryptology, are absolutely amazing and without whose work, friendship, and dedication this book would have been sheer fantasy. I promise never to inflict such agony again.

I would also specifically like to thank K. Heyde, M. Buescher, W. Krips, R. Schuhmann, and Zhang, Jing-ye for very careful reading of many parts of the manuscript and for pointing out numerous errors.

I am very happy to acknowledge Brookhaven National Laboratory for permission to pursue this project and for the infrastructure that made it possible.

Finally, I am grateful to Oxford University Press for asking me to write this book, for forbearance during several delays and lapsed deadlines, and for making the whole process as pleasant as it has been.

## NOTATION

In a work such as this, the question of notation always presents a dilemma—whether to adopt a rigorously unique set of symbols or to use those commonly found in the literature. With one significant exception (so noted at the appropriate place in the text), I have followed the latter course since it facilitates further study by the reader and because, in practice, there should be little ambiguity of meaning. Generally, different uses of a given symbol are widely separated in context and location (with one awful exception in Chapter 4 concerning the “A” dependence of the interaction strength). To further help avoid confusion it may be useful to list a few of the notational choices.

$\psi$  refers to a physical wave function while  $\phi$  usually refers to a basis state or an unperturbed wave function.

$E$  is used for excitation energies but also for quasiparticle energies.

$\epsilon$  is used for single particle shell model energies and for one of the quadrupole deformation parameters.

$\delta$  refers to the “contact like” residual interaction and also to a quadrupole deformation parameter.

Generally  $p, n$  are used for proton and neutron (although very occasionally  $\pi$  and  $v$  are substituted). However,  $p$  also refers to particle as is  $p-p$  or  $p-h$  (particle-particle or particle-hole excitation).

$N$  refers alternately to neutron number, boson number in the IBA, and to oscillator shell number.

$A$  is the mass number of a nucleus but also the angular part of a residual interaction (especially in Chapters 4 and 5).

$\alpha$  is an amplitude of a mixed wave function and also the alignment quantum number in the rotation alignment scheme.

$J$  is used to denote the total angular momentum quantum number (colloquially, “the spin”) of a level. Note that, quantum mechanically, the actual total angular momentum is  $\sqrt{J(J+1)} \hbar$ .  $j$  is used for the angular momentum of a single particle.

Finally, operators, matrices, and vectors are given in bold face. The same symbol (e.g.,  $Q, n_a$ ) in normal face stands for the eigenvalue of that operator.

*This page intentionally left blank*

## CONTENTS

### PART I INTRODUCTION

1. INTRODUCTION, 3
  - 1.1 Introduction, 3
  - 1.2 The Nuclear Force, 6
  - 1.3 Pauli Principle and Antisymmetrization, 16
  - 1.4 Two-State Mixing, 17
  - 1.5 Multistate Mixing, 22
  - 1.6 Two-State Mixing and Transition Rates, 25
2. THE NUCLEAR LANDSCAPE, 28

### PART II SHELL MODEL AND RESIDUAL INTERACTIONS

3. THE INDEPENDENT PARTICLE MODEL, 47
4. THE SHELL MODEL: TWO-PARTICLE CONFIGURATIONS, 67
  - 4.1 Residual Interactions: The  $\delta$ -Function, 69
  - 4.2 Geometrical Interpretation, 85
  - 4.3 Pairing Interaction, 93
  - 4.4 Multipole Decomposition of Residual Interactions, 94
  - 4.5 Some Other Results (Average Shifts, Hole, and Particle-Hole Configurations), 104
5. MULTIPARTICLE CONFIGURATIONS, 109
  - 5.1  $J$  Values in Multiparticle Configurations: The  $m$ -Scheme, 109
  - 5.2 Coefficients of Fractional Parentage (CFP), 111
  - 5.3 Multiparticle Configurations  $j^n$ : The Seniority Scheme, 115
  - 5.4 Some Examples, 125
  - 5.5 Pairing Correlations, 130

**PART III COLLECTIVITY, PHASE TRANSITIONS,  
DEFORMATION**

6. COLLECTIVE EXCITATIONS IN EVEN-EVEN NUCLEI:  
VIBRATIONAL AND ROTATIONAL MOTION, 141
  - 6.1 An Introduction to Collectivity, Configuration Mixing, and Deformation, 141
  - 6.2 Collective Excitations in Spherical Even–Even Nuclei, 145
  - 6.3 Deformed Nuclei: Shapes, 161
  - 6.4 Rotations and Vibrations of Axially Symmetric Deformed Nuclei, 165
  - 6.5 Axially Asymmetric Nuclei, 186
  - 6.6 The Interacting Boson Model, 197
  - 6.7 The Development of Collectivity: Phenomenology and Microscopic Basis, 234
7. THE DEFORMED SHELL MODEL OR NILSSON MODEL, 247
  - 7.1 The Nilsson Model, 248
  - 7.2 Examples, 260
  - 7.3 Prolate and Oblate Shapes, 263
  - 7.4 Interplay of Nilsson Structure and Rotational Motion, 264
8. NILSSON MODEL: APPLICATIONS AND REFINEMENTS, 271
  - 8.1 Single Nucleon Transfer Reactions, 271
  - 8.2 The Coriolis Interaction in Deformed Nuclei, 280
  - 8.3 Coriolis Mixing and Single Nucleon Transfer Cross Sections, 290
  - 8.4 Coriolis Effects at Higher Spins, 300
9. MICROSCOPIC TREATMENT OF COLLECTIVE VIBRATIONS, 313
  - 9.1 Structure of Collective Vibrations, 314
  - 9.2 Examples: Vibrations in Deformed Nuclei, 322

**PART IV EXPERIMENTAL TECHNIQUES**

10. A FEW SELECTED EXPERIMENTAL TECHNIQUES, 335
  - 10.1 Coulomb Excitation, 335
  - 10.2 Spectroscopically Complete Techniques, 344
  - 10.3 Heavy Ion Compound Reactions and High Spin States, 356
  - 10.4 Heavy Ion Transfer Reactions, 361

REFERENCES, 365

INDEX, 371

PART I  
INTRODUCTION

*This page intentionally left blank*

# 1

## INTRODUCTION

### 1.1 Introduction

The atomic nucleus is not a single object but a collection of species ranging from hydrogen to the actinides, and displaying an unbelievably rich and fascinating variety of phenomena. The nucleus is extremely small, namely about  $10^{-12}$  to  $10^{-13}$  cm in diameter, and can contain up to a couple of hundred individual protons and neutrons that orbit relative to one another and interact primarily via the nuclear and Coulomb forces. This system may seem so complex that little could ever be learned of its detailed structure. Indeed, many of us involved in research into nuclear structure proclaim loudly and strenuously that we have barely scratched the surface (both literally and figuratively, as we shall see) in our understanding of nuclear structure. From another perspective, however, we have an immense number of facts about nuclei and we understand an enormous amount, often in great detail, concerning what the individual nucleons do in atomic nuclei, how this leads to the observed nuclear phenomena, how and why these phenomena change from nucleus to nucleus, and how certain nucleons interact with each other in the nuclear medium. We have basic models—the shell model and collective models—both geometric and algebraic, that provide a framework for our understanding and that are extremely simple, and yet subtle and refined. It is only after these models and framework are appreciated that the limitations in our knowledge become focused and identifiable; the identification of the problems that persist is a prerequisite to further advancement. In this book we emphasize the known and understood as a background, map, and guide to the unknown.

We hope the reader perusing this book will come to appreciate two principle facts: namely, the beautiful richness and variety of nuclear physics and the extent to which we can understand nuclear data and models by invoking a few extremely basic ideas and drawing upon arguments that are physically transparent and intuitive. We will see that it is possible, in many if not most cases, to understand the detailed results of complex calculations with an absolute minimum of formalism and often by inspection. As an example, even such seemingly complicated results of nuclear models such as the famous Nilsson diagram and the detailed structure of Nilsson wave functions, or of the microscopic RPA wave functions of collective vibrations, can be derived, nearly quantitatively, without any calculation whatsoever.

We emphasize that one must make a careful distinction between this approach and what is commonly called *handwaving*. The latter, to this author's mind, is what one does when one does not really know an answer or explanation and tries to explain some piece of nuclear data or the result of some calculation by an offhand, qualitative, "explanation" that is often little more than a slogan or a repetition of key words or venerated phrases. We have all encountered examples of such handwaving: supposedly forbidden  $\gamma$ -ray transitions glibly explained as "due to mixing," extra or unexpected excited states dismissed as "due to neglected degrees of freedom," unexplained peaks in transfer reaction spectra ascribed to "higher order processes in the reaction mechanism," or explanations of model calculations as "resulting from the symmetry properties," or "from an energy minimization" (of course but why, how?). Indeed, in many cases, such statements are true and are reasonably accurate descriptions. Otherwise they would not have become catch phrases. But abuses abound to such an extent that they often represent a watered down substitute for real understanding that is to be discouraged.

The approach here, in contrast, attempts to *extract the basic physics ideas* that emerge either from an inspection of nuclear data or that lie behind the results of some model or calculation, and to do this by applying a minimum of key physical and geometrical ideas about the nucleus. When attempting such a program, there is always the danger of losing sight of important subtleties and of ignoring the importance of formal rigor that is so necessary in detailed and realistic model calculations. Undeniably, there are certain results of such calculations and certain model predictions that can only be understood by carrying out the fully detailed, often tedious, calculations. However, the author has always felt, and hopes that the reader will be convinced, that it is remarkable how far one can go in understanding complex nuclear structure phenomena by careful but simple physical arguments. Of course, this approach has the lurking danger of itself slipping into handwaving. If such sins are kept to the minimum here, there is a chance that the reader may emerge with an appealing physical understanding and intuition into nuclear structure that many working physicists have attained but that is seldom spelled out in textbooks because of a hesitancy or reluctance to commit to writing the nonrigorous and intuitive arguments that all of us use and, mentally, rely upon. If anything, the philosophy of this book is that such ideas and such an approach should not be a skeleton hidden in a closet for fear of ridicule but rather an important aid that is a constant and continual complement to necessary formal and rigorous calculations. As frequently as possible, qualitative physical explanations or "derivations" will not be left to stand alone; rather, the physical intuition behind them will be tested by, confirmed, and confronted with the results of actual calculations or with the data on atomic nuclei themselves.

We have already stated that many of the arguments here will rely on "a few basic simple ideas." In fact there are three of these that are of absolute and essential importance. They are:

- The generally attractive and short-range nature of the nuclear force.

- The effects of the Pauli principle.
- An understanding of two-state mixing—that is, the effects on energies and wavefunctions when two nuclear states mix due to some residual interaction.

These ideas, plus a constant reference to a kind of geometrical picture of the nucleus, form the basic ingredients behind many of the arguments to be presented.

A general outline of the book is as follows: After the discussion of these three basic ingredients in Chapter 1, Chapter 2 departs from the usual way of presenting nuclear structure by “surveying the nuclear landscape,” that is, by collecting a number of examples of nuclear data, level schemes, transition rates, systematics, and so on. In a normal text that relies on a systematic, step-by-step progression of ideas, such a chapter would be out of place since it utilizes terminology and concepts that will be formally introduced later. It is inserted here so that the beautiful and elegant consequences of nuclear models discussed in subsequent chapters will not be presented in a contextual vacuum. Often such results, when first encountered, seem highly abstract and of little practical importance and it is, unfortunately, often only years later, when the practicing nuclear physicist has gained a deeper familiarity with nuclear data, that their significance is finally understood.

One reason we feel justified in this approach is that this book is aimed not only at beginning nuclear physics graduate students, to whom much of the jargon in Chapter 2 will be unfamiliar, but also to practicing and experienced nuclear physicists who may be interested in the kind of alternative and complementary approach emphasized here.

Chapters 3, 4, and 5 will deal with the shell structure of nuclei, as is traditional, starting with the independent particle model and going on to the shell model for multiparticle configurations. The formalism and mathematical development of the shell model is one of the most remarkable creations of nuclear physics and allows one to account for many empirically observed features of atomic nuclei with an absolute minimum of physical input (e.g., many detailed predictions can be made without ever specifying the nature of the central shell model potential or the detailed structure of a residual interaction). Unfortunately, the shell model formalism, and derivations based on it, are often complex and, quite honestly, terrifying. This has the unfortunate consequence that this subject is often skimmed or glossed over by students. These chapters attempt to highlight and give plausibility arguments for many shell model results while at the same time avoiding, as much as possible, such formal treatments. Simpler derivations are sometimes possible and are given in appropriate cases.

The next section of the book (Chapter 6) deals with collective models for even–even nuclei, starting with macroscopic models of vibrational and rotational motion. This material also emphasizes the profound importance of the residual proton–neutron interaction (especially the  $T = 0$  component) and its role in the onset of collectivity, configuration mixing, and deformation in nuclei, in inducing nuclear phase transitions, and the assistance its understand-

ing can provide in simplifying the systematics of nuclear data. Following this, a brief treatment of algebraic models, principally the interacting boson approximation (IBA) model is given.

In Chapters 7 and 8, the discussion turns to odd mass nuclei, with primary emphasis on deformed nuclei, and an extensive discussion of the Nilsson model and its consequences, extensions, and testing via single nucleon transfer reactions.

Most of the collective models discussed up to this point will have been phenomenological or macroscopic. We will not discuss detailed microscopic approaches at length but will introduce such approaches in Chapter 9 since they provide both the microscopic justification of macroscopic models and a simple physical picture of collective excitations (especially vibrations) that will allow the reader to anticipate their detailed structure without calculation.

Finally, in Chapter 10, a few selected experimental techniques for studying atomic nuclei will be discussed, primarily to give the reader a glimpse of the richness of experimental probes available, of their differences and of the different types of nuclear data and structure that they elucidate, and to provide some simple physical ideas that may be helpful in understanding the “parameters” that govern the design of such experiments and the extraction of information from them.

With this discussion of the philosophy and outline of the material to follow, we turn now to the three “cornerstones” mentioned earlier that are of such central importance to everything that follows. Many readers know that the nuclear force is attractive, that the Pauli principle is important, and understand that residual interactions can mix neighboring states. They might be tempted to skip over these sections and of course that is their prerogative; indeed, these pages contain nothing that is new or not to be found elsewhere. However, they do present a somewhat different perspective and provide a ground and background for what follows.

## 1.2 The Nuclear Force

Nuclei exist and are composed of neutrons and positively charged protons. Were the nuclear environment dominated by the repulsive Coulomb force, this could not be the case: one therefore deduces immediately that there must be a strong, attractive, interaction that can overcome the repulsive Coulomb force and bind nucleons together. The nuclear force is at first glance a mysterious one since it has few if any recognizable consequences in macroscopic matter (i.e., everyday phenomena). And, in fact, the exact nature of this force is still largely unknown. Nevertheless, it is remarkable how much we can learn about it from a few simple empirical facts. We have already stated that the very existence of nuclei implies a new force—the strong interaction that can overcome the Coulomb repulsion between protons. Beyond this many experiments point to two basic facts:

- Nuclei are small, on the order of  $10^{-12}$  to  $10^{-13}$  cm in diameter.

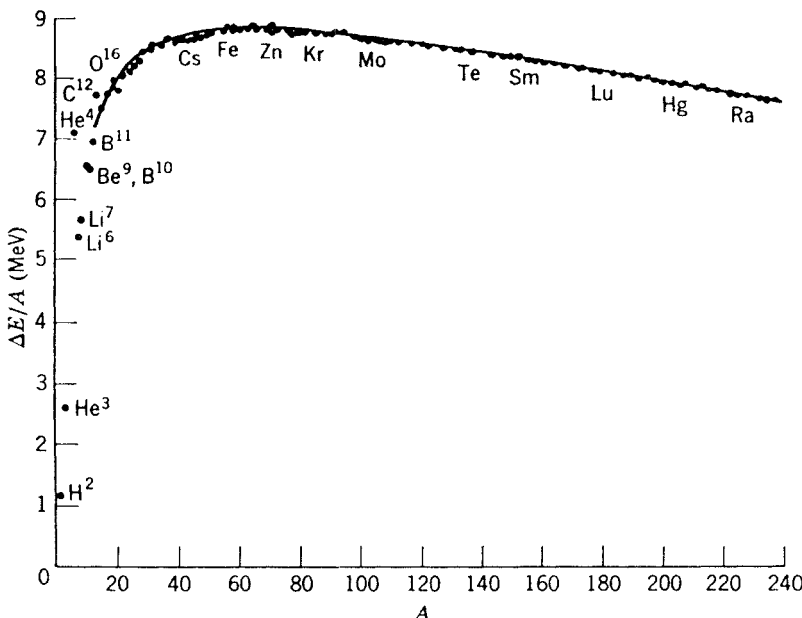


**Fig. 1.1.** Binding energies per nucleon. The solid curve is the result of a typical semi-empirical mass formula that includes corrections for surface effects, Coulomb repulsion, the Pauli principle, and pairing effects. Many of these topics will be discussed later on. (Based on Eisberg, 1974.)

- For all practical purposes, the nuclear force can be neglected when considering atomic and molecular phenomena.

These two facts tell us that the nuclear force must be short range. A few further empirical observations allow us to refine this considerably.

- Nuclear binding energies, per nucleon, at first increase rapidly with  $A$ , until about  $A \sim 10$  to 20, where they level off at approximately 8.5 MeV and remain roughly constant thereafter. These binding energies per nucleon are shown in Figure 1.1.
- The masses of mirror nuclei, which are defined as pairs of nuclei with interchanged numbers of protons and neutrons,  $(Z, N)_1 = (N, Z)_2$ , are nearly identical, after correcting for the different strengths of the Coulomb interaction in the two nuclei.
- The sequencing, spin parity ( $J^\pi$ ) values, and excitation energies of excited states in mirror nuclei are also nearly identical.
- Proton and neutron separation energies, denoted  $S(p)$  and  $S(n)$ , are defined as the energies required to remove the last proton or neutron to infinity, and have a characteristic behavior with changing proton number and neutron number. Typical examples of such separation energies are

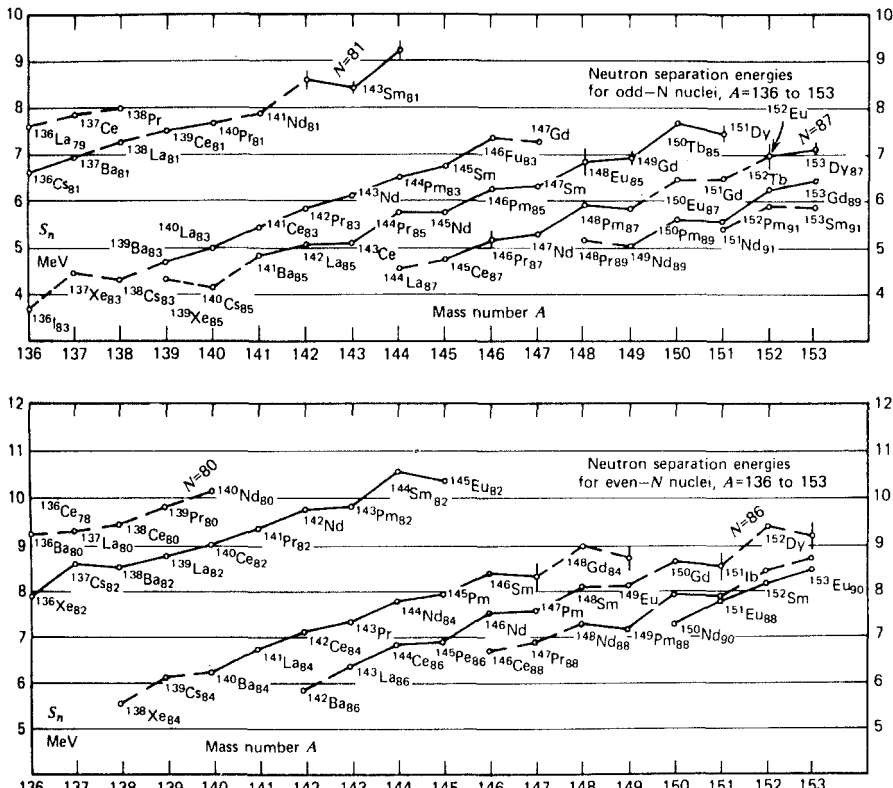


Fig. 1.2. Neutron separation energies near the  $N = 82$  magic number (de Shalit, 1974).

shown in Figs. 1.2 and 1.3 from which it is evident that  $S(p)$  decreases with increasing  $Z$  and increases with increasing  $N$  while  $S(n)$  decreases with increasing  $N$  and increases with increasing  $Z$ . That is, each *decreases* with an increasing number of the *same* type of nucleon and *increases* with an increasing number of the *other* type. Although not exactly germane to the present discussion, we note for later use that the separation energies also show particularly large and sudden drops at certain special numbers of protons and neutrons, called *magic numbers*, namely  $N$  or  $Z = 2, 8, 20, 40, 50, 82, 126$ . Those at 82 are evident in Figs. 1.2 and 1.3.

- Measurements of electron scattering provide abundant evidence of a nearly constant nuclear density independent of the number of nucleons  $A$ . This, in turn, implies that the nuclear volume must increase linearly with  $A$ . Neither of these facts may seem particularly surprising at first but it should be recalled that such is not the case with atomic systems whose sizes are nearly independent of  $Z$ . Note that if the nuclear volume  $V \propto A$ , then, assuming a roughly spherical nucleus, the nuclear radius scales as  $A^{1/3}$ . Innumerable studies have shown that a good approximation to the nuclear radius is  $R = R_o A^{1/3}$  where  $R_o \sim 1.2$  fm.

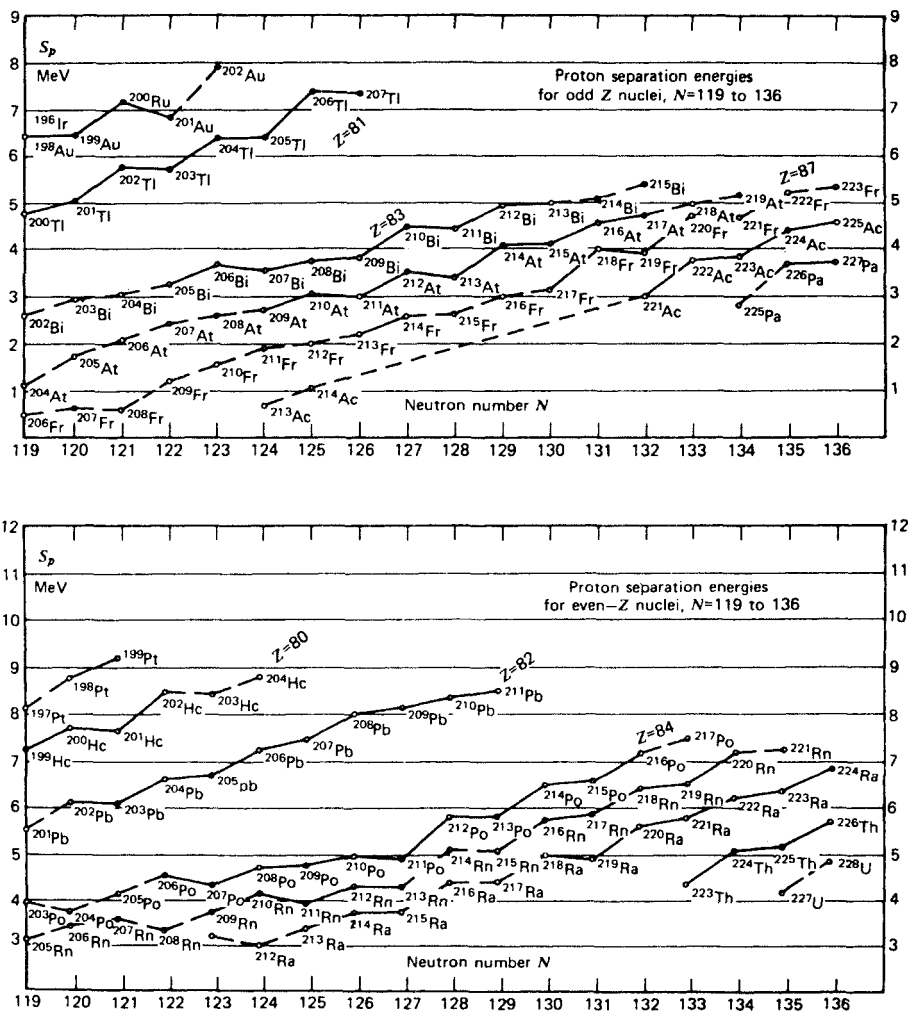


Fig. 1.3. Proton separation energies near the  $Z = 82$  magic number (de Shalit, 1974).

- There is only one bound state of the deuteron, the simplest nuclear system, with one proton and one neutron.
- This bound state has total angular momentum  $J = 1$ , that is, in the deuteron, the intrinsic spins ( $1/2$ ) of the neutron and proton are aligned parallel to each other, not antiparallel. (This result assumes that the two nucleons have no relative orbital angular momentum, a result that will be justified in Chapter 3.)
- The deuteron has a nonzero quadrupole moment, that is, it has, on average, a preference for a nonspherical shape.

Let us consider each of these facts in turn and see what we can learn about the nuclear force. Note that, except for the listing of the magic numbers, the



preceding list contains virtually no specific nuclear structure information, although what we will learn from these facts about the nuclear force has many consequences for nuclear structure throughout the periodic table.

We have already deduced that the nuclear force is predominantly attractive and short range. (We neglect the short range repulsive core component.) The binding energy results, Fig. 1.1, and the fact that the nuclear density is approximately constant, allow us to go much further. The nuclear size, corresponding to a radius of  $\sim 10^{-12}$  to  $10^{-13}$  cm, tells us that the range of the force must be roughly this order of magnitude. However, the density and binding energy data tell us that the force is actually of a considerably smaller range than that of most nuclei. If the nuclear force extended more or less equally to all  $A$  nucleons, then the binding energy would increase roughly as  $A(A-1)/2$ , or the binding energy per nucleon ( $B.E./A$ ) would increase with  $A$  and therefore so would the nuclear density. That such is not the case, at least for  $A \geq 10$ , shows that the nuclear force saturates. The contrary fact that the binding energy per nucleon *does* increase for very light nuclei allows us to quantify this saturation and to make at least a crude estimate of the number of nucleons with which each other nucleon interacts.

To do this, we assume that all such interactions are equal and count the number of interactions assuming that each nucleon interacts with various numbers of other nucleons. Fig. 1.4 gives a pictorial illustration of the connections and shows a plot of  $B.E./A$  deduced under different assumptions for the numbers of connections per nucleon. If one works through this figure, it becomes obvious how saturation arises when each nucleon interacts only with a finite number,  $n_i$ , of others. For example, if  $n_i = 3$ , the number of interactions of each nucleon (and hence its binding energy) has already reached its maximum value when  $A = 4$ . We can use this approach to set some rough limits on  $n_i$ . Clearly  $n_i = 2$  is unacceptable since it leads to immediate saturation at  $A = 3$ . Similarly  $n_i = 3$  leads to premature saturation, but somewhere on the order of 6 to 10 mutual interactions leads to  $B.E./A$  values that approach saturation roughly where the data do. Thus, the empirically observed saturation in binding energy per nucleon data suggest that the range of the nuclear force is on the order of the size of nuclei such as Li or Be (i.e., approximately 2 to 4 fm). Crude as this analysis is, the idea behind it is qualitatively valid and the conclusion is more quantitatively correct than one might expect.

The properties of mirror nuclei also tell us much about the nuclear force. The data for three  $A = 27$  nuclei are shown in Fig. 1.5 (note that  $^{27}\text{Mg}$  is not mirror to the other two; it is shown for comparison and contrast). At the right, the figure gives the relative binding energies or masses of the three nuclei and on the left the low-lying excited states with their  $J^\pi$  values. The remarkable feature is the nearly identical spectra for the two mirror nuclei. The interactions between two nucleons can be divided into three categories: p-p, n-n, and p-n interactions. The data from mirror nuclei suggest that the nuclear force is "charge symmetric" (i.e., the p-p and n-n, interactions are equal). The fact that the absolute binding energy of  $^{27}\text{Al}$  is greater than  $^{27}\text{Si}$  does not reflect a breakdown of this idea, but rather the influence of the Coulomb interaction:  $^{27}\text{Si}$  has more protons than  $^{27}\text{Al}$  and, therefore, has a greater total repulsive Coulomb interaction that leads to lower total binding.

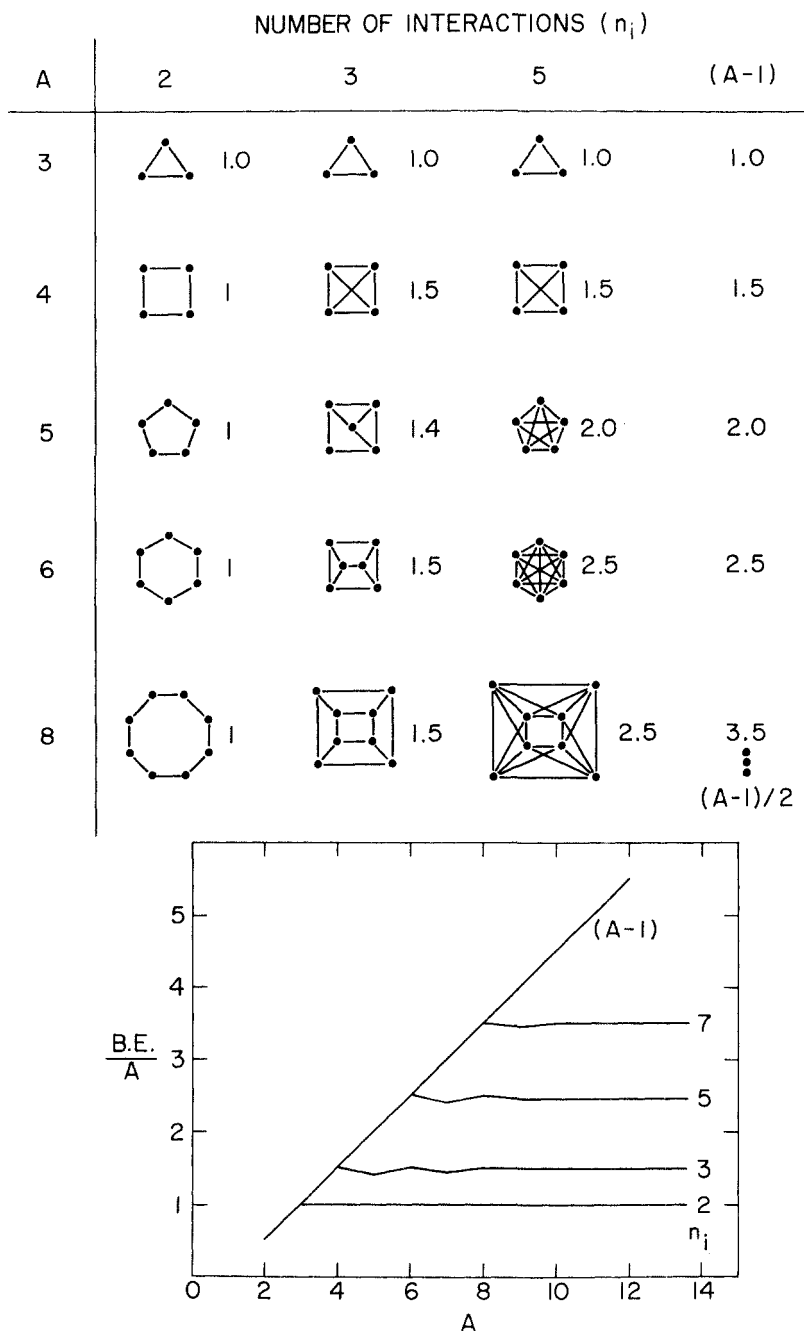


**Fig.1.4.** Highly schematic calculation of the binding energy per nucleon under different "saturation" assumptions concerning nuclear forces. The number of connections indicated,  $n_i$ , is the number of nucleons with which each other nucleon is assumed to interact. All such interactions are considered to be of equal strength. The lower part shows a plot of the resulting binding energies per nucleon.

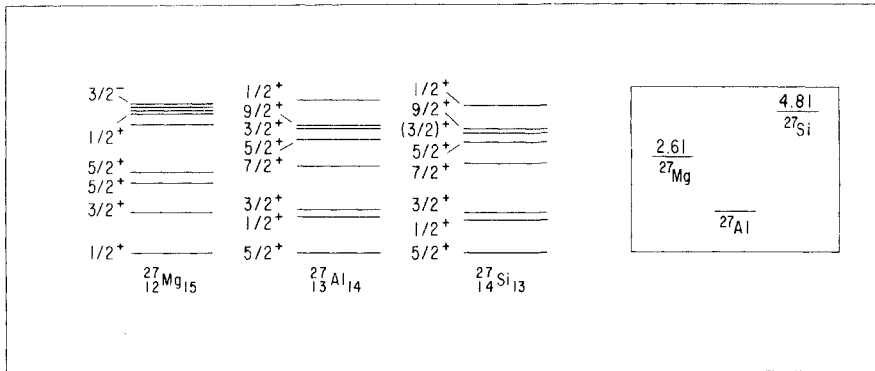


**Fig. 1.5.** Level schemes and binding energies (inset box at right with binding energies in MeV relative to  $^{27}\text{Al}$ ) of the mirror nuclei  $^{27}\text{Al}$  and  $^{27}\text{Si}$ , as well as the isobar  $^{27}\text{Mg}$ .

A more general characteristic of the nuclear force is charge *independence*, which means that the p-p, n-n, *and* p-n forces are equal. To examine this question, consider an isobar triplet such as  $^{12}\text{Mg}_{14}$ ,  $^{13}\text{Al}_{13}$ , and  $^{14}\text{Si}_{12}$ . The low-lying levels of  $^{26}\text{Mg}$  and  $^{26}\text{Si}$  are similar as expected:  $^{26}\text{Mg}$  has excited states  $2^+(1.81 \text{ Mev})$ ,  $2^+(2.94 \text{ MeV})$ ,  $0^+(3.59 \text{ MeV})$ , and so on, while  $^{26}\text{Si}$  has  $2^+(1.80 \text{ MeV})$ ,  $2^+(2.78 \text{ MeV})$ ,  $0^+(3.33 \text{ MeV})$ , and so on. At first glance, the nucleus  $^{26}\text{Al}$  appears quite different, but careful inspection of its level scheme shows a subset of excited states with similar binding energies as its isobars. Specifically, at energies *relative* to the lowest  $0^+$  state there are  $2^+(1.84 \text{ MeV})$ ,  $2^+(2.93 \text{ MeV})$ ,  $0^+(3.52 \text{ MeV})$  levels, and so on. This would seem to suggest that charge independence has approximate validity. However, there are other states that have no analogues in  $^{26}\text{Mg}$  and  $^{26}\text{Si}$ . We also note in Fig. 1.5 that  $^{27}\text{Mg}$  is quite different than  $^{27}\text{Al}$  and  $^{27}\text{Si}$ , even though Table 1.1 shows that all three  $A = 27$  isobars have the same total number of interactions (351). These results focus on a crucial aspect of the p-n system: it can exist in two different configurations. The concept of the proton and neutron as merely two states of the same particle, the *nucleon*, leads to the concept of *isospin*, which is similar to intrinsic spin. In analogy with intrinsic spin, each nucleon is assigned an isospin  $t = 1/2$ : protons and neutrons are distinguished by the projection of this isospin on an imaginary isospin  $z$ -axis. This projection  $t_z$  is  $-1/2$  for protons and  $+1/2$  for neutrons. Then, just as one can couple the intrinsic spins of two identical nucleons parallel or antiparallel to  $S = 1$  and  $S = 0$ , the total isospin projection of a proton-neutron system can either be  $T_z = 1$  if the two isospins are aligned and  $T_z = 0$  if they are antialigned. Since  $T$  cannot be less than its projection, a proton-proton or a neutron-neutron system must have  $T = 1$  with  $T_z = -1$  for the proton case and  $+1$  for the neutron case. However, a proton-neutron system with  $t_z$  components of  $-1/2$  and  $+1/2$  can couple to  $T_z = 1$  or  $0$  and hence  $T = 1$  or  $0$ . It turns out that the p-n interaction is not identical in the  $T = 1$  and  $T = 0$  modes. By charge independence, the interaction in the  $T = 1$  p-n system must be identical to that in the p-p and n-n

**Table 1.1.** Nucleon–nucleon interactions in  $A = 27$  Nuclei

	$^{27}_{12}\text{Mg}_{15}$	$^{27}_{13}\text{Al}_{14}$	$^{27}_{14}\text{Si}_{13}$
p–p	66	78	91
n–n	105	91	78
p–n	180	182	182
Total	351	351	351

Based on deShalit, 1974.

systems. However, the interaction in the  $T = 0$  p–n system need not be the same. (As we will see, it is considerably stronger.) Thus there is no a priori reason to expect that  $^{27}\text{Mg}$ , with fewer p–n interactions, should have the same sequence of energy levels as  $^{27}\text{Al}$  or  $^{27}\text{Si}$  and, indeed, it does not. Furthermore,  $^{27}\text{Mg}$  is less bound than  $^{27}\text{Al}$ , even though it has fewer protons and might, therefore, be expected to be more tightly bound. The reason is that it also has fewer  $T = 0$  p–n interactions (see Table 1.1). This is already one piece of evidence suggesting the  $T = 0$  interaction is stronger than the  $T = 1$ . The concept of the different and stronger, p–n interaction in the  $T = 0$  channel will be of enormous importance later. For example, it determines why the excitation spectra of odd–odd nuclei differ so substantially from those of even–even nuclei. Moreover, its effects are intimately connected with those of the Pauli principle since  $T = 1$  corresponds to a symmetric alignment of the two isospins in the p–n system, while  $T = 0$  corresponds to an antisymmetric alignment.

Nuclear separation energies provide crucial information about the outermost nucleons and therefore about certain subtle aspects of the nuclear force in the “valence” region. As we will see, the most important nuclear model, the shell model, treats nuclei in terms of individual nucleons that orbit as independent particles in a central potential. Each orbit carries certain quantum numbers and a specific wave function. This is an excellent approximation of the actual motion except that there are important “residual interactions” beyond those encompassed by the central potential that must be considered when dealing with nuclei containing several particles outside closed or magic configurations. This will be a major topic of discussion in Chapters 4 and 5. We showed examples of separation energy data in Figs. 1.2 and 1.3 earlier and summarized the trends, which are valid for all mass regions: that  $S(p)$  decreases with increasing  $Z$ , that  $S(n)$  decreases with increasing  $N$ , and that each increases with increasing number of particles of the other type. Superimposed on this general behavior is a fine structure in that  $S(p)$  and  $S(n)$  display odd–even oscillation in  $Z$  and  $N$  such that nuclei with even numbers of either protons or neutrons have larger separation energies (i.e., are more bound). Though these separation energy data are widely familiar, it is seldom appreciated how much they tell us about the nuclear force.

The separation energies refer to the ground states of their respective nuclei: in nuclei with even numbers of protons and neutrons the ground state always has spin and parity  $J^\pi = 0^+$ . Invariably, this state is much lower in energy than any intrinsic excitation. The fact that  $S(p)$  and  $S(n)$  are larger when  $Z$  and  $N$

are even thus implies that there is a special attractive interaction in pairs of protons or neutrons coupled to  $J^{\pi} = 0^+$ . Later, we shall see that this is a property of short-range interactions resulting from the Pauli principle. The separation energy data also shows that the p–n interaction is strong and attractive since  $S(p)$  increases with increasing  $N$  and  $S(n)$  increases with increasing  $Z$ . In contrast, the decrease of each separation energy with increasing numbers of nucleons of the *same* type gives the fundamentally critical result that, *aside from the pairing interaction*, the *residual* interaction between *like* nucleons is repulsive. This fact, pointed out in the early 1960s by Talmi, is seldom recognized or remembered; however, its consequences, are profound. For example, anticipating some concepts and jargon from upcoming chapters, it is one reason why singly magic nuclei do not become deformed and why the accumulation of proton neutron interaction strength is essential for the onset of collectivity and deformation in nuclei.

The properties of the simplest bound nuclear system, the *deuteron*, tell us still more about the nuclear force. The essential features, summarized earlier, are that there is only one bound state, that it has  $J^{\pi} = 1^+$ , and that the deuteron has a finite quadrupole moment. The fact that there is only one bound state and, moreover, that it is only weakly bound (the deuteron binding energy is 2.23 MeV) serves to emphasize the essential *weakness* of the so-called strong nuclear force. By *weak* here we mean weak in comparison to the kinetic energy of relative motion of the two nucleons. For example, this implies that the relative kinetic energy of two nucleons cannot be changed substantially by the strong interaction. This will be important in Chapter 3, when we discuss the reason why essentially independent particle motion is possible in a densely packed, strongly interacting nuclear medium.

It will also be shown in Chapter 3 that for a rather general central potential, the lowest energy state corresponds to zero orbital angular momentum (an *S* state). Thus, both the proton and the neutron in the deuteron must be in *S* orbital angular momentum states and the total angular momentum in the ground state can arise only from the proton and neutron intrinsic spins,  $1/2 \hbar$  (henceforth, in this book, we shall generally omit the units  $\hbar$  in referring to angular momentum and intrinsic spin). There are two possible ways of coupling these two spins: to a total spin  $S = 0$  or  $1$ . The fact that the deuteron chooses the latter highlights an essential point: even though the nuclear force may have no explicit spin dependence, there can be large energy differences between states of different spins in multiparticle configurations. We shall discuss this point extensively in Chapter 4 where we shall see that the *implicit* spin dependence of nuclear forces is a reflection of the Pauli principle and that this has critical nuclear structure consequences.

Finally, the nonzero quadrupole moment of the deuteron is our first indication of the tendency of the proton–neutron interaction to lead to nonspherical nuclear shapes. Moreover, it is an indication that the nuclear force cannot be completely described by a spherically symmetric central potential. (In the particular case of the deuteron the finite quadrupole moment is evidence for tensor forces that couple a spin dependent component to a central potential,

but this is not of particular importance in the present context.)

It is worthwhile at this point to reiterate what we have learned about the nuclear force, and to emphasize that this rather detailed knowledge stems from some of the simplest empirical facts concerning nuclei. The essential characteristics of the nuclear force are:

- It is predominantly attractive
- It is short range
- It saturates
- It is charge independent (excluding, of course, the Coulomb part)

Moreover, we have learned that the residual interaction (the internucleon force not contained within an overall central potential) has the following properties:

- It exhibits the pairing property that favors the coupling of the angular momenta of like nucleons to  $0^+$ .
- Aside from the pairing interaction, the like-nucleon residual interaction is, on average, repulsive.
- The  $T = 0$  component of the p–n interaction, on the other hand, is predominantly attractive.
- The supposedly “strong” nuclear force is strong only in comparison with other forces: in the nuclear context, it is barely strong enough to overcome the relative kinetic energies of two nucleons in low energy orbits.
- On balance, as evidenced by the deuteron, the p–n interaction favors the coupling of the proton and neutron intrinsic spins to  $S=1$  rather than  $S=0$ . In Chapter 4, we shall see that this is in striking contrast to the like-nucleon residual interaction that favors  $S = 0$ . Both of these are intimately connected with the effects of the Pauli principle.
- The proton–neutron system has a tendency to produce nonspherical shapes and provides evidence for spin-dependent tensor forces.

Before we end this discussion of the nuclear force, there is one other interesting point concerning its range. The short range,  $\sim 10^{-12}$  to  $10^{-13}$  cm, is not at all accidental, but may actually be derived by a simple consideration of its source. It is now generally accepted that all forces in nature result from the exchange of specific kinds of particles between the interacting entities. Between the time one of these entities emits such a “virtual” particle and the other absorbs it, there is a nonconservation of energy. Therefore, by the Heisenberg uncertainty principle,  $\Delta t \Delta E \geq \hbar$ , there is only a finite amount of time during which the exchange can occur. Clearly, there is a relation between the mass of the exchanged particle and the possible range of the force: lighter (low  $E$ ) virtual particles induce smaller violations of energy conservation and therefore can exist for longer periods of time, thus permitting longer-range forces. The outstanding example of this is the Coulomb interaction, which is mediated by massless virtual photons and is therefore of extremely long range. In the nuclear case, the mediation is carried by virtual mesons of which the lightest are the pions with mass  $\sim 140$  MeV. Assuming that they travel at the

speed of light, we immediately obtain an upper limit on their “lifetime:”

$$\Delta t \leq \hbar/140 \text{ MeV} = \hbar/mc^2$$

where  $m$  is the pion mass. The distance they can travel in this period is

$$r = c\Delta t = \hbar/mc = 1.4 \times 10^{-13} \text{ cm}$$

which is remarkably close to the typical range of the nuclear interaction.

### 1.3 Pauli Principle and Antisymmetrization

The Pauli principle is of fundamental importance to nuclear structure. For example, we will see in later chapters that it is essential in determining which nuclei are stable, that it provides a justification for the idea of independent particle motion in a dense nucleus, that it is the determining factor in the energy shifts that occur with various residual interactions in the shell model and, perhaps most importantly, that it is the principle reason why single nucleon configuration mixing depends on the valence proton–neutron interaction. In fact, these last two points may seem like structural details, but they explain in one stroke why all even–even nuclei have  $0^+$  ground states, why the low-lying states of these nuclei increase in energy with spin, why most low-lying negative parity states have odd spin, and, remarkably, the entire systematics of where collectivity, phase transitions, and deformation occur in nuclei.

The Pauli principle, in its simplest form, embodies the notion that no two identical nucleons can occupy the same place at the same time. More formally, no two nucleons can have identical quantum numbers. In this second form it plays an important role in proton–neutron systems where the two nucleons can be treated as two states of the same nucleon. Many applications of the Pauli principle, however, are best expressed in terms of a generalized mathematical formulation of it that the nuclear wave function must be totally antisymmetric—*totally* meaning antisymmetric in all coordinates, spatial, spin, and isospin (i.e., that the wave function must reverse its sign if all these coordinates are interchanged). To see the relation of this requirement of antisymmetry to the Pauli principle, consider a wave function of two identical particles,  $\psi_{ab}(r_{12})$ , where the orbits occupied by the particles are labeled a and b and where  $r_{12}$  is the distance between the two particles. Clearly, the Pauli principle requires that the wave function must vanish when  $r_{12} = 0$  that is, when the particles are at the same point in space. A wave function such as  $\psi_a(r_1)\psi_b(r_2)$  need not vanish at  $r_{12} = 0$ , and thus is not an acceptable two-particle state. However, consider the wave function

$$\psi_{ab}(r_{12}) = \psi_a(r_1)\psi_b(r_2) - \psi_a(r_2)\psi_b(r_1)$$

Obviously,  $\psi_{ab}(r_{12}) = 0$  for  $r_1 = r_2$  and thus satisfies the Pauli principle. But, for any  $r_{12}$ , it also follows that

$$\begin{aligned} \psi_{ab}(r_{12}) &= [\psi_a(r_1)\psi_b(r_2) - \psi_a(r_2)\psi_b(r_1)] \\ &= -[\psi_a(r_2)\psi_b(r_1) - \psi_a(r_1)\psi_b(r_2)] = -\psi_{ba} \end{aligned} \quad (1.1)$$

So, the Pauli principle can be formulated mathematically by the statement that a two-particle nuclear wave function  $\Psi$  must be antisymmetric with respect to the interchange of the two partners. For multiparticle states, the antisymmetry must extend to interchanges of any pair of particles.

Although the present argument was phrased in terms of spatial coordinates, it can be extended to other spaces leading to the generalized antisymmetrization condition given earlier.

It is impossible to overemphasize the importance of the Pauli principle in nuclear physics. It has obvious and direct consequences as well as subtle, indirect, but no less real, effects. We shall encounter it continually.

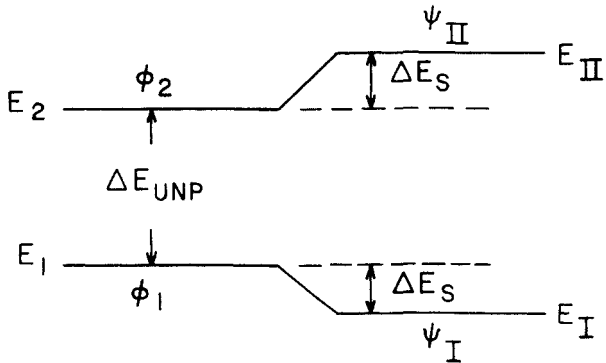
#### 1.4 Two-State Mixing

In realistic calculations of nuclear spectra, pure configurations are seldom encountered. Frequently, the actual nuclear states are complex admixtures of many components; an accurate treatment must involve the diagonalization of a large Hamiltonian matrix. Although this is simple, it is tedious and one often loses sight of the basic physics. In many, if not most cases, however, it is possible to regain a feeling for the underlying physics and at least a semiquantitative calculation by a simple two-state mixing calculation. In many cases, one can simulate the full diagonalization reasonably well using sequences of a few two-state mixing calculations. Two-state mixing is completely trivial. We will present the results in a slightly different form than normally encountered so that we will obtain universal analytic expressions. It is of the utmost importance to understand and to have an intuitive grasp of the relationships between the initial energy spacings and the mixing matrix element, on the one hand, and the final separations and admixed wave functions on the other. These ideas are exploited throughout this book. This section outlines the basic ideas and formulas, presents the universal mixing curve, and discusses some useful limiting cases. In addition, a few sample schematic multistate mixing calculations will be described in the next section.

Consider the situation illustrated in Fig. 1.6, in which two initial levels with energies  $E_1$  and  $E_2$  have wave functions  $\phi_1$  and  $\phi_2$ . For an arbitrary interaction,  $V$ , the mixing matrix element is  $\langle \phi_1 | V | \phi_2 \rangle$ , which we denote simply by  $V$ . The final energies and wave functions are obtained by diagonalizing the  $2 \times 2$  matrix

$$\begin{pmatrix} E_1 & V \\ V & E_2 \end{pmatrix}$$

The final wave functions are denoted by Roman numerals,  $\Psi_I$  and  $\Psi_{II}$ , and have energies  $E_I$  and  $E_{II}$ . In general, the mixing depends both on the initial separation and on the matrix element. A large spacing reduces the effect of a given matrix element. Conversely, even a small matrix element may induce large mixing if the unperturbed states are close in energy. In order to present the results so that this two-parameter aspect is circumvented, yielding a single universal mixing expression valid for *any* interaction and *any* initial spacing, we define the ratio



## INTERACTION: V

**Fig. 1.6.** Two-state mixing: definitions and notation.

$$R = \frac{\Delta E_u}{V} \quad (1.2)$$

of the unperturbed energy spacing to the strength of the matrix element. Then the perturbed energies are

$$\begin{aligned} E_{II} &= \frac{1}{2}(E_1 + E_2) \pm \frac{1}{2}\sqrt{(E_2 - E_1)^2 + 4V^2} \\ &= \frac{1}{2}(E_1 + E_2) \pm \frac{\Delta E_u}{2} \sqrt{1 + \frac{4V^2}{\Delta E_u^2}} \\ &= \frac{1}{2}(E_1 + E_2) \pm \frac{\Delta E_u}{2} \sqrt{1 + \frac{4}{R^2}} \end{aligned} \quad (1.3)$$

where the + sign is for  $E_{II}$  and the - sign for  $E_I$ . It follows that the final energy difference is

$$E_{II} - E_I = \Delta E_u \sqrt{1 + \frac{4}{R^2}} \quad (1.4)$$

or, in units of the unperturbed splitting  $\Delta E_u$ , the final separation is given by the simple result

$$\frac{E_{II} - E_I}{\Delta E_u} = 1 \sqrt{1 + \frac{4}{R^2}} \quad (1.5)$$

A more useful result is the amount,  $|\Delta E_s|$ , by which *each* energy is *shifted* by the interaction.  $|\Delta E_s|$  is given by

$$|\Delta E_s| = |E_{II} - E_2| = |E_I - E_1| = \frac{\Delta E_u}{2} \left[ \sqrt{1 + \frac{4}{R^2}} - 1 \right]$$

or, again, in units of  $\Delta E_u$ , one obtains a result *independent of the initial spacing*:

$$\frac{|\Delta E_s|}{\Delta E_u} = \frac{|E_{II} - E_2|}{\Delta E_u} = \frac{|E_I - E_1|}{\Delta E_u} = \frac{1}{2} \left[ \sqrt{1 + \frac{4}{R^2}} - 1 \right] \quad (1.6)$$

The mixed wave functions are

$$\begin{aligned}\psi_I &= \alpha \phi_1 + \beta \phi_2 \\ \psi_{II} &= -\beta \phi_1 + \alpha \phi_2\end{aligned}\quad (1.7)$$

where the smaller amplitude  $\beta$  is given by

$$\beta = \frac{1}{\sqrt{1 + [R/2 + \sqrt{1 + R^2/4}]^2}} \quad (1.8)$$

The essential point of Eqs. 1.6 and 1.8 is that both the final energy difference (in units of  $\Delta E_u$ ) and  $\beta$  are functions *only* of  $R$ , the ratio of the unperturbed energy splitting to the mixing matrix element. Equations 1.3–1.6 and 1.8 are *universal expressions* completely independent of the nature of the interaction or the initial splitting. The same ratio,  $R = \Delta E_u / V$  always gives the same final wave functions, energies, and energy shifts (in units of  $\Delta E_u$ ).

These results are so important, and will be referred to, either quantitatively or qualitatively, so frequently that it is useful to dwell on them. Equations 1.6 and 1.8 are plotted in Fig. 1.7. To illustrate the results and get a feeling for the

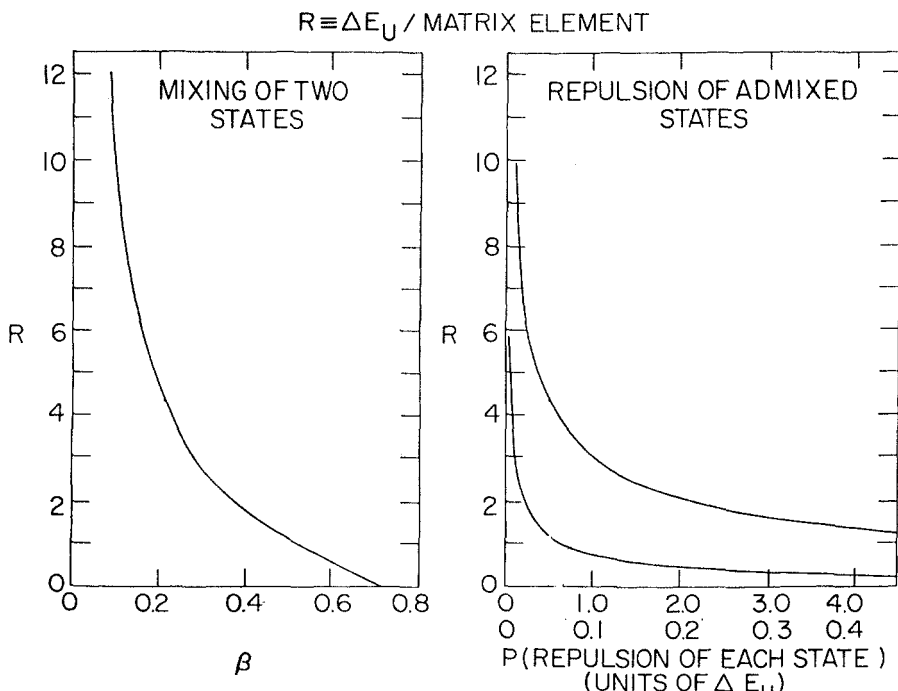


**Fig. 1.7.** Universal two-state mixing curves. The one on the left gives the smaller of the two mixing amplitudes,  $\beta$ , while the curves on the right give the energy shift of each level in units of the unperturbed energy separation. Here the lower curve goes with the upper abscissa scale, while the upper curve goes with the lower scale.

**Table 1.2.** Examples of two-state mixing energy shifts and mixing amplitudes (from Eqs. 1.6 and 1.8).  $R = \Delta E_u / V$

$R$	$\Delta E_s / \Delta E_u$	$\beta$	Specific case: $\Delta E_u = 100 \text{ keV}$	
			$V (\text{keV})$	$\Delta E_s (\text{keV})$
0.2	4.52	0.67	500	452
0.5	1.56	0.61	200	156
1	0.62	0.53	100	62
2	0.207	0.38	50	20.7
3	0.101	0.29	33.3	10.1
5	0.0385	0.19	20	3.85
10	0.0099	0.099	10	0.99
20	0.0025	0.050	5	0.25

\*For  $R = 0$ ,  $\beta = 0.707$ , and  $\Delta E_s = V$ .

numbers involved, let us consider a couple of examples. Suppose two initial states are separated by 100 keV and admixed with a matrix element of 50 keV (a not uncommon situation, for example, in Coriolis mixing). Then  $R = 2$ , and we find that the mixing amplitude  $\beta = 0.38$  and that each state is shifted by an amount 0.207 times the initial separation or, in this case, by 20.7 keV. Clearly, the final separation is 141.4 keV. Another common situation is that of rather weak mixing. Taking two states initially an MeV apart that mix with a 10 keV matrix element ( $R = 100$ ), then Fig. 1.7 or Eqs. 1.6 and 1.8 instantly show that the mixing is negligible and the energy shift is virtually nil. Table 1.2 gives examples of  $\Delta E_s$  and  $\beta$  for a range of  $R$  values.

Of course, in using these expressions in practical situations one normally knows the final perturbed energies not the initial separations. One often wants to extract the amount of mixing ( $\beta$ ) or to deduce the interaction strength from some experimental measure of the mixing (e.g., the ratio of two transition strengths from the mixed state, one of which is allowed, the other forbidden in the unmixed limit: the branching ratio is then directly related to  $\beta^2$ ). In principle it is then necessary to work the equations backward to solve first for  $V$  or for  $\Delta E_u$ , and then for  $\beta$ . In practice, however, the mixing is often small and  $\Delta E_s$  is a small fraction of  $\Delta E_u$  so that an accurate approximation is obtained by taking  $R \approx \Delta E_{\text{final}} / V = (E_{\text{II}} - E_1) / V$ . For example, for  $R \geq 5$ , the initial and final separations differ by less than 10 percent.

Having dealt with some examples and these practical comments, we now consider two extremely important limiting cases where Eqs. 1.6 and 1.8 simplify: the situations of infinitely strong and relatively weak mixing illustrated in Fig. 1.8. The results in both cases have many useful and even profound implications and, for the latter case, the limiting situation has very wide applicability.

1. Consider first, then, the strong mixing limit. Suppose the two initial states are degenerate ( $\Delta E_u = 0$ ), as in Fig. 1.8 (left). Of course, then, Eq. 1.6 cannot be used, but Eq. 1.3 tells us that

$$E_{\text{I},\text{II}} = \frac{1}{2} [(E_1 + E_2) \pm 2V] = E_0 \pm V \quad (1.9)$$

where  $E_0$  is the (common) initial energy. Thus each state is shifted by the

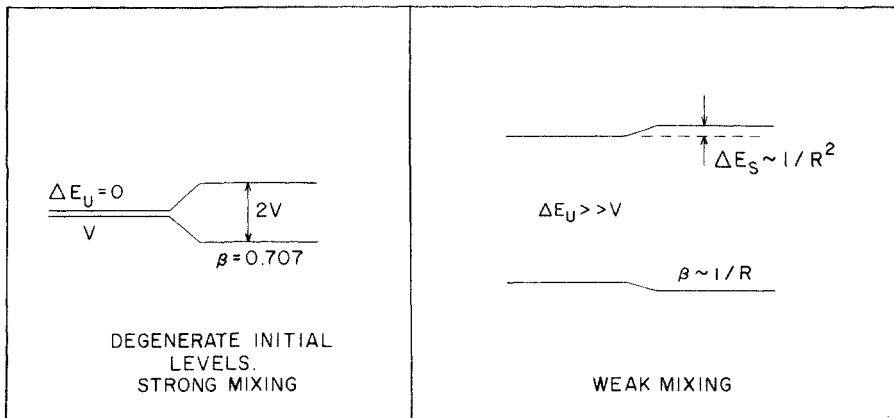


**Fig. 1.8.** The two limiting cases of strong and weak mixing.

*mixing matrix element.* This illustrates the important result that, for any isolated two-state system, the final separation can never be closer than twice the mixing matrix element. As trivial as this sounds, it is often forgotten but is extremely useful. For example, it was one of the early arguments used to demonstrate that Coriolis matrix elements had to be attenuated: examples of isolated pairs of  $13/2^+$  states were found that were closer than twice the calculated Coriolis mixing matrix elements.

In the case of degenerate orbits, it is clear that  $\beta = 1/\sqrt{2} = 0.707$ . Thus  $\alpha$  is also 0.707 and the two states are completely mixed. This is conceptually obvious since the matrix element is “infinitely” stronger than the initial separation (i.e.,  $1/R \rightarrow \infty$ ). This seemingly trivial result also has profound consequences. For example, it means that the mixed wave functions for two initially degenerate states are *independent* of the strength of the interaction between them. (This argument will be used in Chapter 6 to show why the wave functions in the limiting symmetries of the IBA are independent of the coefficients—parameters—of the Hamiltonian as long as the *structure* of that Hamiltonian corresponds to the symmetry involved.)

2. The weak mixing limit corresponds to  $R \gg 1$  (see Fig. 1.8, right). Equation 1.8 becomes

$$\beta \approx \frac{1}{R} \quad (1.10)$$

Hence,

$$V \approx \beta \Delta E_u \approx \beta \Delta E_{\text{final}} \quad (1.11)$$

since  $\Delta E_s$  is small. Frequently (for example, from measured  $\gamma$ -ray branching ratios) one has empirical information on  $\beta$  and therefore Eq. 1.10 (or the exact Eq. 1.8) can be used to deduce  $V$  from the data. Similarly, for  $R \gg 1$ , Eq. 1.6 becomes

$$\frac{|\Delta E_s|}{\Delta E_u} \approx \frac{1}{2} \left[ 1 + \frac{2}{R^2} - 1 \right] = \frac{1}{R^2} \quad (1.12)$$

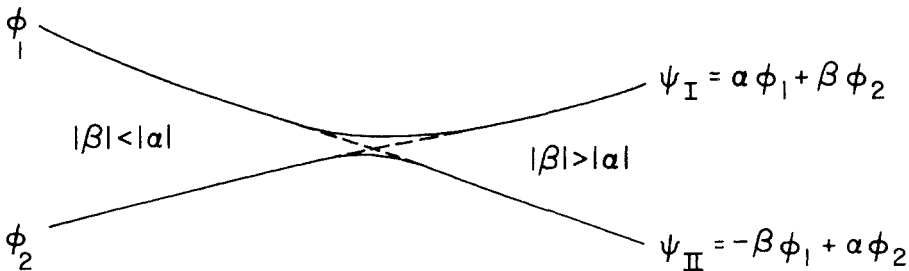


**Fig. 1.9.** Illustration of the noncrossing of two admixed levels.

An example is useful. Suppose  $R = 10$ . Equations 1.10 and 1.12 then give

$$\beta = 0.1 \quad \text{and} \quad \Delta E_s / \Delta E_u = 0.01$$

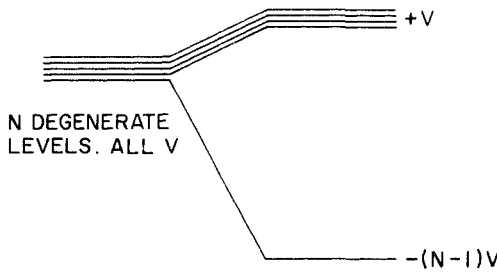
The exact results are  $\beta = 0.0985$  and  $\Delta E_s / \Delta E_u = 0.0099$ . In fact, even for  $R = 4$ , Eqs. 1.10 and 1.12 are already quite satisfactory:  $\beta$  is correct to better than 10 percent and  $\Delta E_s$  to 6 percent. Except in the case of rather strong mixing, Eqs. 1.10 and 1.12 thus provide quite accurate (instantaneous) results for two-state mixing.

There is one other important aspect of two-state mixing. Suppose we consider two states, 1 and 2, whose energies depend on some nuclear structure parameter  $x$  (as illustrated schematically in Fig. 1.9). For example,  $x$  could be the deformation and the states might be two Nilsson orbits. For some  $x$  value,  $x_{\text{crit}}$ , the orbits cross. Now suppose that the two levels mix. They can now never cross since they repel, and can never be closer than twice the mixing matrix element after mixing. Thus the actual behavior of the mixed states, labeled I and II, is as sketched by the solid lines in Figure 1.9. The energies have an *inflection point*. However, for  $x > x_{\text{crit}}$ , the wave function of state I will have a larger amplitude for unperturbed state 2 than for its own “parent” and vice versa. Such behavior is very common in structure calculations and is nearly always an indication of strong mixing. The point of closest approach of the two curves corresponds to the point where the mixed wave functions contain equal admixtures of each of the unperturbed states. In fact, from the separation at this point the mixing matrix element can be derived by inspection, as one-half the separation. This is another illustration of the usefulness of the limiting case of Eq. 1.9.

## 1.5 Multistate Mixing

In general, a multistate mixing situation must be handled by explicit diagonalization. As noted earlier, this can often be simulated by a sequence of two-state mixing calculations. In addition, a couple of idealized situations are particularly simple, often useful, and provide physical insight into the often misunderstood results of complex calculations (e.g., RPA calculations).

First, let us consider the case of  $N$  degenerate initial states and allow each of



$$\psi_{\text{LOWEST}} = \frac{1}{\sqrt{N}} [\phi_1 + \phi_2 + \dots + \phi_N]$$

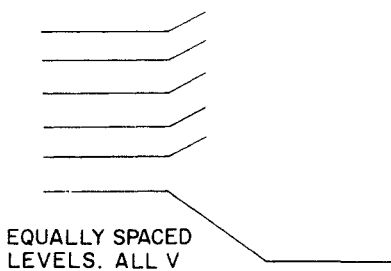


**Fig. 1.10.** Illustration of two multistate mixing situations: (Top)  $N$  degenerate levels, all of which mix by equal matrix elements  $V$ ; (Bottom) The same, except the initial levels are equally spaced.

these levels to mix with each of the others with *equal* matrix elements (i.e., between all pairs). This idea is illustrated in Fig. 1.10. It is then easy to show by explicit diagonalization that one state is lowered by  $(N - 1)V$  and each of the other states is raised by one unit in  $V$ . The wave function for the lowest state is totally mixed:

$$\psi_I = \frac{1}{\sqrt{N}} \phi_1 + \frac{1}{\sqrt{N}} \phi_2 + \frac{1}{\sqrt{N}} \phi_3 + \dots + \frac{1}{\sqrt{N}} \phi_N \quad (1.13)$$

Although this is a clear case of (optimum) multistate mixing, the result for the lowest eigenvalue is exactly what would result from applying a sequence of two-state mixing calculations: mixing with *each* of the other  $N - 1$  degenerate states lowers this state by  $V$ , giving a total lowering of  $(N - 1)V$ .

This feature of one state emerging with special character, low energy, and a highly coherent wave function, is ultimately the microscopic basis for and physical idea behind the development of collectivity. Collective states result from many interactions of simpler (e.g., single particle or two quasi-particle)

entities, and appear at low energies. As we shall see the RPA approach to the microscopic generation of collective vibrations is a prime illustration of this effect. So also is the effect of pairing among  $0^+$  states that leads to the well-known energy gap in even-even nuclei.

A second case is analogous, except that we lift the initial degeneracy and consider a set of  $N$  equally spaced levels. This situation is depicted in Fig. 1.10 for the case of  $N = 6$ . As before, one state is considerably lowered. Of course, the wave functions are now more complex, and are not of particular interest here. What is interesting is that the *ratio* of the lowering of the lowest level in the nondegenerate (ND) case to the lowering in the degenerate (D) case just considered

$$L_N(R) = \frac{\Delta E_{ND}}{\Delta E_D} = \frac{\Delta E_{ND}}{(N-1)V} \quad (1.14)$$

is nearly independent of  $N$ . For  $R = 1$ ,  $L(R)$  for  $N = 2, 4, 8$ , and  $12$ , respectively, is found, by diagonalization, to be  $0.62, 0.60, 0.59, 0.59$ : that is the lowest state is lowered by about 60 percent of what it would be if the initial states had been degenerate. The near-independence of  $N$  means that one can estimate the lowering, without calculation, simply by taking the two-state mixing result for the appropriate  $R$  value. As a test, suppose the (equal) spacings are all twice the matrix element  $V$ . Then, from Table 1.2,  $\Delta E_s$  (two-state) is  $0.414 V$ . For the degenerate case, it is of course  $(2-1)V = V$ . So  $L_2(R=2)$  is  $0.414$ , which should now be approximately applicable to multistate mixing. The value for  $N = 8$ , obtained by diagonalization, is  $L_8(R=2) = 0.35$ .

Finally, a third idealized case again concerns  $N$  degenerate levels, except that each level mixes with only the “adjacent” level (as shown in Fig. 1.11). This statement, however, is meaningless for degenerate levels, but it is clear that we can circumvent it by introducing an infinitesimal spacing, and therefore an “order” to the unperturbed levels,  $1, 2, 3 \dots N$ . This limit, in fact, is not so far from the realistic situation of Coriolis mixing among a series of bands with  $K = K_i, K_i + 1 \dots K_f$ , which frequently occurs in heavy nuclei. Again, one level is lowered, but now the mixed levels are symmetrically distributed with respect to the initial energy and the lowest state is not lowered nearly as much. One can write  $\Delta E_{\text{lowest}} = f(N)V$  where the function  $f(N)$  has the rough dependence sketched in Fig. 1.11.

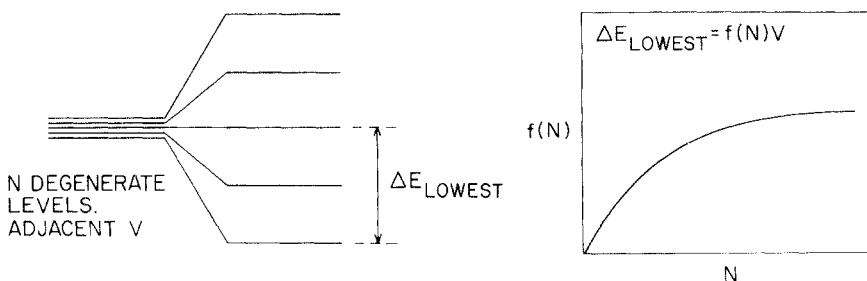


**Fig. 1.11.** Multistate mixing:  $N$  degenerate levels in which only “adjacent” levels are mixed with (equal) matrix elements  $V$ .

Finally, note that in all the multistate mixing cases considered, *all* of the components of the lowest lying wave function have the *same* sign. Though this result depends on the phase conventions chosen, if consistent conventions are used for both wave functions and operators, then matrix elements (observables) will contain coherent, in-phase sums, and can be extremely large. The wave function has *coherence*, and such multistate mixing can lead to *collectivity* as reflected in enhanced transition rates, cross sections, and the like. Also, note that the sum of the initial and final energies is the same, as, of course, it must be. Since these energies appear on the diagonal of the matrix to be diagonalized, this is equivalent to the formal statement that the trace is conserved.

The importance and usefulness of the results in this section cannot be overemphasized. With them, and an understanding of the basically attractive nature of the nuclear force, and of the effects of the Pauli principle and of antisymmetrization, it is possible to understand nearly all of the detailed results of most nuclear model calculations in an extremely simple, intuitive way that illustrates the underlying physics that is often lost in complex formalisms and computations.

## 1.6 Two-State Mixing and Transition Rates

One application of the concept of two-state mixing that is worth discussing, even though it invokes concepts and excitation modes that will be introduced later, is the effect of certain types of mixing on transition rates. Consider the simple level scheme in Fig. 1.12 with  $2_1^+$  levels from different intrinsic excitations (say, belonging to two bands of a deformed nucleus). Suppose that, according to some model, one  $2_1^+$  level has an allowed (A) ground state transition and the other has forbidden (F) transitions to both  $0_1^+$  and  $2_1^+$  states. One occasionally encounters statements of the following kind: "While the  $2_2^+ \rightarrow 0_1^+$

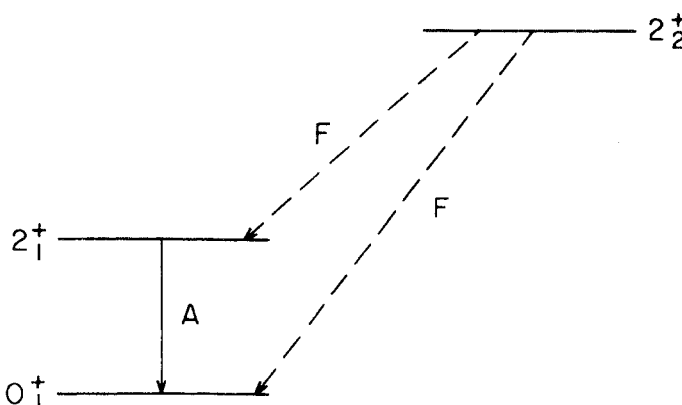


**Fig. 1.12.** Effect of mixing on allowed (A) and forbidden (F)  $\gamma$ -ray transitions.

transition is normally forbidden, its strength results from mixing the two  $2^+$  states: a similar argument accounts for the  $2_2^+ \rightarrow 2_1^+$  transition." At first, this certainly sounds plausible: if the two  $2^+$  states mix, some of the strength of the allowed transition should be "distributed" to the forbidden one. Moreover, the two  $2^+$  states now share some of the same character and should be interconnected. Let us calculate the actual E2 matrix elements for the mixed states to see if the preceding conclusions are warranted. Using the notation of Fig. 1.6 (Roman subscripts for the perturbed wave functions, arabic for the unperturbed), we have

$$\begin{aligned} \langle 2_{II}^+ | \mathbf{E2} | 0_1^+ \rangle &= \langle -\beta 2_1^+ + \alpha 2_2^+ | \mathbf{E2} | 0_1^+ \rangle \\ &= -\beta \langle 2_1^+ | \mathbf{E2} | 0_1^+ \rangle + \alpha \langle 2_2^+ | \mathbf{E2} | 0_1^+ \rangle \\ &= -\beta \langle 2_1^+ | \mathbf{E2} | 0_1^+ \rangle \end{aligned} \quad (1.15)$$

since the unpreturbed  $2_2^+ \rightarrow 2_1^+$  matrix element is forbidden. Thus the  $2_{II}^+ \rightarrow 0_1^+$  transition is now finite and arises solely from the mixing with the  $2_1^+$  level as claimed. For the  $2_{II}^+ \rightarrow 2_1^+$  transition we have

$$\begin{aligned} \langle 2_{II}^+ | \mathbf{E2} | 2_1^+ \rangle &= \langle -\beta 2_1^+ + \alpha 2_2^+ | \mathbf{E2} | \alpha 2_1^+ + \beta 2_2^+ \rangle \\ &= -\alpha \beta \langle 2_1^+ | \mathbf{E2} | 2_1^+ \rangle + \alpha \beta \langle 2_2^+ | \mathbf{E2} | 2_1^+ \rangle \\ &\quad - \beta^2 \langle 2_1^+ | \mathbf{E2} | 2_2^+ \rangle + \alpha^2 \langle 2_2^+ | \mathbf{E2} | 2_1^+ \rangle \end{aligned} \quad (1.16)$$

Since the  $2_2^+ \rightarrow 2_1^+$  transition is assumed forbidden, the last two terms vanish and

$$\langle 2_{II}^+ | \mathbf{E2} | 2_1^+ \rangle = \alpha \beta [\langle \phi_2 | \mathbf{E2} | \phi_2 \rangle - \langle \phi_1 | \mathbf{E2} | \phi_1 \rangle] \quad (1.17)$$

The  $2_{II}^+ \rightarrow 2_1^+$  transition vanishes in the limit of no mixing ( $\beta = 0$ ). However, it is by no means clear that mixing will produce a strong transition. The resulting matrix element is proportional to the *difference* in the quadrupole moments of the two states. If the low-lying levels have nearly the same deformation, as is likely in a well deformed nucleus, this difference will be very small, and thus the second conclusion is at best risky. We have worked out this example explicitly because the error just discussed is widespread and partly because the derivation just given will be useful later in understanding the microscopic structure of the  $\beta$  vibration. The point can be summarized as follows: Consider two states (of the same spin) one of which has an allowed transition to some other level while the decay for the other is forbidden. The forbidden transition becomes finite if the two initial states mix, and its matrix element is proportional to the mixing. However, a forbidden transition *between* the two unper- turbed levels becomes finite only if the states mix and if the intrinsic structure of the two unperturbed states differs in the moment corresponding to the operator for this transition.

With the background provided in this chapter on the properties of the

nuclear force, the comments on the Pauli principle and our discussion of two- and multistate mixing, we can now begin to develop an understanding of the rich diversity and unity of nuclear phenomena. We start with a cursory survey of some empirical features and then develop at some length the foundation models through which we try to understand these data and out of which new models and extensions arise.

# 2

## THE NUCLEAR LANDSCAPE

One of the difficulties often faced by the student trying to understand nuclear models is that he/she cannot fully appreciate many of the truly simple and beautiful results that emerge from these models because there is no reservoir of familiar nuclear data to call upon. Therefore, when one derives the spin sequence for a  $\delta$ -function interaction between two identical nucleons in the same orbit, the results are only of mathematical interest if he or she does not see that this instantly explains the low lying levels of literally dozens of near-closed shell even-even nuclei. The entire seniority scheme seems nothing but a labyrinth of Racah algebra when one does not understand how many well-known facets of nuclear structure are thereby trivially explained. Similarly, the simplicity and intuitiveness of many of the results of the Nilsson model may fall on barren ground unless one realizes the vast number of deformed heavy nuclei that display exactly these properties.

The main purpose of this chapter is to survey the nuclear landscape to display a few (definitely not all) typical patterns of nuclear spectra as well as some of the systematic changes in these patterns over sequences of nuclei, so that the reader will understand the motivation for each model and will benefit from an empirical context for their characteristic predictions. We will refer to the figures in this chapter frequently.

While this approach necessitates some repetition later, it allows us to see exactly *what* we are trying to explain with these models beforehand, and what kinds of data characterize atomic nuclei and are the most useful as tests of various models.

In principle, at this stage the data should be shown “blindly,” without commentary on its meaning or implications. However, the purpose of this book is not to develop nuclear physics ab initio and, indeed, most readers will already be familiar with many of the major concepts and terminology. A “purist” approach here would be needlessly tedious and artificial. In the pages that follow, we will use many words and concepts freely that will be introduced formally later on. Those to whom these concepts are unfamiliar should concentrate simply on absorbing the data with the idea of using this base as a touchstone later.

When we speak of nuclear data, we are referring to a vast, varied, and rich reservoir of information about atomic nuclei—from the deuteron to the actinides—obtained by a most diverse array of techniques. The simplest informa-

tion is the mass of atomic nuclei. A more useful form for these is nuclear binding energies, which focus on the *interactions* between nucleons in the nucleus when the masses of the individual nucleons are subtracted. Still more useful (in many cases) are nucleon separation energies, or the energy required to remove the last, outermost nucleons from the nucleus. (We have discussed these already in Chapter 1.) The nucleon separation energies give important data on the surface regions of nuclei. Later, we will show that the individual nucleons tend to orbit the nuclear center of mass in discrete shells and that, for many applications, it is possible to neglect all the underlying shells that are filled. Therefore, the outermost nucleons are frequently most crucial to understanding the observed properties of nuclear level schemes.

More detailed nuclear data consists of nuclear level schemes: the energies, and angular momenta, and parity values ( $J^\pi$ ), of the ground state and low-lying excited states. The mirror nuclei shown in Fig. 1.5 were our first encounter with such schemes. Careful measurements of the  $\gamma$ -rays emitted when excited levels de-excite to lower lying ones are fundamental to both understanding and constructing nuclear level schemes. The crucial information here is, of course, the  $\gamma$ -ray energies, which help define their placements between nuclear levels and their absolute and relative intensities, which give direct measures of nuclear transition matrix elements.

A large amount of data has resulted from the study of scattering processes of one nucleus on another and direct reaction processes in which two interacting nuclei exchange one or more individual nucleons. Scattering experiments often use low energy projectiles with long wavelengths comparable in size to the nucleus itself. In such cases, they provide information on the overall nuclear shape and on the macroscopic, or collective, excitations of the nucleus as a whole (e.g., rotations and vibrations). Nuclear reactions, examples of which are single nucleon transfer reactions such as (d, p) or two-nucleon transfer reactions such as (p, t), can proceed by a direct process in which individual nucleons are inserted into or removed from specific orbits. These reactions provide detailed and microscopic information on the semi-independent particle motion characterizing atomic nuclei.

Heavy ion fusion reactions, which can bring in enormous amounts of energy and angular momentum and access neutron-deficient nuclei, or  $\beta$  decay experiments on fission product nuclei, which are extremely neutron rich, provide valuable sources of information, especially on unstable nuclei.

Of course, this listing of techniques barely touches the surface and highlights only a few that are most useful for studying low-energy nuclear structure. A few of these will be discussed in some detail in Chapter 10. For now, we turn to the picture of the nuclear landscape they have provided us.

The most basic data for nuclei, of course, is a listing of which nuclei exist. Such a list is usually presented in an  $N$ - $Z$  plot as in Fig. 2.1, where the hatched area approximately outlines the stable nuclei. This is the so-called valley of stability (i.e., the valley of energy *vs.*  $Z$  and  $N$ : because nature prefers to minimize energies, the stable nuclei have the lowest energies). The general features are that  $N \approx Z$  for light nuclei, and a preference for a neutron excess

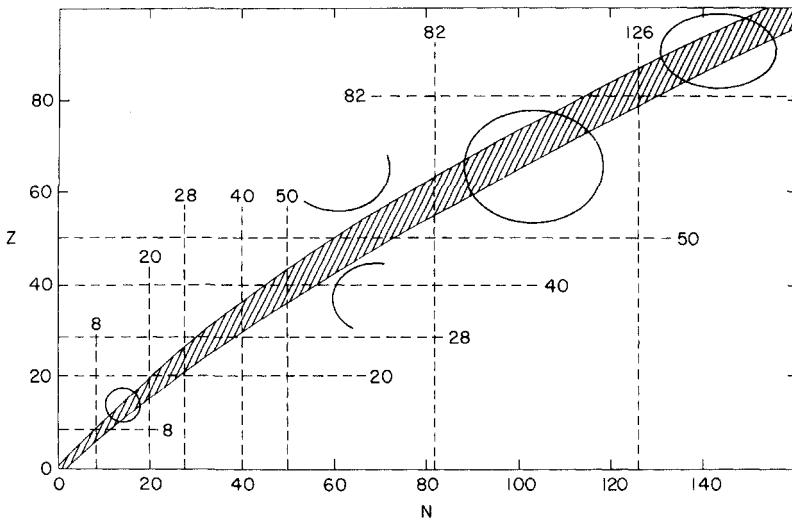


**Fig. 2.1.** The nuclear chart showing the path of stable nuclei (crossed hatched), as well as the magic numbers and midshell deformed regions (circles or circular segments).

in heavier nuclei. We shall see that this pattern is easily explained by combining the concepts of independent particle motion, the Pauli principle, and the Coulomb force.

We have already seen some other examples of significant nuclear data, namely binding energies as a function of  $A$ , separation energies  $S(n)$  and  $S(p)$  and a couple of examples of level schemes for so-called mirror nuclei. These

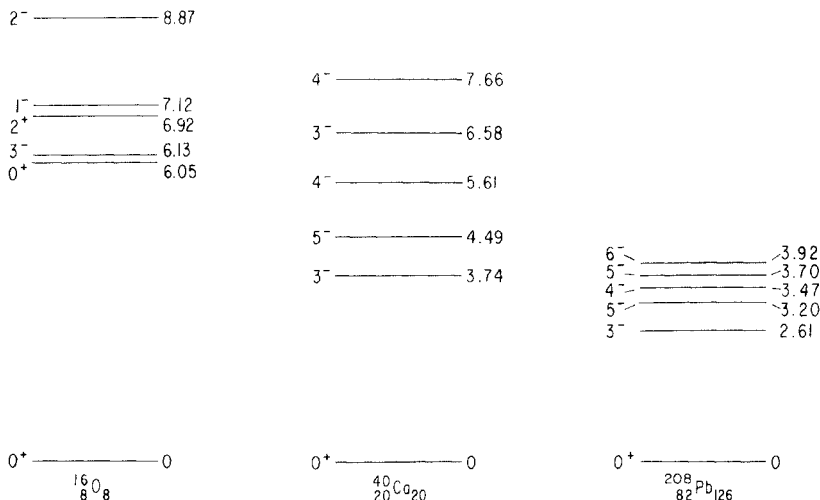


**Fig. 2.2.** Low-lying levels of three doubly magic nuclei. Energies on the right of each line are in MeV.

data were shown early on because they provide basic information on the nuclear force itself, which was already discussed in Chapter 1. Here we are concerned with a somewhat more detailed and much more extensive survey of nuclear excitations.

As noted in Chapter 1, there are large gaps in the nucleon separation energies that define so-called magic numbers, and point to the existence of nuclear shells, analogous to those in atomic physics. That is, certain *magic* numbers of nucleons of a given type correspond to the filling of a set of orbits constituting a "shell." Additional nucleons must then fill the next higher shell and are considerably less bound. In Figs. 1.2 and 1.3 we saw such data for the magic number 82. The complete set of the most important, empirically observed, magic numbers is 2, 8, 20, 28, 50, 82, and 126. There are also gaps or subshell gaps at 40 and 64, especially for protons, which exist for certain neutron numbers only (see further discussions in Chapters 3 and 6). Figure 2.2 shows examples of nuclei where *both* the proton and neutron numbers are magic. Note the extremely high energy of the first excited state, and the predominance of negative parity states. Figure 2.3 shows the Ca isotopes, two of which,  $^{40,48}\text{Ca}$ , are "doubly" magic, while the others are singly magic. The abrupt change of  $2^+$  energies in  $^{42-46}\text{Ca}$  compared to  $^{40,48}\text{Ca}$  is dramatic evidence of the difference in their *magic* structure.

One of the great successes of the independent particle model (Chapter 3) is the prediction of level sequences for nuclei near closed shells, in particular odd

$$B(E2: 0_1^+ \rightarrow 2_1^+) e^2 b^2$$

0.010      0.042      0.047      0.018      0.008

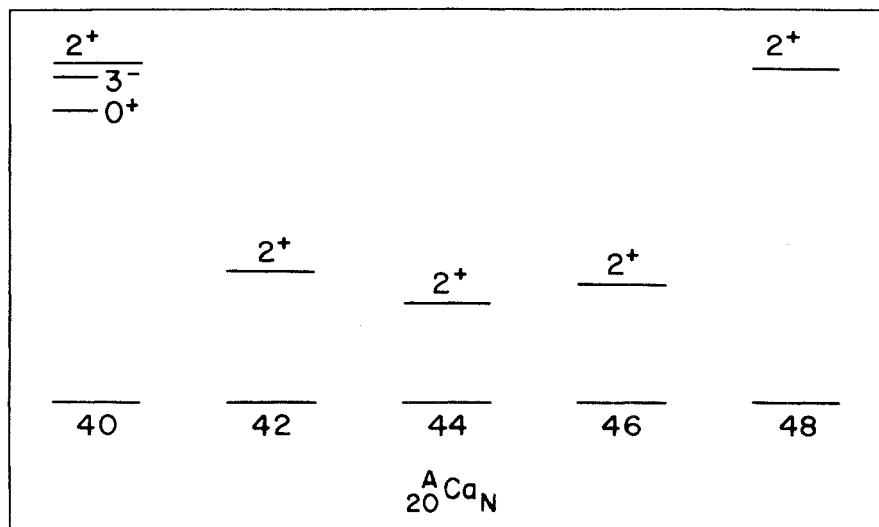


**Fig. 2.3.** Low-lying levels and  $B(E2)$  values for the even-even Ca nuclei.  $^{40}\text{Ca}$  and  $^{48}\text{Ca}$  are doubly magic.

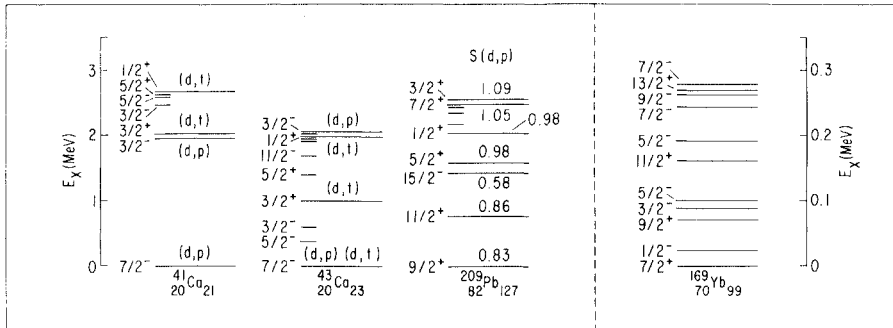


**Fig. 2.4.** Low-lying levels of two nuclei,  $^{41}\text{Ca}$  and  $^{209}\text{Pb}$ , with one nucleon beyond a doubly magic core, and two other nuclei,  $^{43}\text{Ca}$  and  $^{169}\text{Yb}$ , for comparison. Note that the energy scale for Yb is expanded by a factor of 10. The notations (d, t) and (d, p) indicate which levels are primarily populated in these single nucleon transfer reactions. The S(d, p) values given for  $^{209}\text{Pb}$  are the single neutron transfer spectroscopic factors; values near unity indicate nearly pure single-particle structure.

mass nuclei where, as we shall see, the total angular momenta  $J$  (this will often be colloquially referred to later as the “spin” of the level, although this nomenclature is clearly inaccurate) of the ground and low-lying excited states are given by the  $j$  values of the orbits into which the last odd nucleon can be placed. To illustrate this, we show the level schemes of two nuclei ( $^{41}\text{Ca}$ ,  $^{209}\text{Pb}$ ) with one particle beyond a doubly magic nucleus in Fig. 2.4. The specific order and energies of these levels will be easy to understand and predict after we

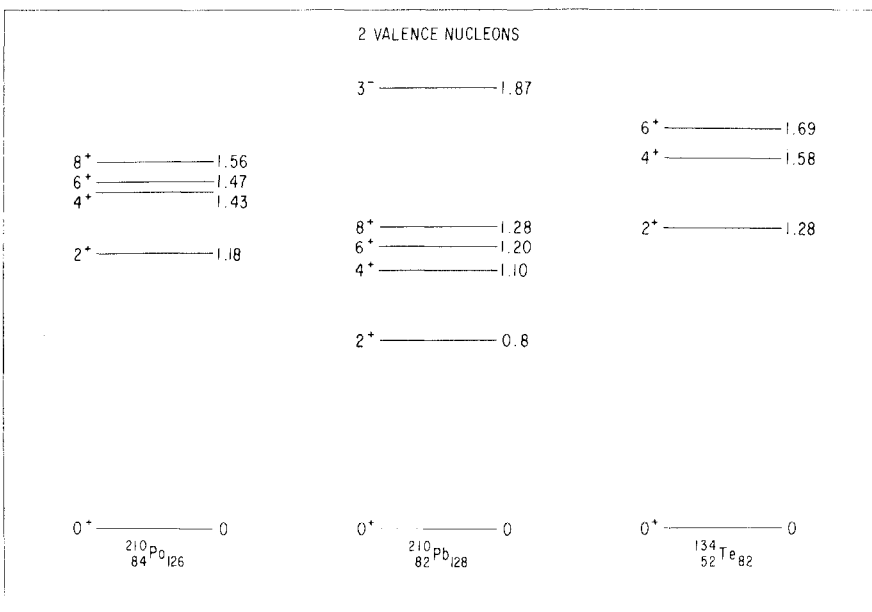


**Fig. 2.5.** Low-lying levels of three nuclei with two valence nucleons.

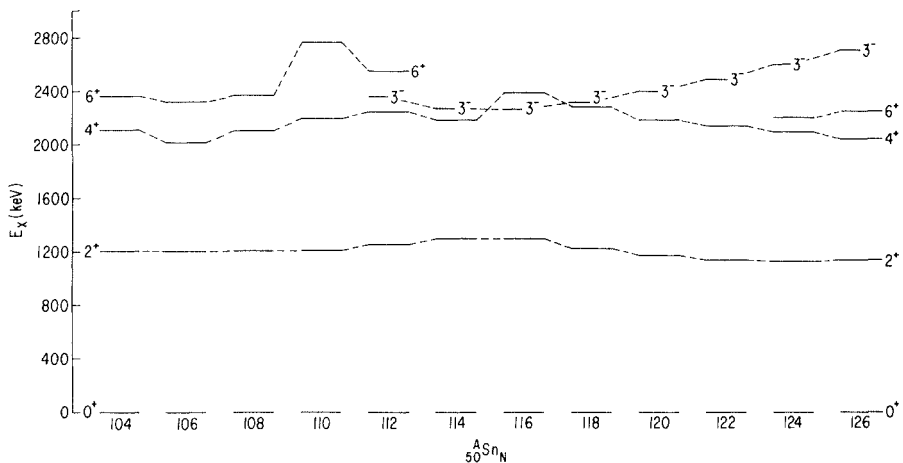


**Fig. 2.6.** Systematics of the lowest levels of the Sn nuclei.

discuss the independent particle model in the next chapter. At this point, these sequences appear as unintelligible jumbles.

Of course, most nuclei have more than one valence nucleon. Two examples are included in the figure. One is  $^{43}\text{Ca}_{23}$  with three valence neutrons. It is similar in many ways to  $^{41}\text{Ca}$  but, with three valence nucleons, a proper treatment requires the study of multinucleon configurations and of the “residual interactions” occurring among nucleons in the *valence* shell.

The other is  $^{169}\text{Yb}$ , which is far from magic in either protons or neutrons. This scheme, both in terms of its complexity (only hinted at in the figure) and its compressed energy scale, sets it completely apart from the other nuclei in the figure. We will see another example of this type of nucleus in a moment.

In treating multivalence particle nuclei such as these, a number of different approaches are used. Close to closed shells (e.g.,  $^{43}\text{Ca}$ ), an extension of the independent particle model that includes residual interactions among the valence nucleons, has been enormously successful. Further from closed shells (e.g.,  $^{169}\text{Yb}$ ), nonspherical shapes appear, and a deformed shell model (the Nilsson model) becomes appropriate. In the case of the shell model, it is often appropriate to consider a coupling scheme in which each nucleon has a given total angular momentum  $j$ . The coupling of these individuals  $j$  values leads to the final  $J$  for the state in question. The energy of such a state clearly depends on the residual interactions among the nucleons in these orbits. It is certainly one of the triumphs of the shell model that one can easily derive expressions for these energies, often without a detailed knowledge of the residual interaction itself, that account reasonably well for a large body of data in both odd and even nuclei.

Figures 2.5–2.7 show the level spectra of some even mass nuclei in the general vicinity of closed shells. Typical of such nuclei, all have  $0^+$  ground states, first excited levels with  $J^\pi = 2^+$ , and mostly even-parity, low-lying excitations.

All of these features will emerge later from very general considerations of

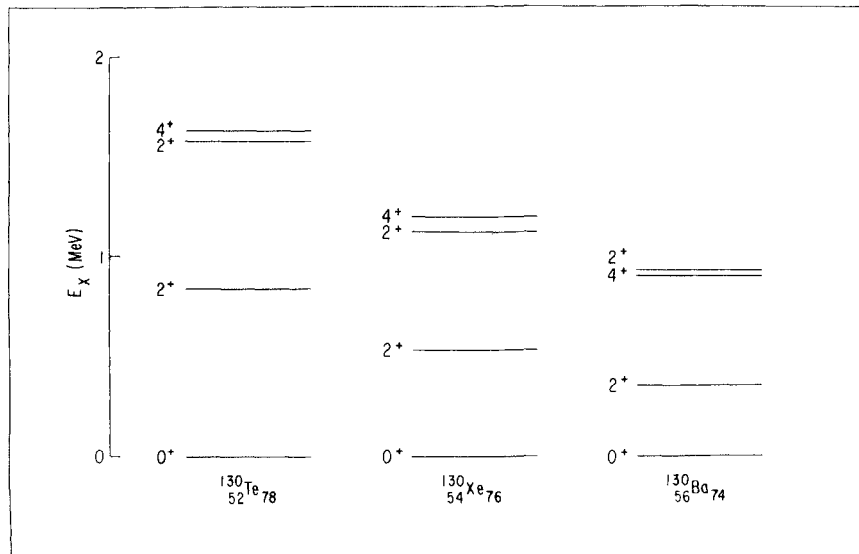


Fig. 2.7. Low-lying levels of the  $A = 130$  isobars that show the effect of adding valence nucleons (in this case neutron holes relative to  $N = 82$ ).

the dependence of the like-nucleon interaction on total angular momentum and of the effects of the Pauli principle. Figures 2.5 and 2.6 deal with singly magic nuclei. They show two interesting features: relatively high-lying, first excited states and a compression of positive-parity energy levels as  $J$  increases. Both features contrast sharply with “collective nuclei.” Note that these features persist in the Sn isotopes even when there are many valence neutrons. It is only when there are both valence protons and neutrons that the excitation patterns change rapidly. Figure 2.7 shows this for three  $A = 130$  nuclei. Note the systematic change as the total number of valence nucleons increases (here we count proton particles plus neutron *holes* relative to the nearest closed shells). Figure 2.8 illustrates this even more systematically and dramatically. Here, there is a sharp drop in  $E_{2_1^+}$  from magic Sn to nonmagic nuclei and the lowering is greater for more and more valence neutrons. There is an additional drop when going from two valence protons (Te, Cd) to four (Xe).

In nuclei far from closed shells where the shell model is either intractable or unreliable, one normally takes recourse in other theoretical frameworks. One of the significant and most fruitful of these approaches can be called *geometrical* or *collective models*, which bypass the shell model by taking a more macroscopic approach of assigning a specific *shape* to the nucleus and examining the rotations and vibrations of such a (generally nonspherical) shape. Of course, a critical issue is whether or not such structures can in fact be derived microscopically from the shell model, and this will be a topic of some importance in a later chapter. Be that as it may, it is an undeniable *empirical* feature of many heavy nuclei that they exhibit properties that *seem* at variance with the concept of a shell model, and show evidence of “collective” behavior.

Individual nuclei exhibit several easily discernible types of collective behav-

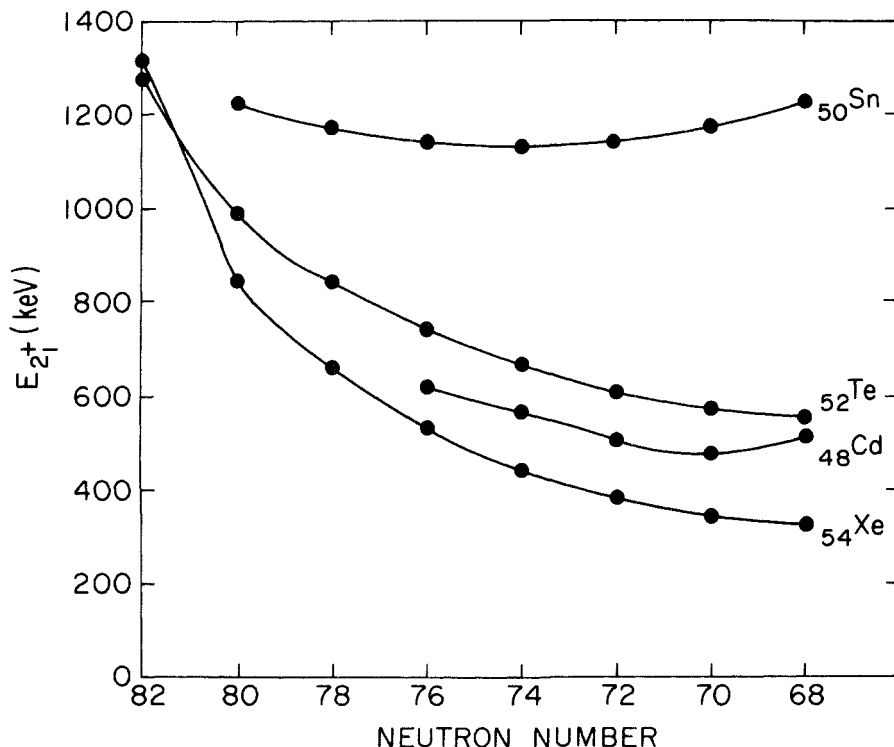


Fig. 2.8.  $E_{2^+}$  values for nuclei in the Sn region.

ior. Figure 2.9 shows typical *vibrational* nuclei, especially  $^{118}\text{Cd}$ , where the first excited state is a quadrupole phonon excitation of a basically spherical shape. At about twice and three times this energy there are groups of states that can

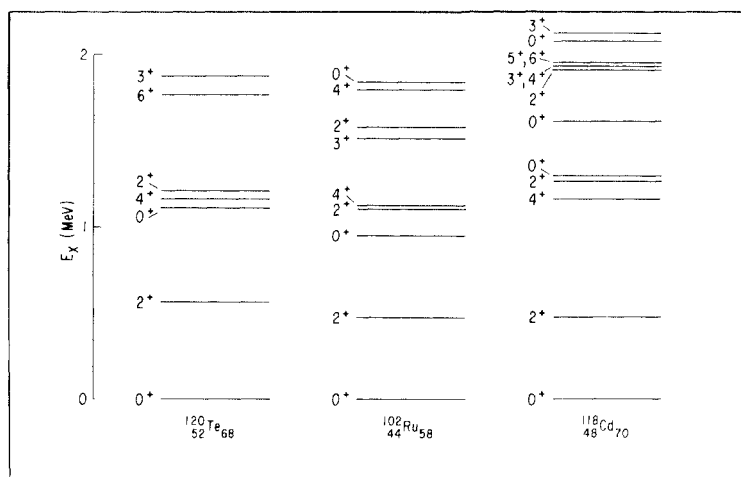
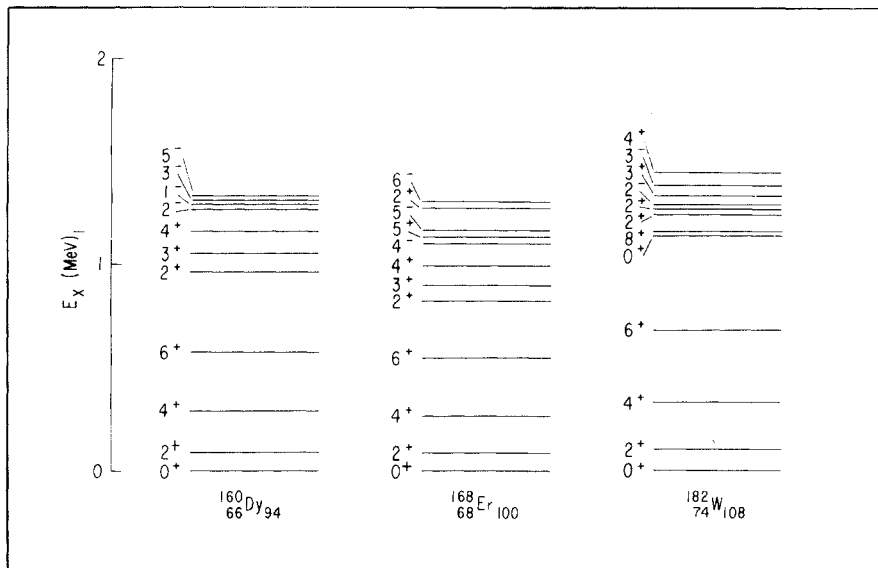


Fig. 2.9. Low-lying levels of some typical, near harmonic vibrational nuclei.



**Fig. 2.10.** Low-lying rotational and vibrational levels of some typical deformed rare earth nuclei.

be described as two- and three-phonon excitations of the basic spherical structure.

Figure 2.10 shows three even-even deformed nuclei in the rare earth region. The lowest levels of spin  $J = 0, 2, 4, 6, \dots$  form a rotational structure whose energies closely follow the  $J(J + 1)$  law for a rotating symmetric top. Above these are groups of levels, some of which we will interpret in Chapter 6 in terms of intrinsic excitations called  $\beta$ ,  $\gamma$ , and octupole vibrations, each with rotational bands superimposed. Finally, Fig. 2.11 shows a typical odd mass deformed nucleus. Here, the levels, which look hopelessly complicated on the

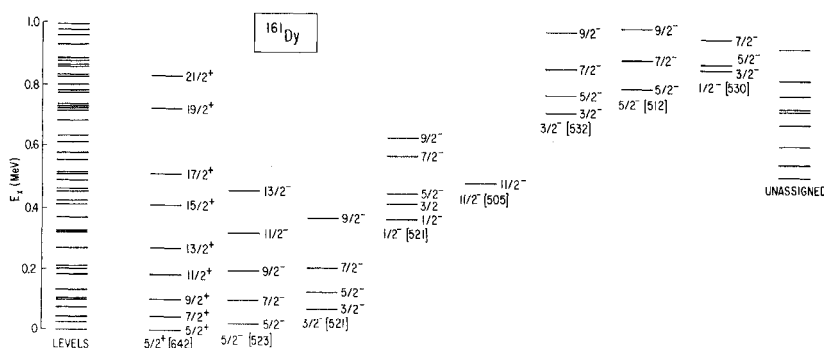


**Fig. 2.11.** Level scheme of  $^{161}\text{Dy}$ . (Left) All levels. (Right) Levels arranged into rotational bands with Nilsson assignments.

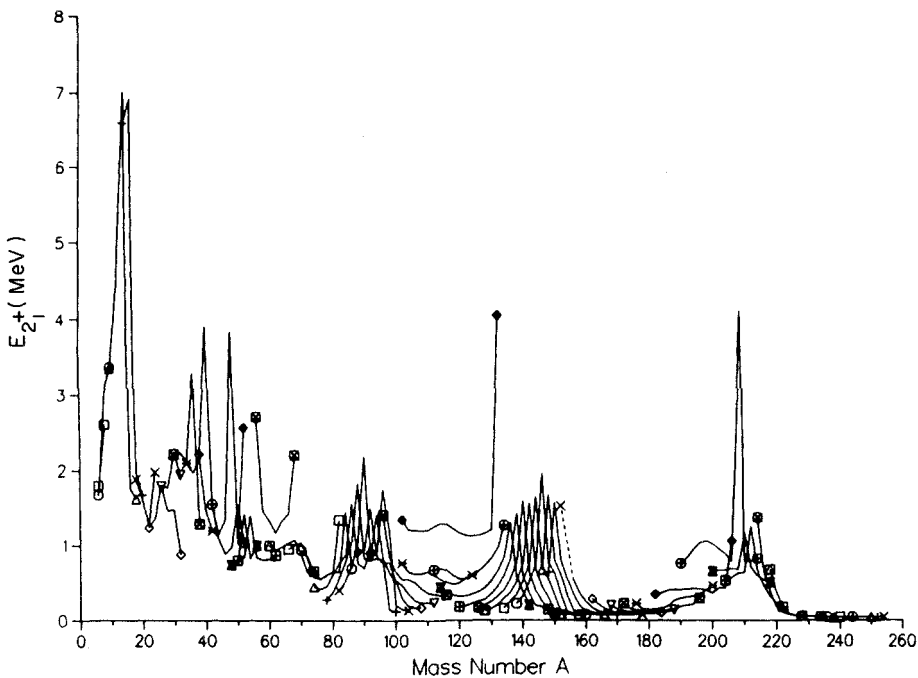


**Fig. 2.12.**  $E_{2_1^+}$  values for all even–even nuclei (Raman, 1987).

left, are arranged in sequences of *single particle* intrinsic (Nilsson) states, each with a rotational band built on top of it on the right. Another example of a nucleus that can be classified in similar manner is  $^{169}\text{Yb}$ , which we looked at in Fig. 2.4.

We note that the rotational bands in  $^{161}\text{Dy}$  range in character from several examples (labeled 5/2-[523], 3/2-[532], 5/2-[512]) with regular spacings that in-

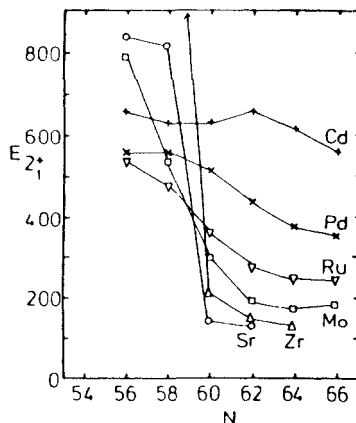


**Fig. 2.13.**  $E_{2_1^+}$  values (in keV) plotted against  $N$  for the  $A = 100$  region.

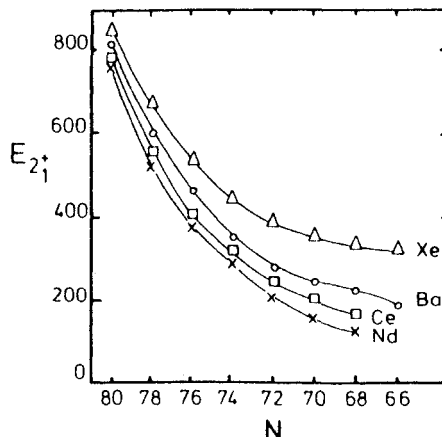


**Fig. 2.14.**  $E_{2_1^+}$  values (in keV) against  $N$  for the  $A = 130$  region.

crease smoothly with  $J$ , to some with highly irregular sequences [e.g.,  $5/2^+[642]$ ,  $1/2^-[521]$  and  $1/2^-[530]$  (with missing  $1/2^-$  level)]. An acceptable model for odd mass deformed nuclei must be able to account for both types of behavior. We will discuss these intrinsic excitations and their connection to rotational motion in detail in Chapters 7 and 8.

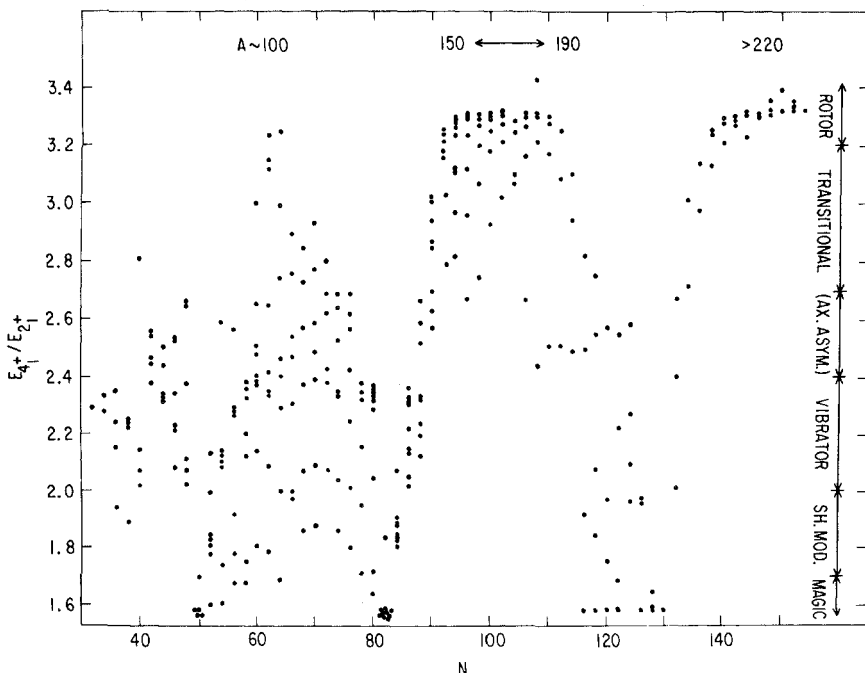


**Fig. 2.15.**  $E_{4_1^+}/E_{2_1^+}$  values plotted against  $N$  for the nuclei with  $N \geq 30$ .

A dramatic way to illustrate both the collective behavior of nuclei far from closed shells and the evolution of structure is to examine a particular property over extended sequences of nuclei—that is, to examine nuclear *systematics*. Three of the most telling data are collected in Figs. 2.12–2.16. Figure 2.12 shows the energies of the first excited  $2_1^+$  states ( $2_1^+$  levels) in even–even nuclei throughout the periodic table. Figures 2.13 and 2.14 show a more detailed view of the same data in two particular regions: nuclei around mass  $A = 100$ , and those near  $A = 130$ . As we have seen near closed shells,  $E_{2_1^+}$  is rather high lying, typically 1 to 2 MeV. In contrast, in collective nuclei, the  $2_1^+$  state can be described as either a vibrational or rotational excitation and occurs at much

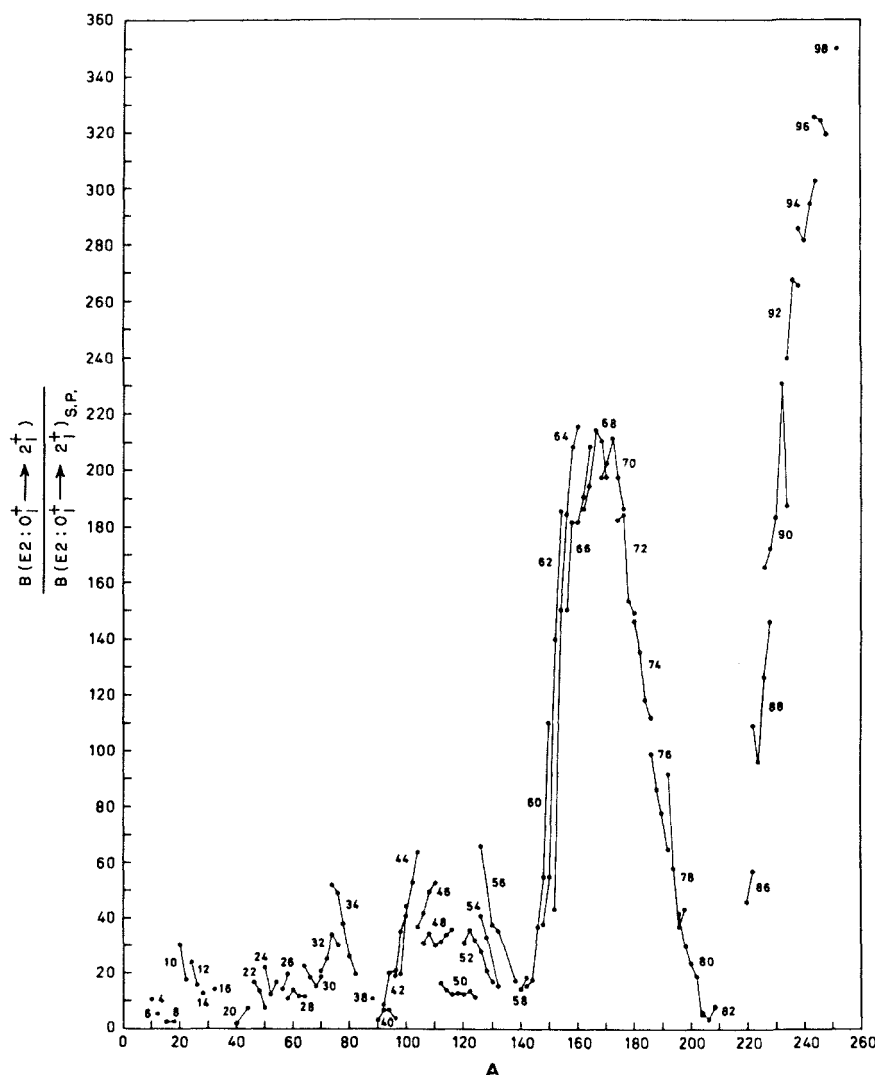


**Fig. 2.16.**  $B(E2:0_1^+ \rightarrow 2_1^+)$  values for all even–even nuclei. (Bohr, 1975.)

lower energy. These figures highlight the enormous differences in  $E_{2_1^+}$  characteristic of these different structures and the transition regions between them as well as the complexity of some individual regions. Figure 2.15 shows a plot of the energy *ratio* of the energy of the  $4_1^+$  state (first  $4^+$  state) to the  $2_1^+$  state in even–even nuclei. As will become evident throughout the subsequent chapters, this ratio is one of the most important structural signatures and, moreover, is one of the few whose *absolute* value is directly meaningful. At first glance, Fig. 2.15 appears to be a semirandom scattering of points. More careful inspection, and some hindsight from subsequent chapters, shows that  $E_{4_1^+}/E_{2_1^+}$  tends to fall into three ranges, values below 2.0 near magic nuclei (see Fig. 2.5), between 2.0 and 2.4 slightly further away from magic numbers (see Fig. 2.9), and values very close to 3.33 in midshell regions corresponding to rotational motion (see Fig. 2.10). The transitions between the latter two clusters are abrupt indeed.

Most low-lying nuclear states, including essentially all that we will consider, are below the energy threshold for particle emission and hence de-excite primarily by electromagnetic processes. These are usually  $\gamma$ -ray transitions, although electron conversion is an important process. The matrix elements for  $\gamma$ -ray transitions often directly give critical nuclear structure information.

We will have many occasions later on to discuss such radiation from excited nuclear states. This is therefore an appropriate place to deal with the crucial issue of the angular momenta,  $\lambda$ , carried by such radiation and the characteristic probability of each. As is well known, the electromagnetic field can be expanded in multipoles of either electric,  $E\lambda$ , or magnetic,  $M\lambda$ , type. We note that the parity carried by such photons is  $(-1)^\lambda$  for electric and  $(-1)^{\lambda+1}$  for magnetic multipoles. Thus, for example, E2 and M1 transitions conserve parity while E1 transitions change it. The probability of emission of radiation of a given multipole is governed by the intrinsic probability of that multipole times a nuclear matrix element. The latter depends on the detailed structure of the initial and final states involved, while the former is a general characteristic of the electromagnetic field and of the “source” of the radiation (the nucleus). We will discuss the properties of the transition matrix elements in a number of different models. Here, we wish to demonstrate in a simple way (ignoring the intrinsic spin of the photon) that such radiation is nearly always characterized by low multipoles, or at least by the lowest multipoles allowed by angular momentum conservation. The argument is very simple. We start by recalling that the orbital angular momentum  $\mathbf{l} = \mathbf{r} \times \mathbf{p}$ . The linear momentum carried by a photon is  $\mathbf{p} = E_\gamma \mathbf{v}/c$ . Therefore the maximum angular momentum (in units of  $\hbar$ ) is given by  $\mathbf{l} = E_\gamma R/\hbar c$  where  $R$  is the nuclear radius. Since  $\hbar c \approx 200$  MeV fm, dipole ( $\lambda = 1$ )  $\gamma$ -rays emitted at typical distances of 10 fm from the nuclear center must have  $E_\gamma \approx 20$  MeV. Since most transitions involved in low-energy nuclear structure are less than 2 MeV, it is obvious, first, that the electromagnetic de-excitation process is relatively slow on a nuclear scale (it must proceed by virtue of the tails of nuclear wave functions extending out to large distances) and, secondly, that high multipoles ( $\lambda > 2$ ) are extremely unlikely. Both these features are very important and are empirically well known. Indeed, it is

often assumed that all transitions are E1, M1, or E2, when assigning  $J^\pi$  values, if the multipolarities have not been measured.

Since the ground state of even-even nuclei is  $0^+$ , the first excited state (normally  $J^\pi = 2^+$ ) can only decay by electric quadrupole or *E2 radiation*. Since we shall see that “collective” effects in low-lying states are quadrupole in geometric character (most deformed nuclei are prolate shaped), it should not be surprising that E2 or *electric quadrupole radiation* is of paramount interest. The usual quantitative measure of E2 transition strengths is called a  $B(E2)$  value, defined as

$$B(E2: J_i \rightarrow J_f) = \frac{1}{2J_i + 1} \langle \psi_f | E2 | \psi_i \rangle^2 \quad (2.1)$$

in terms of the reduced E2 matrix element between initial and final states.

Figure 2.16 shows the systematics of  $B(E2: 2_1^+ \rightarrow 0_1^+)$  values across the nuclear chart in units of so-called single particle values that roughly correspond to the strength expected if a single nucleon changes orbit. The most obvious feature of the data is the relatively small values near closed shells and the enormous ones that occur in midshell regions, such as those near mass 160 and 240. These peaks offer the most dramatic evidence known for nuclear

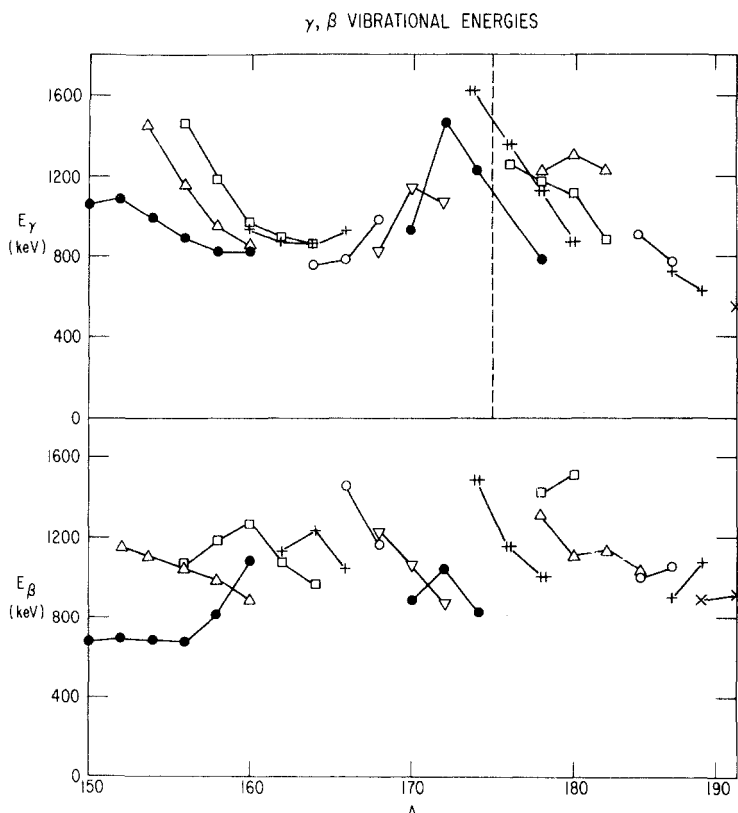
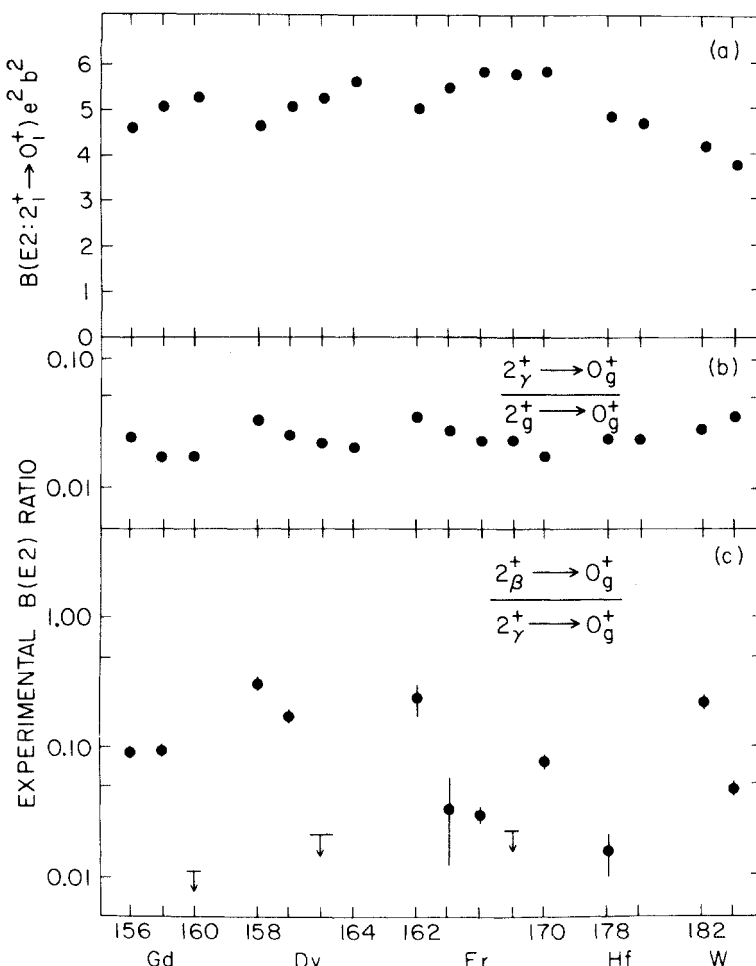


Fig. 2.17. Systematics of  $\beta$  and  $\gamma$  vibrational energies in the rare earth region.

collectivity. Within such peaks, there is a characteristic structure: at first, a rapid increase with increasing valence nucleon number and then a saturation near midshell. We shall discuss these points, and their implications, in Chapter 6.

It is interesting to make a correlation between  $E_{2_1^+}$ ,  $E_{4_1^+}/E_{2_1^+}$ , and  $B(E2: 2_1^+ \rightarrow 0_1^+)$  values. Using our classification of the  $E_{4_1^+}/E_{2_1^+}$  ratios, we see that low values of  $E_{4_1^+}/E_{2_1^+}$  near closed shell correlate with low values of  $B(E2: 2_1^+ \rightarrow 0_1^+)$  and high values of  $E_{2_1^+}$ . As  $E_{2_1^+}$  begins to drop as one proceeds through a major shell,  $E_{4_1^+}/E_{2_1^+}$  rises slightly to just above 2 and the  $B(E2)$  values also begin to increase. Finally, far from magic numbers where  $E_{2_1^+}$  drops dramatically and becomes asymptotically constant,  $E_{4_1^+}/E_{2_1^+}$  approaches 3.33 and the  $B(E2)$  values increase rapidly toward their peak values.



**Fig. 2.18.** Systematics of some typical  $B(E2)$  values and branching ratios relating to rotational and vibrational excitations in the rare earth nuclei (Casten, 1988a).

As we will study in detail later, the structural transition involved here is one from spherical nuclei near closed shells ( $E_{4_1^+} / E_{2_1^+} < 2$ ) toward spherical, but vibrational, nuclei and culminates in a phase transition to strongly deformed (nonspherical axially symmetric) nuclei whose low-lying states reflect rotational behavior. If we recall the discussion of multistate mixing in Chapter 1 (for example, see Eq. 1.13) we see that both the drop in  $E_{2_1^+}$  and the rise in  $B(E2)$  values can be understood in terms of the correlations or collectivity that develop from multistate configuration mixing as one goes from closed shell regions toward midshell. Many of these ideas will be quantified and specific later.

Finally, a crucial test of our detailed microscopic understanding of the macroscopic collective shape vibrations is whether we can understand their systematics. Figure 2.17 shows the energies of  $\beta$  and  $\gamma$ vibrations in the rare earth region of deformed nuclei. Figure 2.18 gives some crucial  $B(E2)$  values relating to the lowest states in even–even nuclei and to their low-lying  $\beta$  and  $\gamma$  vibrations. The top panel shows  $B(E2: 2_1^+ \rightarrow 0_1^+)$  values that describe the matrix elements connecting rotational states. (This is a small subset of those in Fig. 2.16.) The middle and lower panels give the ratios of  $\gamma$ -vibrational to ground state  $B(E2)$  values to  $B(E2: 2_1^+ \rightarrow 0_1^+)$ , and the ratio of “ $\beta \rightarrow g$ ” over “ $\gamma \rightarrow g$ ” transition strengths. The *intraband* values are a couple of orders of magnitude larger than *interband*  $B(E2)$  values and “ $\gamma \rightarrow g$ ” matrix elements dominate “ $\beta \rightarrow g$ ” values. A successful collective model must account for all these results.

In closing this chapter it is appropriate to summarize the nuclear landscape in a compact form that will later allow us to make instant, *a priori*, estimates of the likely structure of any given nucleus. We do this by recalling Fig. 2.1, which shows the nuclear chart in an  $N$ – $Z$  plane. The magic numbers are indicated by vertical and horizontal lines and the known and expected midshell regions of deformed nuclei are encircled. Much of the rest of this book is devoted to understanding nuclei of each specific type occurring in the chart as well as the evolution of structure from one type to another.

*This page intentionally left blank*

## PART II

### SHELL MODEL AND RESIDUAL INTERACTIONS

*This page intentionally left blank*

# 3

## THE INDEPENDENT PARTICLE MODEL

In Chapter I we discussed some of the basic characteristics of the nuclear force, establishing that, aside from a very short-range repulsive core, it is principally attractive in nature, rather short range, saturates, and is charge-independent (excluding, of course, the Coulomb interaction). We also noted that, while the nuclear force is much stronger than the electromagnetic interaction (indeed, if this were not the case, nuclei would not be bound), it is nevertheless a rather weak interaction when compared to the typical kinetic energies of nucleons inside the nucleus.

In this chapter we discuss the independent particle model, which provides an indispensable theoretical framework for all that follows. It is the basis for the multiparticle shell model, which in turn remains the standard of comparison for other models and provides the justification, rationale, and microscopic basis for macroscopic, collective models.

To be clear from the outset, we define some terminology. By independent particle model we refer to the description of a nucleus in terms of noninteracting particles in the orbits of a spherically symmetric potential  $U(r)$ , which is itself produced by all the nucleons. Because of this, we immediately anticipate that the resulting orbit energies are mass dependent. The independent particle model is applicable in principle only to nuclei with a single nucleon outside a closed shell and, even then, incorporates certain results from the shell model. By the latter we refer to a model applicable to nuclei with more than one *valence nucleon* that includes residual interactions between these nucleons and allows for the breaking of closed shells.

Anyone who has studied nuclear physics at all is aware that the basic tenet of the independent particle model is that the nucleons move essentially freely in a central potential that is usually taken as a modified harmonic oscillator or modified square well potential. A little thought, however, raises two apparently serious difficulties before one even attempts this type of approach to the nuclear problem. The first centers on the question of how one can validly speak of independent particle motion in the presence of the strong nuclear interaction and a densely packed nucleus. The answer involves the Pauli principle and the essential weakness rather than strength of the nuclear force referred to earlier. The second question relates to the apparent conflict between a short-range nuclear force and the nature of a harmonic oscillator potential that actually becomes stronger as the distance from the origin (the center of mass) increases. We will return to both issues later.

We saw in Chapters 1 and 2 that the nuclear force is attractive and short range, and that the systematics of certain gross nuclear properties, such as nucleon separation energies, are generally smooth, except at certain specific nucleon numbers, called **magic numbers**, where they exhibit discreet jumps. The concept of magic numbers and the *shell structure* that they imply is of paramount importance in nuclear physics. Thus we summarize a bit of the voluminous evidence of their existence. Beside the sharp drop in  $S(n)$  and  $S(p)$  just after magic numbers (see Figs. 1.2 and 1.3), the lowest excited states in nuclei with magic numbers of either protons or neutrons are, on average, extremely high lying. In particular, in nuclei with even numbers of protons and neutrons the energy of the first excited state is nearly always a  $2^+$  state, and is much higher in magic nuclei. This was illustrated by the Ca isotopes in Fig. 2.3:  $^{40}\text{Ca}$  and  $^{48}\text{Ca}$  correspond to the magic numbers at 20 and 28. Across the even  $^{50}\text{Sn}$  nuclei that have a magic number of protons, the first excited state ( $2^+$ ) has an energy  $E_{2+} \approx 1200$  keV (see Fig. 2.6) as opposed to  $E_{2+} \approx 500$  keV for the isotones of Cd or Te (see Fig. 2.8). Even more striking, when Sn becomes doubly magic at  $^{132}\text{Sn}$ ,  $E_{2+}$  suddenly jumps to several MeV. Further support for the idea of magicity stems from the fact that elements with magic proton numbers have higher relative abundance, a larger number of stable isotopes, and relatively low neutron absorption cross sections. The nucleosynthesis of such elements predominantly occurs in stellar supernova explosions where an intense neutron flux leads to rapid, successive neutron capture reactions. This is the so-called  $r$ -process (“ $r$ ” for rapid). As we shall see in Chapter 10, the cross sections for such reactions depend mostly on the level density at excitation energies near the neutron separation energy. Such level densities are particularly low in magic nuclei. Therefore, for magic nuclei, the low neutron cross sections imply that, once formed, it is unlikely that a sufficient number of neutron captures take place in the short-lived astrophysical environment to deplete their numbers. In essence, they tend to block the  $r$ -process path.

Thus, we see several lines of evidence pointing to the importance of magic numbers. Moreover, we notice a relationship in these lines of evidence; many stem ultimately from the difficulty of exciting a magic or closed shell structure, and the consequent low-level density at low excitation energies.

Combining all the evidence, we can summarize the relevant magic numbers for nuclei as

$$2, 8, 20, 28, 50, 82, 126 \quad (3.1)$$

As we shall see in the discussion of nuclear phase transitions, 40 and 64 are in some cases weakly magic over limited ranges of  $N$  and  $Z$ .

It is well known in atomic physics that electron binding energies undergo sharp changes just after a closed electron shell. Analogously, it is reasonable to suppose that in the nuclear case, these magic numbers correspond to closed shells of nucleons. Of course, this viewpoint already presupposes a shell model and we will have to see later whether this provides an apt description of nuclear properties for nonclosed shell nuclei. Nevertheless, if one wants to pursue a shell model approach, it is clear that one of the basic features it must

reproduce is the particular stability of nuclei with these magic numbers. One would therefore like to construct a nuclear potential that automatically and naturally produces gaps in single particle level energies at the magic numbers.

It is worth noting an often misunderstood point here: One often hears that closed shell nuclei are the most stable nuclei. This is not true, however, as a glance at the chart of separation energies in Figs. 1.2 and 1.3 clearly indicates. As nucleons of a given type (e.g., neutrons) are added, neutron separation energies systematically decrease. Just after a closed shell, the separation energy undergoes a *much larger* drop. Thus, closed shell nuclei are only more stable *relative to succeeding* nuclei.

In considering an appropriate potential for the nuclear case, a tremendous simplification results if the potential is central, that is, if it depends only on the radial distance from the origin to a given point. This is equivalent to requiring that the potential is spherically symmetric. Then, the *angular* dependence of a particle wave function is independent of the detailed radial behavior of the central potential. Moreover, the orbital angular momentum operator,  $\mathbf{l}$ , commutes with the energy ( $H$ ) and is a constant of the motion. All detailed effects of the particular choice of central potential will therefore show up *only* in the radial behavior of the wave functions.

Before considering the specific choice of central potential for the nuclear case, it is useful to summarize a few general properties of such potentials. We denote an arbitrary central potential by  $U(r)$  and only require that  $U(r)$  is attractive and  $U(r) \rightarrow 0$  as  $r \rightarrow 0$ . The Schrödinger equation for such a potential is

$$H\psi = \left( \frac{\mathbf{P}^2}{2M} + U(r) \right) \psi_{nlm}(\mathbf{r}) = E_{nlm} \psi_{nlm}(\mathbf{r}) \quad (3.2)$$

This equation is separable into radial and angular coordinates and therefore the solutions  $\psi_{nlm}$  can be written

$$\psi_{nlm}(\mathbf{r}) = \psi_{nlm}(r\theta\phi) = \frac{1}{r} R_{nl}(r) \psi_{nl}(\theta\phi) \quad (3.3)$$

Here,  $n$  is the radial quantum number,  $l$  the orbital angular momentum and  $m$  the eigenvalue of its  $z$ -component,  $l_z$ . It is conventional in nuclear physics to give names to different  $l$  values following the convention:

$$l = 0, 1, 2, 3, 4, 5, \dots \quad s, p, d, f, g, h, \dots$$

For a given  $l$ ,  $m$  takes the values  $l, l-1, l-2, \dots, 0, -1, -2, \dots, -(l-1), -l$ . Since  $U(r)$  is spherically symmetric the  $(2l+1)$  energies are independent of  $m$  and we will usually delete this index. The radial Schrödinger equation is

$$\frac{\hbar^2}{2M} \frac{d^2 R_{nl}(r)}{dr^2} + \left[ E_{nl} - U(r) - \frac{\hbar^2 l(l+1)}{2M r^2} \right] R_{nl}(r) = 0 \quad (3.4)$$

Its solutions have some interesting properties. First, outside the potential, the wave function decreases exponentially and therefore vanishes as  $r \rightarrow \infty$ . The quantum number  $n$  specifies the number of nodes (zeros) of the wave function with the usual, but not universal, convention that one counts the node at infinity but not that at  $r = 0$ , that is,  $n = 1, 2, \dots$ .

It is easy to prove an important property for such a general central potential—given two wave functions with different  $n$  values and the same  $l$  value, the one with the higher  $n$  (more nodes) will have higher energy. Physically, it is easy to see why this is so since, except for a final exponential falloff, the wave function must be contained within the range of the potential. Since the solution with higher  $n$  has more nodes, the wave function must “turnover” more rapidly within the range of the potential. The kinetic energy must therefore be larger (smaller wave length).

Similarly, for two states with the same  $n$  value, but two different  $l$  values, that wave function with the higher  $l$  also has the higher energy. This is also easy to see from Eq. 3.4, since the centrifugal potential is higher for the particle with larger  $l$ . Therefore this particle has higher transverse motion and is, on average, further from the nucleus and therefore less bound. These two results, for the behavior of  $E_{nl}$  with  $n$  and  $l$ , provide the basic reason why shell structure exists. From these very general and intuitive results one can already deduce an important conclusion: For any well-behaved central potential, the lowest single particle state is always an  $s$  state ( $l = 0$ ) and has  $n = 1$ . In particular, this simple result explains why the ground state of the deuteron is primarily an orbital angular momentum  $s$  state. (The small  $d$  state admixture is due to noncentral potentials, which do not have the properties just discussed).

We now turn to the harmonic oscillator potential. This potential is particularly popular in nuclear physics for two principle reasons: It provides a remarkably good approximate solution to many nuclear problems and it is particularly easy to handle mathematically, thus yielding many results analytically. It is given simply by:

$$V(r) = \frac{1}{2} M \omega^2 r^2 \quad (3.5)$$

The eigenvalues  $E_{nl}$  are:

$$E_{nl} = \left(2n + l - \frac{1}{2}\right) \hbar \omega \quad (3.6)$$

The wave functions,  $\psi_{nlm}$ , are given by Eq. 3.3.

The detailed specifications of the radial wave functions  $R_{nl}$  are of little practical importance in the present discussion except to note that they are proportional to Laguerre polynomials in  $r^2$ . Figure 3.1 shows the form of a harmonic oscillator potential as well as a square well and a typical modified harmonic oscillator potential.

The energy levels of the harmonic oscillator potential are shown in Fig. 3.2. They display two important properties that are evident from the expression for  $E_{nl}$ . First, the energy levels fall into degenerate multiplets defined by the (integer) values of  $2n + l$ . Secondly, a given multiplet generally contains more than one value of the principle quantum number  $n$  and of the orbital angular momentum  $l$ . A change of 2 units in  $l$  is equivalent to a single unit change in  $n$ . Thus, as evident in the figure, the levels 3s, 2d, and 1g are all degenerate. Physically, this is entirely reasonable in view of the arguments above concerning the sequencing of energy levels in an arbitrary central potential as a function of  $n$  and  $l$ . Specifically, since the energy due to centrifugal effects must

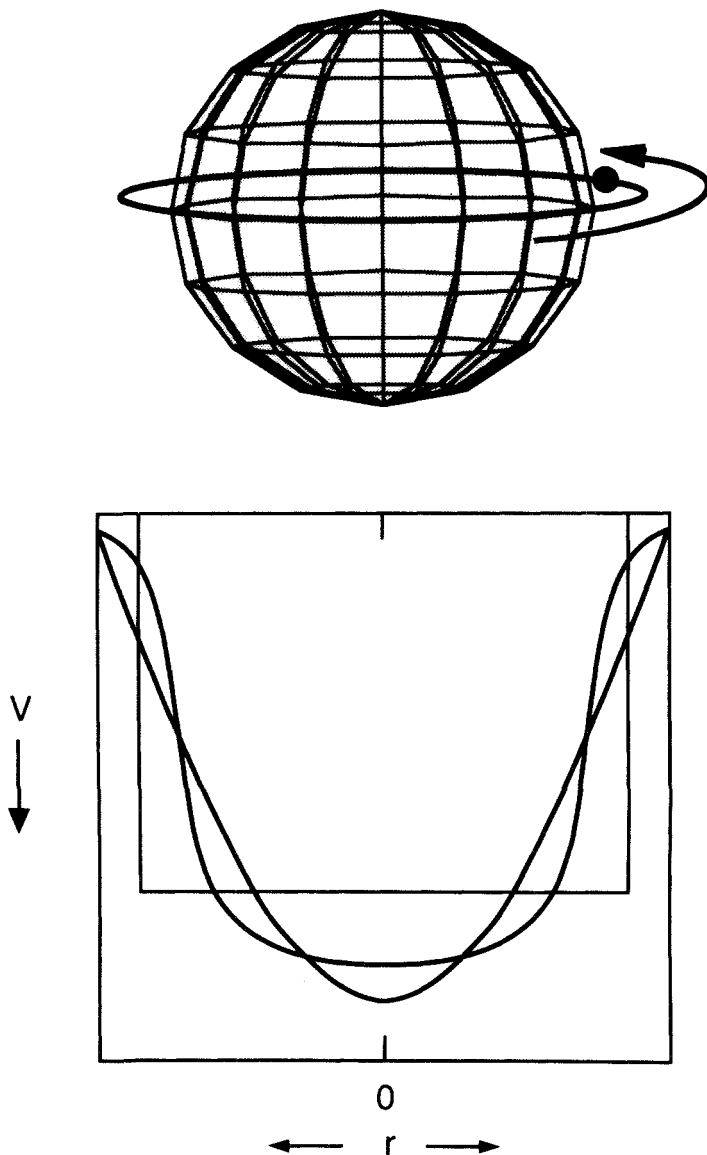


**Fig. 3.1.** (Top) Illustration of a single valence nucleon orbiting a doubly magic nucleus. (Bottom) Schematic illustration of three shell model potentials, a simple harmonic oscillator, a square well, and an intermediate shape or modified harmonic oscillator. The latter simulates, to some degree, the effect of an  $\vec{l}^2$  term.

increase with  $l$  as well as with the number of nodes ( $n$ ) in the wave function, it is clear that, at least qualitatively, one can compensate an increase in  $n$  with a decrease in  $l$ . The factor connecting these effects is exactly 2 for harmonic oscillator potential: it is also 2 for a square well potential.

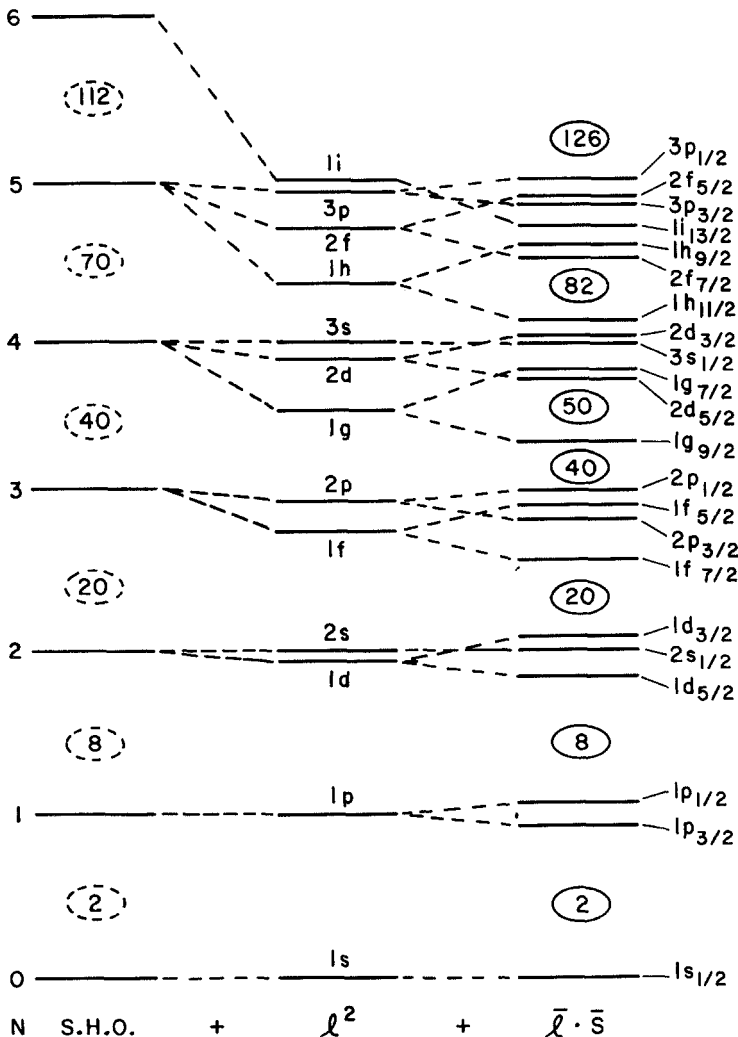


Fig. 3.2. Single-particle energies for a simple harmonic oscillator (S.H.O.), a modified harmonic oscillator with  $\ell^2$  term, and a realistic shell model potential with  $\ell^2$  and spin orbit ( $\ell \cdot s$ ) terms.

It is this grouping of levels that provides the shell structure required of any central potential useful for real nuclei. If we recall that each energy level has  $2(2l+1)$  degenerate  $m$  states, then, by the Pauli principle, each  $nl$  level can contain  $2(2l+1)$  particles. Therefore, if we imagine filling such a potential well with fermions, each group or shell can contain, at most, the specific numbers of particles indicated in the figure. Hence, such a potential automatically gives a shell structure rather than, say, a uniform distribution of levels.

Unfortunately, except for the lowest few, these shells do not correspond to the empirical magic numbers. Therefore, while the harmonic oscillator poten-

tial is a reasonable first order approximation to the effective nuclear potential, it must be modified to be useful. It was, in fact, the monumental achievement of Mayer and, independently, of Haxel, Jensen, and Suess, to concoct a simple modification to the harmonic oscillator potential that enabled it to reproduce the empirical magic numbers. This step revolutionized forever the subsequent history of nuclear physics and has led, either directly or indirectly, to essentially all the progress that has been made since. Their achievement, in effect, is the creation of a realistic shell model. Following their discovery in 1948, the extensive and very detailed development of this model has led to an elaborate formalism that provides not only a direct description of many nuclei but also the microscopic basis for many macroscopic models of collective properties of nuclei. Since their work, there have been extensive efforts to derive the nuclear shell model potential from more fundamental data on the nucleon–nucleon interaction. We shall not concern ourselves with such efforts here, but shall consider the potential they proposed, discuss it physically, and here and in the remaining chapters, draw out many of its implications.

It is possible to use some rather general arguments, based on the short-range nature of the nuclear force, to suggest some plausible modifications to the harmonic oscillator potential  $V$ . Consider a relatively heavy nucleus with dimensions significantly larger than the range  $R_N$  of the nuclear force. Then, as long as a given nucleon lies inside the nuclear surface by a distance greater than  $R_N$ , it should be surrounded rather uniformly by nucleons on all sides. It is screened from the asymmetric distribution that appears at the boundary. Therefore, it should experience no net force. In other words, the central part of the nuclear potential should be approximately constant. Thus, from this point of view, a square well potential might be an improvement on the harmonic oscillator. Another possibility is to add an attractive term in  $l^2$  to the harmonic oscillator potential. It is easy to see why this is equivalent to a flattening of the effective radial shape of the potential. The effects of an  $l^2$  term increase with the orbital angular momentum of the particle. Therefore high angular momentum particles feel a stronger attractive interaction that lowers their energies. However, these are precisely the particles that, because of the centrifugal force, spend a larger fraction of their time at larger radii. Therefore the addition of an  $l^2$  term is equivalent to a more attractive potential at larger radii and comes closer to the desired effect of a more constant interior potential. In fact, it gives a potential intermediate between that of the harmonic oscillator and the square well. A Wood-Saxon potential has a flatter bottom than the harmonic oscillator and also produces effects similar to an  $l^2$  term. In the deformed shell model (Nilsson model), that we will discuss in Chapters 7 and 8, the spherical limit for the single particle energies is explicitly expressed in terms of such an  $l^2$  contribution.

The relation of the single particle levels produced by a harmonic oscillator potential, along with the addition of an  $l^2$  term is illustrated in the middle panel of Fig 3.2, which shows how the  $2n + l$  degeneracy of the harmonic oscillator levels is broken as high angular momentum levels are brought down in energy.

It is clear that neither of these alternatives yet produces the magic numbers observed experimentally. It is easy to do so, however, if one introduces a so-called spin-orbit force. Thus far, we have not discussed the spin quantum number explicitly. Nevertheless, it is well known that the nucleon, either proton or neutron, has an intrinsic spin  $1/2$ , and therefore the total angular momentum of a nucleon in any orbit is given by the vector coupling of the orbital angular momentum  $\mathbf{l}$  with a spin angular momentum  $\mathbf{s} = 1/2$ . With a spin-orbit component, the force felt by a given particle differs according to whether its spin and orbital angular momenta are aligned parallel or antiparallel. If the parallel alignment is favored, and if the form of the spin-orbit potential is taken as  $V_{l\bullet s} = -V_{ls}(r)\mathbf{l} \bullet \mathbf{s}$  so that it affects higher  $l$  values more, then its effects will be similar to those illustrated on the far right in Fig. 3.2. Each  $nl$  level, such as  $1g$ , will now be split into two,  $1g_{9/2}$  and  $1g_{7/2}$ , orbits with the former lowered and the latter raised in energy. This instantly reproduces all the known magic numbers.

The absolute strength of the spin orbit force must be substantial (see Fig. 3.2) to produce the correct magic numbers: indeed, the splittings it produces must be comparable to those between adjacent multiplets of the harmonic oscillator potential. Since the constant  $\hbar\omega$  of the harmonic oscillator potential is found to be  $\hbar\omega = 41/A^{1/3}$  (e.g.,  $\hbar\omega \approx 8$  MeV for medium and heavy nuclei), it follows that the  $V_{ls}(r)$  must attain nearly such magnitudes.

Since the spin-orbit force is an inherently quantum relativistic effect, it is not as easy to give a physical picture for it as for the relation between an  $l^2$  force and the effective change in the behavior of the central potential just discussed. It has been shown, however, to arise naturally, and with the correct sign, from relativistic effects of the nucleonic notion. It is possible, though, to give plausible arguments for the *radial* shape of the spin-orbit potential. These rely again on the notion that, in the interior of the nucleus, a nucleon should experience no net force. If the spin-orbit force were large in the nuclear interior there would be a preference for nucleons with spins aligned parallel to their orbital angular momentum rather than vice versa and therefore such a nucleon would not be surrounded by an equal number of nucleons with all spin orientations. This suggests, although it certainly does not prove, that the spin orbit force is primarily a surface phenomenon. It is therefore customary to write:

$$V_{l\bullet s} = -V_{ls} \frac{\partial V(r)}{\partial r} \mathbf{l} \bullet \mathbf{s} \quad (3.7)$$

where  $V(r)$  is whatever potential is chosen for the central potential itself and  $V_{ls}$  is a strength constant.

It is worth pausing at this point to emphasize the importance of the spin-orbit interaction. It is not merely a device that ensures the appropriate magic numbers. Rather, a significant fraction of nuclear structure research in the last two decades has relied on and exploited the particular consequences of the spin-orbit force. To see this, it is necessary to refer more explicitly to the concept of parity. The parity of a wave function  $\psi_{nlm} = R_n(r)Y_{lm}(\theta, \phi)$  is given by the behavior,  $(-1)^l$ , of the spherical harmonic  $Y_{lm}$  under reflection, since the

radial wave function does not depend on the sign of  $r$ . Thus  $\pi_{nlm} = (-1)^l$ . For a multiparticle system of  $N$  independent particles,  $\psi = \psi_{n_1 l_1}(r_1) \psi_{n_2 l_2}(r_2) \dots \psi_{n_N l_N}(r_N)$ , and the total parity is

$$\pi = \prod_{i=1}^N (-1)^{l_i} = (-1)^{\sum_i l_i}$$

In the harmonic oscillator potential, the particular  $2n + l$  degeneracy led to shells containing sets of  $l$  values differing by even numbers. Therefore all the levels of a given harmonic oscillator shell have the same parity. The addition of a modest  $l^2$  term in the potential does not alter this qualitative fact but a spin-orbit potential can lower the energy of the  $j = l + 1/2$  orbit sufficiently so that, at least in the higher shells, it is brought down among the levels of the next lower shell. Indeed, this is precisely the effect required in order to reproduce the magic numbers. For example, the positive parity  $1i_{13/2}$  orbit now appears in the 82 to 126 shell among the negative parity  $2f_{7/2}$ ,  $1h_{9/2}$ ,  $2f_{5/2}$ ,  $3p_{3/2}$  and  $3p_{1/2}$  orbits. Thus, a real shell, bounded by the magic numbers, contains a majority of levels of one parity and one level of the opposite parity. It is conventional to call these the *normal parity orbits* and the *non-normal* or *unique parity orbits*, respectively.

The significance of this will only become clear when we consider certain *residual* interactions experienced by the nucleons in the shell model potential. However, the general point can be made easily. In some cases, these residual interactions are diagonal, providing contributions only to the energies of the various levels. In others, however, they have important nondiagonal effects that mix different configurations. Whatever mixing does occur, however, cannot mix levels of different parity. (We neglect here the very weak parity-nonconserving part of the weak interaction.) We recall from the discussion of two- and multistate mixing in Chapter 1 that such mixing effects are strongly dependent on the energy separation of the mixed states. Since the unique parity orbit cannot be admixed with its neighbors in a given major shell and because it is so far separated from the other orbits of the  $2n + l$  multiplet from which it originated, it mixes only very weakly with other levels. Therefore, configurations stemming from the unique parity orbit are particularly pure even though they occur amid an enormous complexity of mutually admixed states characteristic of many heavy nuclei. These levels therefore provide an ideal laboratory for testing various nuclear models, since one deals with particularly pure, simple, and well-known wave functions. This fact has been exploited in countless experimental and theoretical studies in recent years. Perhaps the most well known involve the interesting physics of high spin states in deformed nuclei. Indeed, it should not be surprising that the first, and often the majority of tests, of virtually every new approach to the study of high-spin states deals with unique parity levels. Only after whatever new effects are involved are well understood for these levels does one generally dare to look at the normal parity levels.

Unique parity levels are also of particular importance for low-spin states and for reasonably light nuclei. In the next chapter we shall study the effects of

residual interactions on nuclear level schemes. In general, these are quite complex and can lead to significant *configuration mixing*. However, we shall see that many of the complexities are eliminated, and indeed, rather simple, analytic, physically-reasonable results emerge, if the nucleons are restricted to occupying a “single  $j$ ” orbit. Clearly the testing ground par excellence for such ideas, will again be unique parity orbits. The fact that these are also the highest  $j$  orbits in a given shell and thus can contain the most particles, further enriches the phenomena that can be studied.

Now that we have outlined the basic features of the nuclear potential and seen the single particle energy levels to which it leads, we are nearly ready to consider the predictions of this model for various nuclei. The basic idea is simply to fill the levels of the potential sequentially, as one adds nucleons in going from nucleus to nucleus. With the help of some simple arguments we will see that we are immediately able to make many predictions concerning the low-lying levels of a number of nuclei.

One caveat is appropriate here. When looking at a sequence of levels in a central potential, as in Fig. 3.2, the overall scale is illustrative only and in fact changes with mass according to the well-known expression  $\hbar\omega \approx 41/A^{1/3}$ ; there is a gradual scale compression for heavier nuclei. Moreover, residual interactions affect the single particle energies themselves, as we shall discuss later. Thus, such sequences are a guide only. In practical use, specific single particle energies for each mass region must be used.

Before applying the model there are several rather profound issues, seldom thought about explicitly, that must at least be mentioned. The entire concept of “filling the levels... sequentially” is in fact one of the most important applications of the Pauli principle. Without this dictum, any number of nucleons could go in the lowest orbit. That being the case, there would be no reason (energetically) to favor the addition of a neutron or a proton (neglecting the Coulomb force—see the following). A nucleus with  $Z = 2, N = 300$  would be as stable as any other. It is one of the most significant consequences of the Pauli principle that stable nuclei have  $N \approx Z$  since a large excess of either would involve the filling of higher-lying levels at an extra cost in energy. Indeed, the entire shape of the valley of stability (Fig 2.1) results from the countervailing effects of the Pauli principle that favors  $N = Z$  and the Coulomb repulsion that favors a large neutron excess. For low  $Z$ , the former effect dominates, while for higher  $Z$  the valley of stability curves toward the neutron rich side (see the next paragraph). It is the same effect of the Pauli principle that determines nuclear radii: without it (and the Coulomb force), all nuclei would be comparable in size to an  $\alpha$  particle.

This discussion leads naturally into a few comments about the Coulomb force, which is simply an extra, repulsive, long-range potential ( $V_{\text{Coul}} \approx 1/r$ ) felt by the protons. We will not discuss this in detail, but it is obvious that its principle effect is to *raise* the single particle proton energy levels. As we have just seen, in the absence of the Coulomb force, proton and neutron energy levels would fill with equal likelihood, there being no distinction between the two, and the valley of stability would correspond to  $N = Z = A/2$ . However,

because of the Coulomb interaction, there is an extra cost in adding additional protons. This effect is clearly more important for heavier nuclei since the Coulomb force is a long range interaction that scales roughly as  $Z(Z - 1)$ , the total number of interacting proton pairs. Therefore, as  $A$  increases it becomes energetically preferable to add additional neutrons, and thus stable heavy nuclei have a neutron excess.

A second issue of importance concerns the very concept of independent particle motion in a central potential. As noted earlier in this chapter, this seems to be at odds with the idea of a strong nuclear force. Empirically, nuclear radii can be described by the relation  $R = 1.2A^{1/3}$ . If we take 1 fm as the radius of a nucleon, and imagine the nucleus to be uniformly filled, then the ratio of the nuclear volume to that of a single nucleon is just  $(1.2)^3 A$ , or hardly more than  $A$  times the volume of each nucleon! Therefore, it would seem unlikely that an individual nucleon could execute countless undisturbed orbits in such a densely packed medium. (Note that this is in stark contrast to the emptiness through which atomic electrons follow their orbits. Bohr did not need to address this issue, nor could he, since its solution is yet another consequence of the Pauli principle.)

The resolution of the paradox rests on the conjunction of the Pauli principle with the essentially weak nature of the attractive nuclear force where, by “weak,” we mean relative to typical kinetic energies of nucleons within the nuclear volume. This weakness is illustrated by the fact that in the deuteron, the simplest nuclear system, the attractive nuclear interaction is only sufficiently strong to produce one bound state.

To understand the possibility of independent particle motion, consider a central potential with various energy levels, defined by the quantum numbers  $nl$  (we ignore spin for this argument), in which the nucleons, either protons or neutrons, sequentially fill each level. Since the central potential is spherically symmetric, the energy levels are independent of the magnetic quantum number  $m$  and therefore, each such orbit is  $2l + 1$  degenerate (for any  $l$  there are  $2l + 1$  magnetic substates). By the Pauli principle, which states that no two fermions can occupy the same configuration, such an orbit can contain at most  $2l + 1$  particles. Therefore, as more and more nucleons are added to the nucleus, orbits of successively higher  $n$  and  $l$  values, and therefore higher energies, are filled. Now, imagine a pending collision between two nucleons in relatively inner orbits. By the Pauli principle, unless the impact of the collision is sufficiently strong to raise one of these nucleons to an unoccupied orbit (i.e., above the Fermi surface), the interaction can have no effect on the motion of these two nucleons. Therefore only the outermost nucleons are likely to be affected by such collisions. Thus, just as it is the Pauli principle that prevents the nucleus from collapsing on account of the attractive nuclear potential, it is also the Pauli principle that leads to independent particle motion for most nucleons in the nucleus. This does not mean that there cannot be correlations in two-body nuclear wave functions, but those correlations must be consistent with the Pauli principle and with the strength of the attractive nucleon–nucleon interaction. Later, we shall see later that many of those correlations that do

occur are an implicit effect of the antisymmetrization of nuclear wave functions associated with the Pauli principle.

Another question worth mentioning is inherent in the use of a harmonic oscillator potential in the shell model: How does one reconcile the idea that a nucleon at large distances from a real nucleus cannot experience a nuclear force with the fact that a harmonic oscillator potential increases in strength with radius? This point is rather subtle and relates to the problem of separating the internal motion of the nucleons from that of the nuclear center of mass. This problem has been elegantly discussed in de Shalit and Feshbach, and we will not dwell on it here except to comment that in a typical nuclear potential  $V$ , such as the harmonic oscillator, where  $V \rightarrow \infty$ , the falloff of nuclear wave functions with increasing distance from the origin behaves rather differently (as  $e^{-\alpha r^2}$ ) than is the case for quantum mechanical tunneling through a finite potential ( $e^{-\alpha r}$ ). However, this difficulty is primarily a “long distance” problem: the two wave functions are similar within the nuclear volume. Significant errors may accumulate in studying the tails of nuclear wave functions. Such effects can be important, for example, in studying single nucleon transfer reactions that occur primarily in “grazing” collisions at the nucleus surface.

As a final preliminary, we must consider the structure of closed shells and their effects on the valence particles. Consider a system of  $A$  nucleons (either protons or neutrons, which, for the present purposes, we treat independently: the interactions between them will be considered later). Each orbit of spin  $j = l \pm 1/2$  has  $2j + 1$  degenerate magnetic substates. By the Pauli principle, once  $2j + 1$  nucleons are in a given orbit, it is filled (closed) and the next one begins to fill. To predict the spins and parities ( $J^\pi$  values) of low-lying levels in nuclei, we need to consider the effects of the (filled) closed shells. First, we show that the total angular momentum of a closed single- $j$  shell is identically zero. This is trivial. It is immediately clear that the total magnetic quantum number  $M$  of a closed shell is  $M = \sum m_i = j + (j - 1) + \dots + (-j) = 0$ . Since this is the only possible  $M$  value, it follows that the total angular momentum  $J = 0$  since  $J$  can never be larger than the largest  $M$ . Alternately, for each state  $j, m$  there is a state  $j, -m$ , and therefore the vector sum  $\mathbf{J} = \mathbf{j} + \mathbf{j}$  vanishes. Since this is true for each pair of states (with  $\pm m$  values) and, of course, for  $m = 0$ , it is true for the full set of  $2j + 1$  states. Furthermore, since it is true for a given  $j$  value, it must be true for an entire major shell consisting of several  $j$  values.

Note the importance of this result: without it, it would be impossible to apply the independent particle model to any nuclei except hydrogen or a neutron where, of course, the idea of the central potential itself would not be valid. With it, however, one can at least predict the ground state spins and low-lying excited states of any nucleus consisting of one particle, either proton or neutron, outside a closed shell. Since the core—that is, all closed shells (major or single  $-j$ )—contributes only  $J^\pi = 0^+$ , the angular momentum of the ground state of a nucleus with one particle in a shell  $nlj$ , is therefore just  $J = j$  with parity  $\pi = (-1)^j$ .

Any program of predicting ground state  $J$  values, or the  $J$  values and energies of single-particle excited states, presupposes that we know the order

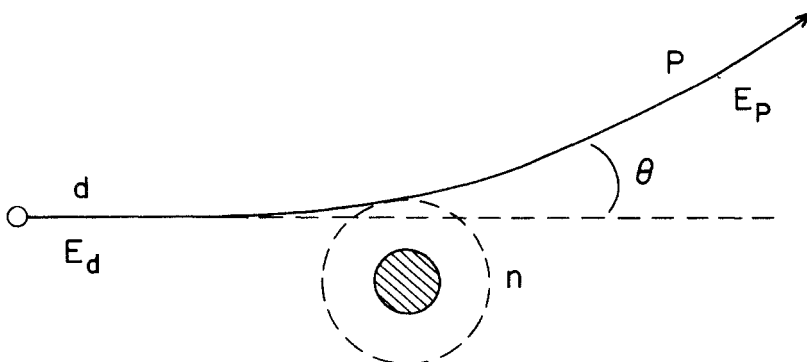
and spacings of the single-particle levels. The reader may perhaps think that we have already dealt with and solved this question by the sequence on the right of Fig. 3.2. However, this ignores the fact that the single-particle energies themselves depend on the number of nucleons in the nucleus since the single-particle potential arises from these same nucleons. Considering nuclei with one valence particle (beyond closed shells), this means considering the effect of the closed shells.

The reader has undoubtedly encountered the idea that closed shells can be ignored. There is considerable truth in this, as we shall see, but it is not the whole story. Especially in recent years, with the advent of much new data far off stability, this issue takes on real importance. In the next few paragraphs we discuss the effects of closed shells on single-particle energies. An extension to multiparticle configurations will be discussed early in the next chapter.

The basic result is absolutely trivial. Since a closed shell has  $J = 0$ , its wave function is spherically symmetric. Therefore, imagine a single valence nucleon outside this shell in an orbit  $j$  and magnetic substate  $m$ . Since the closed shell has no preferred direction in space, its interaction with this nucleon must be independent of  $m$ . This does not mean that the interaction can be ignored. It can, and does, exist but it is only equivalent to a *change in the spherically symmetric central potential*. A particle in a particular valence  $j$  shell certainly interacts with the closed  $j$  shells below it and its *single-particle energy* is altered by that interaction. The preceding argument simply means that this interaction is independent of direction. [Incidentally, to anticipate our later discussion of the multipole expansion of an interaction in  $P_k(\cos\theta)$ , this shift is due exclusively to the *monopole* ( $k = 0$ ) part of the interaction between the closed and open shell nucleons, since that is the only multipole that is  $\theta$  independent ( $P_0(\cos\theta) = \text{constant}$ )].

This interaction of an open shell with underlying filled shells has an important consequence. A *major* shell generally consists of several constituent  $j$  shells. Each of the  $j$ 's of a closed major shell can have a different (spherically symmetric) effect on each of the valence  $j$  orbits. Thus, the *relative* single-particle energies in a given major shell depend critically on the specific lower-lying, filled closed shells.

We can illustrate this effect and understand its importance with some examples. Empirically, it is possible to map out single particle energies with one-nucleon transfer reactions. These will be discussed extensively for deformed nuclei in Chapter 8. Suffice it to say here that in a reaction like  $(d, p)$ , illustrated in Fig. 3.3, a neutron is stripped off the incoming deuteron into a specific orbit around the target nucleus, leaving an outgoing proton. Clearly, such a reaction can disclose sequences of states with single-particle structure, each corresponding to different  $j$  orbits. Moreover, once the "kinematical" aspects of the reaction collision are removed, the cross sections yield a nuclear matrix element, which is the *purity* of the single-particle state. This information is embodied in the so-called spectroscopic factor:  $S(d, p) = 1$  corresponds to a pure single-particle neutron wave function coupled to the target nucleus. While a reaction like  $(d, p)$  can only populate a state to the extent that the



### DIRECT ( $d, p$ ) REACTION

**Fig. 3.3.** Schematic illustration of a direct ( $d, p$ ) reaction.

corresponding orbit was empty in the target, “pickup” reactions like ( $d, t$ ) extract a neutron from an already filled orbit: they produce *hole excitations* and sample single-particle energies below the current valence shell.

Extensive data collected over several decades, much of it from such reactions, has allowed us to map out the empirical single-particle energies in a number of nuclei that are one particle or hole removed from various major closed shells. The recent extension of such data to nuclei far off stability has greatly expanded the overview of single-particle energies thus provided.

We summarize some of the results in Fig. 3.4. Each panel gives the observed single-particle or hole energies for two nuclei, along with schematic illustrations of the orbits involved. The point is to compare these energies for different systems, *cores*, and types of nucleon.

The top left panel of Fig. 3.4 shows proton and neutron single-particle energies in the 82 to 126 shell extracted from the particle levels of  $^{209}\text{Bi}$  and the hole states of  $^{207}\text{Pb}$ . The energies are nearly identical. (The slight expansion of the proton energy scale is probably a Coulomb effect.) This is reasonable. In each of the nuclei, the valence particle or hole “feels” interactions with essentially the same underlying orbits. The only notable difference is that the neutron holes in  $^{207}\text{Pb}$  interact with 43 other neutrons in the 82 to 126 shell, while the proton particles in  $^{209}\text{Bi}$  interact with the full major shell of 44 neutrons. As individual nucleon–nucleon interactions are on the order of a few hundred keV, and  $j$ -dependent differences considerably less, this should be a minor effect. On the top right panel in Fig. 3.4, a similar situation is shown for the 50 to 82 shell with identical results.

However, in the bottom panel, the neutron holes in  $^{131}\text{Sn}$  interact with the same 50 neutrons and 40 protons as in Zr but, in addition, with the  $Z=40$  to 50 closed proton shell and with other neutrons in their own shell. As a consequence, their energies are very different from  $^{91}\text{Zr}$ .

This particular example is actually of great structural consequence. (We

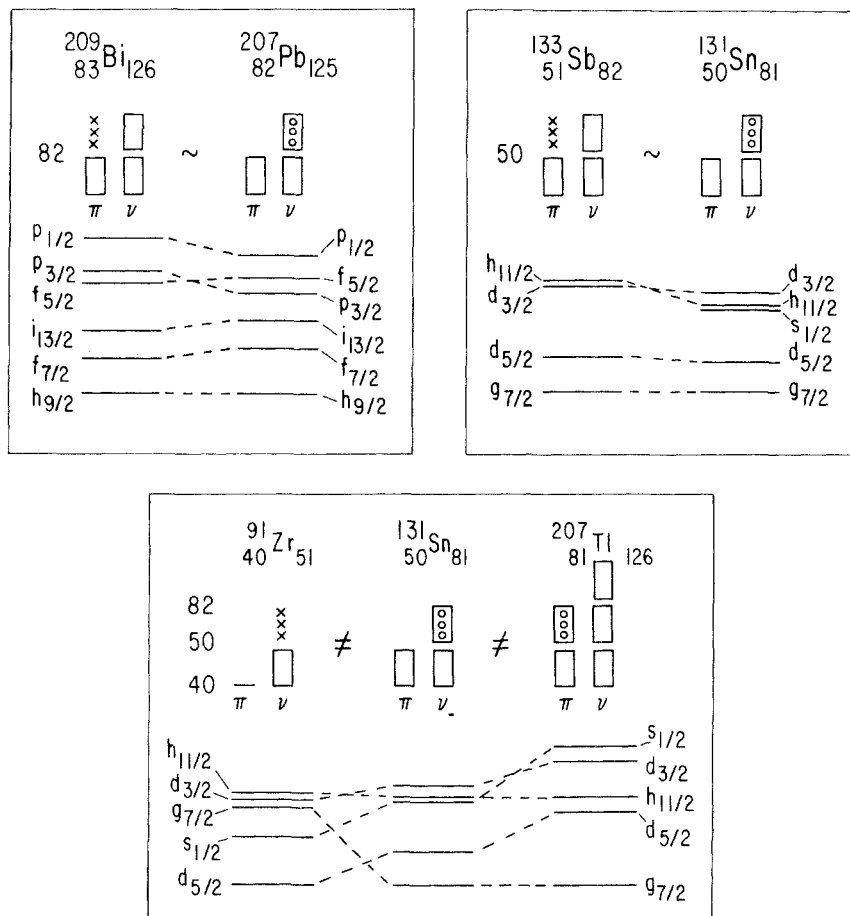


**Fig. 3.4.** Changes in single-particle energies in different nuclei that illustrate the effect of closed shells on the valence orbits. Since we are interested in relative changes only, one energy is normalized in each box.

will see later that it accounts for the onset of deformation near  $A = 100$ .) The point is that the interaction of a given shell,  $j_1$ , with another (closed or open),  $j_2$ , depends on the overlap of the respective wave functions; the only difference if  $j_2$  is closed is that, then, the interaction is angle independent, so it is the *radial* overlap that counts. Orbitals with similar quantum numbers  $nlj$  have higher overlaps. This is demonstrated in Fig. 3.5, where the dependence of the radial overlaps of various orbits with a  $1s$  orbit on  $\Delta n = n_1 - n_2$  and  $\Delta l = l_1 - l_2$  is illustrated. The falloff with  $\Delta n$  and  $\Delta l$  is clear. (Incidentally, the simple estimate that the interaction goes roughly as  $1/(\Delta n + \Delta l)$  is not a bad guide).

In this particular case, as the proton  $1g_{9/2}$  orbit fills from  $Z = 40$  to 50 it exerts a strong attractive *pull* on the  $1g_{9/2}$  neutron orbit, drastically lowering the energy as seen so clearly in Fig. 3.4. In contrast, an orbit like  $3s_{1/2}$  has poor overlap with  $1g_{9/2}$  and, relatively, its energy increases.

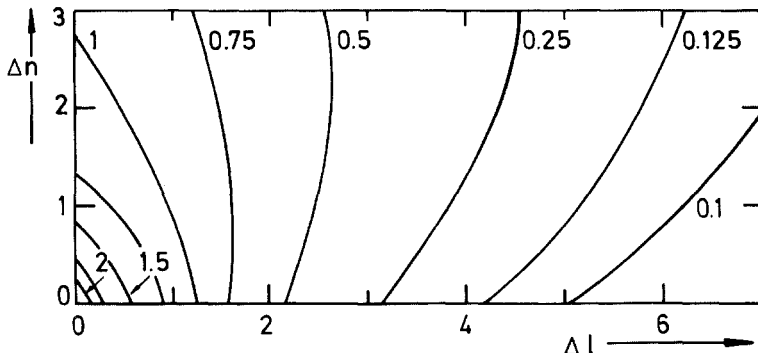


**Fig. 3.5.** Indication of the dependence of a residual interaction on the difference in principle ( $n$ ) and orbital angular momentum ( $l$ ) quantum numbers of the two orbits involved. The contours give constant values of the radial overlap integrals of a  $1s_{1/2}$  orbit with orbits of different  $n, l$  (Heyde, 1987).

The sensitivity of relative single-particle energies in a given shell to the occupation of different underlying shells is further illustrated in the same panel by the extension to  $^{207}\text{Ti}$ . Here, one observes the proton orbits in the 50 to 82 shell, but now an additional neutron shell (82 to 126) has been filled. Since this extra neutron shell has, on average, higher  $j$  values (1/2 to 13/2 instead of 1/2 to 11/2 for 50 to 82 or 1/2 to 9/2 for 28 to 50), the main effect is to further lower the higher  $j$ -proton single-particle energies (7/2, 11/2) relative to the lower ones (1/2, 3/2, 5/2).

This rather lengthy discussion is important because it highlights the three points that (1) a closed shell has the *same* effect on all *magnetic substates* of a particle in an open shell, (i.e., it is equivalent to a change in the spherical potential), (2) the energies of *different j* shells may be very differently affected by underlying shells, and (3) different underlying closed shells ( $j$  or major) may affect a given open shell *very* differently. It also serves to re-emphasize that an illustration of the “shell model levels,” as shown in Fig. 3.2, can only give a semiquantitative guide: the energies are mass dependent.

With this background, we now turn to actual predictions of the independent particle model. Despite the caveat just made, for convenience, we will use Fig. 3.2 as a single-particle energy reference. (Note: in most of the following discussion we will denote orbits by the  $lj$  quantum numbers alone, as in  $f_{7/2}$ , since omission of  $n$  simplifies the notation and seldom causes confusion.)

This simple model works extremely well for a large number of nuclei. For example, by inspection of the right-hand panel of Fig. 3.2, we would expect the ground state of  $_{20}^{41}\text{Ca}_{21}$ , which has one neutron beyond the  $N = 20$  closed shell, to be  $7/2^-$ . Similarly,  $_{21}^{41}\text{Sc}_{20}$  should have a  $7/2^-$  ground state, while the ground states of  $_{41}^{91}\text{Nb}_{50}$  and  $_{40}^{91}\text{Zr}_{51}$  should be  $9/2^+$  and  $5/2^+$ , respectively. These predictions are verified experimentally.

It is also trivial to predict excited states in the independent particle model: these can be formed simply by elevating a particle from the ground state orbit

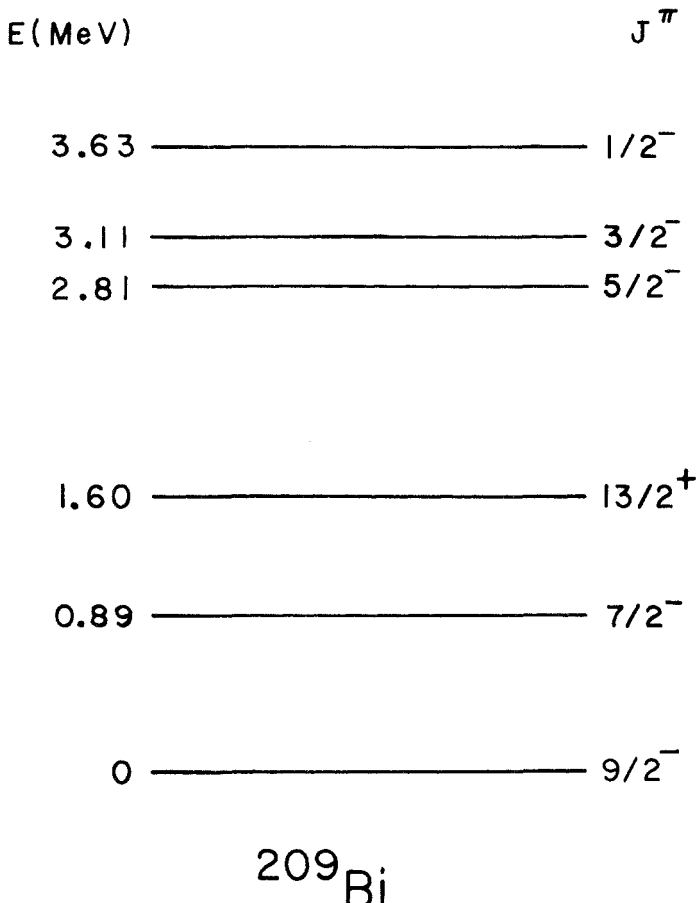


Fig. 3.6. Low-lying single-particle levels of  $^{209}\text{Bi}$ .

to a higher level. The excitation energy is given by the energy differences between the orbits in a shell model potential such as that in Fig. 3.2.

For example, in  $^{41}\text{Ca}$ , there should be a low-lying  $3/2^-$  state and slightly higher  $1/2^-$  and  $5/2^-$  states. Another means of forming an excited state is to elevate a particle from a lower, filled level. Suppose an  $s_{1/2}$  nucleon is raised to the  $f_{7/2}$  orbit. In principle, we now have to deal with a “hole” in the  $N = 8$  to 20 shell and two particles above  $N = 20$ . Anticipating a result from the next chapter, while the two  $1f_{7/2}$  particles can couple their angular momenta to form several  $J$  values, the  $J^\pi = 0^+$  state lies the lowest by far for any realistic interactions between these particles. Therefore the *three-particle* state  $|(s_{1/2})^{-1}(f_{7/2})^2 J\rangle$  (to use an obvious notation where exponents count particles and negative exponents count holes), has  $J^\pi = 1/2^+$  as its lowest state. We thus expect a  $1/2^+$  level in  $^{41}\text{Ca}$  at an excitation energy given roughly by the  $\epsilon_{f_{7/2}} - \epsilon_{s_{1/2}}$  orbit

energy difference. Although this estimate neglects some residual interaction effects, it is good enough for the present purposes.

The  $^{41}\text{Ca}$  level scheme thus should exhibit low-lying  $7/2^-$ ,  $3/2^-$ ,  $3/2^+$ , and  $1/2^+$  levels. The empirical scheme was shown in Fig. 2.4. Clearly there are many more levels than we have accounted for. This is not exactly a discrepancy, but rather a caveat, since the extra states arise from more complex configurations and can be understood by techniques developed in the next two chapters. In Fig. 2.4, we indicated those levels identified in (d, p) or (d, t) and we can see that this “single particle” subset of states in  $^{41}\text{Ca}$  is exactly that demanded by the independent particle model. While this confirms some basic predictions of the model, the wealth of other states hints at the greater complexity to come.

In the same way, the single-particle states in  $^{209}\text{Pb}$  and  $^{209}\text{Bi}$  and many other nuclei have been identified. For example, the results for proton levels in the 50 to 82 shell and for neutron levels below the magic number 82 were shown for  $^{133}\text{Sb}$  and  $^{131}\text{Sn}$ , respectively, in Fig. 3.4. Those for the particle excitations of the  $Z = 82$  to 126 shell are given for  $^{209}\text{Bi}$  in Fig. 3.6. In all three cases, the expected ordering and spacing is approximately observed. The results for  $^{209}\text{Pb}$  are included in Fig. 2.4, along with their spectroscopic factors,  $S(d, p)$ . (The  $S(d, p)$  values have a maximum theoretical value of unity: those empirical values slightly exceeding unity may be due to experimental errors or difficulties in removing reaction kinematics from the observed cross sections.) Except for the  $15/2^+$  levels, the states have remarkable purity and display an order in basic agreement with Fig. 3.2.

Notice that all of the nuclei considered so far have only one nucleon outside a doubly magic nucleus. In considering excited “hole” states in  $^{41}\text{Ca}$ , we have already encountered three-particle states and used a result from Chapter 4 for the relative energies of states in a  $|j^2J\rangle$  configuration. By generalizing this with a further conclusion from Chapter 5, we can greatly extend the usefulness of the independent particle model. We stated earlier that it is energetically favorable for two particles in an orbit to couple their angular momenta  $j$  to  $J=0$ . As discussed in Chapter 5, this tendency persists for any even number,  $n$ , of particles in an orbit  $j$ , that is, in the configuration  $j^n$ . Therefore, the lowest state of a  $j^{n+1}$  configuration can be thought of in the form  $|j^n(J_1=0)j, J=j\rangle$  where  $J_1$  is the “intermediate”  $J$  value for  $n$  nucleons. Thus, again  $J=j$  of the last odd nucleon; this now allows us to predict sequences of ground and excited state  $J$  values for odd mass nuclei relatively far from closed shells.

For example, from Fig. 3.2, the odd neutron in the Ca isotopes from  $^{41}\text{Ca}$  to  $^{47}\text{Ca}$  should fill the  $f_{7/2}$  orbit above the  $N = 20$  magic number. These nuclei should all have  $J^\pi = 7/2^-$  ground states. The  $f_{7/2}$  orbit is filled by  $^{48}\text{Ca}$  and the ground state of  $^{49}\text{Ca}$  should have an odd neutron in the  $p_{3/2}$  orbit.

If we consider  $^{37,39}\text{Ca}$ , we are dealing with holes in the  $N = 20$  neutron shell (i.e., the  $d_{3/2}$  orbit). It is easy to show that a state with one hole in a  $j$  shell also has  $J=j$ . Since  $2j$  must be odd, the first  $(2j-1)$  nucleons will “pair” off to  $J=0$ , using our previous argument, leaving one particle in the orbit  $j$ , and hence, giving  $J=j$ . Another proof is simply the statement that since the  $(2j+1)$ -particle closed shell has  $J=0$ , the only angular momentum in the system of a

GROUND STATE  $J^\pi$  VALUES OF  
SOME ODD MASS NUCLEI

$Z=20$	$\frac{3/2^+}{^{37}\text{Ca}}$	$\frac{3/2^+}{^{39}\text{Ca}}$	$\frac{7/2^-}{^{41}\text{Ca}}$	$\frac{7/2^-}{^{43}\text{Ca}}$	$\frac{7/2^-}{^{45}\text{Ca}}$	$\frac{7/2^-}{^{47}\text{Ca}}$	$\frac{3/2^-}{^{49}\text{Ca}}$
$Z=50$		$\frac{9/2^+}{^{87}\text{Zr}}$	$\frac{9/2^+}{^{89}\text{Zr}}$	$\frac{5/2^+}{^{91}\text{Zr}}$	$\frac{5/2^+}{^{93}\text{Zr}}$	$\frac{5/2^+}{^{95}\text{Zr}}$	
$Z=39$	$\frac{1/2^-}{^{85}\text{Y}}$	$\frac{1/2^-}{^{87}\text{Y}}$	$\frac{1/2^-}{^{89}\text{Y}}$	$\frac{1/2^-}{^{91}\text{Y}}$	$\frac{1/2^-}{^{93}\text{Y}}$	$\frac{1/2^-}{^{95}\text{Y}}$	$\frac{1/2^-}{^{97}\text{Y}}$
$Z=41$		$\frac{9/2^+}{^{91}\text{Nb}}$	$\frac{9/2^+}{^{93}\text{Nb}}$	$\frac{9/2^+}{^{95}\text{Nb}}$	$\frac{9/2^+}{^{97}\text{Nb}}$	$\frac{9/2^+}{^{99}\text{Nb}}$	
$N=50$	$\frac{3/2^-}{^{35}\text{Br}}$	$\frac{3/2^-}{^{37}\text{Rb}}$	$\frac{1/2^-}{^{39}\text{Y}}$	$\frac{9/2^+}{^{41}\text{Nb}}$	$\frac{9/2^+}{^{43}\text{Tc}}$	$\frac{9/2^+}{^{45}\text{Rb}}$	

**Fig. 3.7.** Ground state  $J^\pi$  values for a number of odd-mass nuclei for comparison with the predictions of the independent particle model (compare Fig. 3.2).

one-hole state is the hole angular momentum  $j$ . (Implicitly, of course, we already used this result in predicting the  $J^\pi$  values of  $^{47}\text{Ca}$ , another one-hole nucleus.) Thus the ground state of  $^{39}\text{Ca}$  should have  $J^\pi = 3/2^+$ . In  $^{37}\text{Ca}$ , the first two holes pair to  $J = 0^+$  and the third odd particle again gives the  $J = 3/2^+$  ground state spin. These predictions are verified by the empirical ground states in Fig. 3.7 (top row).

This figure shows several other empirical sequences illustrating the predictions of the independent particle model. The nucleus  $^{90}_{40}\text{Zr}_{50}$  is doubly magic. Isotopes with  $N > 50$  should be filling the neutron  $d_{5/2}$  orbit until  $N = 56$ . Below  $N = 50$  there will be holes in the  $g_{9/2}$  orbit. So we expect ground state spins  $J = 9/2^+$  for  $^{87},^{89}\text{Zr}$  and  $5/2^+$  for  $^{91},^{93},^{95}\text{Zr}$ . The next line in the figure shows the odd proton  $^{39}\text{Y}$  isotopes. Note that they *all* have a  $1/2^-$  ground state. This is the expected orbit for the 39th proton. The interesting point here is that the  $1/2^-$  level remains the ground state, regardless of the number of neutrons over a very wide range of nuclei. The  $^{41}\text{Nb}$  nuclei in the next line exhibit the same feature, except the 41st proton is in the  $g_{9/2}$  orbit. (Interestingly, the first excited state in each of these Nb isotopes is  $1/2^+$ , which can be obtained by

elevating a proton from below the  $N = 40$  closed shell to pair off with the odd  $g_{9/2}$  proton, leaving a  $1/2^-$  hole.)

As a final illustration, if two of the three valence neutrons in  $^{43}\text{Ca}$  couple to  $J = 0$ , its excited states, identified in (d, p) or (d, t), should resemble those in  $^{41}\text{Ca}$ . Figure 2.4 confirms this.

From our earlier discussion of Fig. 3.4, it is obvious that deviations from Fig. 3.2 must occur. The bottom row of Fig. 3.7 is a sequence of  $N = 50$ , odd  $Z$  nuclei from  $Z = 35$  to 45. From Fig. 3.2 we would expect the 35th and 37th protons to fill the  $f_{5/2}$  orbit with a low-lying  $p_{3/2}$  excitation, the 39th to occupy the  $p_{1/2}$  orbit and the 41st to 45th the  $g_{9/2}$  orbits. The predictions for  $Z = 39$  to 45 are confirmed empirically, but there is an inversion of the  $f_{5/2}$  and  $p_{3/2}$  levels. As another example, the level order ordinarily associated with the 50 to 82 shell is a low-lying pair of  $g_{7/2}$ ,  $d_{5/2}$  orbits with a small gap before a cluster of  $s_{1/2}$ ,  $d_{3/2}$ , and  $h_{11/2}$  orbits. This pattern is seen clearly in  $^{131}\text{Sn}$  in Fig. 3.4. However, this figure also shows the very different order in  $^{91}\text{Zr}$ . While we are able to predict the  $d_{5/2}$  ground state for Zr, Fig. 3.2 would have suggested a  $7/2^+$  first excited state, instead of the  $1/2^+$  state observed empirically. Indeed,  $^{97}\text{Zr}$  (with filled  $d_{5/2}$  orbit) also has a  $1/2^+$  ground state. The inversion of the ground and first excited states of  $^{209}\text{Bi}$  is a third example (Compare Figs. 3.2 and 3.6). These are not deficiencies in the model, just a fact of life in its use. As discussed in the context of Fig. 3.4, one *must* deal with changes in single-particle ordering, especially when the same major shell is inspected in nuclei that are far apart in mass so that the interactions of the intervening nucleons will have altered the single particle potential. Also, because of the Coulomb potential, proton and neutron single-particle sequences are expected, and found to be, slightly different, especially in heavy nuclei.

Of course, there are also real discrepancies with the predictions of the independent particle model. Figures 2.4 and 2.11 showed the examples of  $^{169}\text{Yb}$  and  $^{161}\text{Dy}$ , where a totally different empirical picture, completely at variance with Fig. 3.2, is observed. We will see the reasons for this later.

There is one last prediction of the independent particle model that accounts nicely for a characteristic aspect of doubly magic nuclei. Clearly, any excitation of a nucleon to the next higher shell nearly always involves excitation into an orbit with the opposite parity. Therefore, the low-lying excited levels of such nuclei should be negative parity. This is empirically well known, as exemplified in Fig. 2.2.

Although we will not discuss it here, there are many other predictions, for example magnetic moments or single-particle electromagnetic transition rates, that are reasonably well reproduced by the simple independent particle approach.

Finally, we caution that, while  $J = 0^+$  is the lowest-lying configuration for the  $j^p$  configuration of identical nucleons, other  $J$  values are possible at higher energy. Empirically, the next energy level nearly always has  $J = 2^+$ . Therefore it is risky to extend the predictions for odd mass nuclei above excitation energies comparable to  $E_{2+}^1$  in the neighboring even-even nucleus, since configurations of the form  $|j \otimes 2^+, J\rangle$  in which a particle in orbit  $nlj$  is coupled to a "core" excitation (the first  $2^+$  state) of the under-lying even-even nuclei can then compete with single-particle excitations.

## THE SHELL MODEL: TWO-PARTICLE CONFIGURATIONS

In order to proceed, we must deal more deeply and systematically with the problem of multinucleon configurations. By this we mean "valence" configurations of two or more particles outside a core, which is usually assumed to consist of inert closed shells. There are really two issues here: First, which  $J$  values are allowed by the Pauli principle, and, second, what is their relative energy ordering. The first question can be answered without reference to any discussion of a central potential or residual interaction, while the second depends on the details of those interactions, although many properties can be deduced from the simple fact that the radial and angular parts of a wave function in a central potential can be separated and that predictions for the latter are independent of  $J$  value, and for the radial part, many results can be obtained by rather general arguments based on its short- or long-range character or by considering a multipole expansion of it. This chapter addresses these issues. We will start by considering the simplest case of two identical nucleons in the same or different orbits. Then we will turn briefly to the case of two nonidentical nucleons (proton and neutron) and the role of isospin and exchange terms in the residual interaction. In the next chapter we will consider the case of larger multinucleon configurations of the form  $j''$ .

A complete treatment of many of these issues involves extensive and sophisticated familiarity with the formalism of angular momentum and tensor algebra. Indeed, many of the results can only be proved by rather formal manipulation of the various angular momentum coefficients ( $3-j$  symbols, Racah coefficients, coefficients of fractional parentage, and so on.) and a deep understanding of their symmetry properties. It is both contrary to the spirit of our presentation and entirely beyond the competence of this author to present this formal material fully. Moreover, there are numerous existing texts that deal with it at great length in superb fashion. Two of the best are those of de Shalit and Feshbach and de Shalit and Talmi, to which the reader is encouraged to refer. In the following presentation, we will make explicit use of their results, but our principle effort is to provide a physical understanding and motivation for the results and to present arguments for their plausibility. The excellent recent book by Heyde also develops these ideas in a more formal way. It is complementary to the present treatment and is highly recommended.

Before discussing the particular characteristics of multinucleon configurations under the influence of residual interactions, it is crucial to discuss the role

of closed shells on the valence nucleons. As with the energy levels of single nucleons in shell model orbits, it is only if the effects of closed shells can be neglected that the study of multinucleon configurations will be applicable to other than the lightest nuclei.

Since a closed shell is spherically symmetric, the interaction of a valence nucleon in the state  $jm$  cannot depend on  $m$ : hence, the closed shell particles have the same effect on all valence nucleons in a given  $j$  orbit. In multiparticle configurations, the effects of the closed shell nucleons are independent of the way (the relative orientations) that the individual  $jm$  values are coupled to the total  $J$ . Therefore, the closed shell can have no effect on energy *differences* of these different  $J$  states. As discussed in Chapter 3, this does not rule out an additive energy for the entire group of states and different  $j$  values can lead to different shifts. Thus, the “rule” for spacings refers only to those within a given configuration, not to the relative energies of different  $j$  shells in a major shell.

With these preliminaries in hand, we can now discuss two-particle configurations. First, we need to determine which  $J$  values result from coupling of a nucleon in orbit  $j_1$  with one in orbit  $j_2$ . If  $j_1 \neq j_2$ , these are simply the integer values from  $|j_1 - j_2|$  to  $|j_1 + j_2|$ . If the orbits are equivalent,  $n_1 l_{j_1} = n_2 l_{j_2}$  (which we shall often abbreviate to  $j_1 = j_2$  when no confusion should arise) we distinguish two cases—identical and nonidentical nucleons. For the latter (proton–neutron) case,  $J$  takes on all integer values from 0 to  $2j$ , as there is no Pauli principle restriction on the occupation of identical  $m$  states. However, for identical nucleons, one must explicitly consider the effects of the Pauli principle, which requires the *total* wave function to be antisymmetric.

For identical nucleons, the isospin projection  $T_z = t_1(1) + t_2(2) = 1$  and hence the total isospin  $T = 1$ . (Clearly,  $T$  cannot be less than its projection, nor greater than the sum of the individual  $t_z$  values.) This is a symmetric wave function. Hence, the space-spin part must be antisymmetric. When we impose this requirement, only certain  $J$  values are allowed. To see this, we have to look at the particular  $m$  states occupied by the particles, 1 and 2. The Pauli principle requires that

$$\psi_1(jm)\psi_2(jm') = -\psi_2(jm)\psi_1(jm') \quad (4.1)$$

A properly antisymmetrized wave function that has this property is given by

$$\begin{aligned} \psi(j^2 JM) &= N \sum_{m,m'} (jmjm' | jjJM) [\phi_1(m)\phi_2(m') - \phi_1(m')\phi_2(m)] \\ &= N \sum_{m,m'} [(jmjm' | jjJM) - (jm'm | jjJM)] \phi_1(m)\phi_2(m') \end{aligned}$$

where  $N$  is a normalization factor. The relation between the two Clebsch-Gordon coefficients on the right-hand side is well known and given by the phase factor  $(-1)^{2j-J}$ . Hence

$$\psi(j^2 JM) = N [1 - (-1)^{2j-J}] \sum_{m,m'} (jmjm' | jjJM) \phi_1(m)\phi_2(m') \quad (4.2)$$

Since  $2j$  is odd, this vanishes unless  $J$  is even: the only *allowed*  $J$  states for two

*identical* fermions in *equivalent* orbits are those with even total angular momentum  $J = 0, 2, 4, \dots, (2j - 1)$ . In Chapter 5, we will see that the same result is even simpler to obtain in the  $m$ -scheme, which provides a general, though sometimes tedious, way of finding the possible  $J$  states for *any* multiparticle configuration.

With this result for identical nucleons in hand, we have an alternate way to look at the complete set of  $J$  values  $0 - 2j$ , available in the p–n system. We consider the isospin structure of this system and use the result just obtained. The p–n system can have  $T_z = 1/2 \pm (-1/2) = 0$  or 1 and hence  $T = 0$  or 1. The  $T = 1$  case is identical in all respects to the preceding p–p and n–n  $T = 1$  cases and therefore consists of the even  $J$  values  $0, 2, 4, \dots, (2j - 1)$ . The  $T = 0$  case is antisymmetric in isospin so the space-spin part must be symmetric. By a derivation exactly analogous to that just given, one finds that the  $T = 0$  p–n system contains the odd  $J$  values. Together, the  $T(p-n) = 0 + 1$  parts give all  $j$  values from 0 to  $2j$ . (Note that, for  $j_p \neq j_n$ , each two-particle  $J$  state is now a mixture of  $T = 0$  and  $T = 1$  parts: a total nuclear wave function of good isospin is constructed by coupling this two-particle state to the core.)

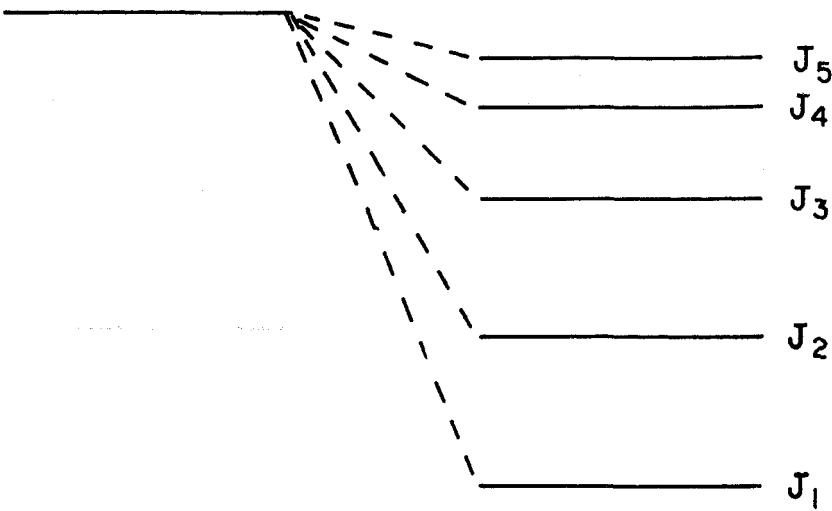
#### 4.1 Residual Interactions: The $\delta$ -Function

We now turn to the energies  $E(j_1 j_2 J)$  of a two-particle configuration of identical nucleons denoted  $|j_1 j_2 JM\rangle$ , in the presence of a residual interaction. We have noted earlier that for any central or scalar interaction, the wave function can be separated into radial and angular parts. Since the radial behavior of the two interacting particles does not differ for different  $J$ , many results are independent of the detailed specification of the radial nature of the interaction. This is certainly true for the ordering and *relative* spacings of different  $J$  states: absolute values, of course, depend on detailed integrations over the radial coordinates and on the strength of the interaction. Even in this case, however, the results for different interactions are roughly similar.

Of course, with no residual interaction, all  $J$  states of the two-particle configuration are degenerate, as shown on the left in Fig. 4.1. In the presence of a residual interaction, the energy *shifts* (Fig. 4.1 right) relative to the degenerate case are given schematically by

$$\Delta E(j_1 j_2 J) = \langle j_1 j_2 J M | V_{12} | j_1 j_2 J M \rangle = \frac{1}{\sqrt{2J+1}} \langle j_1 j_2 J || V_{12} || j_1 j_2 J \rangle \quad (4.3)$$

where the last step utilizes the Wigner-Eckart theorem. Most of the discussion in this chapter centers on the crucial properties of these energy shifts due to the residual interactions. Because of the independence of  $M$ , we shall generally omit the magnetic quantum numbers in the discussion that follows. We have already stated that it is possible to separate the radial and angular coordinates for many residual interactions. To illustrate this, it is useful to consider the simple  $\delta$ -function interaction: by definition, this interaction vanishes unless the particles occupy the same spatial position. The reason for choosing a  $\delta$ -function residual interaction is not simply mathematical convenience. More importantly, it is preeminently a short-range interaction, and we know that the

$|j_1 j_2 J\rangle$ 
 $|j_1 j_2 J\rangle$ 


**Fig. 4.1.** Schematic illustration of the energy shifts in a configuration with particle 1 in orbit  $j_1$  and particle 2 in orbit  $j_2$  coupled to various spins  $J$ .

nuclear force, including residual interactions, has just this character. At least qualitatively, a  $\delta$ -function residual interaction reproduces many observed properties of nuclei.

Moreover, it can be shown that a  $\delta$ -interaction in a  $j^*$  configuration is equivalent to an odd tensor interaction. Such interactions are diagonal (see Chapter 5), in the so-called seniority scheme and as such are particularly useful for treating multiparticle configurations, since many important results reduce to the two-particle case. Thus, a discussion of the  $\delta$ -interaction in  $|j_1 j_2 J\rangle$  configurations has profound implications throughout the study of nuclear structure.

We can write the  $\delta$ -interaction as

$$\begin{aligned} V_{12}(\delta) &= -V_0 \delta(\mathbf{r}_1 - \mathbf{r}_2) \\ &= \frac{-V_0}{r_1 r_2} \delta(r_1 - r_2) \delta(\cos \theta_1 - \cos \theta_2) \delta(\phi_1 - \phi_2) \end{aligned} \quad (4.4)$$

where the second form expresses the interaction in polar coordinates. This is

particularly useful when separating the angular and radial parts. The  $1/r_1 r_2$  factor is necessary because the integration over the angular coordinates introduces a factor  $4\pi r^2$ .

Using the polar coordinate form and performing some straightforward but tedious angular momentum algebra (see de Shalit and Feshbach, Chapter 5) we obtain for the energy shifts in the identical particle configuration  $|j_1 j_2 J\rangle$

$$\Delta E(j_1 j_2 J) = -V_0 F_R(n_1 l_1 n_2 l_2) A(j_1 j_2 J) \quad (4.5)$$

where

$$F_R(n_1 l_1 n_2 l_2) = \frac{1}{4\pi} \int \frac{1}{r^2} R^2_{n_1 l_1}(r) R^2_{n_2 l_2}(r) dr \quad (4.6)$$

and

$$\begin{aligned} A(j_1 j_2 J) &= (2j_1 + 1)(2j_2 + 1) \begin{pmatrix} j_1 & j_2 & J \\ \frac{1}{2} & -\frac{1}{2} & 0 \end{pmatrix}^2 && (\text{if } l_1 + l_2 - J \text{ is even}) \\ &= 0 && (\text{if } l_1 + l_2 - J \text{ is odd}) \\ &&& (\text{Non-equivalent orbits}) \end{aligned} \quad (4.7)$$

$F_R$  depends only on the *radial* coordinates, while the quantity  $A$  results from an integration over the *angular* coordinates.

Therefore, one obtains the extremely important result that the *relative* splittings depend *only* on *universal angular functions*  $A$ , which are totally independent of the nature of the central potential. They are also independent of the principle quantum numbers  $n_1$  and  $n_2$  (except for an overall scale incorporated into the factors  $F_R$ ); for this reason, we shall not specify the  $n$  values unless it is necessary in a particular case. Although Eqs. 4.6–4.7 apply in detail only to a  $\delta$ -function interaction, the general separability into radial and angular parts is valid for *any* residual interaction that depends only on the separation ( $\mathbf{r}_1 - \mathbf{r}_2$ ) of the two nucleons.

We will soon discuss the meaning and implications of Eq. 4.5 at considerable length. First, however, it is useful to give the expression for the specific case of *equivalent* orbits  $l_1 j_1 = l_2 j_2$ . Hence  $l_1 + l_2$  must be even. Moreover, proper normalization of the wave functions introduces a factor of  $1/2$  in the energies that are now given by

$$\Delta E(j^2 J) = -V_0 F_R(n l) A(j J) \quad (J \text{ even}) \quad (4.8)$$

where

$$F_R(n l) = \frac{1}{4\pi} \int \frac{1}{r^2} R^4_{nl}(r) dr \quad (4.9)$$

and

$$A(j^2 J) = \frac{(2j+1)^2}{2} \begin{pmatrix} j & j & J \\ \frac{1}{2} & -\frac{1}{2} & 0 \end{pmatrix}^2 \quad (J \text{ even}) \quad (4.10)$$

(Equivalent orbits)

Note that for  $J = 0$ ,  $A \propto (2j+1)/2$ , so that  $\Delta E(j^2 J=0) = \text{const} (2j+1)/2$ , that is,

the energy lowering of  $0^+$  states is larger for large  $j$  and is in fact proportional to the number of magnetic substates in the orbit  $j$ . This property is identical to that defined for a pairing interaction. Here, its physical basis is that, for high  $j$ , there are more magnetic substates spanning the same angular range of orbit orientations. Hence, the wave function for a given substate is more localized in angle. Two particles with the same  $|m|$  value thus have greater overlap and hence a larger interaction. Similar overlap arguments will help us understand many of the effects of residual interactions. They will be formalized later and will pervade this chapter.

Returning to the general case of any  $j_1, j_2$ , we note that, while the relative energies of individual  $J$  values depend only on the angular structure of the wave functions, the overall *scale* of the interaction and the *average* interaction strength for particles in orbits  $j_1$  and  $j_2$  depend on the radial integral (Eq. 4.6). As we stated in Chapter 3, this will be largest for similar  $n_1 l_1$  and  $n_2 l_2$  values.

Shortly, we will calculate explicit numerical values of  $\Delta E(j_1 j_2 J)$ , or rather, of  $A(j_1 j_2 J)$ . First, however, it will help us understand two-particle configurations and, later, multiparticle situations, if we momentarily ignore the analytic formula and try to understand the basic results for the energies  $\Delta E(j_1 j_2 J)$  from simple physical arguments. It is remarkable how far this will take us.

We start with the obvious statement that the attractive  $\delta$ -function interaction can only be large when there is large spatial overlap between the orbits of the particles. As we have seen, for a given  $j_1$  and  $j_2$ , the overlap for different  $J$  values depends on the *orientation* of the orbits in space. We shall see in Section 4.2 the explicit relation between the  $3-j$  symbols in Eqs. 4.7 and 4.10 and the relative angular orientation of the semiclassical orbit planes. For now, we proceed more qualitatively. From overlap considerations alone, one might think that the interaction would be largest either for  $J=0$  or  $J=J_{\max}$ , which are simply the two cases for which the angular momentum vectors  $j_1$  and  $j_2$  are most nearly antiparallel or parallel, respectively, and therefore those in which the nucleons orbit the nucleus most nearly in the same plane.

While this simple view has an element of truth to it, the requirements of antisymmetrization refine it considerably. Antisymmetrization, or the Pauli principle, has enormous and profound implications throughout the study of nuclear structure. We have seen how it determines the valley of stability, validates the fundamental concept of independent particle motion in a dense sea of nucleons, and gives the magic numbers and attendant shell structure. These (or at least the first and last) are straightforward and obvious effects. Others are subtle, even unexpected, and are certainly seldom appreciated. Our case of two nucleons interacting via a short-range residual interaction is just such a case. We start by considering the configuration of two identical particles (two protons or two neutrons) in orbits  $j_1, j_2$ .

In this case, the two-particle wave function must be totally antisymmetric, that is, antisymmetric in space, spin, and isospin. A careful understanding of this requirement leads to some beautiful, remarkable, and profound results.

Since we are dealing with two identical particles, the states involved must have total  $T_z=1$  and hence  $T=1$ : they are symmetric with respect to the isospin coordinates. Therefore they must be antisymmetric in space and spin coordinates.

Thus far we have carried out the discussion in what is known as a  $jj$  coupling scheme, in which the total angular momentum  $j_1$  of particle 1 is coupled to the total angular momentum  $j_2$  of particle 2 to produce a final total angular momentum  $J$ . One can also think of the problem in terms of the so-called  $LS$  coupling scheme, in which the orbital angular momenta of the two particles  $l_1$ ,  $l_2$  are first coupled to total  $L$  and the intrinsic spins ( $1/2 \hbar$ )  $s_1$  and  $s_2$  are coupled to  $S = 1$  or 0. Generally the  $jj$  coupling scheme is more useful in most nuclear structure applications, but in the present case the  $LS$  coupling scheme separates out the angular and spin coordinates nicely and allows a simpler understanding of the effects of antisymmetrization.

To see how this works, let us take a particular example that gives a simple result. Consider the case of two particles in a  $|d_{5/2} f_{7/2} J\rangle$  configuration as shown in Fig. 4.2. The  $l$  values are  $l_1 = 2$  and  $l_2 = 3$ , respectively, and in both orbits,  $j = l + 1/2$ . The allowed  $J$  values range from 1 to 6. If we picture the vector coupling of  $j_1$  and  $j_2$  to form various  $J$  values, it is clear that the orbital planes of the two particles will overlap the most when  $J = J_{\max}$  and  $J_{\min}$ . We therefore expect one or both of these to be the most affected (lowered) by an attractive short-range interaction. To proceed further, we note that  $J_{\max}$  is greater than  $l_1 + l_2 = 5$ . Therefore, the  $J_{\max}$  state can *only* be formed by aligning the orbital angular momenta to  $L = 5$  and the intrinsic spin angular momenta to  $S = 1$ , and then aligning  $L$  and  $S$  to  $J = 6$ .

Since  $S = 1$ , the two intrinsic spins point in the same direction and thus the spin part of the wave function is symmetric. Therefore, antisymmetrization of the total wave function requires that the spatial part be antisymmetric. Denoting the angular part of the  $i$ th particle wave function by  $\phi_i(\mathbf{r}_i)$ , the requirement of antisymmetrization in the angular coordinates is equivalent to  $\phi_{j_1}(\mathbf{r}_1)\phi_{j_2}(\mathbf{r}_2) = -\phi_{j_2}(\mathbf{r}_1)\phi_{j_1}(\mathbf{r}_2)$ . However, the  $\delta$ -function interaction is only effective when the particles are in contact, when  $\mathbf{r}_1 = \mathbf{r}_2$ . At this point, this expression for the antisymmetrization condition, however, requires that the wave function equal its negative [ $\phi_{j_1}(\mathbf{r})\phi_{j_2}(\mathbf{r}) = -\phi_{j_1}(\mathbf{r})\phi_{j_2}(\mathbf{r})$ ], which of course can only happen if each side vanishes. Therefore the wave function *vanishes* at the *only point in space* where the  $\delta$ -function interaction acts, so the residual interaction has no effect whatsoever in this particular  $J = 6$  state. Turning the argument around, a  $\delta$ -function interaction between identical nucleons can *only affect states through amplitudes* in which  $S = 0$ , in which case the spin part of the wave function is antisymmetric and the spatial part is symmetric and need not vanish at  $|\mathbf{r}_1 - \mathbf{r}_2| = 0$ . Interestingly, although the  $\delta$ -function interaction has no explicit spin dependence, its effects depend critically on the relative orientations of the spins of the two nucleons. In other words, antisymmetrization introduces an implicit spin dependence.

Clearly, to determine which states are affected by a  $\delta$ -interaction we would like to know which have  $S = 0$ . Unfortunately, except for the configuration  $|s^2_{1,2} J=0\rangle$ , where  $S$  obviously must be zero, all two-particle configurations that can have  $S = 0$  amplitudes will also have  $S = 1$  amplitudes. For example, it might be thought that the  $J = 1$  state of the  $|d_{5/2} f_{7/2} J\rangle$  configuration would be pure  $S = 0$  since this state is made by antialigning  $j_1 = 5/2 (l+1/2)$  and  $j_2 = 7/2 (l+1/2)$ . Therefore the two intrinsic spins are also antialigned, giving  $S = 0$ . Though this argument does identify the main component of the configuration, it is a bit

naive: one must be careful of mentally mixing the  $LS$  and  $jj$  schemes. In fact, the  $J = 1$  state can be made in three ways—by coupling  $l_1$  and  $l_2$  to  $L = 1$ , with  $S = 0$  as just stated, but also with the same  $L$  value and vector coupling  $S = 1$  to again give  $J = 1$  and, finally, by coupling  $l_1$  and  $l_2$  to give  $L = 2$  and then antialigning a  $S = 1$  vector to give  $J = 1$ .

In general, the relative amplitudes of  $S = 0$  and  $1$  in a given  $J$  value for the configuration,  $| (l_1 s_1) j_1 (l_2 s_2) j_2; JM \rangle$  are given by the  $9-j$  symbol

$$\left\{ \begin{array}{c} l_1 \frac{1}{2} j_1 \\ l_2 \frac{1}{2} j_2 \\ L S J \end{array} \right\}$$

Returning to the issue of determining which state is most affected by a  $\delta$ -interaction without actually carrying out the calculation of Eqs. 4.7 or 4.10, there are three practical methods. All depend on the fact that the  $J_{\min}$  and  $J_{\max}$  states are most nearly coplanar, and therefore one of these will be the most lowered, while the other is unaffected. Determining either, then, answers the question.

The most straightforward approach is the one we have just used in the  $|d_{5/2} f_{7/2} J\rangle$  case, namely to look for a state that is pure  $S = 1$ : this state will be unaffected, as we have seen.

There will be such a state (either  $J_{\min}$  or  $J_{\max}$ ) with pure  $S = 1$  only when there is an allowed  $J$  value that is greater than  $(l_1 + l_2)$  or less than  $(l_1 - l_2)$ . This occurs, for example, for  $J = 6$  in  $|d_{5/2} f_{7/2} J\rangle$ , or  $J = 1$  in  $|d_{5/2} g_{7/2} J\rangle$  where  $L_{\min} = 2$  (see Fig. 4.2), for  $J = 8$  in  $|d_{5/2} h_{11/2} J\rangle$ , but not for any state in  $|g_{7/2} h_{11/2} J\rangle$  or for the allowed (even)  $J$  values in any configuration of the type  $|j^2 J\rangle$ . A useful rule is that a state with pure  $S = 1$  always exists if  $j_1 \neq j_2$  and  $j_{\text{lower}}$  is  $l + 1/2$ .

When no such state exists, a second method uses the fact that a  $\delta$ -interaction only affects half of the states in a multiplet; either those with even  $J$  or those with odd  $J$ . We have seen an example of this in the  $|d_{5/2} f_{7/2} J\rangle$  configuration where the  $J'' = 6^-$  level is unaffected, and the  $1^-$  level is lowered the most. In contrast, in the  $|d_{5/2} g_{7/2} J\rangle$  configuration,  $J_{\min}$  again equals 1. But here  $L_{\min} = |l_1 - l_2| = 2$  and therefore the  $1^+$  state can only be found by antialigning  $S = 1$  to  $L = 2$ . Thus, here it is the  $1^+$  state that is unaffected, while the  $6^+$  state is lowered the most. These two cases are just examples of the general rule that for positive parity configurations only even  $J$  levels are lowered, while for negative parity only odd  $J$  levels are lowered. This rule is clear from the restrictions on the right in Eq. 4.7: for positive parity  $l_1 + l_2$  is even, so  $l_1 + l_2 - J$  is even only for  $J$  even and vice versa for negative parity. We use this rule, which arises simply from the parity of the interaction matrix elements that involve the spherical harmonics  $Y_L''(\theta)$  where  $\theta$  is the angle between the orbital planes (see Section 4.2), as follows. For any  $j_1 j_2$ , one of  $J_{\min}$  or  $J_{\max}$  will be odd and the other even. That state that falls into the class of states affected by the interaction will be lowered the most, and the others in the same class successively less so as their  $J$  values deviate more from  $J_{\max}$  or  $J_{\min}$ . Let us consider a couple of examples. Starting with the familiar  $|d_{5/2} f_{7/2} J\rangle$  case,  $J_{\min}$  and  $J_{\max}$  are 1 and 6, the parity is negative and thus only the odd  $J$  states will be

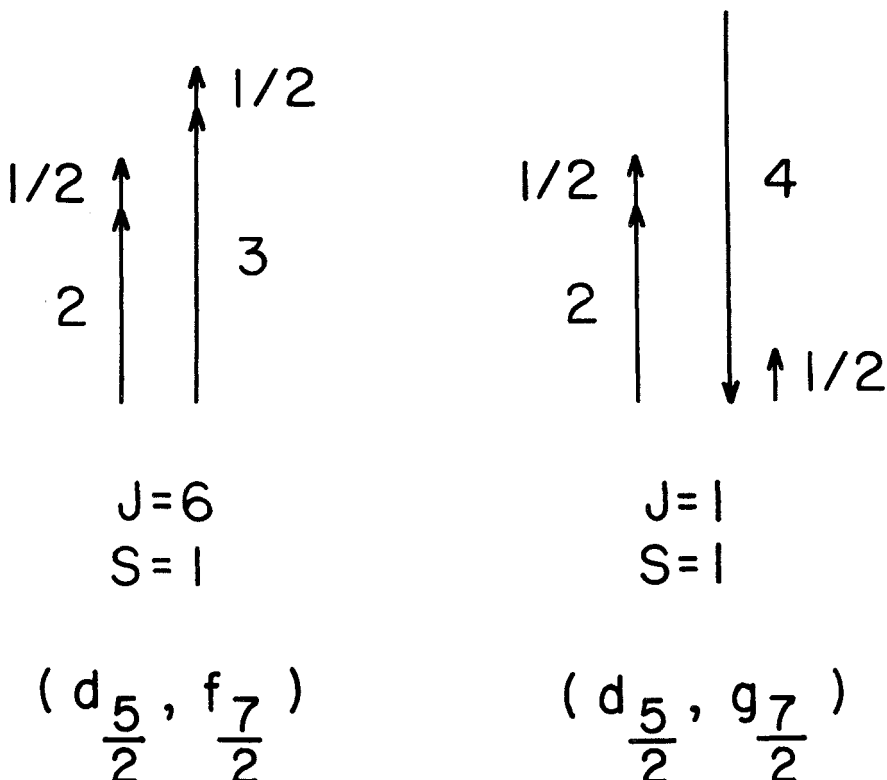


**Fig. 4.2.** Semi-classical illustration of the coupling of intrinsic spins and orbital angular momenta for two configurations  $(d_{5/2} f_{7/2})$  and  $(d_{5/2} g_{7/2})$

affected, that is  $J^\pi = 1^-, 3^-, 5^-$ . Therefore the  $J = 1^-$  state is lowered the most, the  $J = 3^-, 5^-$  states successively less so, and the  $J = 2^-, 4^-$  and  $6^-$  states not at all. For the  $|d_{5/2} g_{7/2} J\rangle$  configuration,  $J_{\min} = 1$ ,  $J_{\max} = 6$ , as before but here  $\pi = +$  so that  $J = 6$  is lowered the most and the order is (from lowest to highest)  $6^+, 4^+, 2^+$  ( $1^+, 3^+, 5^+$  degenerate at the unperturbed position). Finally, for  $|g_{7/2} h_{11/2} J\rangle$ ,  $J_{\min} = 2$ ,  $J_{\max} = 9$ ,  $\pi = -$ , and so the order (again, lowest to highest) is  $9^-, 7^-, 5^-, 3^-$  (with  $2^-, 4^-, 6^-, 8^-$  unperturbed). We note an interesting point, namely that, just as with  $S$  values, although the  $\delta$ -function has no explicit parity dependence, the resulting energies of states  $|j_1 j_2 J\rangle$  are, in fact, different for the two different parities.

Although no states (other than  $|s^2_{1/2} J = 0\rangle$ ) have pure  $S = 0$ , a third method, which is formally incorrect, emphasizes the  $jj$  coupling picture and does always give the right answer. To illustrate this procedure, in  $|g_{7/2} h_{11/2} J\rangle$ , all states  $J = 2$  to 9 can be formed with  $S = 0$  or 1. The naive argument would say that, since  $j_1 = l_1 - 1/2$  and  $j_2 = l_2 + 1/2$ , the  $J_{\min} = 2$  state formed by antialigning  $j_1$  and  $j_2$  would correspond to  $S = 1$  and therefore be unaffected by a  $\delta$ -interaction. The same argumentation would imply that the  $J_{\max} = 9$  state is  $S = 0$ , and therefore would be lowered the most.

This approach can be used for equivalent orbit cases to obtain a very important result. Consider a configuration  $|j^2J\rangle$  such as  $|(\text{f}_{7/2})^2J\rangle$ . The  $j$  value corresponds to  $l + 1/2$ , and therefore the antialigned  $J_{\min}$  state,  $J = 0$ , should have  $S = 0$  and be most affected. Again, although the argument is not really correct, the result is. Since the overlaps of the particle orbits are reduced with increasing  $J$ , the excitation energies increase monotonically with  $J$ . Note that the same result applies for any case of identical particles in equivalent orbits: the  $J^\pi = 0^+$  state will always lie lowest. Note also that, in this respect, the  $\delta$ -function interaction resembles the well-known effects of the pairing force that is designed (defined, actually) to lower states in which pairs of identical particles are coupled to spin 0. As pointed out just after Eq. 4.10, and as seen in the upper panels in Fig. 4.3, this effect of the  $\delta$ -interaction in  $|j^2J\rangle$  configuration is greater for higher  $j$  (proportional to  $(2j + 1)$ ).

This lowering of the  $0^+$  state is an extremely important result. Ultimately, it is the underlying reason why all even–even nuclei have  $0^+$  ground states and, often, large spacings to the  $2^+_1$  level. It directly explains this result only for nuclei two nucleons away from closed shells. However, we shall see in Chapter 5 that our two-particle result can be generalized to  $j^n$  configurations, and by extension, to wave functions that are linear combinations of several  $j_i^n$  configurations. Further generalizations to vibrational excitations and deformed nuclei will be seen in later chapters.

There is an easy geometrical way of viewing this case of identical nucleons in equivalent orbits that provides a physical rationale for the lowering of the  $0^+$  states. Intuitively, it might seem that the overlap of the two particles in the  $J_{\min}$  and  $J_{\max}$  states would be comparable: the two orbits are essentially coplanar in both cases. Once again, however, the Pauli principle plays a key role in distinguishing these situations. We show a schematic illustration in Fig. 4.4. In the  $J = J_{\max}$  state, the near alignment of the two  $j$  values implies nearly coplanar orbits in which the two particles orbit in the same direction. The Pauli principle, however, forbids contact. In effect, this means that the two particles must repel each other at short distances: therefore they track each other around the nucleus on opposite sides of an orbit so that they always remain apart. Thus, there can be no  $\delta$ -function interaction between them. For  $J^\pi = 0^+$ , the orbits once again are coplanar but now the two particles orbit in opposite senses. As they do so, their separation will vary but the average separation will clearly be much less than in the  $J_{\max}$  state, “contact” situations occur, and a large  $\delta$ -function interaction results. The actual values of  $A(j_1 j_2 J)$  for a number of different spin combinations are summarized in Table 4.1, and Fig. 4.3 shows several examples (including those used most often in the preceding discussion) of  $\Delta E(j_1 j_2 J)$  values under the influence of a  $\delta$ -function interaction. In studying Table 4.1, recall that the interactions are attractive so that larger values of  $A(j_1 j_2 J)$  correspond to lower-lying levels. Perusal of the table and figure shows that the preceding rules are always satisfied.

It is possible to summarize these results succinctly, as is done in Table 4.2. (The trigonometric functions in column 6 of Table 4.2 will be explained in Section 4.2.) To illustrate the construction of the table, let us consider the top row. A little thought, or working out a few examples of the preceding rules,

MULTIPLLET SPLITTINGS;  $\delta$  INTERACTION (Identical Particles)

77

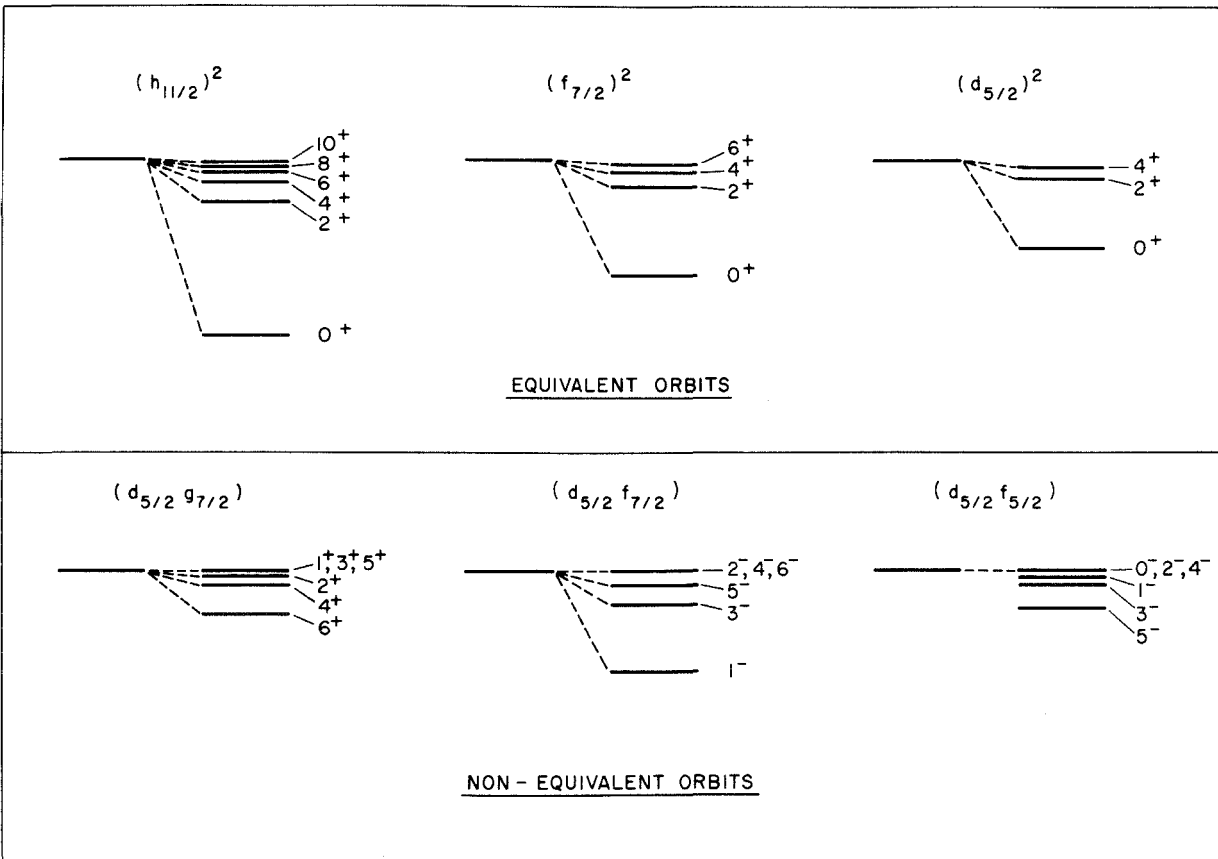
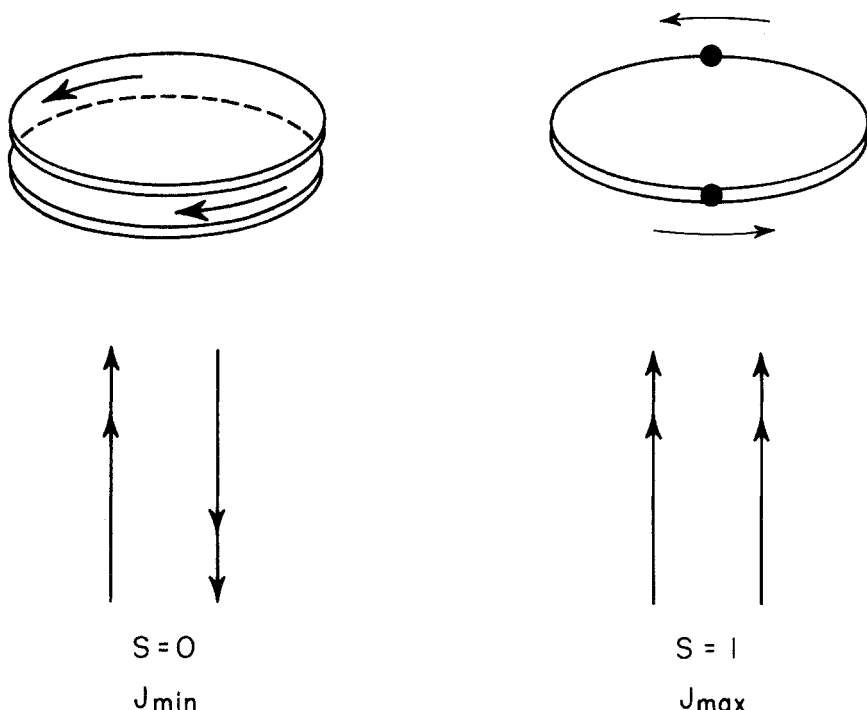


Fig. 4.3. Energy shifts for a  $\delta$ -function residual interaction for identical nucleons in several different orbit combinations.



### IDENTICAL NUCLEONS EQUIVALENT ORBITS

**Fig. 4.4.** Pictorial illustration of the motions of two identical nucleons in equivalent orbits for the cases of maximum and minimum total spin  $J$ , showing the effects of the Pauli principle.

will convince the reader that, for positive parity, the state most affected will be  $J_{\min}$  if  $(j_1 - j_2)$  is even (as in  $|d_{5/2} g_{9/2} J\rangle$ ). Note that even values of  $(j_1 - j_2)$  are equivalent to odd values of  $(j_1 + j_2)$ . Moreover, since only even  $J$  states are affected for positive parity states, odd values of  $(j_1 + j_2)$  are the same as odd values of  $(j_1 + j_2 + J)$ . The consistent element in the table is that, if  $j_1 + j_2 + J$  is odd (even) for the affected states, then the lowest-lying state will be  $J_{\min} = |j_1 - j_2|$  ( $J_{\max} = j_1 + j_2$ ). We will encounter the important role of the quantity  $j_1 + j_2 + J$  later in dealing with interactions in p-n multiplets.

To illustrate how these ideas relate to empirical data on nuclei with two valence nucleons, we recall Fig. 2.5, which showed the yrast states for the typical shell model nuclei  $^{210}\text{Po}$ ,  $^{210}\text{Pb}$ , and  $^{134}\text{Te}$ . We repeat those data here in Fig. 4.5, along with the predictions for a  $\delta$ -interaction normalized to the  $E_{2+1}^+$  energy for the relevant configuration [ $(h_{9/2})^2$  for  $^{210}\text{Po}$ ,  $(g_{9/2})^2$  for  $^{210}\text{Pb}$  (these two cases are actually identical as seen in Eq. 4.10), and  $(f_{7/2})^2$  for  $^{134}\text{Te}$ .] The agreement is quite good. Note the strong lowering of the  $0^+$  ground state. From data such as this, known for many nuclei, it is possible to estimate the absolute strength of the interaction. One obtains, as a rough guideline, that  $\Delta E(j_1 j_2 J) \sim (30 \text{ MeV}/A) A(j_1 j_2 J)$ , where the  $A$  in the denominator is the

**Table 4.1.** Relative  $J$  state energy values for various identical two-particle configurations  $|j_1 j_2 J\rangle$  with an attractive  $\delta$ -interaction.\*

$j_1$	$j_2$	$(lj)_1$	$(lj)_2$	$\pi$	J											
					0	1	2	3	4	5	6	7	8	9	10	11
5/2	5/2	$d_{s2}$	$d_{s2}$													
		$f_{s2}$	$f_{s2}$	+	3.00	—	0.685	—	0.286	—	—	—	—	—	—	—
		$d_{s2}$	$f_{s2}$	—	0	0.173	0	0.457	0	1.29	—	—	—	—	—	—
	7/2	$g_{7/2}$	$g_{7/2}$													
		$f_{7/2}$	$f_{7/2}$	+	4.00	—	0.95	—	0.467	—	0.233	—	—	—	—	—
		$g_{7/2}$	$f_{7/2}$	—	0	0.127	0	0.312	0	0.599	0	1.52	—	—	—	—
11/2	11/2	$h_{11/2}$	$h_{11/2}$													
		$i_{11/2}$	$i_{11/2}$	+	6.00	—	1.47	—	0.785	—	0.493	—	0.318	—	0.180	—
		$h_{11/2}$	$i_{11/2}$	—	0	0.084	0	0.196	0	0.329	0	0.509	0	0.818	0	1.89
	3/2	$d_{3/2}$	$d_{s2}$													
		$p_{3/2}$	$f_{s2}$	+	—	0	0.343	0	1.14	—	—	—	—	—	—	—
		$d_{3/2}$	$f_{s2}$	—	—	2.4	0	0.686	0	—	—	—	—	—	—	—
5/2	7/2	$d_{s2}$	$g_{7/2}$													
		$f_{7/2}$	$f_{7/2}$	+	—	0	0.230	0	0.518	0	1.40	—	—	—	—	—
		$d_{s2}$	$f_{7/2}$	—	—	3.41	0	1.14	0	0.518	0	—	—	—	—	—
	5/2	$f_{s2}$	$g_{7/2}$													
		$d_{s2}$	$g_{9/2}$	+	—	—	2.85	0	1.04	0	0.490	0	—	—	—	—
		$f_{s2}$	$h_{9/2}$	—	—	—	0	0.258	0	0.558	0	1.47	—	—	—	—
5/2	9/2	$d_{s2}$	$g_{9/2}$													
		$f_{s2}$	$h_{9/2}$	+	—	—	0	0.258	0	0.558	0	1.47	—	—	—	—
	9/2	$d_{s2}$	$f_{s2}$	—	—	—	0	0.258	0	0.558	0	1.47	—	—	—	—
		$f_{s2}$	$g_{9/2}$													
5/2	11/2	$d_{s2}$	$i_{11/2}$													
		$f_{s2}$	$h_{11/2}$	+	—	—	—	0	0.279	0	0.587	0	1.52	—	—	—
	11/2	$d_{s2}$	$h_{11/2}$	—	—	—	2.65	0	0.979	0	0.470	0	—	—	—	—
		$f_{s2}$	$i_{11/2}$													

\*The table gives values of  $A(j_1 j_2 J)$  from Eqs. 4.7 and 4.10. Dashes indicate  $J$  values not allowed for the given configuration. States that are unaffected by the interaction (i.e.,  $J$  even for  $\pi = -$ ,  $J$  odd for  $\pi = +$  configurations) are given a value of 0. Other numbers are proportional to the decrease in energy of the state  $J$ .

**Table 4.2.** Rules for the effects of a  $\delta$ -function interaction on two-particle identical nucleon configurations

Parity	Configuration Category		States Affected	Lowest State	Semi-classical dependence on $\theta^*$
	$j_1 + j_2$	$j_1 + j_2 + J$			
Positive	odd	odd	even $J$	$J_{\min}$	$\tan \theta/2$
Negative	even	odd	odd $J$	(antialigned)	
Positive	even	even	even $J$	$J_{\max}$	$\cot \theta/2$
Negative	odd	even	odd $J$	(aligned)	

$$*\theta \text{ is defined by } j_1, j_2, J \text{ as } \theta = \cos^{-1} \left[ \frac{\mathbf{j}_1^2 - \mathbf{j}_1 \cdot \mathbf{j}_2 - \mathbf{j}_2^2}{2|\mathbf{j}_1||\mathbf{j}_2|} \right] = \cos^{-1} \left[ \frac{J(J+1) - j_1(j_1+1) - j_2(j_2+1)}{2\sqrt{j_1(j_1+1)}\sqrt{j_2(j_2+1)}} \right]$$

mass number. Recalling that  $A(J^2 J=0) = (2j+1)/2$ , this gives a typical lowering of the ground state of several MeV in light nuclei and of 1 to 1.5 MeV in heavy nuclei where the interaction strength is only  $\sim 200$  keV. Both of these are well-known features of the data (e.g., Figs. 2.6–2.10), and again show that a  $\delta$ -function naturally produces the famous “energy gap” in even–even nuclei usually associated with the pairing force (see the following).

In all these examples, there is another important feature we have not yet commented on: the lowest level for a given multiplet is substantially lowered, but the *differences* in interaction strength for the others monotonically de-

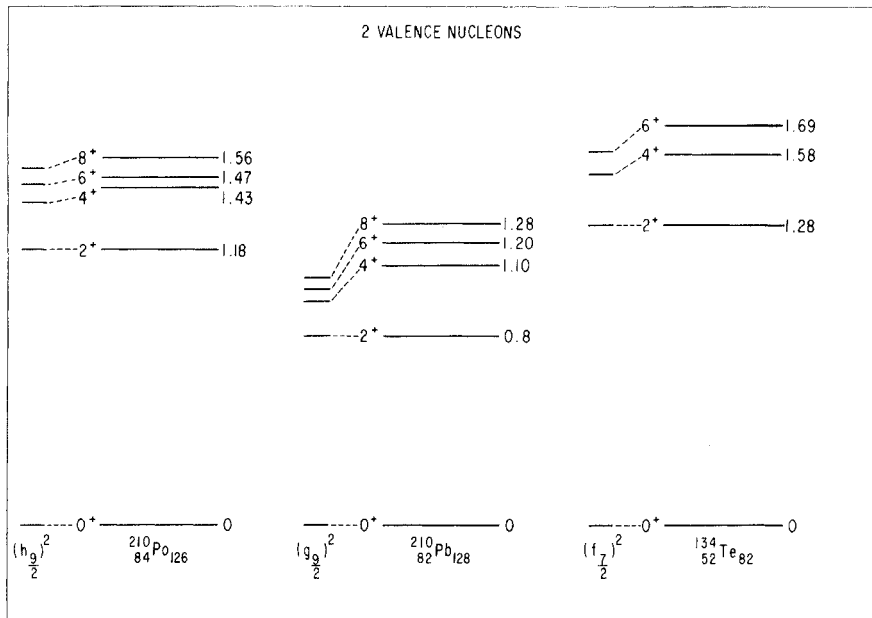


**Fig. 4.5.** Comparison of experimental and calculated low-lying even spin (yrast) states in three nuclei with two valence nucleons. The orbits used for the two identical nucleons are indicated in each case.

crease. That is, there is a relative compression of levels near the *unperturbed* position. This is not just an accident of the  $3-j$  symbols, but has a simple physical origin that we shall discuss shortly. As we noted in Fig. 2.5 and, here in Fig. 4.5 for the case of  $j_1 = j_2$ , it is also a well-known empirical effect characteristic of the low levels of many “shell model” nuclei.

We have been discussing the effects of a  $\delta$ -interaction between identical nucleons. Such states have  $t_z(1) = t_z(2)$ , hence  $T_z = \pm 1$ , and  $T = 1$ . The proton–neutron system also exists in a  $T = 1$  state. By charge independence of the non-Coulomb part of the nuclear force, the p–n  $T = 1$  system must then also satisfy Eqs. 4.5–4.7. Indeed, the familiar statement of charge independence that p–p, n–n, and n–p forces are equal applies specifically (and only) to the  $T = 1$  mode for the p–n system.

As we have seen, however, the p–n system can also exist in a  $T = 0$  state for which there is no need for equality to the p–p or n–n forces. Empirically, in fact, the  $T = 0$  interaction seems to be significantly stronger than the  $T = 1$  (see the following). This  $T = 0$  coupling is extremely important in nuclear structure, as it is now thought to be responsible for single-particle configuration mixing and the onset of collectivity, phase transitions, and deformations. We shall return to these points in later chapters. For now, we are interested in simple two-particle p–n configurations in shell model (noncollective, nondeformed) nuclei under the action of a  $\delta$ -interaction.

In order to address this issue, we must deal with a specific complication that arises in the p–n system. Suppose we imagine such a system occupying levels  $a$  and  $b$  as shown on the left in Fig. 4.6a. Then, if we treat the proton and neutron as two states of the same particle (the nucleon), the orbits or the charges call be exchanged indistinguishably. Thus, the wavefunction for the

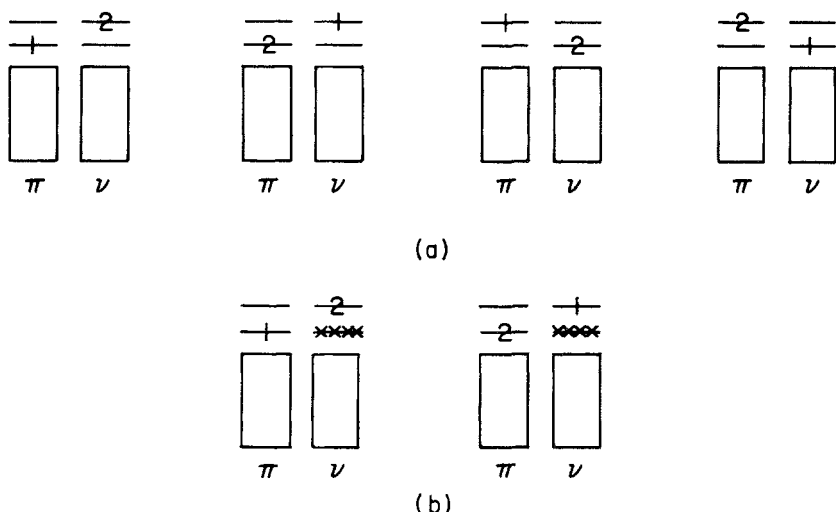


**Fig. 4.6.** “Direct” and “exchange” configurations for protons and neutrons treated as indistinguishable particles (a) filling the same shell, and (b) where the neutron shell corresponding to the valence protons is already filled.

two-particle system will have components of all the types illustrated. An interaction matrix element will then contain, for example,

$$\begin{aligned} & \langle \phi_1^a(p) \phi_2^b(n) | V_{12} | \alpha \phi_1^a(p) \phi_2^b(n) + \beta \phi_1^b(n) \phi_2^a(p) \\ & + \gamma \phi_1^b(p) \phi_2^a(n) + \delta \phi_1^a(n) \phi_2^b(p) \rangle \end{aligned} \quad (4.11)$$

The four terms on the right correspond to the four cases of particles 1 and 2, each occupying levels a or b, and each identified as either a proton or a neutron. The term in  $\alpha$  in Eq. 4.11 is a *direct* term that should be relatively large since the overlap of the wave functions on the two sides is unity. The last term keeps the particles in the same orbits (1 in a, 2 in b) as on the left side but exchanges their type ( $p \rightarrow n, n \rightarrow p$ ). This can also be large if the interaction contains terms that can change a proton into a neutron and vice versa. The second and third terms involve overlaps in which the particles change orbits: therefore they are normally small. In principle, however, all must be taken into account. Clearly, this is both complicated and tedious. The isospin formalism for doing so is well known and is discussed in standard texts, so we will not consider this situation. Here we are largely concerned with medium and heavy nuclei, which greatly simplifies the problem since protons and neutrons are usually filling different major shells. This situation is illustrated in Fig. 4.6b, where the neutron shell corresponding to the proton shell is already filled: hence, exchange matrix elements such as those in the  $\gamma$  and  $\delta$  terms in Eq. 4.11 (the rightmost two terms in Fig. 4.6a) are impossible ("blocked"), since the neutron orbits in that shell are filled. The only remaining exchange term is one of those expected to be small. We can consider only the direct term to good approximation in such a case. This is equivalent to treating the protons and neutrons as *distinguishable particles*. Note that, while we can choose to do so in this case, because of the blocking of exchange terms, it is not mandatory: we could (and will momentarily) use the isospin formalism as well. The proton-neutron and isospin formalisms are equivalent ways of obtaining the same result. Which one is used in a given case is a choice based on practical simplicity. When exchange effects are known, *a priori*, to be inconsequential, the proton-neutron formalism may be simpler.

In the present case, treating the protons and neutrons as distinguishable means that the Pauli principle places no restrictions on their coupling. Their wave functions need not be antisymmetrized. We can write the two-particle p-n wave function as  $\psi_{pn} = \phi_p \phi_n$ . To see the relation to the isospin approach, this can be rewritten as  $\psi_{pn} = 1/2[(\phi_p \phi_n + \phi_n \phi_p) + (\phi_p \phi_n - \phi_n \phi_p)]$ . The first term is symmetric with respect to interchange of protons and neutrons, the second antisymmetric. These two terms therefore correspond to  $T = 1$  and  $T = 0$ , respectively, and the energy shifts in the presence of a residual interaction can be written as the average of their values in the two isospin channels, that is, as  $1/2[\Delta E(T = 1) + \Delta E(T = 0)]$ . In the like-nucleon case, antisymmetrization requires that the  $S = 1$  (symmetric) spin coupling be accompanied by an antisymmetric spatial part of the wave function (which vanishes when the two particles are in contact): such states do not feel the  $\delta$ -interaction. Here, there is no such limitation. Both  $S = 0$  and  $S = 1$  states can be accompanied by

symmetric spatial wave functions and will be shifted by the interaction. Generally, the interaction need not be of the same strength in the two cases, and so we specify two interaction strengths  $V_{S=0}$  and  $V_{S=1}$

$$V_{12} = (V_{S=0} + V_{S=1}) \delta(|\mathbf{r}_1 - \mathbf{r}_2|) \quad (4.12)$$

where it is implicit that the  $V_{S=0}$  ( $V_{S=1}$ ) term acts only on the  $S = 0$  ( $S = 1$ ) components.

We can get the same result in terms of isospin. We saw before that the unsymmetrized two-particle wave function can be written in terms of an average over  $T = 1$  and  $T = 0$  parts. In this case, the wave function for each isospin term must be separately antisymmetric. Specifying to a  $\delta$ -function interaction, the only states affected must have symmetric spatial wave functions. Therefore, the isospin-spin part must be antisymmetric: hence, the  $T = 0$  part goes with  $S = 1$  and the  $T = 1$  with  $S = 0$ . Again, we get  $S = 0$  and 1 terms as in Eq. 4.12. (Recall that the total nuclear wave function must have good isospin, which is obtained by coupling the isospin of the two-particle system to that of the ( $T \neq 0$ ) core.)

Thus, the analogues of Eqs. 4.5–4.7 for a p–n system under the action of a  $\delta$ -interaction given by Eq. 4.12 become:

$$\Delta E(j_p j_n J) = F_R(n_p l_p n_n l_n) A(j_p j_n J) \quad (4.13)$$

where

$$F_R(n_p l_p n_n l_n) = \frac{1}{8\pi} \int \frac{1}{r^2} R_{n_p l_p}^2(r) R_{n_n l_n}^2(r) dr \quad (4.14)$$

and

$$A(j_p j_n J) = (2j_p + 1)(2j_n + 1) \left\{ \begin{array}{c} j_p \quad j_n \quad J \\ \frac{1}{2} \quad -\frac{1}{2} \quad 0 \end{array} \right\}^2 \left\{ \begin{array}{l} V_{S=0} \frac{(1 + (-1)^{l_p + l_n + J})}{2} \\ + V_{S=1} \left[ \frac{\left(1 - (-1)^{l_p + l_n + J}\right)}{2} + \frac{\left[(2j_p + 1) + (-1)^{l_p + j_n + J}(2j_n + 1)\right]^2}{4J(J+1)} \right] \end{array} \right\} \quad (4.15)$$

The  $3-j$  symbol is identical to that appearing in the like-nucleon case, but now there are two terms with different  $J, j_p, j_n$  dependencies. Note that, in the first, or  $V_{S=0}$ , term in Eq. 4.15, only half of the levels are affected, namely those with even  $J$  for positive parity or with odd  $J$  for negative parity. This is the same condition we saw for like nucleons, as it must be since this is the  $S = 0$  ( $T = 1$ ) term. The other  $J$  values are then affected by the first of the  $V_{S=1}$  terms. For  $j_p \neq j_n$ , the second  $V_{S=1}$  term itself affects all  $J$  values, and small  $J$  values the most.

As in the like-nucleon case, this equation simplifies for equivalent orbits ( $j_p^\pi = j_n^\pi = j$ ) to

$$\Delta E(j j J) = F_R(n l) (2j+1)^2 \left\{ \begin{array}{c} j \quad j \quad J \\ \frac{1}{2} \quad -\frac{1}{2} \quad 0 \end{array} \right\}^2 \times \left[ V_{S=0} \delta_{J,\text{even}} + V_{S=1} \delta_{J,\text{odd}} \frac{(2j+1)^2}{4J(J+1)} \right] \quad (4.16)$$

Here we can easily see the explicit relation to the isospin formalism. The  $T = 1$  p–n interaction must be identical to the p–p and n–n interactions. We saw earlier that, for equivalent orbits, only even  $J$  states are allowed for the  $T = 1$  p–p and n–n systems, and hence, for a p–n system, which has all  $J$  values from 0 to  $2j$ , the even  $J$  values must have  $T = 1$  and the remaining levels, namely those with odd  $J$ , must be  $T = 0$ . Thus, in Eq. 4.16, the first term corresponds to the interaction in the  $T = 1$  channel and the second term to the  $T = 0$  channel.

We now need to consider the relative strengths  $V_{S=0}$  and  $V_{S=1}$ . From the fact that the deuteron has an  $S = 1$  ground state, it is clear that  $V_{S=1}$  is stronger than  $V_{S=0}$ . However, there is additional evidence for this from such simple data as neutron separation energies that is directly applicable to nuclei with all  $A$  values. As we have just seen (Eq. 4.16) the  $T = 1$  and 0 interactions can be associated with the  $S = 0$  and 1 terms, respectively. We saw in Chapter 1 from the separation energy data that the nonpairing, like-nucleon ( $T = 1$ ) residual interaction is, on average, repulsive, where by the phrase “on average” we mean averaged over all final  $J$  states and by “nonpairing” we mean excluding the  $0^+$  state (if any). So, by charge independence, the p–n  $T = 1$  interaction must on average also be repulsive. Yet, we also noted in Chapter 1 that both  $S(p)$  and  $S(n)$  increase with increasing numbers of particles of the *opposite* type. The interaction between protons and neutrons has both  $T = 0$  and  $T = 1$  components. So, on balance, the total ( $T = 0 + T = 1$ ) p–n interaction must be attractive. This can only occur if the  $T = 0$  component is both *attractive* and *stronger* than the  $T = 1$ , that is, if the  $|V_{S=1}|$  is greater than  $|V_{S=0}|$ .

Of course, the strength of the two isospin components of the interaction can also be obtained by fitting actual p–n multiplets (groups of states with pure proton and neutron configurations  $j_p$  and  $j_n$  and  $J$  values ranging from  $|j_p - j_n|$  to  $j_p + j_n$ ). Schiffer and True and Molinari and co-workers have carried out extensive surveys of this type near all closed shells from  $^{160}$ O to  $^{208}$ Pb. We will discuss their results in Section 4.2 in terms of a simple geometrical analysis. Here it is useful to convey a feeling as to how the data on individual isospins can be deduced. The nuclei near  $^{208}$ Pb offer a nice example. Consider, for example, the states of  $^{210}_{84}\text{Po}_{126}$  in a  $|1\text{h}_{9/2}1\text{l}_{13/2}J\rangle$  two-proton  $T = 1$  multiplet. (These can be found from the  $^{209}\text{Bi}(^3\text{He}, d)^{210}\text{Po}$  reaction since  $^{209}\text{Bi}$  has a single proton in the  $1\text{h}_{9/2}$  orbit.) The energy shifts in this multiplet can be used to extract the  $(1\text{h}_{9/2}1\text{l}_{13/2})T = 1$  interaction. The same multiplet exists in  $^{208}_{83}\text{Bi}_{125}$  as a particle–hole p–n multiplet. The energy shifts  $\Delta E(j_p j_n J)$  can be converted (see end of chapter) to an equivalent set of particle–particle shifts and the total p–n interaction obtained for each  $J$  state. The difference of the  $T = 1$  and total interactions then yields the net  $T = 0$  strengths. Extraction of  $T = 1$  and  $T = 0$  strengths is even simpler in the case of equivalent orbits ( $j_p = j_n$ ), of course, where the even and odd  $J$  states directly give the  $T = 1$  and 0 interactions, respectively. This approach is useful in light nuclei where the protons and neutrons are filling identical orbits (e.g., the  $f_{7/2}$  orbit in  $^{42}\text{Sc}$ ).

To illustrate the application of these ideas, we consider the classic example of  $^{38}_{17}\text{Cl}_{21}$ . Since the  $N = 8$  to 20 neutron shell is filled, this is an appropriate case to ignore exchange terms. In the lowest-lying states, the configuration is  $(d_{3/2,p}f_{7/2,n})$  giving states  $J = 2^-, 3^-, 4^-, \text{ and } 5^-$ . Since  $V_{S=1} > V_{S=0}$ , the second group

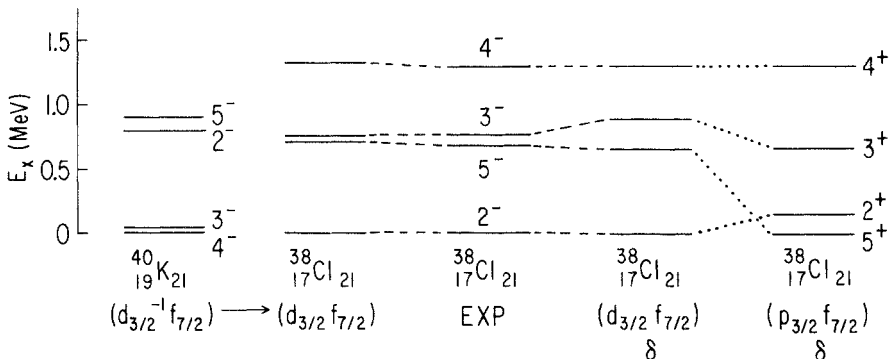


**Fig. 4.7.** Comparison of low-lying empirical and calculated energies for  $^{38}\text{Cl}$ . The two panels on the right correspond to calculations with a two-body  $\delta$ -function residual interaction, assuming two different orbits for the proton. Clearly, the  $(d_{3/2}^- f_{7/2})$  configuration is favored. The calculation on the left uses the empirical levels of the  $(d_{3/2}^- f_{7/2})$  particle-hole configuration in  $^{40}\text{K}$  in conjunction with Eq. 4.34 to predict the particle-particle levels of  $^{38}\text{Cl}$ . (See deShalit, 1974.)

of terms in Eq. 4.15 will generally dominate and the overall ordering of levels in the p-n system will tend to be contrary to that in the like nucleon case. Moreover, whereas only half the states are affected for like nucleons ( $J$  odd for  $\pi = -$ ;  $J$  even for  $\pi = +$ ), all states will be shifted in the p-n case. We therefore may expect the lowest level to be the even  $J$  state with highest overlap, the  $J = 2^-$  level. The  $^{38}\text{Cl}$  experimental spectrum and that calculated with  $V_{S=1} = 2V_{S=0}$  are shown on the right in Fig. 4.7. (The part on the left describes an alternate approach to calculating  $^{38}\text{Cl}$ , to be discussed near the end of this chapter.) The  $2^-$  level does in fact occur lowest, and the agreement is reasonable. The figure also shows that the calculated levels for an alternate configuration with the same  $j$  values,  $(p_{3/2}, f_{7/2})$ , have a rather different pattern since, here, the orbital phase factors in Eq. 4.15 are different ( $l_p + l_n$  is now even) and the  $J = 5, 3$  set is lowered relative to the  $J = 2, 4$  pair in disagreement with the data. This indicates how one can even sometimes suggest  $j$  configurations and  $J''$  values by examining energy sequences and spacings in p-n multiplets.

## 4.2 Geometrical Interpretation

Having dealt extensively now with both like and unlike two-particle configurations under the influence of a  $\delta$ -function interaction, we have gained a feeling for the physics behind the analytic results that can be obtained. The physics revolves around the overlaps of the two-particle wave functions. It is possible to approach this entire subject from an alternate viewpoint and actually derive the typical behavior of the 3- $j$  symbol in Eqs. 4.7, 4.15, and 4.16 from a simple geometrical analysis, which will give us additional insight into the interactions in two-particle configurations.

We commented earlier that the characteristic and typical behavior of that  $3 - j$  symbol is a gradual reduction in the spacings as the excitation energy increases (as the interaction weakens). This is not one of those annoying

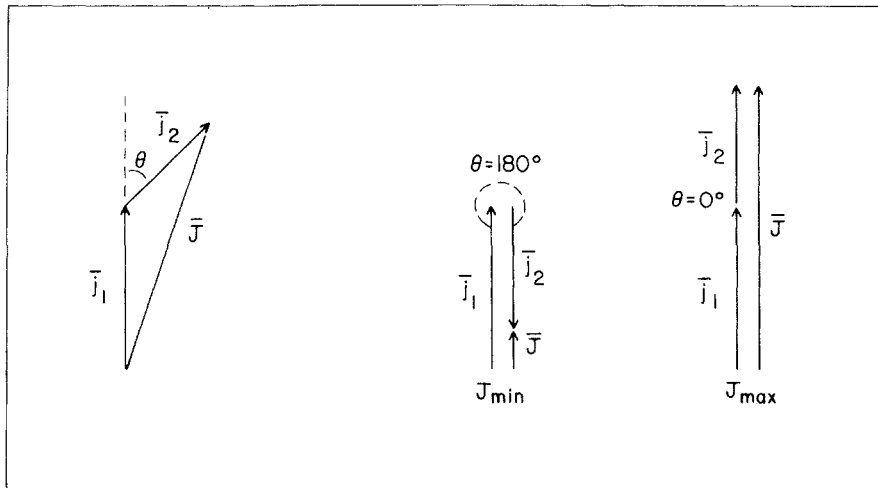


**Fig. 4.8.** Definition and schematic illustration of some of the ideas used in the geometrical analysis of short-range residual interactions.

“accidental” effects of Clebsch-Gordon coefficients that plague many students, but rather it has a very simple physical origin. In pursuing this we will better understand why this  $3-j$  symbol behaves as it does. Moreover, we will see that the energies  $\Delta E(j_1 j_2 J)$  exhibit the same basic pattern for any  $j_1 j_2$  and that this pattern simply reflects the spatial overlaps of the particles and Pauli principle effects.

We start with the semiclassical concept of the angle,  $\theta$ , between the angular momentum vectors  $\mathbf{j}_1$  and  $\mathbf{j}_2$  (hence between the orbital planes) of the two particles as illustrated schematically in Fig. 4.8. Then

$$\mathbf{J}^2 = \mathbf{j}_1^2 + \mathbf{j}_2^2 + 2|\mathbf{j}_1||\mathbf{j}_2| \cos \theta$$

or

$$\cos \theta = \frac{\mathbf{J}^2 - \mathbf{j}_1^2 - \mathbf{j}_2^2}{2|\mathbf{j}_1||\mathbf{j}_2|} = \frac{J(J+1) - j_1(j_1+1) - j_2(j_2+1)}{2\sqrt{j_1(j_1+1)j_2(j_2+1)}} \quad (4.17)$$

From here on, for simplicity, we take the case of identical particles in equivalent orbits ( $j_1 = j_2 = J$ ) and assume that  $j, J \gg 1$  so that terms like  $J(J+1)$  can be approximated by  $J^2$ . Then,

$$\cos \theta = \frac{J^2 - 2j^2}{2j^2} = \frac{J^2}{2j^2} - 1$$

Note that  $\theta = 0^\circ$  corresponds to high  $J$  and  $\theta = 180^\circ$  corresponds to low  $J$ . Thus, for  $j_1 = j_2$ ,  $\theta = 180^\circ$  corresponds to  $J = 0$  and  $\theta_{\min} \rightarrow 0^\circ$  to  $J = J_{\max} = 2j - 1$ .

Before proceeding, we first make use of some simple trigonometric equations. From  $\sin^2 \theta = 1 - \cos^2 \theta$ , we obtain

$$\sin \theta = \frac{J}{j} \left[ 1 - \frac{J^2}{4j^2} \right]^{\frac{1}{2}}$$

And, from  $\sin \theta/2 = [(1 - \cos \theta)/2]^{1/2}$ , we get

$$\sin \frac{\theta}{2} = \left( 1 - \frac{J^2}{4j^2} \right)^{\frac{1}{2}}$$

We also note that  $\tan \theta/2 = (1 - \cos \theta)/\sin \theta$ . Now, the  $3-j$  symbol in Eq. 4.10 can be written

$$\begin{pmatrix} j & j & J \\ \frac{1}{2} & -\frac{1}{2} & 0 \end{pmatrix}^2 = \frac{(2j+1+J)(2j-J)}{(2j+1)^2} \begin{pmatrix} j-\frac{1}{2} & j-\frac{1}{2} & J \\ 0 & 0 & 0 \end{pmatrix}^2$$

A good approximation to this for large  $j, J$  is

$$\begin{pmatrix} j & j & J \\ \frac{1}{2} & -\frac{1}{2} & 0 \end{pmatrix}^2 = \frac{(2j+1+J)(2j-J)}{(2j+1)^2} \frac{1}{2\pi(\frac{1}{2}J)} \frac{1}{\sqrt{(j-\frac{1}{2})^2 - \frac{J^2}{4}}}$$

Neglecting quantities of the order of unity compared to  $j, J$  we get

$$\begin{aligned} \begin{pmatrix} j & j & J \\ \frac{1}{2} & -\frac{1}{2} & 0 \end{pmatrix}^2 &\approx \frac{(2j+J)(2j-J)}{4j^2} \frac{1}{\pi} \frac{1}{Jj \left( 1 - \frac{J^2}{4j^2} \right)^{\frac{1}{2}}} \\ &\approx \frac{4j^2 \left( 1 - \frac{J^2}{4j^2} \right)}{4j^2} \frac{1}{\pi} \frac{1}{Jj \left( 1 - \frac{J^2}{4j^2} \right)^{\frac{1}{2}}} \\ &\approx \frac{\sin^2 \frac{\theta}{2}}{\pi j^2 \sin \theta} \end{aligned}$$

Hence,

$$\Delta E(j^2 J) \approx -\left(\frac{V_0 F_R}{8\pi}\right) \frac{(2j+1)^2 \sin^2 \frac{\theta}{2}}{\pi j^2 \sin \theta} \approx \frac{-V_0 F_R}{2\pi^2} \frac{\sin^2 \frac{\theta}{2}}{\sin \theta}$$

Using the relations for  $\sin \theta/2$  and  $\tan \theta/2$ , we have

$$\Delta E(j^2 J) \approx \frac{-V_0 F_R}{2\pi^2} \frac{\frac{1-\cos \theta}{2}}{\sin \theta}$$

or, finally

$$\Delta E(j^2 J) \approx \frac{-V_0 F_R}{4\pi^2} \tan \frac{\theta}{2} \quad (T=1, J \text{ even}) \quad (4.18)$$

This extremely simple result expresses the shifts in different  $J$  states for a  $\delta$ -interaction between two identical particles in equivalent orbits. It was derived for large  $j, J$ , but is remarkably accurate even for low spins (e.g., as low as  $j = 3/2$  and  $J = 1$  but specifically not for  $J = 0$ ). The function  $\tan \theta/2$  is plotted against  $\theta$  in Fig. 4.9. Since  $\tan \theta/2 \approx \theta/2$  for small  $\theta$  and goes to infinity for

## EQUIVALENT ORBITS

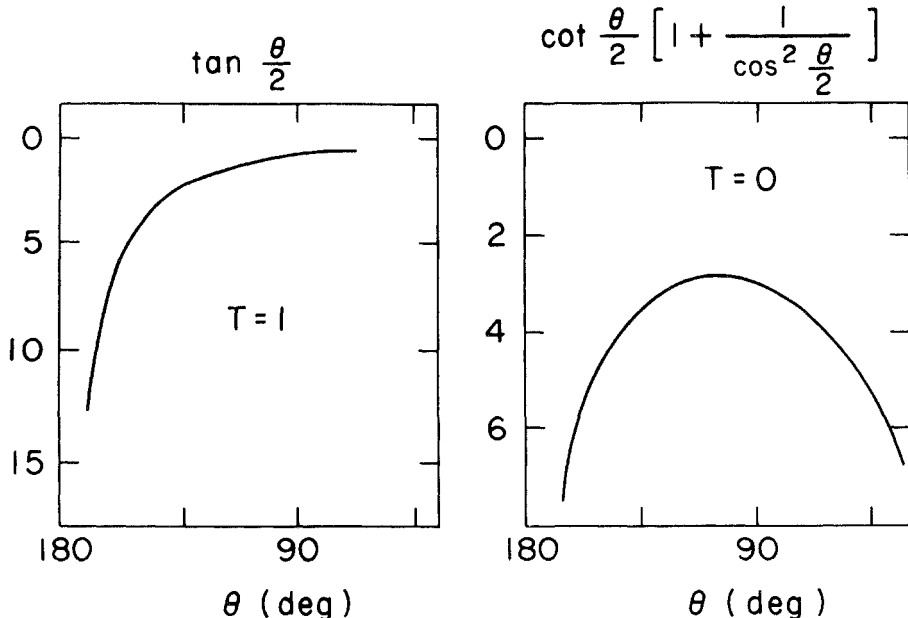


**Fig. 4.9.** Dependence of the  $\delta$ -function residual interaction strength (lower values correspond to more attractive residual interactions) for two particles in equivalent orbits. (Left) The  $T=1$  ( $J_{\text{even}}$ ) states. (Right) The  $T=0$  ( $J$  odd) states. The analytic expressions are indicated above their respective plots.

$\theta \rightarrow 180^\circ$ , Eq. 4.18 simply states that the energy shifts become large (and negative since the force is attractive) for  $\theta \approx 180^\circ$  (for small  $J$  where the two angular momenta are antialigned), while the smallest effect occurs when  $J = J_{\max} \approx j + j$ , since  $\theta \approx 0^\circ$ . Moreover, the curve  $\tan \theta/2$  becomes asymptotically flat for large  $J$ , giving a geometrical interpretation to the compression in spacings discussed above and illustrated for  $^{210}\text{Po}$ ,  $^{210}\text{Pb}$ , and  $^{134}\text{Te}$  in Fig. 2.5.

Note that this formula automatically reflects the Pauli principle arguments discussed earlier, in which the  $\delta$ -interaction affects only  $S=0$  states. The Pauli principle appears here through the 3- $j$  symbol and, in particular, through the spin angular momenta of  $\pm 1/2$  appearing in it.

As we have noted, identical nucleons in equivalent orbits have  $T=1$ , so Eq. 4.18 applies to them. For proton-neutron configurations we have to consider both  $T=1$  and  $T=0$  parts. We still restrict ourselves, though, to equivalent orbits. A  $T=1$  p-n system, which cannot be distinguished from the  $T=1$  p-p and n-n systems, consists of even  $J$  states and is described by Eq. 4.18 as well. However, in a  $T=0$  p-n system (odd  $J$  states)  $\Delta E_{pn}$  ( $j^2 J$ ) has a different  $J$  dependence, reflecting the different  $J$  behavior of the second ( $V_{S=1}$ ) term in Eqs. 4.15 and 4.16 compared to the first term.

For the odd  $J$ ,  $T=0$  case, a similar analysis gives (again for  $j_p = j_n$ )

$$\Delta E(j_p=j_n J) = \frac{-V_0 F_R}{4\pi^2} \left( \cot \frac{\theta}{2} \right) \left[ 1 + \frac{1}{\cos^2 \left( \frac{\theta}{2} \right)} \right] \quad (T=0, J \text{ odd}) \quad (4.19)$$

The behavior of  $\Delta E(J^2 J)$  for  $T=0$  is also indicated in Fig. 4.9. We recall that this only applies to equivalent orbits  $j_p = j_n$ . While the  $T=1$  interaction is largest (lowest-lying on the plot) for  $J_{\min}$  ( $\theta \approx 180^\circ$ ) and is smallest for  $J = J_{\max}$  ( $\theta \rightarrow 0^\circ$ ), the  $T=0$  expression is large for both  $J_{\min}$  and  $J_{\max}$ . For  $T=0$  and  $\theta \approx 180^\circ$ ,  $\Delta E(J^2 J_{\min}) \approx 1/\cos\theta \rightarrow \infty$ ; for  $\theta = 0^\circ$ ,  $\Delta E(J^2 J_{\max}) \approx \cot\theta \rightarrow \infty$ . Both the  $T=0$  and  $T=1$  expressions are small for  $\theta \approx 90^\circ$ .

All these features can be easily understood physically. The interaction should be small for  $\theta = 90^\circ$  for both  $T=0$  and  $T=1$ , since the particles are orbiting in nearly perpendicular planes and are seldom close enough to interact. For  $T=1$  (which, by charge independence, means we can re-use the identical-particle arguments), the interaction is strong when the two nucleons orbit in opposite directions ( $J=0, \theta = 180^\circ$ ). However, it vanishes when they orbit in the same direction ( $J_{\max}, \theta = 0^\circ$ ) since, then, the two particles have identical quantum numbers and the spatial wave function is required to be antisymmetric: it must vanish if the nucleons “touch.” The Pauli principle effectively introduces a short-range repulsion. The only way the particles can orbit in the same direction and yet not touch is if they circulate out of phase at opposite ends of an orbit diameter. This gives an interaction that is small for small  $\theta$ , but large for large angles in agreement with Fig. 4.9. The basic idea is the same as for the identical particle  $T=1$  case (Fig. 4.4). For the  $T=0$  case we treat the particles as distinct and, for both the small and large  $J$  extremes, the orbits are nearly coplanar. Since we need not worry about antisymmetry, there is no restriction on phasing, and “contact” is abundant, leading to a strong interaction for both  $\theta \approx 0^\circ$  and  $\theta \approx 180^\circ$ .

Empirically, these effects are well documented as shown by the examples in Fig. 4.10 taken from the aforementioned empirical analyses of p–n multiplets throughout the periodic table by Schiffer and True. Note the interesting point that for even  $J$ ,  $T=1$ , the empirical interaction is actually slightly positive (repulsive) for small  $\theta$  (high  $J$ ). A  $\delta$ -function interaction cannot give this: at best, it vanishes near  $J = J_{\max}$ . Such an analysis clearly shows the need for a separate repulsive component in the residual interaction. Several studies have successfully carried out multipole analyses of these effective residual interaction, incorporating dipole, quadrupole, etc. components. Evidence for a sizable quadrupole component has been found. This multipole varies as  $P_2(\cos\theta)$  where, again,  $\theta$  is the angle between the two orbits. As is well known, this function crosses zero at  $\theta \approx 55^\circ$  so that even for an overall attractive quadrupole term, the interaction is actually repulsive for angles between  $55^\circ$  and  $125^\circ$ . This is just the region where Fig. 4.10 shows positive (repulsive) empirical  $T=1$  interactions. This repulsive aspect should not be surprising. We have already encountered it. We noted in our discussion of separation energies in Chapter 1 that the like nucleon ( $T=1$ ) nonpairing residual interaction was, on

balance, repulsive ( $S(n)$  decreases with increasing  $N$ ). From this empirical fact, we also deduced that the  $T = 0$  interaction is on balance stronger (more negative) than the  $T = 1$ . This is also evident in Fig. 4.10.

Finally, note that for  $J^\pi = 0^+$ , the interaction deviates from the geometric expression. The  $0^+$  behavior, however, is physically reasonable. As with the like-nucleon case, the interactions are ordered by  $j$ ; they are largest for large  $j$ . The larger the  $j$  value, the more magnetic substates there are, and the smaller the permissible angular range of an orbit for a given  $m$ . Thus the orbit planes are more tightly defined and the overlaps of particles in  $\pm m$  substates are greater.

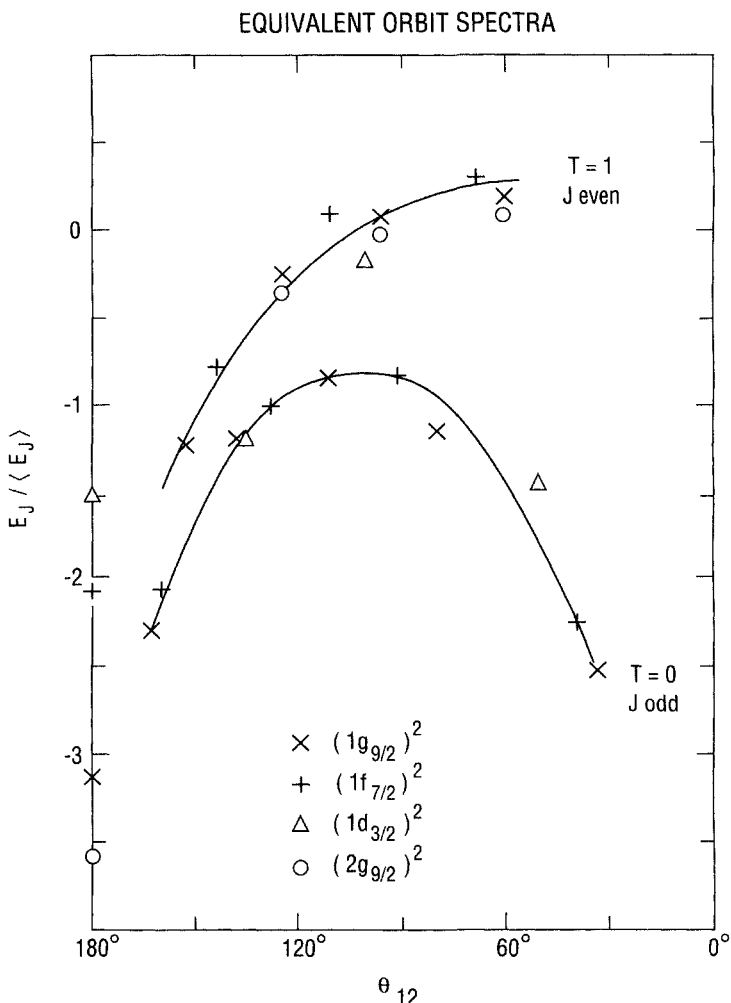


**Fig. 4.10.** Empirical proton-neutron multiplets for two particle equivalent orbit configurations for comparison with the behavior shown in Fig. 4.9. The curves are drawn through the data (Schiffer, 1971).

Thus far, for simplicity, we have carried out the geometrical analysis for the simple case of  $j_1 = j_2$ . For  $j_1 \neq j_2$  and the identical particles, we saw in Section 4.1 that either the  $J_{\min}(\theta \rightarrow 180^\circ)$  or the  $J_{\max}(\theta \rightarrow 0^\circ)$  state can be lowest depending on the particular  $j$  values and their  $j = l \pm 1/2$  character. Table 4.2 summarized the different cases leading to these two situations. These two categories of two-particle configurations should be and are reflected in the geometrical analysis. One obtains two curves now, of which one is identical to Eq. 4.18 ( $\Delta E = \tan \theta/2$ ) giving the lowest energy for the antialignment of the two values ( $J_{\min}$ ,  $\theta$  close to  $180^\circ$ ), and the other curve goes as  $\cot \theta/2$  so that the lowest energy occurs for parallel alignment ( $J_{\max}$ ) and  $\theta$  close to  $0^\circ$ . The correspondence of these two trigonometrical functions and different sets of  $j_1, j_2$  values is made explicit in the sixth column of Table 4.2. Finally, note that the equivalent-orbit situation is actually a special case of this. Here,  $\pi = +$ ,  $j_1 + j_2 = 2j$  is always odd and so the  $\tan \theta/2$  dependence applies and the  $J_{\min}$  (in this case  $0^\circ$ ) state is lowest.

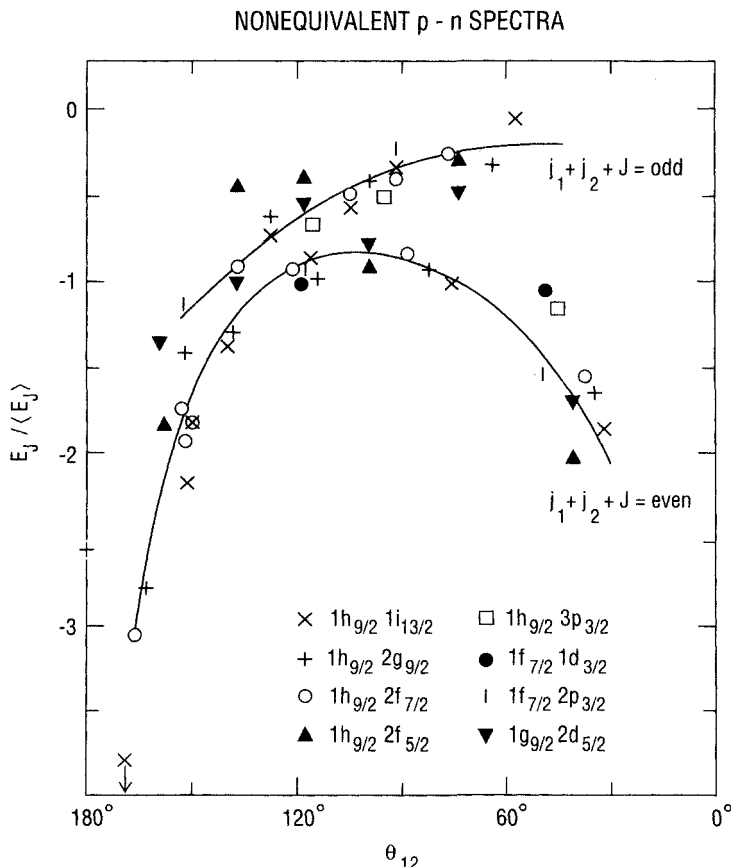


**Fig. 4.11.** Comparison of empirical and calculated multiplet splittings for two-particle configurations of nonequivalent orbits (Schiffer, 1971).

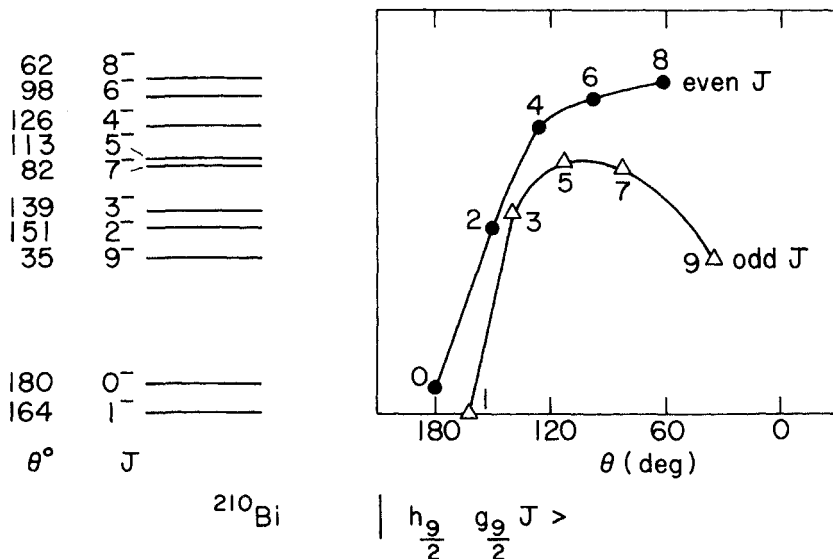


**Fig. 4.12.** A geometrical analysis of the  $|h_{9/2}g_{9/2}J\rangle$  p–n multiplet in  $^{210}\text{Bi}$ . The empirical levels are shown on the left along with the semiclassical angle between the orbits of the two nucleons. The right side shows that the levels split into two families, according to  $J$  even or  $J$  odd. The solid lines are drawn to connect the points.

For the p–n case, a similar analysis again leads to two distinct curves as in the  $T = 1$  and  $T = 0$  cases for equivalent orbits. However, the classification is slightly different. Recall that, for equivalent orbits, the  $T = 1$  states are even  $J$  only. Thus  $j_1 + j_2 + J = 2j + J$  is odd. The  $T = 0$  case, with  $J$  odd, has  $j_1 + j_2 + J = 2j + J$  even. It is this distinction that persists when  $j_1 \neq j_2$  for a p–n multiplet. Again, we obtain two curves, but distinguished according to the odd or even character of  $j_1 + j_2 + J$  and describable by geometrical functions of  $\theta$  very similar to Eqs. 4.18 and 4.19. This is beautifully illustrated by the data for several multiplets collected in Fig. 4.11, and exemplified in depth for  $^{210}\text{Bi}$  in Fig. 4.12. In all these cases the empirical energy distributions within the p–n multiplets follow the expected energy patterns quite well.

One last point worth mentioning is that extensive surveys of empirical p–n interaction multiplets show that the strength of the interaction, especially in  $T = 0$  states, smoothly decreases with increasing mass. This is quite plausible since the average radius of shell model orbits increases with higher oscillator numbers, while the interaction range is constant so that the average interaction strength decreases. In heavy nuclei, typical  $V_{pn}$  interaction matrix elements are  $\approx 200$  to  $300$  keV but of course this depends on the orbits involved.

What is perhaps most important to emphasize in concluding this part of the discussion is that, without ever having dealt with the radial parts of the wave functions, or indeed, calculating anything, it has been possible to predict the qualitative energy ordering of the different  $J$  states in two-particle configurations. Moreover, exact quantitative results for the relative spacings involve only the evaluation of a single  $3-j$  symbol. (Of course, the absolute spacings

depend on the radial integrations and the strength of the interaction.) This is but one example of how far one can go in a shell model treatment of multiparticle configurations by invoking only very general arguments.

### 4.3 Pairing Interaction

We re-emphasize that these results for the  $\delta$ -function interaction are of more than passing interest since, representing the short-range interaction par excellence, this interaction simulates in many respects results from more realistic short-range interactions. In particular, it is closely allied to the pairing interaction specifically designed to mock up a strong, attractive interaction in the  $J = 0$  configuration of two identical nucleons. The motivation is similar to that for the  $\delta$ -function interaction—the pairing interaction is only effective when the particles have extremely high spatial overlaps. Formally, one can define the pairing interaction by

$$\langle j_1 j_2 J | V_{\text{pair}} | j_3 j_4 J' \rangle = -G(j_1 + \frac{1}{2})(j_3 + \frac{1}{2}) \delta_{j_1 j_2} \delta_{j_3 j_4} \delta_{J J'} r_0 \quad (4.20)$$

where  $G$  gives the overall strength in the interaction. Note that this interaction is attractive and, by definition, only effective for  $0^+$  states of identical nucleons in equivalent orbits. It is not, however, limited to diagonal matrix elements  $\langle j_1^{20^+} | V_{\text{pair}} | j_1^{20^+} \rangle$ , but rather allows nondiagonal scatterings,  $\langle j_1^{20^+} | V_{\text{pair}} | j_3^{20^+} \rangle$ , in which the pair of particles switches to another orbit as a pair. This feature is critical to the build-up of pairing correlations and the so-called pairing gap in even-even nuclei, and will be treated in more detail in a later chapter. For diagonal matrix elements  $| j_1 = j_2 = j_3 = j_4 \rangle$  the pairing interaction strongly lowers the  $0^+$  state without affecting the others.

Both the  $\delta$ -function force and the pairing force are intended to represent the short-range component of the nuclear interaction. However, the residual interaction also contains a long-range component, that, as we shall see, is

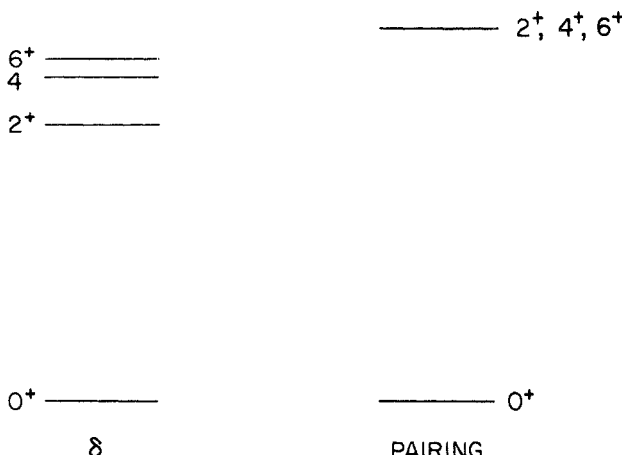


**Fig. 4.13.** Comparison of levels of a  $(j = 7/2)^2$  configuration for a  $\delta$ -function and a pairing interaction.

crucial in producing collective properties and nonspherical nuclei. It is common to mock this up by the so-called quadrupole interaction. (In recent years higher order multipoles, such as hexadecapole interactions, have also been considered, but we shall ignore their effects here.) The combination of these two forces, the so-called pairing plus quadrupole interaction, has been perhaps the most widely used simulation of nuclear interactions in heavy nuclei in the last couple of decades. It can be written as:

$$V_{ppq} = V_{\text{pair}} + \kappa r_1^2 r_2^2 P_2(\cos \theta) \quad (4.21)$$

where  $\theta$  is the angle between the radius vectors to each particle (see Fig. 4.8) and  $\kappa$  is the strength of the quadrupole part. Clearly, while  $V_{\text{pair}}$  is short-range, the quadrupole component simulates at least part of the long-range aspect of the residual interaction (see the following section).

The popularity of the pairing interaction, or of any other that reproduces the low energy of  $J=0$  coupled pairs of nucleons, clearly lies in the fact that all even-even nuclei have  $0^+$  ground states. The quadrupole interaction is motivated, empirically, by the fact that nearly all nuclei more than a few mass numbers away from closed shells display properties that can be described in terms of quadrupole distortions of the spherical shape. Figure 4.13 shows the differences between the pairing and  $\delta$ -function interactions. For the case of identical nucleons in equivalent orbits, both produce a low-lying  $0^+$  state and a grouped cluster of states with higher angular momentum. With the pairing interaction, this latter group is unaffected, remaining degenerate. The  $\delta$ -function interaction seems to be a better approximation, as is clear in Fig. 4.5, as well as Fig. 2.6 for the Sn isotopes. For many-particle configurations, the quadrupole force dominates both the pairing or  $\delta$ -function interactions and the differences in their properties are washed out.

#### 4.4 Multipole Decomposition of Residual Interactions

It is useful at this point to consider a more general approach to calculating nuclear interactions and their effects on energy levels in two-particle configurations. This will help us understand, in a simple manner, the different effects of different residual interactions. It will lead to a deeper appreciation of the  $\delta$ -function results, in particular the origin of the 2 curves in Figs. 4.9–4.12, and it will shed more light on the relation between the pairing and  $\delta$ -interactions. We can expand any interaction that depends on the separation of the two particles as

$$\begin{aligned} V(|\mathbf{r}_1 \mathbf{r}_2|) &= \sum_k v_k(r_1 r_2) P_k(\cos \theta) \\ &= \sum_{km} v_k(r_1 r_2) \frac{4\pi}{2k+1} Y_{km}^*(\theta_1 \phi_1) Y_{km}(\theta_2 \phi_2) \end{aligned} \quad (4.22)$$

where the  $v_k(r_1 r_2)$  are given by

$$v_k(r_1 r_2) = \frac{2k+1}{2} \int V(|\mathbf{r}_1 - \mathbf{r}_2|) P_k(\cos \theta) d \cos \theta \quad (4.23)$$

In the following we do not consider the effects of antisymmetrization explic-

itly, but the results are still valid for identical particles and for p–n systems involving different major shells. If we write the wave function as a product of radial and angular parts, we can then achieve a similar separation of the energy shift into radial and angular parts and, moreover, separate the angular parts of particles 1 and 2. We obtain, as in Eq. 4.5

$$\Delta E(j_1 j_2 J) = \sum_k F_R^k A_k \quad k \leq \min(2j_1, 2j_2, 2l_1, 2l_2) \quad (4.24)$$

where

$$F_R^k = \int |R_{n_1 l_1}(r_1)|^2 |R_{n_2 l_2}(r_2)|^2 v_k(r_1 r_2) dr_1 dr_2 \quad (4.25)$$

and

$$A_k(J) = \frac{(-)^{j_1+j_2+J} (4\pi)}{(2k+1)} \langle l_1 j_1 || \mathbf{Y}_k || l_1 j_1 \rangle \langle l_2 j_2 || \mathbf{Y}_k || l_2 j_2 \rangle \left\{ \begin{matrix} j_1 j_2 J \\ j_2 j_1 k \end{matrix} \right\} \quad (4.26)$$

As before,  $F_R$  is a purely radial integral and depends on the details of the specific interaction chosen, while  $A_k$  depends only on the angular coordinates and is therefore *completely independent* of the interactions involved.

We now note a significant point. The summation in Eq. 4.24 is limited to even  $k$  values from 0 to  $\min(2j_1, 2j_2, 2l_1, 2l_2)$ . These limitations arise simply by angular momentum conservation in the reduced matrix elements of  $Y_k$  and as specified by the triangle conditions involving the  $9-j$  symbol. This severely constrains the number of multipoles that go into the calculation of any given interaction. For example, for *any* interaction  $V(\mathbf{r}_1 - \mathbf{r}_2)$  in a  $(d_{3/2}, f_{1/2})$  configuration,  $k_{\max} = 2$  and hence  $k$  takes on *only* the values 0 and 2. Regardless of the interaction, then, the energies of the four final states with  $J = 2, 3, 4, 5$  are given in terms of only two equations. Indeed, as discussed by de Shalit and Feshbach, one can show that

$$E(5^-) - E(2^-) : E(3^-) - E(2^-) : E(4^-) - E(2^-) : = 1:2.5:3.5$$

independent of the interaction. This case of  $d_{3/2}, f_{1/2}$  particles should actually describe the lowest states of  $^{38}\text{Cl}_{21}$ . The experimental spacings are in the ratios 1:1.1:2.0. They have the same sequencing of levels as in the calculation (2<sup>-</sup>, 5<sup>-</sup>, 3<sup>-</sup>, 4<sup>-</sup>), but the magnitudes of the spacings disagree. Without ever having specified an interaction, or evaluated any radial wave functions, we can unambiguously conclude either that an accurate description of these  $^{38}\text{Cl}$  states requires more complex configurations, or that the interaction depends on something other than  $(\mathbf{r}_1 - \mathbf{r}_2)$  (e.g., spin). Note that this is the same nucleus that we treated earlier with a  $\delta$ -function interaction (Fig. 4.7). The earlier results are different than these precisely because we used different strengths (i.e., a spin dependence) for the  $S = 0$  and  $S = 1$  terms.

Equation 4.24 applies to any interaction that can be written in terms of the separation of the two particles, that is, as  $V(|\mathbf{r}_1 - \mathbf{r}_2|)$ . However, one sometimes encounters spin-dependent interactions. Then we obtain a result similar to Eq. 4.24, with the same limitation on  $k_{\max}$ , but including odd  $k$ . This point is very important, since the  $\delta$ -interaction can be shown to be equivalent to an interaction  $V(|\mathbf{r}_1 - \mathbf{r}_2|)$  times a spin-dependent operator. Thus, a  $\delta$ -function interaction is equivalent to an odd tensor interaction, even though its mul-

tipole expansion contains only even  $k$ . The reason is beyond the scope of our treatment but involves the fact that the interaction takes place only at “contact,” and therefore a  $\delta$ -function interaction can be multiplied by various “exchange” interactions that have odd tensor character. This class of interactions is crucial in nuclear structure since they have the special property of conserving seniority (see Chapter 5).

For a  $\delta$ -interaction,  $v_k(r_1 r_2)$  is given by

$$v_k(r_1 r_2) = \frac{2k+1}{4\pi} \frac{\delta(\mathbf{r}_1 - \mathbf{r}_2)}{r_1 r_2} \quad (4.27)$$

Note that, despite its short-range, the  $\delta$ -interaction has a monopole component ( $k = 0$ ) corresponding to a part of the interaction that is *independent* of angle [ $P_0(\cos\theta) = \text{constant}$ ]. This is a long-range piece par excellence and it says that a “contact” interaction has a component that pays no heed to the angular separation of the particles! Of course, since the monopole part is constant over all (angular) space, it is the same for all relative orientations of  $j_1$  and  $j_2$ , that is, all  $J$  values. Hence, it does *not* contribute to splittings of a multiplet but does give an overall shift to the multiplet. In practical calculations, the situation in regard to allowed multipoles can be even more bizarre. Consider a  $\delta$ -interaction between two  $d_{3/2}$  particles. Not only does the  $k = 0$  multipole contribute, but the triangle conditions on  $k$  limit the multipoles to only the values  $k \leq 3$ . No really short-range multipoles appear.

This seemingly paradoxical situation of an infinitely short-range interaction being simulated only by relatively long-range multipoles is actually easy to understand. This understanding reveals much about the relationship between forces and the orbits and wave functions of the interacting particles. More accurately, it clarifies the way particles from different orbits can “probe” different interactions. It relates in a general philosophical way to how one determines structure in any physical system. The general rule is that in order to sample the structure of a given scale, the probe must be comparable to or smaller than that scale. (It is difficult to distinguish between a potato and a carrot by bombarding either with a truck.)

Imagine a proton and a neutron in an  $s_{1/2}$  orbit. They have only one  $m$  state and are spherically symmetric wave functions: the orbit is uniformly spread out, at a given radius, over time, in a spherical shell. The two particles are therefore always in “contact” and are simply unable to sense *any* details of the residual attraction. To them, a  $\delta$ -force is identical to a constant force over all space. The higher the  $j$  value of the interacting particles, the more sensitive they are to the details of the force simply because higher  $j$  values have more magnetic substates. This set of magnetic substates spans the same angular range around the body of the nucleus and hence, each magnetic substate is restricted to a narrower angular range. Thus, two particles in  $j = 13/2$  orbits coupled to  $J = 12$  can sense the fine details of an interaction: each substate  $M$  samples a different angular range of the force. In contrast, even though the residual interaction may be a  $\delta$ -force, two low  $j$  (e.g.,  $s_{1/2}$ ,  $p_{1/2}$ ,  $p_{3/2}, \dots$ ) orbits cannot “know” this. They are the wrong probe.

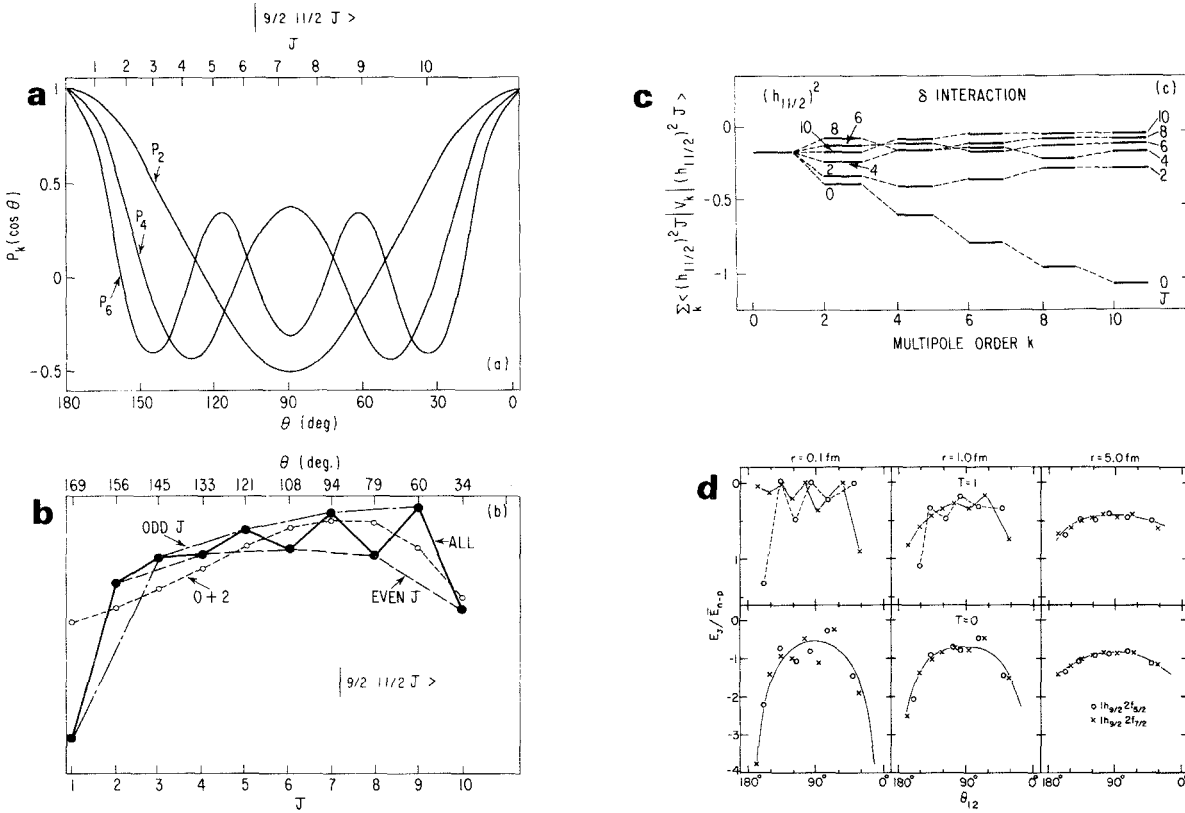


**Fig. 4.14.** Multipole decomposition of residual interactions: (a) Legendre polynomials  $P_k(\cos \theta)$  plotted against  $\theta$  and  $J$  value for a  $(9/2, 11/2)$  configuration. (b) Contribution of different multipoles to  $\Delta E$  ( $g_{9/2} h_{11/2} J$ ) with a  $\delta$  function residual interaction. The short-dashed, and solid curves correspond to the multipoles  $k = 0, 2, 4, 6$ , and  $8$ , respectively. For the complete ( $k = 0-8$ ) case, the even and odd  $J$  states are separately connected by broken lines. (c) Effect of the addition of each successive multipole on the energies of an  $(h_{11/2})^2$  configuration. (Parts (b) and (c) are based on Heyde, 1989.) (d) Effect of forces of different ranges on the relative energy shifts as a function of  $\theta$ , that is, of  $J$ , for two different two-particle configurations. (Schiffer and True, 1976.)

Coupled with the practical historic fact that most shell model calculations have dealt with light nuclei and, therefore, low  $j$  states, we now see why different interactions are often used to account for the same data, and why it often is difficult to determine the details of the interaction.

The other extreme of  $k$  values (multipole order) can also be discussed. Neglecting the limitation given by the  $j_1 l_1, j_2 l_2$  quantum numbers (or, equivalently, assuming a large  $j$  shell), we can relate the largest relevant  $k$  values to the range of the force. Consider the classical picture shown in Fig. 4.8, where  $\theta$  is the angular separation of the two particles. The distance between the two particles is given by  $r^2 = r_1^2 + r_2^2 + 2 r_1 r_2 \cos \theta$ . If we approximate the range by a single number  $r$ , the integration over  $\theta$  will be limited to  $\theta \leq r/r$ . The Legendre polynomial  $P_k(\cos \theta)$  oscillates more rapidly as  $k$  increases (see Fig. 4.14a). If  $P_k$  oscillates many times within the allowed integration range, the integral will be small because of cancellation effects. In practice, therefore, for a given force range,  $k$  is limited to value satisfying  $\pi/k \ll r/r$ . Clearly, then, as the range decreases, more and more  $k$  values are required. The limiting case is of course, the  $\delta$ -interaction, although other factors ( $l, j$  values) relating to the ability of a given wave function to “sample” an interaction will come into play to limit the allowed range of  $k$  values.

The idea of the multipole expansion of a residual interaction can be used to obtain some earlier results in a physically transparent way that offers new insights. This idea can also be used to derive a famous result known as the *parabolic rule* for energies of states in p–n multiplets. We have already seen how one can understand the  $J$ -dependence of the residual interaction in terms of the angle between the two orbits involved (see Eqs. 4.18, 4.19 and Figs. 4.9–4.12). We can apply similar arguments to specific multipoles.

Each multipole,  $k$ , has an angular dependence  $P_k(\cos \theta)$ . The lowest few are  $P_0 = \text{constant}$ ,  $P_2 = 1/2(3\cos^2 \theta - 1)$ ,  $P_4 = 1/8(35\cos^4 \theta - 30\cos^2 \theta + 3)$ . The  $P_k$  were shown in Fig. 4.14a. As Eq. 4.17 indicates, for a given  $j_1, j_2$  there is a specific relation between the total angular momentum  $J$  and the angle  $\theta$ : thus, one can plot  $P_k(\cos \theta)$  equally well against  $J$  or  $J(J+1)$  (as is sometimes done). This alternate scale is included in Fig. 4.17a for the example of  $j_1 = 9/2, j_2 = 11/2$  (e.g., a  $(g_{9/2} h_{11/2})$  configuration).

Obviously, since each multipole is proportional to  $P_k(\cos \theta)$ , the interaction in the  $k^{\text{th}}$  multipole is strongest when  $P_k$  is largest. Thus, we can tell directly which spin states will be most affected for each multipole.

The monopole ( $k = 0$ ) component is constant, affects all states equally, and simply gives an overall shift to the entire multiplet. This is an important effect, altering the relative excitation energies of different multiplets, but it contributes nothing to the splitting.

It is the principal origin of the mass dependence of single-particle energies that we discussed at the end of Chapter 3. In particular, the monopole p–n interaction leads to the changes noted there (Fig. 3.4) in neutron single-particle energies as a function of proton number and vice versa. In this chapter, however, we are focusing on energy *splittings* due to residual interactions and so we turn now to other multipoles.

The quadrupole ( $k = 2$ ) component is strongest when  $\theta = 0^\circ$  and  $180^\circ$  and actually changes sign around  $90^\circ$ . (Recall that there is an overall minus sign to be applied to Fig. 4.14a for an attractive interaction so that negative values on the figure refer to repulsive effects.) Thus, a quadrupole interaction lowers the energies of the extreme  $J$  values the most, but can in fact raise the energies of intermediate spins. The general behavior of the quadrupole term is similar to the  $j_1 + j_2 + J$  even curve in Fig. 4.11 but this is somewhat accidental and we shall return to the relationship between these results in a moment. We can easily derive the specific dependence of  $\Delta E(j_1 j_2 J)$  on  $J$  for a  $k = 2$  multipole. The  $\Delta E$  are just proportional to  $P_2(\cos\theta)$  and, by Eq. 4.17,

$$\begin{aligned}\Delta E(j_1 j_2 J) &\propto \frac{[J(J+1) - j_1(j_1+1) - j_2(j_2+1)]^2}{4j_1(j_1+1)j_2(j_2+1)} \\ &\propto A[J(J+1)]^2 + BJ(J+1) + C\end{aligned}\quad (4.28)$$

where  $A$ ,  $B$ , and  $C$  are functions of  $j_1$ ,  $j_2$ , but are independent of  $J$ . This is a parabola in  $J(J+1)$  and is the *parabolic rule* discussed frequently by Paar. By differentiating we can find the vertex,  $J_v$ :

$$J_v(J_v+1) = j_1(j_1+1) + j_2(j_2+1) - \frac{1}{2}$$

and, solving the quadratic,

$$J_v = [j_1(j_1+1) + j_2(j_2+1) - \frac{1}{2}]^2 - \frac{1}{4} \quad (4.29)$$

Note that  $J_v$  is normally the *highest-lying* member of a downward pointing parabola since the overlap of the particles is largest for  $J_{\max}$  and  $J_{\min}$ . In the  $g_{9/2} h_{11/2}$  case in Fig. 4.14a, this gives  $J_v \approx 7$ , which is indeed where the  $P_2(\cos\theta)$  minimum occurs. For this multiplet, the  $J=1, 10$  states are lowest,  $J \approx 7$  highest.

The relationship of these ideas to the  $J$ -dependence in Figs. 4.9–4.12 is informative, particularly the split into two curves\*. In general, points falling alternately (for odd and even  $J$ ) on these two curves cannot be described by a single parabola in  $J(J+1)$  (we will see one exception later). To generate the  $\delta$ -function results, the higher multipoles must be added in. From Fig. 4.14a it is clear that these oscillate more rapidly in  $\theta$  or  $J$ , and this introduces an irregularity or zig-zag pattern to the spin dependence. For example, a hexadecapole component would raise  $E(7)$  and lower that of the  $J=4$  and  $9$  states. It also broadens the minimum and tends to shift it toward the spin 8 level. A  $P_6(\cos\theta)$  term will add further perturbations. When all the multipoles are summed, with amplitudes appropriate to the  $\delta$ -interaction, two curves similar to those of Fig. 4.11 are reproduced.

This is evident in Fig. 4.14b, which shows the strength of the interaction as a function of  $J$  for different combinations of multipoles (with amplitudes appropriate to a  $\delta$ -function). For the  $|g_{9/2} h_{11/2} J\rangle$  configuration, the  $k = 0 + 2$  curve is smooth and minimizes at  $J = 7$ , as we have just seen. If this curve is replotted against  $J(J+1)$ , an exact parabola is obtained. Adding in all the

\*I am indebted to K. Heyde for much helpful advice in this section and for Figs. 4.14b and 4.14c.

multipoles,  $k = 0, 2, 4, 6, 8$ , gives the solid curve. If we connect just the odd  $J$  states along this curve, we get a dependence just like the  $j_1 + j_2 + J$  odd curve of Fig. 4.11. If we connect the even  $J$  values we get the  $j_1 + j_2 + J$  even curve of Fig. 4.11. Thus we see that the separation of the two curves comes from the higher multipoles and reflects the Pauli effects since these multipoles have shorter ranges.

Figure 4.14c shows this in a particularly illuminating way for the identical particle  $|(\mathbf{h}_{11/2})^2 J\rangle$  configuration. Here, the energies obtained with the addition of each successive multipole in a  $\delta$ -interaction are displayed in level scheme form. For  $k = 0, 2$  only, a parabolic behavior is observed: the  $0^+, 2^+, 4^+$  levels are lowest, the intermediate spins  $6^+, 8^+$  highest and the largest spin,  $10^+$ , lower again. As shorter and shorter range multipoles are added, the levels shift toward the characteristic  $\delta$ -function sequence shown on the right. We have discussed how such a sequence, particularly the weak effects of a  $\delta$ -interaction for the  $J_{\max}$  states (since they have  $S = 1$ ), is a specific Pauli principle effect. Now we see exactly how this comes in through the *shortest*-range multipoles, which are in fact repulsive for these spin states, reflecting the Pauli prohibition against “contact.”

Figures 4.14a and 4.14c also dramatically show why the  $0^+$  state (or, generally, the lowest state of a given multiplet) is lowered so much. This state corresponds to orbit planes closest to  $\theta = 180^\circ$  (or  $0^\circ$ , depending on the  $j$  values if nonequivalent orbits are involved). Here, *all* the multipoles contribute coherently because  $P_k(\cos 180^\circ \text{ or } 0^\circ)$  is always unity. Only for other spins do cancellation effects enter.

Finally, we can use Fig. 4.14c to better understand the relation between  $\delta$ - and pairing forces. Imagine continuing this figure further to the right. The  $0^+ - J$  separation would grow and the separation among the  $J \neq 0^+$  states would diminish relative to their separation from the  $0^+$  level. The limit is the pairing picture shown in Fig. 4.13. Although we do not write the pairing interaction in terms of multipoles, we see that, in effect, it corresponds to the dominance of very high ones. This, incidentally, is the origin and basis for the phrase occasionally encountered that the pairing force is of even “shorter range” than the  $\delta$ -interaction, a statement that sounds paradoxical.

We have now discussed, in several ways, the relation between multipoles and the (angular) ranges of the forces they describe and their effects on different  $J$  states of two-particle multiplets: briefly, attractive short-range (higher multipole order) forces tend to lower especially the  $J_{\max}$  and  $J_{\min}$  states (subject always to Pauli principle constraints). We can see this relation even more explicitly by using forces that are finite (radial) range. To this end, Fig. 4.14d shows the energy shifts calculated for two configurations for a Yukawa type force with range parameter  $r = 0.1, 1.0$  and  $5.0$  fm. In general, the shorter the range, the stronger the effects on the extreme  $J$  (or  $\theta$ ) states where the orbits are most nearly coplanar and the particles, on average, closer. The different patterns for  $r = 0.1$  fm for the  $T = 1$  interaction just reflect the  $\cot \theta/2$  or  $\tan \theta/2$  dependences discussed for the two different configurations (see Table 4.2). This difference, a Pauli effect, is washed out for longer-range forces, as is

most of the  $J$  (or  $\theta$ ) dependence, since the force becomes rather insensitive to the separation of the particles within the nuclear volume.

With this discussion of multipole contributions and force ranges, the reader should now be in a position to estimate, at least qualitatively, the effect of any particular interaction in a given configuration with little or no explicit calculation.

An interesting special case of the multipole decomposition is that of a  $(p_{3/2}d_{3/2})$  p–n configuration. For this configuration, Eq. 4.24 only allows  $k = 0, 2$  values, and the  $k = 0$  multipole is irrelevant for splittings, so the  $\delta$ -interaction in this case should give exactly the parabolic dependence on  $J(J+1)$  characteristic of  $P_2(\cos\theta)$ . Yet, from our previous discussion, we know that the  $J = 0, 2$  ( $j_1 + j_2 + J$  odd) states would occur on the upper curve in Fig. 4.11 and the  $J = 1, 3$  states on the lower curve. Although this hardly seems to yield a parabola, careful inspection of the curves in Fig. 4.11 for the angles appropriate to the  $|d_{3/2} p_{3/2} J\rangle$  configuration shows that these four points have an exact parabolic form against  $J(J+1)$ .

Actually, this result suggests why a quadrupole interaction is more important than it might at first seem: because of the angular momentum constraints on  $k_{\max}$ , many higher multipoles that might normally contribute are eliminated. Moreover, the  $\delta$ -function is not necessarily the best choice of interaction. Other, “finite range” interactions (e.g., Gaussian  $e^{-\alpha(|r_1 - r_2|)}$ ) are often used and have relatively larger low- $k$  amplitudes. Finally, there are often other residual interactions besides the p–n interaction, such as particle–core coupling contributions that are dominated by quadrupole components. Indeed, we saw in Section 4.2 that analyses of empirical two-particle multiplets do suggest evidence for enhanced quadrupole interactions. (We shall see in Chapter 6 that quadrupole core “vibrations” are the dominant low lying “collective” modes in nuclei.)

Thus, the parabolic rule is often an excellent approximation. Figure 4.15 shows a few examples taken from Paar and introduces one final but important point. The  $(g_{7/2}d_{3/2})$  multiplet of  $J = 2^+ - 5^+$  states in  $^{122}\text{Sb}$  is well reproduced by a simple parabola in  $J(J+1)$ , as is the  $(g_{7/2}h_{11/2})$  multiplet.  $^{48}\text{Sc}$  and  $^{116}\text{I}$  also show multiplets with beautiful empirical parabolic behavior, except that they are inverted! The reason is well understood. In  $^{48}\text{Sc}_{27}$ , the  $(f_{7/2p}f_{7/2n})$  multiplet really a particle–hole p–n configuration  $(f_{7/2p}f^7_{7/2n}) \equiv (f_{7/2p}f^{-1}_{7/2n})$ , as is the  $(g_{7/2p}^{-1}h_{11/2n})$  configuration in  $^{116}\text{In}_{67}$ . In this case, the residual interaction has the *opposite* sign of a particle–particle or hole–hole multiplet. In other words, it is repulsive, and the  $J$  states with high p–n overlap ( $J_{\max}, J_{\min}$ ) are *raised* in energy, while  $J_n$  is lowered the most. We note that this change in sign is not always the case; in Chapter 5 we will see it as a characteristic of even multipole interactions such as the quadrupole interaction we are considering here. Interestingly, it does not apply to the  $\delta$ -interaction (even though we have discussed its expansion in even multipoles). For odd multipole interactions  $\Delta E(p-p)$  or  $\Delta E(h-h)$  is identical to  $\Delta E(p-h)$ .

In Chapter 5, we will discuss at length the pairing interaction and the concept of the quasi-particle, which is a state only partially occupied, neither

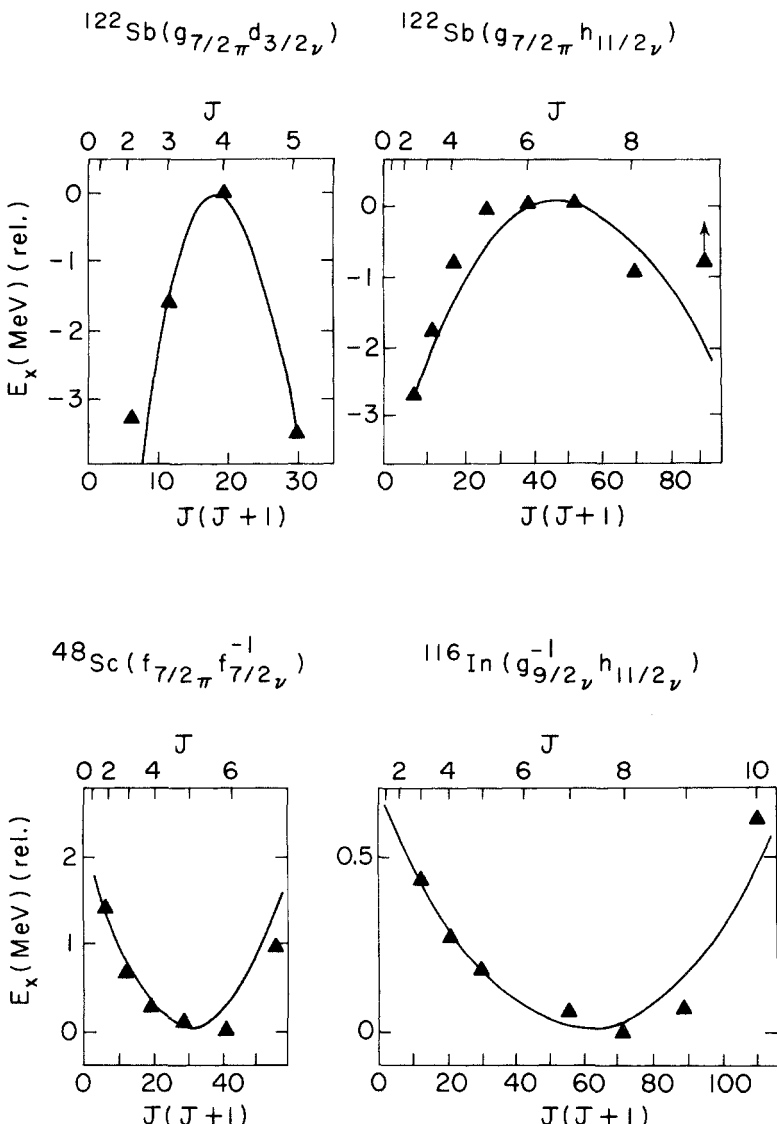


**Fig. 4.15.** Illustrations of the parabolic rule for a quadrupole residual interaction for several p–n multiplets (Paar, 1979).

fully particle nor fully hole. Anticipating that discussion, the *occupancy* of an orbit is given by a probability, denoted  $V_j^2$  (the number of particles in the orbit is  $(2j+1)V_j^2$ ). The orbit *emptiness* is  $U_j^2$ , and  $U_j^2 + V_j^2 = 1$ . Thus, we can rewrite Eq. 4.28 for the general situation of quasi-particles as

$$\Delta E_{qp}(j_1 j_2 J) \sim \Delta E(j_1 j_2 J) (U_1^2 - V_1^2)(U_2^2 - V_2^2) \quad (4.30)$$

Thus, for a given proton number (particle “1”),  $(U_1^2 - V_1^2)$  is constant but  $(U_2^2 - V_2^2)$  changes from +1 to -1 as the neutron orbit (“2”) is filled over a

sequence of isotopes. Therefore, the parabolic rule actually refers to a whole family of possible parabolas for given  $j_1, j_2$ , ranging from bowl-shaped (p-h case) to nearly flat to a convex upward parabola (p-p or h-h cases). The theoretical shapes, for several values of  $V_{h_{11/2n}}$  in a  $(g^{-1}_{9/2p}, h_{11/2n})$  multiplet are illustrated in Fig. 4.16.

It is worth mentioning two applications of these ideas. The fact that different interactions have different multipole composition can sometimes be used to gain information on the nature of the effective interaction. This has been extensively pursued by Schiffer and Molinari and co-workers, who, for example, deduced effective multipole coefficients applicable to broad ranges of nuclei, and by Heyde and co-workers who studied Gaussian and other interactions. In general, stronger quadrupole components are required than given by a  $\delta$ -force, signaling the need for "finite" range interactions.

Secondly, this geometric interpretation of the interaction can provide important intuitive clues to the configurations in certain states without the

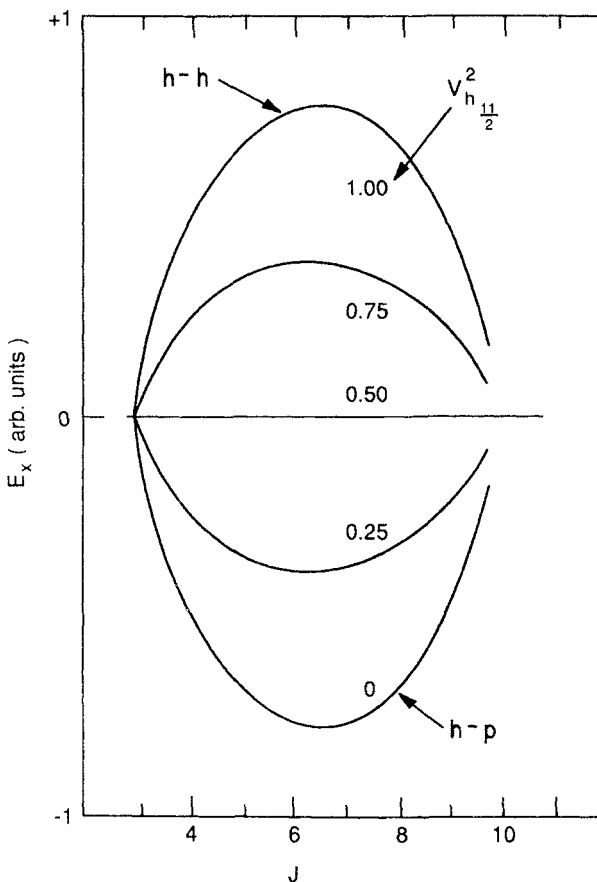


**Fig. 4.16.** Dependence of the shape of  $(g^{-1}_{9/2p}, h_{11/2n})$  multiplet parabolic splittings as a function of the occupancy. The uppermost curve corresponds to a nearly full  $h_{11/2n}$  orbit and therefore a hole-hole configuration. The lowest (h-p) curve corresponds to an  $h_{11/2n}$  orbit with only a few particles and therefore a hole-particle configuration (based on Van Maldeghem, 1985).

need for prior detailed calculations. For example, let us compare the multiplets  $(h_{11/2})^2$  and  $(d_{5/2})^2$ . Clearly, from Eq. 4.17, the angle between the orbits in the  $2^+$  state is less in  $(h_{11/2})^2$  [ $\theta = 24^\circ$  compared to  $49^\circ$  for  $(d_{5/2})^2$ ]. Therefore, the overlap is greater and the  $2^+$  energy lower so that the  $0^+ - 2^+$  spacing will be less (see Fig. 4.3). By comparing  $0^+ - 2^+ - 4^+ - \dots$  intervals, one can sometimes deduce evidence for particular  $j$  components of the wave functions. Care must be taken in this, however, since  $2^+$  states, even in singly magic nuclei, often have several significant components, exhibiting “collective” behavior and lower energies than can be predicted for single two-particle configurations. Nevertheless, changes in spacings of yrast states (the first states of each  $J$  value) across a sequence of nuclei can sometimes signal the emergence of particular shell model components.

#### 4.5 Some Other Results (Average Shifts, Hole, and Particle–Hole Configurations)

In closing the discussion of two-particle systems, we note a few other important results. Consider the case of two identical particles in equivalent orbits and an odd tensor interaction. Only odd  $k$  terms appear in Eq. 4.24 in this case. The total summed interaction energy  $\Delta E_{\text{tot}}$  is given in general by

$$\Delta E_{\text{tot}} = \sum_j (2J+1) \Delta E(j^2 J) \quad (J \text{ even}) \quad (4.31)$$

From the properties of sums over 6- $j$  symbols, without ever considering the radial functions  $F^*$ , we find that by restricting ourselves to *odd tensor interactions*,

$$\Delta E_{\text{tot}} = \sum_{J \text{ even}} (2J+1) \Delta E(j^2 J) = \frac{2J+1}{2} \Delta E(j^2 J=0) \quad (4.32)$$

That is, the total shift of all the levels in a configuration of two identical particles in the same orbit is simply related just to the shift of the  $J=0$  level, for any odd tensor interaction. Since the  $\delta$ -function interaction is equivalent to an odd tensor interaction, it can be expected that Eq. 4.31 will be approximately satisfied in real nuclei. Finally, we re-emphasize that it is the separation into angular and radial coordinates that allows results that are totally independent of the details of the interaction (except, in this case, for the assumption of odd tensors).

Thus far, we have restricted the discussion to two valence particles. Multiparticle configurations will be dealt with shortly. It is useful, however, to consider one simple result that allows a nice generalization of the present discussion. Using the formalism of the seniority scheme, it is possible to relate the matrix elements of any two-body operator in the  $j^n$  configuration to matrix elements in configurations with fewer particles. For the large class of interactions that conserve seniority (including a  $\delta$ -function that is a prototype of short-range interactions) it can be shown that in a multiparticle,  $j^n$  configuration, the more nucleons that are paired off to  $J=0$ , the lower-lying the state will be. Thus, for  $n$  even, the lowest state of the  $j^n$  configuration is a  $J^\pi = 0^+$  state with all nucleons paired to  $J=0$ . (The  $\Delta E(j, j_z J)$  for the levels of the configuration

$|j^2J\rangle$  is just a special case of this). This result is sometimes called the pairing property, and is characteristic of any interaction that conserves seniority. Another key result is that the order and spacing of the  $J \neq 0$  states in the  $j^r$  configuration with two unpaired particles will be exactly the same as in the  $j^2$  configuration. The more realistic situation in which the valence nucleons occupy several  $j$  orbits,  $j_1, j_2, \dots$  in a multiparticle configuration  $|j_1^{n_1}, j_2^{n_2}, \dots, j_r^{n_r}\rangle$  with  $n_i$  even, is just a generalization. By the first result, the  $J = 0$  combination will lie lower than one in which a pair of nucleons is coupled to  $J \neq 0$ . Thus we can generalize these conclusions and state that the ground state of even-even nuclei will always be  $0^+$ . Moreover, since the odd  $J$  levels of  $|j^rJ\rangle$  are unaffected by a  $\delta$ -interaction ( $n$  even), the low-lying *positive* parity states should all have *even* spin and should increase in energy with spin. Remarkably, in view of the simplicity of the argument, this is an almost universally observed situation.

Furthermore, we noted that in  $\pi = -$  two-particle configurations of identical particles,  $|j_1 j_2 J\rangle$ , it is the odd spin levels that are lowered. A simple generalization using the seniority scheme shows that the lowest-lying *negative* parity levels in even-even nuclei should have *odd* spin. This is also almost always observed, and is known as the Talmi-Glaubman rule.

One can go even further. Consider an arbitrary shell in heavy nuclei consisting of several states ( $j$  orbits) from one shell and one unique parity orbit from the next shell. Recall from Fig. 3.2 that the highest normal parity  $l$  value,  $l_{\max}$ , in each succeeding major shell increases by one. The corresponding highest  $j$  value is  $j_{\max} = l_{\max} - 1/2$ . (The  $j = l_{\max} + 1/2$  is the orbit brought down by the spin orbit interaction into the next lower shell.) The next highest  $j$  is  $l_{\max} - 3/2$ . The unique parity orbit is the  $l + 1/2$  coupling from the next highest shell, and so has  $j_{\text{unique}} = l_{\max} + 1 + 1/2 = l_{\max} + 3/2$ . For example, in the 50–82 shell,  $l_{\max} = 4$ , so the highest normal parity orbits are the  $g_{7/2}$ ,  $d_{5/2}$  and the unique parity orbit is  $h_{11/2}$ . In the  $g_{7/2} - h_{11/2}$  configuration, our rules (see Table 4.2) show that the  $J = j_1 + j_2 = 7/2 + 11/2 = 9^-$  state is brought lowest and the  $2^-$  is high-lying at the unperturbed energy. In the  $d_{5/2} - h_{11/2}$  case, the  $J^\pi = 3^-$  is lowest. A little thought shows that this relationship of  $j$  values is generally true for any shell in heavy nuclei. Therefore, we can obtain, without calculation, two general predictions. First, the lowest-spin, negative parity, two-particle state in an even-even nucleus will be a  $2^-$  level: there is no simple spin combination that gives a  $1^-$  level. However, since this  $2^-$  level always results from a  $j = l - 1/2$  normal parity orbit coupled antiparallel to a  $j = l + 1/2$  unique parity orbit, it will always occur rather high in energy. Therefore, the lowest-lying, low-spin, negative parity state will be the  $3^-$  level. This prediction is borne out in nearly all heavy even-even nondoubly magic nuclei (in closed shell nuclei two *different* shells are involved in  $\pi = -$  excitations). Examples were shown in Figs. 2.5 ( $^{210}\text{Pb}$ ) and 2.6 (Sn). The main exceptions to all these predictions are themselves illuminating: they concern nonspherical, or deformed, nuclei in which, to borrow terminology from a later chapter, one sometimes encounters two-quasi-particle, negative parity excitations involving a unique parity Nilsson orbit (e.g., the low-lying  $4^-$  state in  $^{168}\text{Er}$ ). But, as is well known, the nonspherical character of these nuclei is itself induced by a strong residual quadrupole interaction: being an even rank tensor, it does not conserve seniority and

therefore, a priori, one would not expect the preceding arguments to apply.

A final topic to deal with before considering more complex multiparticle systems is the spectra of hole and particle-hole configurations, where, by the former, we mean those of the type  $(j^{-n}) = (j^{2j+1-n})$ . We have briefly mentioned these in our discussion of multipole forces. Here, we obtain a few more explicit results.

For hole states, a diagonal matrix element of any *single particle* operator acting on an  $n$ -hole state  $|j^{-n}JM\rangle$  will be equal in magnitude to its value in the  $n$ -particle system  $|j^rJM\rangle$ . The sign relation will depend on the odd or even tensor character of the operator. This is easy to see by considering all the possible  $m$  states of the  $n$ -hole configuration. There will be  $n$  unoccupied  $m$  states. The expectation value of a single-particle operator  $\mathbf{O}_m$  (which we denote  $\mathbf{O}$  for simplicity) will be the sum of its expectation values over all the particles:

$$\left\langle m_i^{-n} \left| \sum_{i=1}^{2j+1-n} \mathbf{O} \right| m_i^{-n} \right\rangle$$

where  $m^{-n}$  simply indicates the  $n$ -hole state, but where the calculation is carried out over the  $2j + 1 - n$  particles. This is clearly equal to

$$\left\langle m_i \left| \sum_{i=1}^{2j+1} \mathbf{O} \right| m_i \right\rangle - \left\langle m_i^n \left| \sum_{i=2j+1-n}^{2j+1} \mathbf{O} \right| m_i^n \right\rangle$$

that is, equal to the sum over the entire shell minus that for the  $n$  missing particles. But, we have shown above that the first term must vanish since the closed  $j$  shell can have no preferred direction in space and, therefore

$$\left\langle m^{-n} \left| \sum_{i=1}^{2j+1-n} \mathbf{O} \right| m^{-n} \right\rangle = - \left\langle m_i^n \left| \sum_{i=1}^n \mathbf{O} \right| m_i^n \right\rangle$$

Note that the  $n$ -particle and  $n$ -hole states are not exactly equivalent. They have different total  $M$  values. For  $n$  particles in a given  $j$  state occupying  $m$  states  $m_1, m_2, \dots, m_n, M_p = {}^n \Sigma_{i=1}^n m_i$ . For  $n$  holes in the same orbit, one clearly must have  $M_h = -M_p$  (e.g.,  $1/2 + 3/2 = -[5/2 + (-1/2) + (-3/2) + (-5/2)]$ ). So the above matrix element can be written (in simplified notation)

$$\langle J, -M | \mathbf{O} | J, -M \rangle_h = - \langle JM | \mathbf{O} | JM \rangle_p$$

where the subscripts indicate the  $n$ -hole and  $n$ -particle configurations. Using the Wigner-Eckart theorem for a tensor operator  $\mathbf{O}^k$  of rank  $k$  gives

$$\langle J, -M | \mathbf{O}^k | J, -M \rangle = (-1)^k \langle J, M | \mathbf{O}^k | J, M \rangle$$

and hence we can now relate the matrix elements of any single-particle operator in states of the *same*  $JM$  for  $n$ -hole and  $n$ -particle configurations:

$$\langle j^{-n}J | \mathbf{O}^k | j^{-n}J \rangle = (-1)^{k+1} \langle j^nJ | \mathbf{O}^k | j^nJ \rangle \quad (k \neq 0) \quad (4.33)$$

This gives the critical result that the expectation value of any *odd tensor* single-particle operator (e.g., magnetic moment) in an *n-hole* state is the same as the corresponding *n-particle* expectation value, while for even rank tensors (e.g., quadrupole moment), the two expectation values are the negatives of each other.

In Chapter 5 we shall encounter more general results of this special case. This has immediate consequences of great importance. It implies, for example, that magnetic moments or dipole transition rates are the same for corresponding particle and hole configurations, while quadrupole moments or E2 matrix elements change sign. Therefore, such matrix elements must vanish at mid-shell. Of course, these features are well known empirically, although they are partly obscured by configuration mixing effects.

A nice extension of this is to the interaction energies in particle-hole configurations relative to those in particle-particle ones. Compare a proton-neutron particle-particle configuration with a proton hole-neutron particle configuration. The interaction is a product of proton and neutron tensor operators. The effect of the neutron operator on the neutron wave functions (a particle in both cases) is the same for both configurations. Only the proton operator acts on different configurations (particle in one case, hole in the other) and the above results for one-body operators then apply. Thus, for an odd tensor interaction (product of odd tensor one-body operators), the energy shifts  $\Delta E(j_p^{-1} j_n J) = \Delta E(j_p j_n J)$  while, for an even tensor interaction,  $\Delta E(j_p^{-1} j_n J) = -\Delta E(j_p j_n J)$ . The  $U, V$  dependence of a quadrupole force leading to the up-and-down pointing parabolas for p-p (or h-h) and p-h configurations in Eq. 4.30 is an example of this sign change. For the more general case of a mixed-interaction, the results are slightly more complicated and are given by

$$\Delta E(j_p^{-1} j_n JM) = \sum_J (2J+1) \left| \begin{array}{c} j_p \quad j_n \quad J \\ j_p \quad j_n \quad J' \end{array} \right\rangle \Delta E(j_p j_n J' M) \quad (4.34)$$

Note that this gives the energy *differences* for different  $J$  values. The energies themselves can have a constant additive term that is  $J$ -independent (but that can depend on  $j$ ). Thus, while Eq. 4.34, or the simpler relations for odd and even tensor interactions, relates p-h and p-p spectra for a *given j shell*, it does not relate such spectra for different  $j$  orbits in a major shell.

Since, physically, any very short-range interaction cannot give results qualitatively different from that of a  $\delta$ -function (equivalent to an odd tensor interaction), one expects that the odd tensor result will be closer to that observed empirically. In other words, the energies (order and spacing) will be identical in the p-h and p-p configurations. Nevertheless, Eq. 4.34 is very important because it is so general. It is valid for any two-body interaction in a  $jj$ -coupling scheme. Moreover, it has a practical use from a different, empirical, point of view. Without knowing anything about the actual interaction, the knowledge of the order and spacings in a p-p configuration allows one to predict those in the corresponding p-h configuration. A classic example of this is the comparison of  $^{17}_{\text{Cl}} 2_1^+$  and  $^{19}_{\text{K}} 2_1^+$ : the former is expected to be a  $(d_{3/2p} f_{7/2n})$  configuration, while the latter is  $(d^3_{3/2p} f_{7/2n}) = (d^{-1}_{3/2p} f_{7/2n})$ . The comparison is

included in Fig. 4.7, where the empirical  $^{40}\text{K}$  energies were used to calculate the level energies in  $^{38}\text{Cl}$ . The agreement is excellent.

Finally, we consider the interaction energies of the  $(j^nJ)$  configuration relative to those in the  $(j^rJ)$  configuration. By arguments similar to the preceding in the  $m$ -scheme, it is easy to show that the *interaction energy* for any two-body operator in an  $n$ -hole state will be equal to that in the  $n$ -particle state plus an additive constant. Therefore all *spacings* in  $n$ -hole configurations  $|j^nJ\rangle$  should be identical to those in the corresponding  $n$ -particle states  $|j^rJ\rangle$ . Note an important point analogous to a comment we stressed in regard to the effect of closed shells on open shells in Chapter 3. As used here, the term shell refers to a single  $j$  shell, not a *major* shell consisting, generally, of several  $j$  values. The additive constant relating  $n$ -hole to  $n$ -particle configuration need not be independent of  $j$ . Therefore, the full set of spacings in a configuration such as  $|j_1^{-n_1} j_2^{-n_2} \dots J\rangle$  will not generally equal those in  $|j_1^{n_1} j_2^{n_2} \dots J\rangle$ . The equality of spacings applies to each  $j$ , individually. If the realistic wave functions contain admixtures of several  $j$  values, there is no simple general relation of particle and hole energies.

A final point: thus far we have only discussed diagonal matrix elements (energy shifts) due to a  $\delta$ -interaction, but off diagonal effects are equally important. These, of course, give rise to the mixed wave functions characteristic of realistic shell model calculations. Expressions for the off-diagonal matrix elements  $\langle j_1 j_2 | \delta | j_3 j_4 \rangle$  are similar to Eq. 4.7, except there is now a second  $3-j$  symbol involving  $j_3, j_4$ . The strength of a given matrix element then depends on the angular correlation of the two particles in both initial and final states, as well as on the radial overlaps.

It is worthwhile giving a perspective on what we have done in this chapter. We first considered a  $\delta$ -function residual interaction in a rather quantitative way, for both like and unlike particles. Then, we noted the geometrical relation of the orbits in two-body interactions. With a corresponding geometrical understanding of the force between these two particles, it is then trivial to deduce (intuitively or quantitatively) the effects of that force on the various total angular momenta  $J$ . We did this in detail for the  $\delta$ -interaction, recovering the earlier results. We then developed the idea of a multipole expansion of any central interaction that gives the needed geometrical structure, and showed how it can be used to estimate the effects of an arbitrary two-body residual interaction of such type. All this was carried out for two-particle configurations. Now we turn to see how these results can be used for the multiparticle case.

## 5

## MULTIPARTICLE CONFIGURATIONS

We now turn to a more systematic treatment of multiparticle ( $n > 2$ ) configurations of valence nucleons. We have already anticipated a few results from this discussion in Chapter 4. Without having done so, the two-particle results would have been completely useless. We needed to understand, for example, the result that closed shells could be ignored in considering residual interactions, along with some of the results relating p–h to p–p spectra. This allowed us to apply the two-particle discussion to the case of two valence particles or holes relative to any closed shell. We also quoted the enormously important conclusion that (if seniority is conserved) many predictions for  $|j^n J\rangle$  configurations are identical to those for  $|j^2 J\rangle$  configurations. (The requirement of seniority conservation basically means that the other  $(n-2)$ -particles couple pairwise to  $J_{n-2} = 0$ .) Thus the two-particle results could be used for nearly all spherical nuclei.

### 5.1 $J$ Values in Multiparticle Configurations: The $m$ Scheme

Clearly, our first task in the systematic study of multiparticle systems is to consider which values of the total angular momenta  $J$  are permissible for an  $n$ -particle system. The principal consideration here is, of course, the restrictions imposed by the Pauli principle. There are several ways of approaching this issue. The most physically transparent and easy to use is the so-called  $m$ -scheme, to which we now turn. Let us start by working out an explicit case. Consider three identical nucleons in a  $d_{5/2}$  orbit. They cannot couple to a  $J = 15/2$ , since such a state must have an  $M = 15/2$  substate. The only way such a substate can be made is by placing all three particles in  $m = 5/2$  substates, violating the Pauli principle. Similarly,  $J = 13/2$  or  $11/2$  states are impossible since the former would require two of the particles to be in  $m = 5/2$  substates and  $J = 11/2$  would require two particles in  $m = 3/2$  states. However, a  $J = 9/2$  state is indeed possible since it can be formed by placing three particles in the states  $j_1 m_1 = 5/2, 5/2, j_2 m_2 = 5/2, 3/2, j_3 m_3 = 5/2, 1/2$ .

It is easy to see that a slight generalization of this example gives the following result: in the configuration  $j^n$  the maximum angular momentum is given by

$$J_{\max} = nj - \sum_{k=2}^n (k-1) = nj - \frac{n(n-1)}{2}$$

**Table 5.1.**  $m$  scheme for the configuration  $|(7/2)^2J\rangle^*$ 

$j_1 = 7/2$	$j_2 = 7/2$	$M$	$J$
$m_1$	$m_2$		
7/2	5/2	6	
7/2	3/2	5	
7/2	1/2	4	
7/2	-1/2	3	6
7/2	-3/2	2	
7/2	-5/2	1	
7/2	-7/2	0	
5/2	3/2	4	
5/2	1/2	3	
5/2	-1/2	2	4
5/2	-3/2	1	
5/2	-5/2	0	
3/2	1/2	2	
3/2	-1/2	1	2
3/2	-3/2	0	
1/2	-1/2	0	0

\*Only positive total  $M$  values are shown, the table is symmetric for  $M < 0$ .

For the  $(d_{5/2})^3$  case just discussed, this gives  $J_{\max} = 3j - 3 = 9/2$ .

Thus, we see an example of how a consideration of the possible  $m$  substate occupations can give information on permissible total angular momenta  $J$ . Basically, the  $m$ -scheme is a systematic set of procedures for doing this in a general case.

The  $m$ -scheme is best described with a detailed example. Earlier we showed that only even  $J$  values were allowed in the  $j^2$  configuration of identical nucleons. This was argued in terms of the symmetry properties of spherical harmonics. However, it can also be seen by inspecting the possible magnetic substates. Table 5.1 summarizes the allowed magnetic substates for a two-particle configuration  $(7/2)^2$ . (Actually, the  $M < 0$  cases are omitted since they are completely symmetric to the  $M > 0$  cases.) We construct such a table starting with the highest magnetic substate for particle 1 and list all of the possible substates for particle 2 allowed by the Pauli principle, then carrying out the same procedure for the next lower magnetic substate (in this case 5/2) for the first particle. It is necessary to recall that the two nucleons are indistinguishable so a combination 5/2, 7/2, for example, is not allowed, since the 7/2 and 5/2 combination has already been listed. Continuing in this way, we obtain all of the possible  $m$  values for the two-particle system. Since a given total angular momentum  $J$  must have magnetic substates  $M = J, J-1, \dots, -(J-1), -J$ , it is now trivial to deduce the possible final  $J$  values using the table. In the present example, there must be a  $J = 6$  state, since there is a  $M = 6$  configuration. This  $J = 6$  state has magnetic substates  $M = 6, 5, 4, 3, 2, 1, 0$ , and the corresponding negative values. Thus the top seven magnetic substates listed in the table must be used up for this single  $J = 6$  state. There is no  $M = 5$  magnetic substate left over and thus there cannot be a  $J = 5$  state. There can, however, be a  $J = 4$  configuration that consumes the  $M = 4, 3, 2, 1, 0$  magnetic substates

**Table 5.2.**  $m$  scheme for the configuration  $| (5/2)^3 J \rangle$ 

$j_1 = 5/2$	$j_2 = 5/2$	$j_3 = 5/2$	$M$	$J$
$m_1$	$m_2$	$m_3$		
5/2	3/2	1/2	9/2	
5/2	3/2	-1/2	7/2	
5/2	3/2	-3/2	5/2	
5/2	3/2	-5/2	3/2	
5/2	1/2	-1/2	5/2	
5/2	1/2	-3/2	3/2	9/2
5/2	1/2	-5/2	1/2	
5/2	-1/2	-3/2	1/2	
3/2	1/2	-1/2	3/2	
3/2	1/2	-3/2	1/2	3/2

$J = 9/2, 5/2, 3/2$

\*The full set of allowable  $m_i$  combinations that give  $M > 0$  are obtained by the conditions  $m_1 > 0$ ,  $m_3 < m_2 < m_1$  and no two  $m_i$  values identical.

listed next in the table. By continuing this argument, one sees that there is no  $J = 3$  state, but there are a  $J = 2$  and a  $J = 0$  state, thus proving in a different way the result obtained earlier that two identical particles in the same orbit can couple only to even total angular momenta  $J$ .

The case for  $(5/2)^3$  configuration is shown in Table 5.2, which will not be discussed in detail although the reader may go through the example and verify the results just as we did for the  $(7/2)^2$  case. Clearly, for multinucleon configurations where  $n$  is large, this procedure can be lengthy. Other techniques are available. However, the  $m$ -scheme is important because it shows in a transparent way how the physical effects of the Pauli principle arise.

We noted above that the  $m$ -scheme gives a rule for the maximum permissible  $J$  value in a  $j^n$  configuration of identical particles very simply. It also gives, in an equally simple way, the result that a  $j^n$  configuration can never have a state with  $J = J_{\max} - 1$ . We will show this only for the case of two particles, but the generalization is straightforward. (Although the following considerations are general, reference to the specific example in Table 5.1 will clarify the arguments.) The maximum  $J$  in a  $j^2$  configuration is  $J_{\max} = 2j - 1$ . A state  $J = J_{\max} - 1$  would have (if it existed)  $J = 2(j - 1)$ . One value of  $M = J_{\max} - 1$  must be used for the  $J = J_{\max}$  state. Therefore, in order to have a state with  $J = J_{\max} - 1 = 2(j - 1)$ , there must be a second permissible  $M = J_{\max} - 1 = 2(j - 1)$  state. This cannot involve a particle in an  $m = j$  state, since that state is already consumed for the  $J = J_{\max}$  level. Therefore, the only way to make another magnetic substate  $M = 2(j - 1)$  is to have two particles with  $m = j - 1$ . But this violates the Pauli principle, and therefore is impossible, proving that a  $J = J_{\max} - 1$  state never exists in a  $j^n$  configuration. As noted, this can be generalized to the  $j^n$  configuration.

## 5.2 Coefficients of Fractional Parentage (CFP)

Now that we have a feeling for those  $J$  values that can be obtained for any multiparticle configuration, we can discuss the effects of various interactions

on the energies of such  $J$  states and dynamic matrix elements involving such configurations.

Clearly, when considerations such as those discussed in Chapter 4 are attempted for multiparticle configurations, the situation rapidly becomes much more complex. To see this in a simple example, consider a  $(d_{5/2})^3$  configuration of identical nucleons. A  $J = 5/2$  state can be made in three distinct ways by first coupling two particles to an intermediate  $J' = 0, 2, 4$ :

$$\left[ (d_{5/2})^2 J' = 0, j = 5/2 \right]^5$$

$$\left[ (d_{5/2})^2 J' = 2, j = 5/2 \right]^5$$

and

$$\left[ (d_{5/2})^4 J' = 4, j = 5/2 \right]^5$$

However, the  $(5/2)^3$  configuration has only one  $J = 5/2$  state (see Table 5.2). Its wave function must therefore be a totally antisymmetric linear combination of these three basis states. The normalized coefficients in this linear combination are called *coefficients of fractional parentage* (CFP): their squares give the probability that a given final state is constructed from a specific “parent” configuration—in this case, a two-particle state. The relative magnitudes of the three CFP’s for the  $(d_{5/2})^3$  configuration are not arbitrary, but are given by certain angular momentum coupling coefficients. CFP coefficients can be constructed not only for three-particle configurations, but for any  $n$ .

Unfortunately, the complexity of the possible couplings makes the notation for the coefficients rather complex and this has deterred many nuclear physicists from delving into the subject; the formalism can be terrifying. Formal textbooks can be filled with page after page of long, daunting expressions involving sequences of CFP coefficients, angular momentum coefficients, summations over them, and the like. Here, we attempt to cut through much of this by summarizing some of the essential results and their motivations with a few simple examples. This is not entirely satisfactory, since it deprives the reader of an appreciation of the beauty and power of the formalism. Moreover, as the author can personally attest, while a simple presentation of the final results saves the reader from the tedium of struggling through their derivation, it also confers on them an element of mystery—the reader is left with a sense of wonder at how one can start with such general interactions and general configurations and end up with very simple final results. He or she may glance back over the imposing derivations in the hopes of seeing where some simplifying assumption or some restrictive case has been invoked. The real power and beauty of the method, however, is that such assumptions are usually not required: very general results that enormously simplify the treatment of many-particle shell model configurations can often be obtained.

In any case, we will introduce the formal notation for CFP coefficients, but will avoid their manipulation as much as possible. We will derive one simple result that illustrates their power and economy.

Consider a configuration of identical nucleons in equivalent orbits, the  $|j^n JM\rangle$  state ( $\alpha$  specifies any additional quantum numbers needed to describe the states). This  $n$ -particle state can be written in terms of  $(n-2)$ -particle wave functions by using the two-particle CFP coefficients (there are also analogously defined one-particle CFP coefficients). The CFP is denoted

$$\langle j^n J \{ |j^2(J_2)j^{n-2}(J_{n-2})J \} \rangle$$

and determines, as in the preceding three-particle case, the probability that the wave function  $|j^n JM\rangle$  can be written in terms of the  $(n-2)$ -particle configuration  $|j^{n-2}(J_{n-2}M_{n-2})\rangle$  coupled to a two-particle configuration  $|j^2 J_2 M_2\rangle$ . The defining equation is therefore

$$|j^n JM\rangle = \sum_{J_2, J_{n-2}} \langle j^n J \{ |j^2(J_2)j^{n-2}(J_{n-2})J \} | j^2(J_2)j^{n-2}(J_{n-2})JM \rangle \quad (5.1)$$

Clearly, then,

$$\sum_{J_2, J_{n-2}} (\text{CFP})^2 = 1$$

We can see how the concept of CFP coefficients and the parentage of  $n$ -particle configurations is useful. Consider a configuration  $|j^n J\rangle$  and ask what the energy shifts,  $\Delta E(j^n J)$ , are for each final  $J$  value for an arbitrary interaction. (Note that, as usual, we drop the magnetic quantum numbers to simplify the notation.) First, we note that, since the particles are indistinguishable, the *total* interaction energy in any final state  $J$  is given simply by the interaction energy for any pair of nucleons (say, particles 1 and 2) times the total number of possible pairs  $n(n-1)/2$ . However, the two-particle matrix element  $V_{12}$  can only depend on  $J_2$ , and not on the way in which  $J_2$  is coupled with  $J_{n-2}$  for the other  $n-2$  nucleons to give the final  $J$ . The total interaction energy for particles 1 and 2 is just the sum of the interaction energies for each two-particle angular momentum  $J_2$  multiplied by the probability of each  $J_2$  in the state  $|j^n J\rangle$ . We denote this probability  $W(j^n J J_2)$ . Thus, we can immediately write the interaction energy from particles 1 and 2 in the state  $|j^n J\rangle$  as:

$$\left\langle j^n J \left| \sum_{i>j}^n V_{ij} \right| j^n J \right\rangle = \sum_{J_2} W(j^n J J_2) \langle j^2 J_2 | V_{12} | j^2 J_2 \rangle \quad (5.2)$$

where the  $W$  coefficient is the sum of the squares of the CFP coefficients for a given  $J_2$  over all possible values  $J_{n-2}$ . That is,

$$W(j^n J J_2) = \sum_{J_{n-2}} \left| \langle j^n J \{ |j^2(J_2)j^{n-2}(J_{n-2})J \} \rangle \right|^2 \quad (5.3)$$

The interesting point here is that there are in general *fewer* values of  $J_2$  than there are of  $J$ . For example, in the  $(7/2)^3$  configuration,  $J$  can be  $15/2, 11/2, 9/2, 7/2, 5/2, 3/2$  while  $(7/2)^2$  can only couple to  $J_2 = 0, 2, 4$ , and  $6$ . Thus, by Eq. 5.2, the six energies of the configuration  $|j^n J\rangle$  are given in terms of the four matrix elements

$$\langle j^2 J | V_{12} | j^2 J \rangle, \quad J=0, 2, 4, 6$$

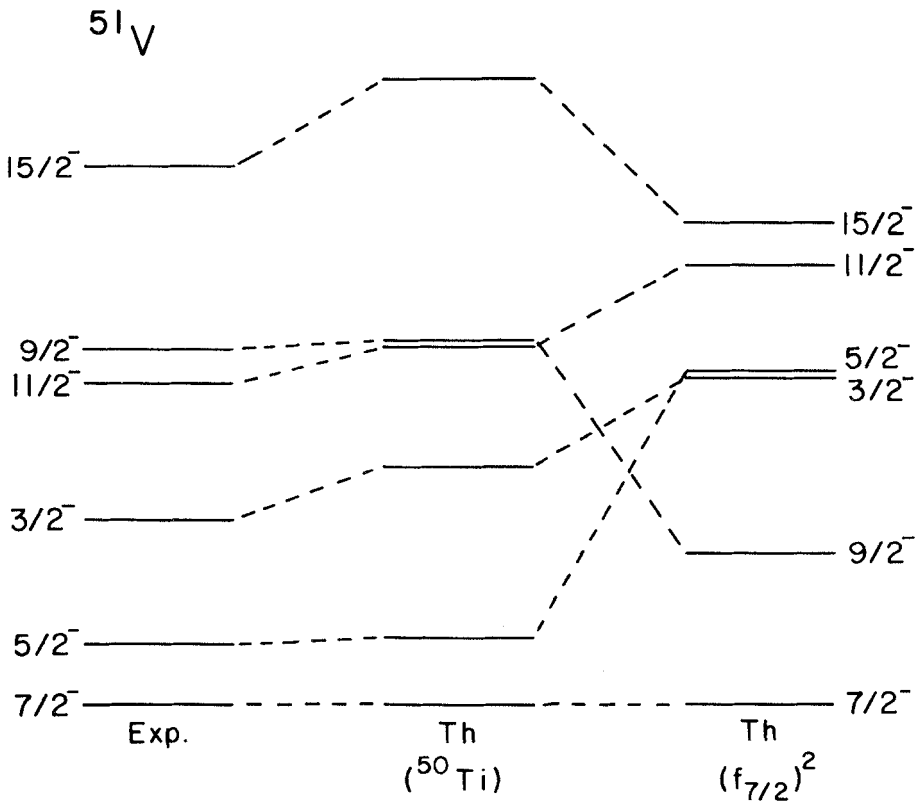


**Fig. 5.1.** Comparison of the low-lying empirical levels of  $^{51}\text{V}$  with calculations obtained by coupling an  $f_{7/2}$  proton to an  $(f_{7/2})^2$  two-particle configuration (right) and by coupling an  $f_{7/2}$  proton to the empirical levels of  $^{50}\text{Ti}$ . (See deShalit, 1974.)

The beauty of this is that these matrix elements are usually easy to calculate for a known interaction and, even when the interaction is not known, empirical values for them can be obtained from the neighboring even-even nucleus (with  $n=2$ ). This can then be used to calculate the energy levels of the adjacent odd mass nucleus.

We have discussed the  $(7/2)^3$  example here because it is treated in detail in de Shalit and Feshbach, where the low-lying  $(f_{7/2})^3$  energy levels of  $^{51}\text{V}$  are calculated in terms of the empirically known  $(f_{7/2})^2$  levels of  $^{50}\text{Ti}$  ( $0^+: 0$ ,  $2^+: 1.55$ ,  $4^+: 2.68$ ,  $6^+: 3.2$  MeV). The results are shown in Fig. 5.1; the agreement is remarkably good for such a simple approach. Note once again that nowhere in this discussion has *any* aspect of the *interaction* been specified, except to assume that it is two-body only. We could also have calculated  $^{51}\text{V}$  with the same formulas using a  $\delta$ -function interaction to simulate  $^{50}\text{Ti}$ , that is, to define the  $(f_{7/2})^2$  matrix elements. Normalizing the  $\delta$ -function strength to the  $0^+-6^-$  spacing in  $^{50}\text{Ti}$  gives calculated  $^{50}\text{Ti}$  energies of  $0^+: 0$ ,  $2^+: 2.68$ ,  $4^+: 3.0$ , and  $6^+: 3.2$  MeV. These have a different distribution than the empirical levels and, when applied to  $^{51}\text{V}$ , give the fit on the right of Fig. 5.1. Clearly, this approach is not

nearly as successful. The point is that the *empirical*  $^{50}\text{Ti}$  spectrum automatically includes *all* relevant interactions in the  $(f_{7/2})^2$  system. The CFP techniques relate this directly to  $^{51}\text{V}$ , independent of a knowledge or guess of the interaction. Thus, an understanding of the makeup of an  $n$ -particle configuration in terms of its  $(n-2)$ -particle structure can greatly simplify the treatment of nuclear spectra in complex systems. The present results can be generalized to  $n > 3$ , and provide comparable, and even greater, simplifications.

### 5.3 Multiparticle Configurations $j^n$ : The Seniority Scheme

When there are numerous particles outside closed shells, they can enter different shell model orbits. For example, in  $^{99}_{40}\text{Zr}_{59}$  the nine valence neutrons might be in a configuration  $(d_{5/2})^6 (g_{7/2})^3$ . Here, the  $d_{5/2}$  shell is filled and the earlier arguments on the effect of closed shells on the values of  $\Delta E(j^{2j+1} j^n J)$  tell us that the  $d_{5/2}$  orbit can be neglected, so this configuration is equivalent to  $(g_{7/2})^3$ . Now, consider  $^{95}\text{Zr}$ . In this case, the lowest expected configuration would be  $(d_{5/2})^5$ . By the particle-hole equivalency discussed earlier, this is exactly equivalent to a single neutron in the  $d_{5/2}$  orbit, leading to a one-state configuration with  $J = j = 5/2$  and, indeed, the ground state of  $^{95}\text{Zr}$  is  $5/2^+$ . However, one could also imagine excited states in  $^{95}\text{Zr}$  of the form  $(d_{5/2})^3 (g_{7/2})^2$ . Normally, at least near closed shells, such configurations are rather high-lying excited states: our primary interest is usually in the lowest-lying levels in which as many particles as possible are packed into the lowest accessible  $j$  value. Thus, at least in simple shell model treatments, one is frequently interested in  $j^n$  configurations. Moreover, even though realistic shell model calculations will often involve important components coupling two  $j$  values, an understanding of the single  $j$  case greatly helps to interpret and even anticipate such calculations. So far, we have ignored the possibility of both valence protons and neutrons. This clearly complicates the situation, as seen in the discussion earlier of the  $\delta$ -function interaction for p-n systems. Moreover, as we shall see later, once one has nucleons of both types outside of closed shells, collective effects rapidly accumulate and other models provide alternate, and often better, approaches. Therefore, it is appropriate to again stress the  $j^n$  configuration of identical nucleons. Despite this restriction, the following considerations have extremely wide applicability.

The tendency of particles to pair to  $J = 0^+$  leads to a scheme in which this property is explicitly recognized and exploited. Consider the  $j^n$  configuration. We ask what is the *smallest* value of  $n$  that can produce a given  $J$  value. Denoting this value by  $v$ , it is clear that there can be no particles coupled in pairs to  $J = 0$  in the configuration  $j^n J$ . (Otherwise, a  $j^{v-2}$  configuration would have a spin  $J$ .) Such a state is then said to have *seniority*  $v$ . From a configuration  $j^{v+2}$  we can make a state of the same spin  $J$  by coupling one pair of particles to  $J = 0$ . This state is also said to have seniority  $v$ . Physically,  $v$  is simply the number of *unpaired* particles in a state of angular momentum  $J$  in the configuration  $j^n$ . The number of paired particles is  $(n - v)$  and the number of such pairs is  $(n - v)/2$ . For  $v = 0$ , all particles are paired and  $J = 0$ .

Let us further illustrate this concept with a simple example. Consider the

$(f_{7/2})^4$  configuration. From the  $m$ -scheme and the simple formula derived earlier,  $J_{\max} = 4j - 4(3)/2 = 8$ . This state can only be made by maximizing the alignment of all  $j = 7/2$  angular momenta as allowed by the Pauli principle. The  $J = 8$  state therefore has seniority 4; there are no particles coupled in pairs to  $J = 0$ . On the other hand,  $J = 2, 4$ , and 6 states can be made by first coupling one pair of particles to  $J = 0$  and then using the remaining  $| (7/2)^2 \rangle$  configuration to produce angular momenta of 2, 4, or 6. Such states have seniority  $\nu = 2$ . Finally, the  $J = 0$  state of the  $(f_{7/2})^4$  configuration obviously has seniority 0, that is, all particles are coupled in pairs to  $J = 0$ . (Note that there may be other  $J = 0, 2, 4, 6$  states of the  $(f_{7/2})^4$  configuration, all with  $\nu = 4$ .) What we have shown is that  $J = 0, 2, 4, 6$  states of  $\nu = 0$  or  $\nu = 2$  can be constructed.

The seniority concept is important for several reasons. First, it leads to many simple, powerful results under very general conditions. For example, various interactions and matrix elements can be classified in terms of whether or not they conserve seniority. As will be seen, they have very different properties as the number of particles in a shell increases. Secondly, and perhaps most importantly, it seems that many realistic residual interactions conserve seniority, so this scheme gives reasonable predictions for actual nuclei. It is impossible within the scope or philosophy of this book to derive all the results of the seniority scheme without adding an undesirable complexity. Such derivations are available in many detailed textbooks on the shell model. The complexity of these derivations often tends to obscure some of the simple ideas lying behind them. It is these ideas that we wish to emphasize here. We will derive or motivate a few crucial results; the others can be obtained by analogous, though more tedious, manipulations.

Perhaps the most important ingredient in understanding the results of the seniority scheme is the following: consider the  $j^2$  configuration and the matrix element of any *odd tensor* interaction. (The introduction of the concept of tensors and their rank here should not be intimidating. The spherical harmonics of order  $k$ ,  $Y_{km}$ , simply form the  $2k + 1$  components of a tensor of rank  $k$ . An example of an odd rank tensor is the magnetic dipole operator. The quadrupole operator is an even rank tensor. As commented earlier, the  $\delta$ -function interaction is equivalent to an odd-tensor interaction.)

For the case of a one-body odd-tensor operator acting in the  $j^2$  configuration

$$\langle j^2 J | \mathbf{O}_k | j^2 J = 0 \rangle = 0 \quad (5.4)$$

The proof of this is trivial. We recall that in the two-particle configuration only even  $J$  values are allowed. Therefore,  $J$  on the left side must be even and, by conservation of angular momentum, there is no way that  $J = 0$  can be coupled to an even  $J$  by an operator carrying odd multipolarity.

Equation 5.4 simply states that *all* matrix elements of one-body odd-tensor operators vanish in the  $j^2$  configuration. This includes the  $J = 0$  case. Odd tensor operators cannot “break” a  $J = 0$  coupled pair, nor can they contribute a diagonal “moment.” The significance of this simple equation cannot be overemphasized.

In many-particle systems, it has three enormously important consequences. For such configurations, one-body operators are normally expressed in terms

of sums over operators acting on each particle. A one-body odd-tensor operator acting in a  $j^n$  configuration is given by  $\mathbf{U}^k = {}^n\Sigma_{i=1} \mathbf{U}_i^k$ . Since an odd tensor operator cannot change any  $|j^2J=0\rangle$  pair to one with  $J \neq 0$  ( $J$  even), odd tensor operators *must conserve seniority*. Equation 5.4 shows that there is no contribution to  $\mathbf{U}^k$  from such pairs of particles coupled to  $J=0$ . Thus matrix elements of one-body odd-tensor operators in  $j^n$  configurations with seniority  $v$ , can be reduced to those in the  $j^v$  configuration. Moreover, they are independent of  $n$  (for  $n \geq v$ ).

These results follow so trivially from Eq. 5.4 that the preceding comments essentially constitute a derivation. However, they are so important and basic that it is worthwhile to go through the arguments more explicitly. Consider a matrix element such as  $\langle j^n v J' | {}^n\Sigma_{i=1} \mathbf{U}_i^k | j^v v J \rangle$ . Since  $v < n$ , the left side can be rewritten in terms of wave functions of the configuration  $|j^{n-v}v(J')^2(J=0)J\rangle$  and similarly for the right side. For simplicity, we take the particles thus separated off as the  $(n-1)$ th and  $n$ th particles. Application of Eq. 5.4 to these two particles contributes nothing to the overall matrix element, and we can replace the operator  ${}^n\Sigma_{i=1} \mathbf{U}_i^k$  with  ${}^{n-2}\Sigma_{i=1} \mathbf{U}_i^k$  extending over  $n-2$  particles. Since the matrix element is now independent of the last two particles, we can integrate over them. Since they are in the same state  $|j^2J=0\rangle$ , this integral is unity by orthogonality. If  $(n-v) \geq 4$ , we can repeat this procedure for another pair of particles. We continue this procedure for any even  $v$  until we are dealing with an operator  ${}^v\Sigma_{i=1} \mathbf{U}_i^k$  acting on the states  $|j^v J\rangle$  and  $|j^v J'\rangle$ . Thus we obtain

$$\left\langle j^n v J' \left| \sum_{i=1}^n \mathbf{U}_i^k \right| j^n v J \right\rangle = \left\langle j^v v J' \left| \sum_{i=1}^v \mathbf{U}_i^k \right| j^v v J \right\rangle \quad (5.5)$$

which shows both the reduction of a matrix element in the  $j^n$  configuration to one in  $j^v$  and the independence of  $n$ .

The other result, conservation of seniority, is equally obtainable. Suppose the two wave functions in the above matrix element have different seniorities  $v, v' < n$ . There is some point in the successive reduction (the successive peeling off of pairs of particles) where an overlap integral over the wave functions  $|j^2J=0\rangle$  and  $|j^2J \neq 0\rangle$  appears. Clearly, by orthogonality, this vanishes. To reiterate, we have the absolutely critical results:

- Odd-tensor single-particle operators conserve seniority in  $j^n$  configurations.
- The matrix elements of odd-tensor single-particle operators in  $j^n$  configurations in the seniority scheme can be reduced to ones in the  $j^v$  configuration.
- These matrix elements are independent of  $n$ .

These rather abstract results have many practical applications. They imply, for example, that the magnetic moment of the  $7/2^+$  state of an  $(f_{7/2})^3$  configuration is identical to that in the single particle  $f_{7/2}$  configuration: in general, magnetic moments in odd mass nuclei where the valence particles occupy a given  $j$  orbit should be independent of the (odd) number of valence nucleons. Similar arguments cannot be applied to even tensor operators like the quadrupole operator. It turns out that these operators are not diagonal in the

seniority scheme, but rather connect states with seniorities  $v$  and  $v \pm 2$ . Using arguments such as these, it is therefore clear why M1 transitions in even mass nuclei are rare—they can only connect states of the same seniority—while E2 transitions dominate even in near-closed shell nuclei. Therefore this dominance is not necessarily a demonstration of collectivity, but a reflection of the seniority structure of low-lying states in  $|j^2J\rangle$  configurations.

Thus far in our discussion of seniority, we have considered single-particle operators representing moments or transitions. Equally important are two-body interactions, which can be either diagonal or nondiagonal. Both are important, although we will emphasize the former since they determine the contribution of residual interactions to level energies. A key example is the  $\delta$ -function interaction. Clearly, interactions can be written as *products* of single-particle operators. We saw an example of this earlier in discussing multipole expansions of arbitrary interactions. We now turn to consider the properties of various interactions in the seniority scheme.

Consider an arbitrary *odd-tensor two-body* interaction  $V_{12}$ . This can be taken as a product of one-body operators,  $\Sigma_{k\text{ odd}} f_1^k f_2^k$ . As with one-body operators, it is extremely useful to be able to relate the two-body interaction matrix elements of seniority  $v$  states in the  $j^v$  configuration ( $n$  even) to the matrix elements in a  $j^v$  configuration. Deriving this desired result is trivial. Consider the matrix element (a subscripted  $k$  labels particles, not rank)

$$\left\langle j^n v \alpha J \left| \sum_{i < k} V_{ik} \right| j^n v \alpha' J \right\rangle$$

where the sum is over the  $n$ -particles, and where  $\alpha$  and  $\alpha'$  denote any additional quantum numbers needed. Since the states have seniority  $v$  (even), there are  $(n - v)$  particles paired off to  $J = 0$ . By the same reasoning that led to Eq. 5.4, the terms in  $\sum_{i < k} V_{ik}$  that act on these particles cannot change their coupling. All that this part of the sum can do is contribute a diagonal matrix element of the form  $\langle j^2J = 0 | V_{ik} | j^2J = 0 \rangle$ . But this is just the lowering of the  $0^+$  energy in a  $j^2$  two-particle configuration. We define this energy lowering by  $V_0$ . The sum contributes this for each such ( $J = 0$ )-coupled pair, of which there are  $(n - v)/2$ . Having thus separated off these particles, we are left with a sum over  $v$  particles of the same interaction. Thus, we obtain,

$$\left\langle j^n v \alpha J \left| \sum_{i < k} V_{ik} \right| j^n v \alpha' J \right\rangle = \left\langle j^v v \alpha J \left| \sum_{i < k} V_{ik} \right| j^v v \alpha' J \right\rangle + \frac{n - v}{2} V_0 \delta_{\alpha\alpha'} \quad (5.6)$$

This interaction matrix element may be either diagonal or nondiagonal (in  $\alpha$ ), but it cannot change  $v$  since it is of odd tensor character. In either case, it is of *absolutely central importance* in nuclear spectroscopy. As with the case of one-body odd-tensor operators, we have an equation relating matrix elements of a two-body interaction in the  $j^v$  configuration to those in the  $j^v$  configuration. Here, however, these matrix elements are not constant across a shell, but *linear* in  $(n - v)/2$ , the number of nucleons paired off to  $J = 0$ . Such matrix elements *peak at midshell*. This feature is sometimes known as the *pairing property*.

To understand other important implications of this, let us first consider

diagonal matrix elements where  $\alpha = \alpha'$ . The second term on the right in Eq. 5.6 is simply the number of pairs of particles coupled to  $J = 0$  multiplied by the interaction energy,  $V_0$ , for each pair. Recalling that we are dealing with attractive residual interactions (larger matrix elements imply lower-lying states), then states with lower seniority  $v$  will lie lower in energy. The  $v = 0$  states, which must have  $J^\pi = 0^+$ , will lie lowest. Immediately, this accounts for the well-known empirical property that the ground states of (spherical) even-even nuclei all have  $J^\pi = 0^+$ .

Similarly for odd mass spherical nuclei, the ground state will usually be a  $v = 1, J = j$  state in which all but one nucleon is paired off in  $|j^2 J = 0\rangle$  combinations.

It is worthwhile to explicitly write Eq. 5.6 for a  $j^n$  configuration in the  $v = 0$ ,  $J = 0$ , and  $v = 1, J = j$  states. For both situations the first term vanishes since there cannot be a two-body interaction in a  $j^{v=0}$  (no particle) or  $j^{v=1}$  (one particle) system. Therefore, the energies are given by the second term:

$$\left\langle j^n J=0 \left| \sum_{i < k}^n V_{ik} \right| j^n J=0 \right\rangle = \frac{n}{2} V_0 \quad (n \text{ even}, v=0) \quad (5.7)$$

$$\left\langle j^n J=j \left| \sum_{i < k}^n V_{ik} \right| j^n J=j \right\rangle = \frac{n-1}{2} V_0 \quad (n \text{ odd}, v=1) \quad (5.8)$$

These equations simply state that the ground state energies in the respective systems depend solely on the numbers of pairs of particles coupled to  $J = 0$ . In the odd particle case, the unpaired nucleon is, from this point of view, just a spectator. Indeed, as de Shalit and Feshbach emphasize, the nuclear force effectively *measures* the number of pairs of particles coupled to  $J = 0$ , at least insofar as it can be approximated by odd tensor interactions.

One of the most crucial uses of Eqs. 5.6 and 5.7 concerns the energies of seniority  $v = 2$  states (the following argument applies to higher seniority states as well, but these are less often identified experimentally). Let us consider the energy difference  $E(j^n v = 2, J) - E(j^n v = 0, J = 0)$ . Simplifying the notation by denoting the interaction by  $V$ , Eq. 5.6 and 5.7 give

$$\begin{aligned} E(j^n, v=2, J) - E(j^n, v=0, J=0) &= \left\langle j^2 J | V | j^2 J \right\rangle + \frac{n-2}{2} V_0 - \frac{n}{2} V_0 \\ &= \left\langle j^2 J | V | j^2 J \right\rangle - V_0 \end{aligned} \quad (5.9)$$

Therefore, the energies of the  $v = 2$  states are independent of  $n$ . Let us also calculate the *spacings* within the  $v = 2$  configuration. These are given by

$$\begin{aligned} E(j^n, v=2, J) - E(j^n, v=2, J') &= \left[ \left\langle j^2 J | V | j^2 J \right\rangle + \frac{n-2}{2} V_0 \right] \\ &\quad - \left[ \left\langle j^2 J' | V | j^2 J' \right\rangle + \frac{n-2}{2} V_0 \right] \\ &= \left\langle j^2 J | V | j^2 J \right\rangle - \left\langle j^2 J' | V | j^2 J' \right\rangle \\ &= E(j^2, v=2, J) - E(j^2, v=2, J') \end{aligned} \quad (5.10)$$

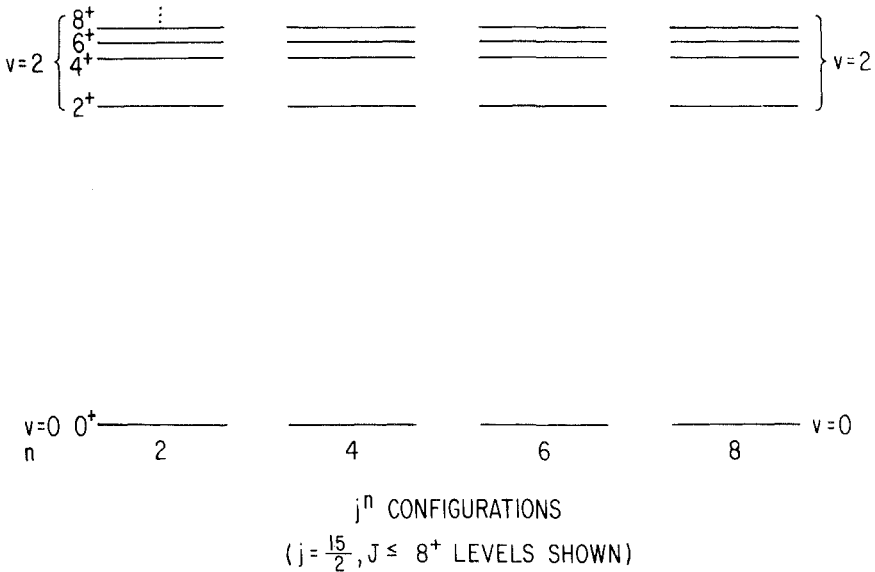


**Fig. 5.2.** Illustration of the constancy of seniority  $v = 2$  levels in  $j^n$  configurations.

Thus, *all* energy differences of seniority  $v = 0$  and  $v = 2$  states in the  $n$ -particle configuration are *identical* to those in the two-particle system and are independent of  $n$ . This is illustrated in Fig. 5.2. This result is crucial because its absence would make it virtually impossible to apply the shell model in a simple way to nuclei other than those within one or two nucleons of closed shells. Indeed, this result was anticipated in the previous chapter in arguing that the shell model has broad applicability. The low-lying levels of good seniority in a  $j^n$  configuration are independent of  $n$ . In practice, more than one orbit  $j$  will be occupied by the valence nucleons. Nevertheless, the present result can be approximately generalized if one writes the wave function in the schematic form

$$\psi = \sum_i \alpha_i |j_i^{ni}\rangle$$

In fact, the incorporation of such two-body configuration mixing is essentially equivalent to a modification of the interaction itself, and thus Eq. 5.6 is widely applicable. The Sn nuclei (see Fig. 2.6) provide a classic example of Eq. 5.10 and its generalization to the multi- $j$  case: the entire known set of  $v = 2$  levels,  $J = 0^+, 2^+, 4^+, 6^+$ , is virtually constant across an entire major shell. The Ca isotopes (Fig. 2.3) provide another example that will be discussed later.

To recapitulate, for the matrix elements of *odd*-tensor operators and interactions between states of good seniority in  $j^n$  configurations:

- One-body *matrix elements* (e.g., dipole moments) are independent of  $n$  and therefore constant across a  $j$  shell. (5.11)

- Two-body *interactions* are linear in the number of paired particles,  $(n - v)/2$ , peaking at midshell. (5.12)

It is possible to derive analogous results for even-tensor operators and interactions. The derivations involve the manipulation of, and recursion relations for, CFP coefficients. These are tedious but straightforward. We will cite two important results. Once again, we look first at one-body operators. As noted, even-tensor operators do not necessarily conserve seniority and can link states with  $\Delta\nu = \pm 2$ . The expression for such matrix elements is given by:

$$\begin{aligned} \left\langle j^n \nu \alpha J \left| \sum_{i=1}^n \mathbf{U}_i^k \right| j^n \nu - 2, \alpha' J' \right\rangle &= \left[ \frac{(n-\nu+2)(2j+3-n-\nu)}{2(2j+3-2\nu)} \right]^{\frac{1}{2}} \\ &\times \left\langle j^\nu \nu \alpha J \left| \sum_{i=1}^\nu \mathbf{U}_i^k \right| j^\nu \nu - 2, \alpha' J' \right\rangle \end{aligned} \quad (5.13)$$

Once again, the power of the seniority scheme allows us to link matrix elements in the configuration  $j^n$  to those in the configuration  $j^\nu$ . The square of Eq. 5.13 gives the behavior of the transition rates induced by the operator throughout a shell. For large  $j$  and  $n$  ( $j, n \gg \nu$ ), this transition probability goes as  $(f(1-f))$  where  $f = n/(2j+1)$  is the fractional filling of the shell. This expression at first increases as  $f$ , then flattens out, peaking at midshell. Moreover, it is clearly symmetric about the midshell point. Probably the most common and important application of this concerns E2 transition rates induced by the operator  $\mathbf{Q} = r^2 Y_2$ . The important quantity  $\langle 2_1^+ | |\mathbf{Q}| | 0_1^+ \rangle^2$  is proportional to the E2 transition rate from the first  $2^+$  state to the ground state in an even-even nucleus, and can be written for the  $j^n$  configuration as [assuming the  $2_1^+(0_1^+)$  state has  $\nu = 2(\nu = 0)$ ]:

$$\langle j^n J=2_1^+ | |\mathbf{Q}| | j^n J=0_1^+ \rangle^2 = \left( \frac{n(2j+1-n)}{2(2j-1)} \right) \langle j^2 J=2_1^+ | |\mathbf{Q}| | j^2 J=0_1^+ \rangle^2 \quad (5.14)$$

For shells that are not too filled, so that  $(2j \pm 1) \gg n$ , this becomes

$$\langle j^n J=2_1^+ | |\mathbf{Q}| | j^n J=0_1^+ \rangle^2 \approx \frac{n}{2} \langle j^2 J=2_1^+ | |\mathbf{Q}| | j^2 J=0_1^+ \rangle^2 \quad (5.15)$$

That is, in the  $j^n$  configuration, the  $B(E2)$  value, defined as

$$B(E2:J_i \rightarrow J_f) = \frac{1}{2J_i + 1} \langle J_f | |\mathbf{Q}| | J_i \rangle^2$$

is just proportional to the number of particles  $n$  in the shell, for small  $n$ . For large  $n$ ,  $n \rightarrow 2j+1$ , it falls off, vanishing, as it must, at the closed shell. For  $j, n \gg 2$ , we see that, as given in the general case above,

$$B(E2:2_1^+ \rightarrow 0_1^+) \propto n \left( 1 - \frac{n}{2j} \right) \approx f(1-f) \quad (5.16)$$

This behavior is commonly observed in real nuclei, with  $B(E2:2_1^+ \rightarrow 0_1^+)$  values rising to midshell and falling thereafter. Data beautifully illustrating this are shown for the  $Z = 50$  to 82,  $N = 82$  to 126 region in Fig. 5.3. (The peak regions of the  $B(E2)$  values in Fig. 2.16 are additional examples of this in condensed form.) In part, this behavior is due to coherent effects involving single-particle configuration mixing of different  $j$  values in the wave functions

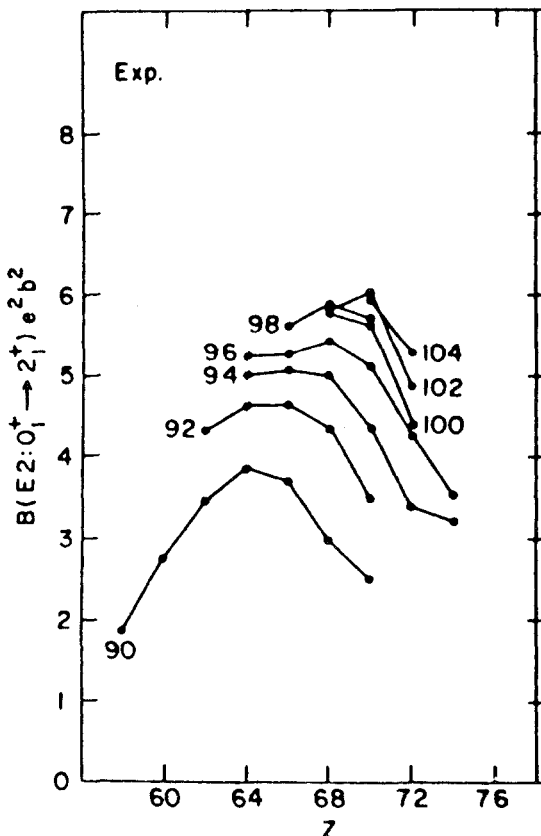


**Fig. 5.3.** Saturation of empirical  $B(E2)$  values in the rare earth region that illustrates Eqs. 5.13 and 5.16. The numbers on each line give the neutron number.

for each particle, but the overall behavior still reflects a generalization of this simple result for the seniority scheme.

For transitions induced by even-tensor operators of rank  $k > 0$  that do *not* change seniority, the expression corresponding to Eq. 5.13 is

$$\left\langle j^n \nu \alpha J \left| \left( \sum_{i=1}^n \mathbf{U}_i^k \right) \right| j'^n \nu' \alpha' J' \right\rangle = \left( \frac{2j+1-2n}{2j+1-2\nu} \right) \left\langle j^n \nu \alpha J \left| \left( \sum_{i=1}^{\nu} \mathbf{U}_i^k \right) \right| j'^n \nu' \alpha' J' \right\rangle \quad (5.17)$$

This equation again expresses an  $n$ -particle matrix element for states of seniority  $\nu$  in terms of the  $\nu$ -particle matrix element. It has an interesting behavior as a function of  $n$ , as given by the factor outside the matrix element. In terms of  $f$  (the fractional filling of the shell), the numerator behaves simply as  $(1-2f)$ . It therefore has opposite signs in the first and second halves of the shell and hence must vanish identically at midshell. This is, of course, an extremely important result, indicating that, for example, quadrupole moments of  $j^n$  configurations in even-even nuclei change sign in midshell. The generali-

zation to many- $j$  shells suggests that such moments should have opposite signs at the beginning and end of major shells. Although the trends in realistic cases are complicated by the different  $j$  shell degeneracies, this qualitative feature is a well-known empirical characteristic of heavy nuclei, and it contrasts markedly with that for odd-tensor operators that are independent of  $n$  (see Eq. 5.5).

We shall see another important application of Eq. 5.17 in our discussion of the p–n interaction in Chapter 6. Moreover, the decrease toward midshell and symmetry about that point will see important reflections even in deformed nuclei (systematics of  $\beta$ : Fig. 6.11, p. 164) where seniority is strongly broken.

Finally, we turn to two-body interactions for even-tensor operators. Some of these interactions can change seniority, connecting states with  $v$  and  $v - 2$ . For this case, the result is trivial to derive. An even-tensor two-body interaction connecting states with seniorities  $v$  and  $v - 2$  must be a product of two one-body operators—one that conserves seniority, another that connects  $v$  and  $v - 2$ . In the reduction to a matrix element in the  $j^v$  configuration, the first gives a factor identical to that in Eq. 5.17, the second gives the factor in Eq. 5.13. Thus, their product yields the result

$$\begin{aligned} \left\langle j^n v \alpha J \middle| \sum_{i < k}^n V_{ik} \middle| j^n, v-2, \alpha' J \right\rangle &= \left( \frac{2j+1-2n}{2j+1-2v} \right)^{\frac{1}{2}} \left[ \frac{(n-v+2)(2j+3-n-v)}{2(2j+3-2v)} \right]^{\frac{1}{2}} \\ &\quad \left\langle j^v v \alpha J \middle| \sum_{i < k}^v V_{ik} \middle| j^v, v-2, \alpha' J \right\rangle \end{aligned} \quad (5.18)$$

Once again, we note the factor  $(2j+1-2n)$ , which vanishes at midshell and has opposite signs in the first and second halves. For  $j, n \gg v$ , this interaction energy varies across a shell as  $(1-2f)f(1-f)$ : at first this increases with  $f$  but it peaks well before the shell is one-quarter filled, tapers off, and crosses zero at midshell; in the second half of the shell, it is symmetric to the first half except for a change in sign.

We will not give the general expression for seniority-conserving matrix elements in the  $j^v$  configuration since they are more complex, involving not only matrix elements of the interaction in the  $j^v$  but in the  $j^{v+2}$  configuration as well.

It is useful at this point to summarize some of these important results. This is done in Fig. 5.4, which shows the behavior of both seniority conserving and nonconserving matrix elements for one-body operators and two-body interactions across a  $j$  shell under the assumption (where applicable) that  $j$  and  $n$  are large and much greater than  $v$ . For the  $v \rightarrow v - 2$  even-tensor case the square of the matrix element is given since it is directly proportional to the most common example of such behavior,  $B(E2: 2_1^+ \rightarrow 0_1^+)$  values. Each panel also gives the (sometimes approximate) analytic formula.

To recapitulate: one-body odd-tensor operators (e.g., magnetic moments) conserve seniority and are constant: one-body even-tensor operators may change seniority, with  $v \rightarrow v - 2$  transition matrix elements (e.g.,  $B(E2: 2_1^+ \rightarrow 0_1^+)$  values) peaking at midshell, while seniority conserving matrix elements (e.g., quadrupole moments) vanish at midshell and are negatives of each other for

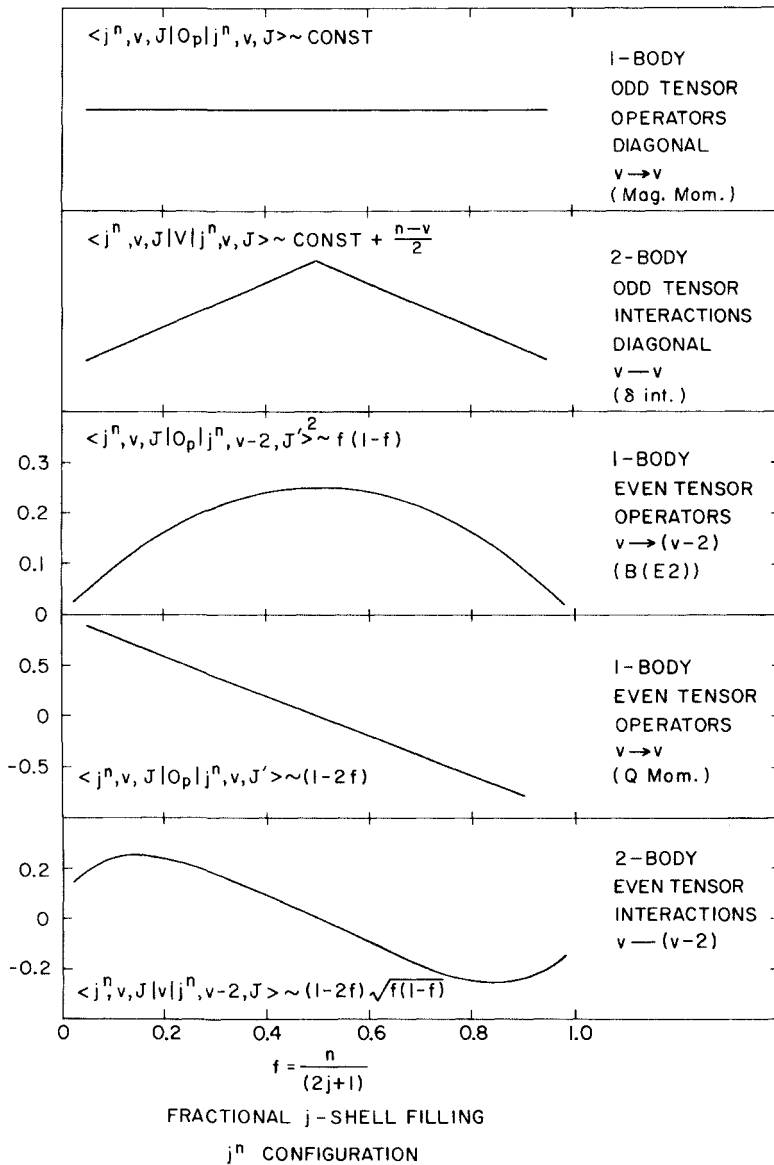


**Fig. 5.4.** Summary of the behavior of various operators and interactions across a shell in the seniority scheme. Note that the middle panel gives the square of the matrix element since this corresponds to the physically interesting case of B(E2) values.

particles and holes; odd-tensor two-body interactions (e.g.,  $\delta$ -interactions) behave as  $(n - v)/2$  (the number of pairs of nucleons in  $J = 0$  couplings), and therefore peak at midshell.

Finally, to relate this discussion to an earlier one regarding the behavior of various matrix elements for particle configurations and the corresponding hole configurations, we note that the results in Eqs. 5.5 and 5.17 are consistent with Eq. 4.33, derived for diagonal matrix elements of one-body operators.

Thus far, the discussion has focused on the  $\delta$ -interaction. A very popular alternative is the surface  $\delta$ -interaction (SDI), which, as its name implies, acts only at the nuclear surface. It is equivalent to the *angular* part of the  $\delta$ -interaction and to the assumption that all radial integrals are equal. Though this is a simplifying assumption, it permits an important generalization of one of the key preceding results: for *degenerate* orbits, the SDI conserves seniority in the multi- $j$  configuration  $|j_1^{n_1} j_2^{n_2} \dots, v, J\rangle$ . (In a single  $j$  shell the  $\delta$  and SDI interactions are identical.) The SDI also has off diagonal matrix elements in multi- $j$  situations that give rise to mixed wave functions. These matrix elements are generally larger than for the volume  $\delta$ -interaction: the reason is simply that, when the interaction can occur throughout the nuclear volume, the effect of non-complete overlap of the particle wave functions is larger.

#### 5.4 Some Examples

With this theoretical background, it is interesting to consider an example that reflects some of these properties of the seniority scheme. Figure 2.3 showed the energies of the first  $2^+$  state,  $E_{2+}$ , for the Ca isotopes as well as the  $B(E2: 2_1^+ \rightarrow 0_1^+)$  values.  $^{20}\text{Ca}$  is doubly magic. The lowest orbit beyond the closed shells is  $1f_{7/2}$  and the ground states of the nuclei from  $^{41}\text{Ca}$  to  $^{48}\text{Ca}$  are formed by adding nucleons in this orbit successively. The low-lying states in the even Ca isotopes can then be viewed as (primarily) an  $(f_{7/2})^n$  configuration.

There is an interesting theorem, which we shall not prove, that states that *any* two-body interaction in the  $j^n$  configuration is diagonal in the seniority scheme, provided it is diagonal in the  $j^3$  configuration, that is, if there are no finite matrix elements connecting  $v = 3$  with  $v = 1$  states. Clearly, since two-body interactions only connect states of the same  $J$  (only states of equal  $J$  can mix), this condition is automatically satisfied for any  $J$  value that is not common to both the  $|j^3 v = 3\rangle$  and  $|j^3 v = 1\rangle$  states. This is useful because it happens for *all*  $j$  values  $j \leq 7/2$ . It is easy to prove this. For  $j = 1/2$  and  $3/2$  it is trivial: they have no  $v = 3$  states since they become maximally filled (midshell) at  $n = 1$  and  $n = 2$ , respectively.

We saw earlier from the  $m$ -scheme that for  $j = 5/2$ , the only allowed states in the  $(5/2)^3$  configuration are  $J = 9/2, 5/2, 3/2$ . The  $J = 5/2$  state can clearly be formed by coupling a  $j = 5/2$  particle to a  $|(j = 5/2)^2 J = 0\rangle$  configuration and so has  $v = 1$ , while the  $J = 3/2$  and  $9/2$  states must have  $v = 3$ .

For  $j = 7/2$  there is, again, only one state with  $J = 7/2$ . Of course, it has  $v = 1$  and, since there are no  $v = 3$  states with the same  $J$  value, the above mentioned matrix elements must vanish. So the preceding theorem is trivially satisfied for all  $j \leq 7/2$ , giving us the useful result that *any* two-body interaction is *diagonal* in the  $j^n$  scheme for  $j \leq 7/2$ .

Note the importance of this result: since the first shell model orbit with  $j \geq 9/2$  is the  $1g_{9/2}$  orbit at the upper end of the 28–50 shell (see Fig. 3.2), this means that seniority is generally a good quantum number for  $j^n$  configurations for *all nuclei* with  $A < 80$ ! These just happen to be the nuclei where shell model calculations are most feasible (the spaces to be diagonalized are not yet too large). Of course, this theorem does not apply to mixed- $j$  configurations  $|j_1^{n_1} j_2^{n_2} J\rangle$ , but it certainly shows why the seniority scheme is so important and

why seniority is often a reasonably good quantum number even in rather complicated configurations.

In any case, the theorem implies that seniority *must* be a good quantum number for the  $(f_{7/2})^n$  states in the Ca isotopes, *independent* of the interaction. This does not mean that the interaction energies are independent of the interaction since, as we saw, the matrix elements of these interactions depend on their odd- or even-tensor character. Nevertheless, knowing that seniority must be a good quantum number, we can confidently choose some reasonable interaction and inspect the predictions of the seniority scheme. We assume that an odd-tensor interaction is a good choice since the  $\delta$ -function can be written in this form. Then, from Eq. 5.6 or, more explicitly, from Eqs. 5.9 and 5.10, the excitation energies of the  $J = 2^+, 4^+$ , and  $6^+$  levels should be constant across the Ca isotopes.

Let us inspect the data in Fig. 2.3. The yrast energies are high at  $^{40}\text{Ca}$  and  $^{48}\text{Ca}$  since both of these nuclei are doubly magic. However,  $^{42}, 44, 46\text{Ca}$  have, as expected, much lower  $2^+$  energies and these are indeed relatively constant. The  $B(E2)$  values in the Ca isotopes are also roughly consistent with the seniority picture since they peak near midshell, although the symmetry about midshell is not particularly evident.

The constancy of  $v = 2$  level energies in singly magic nuclei has long been emphasized by Talmi. His classic example is the Sn isotopes, whose energies were shown in Fig. 2.6.

One can also use the seniority scheme to look at nuclear binding energies,  $B.E.(j^n)$ , ( $n$  even) for a series of nuclei in which an orbit  $j$  is filling. These binding energies are the absolute energies of the  $|j^n, v=0, J=0^+\rangle$  ground states (we assume an odd-tensor interaction). Of course, this is only the residual interaction energy, to which must be added the  $n$  single-particle energies  $E_{n!j}$ . To be slightly more general, there is one other interaction that is diagonal in the seniority scheme—the trivial case of a scalar interaction. Since this is a constant, the interaction matrix element will be equal to that constant multiplied by the total number of pairs of nucleons that can interact,  $n(n - 1)/2$ . Combining these three terms, one then has for the binding energy in a  $j^n$  configuration, relative to the closed shell,

$$B.E.(j^n) = n E_{n!j} + \frac{n(n-1)}{2} B + \frac{n}{2} V_0 \quad (5.19)$$

This formula, which is valid for any interaction that is diagonal in the seniority scheme (and therefore, for *any* interaction for  $j \leq 7/2$ ) displays the well-known parabolic behavior of nuclear masses. We note that the parameter  $B$  always turns out to be negative: the quadratic term is always repulsive. Evidence of this can be seen empirically from the data presented in Chapter 1, which showed that binding energies are approximately proportional to  $A$ . If  $B > 0$  (attractive), binding energies would increase quadratically, instead of linearly, with  $A$ .

This is the same point we have made before, that the nonpairing, residual interaction between *like* nucleons is *repulsive*. We can now carry this one step further. Since the quadratic term stems from the scalar part of the interaction,

which is obviously long range, it is the *long-range* component of the interaction between like nucleons that must be repulsive.

This conclusion, based on the simple form of the binding energies in the seniority scheme and the empirical behavior of separation energies, forces us to conclude that deformation *does not* arise simply from an abundance of valence nucleons outside closed shells, but must specifically involve *both* valence protons and neutrons. We will see later how the properties of the proton-neutron interaction can indeed lead to deformation through the effects of one-body configuration mixing.

Most of the examples of the seniority scheme so far in this chapter have concerned even nuclei. However, the scheme is equally powerful in treating odd mass nuclei near closed shells. We will illustrate this with a simple calculation that is useful in considering low-lying energy levels in sequences of odd  $A$  nuclei.

As we pointed out, the lowest state of the  $j^n$  configuration in an odd mass nucleus normally has  $J = j$  and  $\nu = 1$ . The  $n$ -dependence of its interaction energy is  $[(n-1)/2]V_0$  where  $V_0$  is the interaction energy in the  $J=0$  state of the  $j^2$  configuration. For an odd-tensor interaction, the excitation energies of the  $\nu = 3$  states can be obtained from Eqs. 5.6 and 5.8:

$$\begin{aligned} E(j^n, \nu=3, J') - E(j^n, \nu=1, J=j) &= \left[ \langle j^3, \nu=3, J' | V | j^3, \nu=3, J' \rangle + \frac{(n-3)}{2} V_0 \right] - \left[ \frac{(n-1)}{2} V_0 \right] \\ &= \langle j^3, \nu=3, J' | V | j^3, \nu=3, J' \rangle - V_0 \\ &= E(j^3, \nu=3, J') - E(j^3, \nu=1, J=j) \end{aligned} \quad (5.20)$$

Thus, these excitation energies are identical to those in the  $j^3$  configuration and are independent of  $n$ —that is, they are constant across a shell. Clearly this also means that the spacings *between*  $\nu = 3$  states are  $n$ -independent. This can of course be seen by explicit calculation:

$$\begin{aligned} E(j^n, \nu=3, J') - E(j^n, \nu=3, J) &= \left[ \left( \langle j^3, \nu=3, J' | V | j^3, \nu=3, J' \rangle - \frac{(n-3)}{2} V_0 \right) \right. \\ &\quad \left. - \left( \langle j^3, \nu=3, J | V | j^3, \nu=3, J \rangle - \frac{(n-3)}{2} V_0 \right) \right] \\ &= E(j^3, \nu=3, J') - E(j^3, \nu=3, J) \end{aligned} \quad (5.21)$$

In closing this discussion of multiparticle configurations, it is interesting to take a more complicated level scheme as an example and see how far we can go in interpreting it by exploiting the simple results in this chapter. Consider then the nucleus  $^{60}_{\text{Nd}}{}^{142}_{\text{Nd}}{}^{82}$  with ten protons outside doubly magic  $^{132}\text{Sn}$  (see Fig. 5.5). Although the level scheme seems rather complex, nearly every feature can be easily understood and, indeed, derived analytically, without any complex calculations.

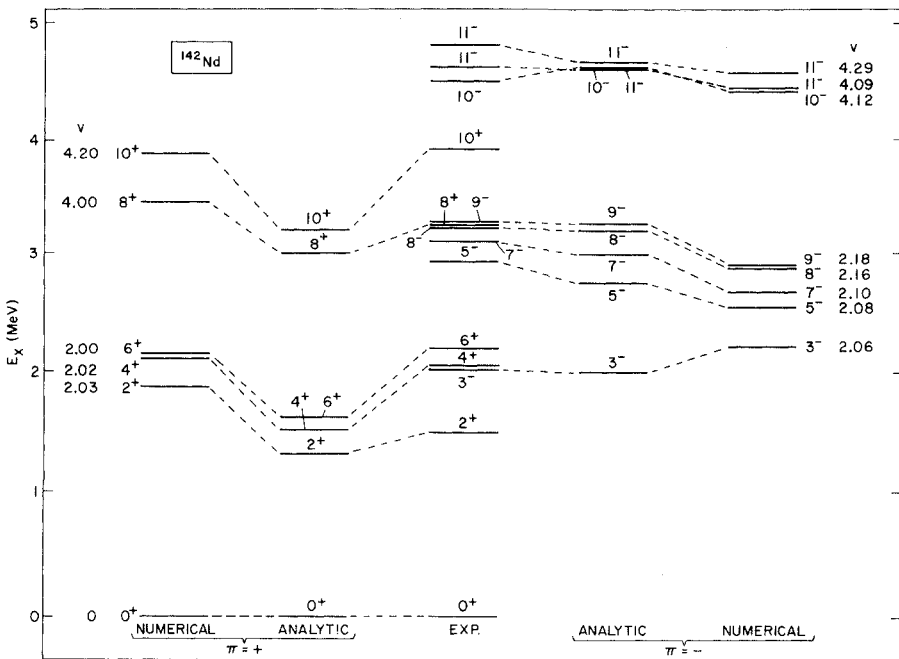


Fig. 5.5. Low-lying levels of  $^{142}\text{Nd}$  in comparison with analytic and numerical shell calculations. (The empirical level scheme is based mainly on Wirowski, 1988.)

To start, we note that the lowest shell model orbits in the  $Z = 50\text{--}82$  shell are  $2d_{5/2}$  and  $1g_{7/2}$ . There are many ways that the protons can be distributed over the two positive parity orbits. If we assume that the splitting of states of a given seniority  $v$  is small compared to the spacings between states of different seniorities (we are neglecting the first term relative to the second in Eq. 5.6), then the  $v = 0$   $J = 0^+$  state will, as usual, lie lowest, by an amount  $V_0$  below the  $v = 2$  states. The  $v = 2$  states, in turn, occur, on average, this same distance below the  $v = 4$  states. Therefore, we can assume that all of the  $J \neq 0$  low-lying positive-parity states ( $J^\pi \leq 6^+$ ) are  $v = 2$ . Since we are dealing with (positive parity)  $j$  values  $\leq 7/2$  we know that seniority is a good quantum number *regardless* of the interaction. Since  $|(\text{d}_{5/2})^n v = 2\rangle$  does not give a  $6^+$  state, let us assume for simplicity that the  $d_{5/2}$  shell is filled, leaving four protons in the  $g_{7/2}$  orbit. By Eq. 5.6 and the preceding discussion, the  $J = 2^+, 4^+, 6^+$   $v = 2$  excitation energies should be identical to those in a  $(g_{7/2})^2$  configuration, and as such can be estimated theoretically using the results for a  $\delta$ -function interaction. We postpone doing so for a moment until we determine how best to estimate the absolute strength of the interaction. The next positive parity state is  $8^+$  and must have  $v = 4$ . By our earlier arguments it should lie higher than the  $v = 2$  states by roughly  $|V_0|$ . The lowest-energy way to construct it is to couple the two  $v = 2$  states with  $J^\pi = 6^+$  and  $2^+$  together. Similarly, the  $10^+$  level must also have  $v = 4$ . The easiest way to form it is by coupling the  $J^\pi = 6^+$  ( $v = 2$ ) and  $J^\pi = 4^+$  ( $v = 2$ ) states.

The negative parity states must involve the  $h_{11/2}$  orbit. The two lowest configurations should involve eight protons coupled to  $J = 0$  in the  $d_{5/2}$  and  $g_{7/2}$  orbits and an  $(h_{11/2}g_{7/2})$  or  $(h_{11/2}d_{5/2})$  pair. The former gives spins  $J = 2^- - 9^-$  while the latter yields  $J = 3^- - 8^-$ . From the rules developed in Chapter 4 for the ordering of different  $J$  states in two-particle configurations under the influence of a  $\delta$ -interaction, we find that the  $9^-$  state should be the lowest in the  $|h_{11/2}g_{7/2}\rangle$  configuration while the  $3^-$  should lie lowest in the  $|h_{11/2}d_{5/2}\rangle$  configuration. In both cases the even-spin negative-parity states are unaffected by the interaction. Empirically, the lowest negative parity state is indeed  $3^-$ , suggesting the  $(h_{11/2}d_{5/2})$  assignment. The lowest  $7^-$  and  $8^-$  levels must also belong to this multiplet (since, if they were part of the  $(h_{11/2}g_{7/2})(J = 2^- - 9^-)$  multiplet they would lie *above* the  $9^-$ ). The  $8^-$  level gives the unperturbed position of the  $(h_{11/2}d_{5/2})$  multiplet, and the energy difference  $8^- - 3^-$  gives the absolute scale of the interaction strength, thus allowing us to predict (using Table 4.1) the  $5^-$  and  $7^-$  energies, as well as the spacings among the positive parity levels. The  $J = 9^-$  state is then the lowest member of the  $(h_{11/2}g_{7/2})$  multiplet. (The lower-spin members would not have been detected in experiments carried out for  $^{142}\text{Nd}$ .) Finally, the  $J^\pi = 10^-$  and  $11^-$  states cannot arise from either  $(h_{11/2}g_{7/2})$  or  $(h_{11/2}d_{5/2})$  couplings. Since, empirically, the latter lies lower, a reasonable configuration for the  $10^-$  level is  $|(h_{11/2}d_{5/2})J = 8^- \otimes 2^+_1\rangle_{10^-}$ , meaning an  $(h_{11/2}d_{5/2})$  pair coupled to  $J^\pi = 8^-$  built on the seniority  $v = 2$   $2^+$  level of the remaining  $(n-2)$  particle system. The energy difference  $E(10^-) - E(8^-) \approx E_{2^+_1}$  is approximately satisfied experimentally. The lowest  $11^-$  levels can be made either by coupling the  $|h_{11/2}g_{7/2}J = 9^-\rangle$  state to the  $v = 2$   $2^+_1$  level or the  $|h_{11/2}d_{5/2}J = 7^-\rangle$  level to the  $v = 2$   $4^+_1$  level.

All these results are incorporated now into Fig. 5.5, where it is evident that the agreement of this extremely simple calculation with experiment is actually remarkably good. The ordering and energies of most of the levels are correctly predicted analytically, in agreement with experiment, and with only three parameters: the single-particle energy differences  $\epsilon_{h11/2} - \epsilon_{g7/2}$  and  $\epsilon_{ds1/2} - \epsilon_{g7/2}$  and the strength of the residual interaction. Figure 5.5 also shows an actual detailed 10-particle diagonalization of the  $^{142}\text{Nd}$  level scheme, using a surface  $\delta$ -interaction (which gives relative spacings, within a configuration  $|J\rangle$ , which are the same as for a volume  $\delta$ -interaction and which is otherwise similar as well, although different in some details) with strength 0.4 MeV and with the single-particle energies (in MeV):  $\epsilon_{g7/2} = 0$ ,  $\epsilon_{ds1/2} = 0.7$ ,  $\epsilon_{h11/2} = 2.5$ . The calculation also shows reasonable agreement with the empirical scheme, but more importantly, it shows that our simple analytic interpretation is a remarkably accurate approximation of a complex shell model diagonalization. This kind of interpretation highlights the power of the methods we have discussed and shows how far we can go in a relatively simple shell model interpretation of rather complex level schemes. The principle difference in the numerical diagonalization is that additional components, such as  $(d_{5/2})^2$  and  $(d_{5/2}g_{7/2})$  or even  $(d_{5/2}g_{7/2}^3)$ , come into play. Similar analyses can be applied to countless other nuclei (e.g., Sn) and greatly help to understand the results of complex realistic calculations.

Improved calculations, compared to Fig. 5.5, have also been carried out.

They allow  $(h_{11/2})^2$  as well as  $(d_{5/2})^{n_1}$  and  $(g_{7/2})^{n_2}$  configurations in the positive parity levels. The inclusion of these amplitudes mainly affects the required  $h_{11/2}$  single particle energy and, of course, changes the strength of the interaction needed to fit the data. The reason is easy to see from Eq. 4.10. Since the lowering of the  $0^+$  state in a configuration  $|j\,{}^2J\rangle$  is proportional to  $(2j+1)/2$  multiplied by the interaction strength,  $V_0$ , the inclusion of  $(h_{11/2})^2$  means that a smaller  $|V_0|$  is required to maintain the same  $J_{\text{yrast}} - J_{0^+}$  spacing. The extra lowering of the  $0^+_1$  level effectively raises the excitation energy of all the others. To regain a fit to the data for the negative parity states, a lower  $\varepsilon_{h_{11/2}}$  is required.

This illustrates two important points. First, the choice of effective residual interaction, single-particle energies and the shell model space are intimately linked. One should be wary of conclusions regarding any of these if there is not supporting evidence for the choices concerning the others. Secondly, despite the beauty of analyticity, a realistic treatment of complex nuclei still requires detailed explicit calculations if really quantitative results are desired.

Finally, note that we have completely ignored core excitations of the protons or neutrons. These can be significant and their effects can vary significantly for different states. In particular, even in singly magic nuclei (e.g.,  $^{142}\text{Nd}$  or Sn), the lowest  $2^+$  and  $3^-$  states are often rather “collective” with a number of major components, including core excited particle-hole components (e.g.,  $(g_{9/2}^{-1} h_{11/2}) J = 3^-$  for neutrons in Nd or protons in Sn). To some average extent, their ignored effects are mocked up by the choices of the single-particle energies of the valence orbits and of the interaction strength. It is no wonder that residual interactions are often called “effective interactions” and that an extensive theory of such interactions has been built up. Indeed, as discussed at the end of Chapter 4, a number of alternates to the  $\delta$ -function interaction are often used. Often, these are more structured, finite-range, interactions such as Gaussian forms. Various so-called Skyrme interactions are also popular, as are interactions defined explicitly in terms of sets of two-body empirical matrix elements. It is clear from the discussion at the end of Chapter 4 that such finite-range interactions have different (often more parabolic)  $J$ -dependencies than the  $\delta$ -function.

## 5.5 Pairing Correlations

In closing this chapter, we want to turn to another interaction, similar in many ways to the  $\delta$ -interaction, which is very important in understanding the structure of heavy nuclei. We saw in Chapter 1 that proton and neutron separation energies exhibited an odd-even effect, indicating an extra binding in the  $0^+$  ground states of even-even nuclei. We have also seen that the  $\delta$ -function force acting on two identical nucleons in equivalent orbits produces a strong lowering of the  $J = 0^+$  state. This behavior is typical of any very short-range interaction and is a direct consequence of the Pauli principle, which allows such interactions to affect only *spatially* symmetric wave functions. Although the  $\delta$ -function force is particularly easy to deal with (and has specific tensor properties that imply conservation of seniority), it has become traditional in

heavy nuclei to describe such behavior more directly in terms of the so-called pairing interaction. This is *defined* (see Eq. 4.20) to be an attractive interaction acting *only* on two identical particles in total angular momentum  $0^+$  states. States with  $J^\pi \neq 0^+$  are unaffected. A comparison of the pairing interaction with a  $\delta$ -function interaction for an  $(f_{7/2})^2$  configuration was shown in Fig. 4.13. The sequence of energy levels for the  $\delta$ -function interaction is the familiar result we have been studying and simply reflects the properties of the  $3-j$  symbol in Eq. 4.10. The pairing force presents a similar overall pattern but with a degenerate multiplet of  $J^\pi \neq 0^+$  states at the unperturbed energy. As we have seen, inspection of the empirical level schemes of two-particle states in singly magic nuclei such as  $^{210}\text{Po}$ ,  $^{210}\text{Pb}$ ,  $^{134}\text{Te}$  (Fig. 4.5), and many others, shows that the  $\delta$ -interaction reproduces empirical spectra much more accurately. Even for multiparticle (but still singly magic) cases, such as the Sn isotopes, the  $\delta$ -function provides a more realistic interpretation (see Fig. 2.6). Nonetheless, it has become nearly universal practice to invoke a pairing interaction and to refer to the lowering of the  $0^+$  state as a pairing effect. (Indeed, we already referred to the second term in Eq. 5.6 as the “pairing property” in analogy with the effect of the pairing force.) Part of the appeal of the pairing force is the ease with which it can be extended to multiparticle systems, where it leads to the desired result of  $0^+$  ground states in even-even nuclei without the need for the seniority apparatus and angular momentum algebra we have discussed.

There are a number of experimental facts that motivate the introduction of a pairing force and the concept of pairing correlations. We have mentioned some, but it is useful to summarize them here. The best known is the simple fact that the ground state of all even-even nuclei has  $J^\pi = 0^+$ . A related point is that this  $0^+$  state is normally far below other noncollective intrinsic states. This is the so-called pairing gap.

Perhaps the most direct evidence for a pairing interaction is the so-called odd-even mass difference. This simply refers to the fact that when nucleons are added to a nucleus, the gain in binding energy is greater when an even-even nucleus is formed than when the neighboring odd mass nucleus is formed. This empirical fact can be inferred from the data of Figs. 1.2 and 1.3 by comparing the absolute values of  $S(n)$  or  $S(p)$  for adjacent odd and even nuclei. An extra attractive interaction that couples pairs of like-nucleons together can accommodate this fact, and indeed, the separation energy data suggest a strength for the pairing interaction of  $\sim 1\text{--}2$  MeV.

There are three other features that can be seen, at least in retrospect, as clearly pointing to the need for a pairing interaction. The pairing interaction clearly favors sphericity since it favors the formation of pairs of particles coupled to a total magnetic substate  $M = 0$ . Therefore, near closed shells, the presence of a strong pairing interaction will inhibit the tendency to deform. Instead of the smooth transition toward deformation that would normally occur as valence nucleons are added, one typically sees, empirically, a sequence of more or less spherical nuclei followed by a rather rapid transition region to deformation. Secondly, for a deformed nucleus of a given shape, it is easy to calculate the moment of inertia. This in turn determines the spacing of

rotational levels (see Chapter 6). Empirical moments of inertia extracted from those energies are systematically lower than calculated in the shell model. The inclusion of pairing correlations essentially removes the discrepancy. Finally, the energy distribution of Nilsson orbits near the ground state in deformed odd mass nuclei is, on average, denser than expected from the Nilsson diagram. This will be seen to be a “compression” effect that occurs in the transformation from particle–hole to quasi-particle energies.

The pairing interaction was defined in Chapter 4 in terms of its matrix elements as:

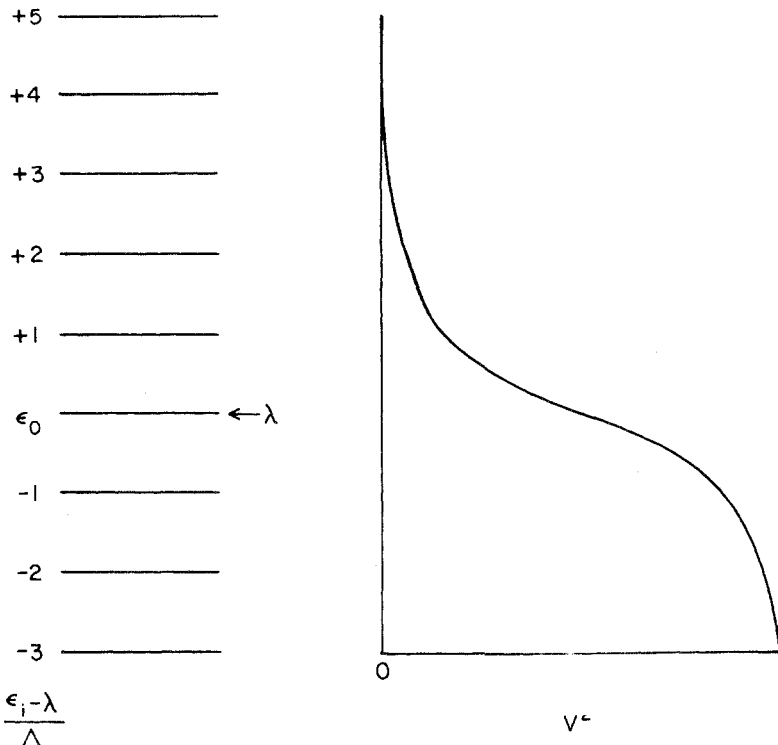
$$\langle j_1 j_2 J | V_{\text{pair}} | j_3 j_4 J' \rangle = -G \left( j_1 + \frac{1}{2} \right) \left( j_3 + \frac{1}{2} \right) \delta_{j_1 j_2} \delta_{j_3 j_4} \delta_{J_0 J'_0}$$

where  $G$  is the so-called strength of the pairing force and the rest of the expression has an obvious meaning. Note that the pairing force is independent of orbit but, since it is identical for each magnetic substate, scales for an orbit  $j$  as  $(2j + 1)$ . It is therefore stronger in high  $j$  orbits. Although  $G$  is orbit independent, it decreases with  $A$  in heavier nuclei where the outer nucleons are generally further apart and so spatial overlaps are likely to be less.  $G$  may be different for protons and neutrons, being lower for the former because of Coulomb repulsion. Commonly used prescriptions are

$$G_p = \frac{17}{A}, \quad G_n = \frac{23}{A} \quad \text{MeV}$$

It is frequently imagined that the pairing force is an interaction only between two particles in the same  $j$  state, coupled with their angular momenta antiparallel, to form a  $J^\pi = 0^+$  state. This, of course, is an important facet of the pairing interaction. However, there is another vital ingredient that is evident from its definition. The pairing force is equally strong for matrix elements connecting a  $|j^2 J = 0^+\rangle$  state with a  $|j'^2 J = 0^+\rangle$  state. That is, the pairing force has *nondiagonal* as well as diagonal components that can “scatter” pairs of particles from one orbit to another. Note the importance of this point. If the force were purely diagonal, then, while  $J = 0^+$  pairs would still be tightly bound, excited states could be formed simply by raising both particles in such a pair to the next unoccupied orbit. On average, this would require twice the energy needed to raise a single particle from orbit  $j$  to orbit  $j'$  in the absence of pairing. The “energy gap” in even–even nuclei would then be only twice the average spacing of low-lying levels in the adjacent odd nucleus and not 5 to 10 times as large, as observed experimentally. Rather, by scattering particles from one  $j$  orbit to another, the pairing force mixes  $0^+$  states and creates partial occupancies near the Fermi surface. Hence it builds up a coherence in the pair wave functions, which further lowers the lowest  $0^+$  state and thereby enlarges the gap: if we picture the pairing force in a perturbation theory context, the amplitudes for scattering a pair of particles from orbit  $j$  to orbit  $j'$  will be proportional to the matrix element  $\langle j^2 J = 0 | V_{\text{pair}} | j'^2 J = 0 \rangle / (\epsilon_j - \epsilon_{j'}) = G / (\epsilon_j - \epsilon_{j'})$ . In the absence of pairing, all levels would be occupied up to some point (the Fermi energy) while those above this energy would be completely empty. With pairing, however, many orbits can be partially occupied. This in turn, radically alters the concept of hole excitations, and thereby, the levels schemes of both odd and even nuclei. We shall see all this a bit more formally when we outline

$$V_i^2 = \frac{1}{2} \left[ 1 - \frac{\epsilon_i - \lambda}{\sqrt{(\epsilon_i - \lambda)^2 + \Delta^2}} \right]$$



## PARTIAL OCCUPANCY DUE TO PAIRING

**Fig. 5.6.** Definition of several quantities used in the calculation of pairing correlations. (Left) Idealized set of equally spaced single-particle shell model levels. (Right) Resultant orbit occupancies  $V^2$ . The calculation is general since the single-particle energies are given in units of  $\Delta$ .

the basic results of pairing theory. We will not derive these standard results but will try to highlight their key effects.

To proceed, we refer to Fig. 5.6 where several quantities important in discussing the pairing interaction are defined: the Fermi energy, denoted  $\lambda$ ; the single-particle energies,  $\epsilon_i$ , with  $\epsilon_0$  being reserved for that level closest to the Fermi surface; and  $\Delta$ , the so-called gap parameter, defined in terms of a sum over orbits  $i, j$  as

$$\Delta = G \sum_{i,j} U_i V_j \quad (5.22)$$

where the usual  $U$  and  $V$  factors are the so-called emptiness and fullness factors that pervade the study of heavy nuclei. They are given by:

$$U_i = \frac{1}{\sqrt{2}} \left[ 1 + \frac{(\varepsilon_i - \lambda)}{\sqrt{(\varepsilon_i - \lambda)^2 + \Delta^2}} \right]^{\frac{1}{2}}, V_i = \frac{1}{\sqrt{2}} \left[ 1 - \frac{(\varepsilon_i - \lambda)}{\sqrt{(\varepsilon_i - \lambda)^2 + \Delta^2}} \right]^{\frac{1}{2}} \quad (5.23)$$

These equations can be solved for  $\Delta$ ,  $U_i$ , and  $V_i$  for a given set of single-particle energies  $\varepsilon_i$ . Or,  $\Delta$  can be estimated from empirical mass differences between adjacent nuclei with odd and even numbers of nucleons. The behavior of  $V_i^2$  against the ratio  $(\varepsilon_i - \lambda)/\Delta$  is shown in Fig. 5.6. We see that  $V_i \rightarrow 1$  for  $(\varepsilon_i - \lambda) \ll 0$  and vanishes for levels far above the Fermi surface. The opposite applies to  $U_i^2$ . Both fall off rapidly for single-particle energies  $\varepsilon_i \sim \lambda$ . Also, from Eqs. 5.23,  $V^2 + U^2 = 1$ .  $U_i^2$  is the probability that the orbit  $i$  is empty, whereas  $V_i^2$  is the probability that it is filled. Pairing smooths out the level occupancies near the Fermi surface over a range  $\sim \Delta$ , which, in turn, is proportional to  $G$ , the “strength” of the interaction. If there were no pairing, the Fermi surface  $\lambda$  would coincide with the last filled orbit being filled and  $(\varepsilon_i - \lambda)$  would be the excitation energy required to excite one of the nucleons in this last orbit to one of the higher orbits  $\varepsilon_i$ . In the presence of pairing, however, this single-particle excitation energy  $(\varepsilon_i - \lambda)$  is replaced by a *quasi-particle* energy  $E_i$  given by

$$E_i = \sqrt{(\varepsilon_i - \lambda)^2 + \Delta^2} \quad (5.24)$$

Thus, particles and holes are replaced by quasi-particles representing partially filled levels, and a particle-hole excitation is replaced by the creation of one quasi-particle and the destruction of another.

The transformation from particles to quasi-particles is of interest not only because the pairing interaction happens to lead to partial occupancy, but because it allows an enormous simplification in shell model calculations with many valence nucleons. It is basically a transformation from a viewpoint based on the closed shell to one based on the Fermi surface. Thus, instead of having to deal with *all* possible ways of constructing each  $J$  state within a major shell, it naturally produces a physically intuitive truncation scheme directly keyed to the scale of excitation energies one is interested in. For low-lying states, one needs to consider only low energy quasi-particles. In the shell model, in contrast, a near-midshell nucleus would involve single-particle energies lying rather high in the shell regardless of the excitation energy. Moreover, pair scattering would give rise to extremely complex wave functions in the shell model. In the quasi-particle picture, all the complexity due to partial pair occupancies induced by the pairing force is effectively absorbed into the ground state (quasi-particle vacuum) and we need only consider quasi-particle excitations relative to the Fermi surface.

The behavior of  $E_i$  is interesting and has important consequences. If  $\varepsilon_i \sim \lambda$ , that is, if the  $i$ th single-particle level is near the energy where the occupation probabilities fall off rapidly,  $E_i \sim \Delta$ . This value is also clearly the minimum value of  $E_i$ .

In an *odd* mass nucleus, however, this is not the minimum energy for an excited state: Rather, excited levels are obtained by *replacing* the quasi-particle defining the ground state by one corresponding to a different single-particle level. Thus the excitation energy  $E_{x_i}^0$  for the  $i$ th quasi-particle in an odd mass nucleus is given by

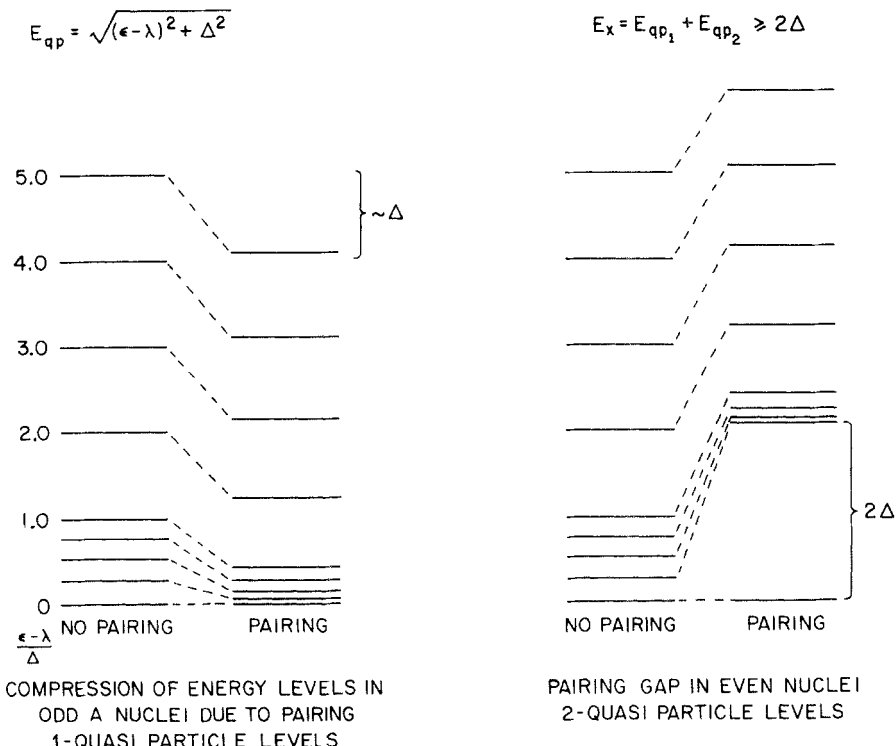


**Fig. 5.7.** Effects of pairing in odd and even nuclei. (Left) Level compression near the ground state for odd mass nuclei. (Right) The energy gap in even-even nuclei.

$$E_{xi}^0 = E_i - E_0 = \sqrt{(\epsilon_i - \lambda)^2 + \Delta^2} - \sqrt{(\epsilon_0 - \lambda)^2 + \Delta^2} \quad (5.25)$$

where  $E_0(\epsilon_0)$  is the quasi-particle (single-particle) energy of that orbit nearest the Fermi energy  $\lambda$ . Thus we see that  $E_{xi}^0$  can take on arbitrarily small values. Indeed, since all  $E_i \sim \Delta$  for  $(\epsilon_i - \lambda) \ll \Delta$ , the effect of pairing is actually to decrease the excitation energies of the low-lying states, compressing the excitation energy spectrum. Figure 5.7 shows this compression of  $E_{xi}^0$  as a function of  $(\epsilon_i - \lambda)$  in units of  $\Delta$ . At higher energies [ $(\epsilon_i - \lambda) \gg \Delta$ ], the effect is to lower all states by an amount  $\sim \Delta$  since  $E_i \rightarrow (\epsilon_i - \lambda)$  and  $E_{xi}^0 = E_i - E_0 \sim (\epsilon_i - \lambda) - \Delta$ .

In even nuclei, the effect of pairing is nearly the opposite: instead of a compression of excited quasi-particle levels, there are no simple excitations below  $E_x^e = 2\Delta$ . This is easy to show. The simplest excitation consists of breaking one pair and raising a particle to the next higher orbit. Without pairing, this is a particle-hole excitation. In the presence of pairing, it appears as a two quasi-particle excitation, one quasi-particle being the hole left behind and the other being the particle excitation newly created. Thus, the excitation energy is given by

$$E_{xi}^e = \sqrt{(\epsilon_i - \lambda)^2 + \Delta^2} - \sqrt{(\epsilon_j - \lambda)^2 + \Delta^2} \quad (5.26)$$

as well. It is immediately clear that the minimum energy is  $E_x = 2\Delta$ , giving the famous "pairing gap" that is a nearly universal feature of even-even nuclei in which few two quasi-particle excitations appear below  $\sim 1.5 - 2$  MeV. In fact, this empirical energy gap is one way of extracting  $\Delta$  experimentally. As noted, typical values of  $\Delta$  range from about 700 keV – 1 MeV.

Although there is a large gap between the ground state of an even-even nucleus and the first excited two-quasi-particle state ( $2\Delta$ ), above this energy the quasi-particle level density will be at least as large as in a neighboring odd mass nucleus.

The energy gap and the high-level density just above it are evident in virtually any even-even nucleus. Figures 2.5, 2.6, and 2.10 show several examples. However, there is another very simple and elegant way of demonstrating the pairing gap empirically without the need for in depth study of each individual excited state. The  $(n, \lambda)$  reaction proceeds by the capture of a neutron of energy  $E_n$  into a target nucleus, forming a residual nucleus at an energy  $E_c = S(n) + E_n$ . This "capture" state then decays by the emission of  $\gamma$ -rays to low-lying levels. Each  $\gamma$ -ray thereby defines an excited state by the equation  $E_{x_i} = E_c - E_\gamma$ . Under appropriate experimental conditions (See Chapter 10) the  $(n, \gamma)$  reaction provides an a priori guarantee of observing all final states in certain spin and excitation energy regions. Thus, a spectrum of  $\gamma$ -ray transitions will reveal a sequence of peaks, each corresponding to a specific excited level, and together, displaying all the excited states with certain  $J^\pi$  values. Because of the "completeness," the pairing gap should be immediately identifiable by a sudden increase in peak density. Figure 5.8 shows such a spectrum for the case of  $^{196}\text{Pt}$ , and includes an insert portraying the reaction process schematically. One sees the ground state, a few low-lying excited states, and

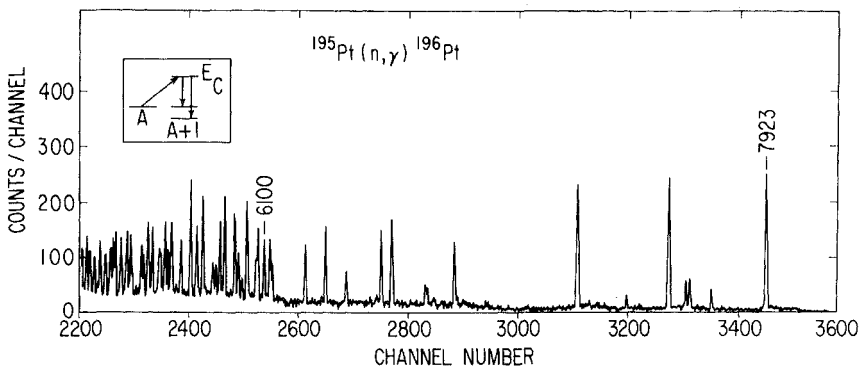


**Fig. 5.8.** Spectrum of primary  $\gamma$ -rays following average resonance capture (ARC) into  $^{196}\text{Pt}$ . The inset schematically illustrates the reaction process. Two peaks in the spectrum are labeled by their  $\gamma$ -ray energies in keV: the rightmost peak corresponds to a transition to the ground state, while that at 6100 keV populates a state at 1823 keV. The increased level density at the pairing gap is immediately obvious at approximately this excitation energy (Cizewski, 1979).

then, at  $E_x \sim 1.8$  MeV, a dramatic increase in level density. By inspection, one can immediately point to an approximate value for  $2\Delta$ .

We also note that, seemingly contrary to the preceding discussion, there are, in fact, a few peaks below the pairing gap. We shall discuss these in considerable detail in later chapters. They correspond to macroscopic "collective" vibrations and/or rotations of the nucleus as a whole and can be viewed as resulting from the interactions among a number of two-quasi-particle states in which the lowest such state is pushed down by mixing, and therefore occurs below the energy gap.

Finally, the defining equation for  $\Delta$  is interesting since it indicates something about the origin of the pairing gap. Clearly  $\Delta$  should vanish in the absence of pairing, which the proportionality to  $G$  in the Eq. 5.22 reflects. Secondly, the range and number of energy levels over which  $U$  and  $V$  are different from 1 and 0 increases with  $G$ , as does the sum in Eq. 5.22.

To summarize the discussion of pairing, it is an extremely important contribution to the structure of medium and heavy nuclei, affecting energy levels,  $\gamma$ -ray transition rates, particle transfer cross sections, moments of inertia, and the microscopic structure of virtually all collective excitations. It modifies most nuclear matrix elements. It is also, as we commented in Chapter 4, one of the two ingredients in the so-called pairing-plus quadrupole (or PPQ) interaction, which is a standard basis for the study of collective excitations (See Chapter 9). We shall see the effects of pairing throughout the rest of this book.

To conclude this chapter and lead into the next part of the book we emphasize that, despite the numerous successes of the shell model over the years, it is apparent that it is not actually applicable for the majority of nuclei. Even the complex  $^{142}\text{Nd}$  case just discussed required simplification by ignoring the excitation of the closed proton and neutron shells. When one deals with valence nucleons of both types, the shell model rapidly becomes intractable, especially in the larger multi- $j$  valence shells of heavy nuclei. Moreover, as we shall see, such nuclei display characteristics that clearly point to nonspherical or deformed shapes. Thus, there are better discussed in the context of geometric (and other) models where such shapes arise naturally. We now turn to a discussion of such models. Later we will show how the collective features that characterize these models can, in fact, be obtained (and therefore justified) microscopically from the shell model.

*This page intentionally left blank*

### PART III

## COLLECTIVITY, PHASE TRANSITIONS, DEFORMATION

*This page intentionally left blank*

# 6

## COLLECTIVE EXCITATIONS IN EVEN-EVEN NUCLEI: VIBRATIONAL AND ROTATIONAL MOTION

### 6.1 An Introduction to Collectivity, Configuration Mixing and Deformation

The shell model is generally considered the fundamental nuclear model. Historically, it was the first model to have considerable, detailed success. Of course, this is not accidental. The shell model works best for light nuclei. Much of the crucial information on nuclear structure comes from nuclear reactions that require the incident projectile to have energies near or above the Coulomb barrier in order to penetrate the nucleus. This requires higher and higher energies for heavier and heavier elements and, consequently, most early studies with low-energy accelerators also focused on light nuclei. The development of nuclear models is intimately connected to the historical progress of experimental techniques.

More fundamental to the shell model's central position in nuclear physics is that it provides a well-defined procedure for the calculation of basic nuclear observables. The principle ingredients needed for any given calculation are a choice of the single-particle energy levels, of the number of these that should be included in the space to be diagonalized, and the residual interaction to be used. Moreover, since the shell model is the only broadly applicable *microscopic* model available, it is the standard against which others are compared, and it is the source and rationalization of macroscopic models. A collective model that can be shown to be inconsistent with the shell model is discarded with little delay.

Unfortunately, the use of the shell model is, in practice, rather severely limited. In previous chapters we considered some simple applications, mostly those in which the particles were confined to a single  $j$  shell. Except for very light nuclei, however, and those very near closed shells, the valence nucleons occupy more than one  $j$  shell. (The pairing interaction assures this if the single-particle spacing is less than or comparable to its "spreading" parameter  $\Delta$ .)

While shell model calculations for multi- $j$ -configurations are certainly possible, the size of the matrices in which the residual interaction must be diagonalized rapidly becomes enormous. For even a few valence nucleons in several  $j$  orbits, it is easily possible to construct hundreds of states of a given  $J^\pi$  value. Even if such calculations are possible using high speed computers, the results are difficult to interpret physically and the consequences of agreement or disagreement with the data are much less intuitively informative. The situation becomes totally intractable when more valence nucleons are added.

To quote the famous example of Talmi, in  $^{154}_{62}\text{Sm}_{92}$ , approximately  $3 \times 10^{14} 2^+$  states can be constructed with protons and neutrons in the  $Z = 50\text{--}82$  and  $N = 82\text{--}126$  major shells. In such a case, no shell model calculation is even remotely feasible, nor could one even begin to understand the resultant wave functions. Since the vast majority of nuclei fall into the many-valence nucleon category, any advance in our understanding of nuclear structure beyond a very select group of nuclei must depend either on some truncation of the shell model or on the development of alternatives to it. This problem is, of course, a common one in physics. One develops a simple model. Later, one introduces first-order perturbations to it to refine its predictions. Further improvements involve incorporating additional degrees of freedom, which enlarge the basis. When the required basis becomes too large or the wave functions too complex in that basis, one looks for a new *physical* picture that allows one to approach the problem from an alternate basis.

The development of nuclear structure in medium and heavy nuclei has followed two related paths, which we shall discuss extensively in the next three chapters. Both involve the concept of a nonspherical shape, but one emphasizes the single-particle motion of nucleons in a field of that shape, while the other stresses the macroscopic motions and excitations of a nucleus having that shape. Ultimately, the former approach (a “deformed shell model”) can be shown or must be shown to be the microscopic justification for the latter, but in practical terms, the two models are often used complementarily in a microscopic-macroscopic combination that has proved to be very powerful. The nonspherical, or deformed, shell model approach is usually called the Nilsson model, while the macroscopic one is a fundamentally *collective* model, generally known as the collective model of Bohr and Mottelson although many others have contributed in essential ways to it. Each of these approaches, of course, has numerous offshoots, extensions, and refinements.

The assumption of a nonspherical macroscopic nuclear shape is a phenomenological or ad hoc one: while the enormous successes of the collective model, its demonstrated predictive power, and the numerous progeny it has spawned over the last three decades leave little doubt that it aptly describes the nuclear structure of perhaps the majority of nuclei, one is left with an uneasiness about the apparent incompatibility of an independent particle picture such as we have been discussing and the clearly collective and coherent motion involved in macroscopic rotations and vibrations. It was a theoretical achievement of basic importance in the early 1960s when it was demonstrated that macroscopic collectivity could indeed result from the shell model with appropriate and reasonable realistic residual interactions. The essence of the method involved is the so-called random phase approximation or RPA method, or its somewhat simpler cousin the Tamm-Dancoff Approximation (TDA). We shall discuss these two methods in some formal detail in Chapter 9.

In the last decade or so, a rather different approach to collective behavior in nuclei has been developed. It exploits the dynamical symmetry structure of nuclei, and utilizes powerful group theoretical techniques to obtain many nuclear properties by simple algebraic techniques, often in analytic form. There are many such algebraic models in use today. However, beyond a doubt,

the most popular, successful, and widely tested to date has been the interacting boson approximation (IBA) model of Iachello and Arima. This model will also be discussed later in this chapter. Other algebraic models, which emphasize the fermions (nucleons) directly, currently offer enticing initiatives that promise to be both more general and more microscopic.

Since the shell model picture of nucleons orbiting in a *spherically* symmetric central field must ultimately be relied upon for the microscopic justification of collective behavior in *nonspherical* nuclear shapes, it is worthwhile to see how this model is capable of producing nonspherical configurations. To many students this is a mysterious point: the explanation is actually quite simple while the confusion stems from a semantic misunderstanding. This discussion will form at least a qualitative justification for the basic concepts of the Nilsson model—the *assumption* of a deformed shell model potential—as well as highlight the central importance of the proton–neutron (p–n) interaction in the development of collectivity and deformation in nuclei. And finally, it will help to foster an appreciation of the key role played by the *distribution* of valence nucleons between protons and neutrons, as opposed to a simple consideration of the *total* number of valence nucleons.

There is really nothing mysterious in the idea of generating deformed shapes from the *spherical* shell model. The model is *spherical* in the sense of the *shape* of the central potential, not the resulting shape of the nucleus. A spherical potential allows no distinction between magnetic substates of a given orbit, all of which are degenerate. A single-particle in a shell model orbit occupies all such substates equally, and overall, its wave function will be spherically symmetric. However, *any* mechanism that yields an *unequal* occupation of  $m$  states gives a nonspherical shape. (An orbit may be circular, but it is a circle in a specific *plane* and therefore gives the nucleus a “bulge” in that plane.) Such mechanisms abound in the shell model without introducing anything fancy (even without residual interactions). Consider, for example, a configuration of two identical nucleons in equivalent orbits, say  $|(\ell_{7/2})^2 J\rangle$ , outside a magic core. The  $0^+$  ground state is spherical, of course, but let us look at the construction of the  $2^+$  state in terms of  $m$  substates. From Table 5.1 we see that many possible  $m_1, m_2$  values, such as  $m_1 = 7/2, m_2 = 1/2$  or  $m_1 = 5/2, m_2 = 3/2$  give  $M = m_1 + m_2 > 2$  and cannot contribute to the  $2^+$  state. This state is then formed from a nonuniform distribution of  $m_1, m_2$  components and must be nonspherical. Indeed, this is why it has a quadrupole moment (see Eq. 5.5).

A nonuniform magnetic substate distribution is in fact so characteristic of deformation that one of the best known features of the Nilsson (deformed shell) model is a filling of orbits based on their  $m$  values instead of their  $j$  values. But that jumps ahead of the discussion. We must discuss how and why  $j$  itself may not always be a good quantum number. This is an essential point since “configuration mixing” of single-particle  $j$  values *ensures* an unequal  $m$  substate distribution and is therefore tantamount to ensuring deformation.

To do this we will show that there is a fundamental difference between the occupation of valence orbits by *like* nucleons (e.g., two protons or two neutrons) and *unlike* nucleons (one proton and one neutron). Consider then, and by way of example, a nucleus with two valence nucleons filling the lower part

of the 8–20 shell in the  $1d_{5/2}$  and  $1d_{3/2}$  orbits, which are separated by  $\approx 5$  MeV.

We want to consider matrix elements that can admix  $d_{5/2}$  and  $d_{3/2}$  components. In Chapter 4 we discussed *diagonal* matrix elements of short-range two-body residual interactions. Now, we are dealing with nondiagonal ones (although the diagonal elements still play an important role in modifying the unperturbed energies of the states that mix). Nevertheless, the basic idea is the same: if the particles are not close to one another in the two two-particle configurations, the matrix element will be small. The Pauli principle must also be considered. In addition, as opposed to the diagonal case, here we also need to consider the unperturbed (initial) energy spacing of the two configurations. The whole issue then is just one of two-state mixing. We consider the possible matrix elements:

$$\langle d_{3/2}^2 J | V | d_{3/2}^2 J \rangle, \quad \langle d_{5/2}^2 J | V | d_{5/2} d_{3/2} J \rangle, \quad \langle d_{3/2}^2 J | V | d_{5/2} d_{3/2} J \rangle$$

and concentrate on qualitative effects, ignoring complexities due to angular momentum coupling coefficients.

For *like nucleons* ( $T = 1$ ) the unperturbed energies of the  $(d_{5/2})^2$  and  $(d_{3/2})^2$  configurations are  $\approx 10$  MeV apart. Though the individual  $J$  states of each are lowered by the diagonal residual interaction (see Fig. 4.3 (top)), this lowering is roughly similar in the two configurations. The spacing thus remains  $\approx 10$  MeV, and it is unlikely that strong mixing will occur. (Recall the pairing discussion:  $\Delta \approx 1$  MeV and states are admixed only over an energy range of that magnitude.)

The mixing is also small for matrix elements like  $\langle d_{5/2}^2 J | V | d_{5/2} d_{3/2} J \rangle$ , since although the unperturbed separation is now only  $\approx 5$  MeV, the Pauli principle enters in an important way. The configuration  $(d_{5/2})^2$  for like nucleons only exists in  $J = 0, 2, 4$  states. The  $(d_{5/2} d_{3/2})$  configuration does not exist as  $J = 0$ . Therefore, the strong  $J = 0$  interaction is forfeited and we are left with only the  $J = 2$  and  $4$  cases. But, we can apply our geometric analysis of Chapter 4 to these cases. For  $J = 4$ , for example, the angle  $\theta$  between the two orbits in a  $(d_{5/2})^2$  configuration is  $\approx 82^\circ$ , while it is  $\approx 49^\circ$  for  $(d_{5/2} d_{3/2})$ . We can see the effect of this if we imagine that one orbit in each configuration is fully aligned with one in the other (the optimum case). Then, to couple these two states (that is, for a finite matrix element), the short-range residual interaction must act over an angular “distance”  $\Delta\theta \approx 33^\circ$ . We have seen in Chapter 4 that such matrix elements are small. Thus, in all these cases, the like nucleon configuration mixing amplitudes will be small.

For *unlike nucleons*, the large energy difference ( $\approx 10$  MeV) between  $(d_{5/2})^2$  and  $(d_{3/2})^2$  configurations again leads to small mixing. However, the *single nucleon mixing* induced by the  $\langle d_{5/2}^2 J | V | d_{5/2} d_{3/2} J \rangle$  matrix element is not necessarily small. First, the spacing is only  $\approx 5$  MeV. Second, both configurations exist in  $J = 1, 2, 3$ , and  $4$  states and, third, the angles involved favor large matrix elements. For example, for  $J = 1$ , the angle between the two nucleons in  $(d_{5/2})^2$  is  $\approx 152^\circ$  while for  $(d_{5/2} d_{3/2})$  it is  $\approx 156^\circ$ . Another way of saying this is that in the  $J = 1$  states, the main difference between  $(d_{5/2})^2$  and  $(d_{5/2} d_{3/2})$  is a flip of one intrinsic spin—the matrix element corresponds to the strong  ${}^3S$  interaction.

Therefore, we conclude that  $T = 1$  configurations of *identical* nucleons are

not very mixed by short-range attractive residual interactions, because of the large energy differences between such configurations, because of the consequences of antisymmetrization in determining which spin states are allowed, and because of the magnitude of the matrix elements that do exist. In contrast, configurations of *nonidentical* nucleons can be *strongly* admixed. Moreover, the mixing is a *single nucleon* effect. Therefore, such excitations cannot be absorbed into an effective two-body interaction. The strong admixtures of different *single* nucleon wave functions, in this case  $d_{5/2}$  and  $d_{3/2}$ , implies that the spherical symmetry of the wave functions is lost since the resultant wave functions must have nonuniform  $m$  state distributions (e.g.,  $(d_{5/2})^2(p-n)$  has a component  $M = 5/2 + 5/2 = 5$  while  $(d_{5/2} d_{3/2})(p-n)$  has  $M_{\max} = 5/2 + 3/2 = 4$ ). Thus, one can write the single-particle nuclear functions as  $\psi = C_{5/2m} d_{5/2} + C_{3/2m} d_{3/2}$ . As we shall see, this is exactly the form of Nilsson wave functions for a deformed shell model potential.

Although we have illustrated the idea for a particular case, the argument is general. It is also interesting to note that the  $C_{jm}$  coefficients *must* depend on the substate  $m$ . In this example,  $C_{3/2 m=3/2}$  can be nonzero, but  $C_{3/2 m=5/2}$  must be zero. Looking ahead for a moment, this, in essence, explains why Nilsson wave functions are  $m$ -dependent ( $m$  is often called  $K$  in the Nilsson model) and also why they are purest for the highest  $K$  values since, in that case, no other orbits can contribute admixed amplitudes.

In closing these introductory pages it is worthwhile to re-emphasize that our arguments for the existence of deformation and configuration mixing arose as a consequence of the Pauli principle, which led to a different behavior of  $T=0$  and  $T=1$  configurations, and of the short-range attractive nature of the nucleon residual interaction. Nowhere was it necessary to specify the interaction in detail. Of course, the choice of a specific residual interaction will affect the detailed wave functions that result, but the possibility of nonspherical wave functions is a rather general feature resulting from the particular configurations and interactions allowed by the Pauli principle when nonidentical nucleons are involved.

## 6.2 Collective Excitations in Spherical Even–Even Nuclei

One of the most characteristic empirical facts of nuclear systematics is that the shell model picture of nearly independent particle motion under the influence of weak residual interactions in simple configurations breaks down as one adds more and more valence nucleons past magic numbers. Simply put, the residual interactions among a growing number of valence nucleons build up to such an extent that they obliterate much of the underlying shell structure. The shell model wave functions become a poor first-order approximation to the real nuclear wave functions. In short, they no longer serve as the most appropriate basis states. In general, in a physical system, one always searches for some suitable set of basis states such that the realistic wave functions are dominated by one or a few components and any admixtures of basis states can be treated as relatively small perturbations. This is not to say that the shell model cannot provide a valid microscopic description of such collective excitations. Indeed,

we shall see in a later chapter that the widely used and extremely important RPA and TDA techniques are just such descriptions. Nevertheless, an alternate viewpoint, that approaches the nuclear structure more macroscopically, emphasizes the nuclear shape and excitations of that shape, providing a much simpler, physically transparent approach.

In this chapter we shall discuss a sampling of the most important models for collective excitations in even-even nuclei. As always, the emphasis will be on the physical ideas.

To begin, we recall some of the systematics shown in Chapter 2. Figure 2.8 showed the energy levels of the Sn, Xe, Te, and Cd nuclei. Sn, with  $Z = 50$ , is singly magic and displays a typical shell model behavior regardless of the number of valence neutrons. The  $2_1^+$  energy remains high and the  $4_1^+, 6_1^+$  levels cluster. As soon as valence nucleons are added, for example in Te and Cd (where the two valence protons are counted as holes),  $E_{2_1^+}$  drops sharply. The decrease grows as the number of valence neutrons increases. The drop is even faster for Xe, which has four valence protons. Figure 2.15 showed the systematics of the energy ratio  $E_{4_1^+}/E_{2_1^+}$ . It ranges from values  $< 2$  for shell model nuclei through  $\sim 2$  for nuclei reasonably close to closed shells, then increases sharply towards the limiting value of 3.33 near midshell. As we shall discuss, values near 2.0, 2.5, and 3.33 are all typical of different types of macroscopic collective shapes: spherical harmonic vibrator, axially asymmetric rotor, and axially symmetric rotor, respectively.

Generally, there is a smooth progression from one to another of these idealized collective limits. However, inspection of Figs. 2.13 and 2.14 shows that the systematics is anything but simple. At the end of this chapter we shall see some easy, physically transparent, ways of understanding this complexity and of parameterizing the behavior of heavy nuclei. Appropriately enough, this approach will be based on a recognition of the importance of the residual p-n interaction among the valence nucleons.

Here, though, we discuss models for each type of behavior, turning later to their evolution from one into another. We start the discussion with the least collective nuclei, which occur soon after closed shells: spherical-vibrational nuclei. The generic concept of vibrational motion in nuclei is widespread and encompasses a great richness of phenomena. We speak here of a particular kind. To put this in context, suppose we expand the residual interaction among the valence nucleons in multipoles, the first few terms will correspond to monopole, dipole, quadrupole, octupole, and hexadecapole components. Each of these carries a parity  $\pi = (-1)^\lambda$  where  $\lambda$  is the multipolarity involved.

The electric dipole mode corresponds, geometrically, to a shift in the center of mass, and therefore plays little role in the low-lying spectrum of even-even nuclei. At higher energies, however, it induces the well-known giant dipole resonance, which can be pictured as an oscillation of the proton distribution against the neutron distribution. As this mode involves a rather large scale displacement of major components of the nucleus, it requires considerable energy, typically between 8 and 20 MeV. Since it is also a negative parity excitation, and since most of the orbits in a given major shell consist of the same parity, it necessarily involves excitations of the particles from one major

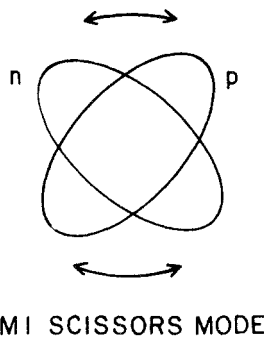


**Fig. 6.1.** The M1 scissors mode.

shell to the next and, once again, we see why it is generally high lying. We shall not discuss the giant dipole resonance, or indeed, other giant resonances, any further. This is in no way meant to minimize their importance: indeed, they are a major focus of current work in nuclear structure physics. Their neglect here stems rather from the emphasis in this book on the low-lying nuclear structure spectrum and from the author's feeling that he has nothing particularly new or innovative to say about the subject.

There is, however, a low-lying magnetic dipole excitation that has recently been discovered in beautiful electron scattering and  $\gamma$  ray inelastic scattering experiments. It occurs, for example, in heavy deformed nuclei at roughly 3 MeV and corresponds to a vibration in which the proton and neutron distributions oscillate with respect to each other with a scissors type of motion, as opposed to the linear vibrational motion of the giant electric dipole resonance. The idea is illustrated in Fig. 6.1. This mode, characterized by strong M1 electromagnetic transitions to the ground state and first  $2_1^+$  state is now known in a number of nuclei and an interesting systematics has been established. It has been studied from both geometric and algebraic (IBM-2) viewpoints. Further discussion of this active area of research is beyond the scope of this book.

### Quadrupole Vibrations

The next vibrational mode, that we shall consider in detail, is the electric quadrupole or E2 vibrational mode. It appears in different guises in different categories of nuclei. Near closed shells, where the nuclei are spherical in their ground state, the action of a quadrupole residual interaction causes the nucleus to oscillate in shape, taking on a range of quadrupole distortions as a function of time. The Hamiltonian for such a state can be schematically written as

$$H = E_0 + \hbar \omega \sum_{\mu} \left( \mathbf{b}_{2\mu}^\dagger \mathbf{b}_{2\mu} + \frac{1}{2} \right) + C \sum_{\mu} \left[ (\mathbf{b}_{2\mu}^\dagger \mathbf{b}_{2\mu})^L (\mathbf{b}_{2\mu} \mathbf{b}_{2\mu})^L \right]^{(0)} \quad (6.1)$$

where  $E_0$  is the zero-point energy and the operators  $\mathbf{b}_{2\mu}^\dagger$  and  $\mathbf{b}_{2\mu}$  create and destroy this quadrupole vibration:  $\psi_{ph} = \mathbf{b}_{2\mu}^\dagger |0\rangle$ .

For simplicity of notation, and to keep the essential physics to the fore, we

shall henceforth usually drop the subscripts on the operators  $\mathbf{b}_{2\mu}$ . In the same spirit, summations over the components  $\mu$  will usually be implied rather than explicit. Since we shall make frequent use of phonon or boson creation and destruction operators, we pause for a moment to recall some key properties of such operators in the formalism of second quantization. The basic defining rules for arbitrary creation and destruction operators  $\mathbf{b}$  and  $\mathbf{b}^\dagger$  are:

$$\mathbf{b}|n_b\rangle = \sqrt{n_b}|n_b-1\rangle \quad (6.2)$$

and

$$\mathbf{b}^\dagger|n_b\rangle = \sqrt{n_b+1}|n_b+1\rangle \quad (6.3)$$

where  $|n_b\rangle$  is a state with  $n_b$  bosons. Here  $\mathbf{b}$  refers to quadrupole phonons; later, in the discussion of the IBA,  $\mathbf{b}$  will refer to either  $s$  or  $d$  bosons. From these definitions

$$\mathbf{b}^\dagger \mathbf{b}|n_b\rangle = \mathbf{b}^\dagger \sqrt{n_b}|n_b-1\rangle = \sqrt{n_b} \sqrt{(n_b-1)+1}|n_b\rangle$$

or

$$\mathbf{b}^\dagger \mathbf{b}|n_b\rangle = n_b|n_b\rangle \quad (6.4)$$

So,  $\mathbf{b}^\dagger \mathbf{b}$  simply counts the number of  $b$ -type bosons. Thus we now recognize that the second term in  $H$  is just the energy, relative to the ground state energy  $E_0$  needed to create the quadrupole phonon excitation, which naturally carries a spin and parity  $2^+$ .

There is no reason, except the limitations provided by the Pauli principle when the microscopic structure of these vibrations is considered, that prevents more than one phonon excitation from simultaneously existing. These multiphonon states  $\psi_{N_{ph}} = (\mathbf{b}^\dagger)^N |0\rangle$  will correspond to higher and higher nuclear levels. From Eq. 6.4, the second term in  $H$  is the product of the number of quadrupole phonons and the energy of each. Clearly, at this stage in the Hamiltonian one has a purely harmonic vibrational spectrum, where the excitation energy is linear in the number of phonons: for an  $N_{ph}$ -phonon state,  $E_x = \hbar\omega(N_{ph} + 5/2)$ , since the quadrupole mode is a 5-dimensional oscillator.

**Table 6.1.**  $m$  scheme for two-quadrupole phonon states.\*

$J_1 = 2$	$J_2 = 2$	$M$	$J$
$m_1$	$m_2$		
2	2	4	
2	1	3	
2	0	2	
2	-1	1	4
2	-2	0	
1	1	2	
1	0	1	
1	-1	0	2
0	0	0	0

\*Only positive total  $M$  values are shown: the table is symmetric for  $M < 0$ . The full set of allowable  $m_i$  values giving  $M \geq 0$  is obtained by the conditions  $m_1 \geq 0$ ,  $m_2 \leq m_1$ .

**Table 6.2.**  $m$  scheme for three-quadrupole phonon states\*

$J_1 = 2$	$J_2 = 2$	$J_3 = 2$	$M$	$J$
$m_1$	$m_2$	$m_3$		
2	2	2	6	
2	2	1	5	
2	2	0	4	
2	2	-1	3	
2	2	-2	2	
2	1	1	4	
2	1	0	3	
2	1	-1	2	
2	1	-2	1	
2	0	0	2	
2	0	-1	1	2
2	0	-2	0	4
2	-1	-1	0	6
1	1	1	3	
1	1	0	2	
1	1	-1	1	3
1	1	-2	0	
1	0	0	1	
1	0	-1	0	
0	0	0	0	0

$J = 6, 4, 3, 2, 0$

\*Only positive total  $M$  values are shown; the table is symmetric for  $M < 0$ . The full set of allowable  $m_i$  values giving  $M \geq 0$  is obtained by the conditions  $m_1 \geq 0$ ,  $m_3 \leq m_2 \leq m_1$ .

To continue, we must now turn to the question of which spin states are allowed in multiphonon excitations. For the two-quadrupole phonon case, it is clear that the maximum possible spin is  $4^+$ . But it turns out that only a triplet of levels with spins  $J^\pi = 0^+, 2^+, 4^+$  is allowed. There are many ways to derive this result. Perhaps the most elegant is the use of Young tableaux, but here we shall use the simpler and more straightforward, though more tedious, method of the  $m$ -scheme. The essential difference between the use of the  $m$ -scheme for phonon excitations and for single-particle excitations is the recognition that phonons, involving particle-hole excitations and integer spins, behave essentially as bosons. Therefore, the Pauli principle is not applicable and the wave functions must be totally *symmetric*. This means that all combinations of  $m$  states are allowed. Table 6.1 shows the  $m$ -scheme counting of substates for the case of two quadrupole phonons and shows that the allowed spins are as stated previously. The  $m$ -scheme analysis for the three-phonon case is given in Table 6.2, which shows that this excitation comprises a quintuplet of levels (at three times the single phonon energy), with spins  $J^\pi = 0^+, 2^+, 3^+, 4^+, 6^+$ . This harmonic picture of single- and multi-phonon excitations is illustrated in Fig. 6.2.

To pursue the study of multiphonon states, it is necessary to delve more deeply into their structure. Consider the three-phonon levels. As Fig. 6.3 illustrates, the  $6^+$  state can only be made in one way: by aligning the angular momentum of a single phonon state with that of the  $4^+$  two-phonon level.

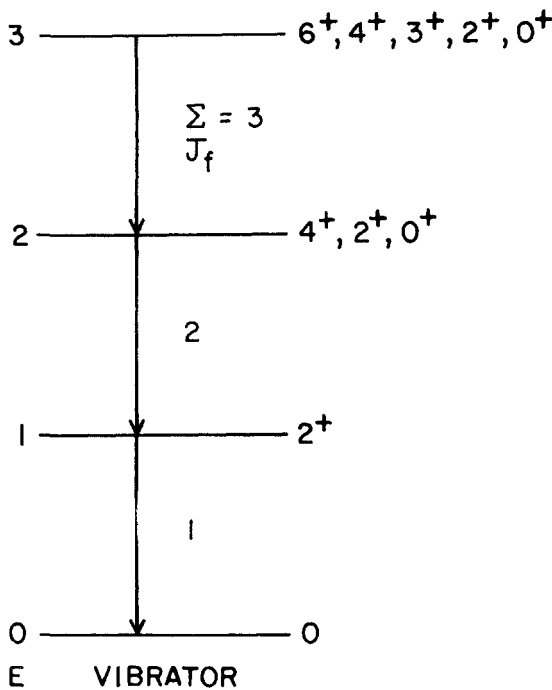
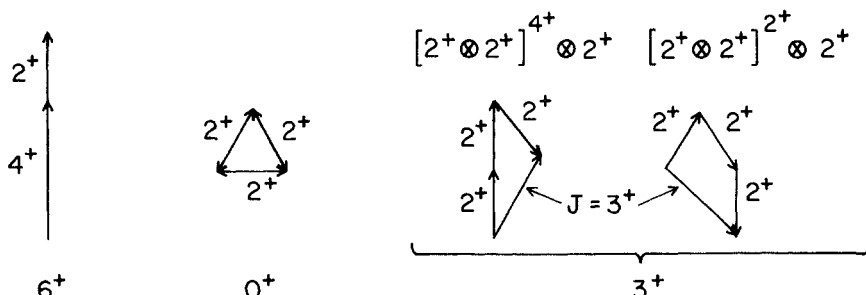


Fig. 6.2. Low-lying levels of the harmonic vibrator phonon model.

Similarly, the  $0_3^+$  three-phonon level can only be constructed by antialigning a single quadrupole phonon with the  $2^+$  two-phonon state. However, the other three-phonon levels can be constructed in more than one way. For example, the  $2^+$  level can be made by coupling a quadrupole phonon with the  $2^+$  two-phonon state or by antialigning a quadrupole phonon with the  $4^+$  two-phonon state. In similar fashion, the  $3^+$  and  $4^+$  three-phonon states can be made by coupling the third quadrupole phonon to more than one of the two-phonon



#### CONSTRUCTION OF SOME 3-PHONON STATES

Fig. 6.3. Two-phonon composition of three-phonon states.

**Table 6.3.** Relative coefficients of fractional parentage for three-phonon quadrupole vibrator states<sup>†</sup>

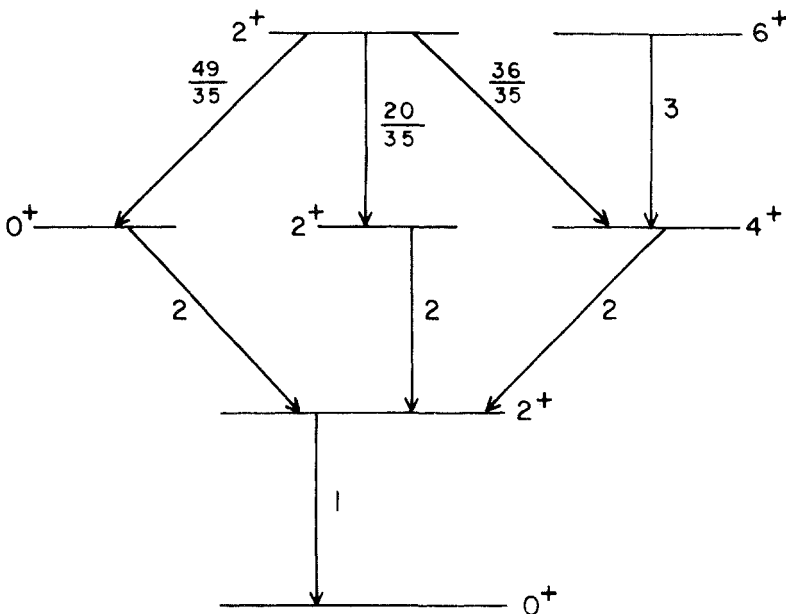
$J_{3\text{ph}}$	$0^+$	$2^+$	$4^+$
$6^+$			$\sqrt{3}$
$4^+$		$\sqrt{11/7}$	$\sqrt{10/7}$
$3^+$		$\sqrt{15/7}$	$-\sqrt{6/7}$
$2^+$	$\sqrt{7/5}$	$\sqrt{4/7}$	$\sqrt{36/35}$
$0^+$		$\sqrt{3}$	

<sup>†</sup>The normalization is to  $\sqrt{N}$ . For the three-phonon states,  $J_{3\text{ph}}$ , the squares of the coefficients for each  $J_{2\text{ph}}$  also give the relative values of  $B(E2; J_{3\text{ph}} \rightarrow J_{2\text{ph}})$ . For example, the  $B(E2; 4^+_{3\text{ph}} \rightarrow 2^+_{2\text{ph}})$  and  $B(E2; 4^+_{3\text{ph}} \rightarrow 4^+_{2\text{ph}})$  values are in the ratio  $11/10 = 1.1$ . See text.

states. The wave functions for the  $2^+$ ,  $3^+$ , and  $4^+$  three-phonon states are therefore linear combinations of two terms, and the relative amplitudes are simply *phonon* coefficients of fractional parentage whose squares give the relative likelihoods that the three-phonon state is made in a certain way. It is often useful to know these coefficients, so we give them for the  $N_{\text{ph}} = 3$  states in Table 6.3. We will encounter two applications of these coefficients momentarily.

An important aspect of the vibrational model centers on electromagnetic transition rates since they are particularly sensitive to coherence properties in nuclear wave functions. We saw, for example, in Fig. 2.16, the systematics of  $B(E2; 0^+_1 \rightarrow 2^+_1)$  values throughout the periodic chart. Although small and comparable to single-particle estimates in light nuclei, they attain values orders of magnitude larger in heavy deformed regions. Intermediate values characterize the realm of spherical-vibrational nuclei we are presently considering.

In general, radiation can be given off when any nucleon changes its orbit. For example, changes in single-particle orbits in shell model nuclei are often accompanied by the emission of  $\gamma$ -radiation. While collective excitations are clearly not of single-particle nature and the destruction of one does not correspond to a single change of orbit by an individual nucleon, we will see in Chapter 9 that their wave functions can be represented as coherent linear combinations of single-particle–hole (or, equivalently, two quasi-particle) excitations. Therefore, not only are  $\gamma$ -ray transitions between phonon levels permitted, but the coherence can make them particularly strong. Since a two-phonon excitation involves a superposition of two linear combinations of one-body excitations, the destruction of two-phonons would require a simultaneous destruction of two particle–hole excitations or four quasi-particles. Therefore, such transitions are forbidden and one has the characteristic phonon model selection rule  $\Delta N_{\text{ph}} = \pm 1$ , where  $N_{\text{ph}}$  is the number of phonons. The argument for this selection rule (obtained here for quadrupole vibrations of spherical nuclei) is rather general and applies to any phonon structure described as a linear combination of one-particle excitations. We will encounter it repeatedly in various applications.



### B(E2) VALUES FOR DECAY OF MULTI-PHONON STATES

Fig. 6.4. B(E2) values in the harmonic vibrator model.

Let us now consider the magnitude of these B(E2) values between phonon states as illustrated in Fig. 6.2 and 6.4, where we assign a value of unity for the decay of the one-phonon  $2^+$  state to the ground state. Since, in first order, multiphonon excitations simply consist of the piling on or superposition of more than one identical phonon, it might seem that the B(E2) value for the decay of the two-phonon state would also be unity. However, this neglects the fact that there are two phonons in the initial state and that either one of them may be destroyed. This gives twice as many decay possibilities and therefore  $B(E2:(N_{ph}=2) \rightarrow 1) = 2$ , as indicated in Fig. 6.2. Continuing this, one can state a general expression for the decay of the  $N_{ph}$ -phonon state to the  $(N_{ph}-1)$ -phonon state. A transition  $N_{ph} \rightarrow N_{ph}-1$  must be accomplished by an E2 operator of the form  $\mathbf{b}$ , that is, a one-phonon destruction operator. By Eq. 6.2

$$\mathbf{b}|N_{ph}\rangle = \sqrt{N_{ph}}|N_{ph}-1\rangle$$

and so the B(E2) value is proportional to  $N_{ph}$ .

This general statement, however, obscures the important point that, for  $N_{ph} \geq 3$ , angular momentum conservation allows the decay of some initial states to more than one final state. For example, the  $2^+$ ,  $3^+$ , and  $4^+$ , three-

phonon levels can each decay to two or more of the two-phonon states. We shall now show that the proportionality of these  $B(E2)$  values to the number of phonons in the initial state actually refers to the *sum* of the  $B(E2)$  values from a given  $N_{ph}$ -phonon level to all possible  $(N_{ph}-1)$ -phonon levels. It is trivial to work out the relative  $B(E2)$  values for each of these decay routes: this exercise is in fact one of the promised applications of the phonon CFP's in Table 6.3. Consider as an example the decay of the  $N_{ph} = 3, 4^+$  level to the  $2^+$  and  $4^+$  two-phonon states.

From Table 6.3, the wave function for the three-phonon  $4^+$  level can be written, in obvious notation, as

$$\psi_3(4^+) = \frac{1}{\sqrt{3}} \left[ \sqrt{\frac{11}{7}} [\psi_2(2^+) \psi_1(2^+)]^{4^+} + \sqrt{\frac{10}{7}} [\psi_2(4^+) \psi_1(2^+)]^{4^+} \right]$$

Then, the E2 matrix element connecting this level to the  $2^+$  two-phonon state is

$$\begin{aligned} \langle \psi_2(2^+) || E2 || \psi_3(4^+) \rangle &= \frac{1}{\sqrt{3}} \left[ \sqrt{\frac{11}{7}} \langle \psi_2(2^+) || b || [\psi_2(2^+) \psi_1(2^+)]^{4^+} \right] \\ &\quad + \sqrt{\frac{10}{7}} \langle \psi_2(2^+) || b || [\psi_2(4^+) \psi_1(2^+)]^{4^+} \rangle \end{aligned}$$

But the second term vanishes because  $\psi_2(2^+)$  and  $\psi_2(4^+)$  are orthogonal. Hence, using Eq. 6.2 and setting  $B(E2:2^+_1 \rightarrow 0^+_1) = 1$ , we get

$$B(E2:4^+_{3ph} \rightarrow 2^+_{2ph}) = \frac{3}{3} \left( \frac{11}{7} \right) = \frac{11}{7} \quad (6.5)$$

Similarly,

$$B(E2:4^+_{3ph} \rightarrow 4^+_{2ph}) = \frac{10}{7}$$

and we see that the three-phonon  $\rightarrow$  two-phonon  $B(E2)$  values are proportional to the squares of the three-phonon CFP coefficients in Table 6.3. The table can be used to obtain the  $B(E2)$  values we have not worked out. The results for the decay of the  $4^+$  and  $2^+$  three-phonon states are illustrated in Fig. 6.4. We also see an example of our general result, namely,

$$\sum_{J_{2ph}} B(E2:4^+_{3ph} \rightarrow J^+_{2ph}) = 3 B(E2:2^+_{1ph} \rightarrow 0^+_{gs}) \quad (6.6)$$

and similarly for the other three-phonon levels.

The reader is cautioned to bear these results in mind, since one occasionally encounters statements such as that the  $B(E2)$  for the decay of a three-phonon state to a two-phonon state is three times that for the decay of the one-phonon state to the ground state. The proper relation involves the sum of the decays to the possible final states.

This discussion of energies and  $B(E2)$  values in the harmonic vibrator model assumes an idealized picture in which all of the phonons in a multiphonon state are identical. However, as we shall see in more detail when we consider the microscopic structure of collective vibrations, a phonon state can be written as a linear combination of individual particle-hole (or two quasi-particle) excitations. Since a multiphonon wave function can be written as a product of single phonon wave functions, multiphonon states effectively corre-

spond to multiparticle–multihole excitations. Since each of these excitations is a Fermion excitation, the Pauli principle must be obeyed. Its effects are significant only when the particle–hole excitations cause significant occupation of individual  $j$  shells. As a trivial example, consider a nucleus where a valence  $s_{1/2}$  orbit has, on average, one valence nucleon in the ground state (i.e., the amplitude for  $(s_{1/2})^2$  is 0.5). Further suppose that a particular vibration has an amplitude of 0.707 for raising a particle to this  $s_{1/2}$  orbit. Clearly, it is not difficult to create a single- or even a double-phonon excitation in this case. The latter would add, on average, one particle to the  $s_{1/2}$  orbit, thereby filling it. This component of the vibrational wave function would be “blocked,” however, in a three-phonon state, since one cannot put more than two particles in an  $s_{1/2}$  orbit. The three-phonon wave function would therefore entail a modification to the basic phonon structure. This, in turn, would entail a change in the  $B(E2)$  values for the decay of this state compared to the harmonic phonon picture. Therefore, in realistic situations, the simple selection rules and the analytic results for the relative  $B(E2)$  values between various phonon states will be at best approximately realized.

Moreover, this blocking leads to anharmonic vibrational spectra in which the degeneracies of the states in multiphonon multiplets are broken. Such degeneracy breaking can also arise from the neglect of those residual interactions not taken into account in the microscopic structure of the phonon itself. In general, the calculation of such anharmonicities is complex and depends on the specific  $j$  shells and residual interactions involved. However, there is one situation in which a very simple and elegant result can be obtained essentially by inspection.

This brings up the second application of the CFP's in Table 6.3. Suppose we assume that degeneracy breaking is caused by residual two-body interactions only. This means that the level energies in a two-phonon state are simply not twice the one-phonon energy, but differ because of a residual interaction between the two-phonons. This, in fact, is the effect of the third term of  $H$  in Eq. 6.1: it represents an interaction between two phonons.

In the three-phonon states, the same residual interactions apply and our assumption simply states that there are no mutual interactions among the three phonons at a given time. In this case, without ever specifying the residual interaction, the nature, or the microscopic structure of the phonon, one can immediately deduce the anharmonic energies of the three-phonon states from those of the two-phonon levels. The situation is illustrated in Fig. 6.5, where the energies of the  $0^+$ ,  $2^+$ , and  $4^+$  two-phonon states are written in terms of the harmonic value  $2E_{2\ddagger}$ , plus a perturbation  $\epsilon_j$  ( $\epsilon_0$ ,  $\epsilon_2$ ,  $\epsilon_4$  are the anharmonicities). Consider now the three-phonon levels. As we have seen, there is only one way to make the  $6^+$  level: by aligning a single  $2^+$  quadrupole phonon with a pair of phonons coupled so as to produce the  $4^+$  two-phonon state. In the three-phonon  $6^+$  state, there are three possible pairs of (indistinguishable) phonons that can couple and interact in forming the intermediate  $4^+$  plus state. Therefore, the anharmonicity (the deviation of  $E_{6+}$  from  $3E_{2\ddagger}$ ) is three times the anharmonicity in the  $4^+$  two-phonon state, or  $3\epsilon_4$ . In the same fashion, the  $0^+$  3-

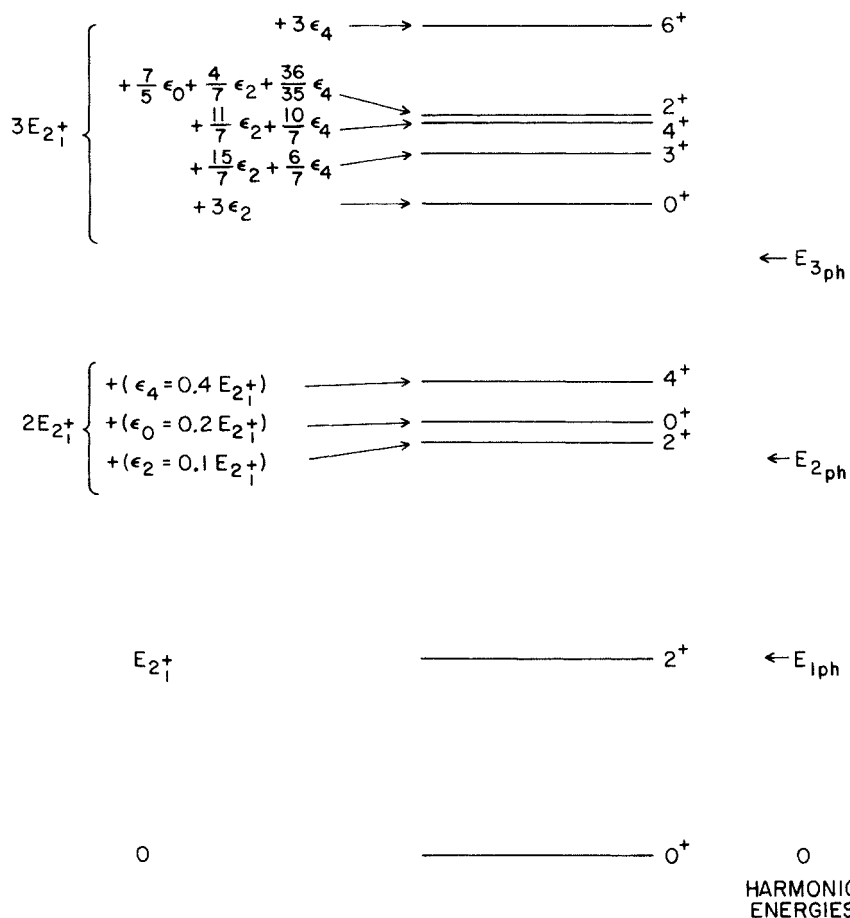


Fig. 6.5. Energy anharmonicities in the vibrator model assuming arbitrary two-body residual interactions.

phonon state can only be made by antialigning one phonon with the  $2^+$  two-phonon state. Again, there are three ways to do this, and the anharmonicity in the three-phonon  $0^+$  energy will be triple the anharmonicity in the two-phonon  $2^+$  level, or  $3\epsilon_2$ . The other three-phonon states, which can be made in two or more ways from the 2-phonon levels, will have total energy anharmonicities given by the relative proportions of their wave functions arising from the various two-phonon states. These relative proportions are given by the CFP coefficients of Table 6.3, and the resulting energy anharmonicities are shown in Table 6.4 and illustrated in Fig. 6.5.

It is worthwhile to reiterate what has been derived here. We have never specified the structure of the phonon itself. We have also never specified the nature of the residual interaction except to state that it is two-body. Neverthe-

**Table 6.4.** Energies of the three-phonon quintuplet states in terms of the two-phonon anharmonicities.

$N_{ph}$	$J$	Energy*
		(relative units)
0	0	0
1	2	1
2	0	$2 + \epsilon_0$
2	2	$2 + \epsilon_2$
2	4	$2 + \epsilon_4$
3	0	$3 + 3\epsilon_2$
3	2	$3 + 7/5\epsilon_0 + 4/7\epsilon_2 + 36/35\epsilon_4$
3	3	$3 + 15/7\epsilon_2 + 6/7\epsilon_4$
3	4	$3 + 11/7\epsilon_2 + 10/7\epsilon_4$
3	6	$3 + 3\epsilon_0$

\* $\epsilon_0$ ,  $\epsilon_2$ , and  $\epsilon_4$  are defined as the deviations of the  $0^+$ ,  $2^+$ , and  $4^+$  level energies of the two-phonon triplet from  $2E_{2,1}^+$ .

less, from the observed anharmonicities in the two-phonon states, we have been able to derive predicted anharmonicities for the three-phonon levels.

This model can be tested by observation of the three-phonon levels. If discrepancies are found, then we immediately know that they must arise either from three-body interactions, from Pauli principle effects in the multiphonon states, or from interactions with other nearby excitations. Our analysis helps to isolate the specific mechanisms leading to the observed anharmonicities.

The vibrational model was originally proposed in the early 1950s, and it was thought that numerous examples of such a structure were observed empirically. Triplets of levels with spins  $0^+$ ,  $2^+$ ,  $4^+$ , were known in many nuclei near closed shells at slightly more than twice the energy (typically,  $E_{2ph}/E_{1ph} \sim 2.2$ ) of the first  $2^+$  state. However, it was commonly found that the energy splitting among the two-phonon levels is comparable to the one-phonon energy; basically, the structural effects leading to anharmonicities are comparable to those involving the phonon itself. Moreover, the predicted phonon model B(E2) values were significantly violated. Perhaps most importantly, over the last decades, additional low-lying levels near the two-phonon states have been detected in many nuclei.

While in many of these nuclei there may be an *underlying* vibrational structure, it is significantly perturbed and admixed with other degrees of freedom. An interesting example is the Cd isotopes shown in Fig 6.6: These nuclei, especially  $^{114}\text{Cd}$ , historically have been considered the best prototypes of vibrational behavior. However, it is clear from Fig. 6.6 that there are four and sometimes five levels clustered together in the two-phonon energy region. The extra states have since been identified as *intruder* levels.

It is worth digressing from our discussion of vibrational excitations to comment on such intruder excitations, which are now known to be widespread in nuclei near closed shells. They are an area of active study, especially in

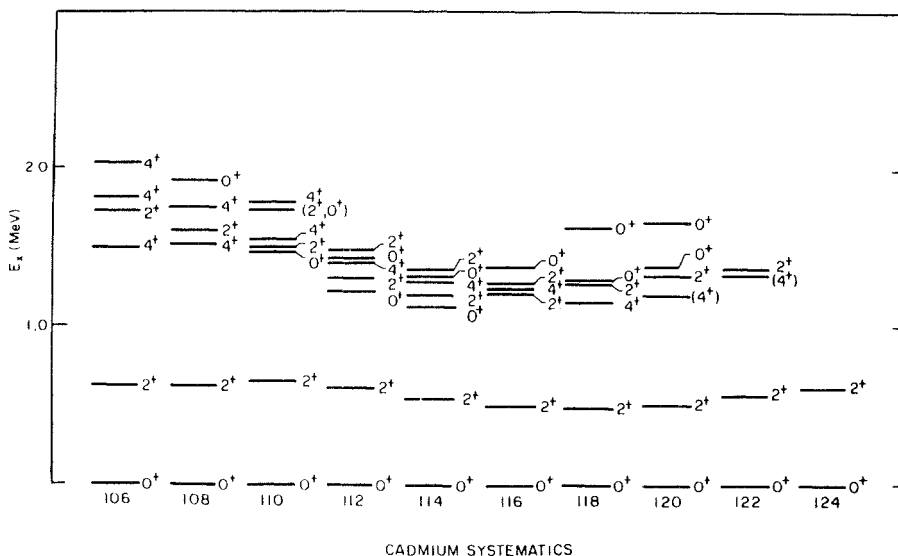


**Fig. 6.6.** Energy systematics in the Cd isotopes. Note the intermingling of two-phonon triplet states with extra levels (Aprahamian, 1984).

nuclear regions far from stability. An understanding of them is, in any case, essential to disentangling the empirical features of many vibrational nuclei. Moreover, the discussion will introduce some basic ideas relating to the p-n interaction, which we shall return to later in this chapter. We have already alluded several times to the idea that this interaction is essential to the development of collectivity and deformation in nuclei. Here we will encounter our first specific example of this.

Cd has  $Z = 48$ , and therefore two proton holes relative to the  $Z = 50$  magic number. It is of course possible to excite the Cd nuclei by elevating two protons from the  $Z = 28\text{--}50$  valence shell into the next higher,  $Z = 50\text{--}82$  shell. The idea is sketched in Fig. 6.7. Normally this requires considerable energy since it involves raising two nucleons across a major shell gap. However, the residual p-n interaction is strong and attractive, and as such introduces a major modification to this first-order energy. In a simple picture, one can view the “normal” states of Cd as consisting of two proton holes interacting with some number of valence neutrons. In the *intruder* state, there are four proton holes in the  $Z = 28\text{--}50$  shell *plus* two proton particles in the  $Z = 50\text{--}82$  shell. In a sense, there are six valence protons that can now interact with the same number of valence neutrons. In this picture the intruder states in Cd are analogous to the normal states in Ba, as suggested in Fig. 6.7.

We have already seen that the more valence nucleons there are of both kinds, the “softer” the structure will be. Sufficient numbers of valence protons and neutrons lead to deformed shapes. Therefore, in this schematic view, intruder levels should be more deformed than the “normal” levels. Moreover, since the attractive interaction is three times greater than in the normal levels,

INTRUDER STATE MODEL  
PROTON LEVELS

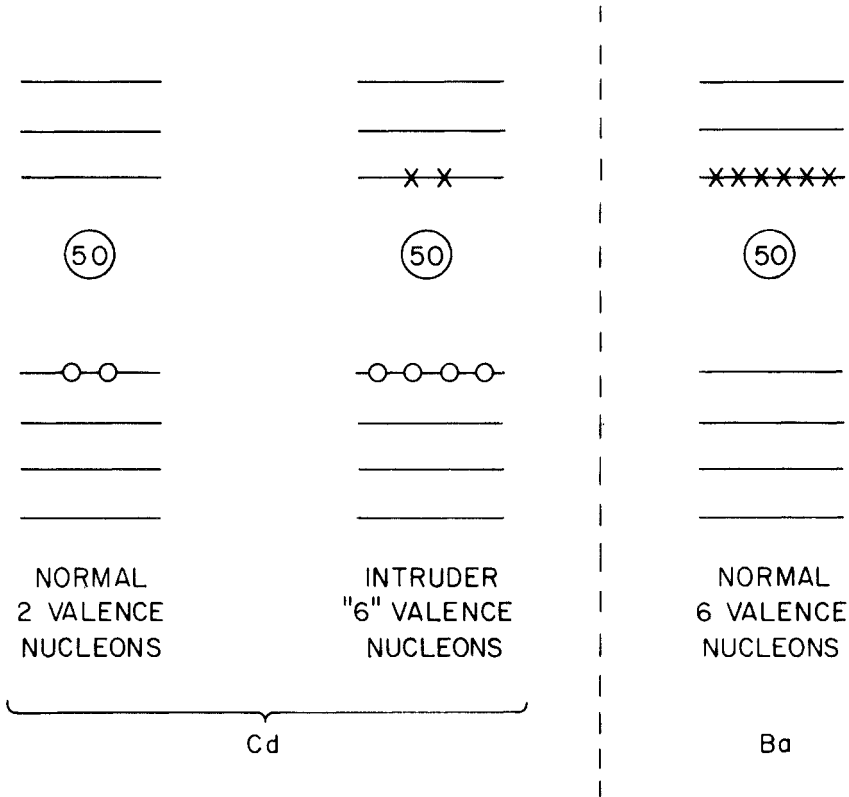


**Fig. 6.7.** Schematic illustration of intruder excitations and normal states in Cd. The normal states of Ba are shown for comparison with the Cd intruders.

the intruder state excitation energies are lowered relative to their unperturbed (no p-n interaction) value. This lowering increases approximately linearly with the number of neutrons, and therefore, one expects the energies of these intruder states to drop from approximately twice the shell gap for  $N \sim 50$  or 82 toward midshell, where the p-n interaction strength is maximum. Inspection of Fig. 6.6 shows that this simple picture is at least qualitatively correct.

As suggested, this intruder state model is quite general and such excitations, once thought to be rare, are now known to abound throughout the periodic table. Perhaps the best known example is in the Pb region, whose systematics are shown in Fig. 6.8.

Most intruder levels observed to date are proton excitations. This is related to the role of a strong p-n interaction in lowering these levels. Since there is a

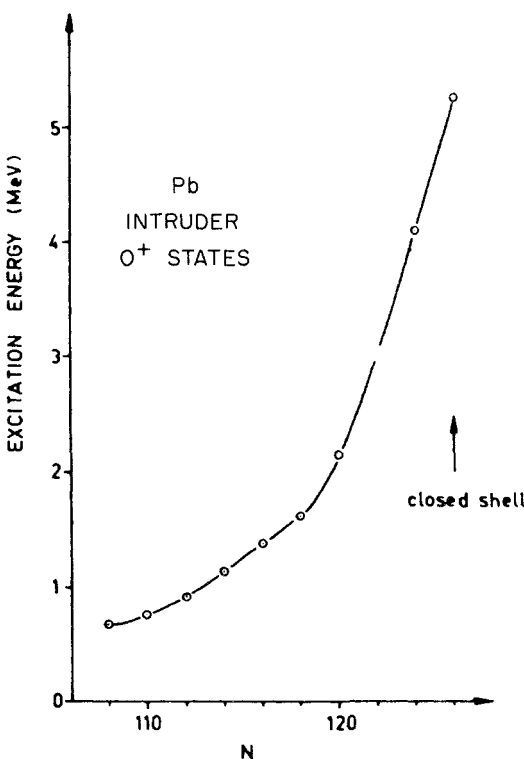
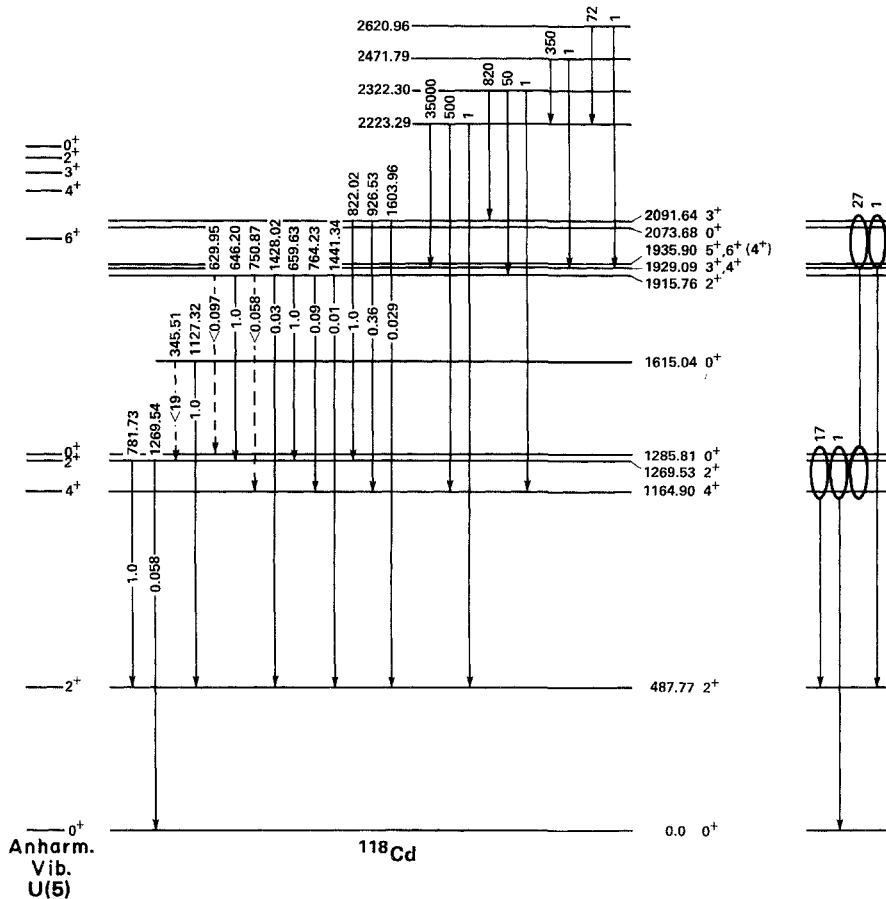


Fig. 6.8. Systematics of  $0^+$  intruder levels in the Pb isotopes (Van Duppen, 1985).

neutron excess in heavy nuclei, the excited valence protons in the intruder state occupy the same shell as the neutrons, thus enhancing the p–n interaction (see Fig. 3.5).

The concept of intruder states is far more important than the explanation of a few bothersome levels. It is closely connected with the origin of deformation itself, as we shall discuss towards the end of this chapter.

These comments relate to our discussion of Cd vibrational states because, as the  $N = 82$  shell closure in Cd is approached, the expected rise in intruder energies should leave behind a reasonable vibrational spectrum. This has led to experiments on  $^{118,120}\text{Cd}$ . The data included in Fig 6.6 seem to confirm this expectation, although studies of absolute  $B(E2)$  values show that the interpretation is not quite so simple. The level scheme for  $^{118}\text{C}$  is illustrated in Fig 6.9, which includes the known information on  $\gamma$ -ray transition rates and relative  $B(E2)$  values. There is a triplet of levels near 1200 keV in which the energy separation is much less than  $E_{2_1^+}$ . Furthermore, and most remarkable, an *entire* closely spaced quintuplet of candidates for the three-phonon multiplet was identified. (In fact, candidates for even higher four-phonon states have been suggested.) Although there are significant deviations from the expected



**Fig. 6.9.** Level scheme of  $^{118}\text{Cd}$  showing the one-, two-, and three-phonon states as well as an intruder  $0^+$  level at 1615 keV and possible candidates for four-phonon excitations above 2.2 MeV. On the right are shown the average  $(\Delta N_{\text{ph}} = 1)/(\Delta N_{\text{ph}} = 2)$  branching ratios. On the left are the predictions for the three-phonon states assuming the empirically observed anharmonicities in the two-phonon states. These are the same predictions one would obtain in the U(5) limit of the IBA (Aprahamian, 1987).

patterns of relative  $B(E2)$  values compared to the phonon model predictions, the overall predominance of  $\Delta N_{\text{ph}} = 1$  transitions is well satisfied. On the right of Fig 6.9, the average ratio of one-phonon to two-phonon changing transitions [ $(\Delta N_{\text{ph}} = 1)(\Delta N_{\text{ph}} = 2)$ ] is indicated: there is at least an order of magnitude preference for the phonon model selection rule. On the left are the predicted energies for the three-phonon quintuplet based on the anharmonicities observed in the two-phonon triplet. Although the agreement with experiment is not at all exact, the observed clustering of the levels into two spin groups is

correctly predicted. Presumably, the remaining deviations are due in part to intruder-normal state mixing or to Pauli principle effects. In fact, calculations by Heyde and co-workers that incorporate such mixing provide a significant improvement in the predicted energy levels.

The observation of E2 transitions in Cd, as well as other near-vibrational nuclei, such as the weak  $\Delta N_{ph} = 2$  transitions that violate the phonon model selection rules are often considered to arise from interactions that mix the number of phonons. From the B(E2) branching ratios, one can make estimates of the mixing amplitudes and thereby extract the interaction matrix elements. A similar approach can be used for intruder states. These states have forbidden E2 transition matrix elements to the normal states, since they cannot be connected to them by a one-particle operator. Once again, however, neglected residual interactions will cause some small mixing of the intruder and normal states, and such mixing can be probed empirically by measuring E2 branching ratios. It is generally estimated that the intruder-normal mixing matrix elements are  $\sim 100$  keV. Therefore, in a nucleus such as  $^{114}\text{Cd}$  where the final energies of the intruder and normal  $0^+$  states near 1.2 MeV are only  $\sim 200$  keV apart, these states must have been nearly degenerate prior to mixing (after mixing, degenerate levels are twice the mixing matrix element apart), and therefore their perturbed wave functions will be nearly equal admixtures of the unperturbed intruder and normal states. In  $^{118}\text{Cd}$ , on the other hand, the final separation, and therefore the initial separation, is much greater; the mixing is correspondingly smaller.

There are other nuclei that display reasonably well-developed vibrational spectra. Examples are  $^{102}\text{Ru}$ , which has a full three-phonon quintuplet but with greater intramultiplet splitting (anharmonicity) than  $^{118}\text{Cd}$ . The Te isotopes near  $A = 120$  also exhibit nice two-phonon triplets, relatively closely bunched. The level schemes for two of these nuclei were included in Fig. 2.9.

Despite these examples, *near-harmonic* vibrational motion is the exception rather than the rule. The reason seems to be that it takes only a few valence protons and neutrons to soften the nucleus to deformation to such an extent that the simple scheme of quadrupole surface vibrations of a spherical shape loses applicability.

### 6.3 Deformed Nuclei: Shapes

Further from closed shells, the accumulating p-n interaction strength leads to additional configuration mixing and deviations from spherical symmetry even in the ground state, and so we now turn to consider nuclei with stable and permanent deformations. The lowest applicable shape component is a quadrupole distortion. There can also be octupole and hexadecapole shapes. These are schematically illustrated in Fig. 6.10a. Nuclei with quadrupole shapes abound throughout the periodic table in midshell regions.

For a nucleus with quadrupole deformation, one can write the nuclear radius as

## SOME NUCLEAR SHAPES AND VIBRATIONS

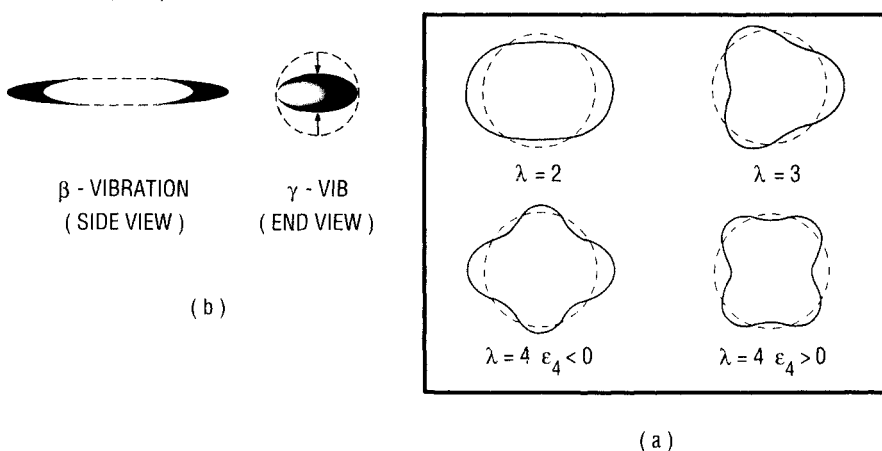
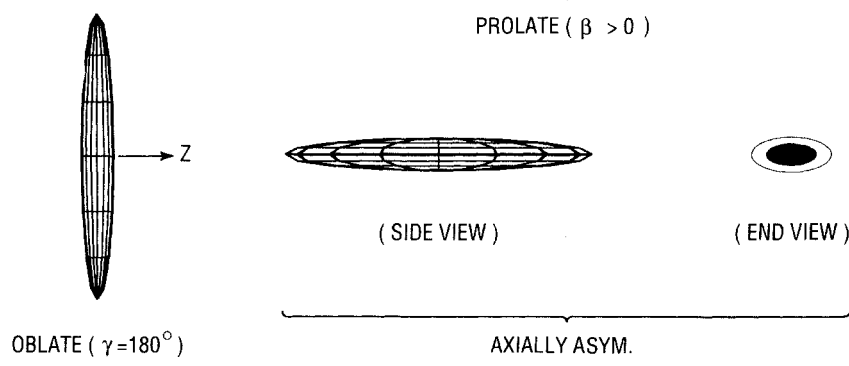
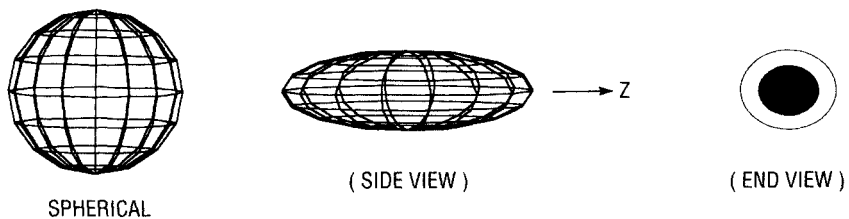


**Fig. 6.10.** (a) Equal potential surfaces for different multipole distortions. (b) Schematic illustrations of various quadrupole shapes (prolate, oblate, axially asymmetric) as well as of  $\gamma$  and  $\beta$  vibrational motions.

$$R = R_0 \left[ 1 + \sum_{\mu} \alpha_{\mu} Y_{2\mu}(\theta, \phi) \right] \quad (6.7)$$

where  $R_0$  is the radius of the spherical nucleus of the same volume.

The  $Y_{2\mu}$  are spherical harmonics of order 2 and the  $\alpha_{\mu}$  are expansion coefficients. It is convenient to change notations here and write the five  $\alpha_{\mu}$  in terms of three Euler angles and two variables  $\beta$  and  $\gamma$ . We set  $\alpha_1 = \alpha_{-1} = 0$ , since

these two coefficients represent only the motion of the nuclear center of mass, and write  $\alpha_0 = \beta \cos \gamma$  and  $\alpha_2 = \alpha_{-2} = \beta \sin \gamma$ . The nuclear shape is then specified in terms of  $\beta$  and  $\gamma$ .  $\beta$  represents the extent of quadrupole deformation, while  $\gamma$  gives the degree of axial asymmetry. Most nuclei are axially symmetric, or close to it, at least in their ground states. For an axially symmetric nucleus, the potential has a minimum at  $\gamma=0^\circ$ . [It is unfortunate that no single notation for deformation parameters exists.  $\beta$  is quite common, but we shall also encounter  $\varepsilon$  and  $\delta$ , especially in Chapters 7 and 8. Often, a subscript "2" is appended to explicitly denote quadrupole deformation.]

The relation between  $\beta$ ,  $\gamma$ , and the nuclear radii can be seen by evaluating the change in radius ( $R_{x,y,z} - R_0$ ) in Cartesian coordinates as a function of  $\beta$  and  $\gamma$ .

$$\delta R_z = \sqrt{\frac{5}{4\pi}} R_0 \beta \cos \gamma$$

$$\delta R_x = \sqrt{\frac{5}{4\pi}} R_0 \beta \cos \left( \gamma - \frac{2}{3}\pi \right)$$

$$\delta R_y = \sqrt{\frac{5}{4\pi}} R_0 \beta \cos \left( \gamma - \frac{4}{3}\pi \right)$$

To see the shapes implied by these expressions, Table 6.5 gives the values of these correction terms to a spherical shape for four  $\gamma$  values in units of  $\sqrt{5/4\pi} R_0 \beta$ . Values greater than zero in the table indicate an elongation in the direction concerned; those less than zero indicate a compression. Note that, for  $\gamma$  values that are a multiple of  $60^\circ$ , two  $\delta R_i$  values are always identical since the nucleus is axially symmetric for these  $\gamma$  values. For  $\gamma=0^\circ$ , the nucleus is extended in the  $z$ -direction and compressed in  $x$  and  $y$ . This is a prolate (American football) shape. Oblate (disk-like) nuclei correspond to  $\gamma=60^\circ$  and  $180^\circ$  and are compressed in the  $y$ - and  $z$ -directions, respectively, and extended in the  $xz$  and  $xy$  planes, respectively.

The essential difference between prolate and oblate shapes is that the former is extended in one direction and squeezed in two, while oblate shapes are extended in two and compressed in one. Intermediate values of  $\gamma$  ( $\gamma \neq n\pi/3$ ), such as the  $\gamma=30^\circ$  example in the table, correspond to axially asymmetric shapes, that is, to a flattening of the nucleus in one of the two directions perpendicular to the symmetry axis. Then all three radii are different.

An attempt has been made to depict several nuclear shapes in Fig. 6.10b (as well as  $\beta$  and  $\gamma$  vibrational motions to be discussed). These pictorial images,

**Table 6.5.** Changes in the radius of a quadrupole ellipsoid in the  $x$ ,  $y$ ,  $z$  directions for several  $\gamma$  values and fixed  $\beta$ .\*

	$\gamma$			
	$0^\circ$	$30^\circ$	$60^\circ$	$180^\circ$
$\delta R_z$	+1	+0.866	+1/2	-1
$\delta R_x$	-1/2	0	+1/2	+1/2
$\delta R_y$	-1/2	-0.866	-1	+1/2

\*All numbers are in units of  $\sqrt{5/4\pi} R_0 \beta$ .

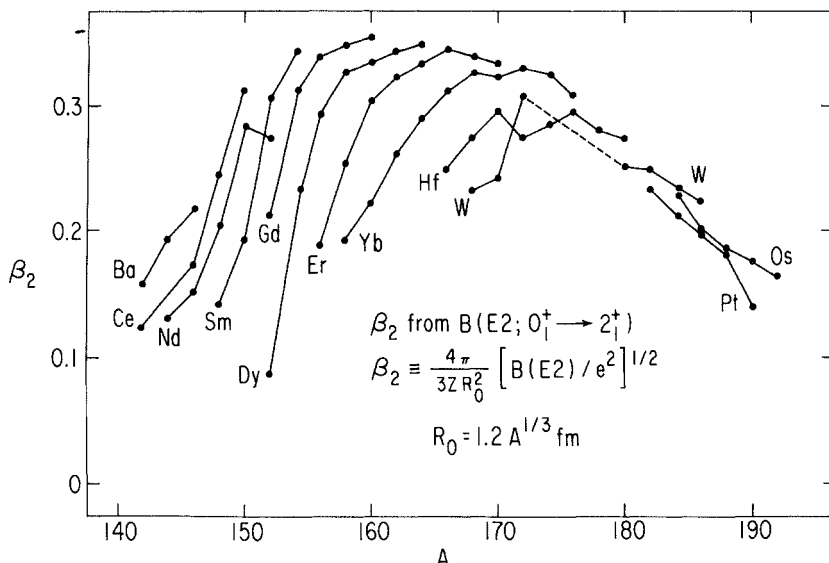


**Fig. 6.11.** Empirical systematics of quadrupole deformation parameters  $\beta$  in the rare earth region.

while crude and too classical, should be helpful to readers unfamiliar with the shapes involved.

The systematics of  $\beta$  values (effectively, quadrupole moments) for the rare earth region is shown in Fig. 6.11. The qualitative behavior is easily understood in terms of a generalization of the seniority argument of Chapter 5 (see Eq. 5.17). Early in a major shell, when softness to deformation first appears, the individual  $j$  orbits are still nearly empty; hence the quadrupole moments for the nucleons in these orbits are positive. Then a large positive  $Q(\beta)$  builds up rapidly. As the shell fills, however, the contribution of successive  $j$  shells to the total quadrupole moment decreases, vanishes, and ultimately turns negative (see Fig. 5.4). On account of these negative contributions, the summation over the individual quadrupole moments steadily decreases and may even go negative (as in Pt, not shown in Fig. 6.11) near the end of the shell.

Two important quantities for a quadrupole deformed nucleus are the moment of inertia and the quadrupole moment of the ellipsoidal shape. Both can be written in terms of  $\beta$  for axially symmetric nuclei. For an ellipsoid, the so-called rigid body moment of inertia is  $I = 2/5 M R^2$ . Integrating the radius over the nuclear surface gives (to first order in  $\beta$ )

$$I = \frac{2}{5} A M R_0^2 (1 + 0.31 \beta) \quad (6.8)$$

The intrinsic quadrupole moment is given by

$$Q_0 = \frac{3}{\sqrt{5}\pi} Z R_0^2 \beta (1 + 0.16 \beta) \quad (6.9)$$

to second order in  $\beta$ .

Note that since  $R_0 \propto A^{1/3}$ ,  $I \approx A^{5/3}$  and is a linear function of  $\beta$ .  $Q_0$  is directly proportional to  $\beta$  in leading order. For the  $\beta$  values typical of actual deformed nuclei,  $\beta \approx 0.3$ , the higher-order terms are rather small.

## 6.4 Rotations and Vibrations of Axially Symmetric Deformed Nuclei

The most obvious characteristic of nonspherical nuclei is that they can undergo rotations about an axis perpendicular to the symmetry axis. They can, of course, also vibrate and, moreover, rotations can be superimposed on vibrational motion. In order to discuss both rotational and vibrational motion, and later, their superposition and interactions, we need to specify the deformed wave functions.

These wave functions incorporate the two aspects of intrinsic excitation and rotational motion. The latter is specified in terms of the well-known rotational  $D$  matrices, the former in terms of the wave functions  $\chi_K$ . The adiabatic assumption of the separability of rotational and intrinsic motions leads to a product wave function in  $D$  and  $\chi$ . In a state  $\psi$ , in a spherical nucleus, all magnetic substates are degenerate since there can be no distinction in energy as a function of angular orientation of the motion. This, of course, is not true for deformed nuclei whose energies depend on the orientation of the wave function with respect to the symmetry axis. However, whether we consider the motion of a single nucleon in a deformed field (as we shall do when we discuss the Nilsson model in the next chapter) or the motion of some collective “wave” around the nucleus, there remains a twofold degeneracy, corresponding to clockwise and counterclockwise motions, which persists even in the deformed field. These two motions can be distinguished by the projection,  $K$ , of their angular momenta on the symmetry axis. States with projections  $K$  and  $-K$  will still be degenerate. The nuclear wave function must reflect this and thus one has the symmetrized product form for wave functions in rotational nuclei:

$$\psi_{JM} = \left( \frac{2J+1}{16\pi^2} \right)^{\frac{1}{2}} [ D_{JMK} \chi_K + (-1)^{J-K} D_{JM-K} \chi_{-K} ] \quad (6.10)$$

Note that for  $K = 0$ , only even  $J$  values are allowed, so wave function collapses to a single term

$$\psi_{JM} = \left( \frac{2J+1}{8\pi^2} \right)^{\frac{1}{2}} D_{J0} \chi_0 \quad (6.11)$$

With these wave functions in hand, we consider axially symmetric nuclei in which the rotation has equal frequencies around the  $x$  or  $y$  axes. The rotational Hamiltonian is simply

$$H = \frac{\hbar^2}{2I} \mathbf{R}^2 \quad (6.12)$$

where  $I$  is the moment of inertia and  $\mathbf{R}$  is the rotational angular momentum operator. If we assume that the ground state is  $J^\pi = 0^+$ ,  $K = 0$ , and if all the angular momentum can be ascribed to rotation (as is normally true for the low-lying, low-spin, positive parity states in deformed even–even nuclei) then the total angular momentum  $\mathbf{J} = \mathbf{R}$  and we obtain the famous symmetric top rotational energy expression

$$E_{\text{rot}}(J) = \frac{\hbar^2}{2I} J(J+1) \quad (6.13)$$

where only even  $J$  are allowed.

It is useful to comment briefly on the assumption of a  $0^+$  ground state. For spherical nuclei, we have seen that a  $\delta$ -interaction between two identical particles in a  $j$  shell produces a  $0^+$  ground state. For the case of multiparticle configurations of identical nucleons in the same  $j$  shell, the seniority  $v = 0$   $0^+$  state also emerges as the lowest energy configuration. This behavior does not result from the special character of the interaction, but is characteristic of any short-range interaction. The same result applies when one has both valence neutrons and protons. It also occurs if  $j$  is not a good quantum number, as when there is single-nucleon configuration mixing. (As we shall see, such mixing characterizes Nilsson model wave functions, which can be written as coherent sums over several  $j$  values.) The reason is that a short-range interaction favors the lowering of the  $0^+$  states in each  $j$ -configuration. The presence of many  $j$  values actually serves to further lower the  $0^+$  state because of a build up of coherence. We have already seen this coherence effect in our discussion of pairing, in which the lowering of the  $0^+$  state is related to the size of the energy gap  $\Delta$ , which in turn depends (see Eq. 5.22) on the number of partially filled orbits near the ground state and the strength parameter  $G$ . Thus the phenomenon of a  $0^+$  ground state persists in deformed even-even nuclei as well.

The symmetric top expression for rotational energies gives the values (where we abbreviate  $\hbar^2/2I$  by  $\vartheta$ ):

$$E_{2_1^+} = 6 \vartheta$$

$$E_{4_1^+} = 20 \vartheta$$

$$E_{6_1^+} = 42 \vartheta$$

and so on. Thus, the energy ratio  $E_{4_1^+}/E_{2_1^+} = 3.33$ . This simple formula is one of the most famous results of the rotational model and still remains one of the best signatures for rotational motion and deformation. We have already seen examples of nuclei that behave according to this relation in Figs. 2.10 and 2.15.

Combining Eqs. 6.8 and 6.13 gives two characteristic features of transitional and deformed nuclei. For a *given* mass region ( $A \approx \text{const}$ ),  $\hbar^2/2I$  decreases as  $\beta$  increases, leading to smaller and smaller rotational spacings as a deformed region is entered. This behavior is one of the signatures of nuclear transition regions, as we pointed out in Chapter 2 (Figs. 2.13 and 2.14). Second, since nuclear radii increase as  $A^{1/3}$ ,  $I \approx A^{5/3}$  and  $\hbar^2/2I \approx A^{-5/3}$ , for constant  $\beta$ . Rotational spacings should therefore decrease for heavier nuclei. Figure 2.10 illustrated exactly this behavior with examples taken from Zr, the rare earth, and the actinide regions.

As we stated earlier, in a geometrical picture (that is, a macroscopic one in which we do not worry explicitly about the Pauli principle), there is no reason why rotational motion cannot be superposed on intrinsic excitations, whether of collective vibrational or two-quasi-particle character. Now consider such an intrinsic excitation in a deformed nucleus.

Each intrinsic excitation carries intrinsic angular momentum  $J_o$ . It can be partially characterized by the projection of that angular momentum onto the symmetry ( $z$ ) axis. Since for axially symmetric nuclei, any rotation of the

nucleus as a whole must be about an axis perpendicular to the  $z$  axis, such rotation has vanishing projection along the  $z$  axis. Therefore, the projection of the *total* angular momentum  $J$  along the  $z$  axis, denoted  $K$ , is the same as that of the intrinsic excitation. One sometimes sees the notation  $\Omega$  for the projection of the *intrinsic* angular momentum. However, the assumption of axial symmetry is generally a good approximation and  $K$  is often used interchangeably for both the projection of the intrinsic and total angular momenta. We shall follow this simplified notation here.

When nuclear rotational motion is superimposed on an intrinsic excitation characterized by projection  $K$ , the total angular momentum can take on values  $J = K, K + 1, K + 2, \dots$ , except when  $K = 0$ , in which case only even spins  $J$  are allowed. Thus, for the *rotational* energies, relative to the "base" energy of the intrinsic excitation, Eq. 6.13 becomes

$$E_{\text{rot}}(J) = \frac{\hbar^2}{2I} [J(J+1) - K(K+1)] \quad (6.14)$$

The energy expressions, Eqs. 6.13 and 6.14, are quite accurate for low spin states in deformed nuclei, thus affirming the basic validity of the rotational concept. An example is shown in Fig. 6.12 for a typical deformed nucleus,  $^{164}\text{Er}$  (the nature of the intrinsic excitations indicated in the figure will be discussed momentarily). The energies for each band are normalized to the bandheads in order to isolate the rotational behavior. The predictions from Eq. 6.14 are reasonable, but there are also clear deviations as  $J$  increases. Also, note the changes in the inertial parameter,  $\hbar^2/2I$ , from band to band. Apparently the deformation is not completely constant.

An understanding of the physics involved in these deviations is extremely

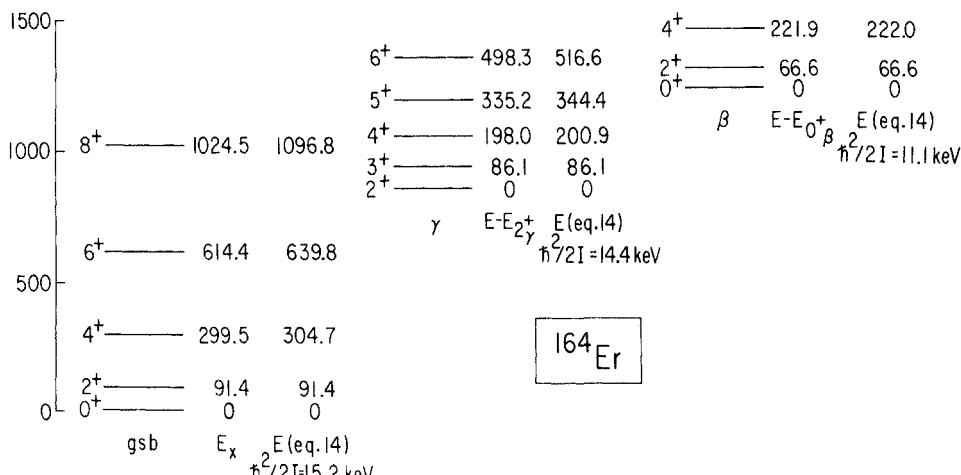


Fig. 6.12. Ground,  $\gamma$ , and  $\beta$  band levels of a typical deformed nucleus  $^{164}\text{Er}$ . For each band the symmetric top rotational energy predictions (Eq. 6.14) are shown.

simple, yet intimately connected with a number of subtle effects involving rotation-vibration coupling, bandmixing, axial asymmetry, and  $\gamma$ -softness. These concepts, and the various models emphasizing different aspects of them (e.g., the Davydov and Wilets-Jean pictures), are so interrelated that a logically ordered pedagogical treatment is difficult. We have chosen to first discuss the basic “Bohr-Mottelson” idea of an axially-symmetric, deformed nucleus susceptible to quadrupole vibrations of so-called  $\beta$  and  $\gamma$  type. This will allow us to proceed to consider their interactions with the ground state band and with each other (that is, bandmixing or rotation-vibration coupling). This, in turn, will provide us with a refinement to Eqs. 6.13 and 6.14. With this in hand, we will turn to approaches that provide closely related viewpoints. In the end, we hope that both the different starting points and the intimate relationships of these models will be clear.

We have seen that the most common distortion of spherical nuclei is quadrupole in nature. Therefore, it should not be surprising that the most common low-lying vibrational excitations in deformed nuclei are quadrupole vibrations. Clearly such modes, which carry two units of angular momentum, can be of two types with  $K = 0$  and  $K = 2$ . The former are known as  $\beta$  vibrations; since  $K = 0$ , the vibration is aligned along the symmetry axis and therefore preserves axial symmetry.

The latter, with  $K = 2$ , is called a  $\gamma$  vibration and represents a dynamic time-dependent excursion from axial symmetry. These names stem from the fact that the  $\beta$  vibration corresponds to fluctuations in the quadrupole deformation  $\beta$ , while the  $\gamma$  vibration corresponds to oscillations in  $\gamma$ . A qualitative depiction of the  $\beta$  and  $\gamma$  modes is included in Fig. 6.10. The  $\gamma$  vibration is more difficult to visualize. It may be viewed as an alternate “squashing” of an American football in two directions  $90^\circ$  to the symmetry or major axis. Note that, although the  $\gamma$  vibration involves a dynamic fluctuation in  $\gamma$  and has an average value of  $\gamma_{\text{ave}} = 0^\circ$ , the rms value of  $\gamma$  is finite and can be quite large. These two vibrational modes appear in essentially all deformed nuclei, usually around 1 MeV for  $A > 100$ . The fact that they occur well below the pairing gap,  $2\Delta \sim 1.5 - 2$  MeV, is not a violation of the concept of pairing correlations but an affirmation of the collective character of these excitations (as we shall see explicitly in Chapter 9). An example of a typical deformed nucleus with  $\beta$  and  $\gamma$  vibrations was shown in Fig. 6.12. Figure 2.17 showed the systematics of the lowest-lying intrinsic  $K = 0$  and  $K = 2$  excitations in deformed rare earth nuclei. Although it is possible that such excitations may involve components from configurations other than  $\beta$  or  $\gamma$  vibrations (such as low-lying “pairing” vibrations or two-quasi-particle excitations), it is safe to assume that nearly all the excitations included in these figures are predominantly of  $\beta$  or  $\gamma$  type.

After our discussion of the microscopic structure of  $\beta$  and  $\gamma$  vibrations in Chapter 9, we will understand the origin of these systematics. For now we simply treat these vibrations as phenomenological macroscopic shape excitations. As we have noted, each of them can have rotational motion superposed. Therefore, we can look on a level scheme such as that in Fig. 6.13 as a prototypical one for a heavy, axially symmetric (or nearly so) deformed nu-

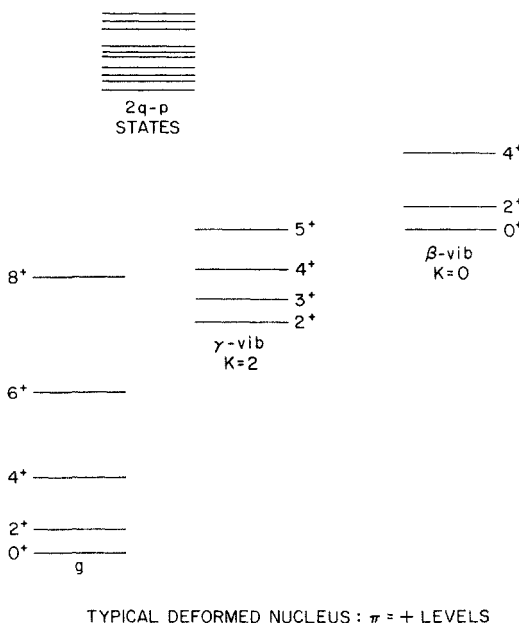


**Fig. 6.13.** Positive parity levels of a typical deformed nucleus.

cleus, with ground,  $\beta$  and  $\gamma$  excitations, and rotational bands. Two-quasi-particle excitations, each with its own rotational band, can also appear above the "pairing gap", as indicated schematically. (Negative parity (octupole) vibrations can also occur low in energy and will be briefly mentioned later.)

It is also possible to have multiphonon deformed vibrations. Since  $K$  values are projections of the angular momentum and not themselves vectors, the  $K$  values for multiple phonon excitations are obtained by simple algebraic sums and differences of the component  $K$  values. Thus, the double  $\beta$  vibration has  $K = 0$ , the  $\beta\gamma$  vibration has  $K = 2$ , and the double  $\gamma$  vibration exists in two forms with  $K = 0$  and  $K = 2$ .

In contrast to spherical vibrational nuclei where one quite frequently encounters at least some two-phonon and occasionally three-phonon levels, albeit with anharmonic distortions, *deformed* multivibrational states ( $\gamma\gamma$ ,  $\beta\beta$ , or  $\beta\gamma$ ) are the exception rather than the rule. (Extensive studies of a few deformed nuclei, such as  $^{168}\text{Er}$  and some of the Dy isotopes, have identified candidates for multiphonon vibrations, but they are probably admixed with other configurations and the data are both fragmentary and ambiguous.) One reason for the dearth of multiphonon vibrations in deformed nuclei is that, while single-phonon spherical vibrations typically occur at about 500–600 keV, placing the two-phonon states around 1.2 MeV,  $\beta$  and  $\gamma$  vibrations are typically at  $\sim 1$  MeV, which would put the two-phonon states above 2 MeV. But the energy gap  $2\Delta$  is also on the order of 2 MeV, so that there is a plethora of two-quasi-particle excitations at the same energies. This fragments the collective states and makes them harder to detect.

In addition to the experimental problem of identifying multiphonon vibrations in deformed nuclei, there is the question of the effects of the Pauli principle. This was discussed for quadrupole vibrations of spherical nuclei—the same arguments apply here, except more so. The reason is that, in spherical nuclei, a given single-particle level such as  $f_{7/2}$  can contain up to eight particles, and the Pauli principle will not play a large role if the level is less than half filled. In deformed nuclei, however, each intrinsic excitation (Nilsson orbit with given  $K$  value) is only two-fold degenerate (see Chapter 7): if the excitation is important in the one-phonon state, there will be a substantial “blocking” effect due to the Pauli principle in a two-phonon vibration. Despite extensive recent discussion, the issue of the inhibition of multiphonon excitations in deformed nuclei is not yet settled. Calculations testing the possibility of such excitations involve large bases that incorporate both quasiparticle and collective degrees of freedom and, in most cases, they are simplified by truncating the space. Different truncation schemes yield different results.

Perhaps the most telling and interesting properties of the  $\beta$  and  $\gamma$  vibrations centers on their electromagnetic decay properties. The basic E2 selection rule here is identical to, and arises from the same arguments as in the phonon case. Microscopically, the  $\beta$  and  $\gamma$  vibrations can be written as linear combinations of two-quasi-particle excitations (or, in nonpairing terminology, particle-hole excitations). Therefore, an electromagnetic transition can create or destroy at most one such vibration or phonon. A  $\beta$  or  $\gamma$  vibration can decay, therefore, by E2 radiation to the ground state band, but transitions *between*  $\gamma$  and  $\beta$  vibrational bands are forbidden since they involve the simultaneous destruction of one vibration and creation of another. For multiphonon vibrations ( $\gamma\gamma$ ,  $\beta\beta$ ,  $\beta\gamma$ ) this selection rule allows  $\gamma\gamma \rightarrow \gamma$ ,  $\beta\beta \rightarrow \beta$  and  $\beta\gamma \rightarrow \gamma$  or  $\beta$  transitions and, indeed, such transitions are among the key signatures used in searching for such excitations.

We shall see in Chapter 9 that the “collectivity” of  $\beta$  and  $\gamma$  vibrations is such that their wave functions typically involve a small handful of orbits comprising a subset of the valence particles. Since collectivity in electromagnetic transitions arises from coherence in the wave functions, we can expect that  $\gamma \rightarrow g$  or  $\beta \rightarrow g$  E2 transitions will be collective (the matrix elements will be much larger than single-particle matrix elements), but that they will be much weaker than transitions occurring *within* a given rotational band since a change in rotational structure involves the whole nucleus (or at least all of the valence nucleons).

We saw in Chapter 2 that rotational transitions in even-even deformed nuclei, typified by  $B(E2: 2_1^+ \rightarrow 0_1^+)$  values, can easily reach several hundred single-particle units. At the same time, vibrational transitions such as  $\gamma \rightarrow g$  are typically 10–30 single-particle units. As we shall see in Chapter 9, while it is relatively easy to construct  $K = 2$  two-quasi-particle states by breaking nucleon pairs and exciting one particle to an excited quasi-particle level, it is not so easy to create  $K = 0$  excitations. This normally involves the excitation of a pair of nucleons *together*. It should not be surprising that  $B(E2)$  values for  $\beta \rightarrow g$

transitions, while collective, are much weaker than  $\gamma \rightarrow g$  transitions, typically a few single-particle units. We illustrated these points in Chapter 2 (Fig. 2.18) by summarizing the transition rate data for deformed nuclei in terms of ratios of  $\gamma \rightarrow g$  and  $\beta \rightarrow g$   $B(E2)$  values to  $B(E2: 2_1^+ \rightarrow 0_1^+)$  values. One remarkable feature is the relative constancy of the  $\gamma \rightarrow g$   $B(E2)$  values. This surely points to a collective, slowly evolving structure.

To further consider  $\gamma$ -ray transitions, both within rotational bands (intra-band transitions) and between intrinsic excitations (interband transitions), we must be a bit more formal. The basic results are extremely simple to derive. Taking the wave function of Eq. 6.10 for deformed nuclei, the  $E2$  transition matrix element (up to constant factors) is:

$$\begin{aligned} \langle \psi_f | E2 | \psi_i \rangle &= \left\langle D_{JMK_f} \chi_{K_f} + (-1)^{J-K_f} D_{JM-K_f} \chi_{-K_f} \right| |E2| \\ &\quad \left. D_{JMK_i} \chi_{K_i} + (-1)^{J-K_i} D_{JM-K_i} \chi_{-K_i} \right\rangle \\ &= \left\langle D_{JMK_f} \right| |E2| \left. D_{JMK_i} \right\rangle \langle \chi_{K_f} | |E2| | \chi_{K_i} \rangle \end{aligned} \quad (6.15)$$

where we have neglected the cross terms of the form  $\langle K_f | |E2| | -K_i \rangle$ , which normally vanish by conservation of angular momentum, and have utilized the fact that the  $K_f \rightarrow K_i$  and  $-K_f \rightarrow -K_i$  matrix elements are identical. The separation of the wave function into rotational and vibrational components thus gives a separation of the matrix element into an intrinsic part (second factor on the right in Eq. 6.15) dependent only on  $\chi$  and a “rotational” part, which in turn depends only on the angular momenta involved and is proportional to the Clebsch-Gordon coefficient  $\langle J_i K_i 2 \Delta K | J_f K_f \rangle$ .

The diagonal matrix elements with  $\chi_i = \chi_f$ ,  $J_i = J_f$  give the intrinsic quadrupole moments  $Q_o$  of the excitation involved. Note that these quadrupole moments are given in the intrinsic body-fixed frame. The *observed* quadrupole moments, that is, the so-called spectroscopic quadrupole moments, involve a transformation to the laboratory frame, giving the well-known result

$$Q = Q_0 \left( \frac{3K^2 - J(J+1)}{(J+1)(2J+3)} \right) \quad (6.16)$$

The dependence on  $K$  and  $J$  reflects the fact that the *perceived* shape of a rotating nucleus is not the same as the shape in the intrinsic frame. This is easy to visualize. When a prolate deformed nucleus rotates about an axis perpendicular to the symmetry axis, the time averaged shape looks more like a disk (an oblate nucleus), which would have a quadrupole moment of the opposite sign. This effect is exacerbated for higher rotational velocities and, indeed, for  $J(J+1) > 3K^2$ , the *spectroscopic* quadrupole moment does have a sign opposite to the *intrinsic* quadrupole moment. In fact, for  $K = 0$  this is always the case. Note that for  $J = 0$  (which implies  $K = 0$  since  $K \leq J$ ),  $Q = 0$ : a state of zero angular momentum can have no preferred direction of the time averaged distribution in space and therefore no quadrupole moment.

For the important case of matrix elements diagonal in  $\chi$  but not in  $J$  (or transitions *within* a band), we have nearly the same result except for a Clebsch-Gordon coefficient connecting  $J_i$  and  $J_f$ . Thus

$$B(E2:J_i \rightarrow J_f) = \frac{5}{16\pi} e^2 Q_0^2 \langle J_i 0 2 0 | J_f 0 \rangle^2 \quad (6.17)$$

For  $0_1^+ \rightarrow 2_1^+$  transitions this gives

$$B(E2:0_1^+ \rightarrow 2_1^+) = \frac{5}{16\pi} e^2 Q_0^2 \quad (6.18)$$

Since the intrinsic quadrupole moment  $Q_o \propto \beta(1 + 0.16\beta)$ ,  $B(E2:0_1^+ \rightarrow 2_1^+) \sim \beta^2$ . The large  $\beta$  values (of about 0.3) that characterize deformed nuclei can lead to a one to two order of magnitude increases in this  $B(E2)$  value above that of near spherical nuclei ( $\beta \sim 0.05$ ). This explains the systematics we showed in Fig. 2.16, which provides the most obvious evidence of deformed collective behavior in nuclei.

Frequently one can extract very sensitive and critical information on structure effects and rotation-vibration interactions from  $B(E2)$  values for a pair of transitions connecting the same two intrinsic states. These transitions can be either both intraband or both interband with the same initial and final bands. Then the *intrinsic* matrix element will clearly be identical for both transitions and will cancel in their ratio. Such branching ratios depend only on the squares of Clebsch-Gordon coefficients, and are therefore model independent in the sense that they do not depend on the microscopic structure of the excitations involved. They depend on the assumption of the separability of rotational and vibrational motions. They are known as Alaga rules.

Specifically, we have

$$\frac{B(E2:J_i \rightarrow J_f)}{B(E2:J_i \rightarrow J'_f)} = \frac{\langle J_i K_i 2 \Delta K | J_f K_f \rangle^2}{\langle J_i K_i 2 \Delta K | J'_f K_f \rangle^2} \quad (6.19)$$

Note that, since the intrinsic structure has canceled out in such ratios, they are equally valid for transitions involving any intrinsic states (e.g., two-quasi-particle states) as well as for those involving vibrational excitations.

As examples of these ratios, we have

$$\frac{B(E2:2_\gamma^+ \rightarrow 0_g^+)}{B(E2:2_\gamma^+ \rightarrow 2_g^+)} = 0.7 \quad (6.20)$$

$$\frac{B(E2:2_\gamma^+ \rightarrow 4_g^+)}{B(E2:2_\gamma^+ \rightarrow 2_g^+)} = 0.05 \quad (6.21)$$

Equally simple but numerically different results are obtained for other transitions. There are two important uses of such ratios. First, since they depend on the  $K$  values of the initial and final states, they can sometimes be empirically used to assign  $K$  quantum numbers to different intrinsic excitations. Secondly, as we shall see momentarily, small admixtures of different intrinsic excitations (bandmixing effects) can induce enormous changes in these branching ratios, so the empirical ratios can provide very sensitive tests of small details of the nuclear wave functions.

It is easy to look up or calculate values of the Clebsch-Gordon coefficients

**Table 6.6.** Some useful Alaga rules for E2 transitions in deformed nuclei\*

$J_i$	$J_f$	$\langle J_i K_i \Delta K   J_f K_f \rangle$			
		$K_i \rightarrow K_f$			
		$0 \rightarrow 0$	$2 \rightarrow 0$	$0 \rightarrow 2$	$2 \rightarrow 2$
0	2	1.0	—	1.0	—
2	0	0.200	0.200	—	—
	2	0.286	0.286	0.286	0.286
	3	—	—	0.500	0.500
	4	0.515	0.014	0.215	0.215
	5	—	—	—	—
3	2	—	0.358	—	0.358
	3	—	—	—	0
	4	—	0.143	—	0.343
	5	—	—	—	0.300
	6	0.455	0.031	0.142	0.340
4	2	0.286	0.120	0.008	0.120
	3	—	—	0.112	0.267
	4	0.260	0.351	0.351	0.042
	5	—	—	0.389	0.234
	6	0.455	0.031	0.142	0.340
5	3	—	—	—	0.191
	4	—	0.319	—	0.191
	5	—	—	—	0.093
	6	—	0.182	—	0.167
	7	—	—	—	0.360
6	4	0.315	0.098	0.021	0.235
	5	—	—	0.154	0.141
	6	0.255	0.364	0.364	0.130
	7	—	—	0.347	0.124
	8	0.431	0.039	0.116	0.371

\*The entries are the squares of the Clebsch-Gordon coefficients for each indicated transition. Thus, relative  $B(E2)$  values connecting states  $J_i, J_f$  in bands with  $K_i, K_f$  are  $B(E2 | J_i K_i \rightarrow J_f K_f |) \propto \langle J_i K_i | \Delta K | J_f K_f \rangle^2$ .

involved in these branching ratios. However, transitions involving  $K = 0$  and  $K = 2$  bands are so important and so common that it is useful to collect the results here. Table 6.6 shows the relative  $B(E2)$  values for transitions involving low-spin states in  $K = 0$  and  $K = 2$  bands.

It is interesting to compare them with the data for deformed nuclei. To this end, we show comparisons for three nuclei in Table 6.7, of which one,  $^{154}\text{Sm}$ , is situated at the beginning of the deformed region while the other two,  $^{168}\text{Er}$  and  $^{178}\text{Hf}$ , are near midshell. The table shows a number of very interesting features:

1. The general agreement is remarkably good, indicating that these simple expressions are a reasonable leading-order approximation. Despite the deviations to be discussed at considerable length next, it is important to stress that the approximate validity of the Alaga rules is one of the strongest arguments for axially deformed nuclei and for the concept of separable rotational motion. Nevertheless, there are substantial devia-

**Table 6.7.** Comparison of some relative  $B(E2: \gamma \rightarrow g)$  values in deformed rare earth nuclei with the Alaga rules\*

$J_i$	$J_f$	Alaga	Relative $B(E2: J_i J_f)$		
			$^{154}\text{Gd}$	$^{168}\text{Er}$	$^{178}\text{Hf}$
2	0	70	43	54	88
	2	100	100	100	100
	4	5	14	6.8	5.8
3	2	100	100	100	100
	4	40	105	65	52
4	2	34	16	20	18
	4	100	100	100	100
	6	9	—	14	—
5	4	100	—	100	100
	6	57	—	123	107
6	4	27	—	12	18
	6	100	—	100	100
	8	11	—	37	—

\*One transition is normalized to 100 for each initial state. The Alaga rule entries are relative values from Table 6.6 for the  $K = 2 \rightarrow K = 0$  case.

tions from them and their study greatly deepens our understanding of deformed nuclei.

2. The deviations increase substantially with increasing spin.
3. Transitions in which the spin increases ( $J_f > J_i$ ) are nearly always empirically larger than the Alaga rules, while spin decreasing transitions ( $J_f < J_i$ ) are nearly always smaller.
4. The deviations can become quite large, leading to factors of three or four discrepancies from the predictions.
5. The deviations are, on average, larger in Sm than in Er and larger in Er than in Hf.

Combined with all the evidence from rotational energy sequences, measurements of quadrupole moments, and the like, point 1 provides a vast body of evidence that supports the idea of a superposition of rotational and intrinsic motion and the approximate separability of the two. Point 5 suggests that this separability is most applicable in midshell and least just after the transition regions from spherical to deformed nuclei. This is reasonable, of course, since the energy scale of rotational motion decreases systematically toward midshell, and therefore, the distinction in energy between rotational and vibrational behavior is larger there than closer to the vibrational regions at the beginning and end of major shells. We shall soon see more dramatic evidence of this point shortly in terms of a systematic measure of the rotation-vibration coupling. First, however, in order to understand points 2, 3, and 4, and in particular why point 4 does not indicate a serious breakdown of the rotational description, we must introduce the concept of bandmixing and discuss a quantitative formalism to treat it in a simple way.

## Bandmixing and Rotation-Vibration Coupling

Bandmixing is a widespread phenomenon in even-even nuclei. We shall limit our discussion to its simplest and most common manifestations, namely  $\Delta K = 2$  mixing between the  $\gamma$  and the ground bands and  $\Delta K = 0$  mixing between  $\beta$  and ground bands. This is not to minimize the importance of  $\beta-\gamma$  mixing or the mixing of two-quasi-particle intrinsic excitations with vibrational states: the same physical concepts and formalism also apply to such cases but the extent and systematic behavior of  $\gamma-g$  mixing makes it the most interesting and informative to study. The basic scheme is simply an example of two-state mixing. For  $\gamma-g$  mixing, the ground and  $\gamma$  band wave functions can be written as

$$\begin{aligned}\psi_g &= \phi_g + \varepsilon'_{\gamma}(J) \phi_{\gamma} \\ \psi_{\gamma} &= \varepsilon'_{\gamma}(J) \phi_g + \phi_{\gamma}\end{aligned}\quad (6.22)$$

where  $\varepsilon'$  is the *small* mixing amplitude of each band in the other. It is convenient to separate the spin dependent and spin independent parts of the mixing by writing

$$\varepsilon'_{\gamma} = \sqrt{2} \varepsilon_{\gamma} f_{\gamma}(J) \quad (6.23)$$

In order to derive the spin dependence, we need to anticipate a result from Chapter 8 on Coriolis mixing in the Nilsson model. Coriolis mixing is a well-known effect in any rotating system and arises from the transition from a body-fixed (nuclear) frame of reference to the laboratory. We will show in Chapter 8 that the Coriolis effect in nuclei mixes intrinsic states differing by  $\Delta K = \pm 1$ . The dependence of the Coriolis mixing matrix element on the total angular momentum  $J$  is contained in the mixing operator  $J_+$ , given by (see Eq. 8.2)

$$\langle K | J_+ | K+1 \rangle = \sqrt{(J-K)(J+K+1)} \quad (6.24)$$

where  $K$  is the lower  $K$  value. We now interpret  $\gamma \rightarrow g$  mixing as proceeding via a two-step Coriolis effect through an intermediate  $K=1$  band (which need not, and generally is not, known empirically). For weak mixing, this can be viewed as a sequence of two separate two-step mixing effects.

We know from the discussion in Chapter 1 of weak two-state mixing that if three states  $\phi_1, \phi_2, \phi_3$  mutually mix, the mixing of states  $\phi_2$  and  $\phi_3$  gives

$$\phi'_2 = \alpha \phi_2 + \beta_{23} \phi_3$$

Then, if the already mixed state  $\phi'_2$  mixes with state  $\phi_1$ , we have

$$\begin{aligned}\psi_1 &= \alpha_1 \phi_1 + \beta_{12} \phi'_2 \\ &= \alpha_1 \phi_1 + \beta_{12} \alpha \phi_2 + \beta_{12} \beta_{23} \phi_3\end{aligned}$$

or, since  $\alpha$  and  $\alpha_1 \sim 1$ ,

$$\psi_1 = \phi_1 + \beta_{12} \phi_2 + \beta_{12} \beta_{23} \phi_3$$

Thus, the overall mixing amplitude of state  $\phi_3$  in state  $\phi_1$  is simply given by the product of the individual two-state mixing amplitudes  $\beta_{12}$  and  $\beta_{23}$ .

Applying this to the present case, we have the mixing sequence  $(K=0) \rightarrow (K=1) \rightarrow (K=2)$ . Hence the spin dependence of the  $\Delta K=2$  mixing amplitude,  $f_\gamma(J)$  is

$$\begin{aligned} f_\gamma(J) &= \sqrt{J(J+1)} \sqrt{(J-1)(J+2)} \\ &= \sqrt{(J-1)J(J+1)(J+2)} \end{aligned} \quad (6.25)$$

Similarly, for mixing between the  $\beta$  ( $K=0$ ) and ground bands, the mixing sequence is  $(K=0) \rightarrow (K=1) \rightarrow (K=0)$ . Then  $f_\beta(J)$  is given by

$$f_\beta(J) = J(J+1) \quad (6.26)$$

Note that both  $f_\beta(J)$  and  $f_\gamma(J) \rightarrow J^2$  for large  $J$ : the band mixing increases rapidly for high spin.

The spin dependence of  $\epsilon'$  explains point 2 concerning the increase of the deviations from the Alaga rules with increasing spin. However, we have yet to explain why these deviations can be so large without implying a corresponding destruction of the entire rotational picture on which the Alaga rules and the present formalism are based.

We can now calculate the interband E2 matrix elements very simply using the admixed wave functions of Eq. 6.22.

$$\langle \psi_g || E2 || \psi_\gamma \rangle = \langle \phi_g || E2 || \phi_\gamma \rangle + \epsilon'_\gamma [\langle \phi_\gamma || E2 || \phi_\gamma \rangle - \langle \phi_g || E2 || \phi_g \rangle] \quad (6.27)$$

The first term in Eq. 6.27 is the direct matrix element in the absence of mixing. Thus, the perturbed matrix element can be written as a sum of a direct term plus a contribution proportional to  $\epsilon'_\gamma$ . In deriving this expression we have dropped terms in  $\epsilon'^2$  since the mixing is assumed to be small. Each of the two terms multiplying  $\epsilon'_\gamma$  is proportional to a Clebsch-Gordon coefficient multiplied by the intrinsic quadrupole moment of the  $\gamma$  or ground band. Therefore, even if we assume these intrinsic moments to be equal (as is commonly done since the deformation does not differ much from band to band), the  $K$  dependence of the Clebsch-Gordon coefficients prevents this term from vanishing.

In the case of  $\beta \rightarrow g$  mixing, exactly the same formalism applies with a substitution of  $f_\beta$  for  $f_\gamma$ . One interesting result for the special case of transitions that do not change spin ( $J_\beta = J_g$ ) follows immediately. For identical quadrupole moments, the two terms multiplying  $\epsilon'_\beta$  are identical and vanish: The  $\beta \rightarrow g$  bandmixing has no effect on transitions which do not change the spin. This is a special case of the result derived in Eq. 1.17.

Incorporating the spin dependence of  $\epsilon'$  and expressions for the Clebsch-Gordon coefficients in Eq 6.27 leads to a general form for the effect of band-mixing on interband B(E2) values. We obtain in this way the well-known expressions:

$$B(E2: J_\gamma \rightarrow J_g) = B_0(E2) [1 + Z_\gamma F_\gamma(J_\gamma, J_g)] \quad (6.28)$$

$$B(E2: J_\beta \rightarrow J_g) = B_0(E2) [1 + Z_\beta F_\beta(J_\beta, J_g)] \quad (6.29)$$

**Table 6.8.** Correction factors  $F_\gamma(J_i, J_f)$  and  $F_\beta(J_i, J_f)$  for  $\gamma \rightarrow g$  and  $\beta \rightarrow g$  reduced E2 matrix elements due to  $\gamma-g$  and  $\beta-g$  bandmixing

$J_i$	$J_f$	Correction factor	
		$\gamma \rightarrow g$	$\beta \rightarrow g$
$J_f - 2$	$J_f$	$1 + (2J_f + 1)Z_\gamma$	$1 + 2(2J_f - 1)Z_\beta$
$J_f - 1$	$J_f$	$1 + (J_f + 2)Z_\gamma$	—
$J_f$	$J_f$	$1 + 2Z_\gamma$	1
$J_f + 1$	$J_f$	$1 - (J_f - 1)Z_\gamma$	—
$J_f + 2$	$J_f$	$1 - (2J_f + 1)Z_\gamma$	$1 - 2(2J_f + 3)Z_\beta$

\*Riedinger, 1969.

Here  $B_0(E2)$  is the unperturbed value and  $Z_\gamma$  and  $Z_\beta$  are bandmixing parameters proportional  $\epsilon_\gamma$  and  $\epsilon_\beta$ , respectively. The functions  $F_\gamma(J_\gamma, J_g)$  and  $F_\beta(J_\beta, J_g)$  are given in Table 6.8 for the three possible cases of  $\Delta J = 0, \pm 1, \pm 2$ . Clearly the case  $\Delta J = \pm 1$  does not apply to the  $\beta \rightarrow g$  transitions, and the result obtained earlier for  $\Delta J = 0$ ,  $\beta \rightarrow g$  transitions is reflected by the value of unity for  $F_\beta(J_\beta = J_g)$ .

One can analyze experimental data in terms of this formalism in several different ways. One is to extract a  $Z_\gamma$  value from each branching ratio between a pair of bands and then test for a consistent value. An example of this is shown in Table 6.9, where the  $Z_\gamma$  values for  $^{152}\text{Sm}$  are given. Clearly in this case,  $Z_\gamma \sim 0.078$  provides good agreement with the data.

Another approach exploits a particularly useful form of Eq. 6.27. We will give it in a form that is applicable to both  $\beta \rightarrow g$  and  $\gamma \rightarrow g$  transitions by combining the spin dependence of the  $f_\beta$  or  $f_\gamma$  functions with that of the Clebsch-Gordon coefficients. We obtain

$$B(E2: J_i \rightarrow J_f) = 2 \langle J_i K_i | J_f 0 \rangle^2 [M_1 - M_2 (J_f(J_f+1) - J_i(J_i+1))]^2 \quad (6.30)$$

For  $\gamma \rightarrow g$  transitions  $M_1$  and  $M_2$  are defined by

**Table 6.9.**  $Z_\gamma$  values for  $^{152}\text{Sm}^*$ 

Branching Ratios	Experiment	Alaga	$Z_\gamma$ ( $\times 10^2$ )
$\frac{4\gamma}{4\gamma} \rightarrow 4g$	11.2(19)	2.94	8.1(8)
$\frac{4\gamma}{4\gamma} \rightarrow 2g$			
$\frac{3\gamma}{3\gamma} \rightarrow 4g$	1.00(5)	4	7.7(5)
$\frac{3\gamma}{3\gamma} \rightarrow 2g$			
$\frac{2\gamma}{2\gamma} \rightarrow 2g$	10.0(14)	20	6.7(18)
$\frac{2\gamma}{2\gamma} \rightarrow 4g$			
$\frac{2\gamma}{2\gamma} \rightarrow 2g$	2.38(18)	1.43	8.8(14)
$\frac{2\gamma}{2\gamma} \rightarrow 0g$			
$\frac{2\gamma}{2\gamma} \rightarrow 0g$	4.16(61)	14.0	7.6(1.1)
$\frac{2\gamma}{2\gamma} \rightarrow 4g$			

\*Errors given on last digit. Riedinger, 1969.

$$M_1 = \langle \phi_\gamma | M(E2) | \phi_g \rangle - 4M_2$$

$$M_2 = \left( \frac{15}{8\pi} \right)^{\frac{1}{2}} Q_0 \epsilon_\gamma \quad (6.31)$$

and are related to  $Z_\gamma$  by

$$Z_\gamma = -\frac{2M_2}{(M_1 + 4M_2)} = -\frac{2M_2}{\langle \phi_\gamma | M(E2) | \phi_g \rangle}$$

$$= \left( \frac{15}{2\pi} \right)^{\frac{1}{2}} \frac{Q_0 \epsilon_\gamma}{\langle \phi_\gamma | M(E2) | \phi_g \rangle}$$

For  $\beta \rightarrow \gamma$  transitions,  $M_1 = \langle \phi_\beta | M(E2) | \phi_\gamma \rangle$  and  $M_2 = (5/16\pi)^{1/2} Q_0 \epsilon_\gamma$ .

Thus,  $M_1$  is essentially the direct intrinsic  $\Delta K = 2$  matrix element (the correction term,  $-4M_2$  for  $\gamma - g$  mixing, is normally very small) and  $M_2$  is proportional to the spin independent mixing amplitude  $\epsilon_\gamma$ . The advantage of this form of Eq. 6.30 is that it can be rewritten as (taking the  $\gamma \rightarrow g$  case to be specific)

$$\frac{\sqrt{B(E2; J_\gamma \rightarrow J_g)}}{\sqrt{2} \langle J_\gamma 22^- | J_g 0 \rangle} = M_1 - M_2 [J_g(J_g+1) - J_\gamma(J_\gamma+1)] \quad (6.32)$$

A plot of the left side against the spin function on the right is a straight line with intercept  $M_1$  at  $J_\gamma = J_g$  and slope  $M_2$ . From such a plot, called a *Mikhailov plot*, one can extract directly from the empirical results both the direct *intrinsic unperturbed  $\Delta K = 2$  matrix element* and the *mixing amplitude*  $\epsilon_\gamma (\propto M_2)$ , provided the data can be fit by a straight line. Deviations from a straight line can arise from several sources: unequal quadrupole moments of the bands, more than two-bandmixing, undetected M1 components in the interband transitions, or two-bandmixing that follows a different spin dependence than that given by the  $f_\rho(J)$  and  $f_\gamma(J)$  functions.

An example of a Mikhailov plot, for  $^{168}\text{Er}$ , is shown in Fig. 6.14 (the dashed line labeled IBA will be discussed later). It is clear that the data points are very well approximated by a straight line, thus validating the use of the Mikhailov formalism. Such data are typical of deformed nuclei.

The use of the bandmixing formalism in either the  $Z_\gamma$  or Mikhailov forms is a powerful tool for analyzing deviations of relative E2 transitions from the rotational (Alaga) values and for studying rotation-vibration interactions. Empirically, it is invariably found that  $M_2 \ll M_1$  and negative (by convention,  $M_1$  is positive): therefore  $Z_\gamma$  is positive. In this way,  $Z_\gamma$  values have been extracted for a number of rare earth nuclei. The results are summarized in Fig. 6.15.

These systematics exhibit a parabolic behavior that minimizes at midshell. This smooth pattern highlights, indirectly, the collective structure of the unperturbed states involved: if the mixing were with single-particle excitations, it would surely be more erratic. As we shall see in Chapter 9, however, the microscopic structure of collective vibrations changes smoothly and slowly with  $N$  and  $Z$ . The minimum in  $Z_\gamma$  at midshell, and the generally small values

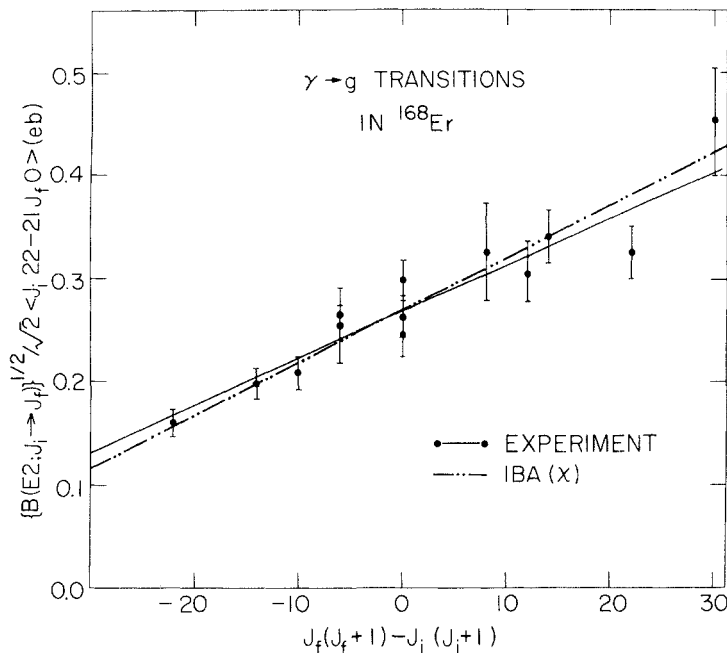


Fig. 6.14. Mikhailov plot for  $\gamma \rightarrow g$  transitions in  $^{168}\text{Er}$  (Warner, 1982).

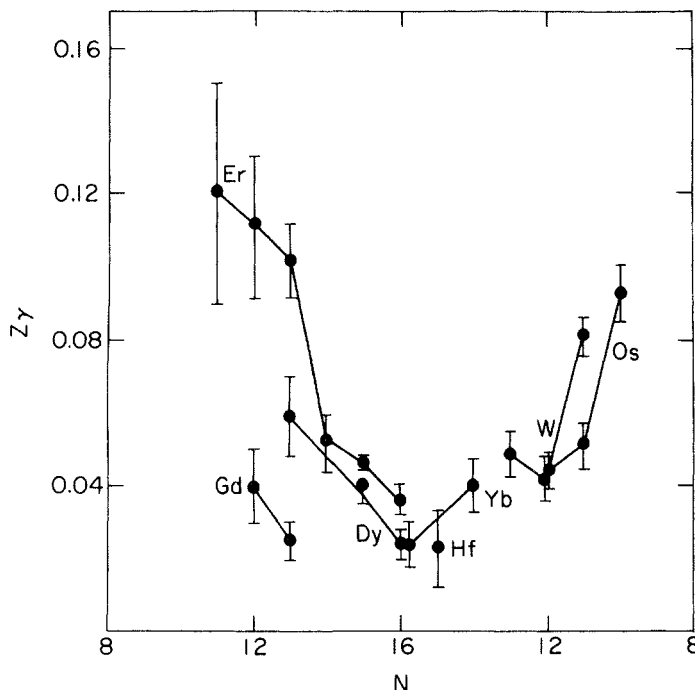


Fig. 6.15. Empirical systematics of  $Z_\gamma$  in the rare earth region (Casten, 1983).  $N$  is half the number of valence nucleons.

of  $Z_\gamma$ , demonstrate the overall validity of the separation of rotational and vibrational degrees of freedom and show that, as expected, this separability is best at midshell.

With this bandmixing formalism and the empirical results in hand, we can now address points 2, 3 and 4 mentioned earlier. First of all, Eq. 6.32 shows that, regardless of the sign of  $M_2$ , the effect of bandmixing (on  $\Delta J \neq 0$  transitions at least) must increase with increasing spin as we anticipated earlier from the spin dependence of the mixing amplitudes  $\epsilon_\gamma$  and  $\epsilon_g$ . Second, the negative values of  $M_2$ , that is, the positive slopes in a Mikhailov plot, and the fact that the abscissa is positive for  $J_f > J_i$ , implies that the B(E2) values are *increased* for *spin-increasing* transitions and *decreased* for *spin-decreasing* transitions, as we observed in the examples given in Table 6.7.

This point is also clear from inspection of the analytic formulas in Table 6.8. Since  $M_2$  has the opposite sign to  $Z_\gamma$ , the data in Figs. 6.14 and similar data for other deformed regions show that  $Z_\gamma$  is always positive. Then, we see from Table 6.8 that, for *spin increasing* transitions, the B(E2) correction factor always has the form

$$[1+g(J)Z_\gamma]^2 \quad (\text{spin increasing}) \quad (6.33)$$

while for *spin decreasing* transitions, we have

$$[1-h(J)Z_\gamma]^2 \quad (\text{spin decreasing}) \quad (6.33)$$

where  $g(J)$  and  $h(J)$  are positive functions of the final spin  $J$ .

It is worth working through an explicit example to see how the bandmixing technique is used. We take the case of  $\gamma$ -ground mixing in  $^{168}\text{Er}$  and use both the analytic approach with Table 6.8 and the Mikhailov formalism.

According to Tables 6.6 and 6.8,

$$\frac{B(\text{E}2:2\gamma^+ \rightarrow 2_1^+)}{B(\text{E}2:2\gamma^+ \rightarrow 0_1^+)} = 1.43 \left[ \frac{(1+2Z_\gamma)}{(1-Z_\gamma)} \right]^{\frac{1}{2}} \quad (6.34)$$

where the first factor is the unperturbed (Alaga) ratio. From the experimental value of 1.85, we obtain  $Z_\gamma = 0.044$ . Similar values are obtained from other transitions. A good average value is  $Z_\gamma \sim 0.038$ . The small magnitude of  $Z_\gamma$  confirms the adequacy of the two-state bandmixing approach.

Turning to the Mikhailov approach, which generally is easier and yields interesting physics more directly, Fig. 6.14 gives

$$M_1 = 0.268 \text{ eb} \quad M_2 = -0.0045 \text{ eb}$$

Thus, we can immediately deduce the direct, unperturbed  $\gamma \rightarrow g$  E2 matrix element

$$\langle \phi_\gamma | E2 | \phi_g \rangle = 0.250 \text{ eb}$$

Using  $Q_0 = 7.61$  eb, the spin independent part of the mixing amplitude is

$$\epsilon_\gamma = \left( \frac{8\pi}{15} \right)^{\frac{1}{2}} \frac{M_2}{Q_0} = -0.00077 \quad (6.35)$$

The full mixing amplitudes  $\epsilon'_\gamma(J) = \sqrt{2} \epsilon_\gamma f_\gamma(J)$  are then  $-0.0053$  ( $2^+$ ),  $-0.012$  ( $3^+$ ), and  $-0.021$  ( $4^+$ ).

We can now calculate the actual mixing matrix element since for such small mixing we have, from Eq. 1.10

$$\epsilon_\gamma(J) \sim \frac{\langle \phi_\gamma(J) | V_{\Delta K=2} | \phi_g(J) \rangle}{[E_\gamma(J) - E_g(J)]_{\text{unp}}} \quad (6.36)$$

Neglecting the tiny difference between perturbed and unperturbed spacings, and taking  $E_{2\gamma^+} - E_{2g^-} = 741$  keV we get

$$\langle \phi_\gamma(2^+) | V_{\Delta K=2} | \phi_g(2^+) \rangle = \epsilon_\gamma(741 \text{ keV}) = 3.9 \text{ keV}$$

In a way, it is remarkable how much detailed information, including a mixing amplitude, an interaction matrix element, and even an absolute unperturbed transition matrix element, can be obtained in this simple way and only from the measurement of *relative* interband B(E2) values, without measuring absolute transition rates.

Finally, we now see that the rather large changes in the interband B(E2) values result from extremely small residual interactions, on the order of a few keV, and mixing amplitudes  $\sim 10^{-2}$ – $10^{-3}$ . Returning to our earlier point 4, we see that the rotational description of the wave functions is still an excellent approximation although certain observables deviate substantially from their rotational predictions. Later we shall see other cases, such as Coriolis mixing, where small disturbances of pure wave functions grossly affect certain observables and, conversely, where the measurement of those observables provides very sensitive probes of specific wave function components.

The fundamental reason that small interactions such as the one we are considering can lead to such large effects is obvious from Eq. 6.27: the mixing introduces an effectively *intraband* contribution to the originally *interband* transition. The  $4_\gamma^+ \rightarrow 2_g^+$  transition, for example, contains small amplitudes for the very large  $4_\gamma^+ \rightarrow 2_g^+$  and  $4_\gamma^+ \rightarrow 2_g^+$  *rotational* matrix elements. From this, we can immediately appreciate the well-known empirical fact that contrary to *interband* transitions, *intraband* transitions are virtually unaffected by band-mixing because the effect is reversed, namely, adding a small *interband* amplitude to a much larger *intraband* amplitude.

By formalizing this argument we can deduce some interesting results. We consider the set of bands shown in Fig. 6.16, where we illustrate states of spin  $J, J+1, J+2$  occurring somewhere in these bands. We do not restrict ourselves to small mixing. First, let us isolate the two-band system of intrinsic states 1 and 2 and actually calculate the relevant B(E2) value for the transition between states of spin  $J'$  and  $J$ . If the mixing is large, we might expect transitions *between* bands to be comparable to those *within* a band. However, we shall see that under one rather reasonable assumption, this is not the case.

We explicitly write the B(E2) value, using an obvious notation for the initial and final wave functions analogous to the notation in Eq. 1.7 except that it distinguishes amplitudes  $\alpha, \alpha', \beta, \beta'$  for the spins  $J$  and  $J'$ . We have, for an *intraband* transition in band 2,

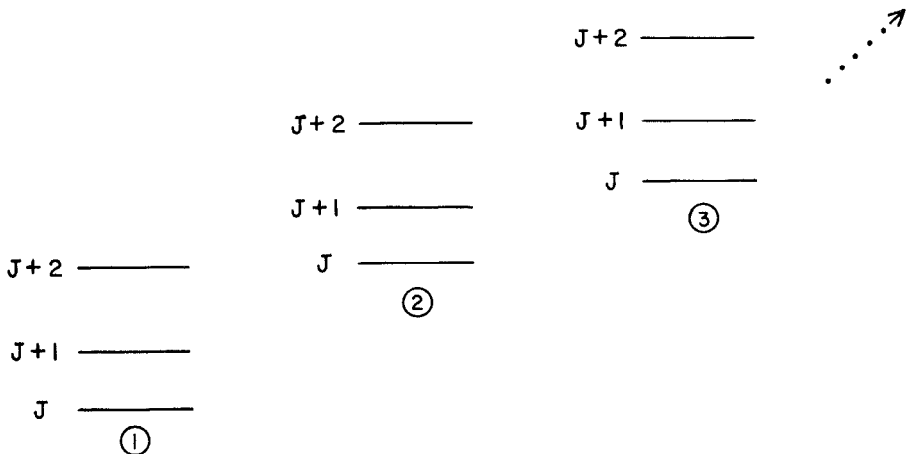


**Fig. 6.16.** Set of admixed bands (see text).

$$\begin{aligned}
 B(E2: (J' \rightarrow J)_2) &= \frac{1}{2J'_2 + 1} [\langle (\alpha' \phi_1 + \beta' \phi_2)_J | E2 | (\alpha \phi_1 + \beta \phi_2)_J \rangle]^2 \\
 &= \frac{1}{2J'_2 + 1} [\alpha \alpha' \langle \phi_1(J') | E2 | \phi_1(J) \rangle + \beta \beta' \langle \phi_2(J') | E2 | \phi_2(J) \rangle \\
 &\quad + \alpha' \beta \langle \phi_1(J') | E2 | \phi_2(J) \rangle + \alpha \beta' \langle \phi_2(J') | E2 | \phi_1(J) \rangle]^2
 \end{aligned}$$

But, here, the interband matrix elements connecting unperturbed states in bands 1 and 2 are negligible compared to the intraband rotational matrix elements. We assume for simplicity that the intrinsic matrix elements are band independent and obtain

$$B(E2: (J' \rightarrow J)_2) \sim \frac{1}{2J'_2 + 1} [(\alpha \alpha' + \beta \beta') \langle \phi_1(J') | E2 | \phi_1(J) \rangle]^2 \quad (6.37)$$

If we now assume that the mixing interaction, though possibly large, is not very spin dependent, then the composition of the mixed wave functions will also not depend much on spin and therefore,  $\alpha \sim \alpha'$  and  $\beta \sim \beta'$ . But, then, the factor  $(\alpha \alpha' + \beta \beta') \sim 1$  by orthonormality and the intraband transition has an identical  $B(E2)$  value as in the unmixed case.

Extending this argument to multiband mixing, the factor  $(\alpha \alpha' + \beta \beta')$  in Eq. 6.37 will simply be replaced by  $(\alpha \alpha' + \beta \beta' + \gamma \gamma' + \delta \delta' + \dots)$ . If, again, the primed and unprimed mixing amplitudes are approximately equal, this is just the orthogonality sum, which is unity. (For *interband* transitions, the amplitude sum is  $(\alpha_1 \alpha'_2 + \beta_1 \beta'_2 + \dots)$ , and in this case nearly vanishes by the same orthogonality argument.) Thus we see that, although the mixing is large, *intraband* transitions are barely affected and retain their normal rotational strengths.

This has many repercussions, two of which are worth citing briefly. It

means, for example, as we argued already, that Alaga rules for *intraband* transitions are essentially unaffected by mixing. Thus, observed deviations from the Alaga rules can be ascribed to other mechanisms (e.g., M1 components) and can be used to estimate these. Second, consider heavy ion reactions that bring large amounts of angular momentum into the nucleus, which then decays by a series of cascade transitions (see Chapter 10). It has been observed that these cascades flow through many rotational bands, but that the population within a band tends to remain intact as  $J$  decreases, even though these relatively high-lying quasi-particle excitations are expected to mix considerably. The preceding derivation provides a simple explanation: the mixing can indeed be strong, but as long as it does not change rapidly with  $J$ , the *intraband* transitions are only slightly affected and remain dominant.

In closing this section, we note that extensions of the formalism to include  $\beta - \gamma$  mixing have also been developed and are available in the literature. One point that will be useful in our later discussion of the IBA can be deduced immediately without a formal development of the mixing expressions. The effects of  $\beta - \gamma$  bandmixing on  $\beta \rightarrow g$  and  $\gamma \rightarrow g$  transitions are second order and generally weak; however, since  $\beta \rightarrow \gamma$  transitions are forbidden in the absence of mixing, such mixing can strongly break this fundamental selection rule. The expression for  $\beta \rightarrow \gamma$  transitions in the presence of  $\beta - \gamma$  mixing is analogous to those we generated for the  $\beta \rightarrow g$  and  $\gamma \rightarrow g$  cases, except that there is no longer a direct term and hence the *entire* transition strength arises *solely* from a mixing term proportional to  $Z_{\beta\gamma}$ . Thus, in *ratios* of  $\beta \rightarrow \gamma$  transitions,  $Z_{\beta\gamma}$  cancels out. Therefore, although the finite transition matrix elements arise from mixing, *branching ratios* are *independent* of the strength of that mixing and are given only by ratios of functions of  $J_\beta$  and  $J_\gamma$ . We note for future reference that in the IBA model,  $\beta \rightarrow \gamma$  transitions are, in contrast, allowed for deformed nuclei but their branching ratios depend on the detailed structure (in effect on the value of the asymmetry parameter  $\gamma$ ). We will discuss this further later in this chapter.

Having discussed the low-lying, intrinsic excitations of axially symmetric nuclei, we can return to the question of rotational energies and corrections to the simple first-order expressions in Eqs. 6.13 and 6.14. It was useful to discuss these intrinsic excitations, in particular, the bandmixing between them, first, because the corrections to the symmetric top formula are intimately connected with excursions from axial symmetry and rotation–vibration coupling. Indeed, the first order rotational expression makes several implicit assumptions, the most important of which are that there is no coupling between rotational and intrinsic degrees of freedom and that  $\beta$  is independent of  $J$ . These two assumptions are, in fact, related. As the nucleus rotates, it experiences a centrifugal force that tends to increase the deformation and moment of inertia and decrease the rotational spacings, and leads to an enhanced coupling to vibrational modes (recall Eqs. 6.25 and 6.26, which show that this increases with spin). There are several ways of incorporating these effects into a rotational energy expression. One of the first and most common is simply to expand the rotational energy in powers of  $J(J + 1)$  and keep the second term.

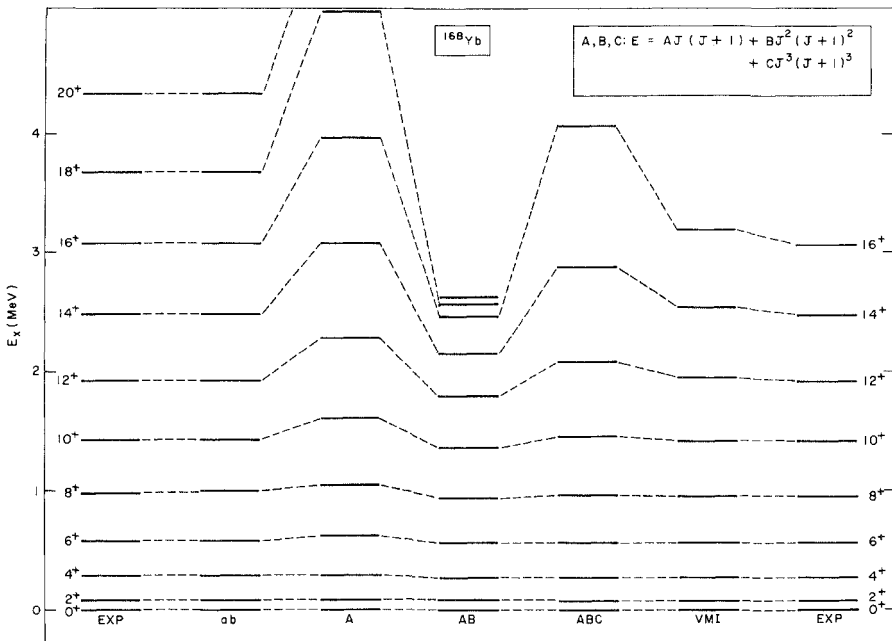


**Fig. 6.17.** Empirical ground band levels of  $^{168}\text{Yb}$  compared with various models. The labels ab and A, AB, ABC refer to the coefficients in Eq. 6.40 and in the expansion of rotational energies in powers of  $J(J+1)$  (see Eq. 6.40 and following discussion).

One then has

$$E = AJ(J+1) + BJ^2(J+1)^2 \quad (6.38)$$

where  $A = \hbar^2/2I$ . (We will derive this formula in a moment.) From our earlier comments, we know that empirical values of  $B$  are negative. If they are also small ( $|B/A| \ll 1$ ), the expansion converges rapidly and Eq. 6.38 will be a significant improvement.

In some cases, still higher-order terms such as  $CJ^3(J+1)^3$  are necessary to produce adequate fits for higher  $J$  values. Rather than explore this, we shall turn shortly to an alternate expression that automatically includes Eq. 6.38 and all higher-order terms. First, we show an example in Fig. 6.17 of the ground state rotational band of  $^{168}\text{Yb}$  compared with the energies calculated from Eqs. 6.13 and 6.38, as well as other expressions to be discussed. Evidently, the first-order expression (Eq. 6.13) is reasonable only for very low-spin states. Equation 6.38 (AB in the figure) is an improvement for higher spins, although it too encounters serious difficulties for still larger  $J$ . A fit with the  $CJ^3(J+1)^3$  term (ABC) included further improves the predictions, but is also inadequate for large  $J$ : the opposite signs empirically deduced for  $B$  and  $C$  tend to produce wild oscillations in predicted energies (compressions of levels, even spin inversions) at high enough  $J$  values.

An alternate approach to incorporating rotation-vibration or centrifugal

effects into the rotational energy expression is to make the moment of inertia spin dependent. This approach is known as the *Variable Moment of Inertia* (VMI) model and has enjoyed considerable success. In general, its predictions are better than those of Eq. 6.38, and it is not limited to the realm of strongly deformed nuclei. Figure 6.17 includes VMI predictions and shows their advantages. We shall not dwell on this approach, as it has been extensively covered in other literature.

Interestingly, it is easy to see how both effects (a change in the moment of inertia and the addition of a higher order term) result immediately from the effects of  $\gamma$ -g bandmixing.

We have seen that the mixing is generally small so we can use the approximation of Eqs. 1.12 to write the energy shift (lowering) of the ground state band as  $\Delta E_s^{gsb}(J) = -V^2/\Delta E_{unp}^2$ . But, from Eq. 1.10, the mixing amplitude  $\epsilon'_\gamma = \sqrt{2}\epsilon_\gamma f_\gamma(J) = V/\Delta E_{unp}$ . So,  $\Delta E_s^{gsb} = 2\epsilon_\gamma^2 f_\gamma^2(J)$ . Hence, from Eq. 6.25,

$$\begin{aligned}\Delta E_s^{gsb}(J) &= 2\epsilon_\gamma^2(J-1)J(J+1)(J+2) \\ &= 2\epsilon_\gamma^2 J(J+1)[(J-1)(J+2)] \\ &= 2\epsilon_\gamma^2 J(J+1)[J(J+1)-2] \\ &= 2\epsilon_\gamma^2 J^2(J+1)^2 - 4\epsilon_\gamma^2 J(J+1)\end{aligned}\quad (6.39)$$

The second term is the promised correction to the standard rotational formula, and can give the variation with  $J$  of the inertial parameter  $\hbar^2/2I$ , while the first gives the required second-order correction term. From this derivation it is clear that Eq. 6.38 is, as we implied earlier, ultimately connected with the concept of rotation-vibration coupling (bandmixing) and also that it implicitly assumes small mixing.

When  $J$  becomes large enough such that  $\epsilon_\gamma f_\gamma(J) \sim 1$  we must anticipate a breakdown of Eq. 6.38 and thus a need for many higher-order terms or an alternate formula. We have seen this effect empirically in the failure of Eq. 6.38 for  $J \geq 14$  in Fig. 6.17.

However, there is a much superior rotational expression that is valid for even higher spins that unfortunately has not been discussed much in the literature. It automatically gives Eqs. 6.13 and 6.38 as limiting cases, automatically includes all the higher order correction terms, and moreover, contains a specific relationship between the coefficients of each successive term. One simply writes the two-parameter formula

$$E(J) = a[\sqrt{1+bJ(J+1)} - 1] \quad (6.40)$$

where  $a$  and  $b$  are parameters.

This expression can be derived in the Bohr-Mottelson picture by including small deviations from axial symmetry. A trivial rationale for this was presented by Lipas many years ago. Suppose that we make the ansatz that we can write the moment of inertia  $I$  as a function of excitation energy:

$$I = \alpha + \beta E(J)$$

Then, substituting this into Eq. 6.13 gives

$$E(J) = \frac{\hbar}{2[\alpha + \beta E(J)]} J(J+1)$$

or

$$2\beta E^2(J) + 2\alpha E - \hbar^2 J(J+1) = 0$$

Hence

$$E(J) = \frac{-2\alpha \pm \sqrt{4\alpha^2 + 8\beta\hbar^2 J(J+1)}}{4\beta}$$

or, taking positive energies,

$$E(J) = \frac{\alpha}{2\beta} \left[ \sqrt{1 + \frac{2\beta\hbar^2}{\alpha^2} J(J+1)} - 1 \right] \quad (6.41)$$

which is simply Eq. 6.40 with  $a = \alpha/2\beta$  and  $b = 2\hbar^2\beta/\alpha^2$ . Note that energy ratios, such as  $E_J/E_{2+}$ , depend only on the single parameter  $b$  in Eq. 6.40. Nevertheless, this formula is far more accurate than any of the expressions we have considered, as shown in Fig. 6.17 for  $^{168}\text{Yb}$  where the predictions are compared with one-, two-, and three-term expansions in  $J(J+1)$  and with the VMI model. Its success extends to softer (transitional) nuclei (e.g.,  $^{152}\text{Sm}$ ,  $^{184}\text{Pt}$ ). Since the expression works so well for higher  $J$ , we anticipate a later discussion to caution that it is only applicable below any “backbend” that may be present.

Aside from its empirical success, Eq. 6.40 is interesting because, for relatively low spins such that  $bJ(J+1) \ll 1$ , expansion of the square root naturally recovers the second (and higher) order terms in the rotational formula of Eq. 6.38:

$$\left[ \sqrt{1 + bJ(J+1)} - 1 \right] = \frac{b}{2} J(J+1) - \frac{b^2}{8} J^2 (J+1)^2 + \dots \quad (6.42)$$

Here, however, the coefficients of each power of  $J(J+1)$  are interrelated, whereas in Eq. 6.38, they are arbitrary parameters. It is remarkable that this constrained version of the expansion in powers of the angular momentum produces such an excellent fit.

For large  $J$  such that  $bJ(J+1) \gg 1$  (this typically requires  $J \sim 30$ ), this expression is almost *linear* in  $J$ , reflecting the enormous compression of the ground band due to both bandmixing effects and to centrifugal stretching. Thus, Eq. 6.40 incorporates the limit of small mixing (Eq. 6.38), but also extends into spin regions where the mixing is large.

## 6.5 Axially Asymmetric Nuclei

The models we have discussed thus far incorporate excursions from axial symmetry that are both *small* and dynamic. Certainly, such an approach accounts reasonably well for the deviations of most well-deformed nuclei from the properties of the pure axial rotor. However, there have long been indications that larger and possibly permanent (static) asymmetries also occur.

Naturally, this would lead to more radical departures from the energy and transition rate expressions we have considered. In fact, in certain limiting cases of large asymmetry, new selection rules appear. In another sense, however, such models for larger asymmetry are extensions of the small excursions from axiality dealt with so far, and their predictions go over into the latter as  $\gamma \rightarrow 0^\circ$ . It also turns out that many predictions of models for large, fixed asymmetries  $\gamma$  are identical, or nearly so, to models incorporating dynamic fluctuations in  $\gamma$  so long as  $\gamma_{\text{rigid}}$  in one equals  $\gamma_{\text{rms}}$  in the other.

The best known model of fixed stable asymmetry (*triaxiality*) is that of Davydov and co-workers developed around 1960. Here, the potential  $V(\gamma)$  is envisioned to have a steep, deep minimum at a particular value of  $\gamma$  so that the nucleus takes on a rigid shape with that asymmetry.

We have seen that, if the rotational and vibrational motions are not completely decoupled, and there is an interaction (mixing) between the  $\gamma$  and ground bands, the latter will acquire a finite  $\gamma_{\text{rms}}$  and  $K$  will no longer be a good quantum number. Therefore, it is not surprising that in the Davydov model  $K$  is not a good quantum number either. Here, however, since  $\gamma$  can be large, the  $K$  admixtures can reach levels far beyond those we have encountered.

The relation between the Davydov model and models with axially symmetric but  $\gamma$ -soft potentials runs deeper than this. In a nucleus with such a potential, the greater the softness the lower the  $\gamma$  vibration will lie, and the larger  $\gamma_{\text{rms}}$  will be in the ground state. In the Davydov model there is no distinction in intrinsic structure between what is normally called the ground state rotational band and the  $\gamma$  vibrational states. The levels of these two bands simply become the so-called normal and anomalous levels of a new ground state band whose energies depend explicitly on  $\gamma$ , which can take on values from  $0^\circ \rightarrow 30^\circ$  (prolate symmetric  $\rightarrow$  maximum asymmetry:  $30^\circ \leq \gamma \leq 60^\circ$  corresponds to the “oblate” region of asymmetry). Figure 6.18 shows the lowest levels as a function of  $\gamma$  and clearly illustrates the descent of the  $\gamma$  vibrational levels. Indeed, for  $\gamma \geq 25^\circ$ ,  $E_{2\gamma}^+ < E_{4_1^+}$ . In contrast, as  $\gamma \rightarrow 0^\circ$ , the normal levels  $0_1^+, 2_1^+, 4_1^+, 6_1^+$ , which are rather insensitive to  $\gamma$ , go over into those of an axially symmetric ground state band, while the “ $\gamma$  band” energies increase rapidly. An important feature of the anomalous levels is their energy “staggering”: They tend to be grouped into couplets as  $(2^+, 3^+), (4^+, 5^+)$ ...

The behavior in Fig. 6.18 is easy to understand. As  $\gamma$  increases, the nucleus becomes increasingly flattened. Therefore, states whose wave functions are predominantly aligned in the direction of the flattening attain lower energies, since the nuclear force is attractive and they are, on average, closer to the bulk of the nuclear matter. This is exactly the case for the  $K = 2$  (and higher  $K$ ) levels which, therefore, rapidly decrease in energy with increasing  $\gamma$ . They also mix with the normal ground state band levels (yrast states) and, as we have seen,  $K$  is no longer a good quantum number. The leveling off of the energies of the anomalous levels for  $\gamma \geq 25^\circ$  is easily understood in terms of that mixing. In Table 6.10 we give a number of interesting quantities relating to the Davydov model, including the amplitude for  $K = 0$  in the  $4_1^+$  and  $4_2^+$  states as a function of  $\gamma$ . For  $\gamma$  between  $25^\circ$  and  $30^\circ$ , the major amplitudes in the  $4_2^+$  state

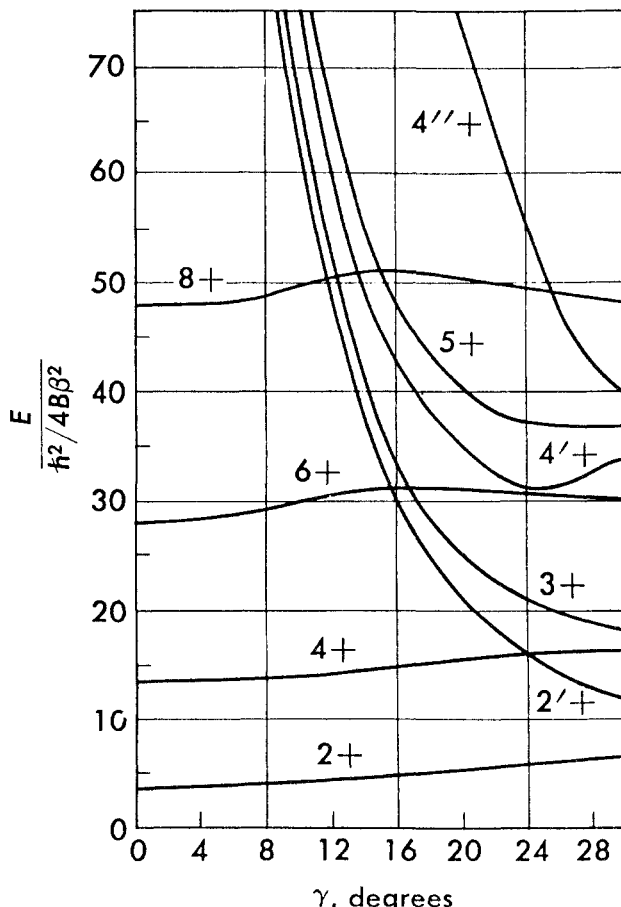


Fig. 6.18. Normal and anomalous levels of the triaxial rotor (Preston, 1975).

actually interchange so that the  $K = 0$  amplitude is larger than the  $K = 2$  one. (The  $4_1^+$  amplitudes do not quite “cross” since there is actually substantial three-state mixing involving the  $4_3^+$  state.) The interchange of amplitudes in the  $4_2^+$  level occurs near the energy inflection point in Fig. 6.18. The decreasing trend of the quasi- $\gamma$ -band, or anomalous level energies, would have caused these energies to cross the normal levels at this point. Instead, the interaction causes a repulsion. This is a nice example of this two-state mixing effect discussed in Chapter 1.

In practical applications of the Davydov model, one usually extracts  $\gamma$  from the energy ratio  $E_{2_2^+}/E_{2_1^+}$  of the first two  $2^+$  states. This ratio is given in Table 6.10 for several values of  $\gamma$  and is plotted in Fig. 6.19 (along with two  $B(E2)$  ratios). It can be calculated for any  $\gamma$  value from the expression

$$\frac{E_{2_2^+}}{E_{2_1^+}} = \frac{[1 + X]}{[1 - X]} \quad (6.43)$$

**Table 6.10.** Some useful predictions of the asymmetric rotor (Davydov) model\*

$\gamma \rightarrow$	0°	5°	10°	15°	20°	25°	27.5°	30°
$E_{2^+2}/E_{2^+_1}$	$\infty$	64.2	15.9	6.85	3.73	2.41	2.10	2.00
$B(E2:2^+_2 \rightarrow 2^+_1)$	1.43	1.49	1.70	2.70	5.35	20.6	82	$\infty$
$B(E2:2^+_2 \rightarrow 0^+_1)$								
$\psi_{4^+1}^{K=0}$	1	1	0.999	0.993	0.955	0.852	0.792	0.739
$\psi_{4^+1}^{K=2}$	0	0.003	0.030	0.114	0.296	0.522	0.605	0.661
$\psi_{4^+2}^{K=0}$	0	-0.003	-0.030	-0.114	-0.296	-0.523	-0.602	0.559
$\psi_{4^+2}^{K=2}$	1	1	0.999	0.993	0.954	0.842	0.754	0.500
$B(E2:2^+_1 \rightarrow 0^+_1)$	1	0.993	0.972	0.947	0.933	0.955	0.985	1
$B(E2:2^+_2 \rightarrow 0^+_1)$	0	0.0074	0.028	0.053	0.067	0.425	0.015	0
$B(E2:2^+_2 \rightarrow 2^+_1)$	0	0.011	0.051	0.143	0.357	0.865	1.23	1.43
$B(E2:2^+_2 \rightarrow 0^+_1)$	0	0.0074	0.0288	0.056	0.072	0.0445	0.015	0
$B(E2:4^+_2 \rightarrow 2^+_1)$	0	0.0004	0.011	0.008	0.0004	0.021	0.018	0
$B(E2:4^+_1 \rightarrow 2^+_2)$	0	0	0.0023	0.010	0.033	0.039	0.016	0
$B(E2:4^+_2 \rightarrow 4^+_1)$	0	0.0138	0.0624	0.167	0.313	0.311	0.271	0.273
$B(E2:4^+_1 \rightarrow 2^+_1)$	1.429	1.418	1.395	1.377	1.372	1.365	1.378	1.389
$B(E2:3^+_1 \rightarrow 4^+_1)$	0	0.006	0.034	0.130	0.406	0.821	0.955	1
$B(E2:3^+_1 \rightarrow 2^+_1)$	0	0.0132	0.0492	0.095	0.12	0.079	0.027	0
$B(E2:3^+_1 \rightarrow 2^+_2)$	1.78	1.77	1.74	1.69	1.67	1.70	1.76	1.78

\*B(E2) values are in units of  $e^2 Q^2 / 16\pi$ .

where

$$X = \sqrt{1 - \frac{8}{9} \sin^2(3\gamma)}$$

The individual energies are equal to the respective numerators and denominators multiplied by  $(9/\sin^2 3\gamma)$ . Note that  $X \rightarrow 1$  for  $\gamma \rightarrow 0^\circ$ . Thus,  $E_{2^+_2}/E_{2^+_1} \rightarrow \infty$  for  $\gamma \rightarrow 0^\circ$  as seen in the Table and figure. Also,  $X \rightarrow 1/3$  for  $\gamma \rightarrow 30^\circ$ . Table 6.11 gives the empirical values of  $E_{2^+_2}/E_{2^+_1}$  for a number of heavy rare earth nuclei as well as the associated  $\gamma$  values. If, on account of the anomalously low  $E_{2^+_2}/E_{2^+_1}$  ratios, these nuclei are considered to have large rigid triaxiality (this is the term usually used for the concept of fixed asymmetries), then these  $\gamma$  values are the only input needed to make Davydov model predictions for other observables. Such predictions are included in Table 6.10 for several  $\gamma$  values. The branching ratio,

$$R_2 = \frac{B(E2:2^+_2 \rightarrow 2^+_1)}{B(E2:2^+_2 \rightarrow 0^+_1)}$$

is also a useful indicator, as shown in the same table and in Fig. 6.19.  $R_2$  can be written analytically and calculated for any  $\gamma$  from

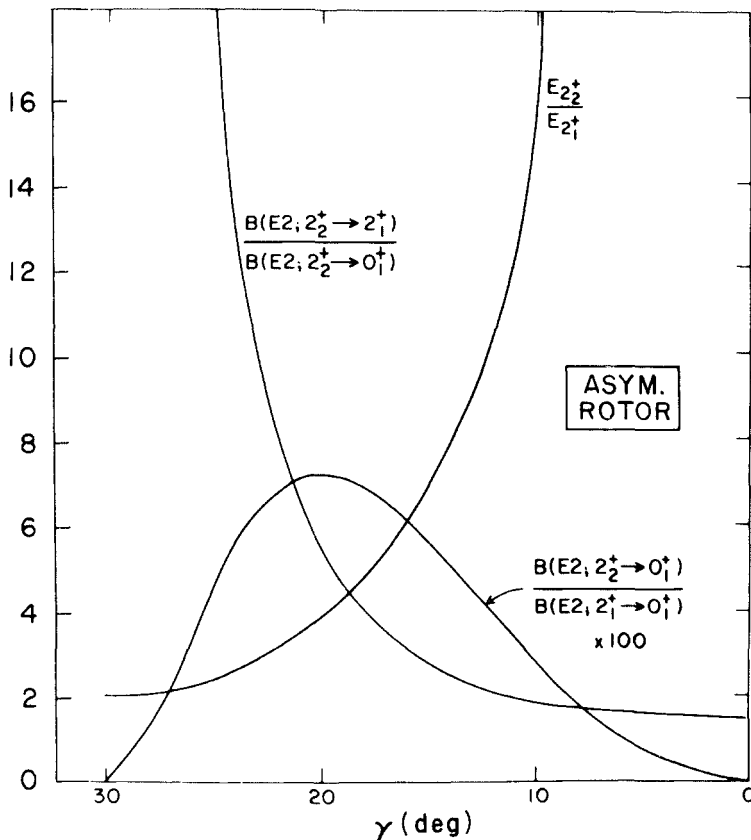


Fig. 6.19. Dependence of several observables on  $\gamma$  (compare Fig. 6.42).

$$R_2 = \frac{\frac{10}{7} \left( \frac{\sin^2(3\gamma)}{9X^2} \right)}{2 \left[ 1 - \frac{3 - 2\sin^2(3\gamma)}{3X} \right]} \quad (6.44)$$

where the numerator and the denominator are the individual  $B(E2)$  values. Note that both  $B(E2)$  values in  $R_2$  vanish for  $\gamma=0^\circ$ , yet they have a finite ratio that is the Alaga rule: the vanishing is reasonable since for  $\gamma=0^\circ$ ,  $E_{2_2}^+ / E_{2_1}^+ \rightarrow \infty$ , corresponding to infinite rigidity in the  $\gamma$  direction and to vanishing vibrational amplitude.  $R_2$  increases rapidly with  $\gamma$  and  $R_2 \rightarrow \infty$  for  $\gamma=30^\circ$ . This latter result is identical to the selection rule for an alternate model of axial asymmetry that we will soon discuss, the  $\gamma$  flat or  $\gamma$ -unstable model of Wilets and Jean in which the  $2_2^+ \rightarrow 0_1^+$  transition is forbidden.

Some other  $B(E2)$  values and branching ratios are given in Table 6.10. Those corresponding to rotational transitions in either the  $\gamma$  or ground bands, are nearly  $\gamma$  independent. Others vanish at both  $\gamma=0^\circ$  and  $30^\circ$  but attain small,

**Table 6.11.** Values of  $E_{2_2^+}/E_{2_1^+}$  for some deformed and transitional nuclei and the corresponding  $\gamma$  values (rounded to nearest degree)

Nucleus	$E_{2_2^+}/E_{2_1^+}$	$\gamma$
$^{152}\text{Sm}$	8.9	13°
$^{160}\text{Dy}$	11.1	12°
$^{168}\text{Er}$	10.3	13°
$^{172}\text{Yb}$	18.6	9°
$^{176}\text{Hf}$	15.2	10°
$^{182}\text{W}$	12.2	12°
$^{184}\text{Os}$	7.9	14°
$^{188}\text{Os}$	4.1	19°
$^{192}\text{Os}$	2.4	25°
$^{196}\text{Pt}$	1.94	30°

finite values for intermediate  $\gamma$  values. These are transitions *between* normal and anomalous levels. The  $2_2^+ \rightarrow 2_1^+$  and  $3_1^+ \rightarrow 4_1^+$  transitions form a third category: small at  $\gamma = 0^\circ$  and rising rapidly toward  $\gamma = 30^\circ$ . This behavior is easily understandable if we note that, in the  $\gamma = 30^\circ$  case, the Davydov model has the same selection rules as both the quadrupole vibrator model and the Wilets-Jean  $\gamma$ -unstable model. For example, at  $\gamma = 0^\circ$ , the  $2_2^+ \rightarrow 2_1^+$  and  $3_1^+ \rightarrow 4_1^+$  transitions are interband ( $\gamma \rightarrow g$ ): given the built-in stiffness in  $\gamma$ , they must be forbidden. At  $\gamma = 30^\circ$ , the  $3_1^+$  state is analogous to a three-phonon level, the  $4_1^+$  level to a two-phonon excitation, so the transition becomes allowed. Similarly the  $2_2^+ \rightarrow 2_1^+$  transition is analogous to a  $2 \rightarrow 1$ -phonon transition.

Since finite  $\gamma$  values correspond to mixed  $K$  values, one might expect a close relation between  $B(E2)$  values for finite  $\gamma$  in the Davydov model and in the bandmixing formalism. This is indeed so. Consider, as an example, the case we worked out earlier of  $^{168}\text{Er}$ . We found that the Mikhailov plot analysis gave a full mixing amplitude in the  $4^+$  states of  $\epsilon'_+(4^+) = 0.021$ . In the Davydov model, the experimental ratio  $R_2 = 1.85$  yields  $\gamma \sim 11^\circ$  (see Table 6.10). This, in turn, corresponds to a  $\gamma \rightarrow g$  mixing amplitude of 0.03, which is quite close to the bandmixing result. The agreement is not exact since the comparison is not quite on an equal footing. In the bandmixing case, the spin independent mixing amplitude was deduced from a Mikhailov plot, which gives an overall average value for all transitions, while the Davydov mixing value was deduced from  $R_2$  alone. In any case the essential point is that both the bandmixing formalism and the Davydov model lead to  $K$  mixtures in  $\gamma$  and ground bands, and give comparable mixing amplitudes and  $B(E2)$  values for small  $\gamma$ . (The bandmixing formalism is a first-order perturbation treatment and is therefore inapplicable for large  $\gamma$ .) Though the physical pictures are different, predictions for many observables are nearly identical.

When we turn to the large  $\gamma$  extreme, one might think that the extremely low-lying  $\gamma$  band levels of the Davydov model would be an appropriate signature for stable axially asymmetric shapes. However, we can also envision large  $\gamma$  values as dynamic quantities by picturing a deformed nucleus that is

totally free to vibrate in the  $\gamma$  degree of freedom. Such a nucleus is completely  $\gamma$ -soft: it is a “ $\gamma$ -unstable” rotor. This corresponds to a nuclear potential centered at a finite  $\beta$  but completely flat in the  $\gamma$  degree of freedom. The nucleus oscillates smoothly from  $\gamma = 0^\circ - 60^\circ$  and has  $\gamma_{\text{rms}} = 30^\circ$ . In the extreme limit of complete  $\gamma$  instability, known as the *Wilets-Jean* model, the “rotational” energies are given by

$$E(\Lambda)_{w_J} = \vartheta \Lambda (\Lambda + 3) \quad (6.45)$$

where  $\vartheta$  is a constant analogous to  $\hbar^2/2I$  and the levels are now classified according to the quantum number  $\Lambda$ . This classification scheme is given in Fig. 6.20. The yrast levels have  $J = 2\Lambda$ . Note that each  $\Lambda$  value (for  $\Lambda > 1$ ) corresponds to more than one level and that the  $\Lambda$  values 2, 3, 4, ... include a low-lying set of levels analogous to the  $\gamma$  vibrational band and to the anomalous levels of the Davydov model for large  $\gamma$ .

Now that we have the three basic extreme geometric models, the harmonic vibrator, the axially symmetric deformed rotor, and the  $\gamma$ -soft axially asymmetric deformed rotor, it is interesting to compare their rotational energies. The results are shown in Fig. 6.21. The spacing of the normal rotational levels of the Wilets-Jean rotor are quite different than in the symmetric rotor. This is easy to see if one notes that for these levels (the yrast states)  $\Lambda = J/2$ , so that  $E_{w_J}(J\text{-yrast}) = (\vartheta/4)J(J+6)$ , which increases with  $J$  considerably slower than the  $J(J+1)$  law for a symmetric rotor. For example,  $E_{4_1^+}/E_{2_1^+} = 2.5$  compared to 3.33 for the rotor and  $E_{6_1^+}/E_{4_1^+} = 4.5$  instead of 7. We note for later reference

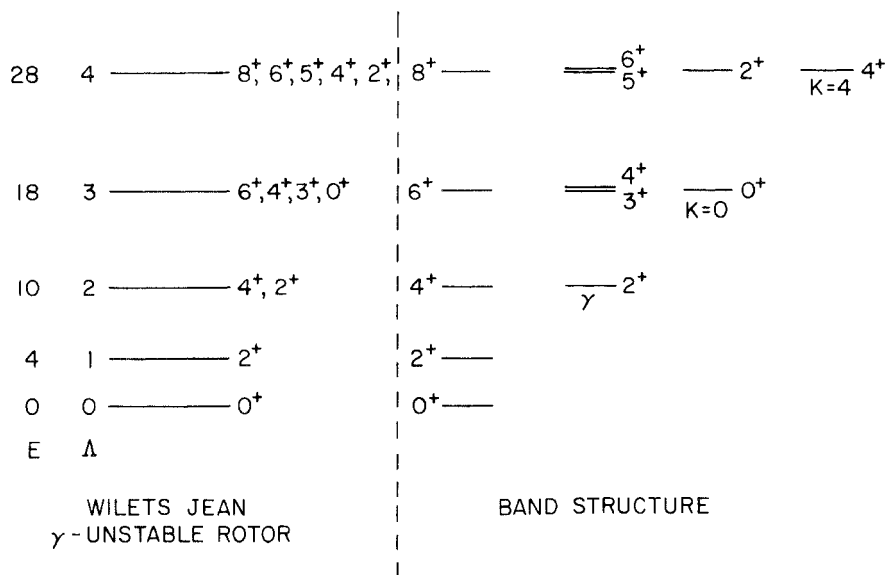


**Fig. 6.20.** Ground band levels in the  $\gamma$ -unstable or Wilets-Jean model. (Left) In terms of  $\Lambda$  multiplets; (Right) Displayed in analogy to the quasi-band structures of a normal rotor.

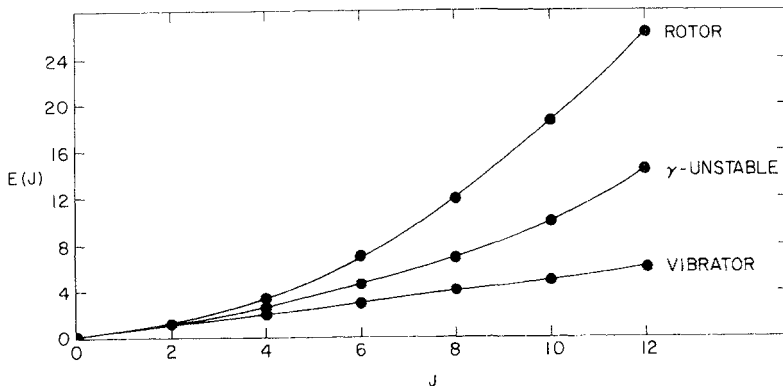


**Fig. 6.21.** Dependence of ground band energies on spin for different models. An identical set of curves is obtained in the U(5), O(6), and SU(3) symmetries of the IBA (see Eq. 6.72).

that the  $\gamma$  unstable limit of Wilets-Jean is very closely related to the 0(6) limit of the IBA Model.

Another characteristic of the Wilets-Jean model concerns E2 selection rules. The allowed transitions must satisfy  $\Delta\Lambda = \pm 1$ . Comparison with Table 6.10 shows that the Davydov model goes over to the same selection rules as the Wilets-Jean model for  $\gamma = 30^\circ$ , again highlighting the similarity of a  $\gamma$ -flat model with  $\gamma_{\text{rms}} = 30^\circ$  to a rigid asymmetric model with fixed  $\gamma = 30^\circ$ . The Wilets-Jean picture also resembles the phonon model in its E2 selection rule and gives some identical predictions. For example, the  $2_2^+ \rightarrow 2_1^+$  transition ( $\Lambda = 2 \rightarrow \Lambda = 1$ ) is allowed, as is  $4_1^+ \rightarrow 2_1^+$ , but the crossover  $2_2^+ \rightarrow 0_1^+$  transition is forbidden ( $\Delta\Lambda = 2$ ), as is the  $4_1^+ \rightarrow 2_2^+$  ( $\Delta\Lambda = 0$ ). These are the same results one would have if the  $0_1^+, 2_1^+$  and  $(4_1^+, 2_2^+)$  doublet were treated as the zero-, one-, and two-phonon vibrational states. This is not surprising since the potential for the spherical vibrator, while parabolic in  $\beta$ , is independent of  $\gamma$ , so it is trivially  $\gamma$ -unstable as well. The real difference between the vibrator and Wilets-Jean limits is that in one  $\beta_{\text{ave}} = 0$ , whereas the other has a deformed minimum. Another difference between the two models (with the vibrator now considered in its harmonic, degenerate multiplet limit) is that the vibrator has a two-phonon triplet of levels  $0^+, 2^+, 4^+$  while the Wilets-Jean scheme has only a  $2^+, 4^+$  doublet, the first excited  $0^+$  state having  $\Lambda = 3$ . Thus, not only is it higher in energy but its allowed decay is to the *second*  $2^+$  level ( $2_2^+$ ) rather than the first as in the vibrator; more precisely,  $B(\text{E2}: 0_2^+ \rightarrow 2_2^+)/B(\text{E2}: 0_2^+ \rightarrow 2_1^+) \rightarrow \infty$  in the  $\gamma$ -unstable limit but is zero in the vibrator. The reader is warned, however, that these differences do not *necessarily* persist in a sufficiently anharmonic vibrator. We will encounter this point, and this close relationship between vibrator and  $\gamma$ -unstable models, again, in our discussion of the U(5) and O(6) symmetries of the IBA model later in this chapter.

Despite the obvious similarities between the Davydov and Wilets-Jean models, there is one outstanding difference by which to distinguish them

empirically: the energy staggering in the low-spin anomalous or  $\gamma$  vibrational levels is *opposite* in the two models. In the  $\gamma$  unstable case, these levels group according to  $(2^+), (3^+, 4^+), (5^+, 6^+) \dots$  as seen in Fig. 6.20: in the simplest version of this model, the levels within each couplet are degenerate.

It is interesting to use a quantitative measure of the asymmetry as a distinguishing signature. To this end, we define the quantity  $\Delta E_J = E_J - E_{J-1}$ , where the energies refer to the  $\gamma$ -band, and then define the energy staggering,  $E_s(J)$ , as

$$E_s(J) = \Delta E_J - \Delta E_{J-1} \quad (6.46)$$

For example,

$$E_s(4) = (E_{4\gamma} - E_{3\gamma}) - (E_{3\gamma} - E_{2\gamma}) \quad (6.47)$$

These double energy differences involve three levels with spins  $J, J-1$ , and  $J-2$ , and we use the convention that the level of spin  $J$  (the starting level) is always of even spin. The usefulness of  $E_s$  in comparing different models is evident if we relate it to the energy of the first  $2^+$  level,  $E_{2\gamma}^\dagger$ . Although the harmonic vibrator is not a rotational scheme, the levels of the “quasi- $\gamma$  band” in that scheme also display a staggering similar to the  $\gamma$ -unstable model and include the same degenerate couplets. We can therefore include this model in this intercomparison as well. For the four cases of the symmetric rotor, the triaxial rotor/ Davydov model with  $\gamma = 30^\circ$ , the  $\gamma$ -unstable or Wilets-Jean model, and the harmonic vibrator, the following analytical expressions result:

$$\begin{aligned} E_s(4) &= \frac{\hbar^2}{2I} \{ [J(J+1) - (J-1)J] - [(J-1)(J) - (J-2)(J-1)] \} \\ &= \frac{\hbar^2}{2I} 2 = \frac{E_{2\gamma}^\dagger}{3} \quad (\text{symmetric rotor}) \\ E_s(4) &= A[(34 - 18) - (18 - 12)] = 10A = \frac{5}{3}E_{2\gamma}^\dagger \quad (\gamma\text{rigid}, \gamma = 30^\circ) \\ E_s(4) &= A\{0 - [3(6) - 2(5)]\} = -8A = -2E_{2\gamma}^\dagger \quad (\gamma\text{unstable}) \\ E_s(4) &= [0 - (3E_{2\gamma}^\dagger - 2E_{2\gamma}^\dagger)] = -E_{2\gamma}^\dagger \quad (\text{vibrator}) \end{aligned} \quad (6.48)$$

Generally, if  $E_s(4) < E_{2\gamma}^\dagger/3$  ( $\gamma$ -soft case), the even spin states are depressed relative to the odd spin; if  $E_s(4) > E_{2\gamma}^\dagger/3$  ( $\gamma$ -rigid), the odd spin levels are depressed relative to the even spin ones.

Before inspecting empirical values of  $E_s(4)$ , we note another interesting feature of the vibrator limit. As we have seen, empirical values of the energy ratio  $R \equiv E_{2\text{ph}}/E_{1\text{ph}}$  for vibrational nuclei are typically  $\sim 2.2$  rather than the strict harmonic limit of 2.0. Table 6.4 gave the energy levels of the three-phonon states, which include the  $3^+$  and  $4^+$  levels of the “quasi- $\gamma$  band” in terms of the two-phonon levels.  $E_s(4)$  cannot be defined analytically in this case since the unknown energies of these  $3^+$  and  $4^+$  levels implicitly involve the energy of the  $4_1^+$  level. However, if we make the approximation that the two-phonon  $2_2^+$  and  $4_1^+$  levels are degenerate (i.e.,  $\epsilon_2 = \epsilon_4$  in the notation of Table 6.4), then the  $3^+$  and  $4^+$  quasi- $\gamma$  band states will still be degenerate at an energy  $3E_{2\gamma}^\dagger$  ( $R - 1$ ).

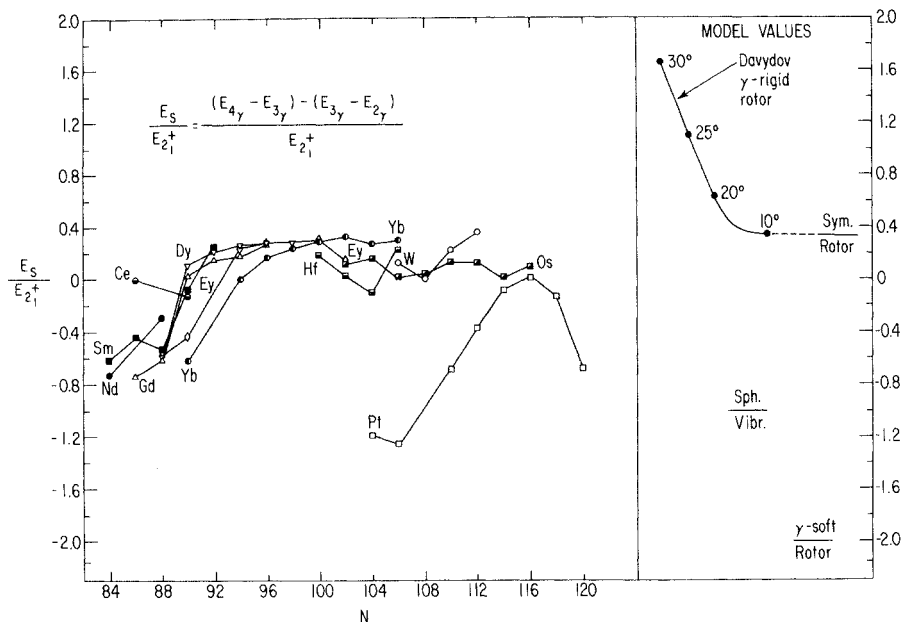


**Fig. 6.22.** Systematics of  $E_s(4)/E_{2_1^+}$  in the rare earth region. Predicted values for several models are given at the right.

The energy anharmonicity of the two-phonon states is tripled in the three-phonon states. Simple manipulations then give  $E_s(4) = -E_{2_1^+}(2R - 3)$ . Of course, in the harmonic limit  $R = 2$ , and this goes to  $E_s(4) = -E_{2_1^+}$  as in Eq. 6.48. For the more typical case of  $R > 2$ , however,  $E_s(4)$  becomes increasingly negative compared to the harmonic value.

We see that  $E_s$  nicely distinguishes different models ranging from vibrational to rotational to axially asymmetric, and is also a useful signature of transitional regions between these ideal limiting cases. We show in Fig. 6.22 the empirical  $E_s(4)$  values for rare earth nuclei. Near the  $N = 82$  closed shell, the nuclei are close to vibrational with only a small component of  $\beta$  softness.  $E_s(4)$  is negative and, in units of  $E_{2_1^+}$ , ranges from  $-0.8 \rightarrow -0.4$ . As the neutron number increases, the  $\beta$  softness rapidly increases and  $E_s(4)$  approaches the rotational limit of  $+E_{2_1^+}/3$ . The fact that most of the deformed rare earth nuclei have  $E_s(4)$  values slightly less than  $E_{2_1^+}/3$  reflects both their predominantly axially symmetric rotational character and the presence of a small amount of rotation-vibration coupling. Towards the end of the  $N = 82-126$  shell, the behavior becomes more erratic, with the Pt isotopes displaying tendencies toward extreme  $\gamma$  softness.

Despite years of popularity of the Davydov model because of its simplicity and analytic formulas, there is virtually no evidence for rigid triaxial behavior. Axial asymmetry in nuclei seems associated with  $\gamma$  softness instead.

In a later section of this chapter we shall see that such  $\gamma$  softness also

characterizes the O(6) symmetry of the IBA and nuclei in O(6)  $\rightarrow$  rotor or SU(3) transitional regions. To anticipate that discussion briefly, it is interesting to note that the classic O(6) nuclei,  $^{192-196}\text{Pt}$ , have larger  $E_s(4)$  values than some of the other Pt isotopes, even though they are supposedly completely  $\gamma$ -soft. We can already guess from Fig. 6.22, however, that nuclei with nearly  $\gamma$  independent potentials but with shallow minima at  $30^\circ$  (that is, with the addition of a small component of triaxiality at  $\gamma=30^\circ$ ) might have  $E_s(4)$  values higher than the extreme  $\gamma$ -unstable limit. This is in fact the case, as will be commented later in the discussion of the IBA.

The  $\gamma$ -rigid– $\gamma$ -soft ambiguity is not the only one that can obfuscate an interpretation of the structure. Figure 6.22 also shows the difficulty in distinguishing near harmonic vibrational structure from  $\gamma$  softness. There is one useful, albeit qualitative, indicator stemming from the systematic behavior of certain absolute energies that can sometimes clarify whether a *transitional* region is vibrational  $\rightarrow$  symmetric rotor or axially asymmetric  $\rightarrow$  symmetric rotor in character. This indicator is the relation between the energy of the  $2_\gamma^+$  (normally  $2_2^+$ ) level and the  $4_1^+$  state of the quasi-ground state band.

In a transition from vibrator to symmetric rotor, the  $2_2^+$  level starts off initially degenerate with the  $4_1^+$  level at rather high energies (since  $E_{2_1^+}$  is then also rather high). As the phase transition develops, the  $4_1^+$  level drops rapidly (as the  $2_2^+$  energy drops) to become a member of the ground state rotational band, while the  $2_\gamma^+$  level remains rather high in energy (although it may drop slightly). In a transition from an axial asymmetric rotor (either soft or rigid) to symmetric rotor, the  $2_\gamma^+$  and  $4_1^+$  levels start out nearly degenerate (for large  $\gamma$ ) and rather low-lying, but the former rises rapidly as  $\gamma \rightarrow 0^\circ$  while the  $4_1^+$  level drops slightly as the deformation increases. These contrasting systematics are shown for the Sm and Os nuclei in Fig. 6.23. This signature, while valid, cannot be quantified as well as the energy staggering since the two levels involved have intrinsically different structure in the rotational limit: the  $4_1^+$  state belongs to the ground state band while the  $2_\gamma^+$  state is an intrinsic excitation whose energy depends on details of its microscopic collective wave function

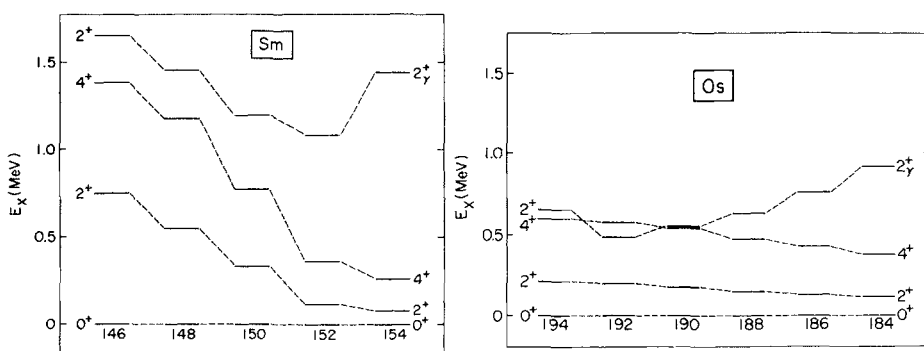


**Fig. 6.23.** Systematics of low-lying levels in the Sm and Os nuclei. The symmetric rotor limit is at the right in each case.

(see the discussion of the RPA in Chapter 9). In any case, it is evident that the Ba–Gd region represents a vibrational–rotational transition, whereas the Pt–Os region is axially asymmetric → rotational.

This completes our brief survey of some of the essential features of geometric models for deformed even–even nuclei. These models have been enormously successful, especially when the first order energy and  $B(E2)$  predictions are modified by incorporating the higher order terms that reflect changes in shape and adiabaticity of the rotational motion as  $J$  increases. These models are all truly phenomenological in that they are applied to real nuclei by inspecting empirical properties in order to *assign* the appropriate shapes ( $\beta$ ,  $\gamma$ , or higher-order moments). The models then provide a framework for the prediction of numerous other observables.

In closing this section, it is important to stress that we have hardly exhausted the collective vibrational modes in even–even nuclei. For example, we have not touched on the most basic low-lying negative-parity excitations—octupole vibrations—nor have we considered hexadecapole excitations. Just as quadrupole vibrations in deformed nuclei can have  $K = 0$  or  $K = 2$ , octupole excitations exist in  $K = 0, 1, 2$ , and 3 forms. In many deformed nuclei, several of these have been identified, primarily via strong E1 and/or E3 transitions to the ground state band. The ordering of these octupole  $K$  values changes systematically through a shell: near the beginning, the low  $K$  modes are lowest, while they are highest toward the end. The basic physics, especially concerning  $\gamma$ -ray transitions into and out of these excitations, is similar in spirit to what we have already outlined for positive parity levels. Though these excitations account for most of the known negative parity states below the pairing gap in deformed nuclei, they have been less well studied than their positive parity quadrupole counterparts. Recently, however, they have taken on a new interest in conjunction with, or rather as an alternative description to, the possible existence of  $\alpha$ -like cluster states, which are expected to have some of the same properties. Hexadecapole vibrations are much less well known: perhaps the most likely manifestation of their particular characteristics are in the low-lying  $K = 4$  bands in the Os isotopes.

We will not pursue a discussion of these higher multipole excitations here; instead, we will return to the question of hexadecapole excitations and stable hexadecapole deformations after our discussion of the Nilsson model in Chapter 8, and to the structure and systematics of octupole excitations in Chapter 9 after our treatments of the TDA and RPA approaches to the microscopic derivation of collective vibrations.

## 6.6 The Interacting Boson Model

Up until the mid-1970s the two principle strains of nuclear structure theory were embodied in the shell model, which emphasized the single-particle aspects of nuclear structure along with a careful accounting of the effects of the Pauli principle, and the collective model pioneered by Bohr and Mottelson and generalized by Gneuss and Greiner, Kumar, and numerous others. Each

of these models, of course, had numerous offshoots: the shell model for spherical nuclei led to the development of the Nilsson model for deformed shapes and the collective models developed refinements that incorporated axial asymmetry, higher moments in the shape such as hexadecapole components, and the like. The link between these models was provided in the early 1960s by the development of microscopic approaches to collective motion utilizing such techniques as the TDA and RPA, which we will discuss in Chapter 9.

In 1974 the *Interacting Boson Approximation* (IBA) model was proposed, which is based on a third approach that is group theoretical or algebraic and that recalled methodology developed in the 1950s by Elliott and co-workers for light deformed nuclei. The IBA has been extraordinarily successful, and has also generated its own family of offshoots inspiring alternate, sometimes competitive algebraic approaches such as the interesting pseudo-SU(3) and symplectic group studies of Draayer and co-workers.

The IBA is a model for collective behavior. It has become customary to refer to collective models of the Bohr-Mottelson type as “geometric” models and those of the IBA or other group theory-based approaches as “algebraic” models. Today one has a situation in which there is a triad of models—shell, geometric, and algebraic—with which one can attack the basic problems of nuclear structure. These models are not generally incompatible, although there are differences in certain important details, but rather reflect three approaches to nuclear structure that emphasize different complementary aspects of that structure.

As we have commented repeatedly, the shell model rapidly becomes intracitable far from closed shells. In order to circumvent this, two basic alternatives have been tried. In one, that of geometric models, the whole microscopic approach is abandoned and replaced by a macroscopic one involving an assumed or deduced nuclear shape, with rotations and vibrations about that shape. The other, of which the IBA is an example, seeks to effectively truncate the shell model space: the practical utility of such an approach depends on the *extent* of the truncation, while its success depends on the *appropriateness* of the truncation in isolating the key configurations involved (at least in the low-lying states).

The truncation inherent in the IBA is shockingly extreme. For example, it reduces the  $3 \times 10^{14}$   $2^+$  shell model basis states in  $^{154}\text{Sm}$  to 26! It is a wonder that such a scheme can work at all, much less have the extensive and repeated success it has enjoyed.

The basic idea of the IBA is to assume that the valence fermions couple in pairs *only* to angular momenta 0 and 2 and that the low-lying collective excitations of medium and heavy nuclei can be described in terms of the energies and interactions of such pairs. These fermion pairs, having integer spin, are treated as bosons (called *s* and *d* bosons for obvious reasons).

More formally, the model is founded on and embodies the following assumptions and ideas:

- Closed shells of either protons or neutrons, and excitations out of them, are neglected.

- The low-lying excitations of even–even nuclei depend only on the valence space.
- The valence nucleons are treated in pairs, as  $s$  and  $d$  bosons, with angular momenta 0 and 2. In the IBA–1 no distinction is made between proton and neutron bosons. The number of bosons is half the number of valence protons and neutrons, both of which are always counted to the nearest proton and neutron closed shells. This counting rule generates a finite, fixed, number of  $s$  and  $d$  bosons. This finite number has profound effects, and leads to numerous predictions that are different from those of the geometric analogues of IBA structures.
- The states of this boson system result from the distribution of the fermions in  $s$  and  $d$  pairs, and thus depend only on the  $s$  and  $d$  boson energies and on interactions *between* bosons. These interactions are assumed to be simple (at most two-body).

A fundamental feature of the IBA that results from these assumptions is its group theoretical structure. Since an  $s$  boson ( $J = 0$ ) has only one magnetic substate and a  $d$  boson ( $J = 2$ ) has five, the  $s$ – $d$  boson system can be looked at mathematically as a six dimensional space. The basis states span that space. It turns out that such a system can be described in terms of the algebraic group structure  $U(6)$ . As we shall discuss at length, such a “parent” group has various subgroups and different “decompositions” of  $U(6)$  into sequences of subgroups that lead to different symmetries (dynamical symmetries, to be exact). There are three of these symmetries that are physically interesting, known by the labels  $U(5)$ ,  $SU(3)$ , and  $O(6)$ . Each has specific, characteristic properties and a definite geometric analogue. Actual examples of nuclei manifesting these symmetries have been identified.

This symmetry structure is central and critical to the IBA. Many predictions can be obtained analytically by powerful group theoretical (algebraic) methods, rather than by tedious numerical diagonalizations. Moreover, the group structure keeps the underlying physical picture close at hand. Even when analytic results are not obtainable (for nuclei with structures “intermediate” between two symmetries) the symmetries act as benchmarks or touchstones that provide a physical backdrop and a simpler starting point for detailed calculations.

As Broglia and others have pointed out, the twin aspects of the grounding of the IBA in fermion pairs, and its symmetry structure with geometrical analogues, confers on the model a “Janus-like” character. On the one hand, it looks to the shell model for its microscopic justification (is it a reasonable truncation to ignore all configurations except those corresponding to  $J = 0$  and  $J = 2$  valence fermion pairs?) and for the ultimate derivation of its parameters and their systematics. On the other, it leads to a picture of the nucleus, and specific predictions, very closely allied to macroscopic geometrical collective models.

To summarize, the two essential distinguishing features of the IBA are its symmetry structure resulting from the  $s$ – $d$  boson truncation and its emphasis on the valence space, with explicit recognition of the finite number of valence nucleons. The first leads to its algebraic formulation and to the dynamical symmetries so intimately associated with the model, while the latter leads to

many key predictions, often different from otherwise closely related geometrical models. As we shall see, it confers a microscopic aspect on an otherwise basically phenomenological model.

We now present a simplified outline of some key elements of the IBA-1 model (protons and neutrons treated together). We first discuss the bosons and the basis states that can be constructed from them, and then a suitable IBA-1 Hamiltonian. We then turn to a discussion of the group theory of the IBA and its symmetry structure. Finally, we consider realistic (nonalgebraic) calculations for actual nuclei and a simplified approach to many of these, the so-called consistent Q formalism. Throughout, we give a number of concrete examples of IBA predictions and stress the relationship to the geometrical models discussed earlier in this chapter.

The basic entities of the IBA are  $s(J = 0)$  and  $d(J = 2)$  bosons, which are assigned energies  $\varepsilon_s$  and  $\varepsilon_d$ . (Note that it is conventional in the IBA literature to use  $L$  for angular momentum both for the individual bosons,  $s$  and  $d$ , and for the total spin of a state. Here, we keep to the convention of this book and use  $J$  for these quantities.) A given nucleus with  $N_p + N_n$  valence protons and neutrons (each counted to the nearest closed shell) has  $N = (N_p + N_n)/2$   $s$  and  $d$  bosons. For example,  $^{152}\text{Sm}$  has  $N = 6 + 4 = 10$  and both  $^{144}\text{Ba}$  and  $^{196}\text{Pt}$  have  $N = 3 + 3 = 6$ . No distinction is made whether the valence nucleons are particles or holes. Ground and excited states are formed by distributing the bosons in different ways among  $s$  and  $d$  states and coupling them to different total  $J$ . The level structures that result depend on these distributions and couplings.

The simplest situation is to imagine all  $N$  bosons in  $s$  boson states. By convention,  $\varepsilon_s = 0$ , the absolute ground state. The lowest excited state will have  $(N - 1)$   $s$  bosons, one  $d$  boson, and an energy  $E = \varepsilon_d$ . The next states, in this simplest case, will be a group with two  $d$  bosons ( $n_d = 2$ ). Clearly, as in the phonon model, the two  $d$  bosons can couple to  $J = 0, 2, 4$ . This triplet will be degenerate. Higher  $d$  boson multiplets will also occur up to  $n_d = N$ . This is a purely harmonic spectrum identical to the harmonic vibrator except for the limitation due to finite boson number.

Since the IBA is configured explicitly in terms of  $s$  and  $d$  bosons, most of the formalism is phrased in terms of creation and destruction operators for these entities,  $s$ ,  $s^\dagger$ ,  $d$ ,  $d^\dagger$ , and combinations thereof. The basic rules for operating with these are the same as for the phonon operators  $\mathbf{b}$ ,  $\mathbf{b}^\dagger$  used earlier in this chapter (Eqs. 6.2–6.4). The Hamiltonian for the harmonic system just described, is simply

$$H = \varepsilon_d (\mathbf{d}^\dagger \mathbf{d})^0 = \varepsilon n_d \quad (6.49)$$

that is, the energies are  $E = \varepsilon n_d$ , where for simplicity here and henceforth we drop the subscript “ $d$ ” on  $\varepsilon$ .

Different states in a multiplet can be distinguished by their angular momentum  $J$  and by the number  $n_p(n_d)$  of  $d$  bosons coupled pairwise (tripletwise) to  $J = 0$ . Sometimes one specifies not  $n_p$ , but the number of bosons *not* coupled to  $J = 0$ , and denotes this “boson seniority” quantum number by  $v$ . These states form a convenient basis set for the IBA and are illustrated in Fig. 6.24. Note that for  $n_d \geq 4$ , more than one state of a given  $J$  can occur.

$8^+(400)$	$6^+(400)$	$5^+(400)$	$4^+(400)$	$4^+(410)$	$2^+(401)$	$2^+(410)$	$0^+(420)$
$6^+(300)$	$4^+(300)$	$3^+(300)$	$2^+(310)$	$0^+(301)$			
$4^+(200)$	$2^+(200)$	$0^+(210)$					
$2^+(100)$			$U(5)$				
$0^+(000)$			$(n_d \ n_\beta \ n_\Delta)$				

Fig. 6.24. Basis states of the IBA. The  $U(5)$  limit (Casten, 1988a).

Having defined the basis states in this way, we can now consider more general IBA Hamiltonians composed of creation and destruction operators for  $s$  and  $d$  bosons limited to a maximum of two-body (boson) interactions. If we keep only those terms relevant to excitation energies (i.e., if we ignore terms contributing to binding energies), we can write

$$H = \varepsilon' n_d + \frac{1}{2} \sum_J C_J (\mathbf{d}^\dagger \mathbf{d}^\dagger)^{(J)} \cdot (\tilde{\mathbf{d}} \tilde{\mathbf{d}})^{(J)} + \frac{v_2}{\sqrt{10}} \left[ (\mathbf{d}^\dagger \mathbf{d}^\dagger)^{(2)} \cdot \tilde{\mathbf{d}} \mathbf{s} + \text{H.c.} \right] + \frac{v_0}{2\sqrt{5}} (\mathbf{d}^{(2)} \mathbf{s}^2 + \text{H.c.}) \quad (6.50)$$

where  $\varepsilon'$ ,  $C_J$ ,  $v_2$  and  $v_0$  are six free parameters. As we have discussed, the first term simply counts the number of  $d$  bosons and multiplies it by a  $d$  boson energy. This gives the unperturbed energy of a state with  $n_d$  noninteracting  $d$  bosons. The second group of three terms introduces interactions between pairs of  $d$  bosons that depend on the angular momentum to which they are coupled but that do not change the relative numbers of  $s$  and  $d$  bosons nor mix the basis states. The other terms have the property of changing the number of  $d$  bosons by  $\Delta n_d = \pm 1, \pm 2$ . These terms mix different basis states of a given  $J$  and, as in the analogous case of the shell model, it is this configuration mixing that leads to a build-up of collectivity and to the appearance of rotation-like behavior.

One often sees another equivalent form of the IBA Hamiltonian,

$$H = \varepsilon'' n_d + a_0 \mathbf{P}^\dagger \mathbf{P} + a_1 \mathbf{J}^2 + a_2 \mathbf{Q}^2 + a_3 \mathbf{T}_3^2 + a_4 \mathbf{T}_4^2 \quad (6.51)$$

where

$$\begin{aligned} \mathbf{P} &= \frac{1}{2} \left( \tilde{\mathbf{d}}^2 - \mathbf{s}^2 \right) \\ \mathbf{T}_J &= \left( \mathbf{d}^\dagger \tilde{\mathbf{d}} \right)^{(J)}, \quad J = 0, 1, 2, 3, 4 \\ \mathbf{Q} &= \left( \mathbf{d}^\dagger \mathbf{s} + \mathbf{s}^\dagger \tilde{\mathbf{d}} \right) - \frac{\sqrt{7}}{2} \left( \mathbf{d}^\dagger \tilde{\mathbf{d}} \right)^{(2)} \\ n_d &= \sqrt{5} \mathbf{T}_0, \quad \hat{J} = \sqrt{10} \mathbf{T}_1 \end{aligned} \quad (6.52)$$

The operators in Eqs. 6.51 and 6.52 are convenient combinations of those in Eq. 6.50 that have simple physical interpretations in terms of, for example, boson pairing and quadrupole operators. The most important point to note in Eq. 6.51 is the  $\Delta n_d$  character of the various terms; those in  $\mathbf{n}_d$ ,  $\mathbf{J}^2$ ,  $\mathbf{T}_3^2$  and  $\mathbf{T}_4^2$  have  $\Delta n_d = 0$ ,  $\mathbf{P}^\dagger \mathbf{P}$  has  $\Delta n_d = 0, \pm 2$  contributions, while  $\mathbf{Q}^\dagger$  has  $\Delta n_d = 0, \pm 1, \pm 2$  parts.

An important aspect of IBA predictions focuses on E2 transitions. The relevant operator,  $T(E2)$ , is simply related to  $\mathbf{Q}$  in Eq. 6.52, by

$$\mathbf{T}(E2) = e_B \mathbf{Q} = e_B [s^\dagger \mathbf{d} + \mathbf{d}^\dagger s + \chi (\mathbf{d}^\dagger \mathbf{d})^2] \quad (6.53)$$

where  $e_B$  is a boson charge similar to the effective charge for fermions and is often treated as a free parameter. In the original IBA formalism, the parameter  $\chi$  in  $\mathbf{Q}$  is fixed at  $\chi = -\sqrt{7}/2$  in the Hamiltonian and treated as a free parameter in  $\mathbf{T}(E2)$ . An alternate formalism, the *consistent Q formalism* (CQF), uses the same  $\chi$  in both  $H$  and  $T(E2)$ , which leads to certain simplifications and to a clearer physical picture of this model. This formalism will be discussed shortly.

We have stated that the  $s$  and  $d$  boson structure of the IBA leads to a six dimensional space and hence to a description in terms of the unitary group  $U(6)$ . We shall not delve into the group theory of the IBA in any detail, but a few ideas are useful to understand how the symmetries so characteristic of this model arise. Much of the following discussion is based on a recent review by the author and D.D. Warner to which the reader is referred for additional material on the IBA and its literature.

The basic concept underlying the group theory of the IBA is that of the “generators” of a group. These are sets of operators that “close on commutation” (i.e., the commutator of any pair  $[\mathbf{A}, \mathbf{B}] = \mathbf{AB} - \mathbf{BA}$  either vanishes or is proportional to another member of the group, or a linear combination thereof). For the IBA, the 36 operators  $s^\dagger s$ ,  $s^\dagger d_\mu$ ,  $d_\mu^\dagger s$  and  $(d_\mu^\dagger d_\mu)^J$  where  $J = 0, 1, 2, 3, 4$  and  $|\mu| \leq J$  satisfy this condition and are the generators of  $U(6)$ . As an example, we show this closure for the particular pair  $d^\dagger s$  and  $s^\dagger s$ .

Using Eqs. 6.2–6.4 we have

$$\begin{aligned} [d^\dagger s, s^\dagger s] |n_d n_s\rangle &= (d^\dagger s s^\dagger s - s^\dagger s d^\dagger s) |n_d n_s\rangle \\ &= d^\dagger s n_s |n_d n_s\rangle - s^\dagger s d^\dagger s |n_d n_s\rangle \end{aligned}$$

or, since  $n_s$  is just a number and is factorable

$$\begin{aligned} &= (n_s - s^\dagger s) d^\dagger s |n_d n_s\rangle \\ &= (n_s - s^\dagger s) \sqrt{n_d + 1} \sqrt{n_s} |n_d + 1, n_s - 1\rangle \\ &= \sqrt{n_d + 1} \sqrt{n_s} [n_s - (n_s - 1)] |n_d + 1, n_s - 1\rangle \\ &= \sqrt{n_d + 1} \sqrt{n_s} |n_d + 1, n_s - 1\rangle \\ &= d^\dagger s |n_d, n_s\rangle \end{aligned}$$

or

$$[\mathbf{d}^\dagger \mathbf{s}, \mathbf{s}^\dagger \mathbf{s}] = \mathbf{d}^\dagger \mathbf{s} \quad (6.54)$$

The other commutators can be similarly evaluated and indeed close on commutation. This set of 36 generators of the group of transformations of U(6) is said to form a Lie algebra.

Another key concept is that of a *Casimir operator* of a group. This is an operator that commutes with *all* of the generators of the group. Such operators can be composed of linear or higher order combinations of the generators and are appropriately called linear, quadratic,... Casimir operators.

The linear Casimir operator of U(6), which commutes with all 36 generators, is the total boson number operator  $\mathbf{N} \equiv \mathbf{d}^\dagger \mathbf{d} + \mathbf{s}^\dagger \mathbf{s}$  whose eigenvalue is  $N$ . This result follows trivially from the fact that all 36 combinations of the  $\mathbf{s}$  and  $\mathbf{d}$  operators must conserve the total boson number. For example,

$$\begin{aligned} [\mathbf{N}, \mathbf{s}^\dagger \tilde{\mathbf{d}}] \psi &= \mathbf{N}(\mathbf{s}^\dagger \tilde{\mathbf{d}}) \psi - (\mathbf{s}^\dagger \tilde{\mathbf{d}} \mathbf{N}) \psi \\ &= \mathbf{N}(\mathbf{s}^\dagger \tilde{\mathbf{d}}) \psi - \mathbf{N}(\mathbf{s}^\dagger \tilde{\mathbf{d}}) \psi = 0 \end{aligned}$$

Suppose now that some smaller set of operators also closes on itself under commutation. This set forms the generators of a smaller subgroup of U(6). It will have linear and/or quadratic Casimir operators associated with it that commute with all the generators of the subgroup. There are several subgroups for U(6), so the reduction process continues until the rotational subgroup O(3) is reached.

It is now necessary to find the quantum numbers that label the states. In general, the generators of a group may change some quantum numbers (e.g.,  $n_d$ ) but there will be one (or more) that are *not* changed by *any* of the generators. For U(6), the 36 generators always conserve  $N$ . The set of basis states that have a particular fixed value of an unchanged quantum number (or numbers) is called an *irreducible representation* of the group.

Since the generators of a given group cannot connect different irreducible representations, the Casimir operator(s) of a group that commute with all the generators by definition must be diagonal and therefore must conserve all quantum numbers, including those of the subgroups. Indeed, each Casimir operator has eigenvalues that are functions only of the conserved quantum numbers of the particular subgroup. Thus we have the central result that a Hamiltonian consisting of Casimir operators of a group and subgroups cannot mix different representations of any of the groups involved. Furthermore, its eigenvalues are simple linear combinations of its component Casimir operator eigenvalues and are functions of the quantum numbers characterizing each group and subgroup. Since the quantum numbers characterizing a subgroup are constant for all the states of the particular representation it defines, all the states of that representation must be degenerate. This degeneracy is broken only by the next step in the chain, which classifies the levels according to another quantum number (for a subsequent subgroup). This whole process is illustrated for one of the group chains (the so-called O(6) limit) of the IBA in Fig. 6.25. The precise meanings of the quantum numbers and eigenvalue terms will be clarified shortly. The key point here is the successive degeneracy

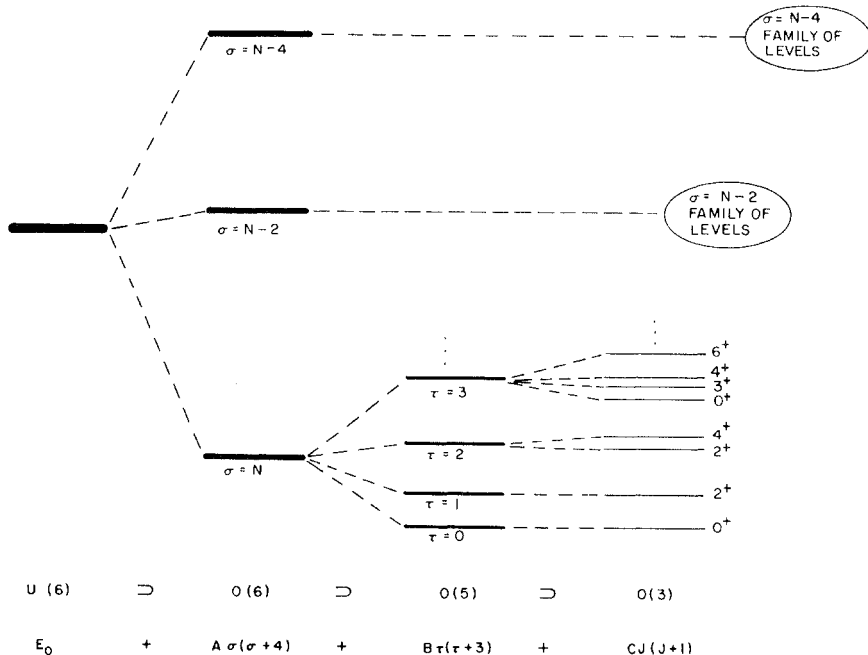


**Fig. 6.25.** Illustration (using the  $O(6)$  symmetry) of the successive degeneracy breaking in a dynamical symmetry group chain (Casten, 1988a).

breaking and the classification of sets of states (representations) of each subgroup by specific quantum numbers. Another important result is now also obvious: a transition operator consisting of generators of a given group or subgroup cannot connect states in different representations of that group. This leads to many essential selection rules.

A central task in developing any group chain or group reduction scheme is to identify the quantum numbers that label the irreducible representations of each subgroup. This is the basic procedure followed in the algebraic treatment of the IBA. Group chains are constructed starting from  $U(6)$ , where all the states are degenerate for a given value of  $N$ , and ending with  $O(3)$ . A Hamiltonian for any such chain is written as a sum over the Casimir operators of the subgroups of the specific chain, and is therefore diagonal in a basis defined by the corresponding representation labels. Each step in the chain reduction introduces one or more free parameters (coefficients of terms in  $H$ ) into the eigenvalue expression and requires one or more quantum numbers to distinguish the representations of the particular subgroup; it also breaks a previous degeneracy. Thus, the solution of the eigenvalue problem for such a chain reduces to that of the (known) eigenvalues of each of the Casimir operators.

The structure defined by such a Hamiltonian is referred to as a *dynamical symmetry*. One of the elegant aspects of these symmetries is that the excitation

energy spectrum can be written down immediately and each state can be labeled by appropriate quantum numbers even though these symmetries may correspond to a complex physical situation and, in terms of Eq. 6.51, to a complex Hamiltonian. Since transition operators can often be written in terms of the group generators, transition selection rules appear naturally, and the rates for allowed transitions can be written analytically. Moreover, many ratios of transition rates depend only on general characteristics of the symmetry (group chain) and are parameter free. This should not be surprising: the Alaga rules for E2 branching ratios in deformed nuclei are a familiar geometrical analogue.

Returning now to the basic problem in the IBA, there are exactly three group chains of U(6) that end in O(3), which is the rotation group. This group is a necessary subgroup in any physical chain because it provides for rotational invariance. The three group chains can be written, along with their relevant quantum numbers (see discussion to follow) as:

$$\text{I. } \begin{array}{cccccc} U(6) & \supset & U(5) & \supset & O(5) & \supset O(3) \\ N & & n_d & & v & & n_\Delta J & & U(5) \\ & & & & & & & & (6.55) \end{array}$$

$$\text{II. } \begin{array}{cccccc} U(6) & \supset & SU(3) & \supset & O(3) & & SU(3) \\ N & & (\lambda, \mu) & & KJ & & (6.56) \end{array}$$

$$\text{III. } \begin{array}{cccccc} U(6) & \supset & O(6) & \supset & O(5) & \supset O(3) & O(6) \\ N & & \sigma & & \tau & & v_\Delta J \\ & & & & & & (6.57) \end{array}$$

We now discuss each of these symmetries in turn.

### I. U(5)

The U(5) symmetry is the IBA version of a vibrator. Its representation labels were already introduced, since this limit provides the basis states used in most treatments of the general IBA Hamiltonian.

The eigenvalues of U(5) are

$$E(n_d, v, J) = \alpha n_d + \beta n_d(n_d + 4) + 2\gamma v(v + 4) + 2\delta J(J + 1) \quad (6.58)$$

where  $\alpha, \beta, \gamma$ , and  $\delta$  are parameters. A harmonic version of U(5) was illustrated in Fig. 6.24. Note, however, that U(5) is a very rich symmetry and allows much anharmonicity. The degenerate multiplets with a given value of  $n_d$  include levels with different values of  $v, J$  and the energies can depend on these quantum numbers. The U(5) wave functions, of course, are trivial. Since they are themselves the normally-used IBA basis states, each wave function has but a single term. Even highly anharmonic U(5) spectra maintain the same simple wave functions: the anharmonicity is a diagonal effect on the energies and does not lead to mixing of the basis states.

An interesting result concerning the anharmonicity follows from the Hamiltonian for U(5) written in the form of Eq. 6.50. Here U(5) includes all terms with  $\Delta n_d = 0$ . Although the interactions that break the degeneracies may

appear to be complex, they never involve higher order interactions in  $\mathbf{d}$  and  $\mathbf{s}$  boson operators (i.e., operators such as  $(\mathbf{d}^\dagger \mathbf{d}^\dagger \mathbf{d}^\dagger)(\mathbf{d}\mathbf{d}\mathbf{d})$ ). Thus the anharmonicities, *whatever* they may be, arise from two-body interactions. This is exactly the ansatz used to discuss the relationship between three-phonon and two-phonon energies in the anharmonic vibrator model earlier. In neither case are the results dependent on the details of the interactions, but only on the *number* of the interacting entities. Thus, these same relationships, listed in Table 6.4, characterize the U(5) limit. No choices of U(5) parameters can violate them.

In each symmetry that we shall discuss, key signatures and tests are provided by E2 transitions. So it is useful to summarize some typical results for each.

The operator  $T(E2)$  has a term that changes  $n_d$  by  $\pm 1$ , and a term with  $\Delta n_d = 0$ . If  $T(E2)$  is chosen to be a generator of U(5), only the latter term is used. (Since  $n_d$  is a good quantum number in U(5), a generator of U(5) cannot change  $n_d$ .) The predicted E2 matrix elements would then vanish between states differing by  $\pm 1 d$  boson, while they would yield nonzero diagonal contributions (quadrupole moments). This situation is essentially the inverse of what is expected and observed for vibrational nuclei, making it customary to use the first term of the E2 operator in the U(5) limit, as this term produces results similar to those of the geometric vibrational picture.

For example, one obtains the general result

$$\sum_{J'} B(E2; J, n_d + 1 \rightarrow J', n_d) = e_B^2 (n_d + 1) (N - n_d) \quad (6.59)$$

The sum on the left side of Eq. 6.59 accounts for the distribution of strength from a given initial state if the angular momentum selection rules allow decay to more than one level of the next lower multiplet. This sum contains more than one term only for decay of  $n_d \geq 3$  states, and is identical in origin to the sum in the phonon model expression, Eq. 6.6.

The factor  $(n_d + 1)$  in Eq. 6.59 is analogous to the phonon model result proportional to  $(N_{ph} + 1)$ . The factor  $(N - n_d)$  in the IBA case has no analogue in the phonon model and arises specifically from the finite boson number. Its origin can easily be seen. The matrix element  $\langle n_d, n_s | s^\dagger \tilde{\mathbf{d}} | n_d + 1, n_s - 1 \rangle$  can be calculated as:

$$\begin{aligned} \langle n_d, n_s | s^\dagger \tilde{\mathbf{d}} | n_d + 1, n_s - 1 \rangle &= \sqrt{(n_d + 1)} \sqrt{n_s} \langle n_d, n_s | n_d, n_s \rangle \\ &= \sqrt{(n_d + 1)} \sqrt{n_s} = \sqrt{(n_d + 1)} \sqrt{N - n_d} \end{aligned} \quad (6.60)$$

In terms of the number of quadrupole excitations only (i.e.,  $d$  bosons or quadrupole phonons) the U(5) limit and the geometrical vibrator are identical. The  $2_1^+$  level has one such excitation, the levels of the  $0^+, 2^+, 4^+$  triplet have two, and so on. The difference is that, in such excitations in the IBA, the restriction to a finite fixed  $N$  imposes another complementary constraint on the number of  $s$  bosons, which gives rise to the second factor on the right in Eqs. 6.59 and

6.60. In the phonon model, a creation (or destruction) of a phonon takes place in isolation: the transition rate is related to the number of phonons available. However, in going from one U(5) representation to another in the IBA, the creation (or destruction) of a  $d$  boson *must* involve the destruction (or creation) of an  $s$  boson to conserve  $N$ . As  $n_d$  grows, there are fewer available  $s$  bosons, and the  $s$  boson factor  $n_s$  (or  $N - n_d$ ) decreases. In an  $(n_d + 1) \rightarrow n_d$  transition in the IBA, larger  $n_d$  values facilitate the transition (there is more freedom in choosing a particular  $d$  boson to destroy) but the smaller number of  $s$  bosons hinders the transition. These two counterbalancing aspects are reflected in the two factors in Eqs. 6.59 and 6.60.

Equation 6.59 gives, for the transitions between the lowest levels,

$$B(E: 2: 2^+_1 \rightarrow 0^+_1) = e_B^2 N \quad (6.61)$$

and

$$B(E: 2: 2^+_2 \rightarrow 2^+_1) = 2e_B^2(N-1) \quad (6.62)$$

The ratio of these two equations gives the useful result

$$R = \left( \frac{B(E: 2: 2^+_2 \rightarrow 2^+_1)}{B(E: 2: 2^+_1 \rightarrow 0^+_1)} \right)_{U(5)} = \left( \frac{N-1}{N} \right) \left( \frac{B(E: 2: 2^+_2 \rightarrow 2^+_1)}{B(E: 2: 2^+_1 \rightarrow 0^+_1)} \right)_{\text{Phonon}} \quad (6.63)$$

Since U(5) is usually relevant only near closed shells where  $N$  is rather small, differences with the geometric model can be significant. For example, Eq. 6.63 gives  $R = 1.6$  for  $N = 5$ , compared to  $R = 2.0$  for the geometric picture. Finally, when the initial state is the fully aligned  $J = 2N$  excitation, the factor  $(N - n_d)$  is reduced to unity. This is an example of the well-known cutoff effect in  $B(E2)$  values involving high spin states, which is another characteristic distinction of the IBA from geometric models.

Whenever some model predicts a symmetry, it is always a critical test to search for empirical examples. This is particularly true for the IBA since it is so intimately connected with the concept of dynamical symmetry. Searches for U(5)-like nuclei naturally focus on those regions where the geometric vibrational model is also appropriate. The nucleus  $^{118}\text{Cd}$  has recently been proposed as a near-harmonic empirical manifestation of U(5). Its level scheme was shown in Fig. 6.9. The E2 selection rules for U(5) (identical to the vibrator) are clearly well-satisfied, and the small anharmonicities in the two-phonon states reasonably account for the three-phonon anharmonicity. It is also possible to fit many nuclei with more highly anharmonic U(5) energy spectra but strong disagreements with the U(5) E2 selection rules and branching ratios nearly always result.

## II. SU(3)

This symmetry is the IBA version of a deformed rotor, but with special characteristics that distinguish it from its geometric analog. The SU(3) limit is

obtained when the  $\mathbf{Q}^2$  term dominates in Eq. 6.51 (a  $\mathbf{J}^2$  term may also be present). Thus

$$H = a_2 \mathbf{Q}^2 + a_J \mathbf{J}^2 \quad (6.64)$$

Here, for  $\mathbf{Q}$  to be a Casimir operator of  $SU(3)$ ,  $\chi$  must equal  $-\sqrt{7}/2$ . We saw before that  $\mathbf{Q}^2$  strongly mixes  $U(5)$  basis states with  $\Delta n_d = 0, \pm 1, \pm 2$ . Therefore,  $SU(3)$  wave functions are no longer simple in terms of an expansion in  $U(5)$ . On the contrary, they are rather complex, and certainly not very physically transparent, combinations of many  $U(5)$  states. The simplicity of  $SU(3)$ , or any IBA symmetry, results from its geometrical structure, from the analytic nature of many results, and from simple selection rules, despite the fact that the wave functions, when expressed in the basis of *another* symmetry, may be complex. Such complexity signals only that the symmetries are different from each other, not that one is more complicated than any of the others. Nevertheless, one gets an insight into the symmetry structure by explicitly showing some wave functions in the same basis. This is done for all three symmetries in a  $U(5)$  basis in Table 6.12.

On account of the mixing of basis states with different  $n_d$  values in  $SU(3)$ , the expectation values of the operator  $(\mathbf{d}^\dagger \mathbf{d})^0 = n_d$  are very different in  $SU(3)$  and  $U(5)$ . They are shown for the ground band states in Fig. 6.26 along with the values for  $O(6)$ . In  $U(5)$ ,  $\langle n_d \rangle = 0, 1, 2, \dots$  etc., up to  $\langle n_d \rangle = N$ . In  $SU(3)$ ,  $\langle n_d \rangle$  is already substantial in the ground state. This has three important effects that we can see without detailed calculation. First, any effects of finite boson number will be relatively larger in the  $SU(3)$  ground state than in  $U(5)$ . Second, since in both cases  $\langle n_d \rangle_{\max} = N$ , the expectation value of  $n_d$  must increase *slower* with  $J$  in  $SU(3)$  than in  $U(5)$ . This will have important consequences for certain  $B(E2)$  values that, we shall see, will increase more

**Table 6.12.** Wave functions expressed in the  $U(5)$  basis for the first three  $0^+$  states in each limit of the IBA

State*	Limit	Basis States ( $n_d n_\beta n_\Delta$ )						
		(000)	(210)	(301)	(420)	(511)	(602)	(630)
$0^+_1$	$U(5)$	1	0	0	0	0	0	0
	$O(6)$	-.43	-.75	0	-.491	0	0	-.095
	$SU(3)$	.134	.463	-.404	.606	-.422	-.078	.233
$0^+_2$	$U(5)$	0	1	0	0	0	0	0
	$O(6)$	.685	.079	0	-.673	0	0	-.269
	$SU(3)$	.385	.600	-.204	-.175	.456	.146	-.437
$0^+_3$	$U(5)$	0	0	1	0	0	0	0
	$O(6)$	0	0	-.866	0	-.463	0	0
	$SU(3)$	-.524	-.181	-.554	.030	-.114	-.068	-.606

\*The states are ordered for pedagogical clarity and not necessarily in the order of increasing energy: indeed, the  $\tau = 3$   $0^+$  state in  $O(6)$  (here labeled  $0^+_3$ ) is usually the  $0^+_2$  state.

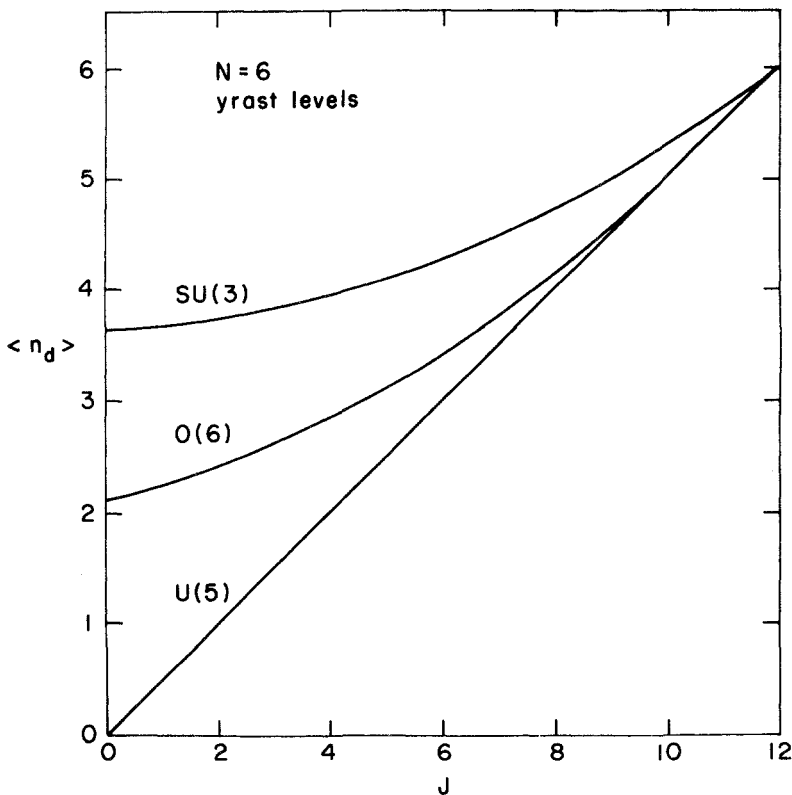


Fig. 6.26. Expectation values of  $n_d$  in the ground band in the three limits of the IBA (Casten, 1988a).

slowly with  $J$  in SU(3) than in U(5). Third, in U(5),  $\langle n_d \rangle$  for a given state is independent of  $N$ , while in SU(3), it is roughly proportional to  $N$ . This has enormously important effects on collective E2 transitions.

The SU(3) energies are given in terms of quantum numbers of the group chain II of Eq. 6.56

$$E(\lambda, \mu, J) = \frac{a_2}{2} (\lambda^2 + \mu^2 + 3\lambda\mu + 3(\lambda+\mu)) + \left(a_1 - \frac{3}{8}a_2\right)J(J+1) \quad (6.65)$$

where  $a_1, a_2$  are the coefficients of the multipole form of the Hamiltonian of Eq. 6.51. Each set of  $(\lambda, \mu)$  values defines a representation of the subgroup of SU(3) and corresponds to a set of one or more rotational bands. Each band is characterized by a quantum number, sometimes denoted  $K'$ , which is almost identical to the usual  $K$  projection quantum of geometrical shape models. (Technically, some SU(3) states contain small admixtures of other  $K$  values; this has notable effects on certain  $B(E2)$  values since it is a bandmixing effect, but as far as the wave functions are concerned, it is an excellent (and useful)

approximation to ignore these mixtures and use the usual notation  $K$ .) The rule that determines the  $K$  values that occur in a given  $(\lambda, \mu)$  representation is  $K = 0, 2, \dots \min(\lambda, \mu), K$  even. For typical values of  $a_2 < 0$ , the ground state band has  $(\lambda, \mu) = (2N, 0)$ . The next representations are  $(\lambda, \mu) = (2N - 4, 2)$  with  $K = 0, 2$  bands,  $(2N - 8, 4)$  with  $K=0, 2, 4$  bands; and  $(2N - 6, 0)$  with a single  $K = 0$  band. These states are illustrated in Fig. 6.27. The similarities to a deformed rotor are clear: we see sequences of states resembling a ground state band,  $\beta$  and  $\gamma$  vibrational bands, and bands that can be characterized as the  $\beta\beta(K = 0)$ ,  $\beta\gamma(K = 2)$ , and  $\gamma\gamma(K = 0, 4)$  two-phonon intrinsic excitations. However, we note two specific features, exemplified by the  $\beta$  and  $\gamma$  bands, that distinguish SU(3) from a general deformed rotor and act as characteristic signatures for the symmetry. They are schematically shown in Fig. 6.28. Since the  $\beta$  and  $\gamma$  bands appear in the same representation, states of the same spin of these two bands must have the same energies. Thus, SU(3) is a *special* case of a deformed rotor with degenerate  $\beta$  and  $\gamma$  bands. We stated that a transition operator consisting of the Casimir operators of a subgroup cannot connect different representations. Therefore, in the SU(3) limit, the E2 operator with  $\chi = -\sqrt{7}/2$  cannot lead to transitions from either the  $\beta$  or  $\gamma$  bands to the ground band! This is in direct contrast to the usual picture of harmonic collective  $\beta$  and  $\gamma$  vibrations in deformed nuclei. Moreover, since these bands are in the same representation, the E2 operator leads to *allowed*, collective  $\gamma \rightarrow \beta$  E2 transitions, again violating the  $\Delta N_{ph} = \pm 1$  selection rule of geometrical models.

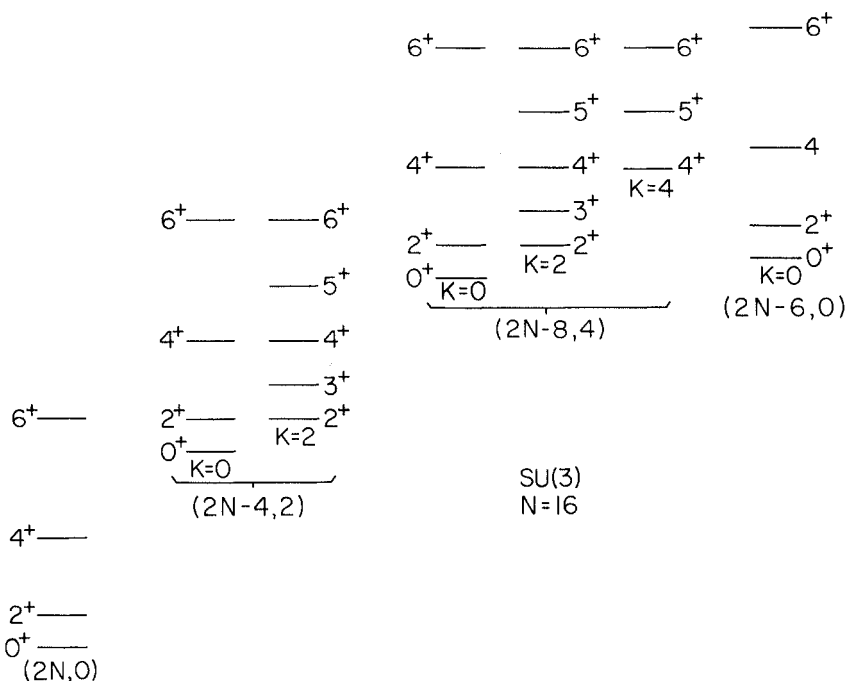


Fig. 6.27. Characteristic spectrum of SU(3) (Casten, 1988a).

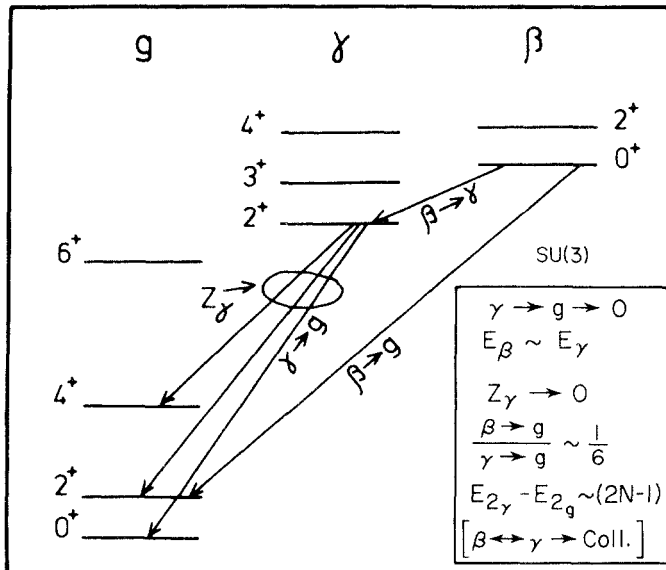


Fig. 6.28. Characteristic signatures of SU(3) (Casten, 1985b).

Given decades of success of the latter model, this would appear to be an argument against the IBA. However, neither the issue nor the data is as simple as at first appears, and both approaches can be made more or less mutually consistent. We will discuss this shortly to help us to better understand the IBA.

There are three more distinguishing characteristics of the SU(3) symmetry shown in Fig. 6.28. Since there is no connection between representations, there can be no  $\gamma$ - $g$  or  $\beta$ - $g$  bandmixing.  $Z_\gamma(Z_\beta)$  are effectively zero in SU(3). And, although both  $\beta \rightarrow g$  and  $\gamma \rightarrow g$  E2 transitions vanish in SU(3), they have a finite ratio. Specifically,

$$\frac{B(E2: 2^+_\beta \rightarrow 0^+_g)}{B(E2: 2^+_\gamma \rightarrow 0^+_g)} \sim \frac{1}{6}$$

Finally, we see from Eq. 6.65 that if we substitute  $(\lambda, \mu) = (2N, 0)$  and  $(2N-4, 2)$  for the ground and  $\gamma$  intrinsic excitations, we obtain the energy difference  $E_\gamma(J) - E_g(J) \propto (2N-1)$ —the  $\gamma$ vibrational energy *increases* with  $N$  in SU(3) towards midshell.

We note that in Fig. 6.28, the collectivity of  $\beta \rightarrow \gamma$  transitions is enclosed in brackets because it persists even with large SU(3) symmetry breaking and, as such, cannot properly serve as a specific signature of the limiting symmetry. It does, however, distinguish the IBA from harmonic geometrical models.

A few specific results of SU(3) are useful to cite for practical applications. The parameters  $a_2$  and  $a_1$  of the eigenvalue expression may be written in terms of specific level energies by inserting appropriate values of  $\lambda$  and  $\mu$ . One obtains, for example,

$$a_2 = \frac{E_{2\gamma} - E_{2\dagger}}{3(2N-1)}, \quad a_1 = \frac{E_{2\dagger}}{6} + \frac{3}{8}a_2 \quad (6.66)$$

Ground band B(E2) values are given by

$$B(E2:J+2 \rightarrow J) = e_B^2 \frac{3}{4} \left[ \frac{(J+2)(J+1)}{(2J+3)(2J+5)} \right] (2N-J)(2N+J+3) \quad (6.67)$$

Hence,

$$B(E2:2_1^+ \rightarrow 0_1^+) = e_B^2 \frac{N(2N+3)}{5} \quad (6.68)$$

Note that these go as  $N^2$  for large  $N$ , in direct contrast with the linearity in  $N$  characteristic of U(5). The reason is obvious and has already been hinted at. The U(5) B(E2) values scale as  $N$  because of the  $(N - n_d)$  factor in Eq. 6.59. The  $n_d$  factor is independent of  $N$  because a given pair of U(5) states (e.g.,  $2_1^+$  and  $0_1^+$ ) always have the *same* pair of  $n_d$  values (e.g., 1 and 0, respectively) regardless of  $N$ . In SU(3), the  $\mathbf{d}$ 's and  $\mathbf{s}^\dagger \mathbf{d}$  operators in T(E2) give factors involving  $N$  from *both* operators in each pair, because, as we just saw, both  $n_d$  and  $n_s$  increase with  $N$ . So, a dependence on  $N$  enters twice, leading to the  $\sim N^2$  dependence.

Finally, we note, from direct substitution in Eq. 6.67, an interesting result that we can illustrate by the ratio

$$\frac{B(E2:4_1^+ \rightarrow 2_1^+)}{B(E2:2_1^+ \rightarrow 0_1^+)} = \frac{10}{7} \left[ \frac{(2N-2)(2N+5)}{(2N)(2N+3)} \right] \quad (6.69)$$

The first factor is the rotational model Alaga rule. The second factor is (another example of) an  $N$ -dependent finite boson number effect, which means that *even* in the strict SU(3) limit, B(E2) ratios deviate from the Alaga rules. Note that the second factor goes to unity as  $N \rightarrow \infty$ . That its predictions go over into those of the usual geometrical models for large  $N$  is a characteristic feature of the IBA. Many of the unique aspects of the model (such as allowed, collective  $\beta \rightarrow \gamma$  E2 transitions) stem directly from the explicit incorporation of finite  $N$ , which in turn, reflects the model's emphasis on the valence space.

Since SU(3) is such a specific type of deformed rotor, we already recognize that it does not characterize most deformed nuclei since such nuclei exhibit nondegenerate  $\beta$  and  $\gamma$  bands, collective  $\beta \rightarrow g$  and (especially)  $\gamma \rightarrow g$  transitions, and finite  $Z_\gamma$ . (See Fig. 6.29.) Moreover, in the first half of the deformed rare earth region  $E_\gamma(J) - E_g(J)$  actually decreases rather than displaying a proportionality to  $(2N-1)$ . We will consider shortly how the IBA can treat such nuclei. First we ask if there are *any* nuclei that do display the limiting characteristics of SU(3). The answer is (probably) yes, the rare earth isotopes of Yb and Hf near neutron number  $N = 104$ . The empirical evidence is displayed in Figs. 6.29 and 6.30, where each of the signatures of SU(3) is approached in the same general  $N, Z$  region (and in no other). At the same time, it is clear that no single nucleus in the  $N = 104$  region displays all the

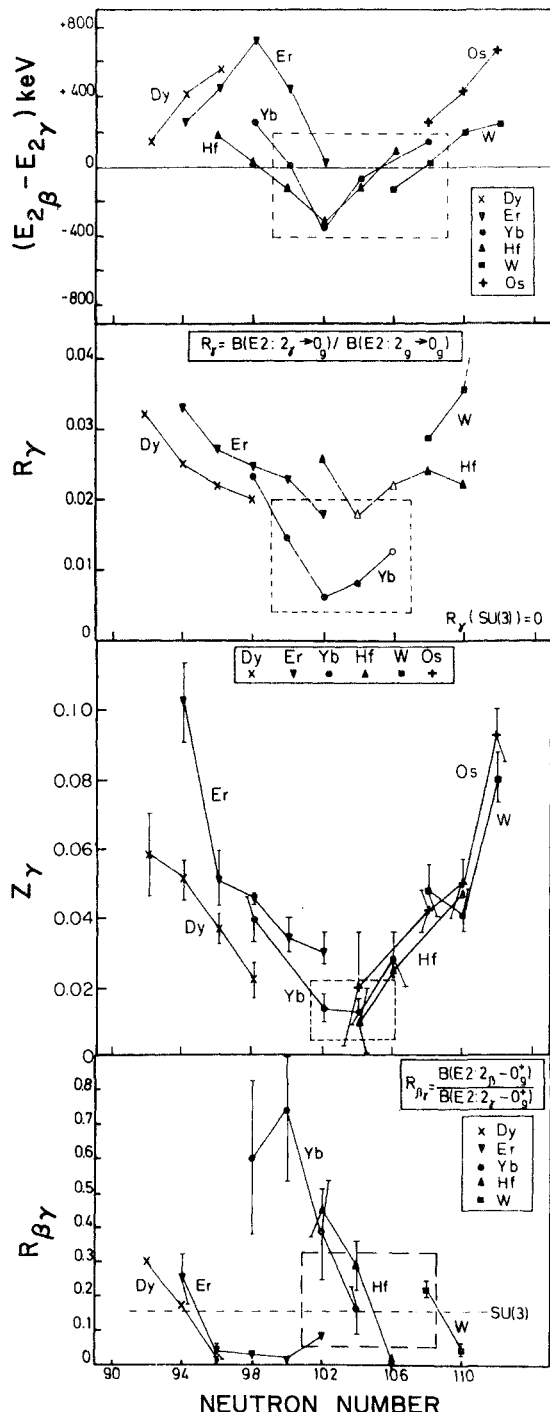


**Fig. 6.29.** Empirical evidence relative to four of the SU(3) signatures near  $N = 104$  (Casten, 1985b).

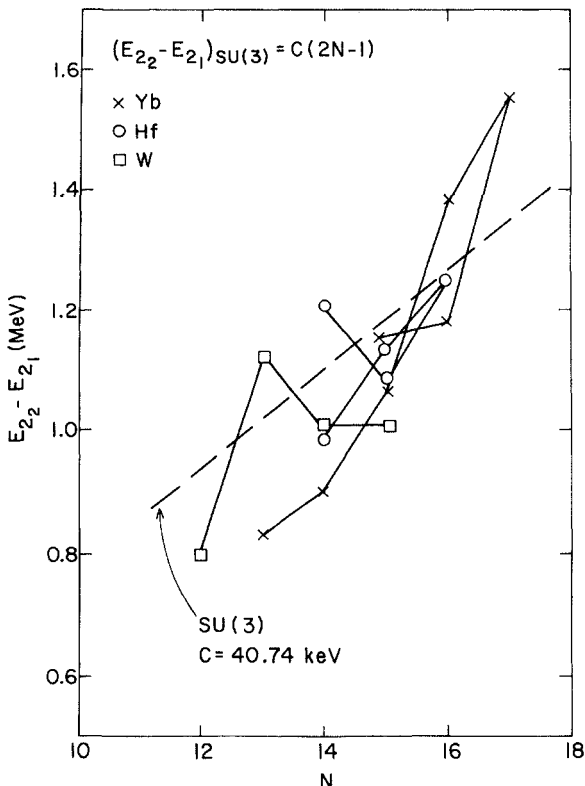


Fig. 6.30. Comparison of empirical and SU(3) values for  $E_{2_2^+} - E_{2_1^+}$  in the rare earth region (Casten, 1988a).  $N$  is the boson number.

SU(3) characteristics. Moreover, some of these same empirical features (high intrinsic  $K = 2$  energies, weak  $B(E2: \gamma \rightarrow g)$  values, small bandmixing) also characterize high-lying noncollective two-quasi-particle excitations. Thus the evidence is ambiguous, although the author feels that it points toward an *underlying* SU(3) character that may be mixed with noncollective degrees of freedom; the coincidence of signatures is too significant to be dismissed as fortuitous.

### III. O(6)

The O(6) symmetry is the least familiar geometrically, although it is now recognized as corresponding to a deformed, axially-asymmetric but  $\gamma$  soft rotor, the Wilets-Jean model. The O(6) Hamiltonian is

$$H = a_0 \mathbf{P}^\dagger \mathbf{P} + a_1 \mathbf{J}^2 + a_3 \mathbf{T}_3^2 \quad (6.70)$$

and the eigenvalue equation is

$$E(\sigma, \tau, J) = A(N-\sigma)(N+\sigma+4) + B\tau(\tau+3) + J(J+1) \quad (6.71)$$

where  $A = a_0/4$ ,  $B = a_3/2$  and  $C = a_1 - a_3/10$  (one sometimes encounters a notation with coefficients  $A/4$  and  $B/6$ ). The characteristic quantum numbers are  $\sigma$  for the O(6) group and  $\tau$  for the U(5) subgroup. A typical O(6) spectrum was used to illustrate the idea of a group chain in Fig. 6.25, and is shown more completely (for  $N=6$ ) in Fig. 6.31. The lowest levels (for  $A, B > 0$ ) have  $\sigma = N$ , and  $\tau = 0, 1, 2, \dots$ . For each value of  $\tau \geq 2$ , there is a multiplet of states whose degeneracy is broken by the  $J(J+1)$  term. For  $\tau = 2$ , there are only  $2^+$  and  $4^+$  levels, and no triplet as in U(5). Major families of O(6) levels are grouped and characterized according to  $\sigma$ , and within each family, by  $\tau$  (and  $J$ , of course). Note the characteristic behavior within a  $\sigma$  family: energies of states with the same  $\tau$  are monotonic in  $J$  (usually decreasing with  $J$  since  $C > 0$ ) and splittings increase rapidly with  $\tau$ . The ground band or yrast levels increase as  $\tau(\tau+3) = (J/2)(J/2+3) \propto J(J+6)$  as in the Wilets-Jean model. As noted for the corresponding geometric models, this increase is faster than in U(5) where  $E(J) \propto J$ , and slower than in SU(3) where  $E(J) \propto J(J+1)$ . These relative ground band energies may be summarized

$$E_2 : E_4 : E_6 : E_8 := \begin{cases} E_{n_d=1} : E_{n_d=2} : E_{n_d=3} : E_{n_d=4} = 1 : 2 : 3 : 4 & \text{U}(5) \\ E_{\tau=1} : E_{\tau=2} : E_{\tau=3} : E_{\tau=4} = 1 : 2.5 : 4.5 : 7 & \text{O}(6) \\ E_{J=2} : E_{J=4} : E_{J=6} : E_{J=8} = 1 : 3.33 : 7 : 12 & \text{SU}(3) \end{cases} \quad (6.72)$$

These expressions are identical to those of the vibrator, Wilets-Jean, and rotor models shown in Fig 6.21. Despite the apparent differences in ground band energies for each of the symmetries, it is important to recall that the curves in Fig. 6.21 are defined by the characteristic quantum number  $n_d$ ,  $\tau$ , and  $J$  for U(5), O(6), and SU(3), respectively. For U(5) and O(6), however, there is also a separate  $J(J+1)$  term in the Hamiltonian and, depending on the strength of its coefficient, the actual ground band energies in these two symmetries can be made to resemble each other or SU(3) itself.

In terms of the U(5) basis states, the nondiagonal term in  $H_{O(6)}$  is  $\mathbf{P}^\dagger \mathbf{P}$ , which has  $\Delta n_d = 0, \pm 2$  matrix elements. Thus the wave functions are mixtures in a U(5) basis, but are not as complex as in SU(3). Table 6.12 illustrates this, showing that in O(6) the finite amplitudes always differ from each other by the addition of a zero coupled pair of  $d$  bosons for a given state. This implies that the number of *unpaired*  $d$  bosons is constant for a given state. It is zero for the  $0_1^+$  and  $0_2^+$  states, and 3 for  $0_3^+$ . But note that this quantity is just the boson seniority  $v$ , and in fact,  $\tau$  and  $v$  are identical. The use of different notations has historical origins only and no physical content. Indeed,  $v$  or  $\tau$  arise in U(5) and O(6) because both chains involve the same subgroup O(5). This has been the source of some confusion since the common occurrence of this subgroup means that many predictions of the two symmetries are identical. Differences between them do exist, but reside principally in transition rates, which depend on the detailed  $d$  boson structure and occur among higher-lying states belonging

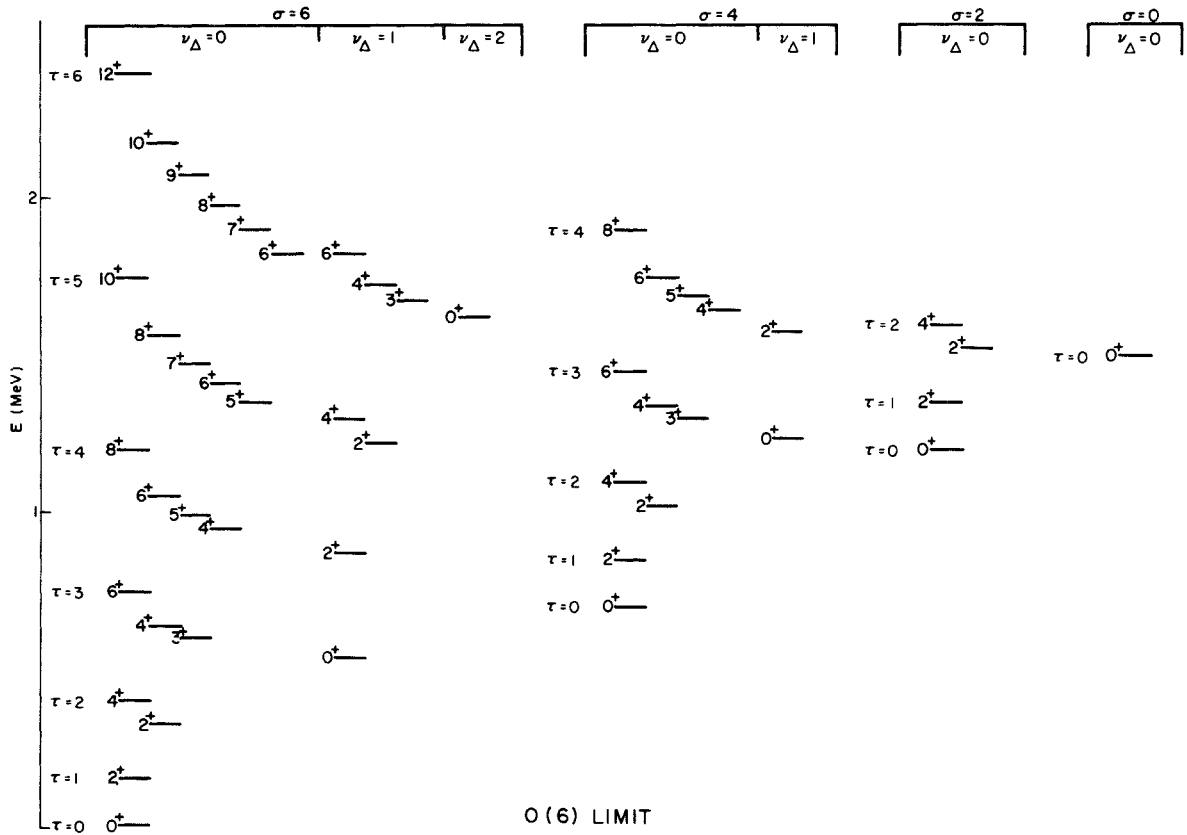


Fig. 6.31. Typical  $0(6)$  spectrum for  $N = 6$ .

ing to higher  $n_d$  multiplets in U(5) and to  $\sigma < N$  representations in O(6). (We shall return to this point momentarily).

The fact that  $\mathbf{P}^\dagger \mathbf{P}$  has only  $\Delta n_d = 0, \pm 2$  terms suggests that one might be able to construct O(6) wave functions in another way. We pointed out that the  $\mathbf{Q}^2$  term has  $\Delta n_d = 0, \pm 1, \pm 2$  components, but that if  $\chi = 0$ , it has only  $\Delta n_d = 0, \pm 2$  terms. Therefore, the Hamiltonian

$$H = a_2 \mathbf{Q}^2 + a_1 \hat{\mathbf{J}}^2 \quad (\text{with } \chi=0) \quad (6.73)$$

also produces O(6) wave functions and spectra. This Hamiltonian has only two terms, so it cannot give three independent terms in the eigenvalue equation. This way of producing O(6) thus leads to a special case of Eq. 6.71 where  $A = B$ . Although this is only one of an infinite set of possible  $A:B$  relations, it turns out to be the one empirically observed in O(6) nuclei, suggesting the usefulness of this alternate form for  $H_{\text{O}(6)}$ . We will see that this alternative is in fact one limiting case of the CQF that offers a simplified approach to many IBA problems. First, however, we need to delineate a few additional O(6) predictions. The E2 transition selection rules are clear from the form of the E2 operator that is a generator of O(6), namely

$$\mathbf{T}(\text{E2}) = e_B \left( \mathbf{s}^\dagger \tilde{\mathbf{d}} + \mathbf{d}^\dagger \mathbf{s} \right)$$

The allowed transitions must satisfy  $\Delta \sigma = 0$  and  $\Delta \tau = \pm 1$ . The first rule is a direct consequence of the fact that a generator of a group cannot connect different representations. It means that there are no allowed transitions from one  $\sigma$  family to another. Eventually, excited levels with  $\sigma < N$  must decay, but only by violations of the strict symmetry. This selection rule provides the most telling contrast with U(5). (See the following.) The  $\Delta \tau = \pm 1$  rule is similar to the  $\Delta N_{ph}$  or  $= \Delta n_d = \pm 1$  rules for the geometrical vibrator and U(5) limits. Naturally, B(E2) values between yrast states are allowed, and given by

$$B(\text{E2}; J+2 \rightarrow J) = B(\text{E2}; 2(\tau+2) \rightarrow 2\tau) = e_B^2 \left( N - \frac{J}{2} \right) \left( N + \frac{J}{2} + 4 \right) \left( \frac{\frac{J}{2} + 1}{J + 5} \right) \quad (6.74)$$

from which we get,

$$B(\text{E2}_1^+ \rightarrow 0_1^+) = e_B^2 \frac{N(N+4)}{5} \quad (6.75)$$

As in SU(3), B(E2) values in O(6) scale approximately as  $N^2$  for large  $N$ . The yrast B(E2) values are illustrated in Fig. 6.32.

There has recently been much discussion of the differences and similarities between O(6) and U(5). The level schemes in Figs. 6.24 and 6.31 appear very different. Specifically, U(5) has the well-known two-phonon triplet, while O(6) lacks the  $0^+$  state. On account of this difference, the first excited  $0^+$  state in U(5) decays to the  $2_1^+$  level, while the first excited  $0^+$  state in O(6) has  $\tau = 3$  and therefore decays to the  $2_2^+$  state. These distinctions have been used as evidence both for or against each of these symmetries. This issue is more subtle, however. Each figure embodies a specific choice of parameters ( $\alpha, \beta, \gamma$ ,

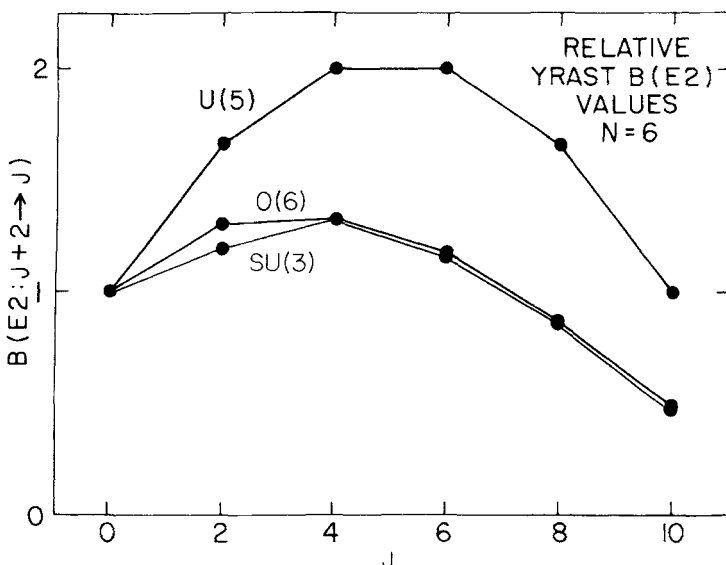


Fig. 6.32. Dependence of ground band  $B(E2)$  values on  $J$  in the three limits of the IBA.

$\delta$  for  $U(5)$  and  $A, B, C$  for  $O(6)$ ); indeed, the  $U(5)$  scheme is the harmonic limit. Actually, both symmetries permit a rich variety of level scheme configurations by appropriate choices of parameters. Since both group chains contain  $O(5)$  and  $O(3)$  subgroups, the only real structural differences center on the  $O(6)$  and  $U(5)$  parent groups. Thus, it turns out that the energies of the entire lowest representation of  $O(6)$ , with  $\sigma = N$ , can be exactly replicated in  $U(5)$ . To do so, the  $0_2^+$  (two-phonon or  $n_d = 2$ )  $U(5)$  level must be forced up in energy above the  $n_d = 3\ 0_3^+$  state in order to reproduce the  $O(6)$  decay pattern in which the first excited  $0^+$  state decays to the  $2_2^+$  level. Such an  $O(6)$ -like  $U(5)$  spectrum would be enormously anharmonic but still valid within the context of this dynamical symmetry.

The real difference between  $O(6)$  and  $U(5)$  occurs in two other realms: absolute transition rates and higher-lying levels. Table 6.12 shows that, though their energies may be identical, the  $U(5)$  and  $O(6)$  wave functions are completely different. Thus,  $B(E2)$  values will be different; in particular, the different expectation values of  $n_d$  imply different finite  $N$  effects. We have seen an example of this in the yrast  $B(E2)$  values in Fig. 6.32. In  $U(5)$ , the yrast band experiences greater changes in  $\langle n_d \rangle$  from state to state (see Fig. 6.26), and hence the  $B(E2)$  values change more rapidly with spin.

High-lying levels in  $U(5)$  have high  $n_d$  and decay to  $(n_d - 1)$  levels. There are many such  $(n_d - 1)$  states and thus many allowed E2 transitions. In  $O(6)$ , high-lying levels often belong to low  $\tau$  states of  $\sigma < N$  representations. These typically have only one allowed deexcitation transition—that permitted by the  $\Delta\tau = \pm 1$  selection rule.

$O(6)$  nuclei are now well known in two regions: the Pt isotopes, especially

QUANTUM NUMBERS  
 $(\sigma, \tau, \nu_\Delta)$

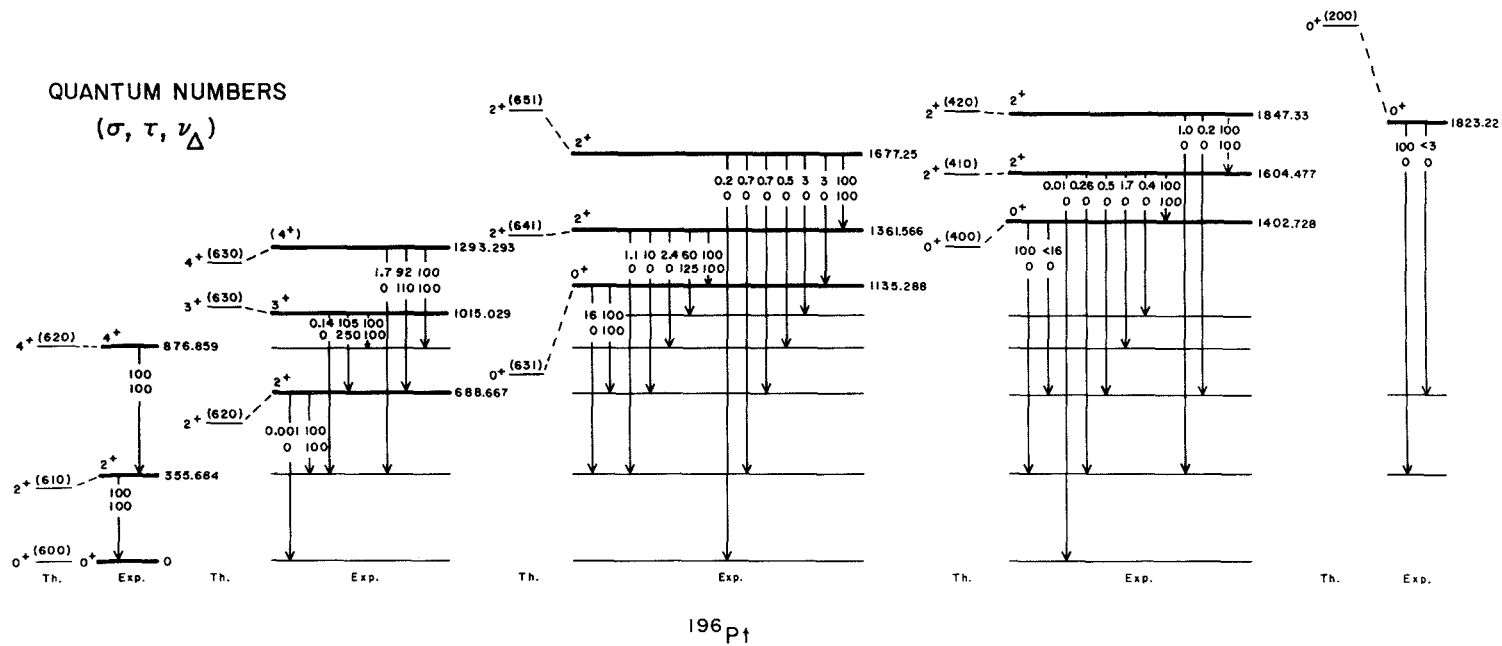


Fig. 6.33. Comparison of empirical energies and E2 branching ratios in  $^{196}\text{Pt}$  with the 0(6) limit. The lower numbers on the transition arrows are the predictions, the upper are the measured values (Cizewski, 1978).

$^{196}\text{Pt}$  and the Xe–Ba nuclei near  $A = 130$ . A comparison of the  $^{196}\text{Pt}$  level scheme with the O(6) limit is shown in Fig. 6.33. The agreement with all the E2 selection rules is impressive. All allowed transitions are observed and dominate the decays of their respective levels; all forbidden transitions are either weak or unobserved. At the same time, there are at least three important discrepancies in energies: the  $\tau = 3\ 0^+$  state is *not* below the  $3_1^+$  level as it should be, the splitting among the high  $\tau$  states (e.g., the  $0^+ - 2^+ - 2^+$ ,  $\tau = 3 - 4 - 5$  states) is much less than predicted, and the energies in the  $\gamma$  band are less staggered than predicted.

The data for Xe and Ba is comparable to Pt: only  $\sigma = N$  and  $N - 2$  levels are known, but many  $\tau = 4, 5, 6$  states have been assigned and the O(6) character extends over a large range of nuclei. There are some striking analogies between Pt and Xe–Ba. Besides their common manifestation of O(6)-like characteristic, fits of the O(6) eigenvalue equation in each region show nearly identical ratios  $A/B \sim 0.9$ . Interestingly, this common value is very close to the special case  $A/B = 1$ , which corresponds to the CQF Hamiltonian of Eq. 6.73. Moreover, exactly the same discrepancies with O(6) that occur in  $^{196}\text{Pt}$  are repeated in Xe–Ba. One of these, the weaker  $\gamma$  band energy staggering, provides a useful clue to the nature of the responsible symmetry breaking. Recall from our earlier discussion of asymmetric rotor models that the rigid triaxial rotor of Davydov is characterized by staggering exactly opposite in phase to that of the Wilets–Jean  $\gamma$  unstable model. The O(6) limit corresponds to the latter, that is, to a completely  $\gamma$  independent potential and to a nucleus whose shape fluctuates uniformly over a range of  $\gamma$  values from  $\gamma = 0^\circ - 60^\circ$  such that  $\gamma_{\text{ave}} = 0^\circ$  but  $\gamma_{\text{rms}} = 30^\circ$ . The staggering data suggests that a realistic potential for Pt and Xe–Ba might contain some small  $\gamma$  dependence that would shift the characteristic  $\gamma$  band energy staggering pattern slightly toward the opposite couplings of the Davydov model. It turns out that the introduction of a very small (3–4%)  $\gamma$  dependence in the potential with a minimum at  $30^\circ$  corrects not only the  $\gamma$  band energy staggering, but the other discrepancies as well. This idea is in line with our earlier discussion in the context of Fig. 6.22 in which we suggested that the  $E_s/E_{2_1^+}$  data could be accounted for by a potential that was predominantly  $\gamma$  independent but with a small minimum near  $\gamma = 30^\circ$ .

We commented earlier that a strict distinction between O(6) and U(5) can not rely on the energies or branching ratios of low-lying levels alone, but requires absolute  $B(\text{E}2)$  values or branching ratios for  $\sigma < N$  states. Both of these types of data are abundant for Pt and for Xe–Ba. As an example, Fig. 6.34 shows the decay of the most telling  $\sigma = (N - 2) = 4$  level for  $^{196}\text{Pt}$  and compares this with O(6) and U(5) predictions. The high  $n_g$  U(5) levels have multiple allowed decay routes while the O(6)  $\sigma < N$  levels often have only one such route. The data clearly support the O(6) interpretation.

As we have suggested in each of the preceding discussions, it appears that good examples of all three IBA symmetries exist. This provides support for the general structure of the IBA model and, moreover, these limiting cases

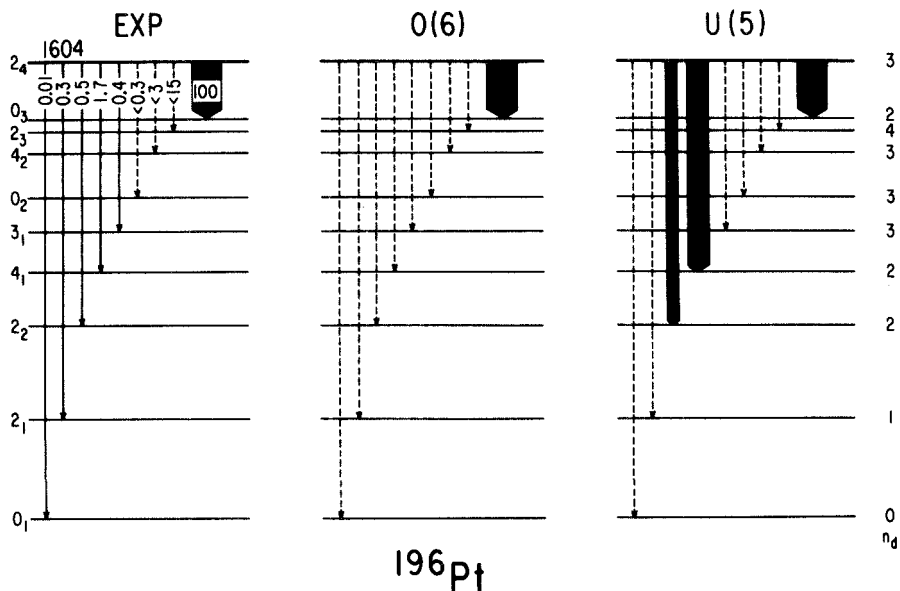


**Fig. 6.34.** Comparison of the decay of the 1604 keV level in  $^{196}\text{Pt}$  with O(6) and U(5) symmetries (Cizewski, 1978).

offer convenient benchmarks to assess the structure of nuclei similar in character to the symmetries but exhibiting some degree of symmetry breaking.

Of course, there is no a priori reason why a particular nucleus should satisfy a given symmetry or, indeed, why any nuclei should satisfy the particular

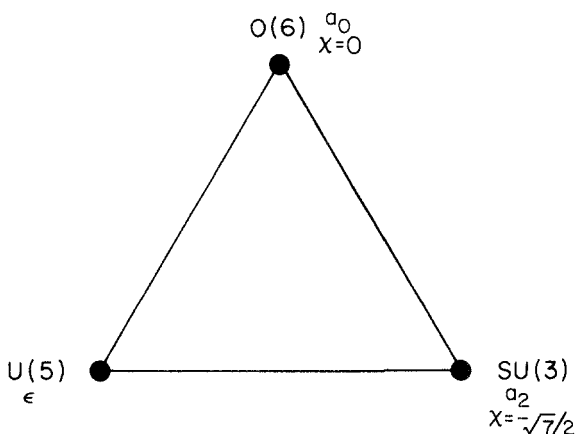


**Fig. 6.35.** Symmetry triangle of the IBA with the coefficients giving each dynamical symmetry.

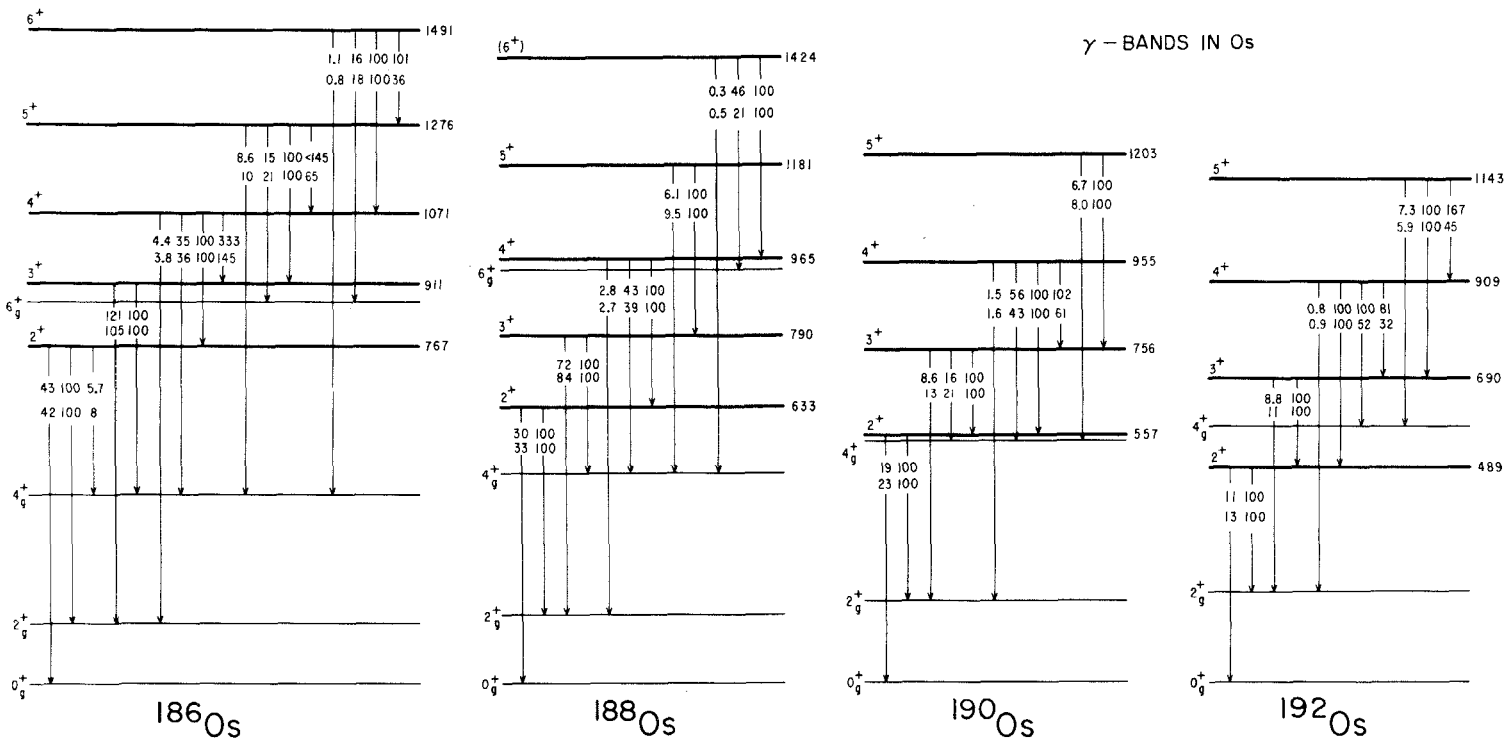


Fig. 6.36. Empirical (upper numbers) and calculated relative  $B(E2)$  values for the Os 0(6)  $\rightarrow$  rotor transitional region (Casten, 1978).

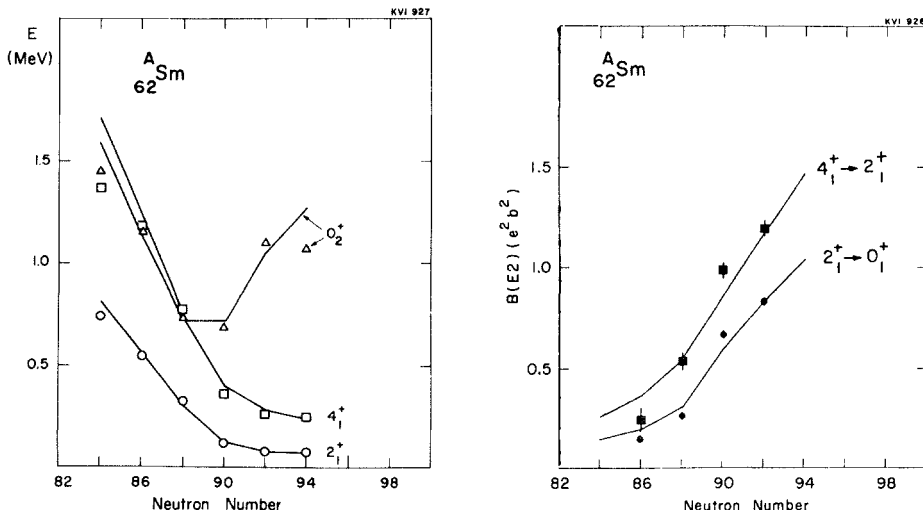


Fig. 6.37. Empirical and calculated properties of the transitional Sm nuclei (Scholten, 1978).

constraints of one of these symmetries. Most nuclei do not, yet the IBA is appealing precisely because it provides a simple way to treat such nuclei. Such treatments also reveal new aspects of collective behavior not heretofore encountered or expected.

To study some of these ideas, we now turn to transitional nuclei between IBA symmetries. A convenient way to picture the symmetry structure of the IBA is in terms of the symmetry triangle shown in Fig. 6.35. The three symmetries mark the vertices. In terms of the Hamiltonian of Eq. 6.51, the characteristic wave functions of each symmetry are generated by a specific term whose coefficient is labeled at the appropriate vertex:  $\epsilon$  for U(5),  $a_2$  for SU(3), and  $a_0$  for O(6). We have also seen that for  $Q$  to be a generator of SU(3) one must set  $\chi = -\sqrt{7}/2$ , and that if  $\chi = 0$ , the same Hamiltonian produces O(6) wave functions. These  $\chi$  labels are also included in Fig. 6.51.

Treating transitional nuclei is trivially simple. Structural evolution from one limiting symmetry to another merely involves changing the ratio of the two parameters associated with the two vertices from 0 to  $\infty$ . For example, a U(5)  $\rightarrow$  SU(3), or vibrator  $\rightarrow$  rotor, transition, such as occurs in the Nd, Sm, and Gd nuclei near  $A = 150$ , is effectuated by varying  $\epsilon/a_2$  and an O(6)  $\rightarrow$  rotor transition, as in the Os isotopes, by changing  $a_0/a_2$ . Examples of such structural evolution are shown for these two cases in Figs. 6.36 and 6.37. The extremely complex changes in level schemes and transition rates in these phase transitions are rather well reproduced in terms of a variation of a single parameter.

While the SU(3) symmetry represents a deformed nucleus, few deformed nuclei satisfy its strict rules. Therefore, to properly calculate the bulk of deformed rare earth and actinide nuclei, one needs to break the SU(3) symmetry either towards U(5) or O(6). Most deformed nuclei have  $E_\beta > E_\gamma$ . We recall that a high-lying  $0_2^+$  state is characteristic of O(6). This suggests that devia-

tions from SU(3) in that direction are appropriate. It is indeed possible to obtain excellent fits to most deformed rare earth nuclei by using finite ratios of  $a_3/a_2$  near -4. We shall not show such results, but rather turn to an alternate method, the *consistent Q formalism* (CQF), an even simpler way of dealing with these nuclei.

In early applications of the IBA, it was customary to keep  $\chi$  in the quadrupole operator in the Hamiltonian fixed at the SU(3) value of  $-\sqrt{7}/2$ , while treating  $\chi$  in the E2 operator as a free parameter. This is certainly permissible, even though one might feel slightly uncomfortable using different forms of the quadrupole operator since it is same quadrupole force that produces deformed nuclei and collective E2 transitions. This discomfort initiated interest in pursuing an approach in which consistent forms of  $Q$  are used throughout. This approach, the CQF, is widely used, perhaps due more to its simplicity than to any philosophical preference. One additional advantage of the CQF is that it involves fewer free parameters, which makes it easier to establish a relationship between the IBA and corresponding geometrical analogues.

In the CQF, the  $O(6) \rightarrow SU(3)$  transition leg in the symmetry triangle is accomplished by varying  $\chi$  from 0 to  $-\sqrt{7}/2$  in both  $H$  and  $T(E2)$ . Now,  $H$  has the form shown in Eq. 6.73

$$H = a_2 \mathbf{Q}^2 + a_1 \hat{\mathbf{J}}^2 \quad \left( \text{with } -\frac{\sqrt{7}}{2} \leq \chi \leq 0 \right) \quad (6.76)$$

Since  $\mathbf{J}^2$  is diagonal and has the same effect on any states of the same spin, it plays no structural role. Thus, if we write

$$H = a_2 \left[ \mathbf{Q}^2 + \frac{a_1}{a_2} \hat{\mathbf{J}}^2 \right] \quad (6.77)$$

we see that  $a_2$  is just a scale factor on energies and has no structural influence. Thus the wave functions, relative  $B(E2)$  values, and relative energies of states of the same spin are determined *solely* by  $\chi$  and  $N$ . Whereas in the traditional form of  $H$  in Eq. 6.51 the structure and relative energies in an  $O(6) \rightarrow SU(3)$  region depend on  $a_0$ ,  $a_2$ ,  $a_3$ , and E2 transitions depend separately on  $\chi$ , now a *single* parameter determines all. The only loss of generality is that the  $O(6)$  symmetry approached and obtained in this way is a special case, with  $A/B = 1$ . However, this does not seem to be a deficiency, since it is this special case that is experimentally observed.

Since predictions of branching ratios and of relative energies (of states of the same  $J$ ) depend only on  $\chi$  and  $N$  in the CQF, it is possible construct *universal* plots for a given  $N$ , or *universal* contour plots against  $\chi$  and  $N$ . Some examples are shown in Figs. 6.38 and 6.39. (In the energy ratio plotted,  $E_{2+}$  is always subtracted to remove the structurally inconsequential effects of the  $\mathbf{J}^2$  term.) Figure 6.38 (top) shows the behavior of the  $\beta$  vibration relative to the  $\gamma$  band energy. These excitations belong to the representation  $(N - 4, 2)$  in SU(3). As  $O(6)$  is approached, the  $\beta$  vibration increases rapidly relative to the  $\gamma$  band. The reason is that the  $\gamma$  band goes over into a quasi- $\gamma$  band sequence starting with the  $\tau = 2$   $2_{\gamma}^{+}$  level of the  $\sigma = N$  family, while the  $\beta$  bandhead

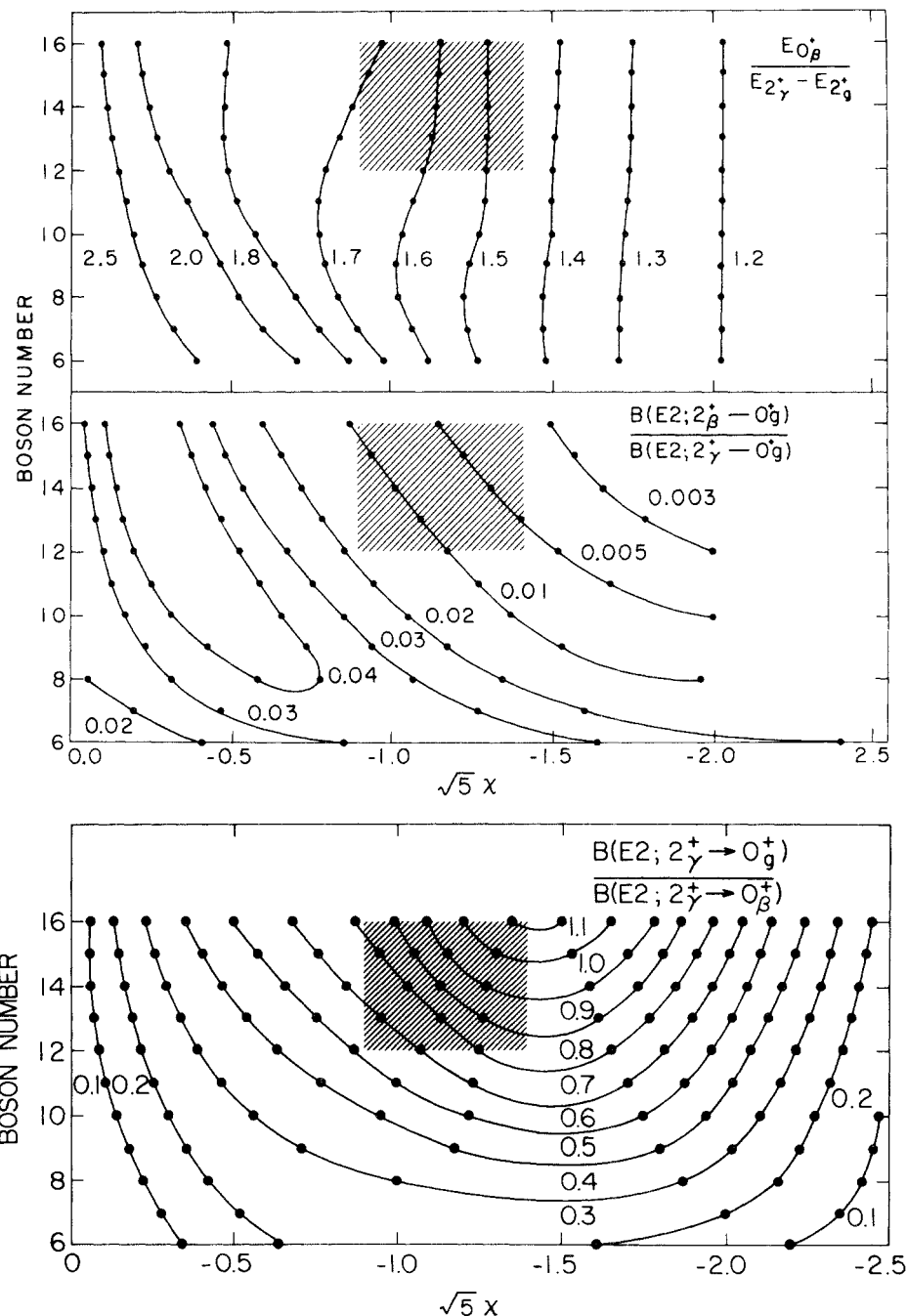


**Fig. 6.38.** Three contour plots in the CQF formalism of the IBA (Warner, 1983).

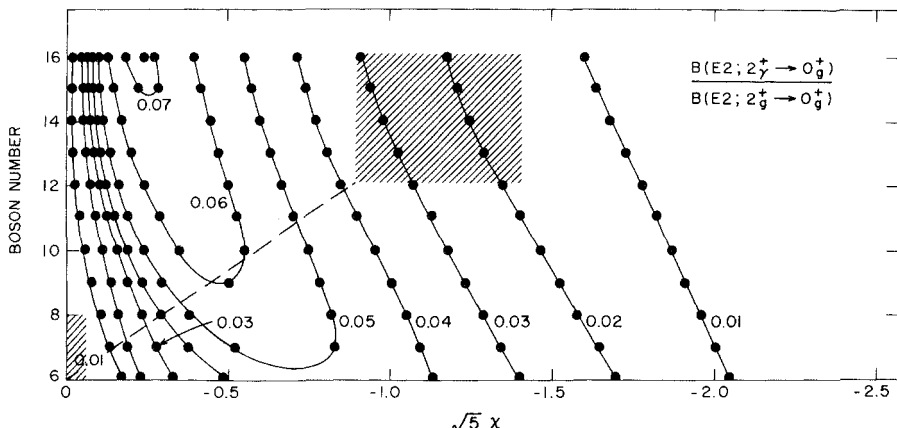


Fig. 6.39. Another CQF contour plot (Warner, 1983).

becomes the *yраст*  $0^+$  level of the higher-lying  $\sigma = N - 2$  family. Figure 6.38 also shows that for essentially all  $\chi$  values, and especially for those values typical of deformed nuclei (cross hatched box), the  $\beta$  band lies well above the  $\gamma$  band. This is in excellent agreement with the data, but not unexpected given our discussion. What is more impressive is that the CQF *automatically* predicts that  $B(E2:\beta \rightarrow g) \ll B(E2:\gamma \rightarrow g)$ .

In Fig. 2.18 we saw that this feature was one of the most characteristic empirical properties of deformed nuclei. It is particularly interesting that the IBA predictions for realistic deformed nuclei come out this way since *both*  $\beta \rightarrow g$  and  $\gamma \rightarrow g$  transitions are forbidden in SU(3). However, in the transition towards O(6), the  $\gamma$  band levels go over into the quasi- $\gamma$  band (in Davydov language, into the anomalous levels of the ground band) with collective transitions to the latter, while the  $\beta$  band goes over into the low-lying states of the  $\sigma = N - 2$  family and the  $\Delta\sigma = 0$  selection rule forbids their decay to the ground band. Thus they remain weak throughout the transition leg while the  $\gamma \rightarrow g$  transitions become collective.

The lowest contour plot in Fig. 6.38 shows one of the most remarkable and surprising predictions of the IBA, that of *collective*  $\beta \leftrightarrow \gamma$  transitions that are comparable in strength to  $\gamma \rightarrow g$  transitions. This is completely contrary to normal expectations and to the traditional perception of the experimental situation. When this prediction of the IBA was initially realized, it was thought to contradict a wide body of empirical evidence showing systematically collective  $\gamma \rightarrow g$  and weakly collective  $\beta \rightarrow g$  transitions but no  $\beta \leftrightarrow \gamma$  transitions. However, given the normal closeness in energy of  $E_\beta$  and  $E_\gamma$  and the fact that E2 transition rates  $T(E2) \propto B(E2) E_\gamma^5$ , such transitions would be extremely weak in *intensity* even if the *matrix elements* are large. Recently, though, extremely sensitive experiments, mostly utilizing the  $(n, \gamma)$  reaction and powerful  $\gamma$ -ray spectrometers installed at an Institute Laue-Langevin in

Grenoble (see Chapter 10), have shown that collective  $\beta \leftrightarrow \gamma$  transitions do indeed exist and appear whenever the appropriate experiments have been carried out.

It is evident in Fig. 6.38 that the  $\gamma \rightarrow g/\beta \leftrightarrow \gamma$  matrix elements generally increase with  $N$ , and in the large  $N$  limit,  $\beta \leftrightarrow \gamma$  matrix elements become negligible relative to either  $\gamma \rightarrow g$  or  $g \rightarrow g$  intraband transitions, thus recovering the geometrical picture. Of course, geometrical models can be modified (perturbed) so as to produce  $\beta \leftrightarrow \gamma$  matrix elements of collective strength simply by introducing mixing between  $\beta$  and  $\gamma$  bands. However, as we pointed out in the bandmixing discussion earlier in this chapter, the  $B(E2)$  values so produced result not as a correction to an unperturbed value (since the latter vanishes), but solely from the mixing. Thus, all  $\beta \rightarrow \gamma$   $B(E2)$  values are proportional to the same mixing parameter (usually called  $Z_{\beta\gamma}$  in analogy with  $Z_\gamma$  or  $Z_\beta$ ) and, hence, their branching ratios must be independent of the amount of mixing;  $\beta$ - $\gamma$  mixing provides no flexibility in the branching ratios predicted in this way and generally disagrees with the data.

The last contour plot, that of Fig. 6.39, is also interesting. It shows a branching ratio that vanishes in both SU(3) and O(6) limits but is finite in between. There is no possible path between these limits that bypasses finite values. Thus, in a totally parameter-free manner, the IBA automatically predicts that such a branching ratio (and, indeed, many others) will peak in transitional regions.

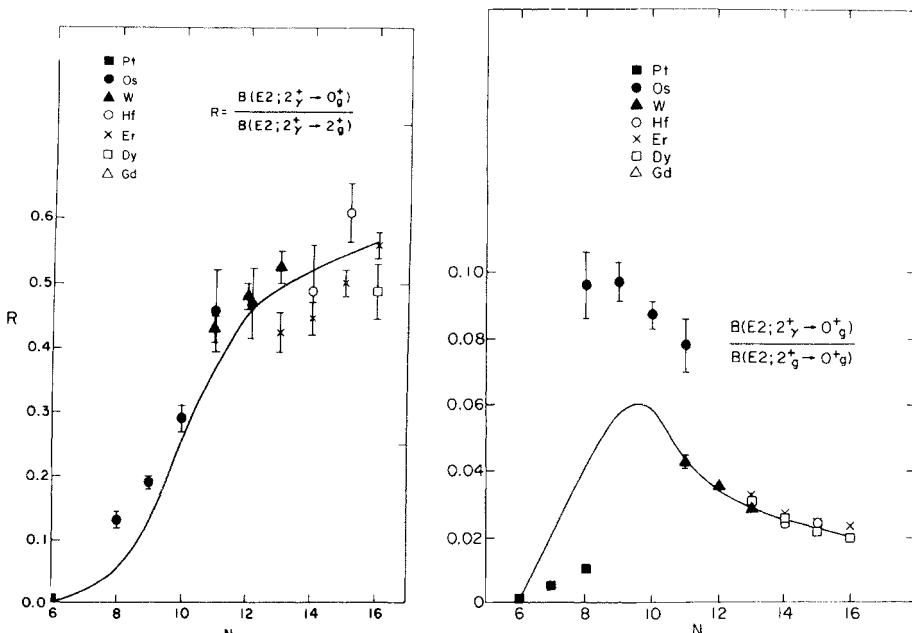


**Fig. 6.40.** Comparison of the data with predictions of the CQF for two observables. In each case a straight-line trajectory in  $\chi$  (see dashed line in Fig. 6.39) was used (Warner, 1983).

When carrying out actual calculations, one generally chooses  $\chi$  to reproduce a specific energy ratio or branching ratio and then inspects other predictions. However, a more generic viewpoint is obtained by taking the simplest possible trajectory in  $\chi$  (shown as the straight dashed line in Fig. 6.39) between O(6) and rotor nuclei. Figure 6.40 shows predictions for such a trajectory for the branching ratio of Fig. 6.39 and for a branching ratio involving the same pair of intrinsic states, and compares them with the data for rare earth nuclei. One does not expect to get exact agreement in such a simplified approach, but the general pattern of the predictions is in remarkably good accord with the data.

It is useful to present a more detailed set of predictions for a typical deformed nucleus situated between SU(3) and O(6) but closer in structure to the former:  $^{168}\text{Er}$  has become, by virtue of the extensive data available for it, the standard case. Calculated and empirical energies are compared in Fig. 6.41. The empirical  $B(E2:\gamma \rightarrow g)$  values were shown earlier in a Mikhailov snapshot in Fig. 6.14. The dashed line is the IBA prediction in the CQF. Table 6.13 also presents this comparison. In either format, the agreement is outstanding and demonstrates the *automatic* incorporation of bandmixing in the IBA.

An interesting feature of this bandmixing is that it decreases with increasing  $N$ . This can be discerned on the left in Fig. 6.40 from the flattening of the

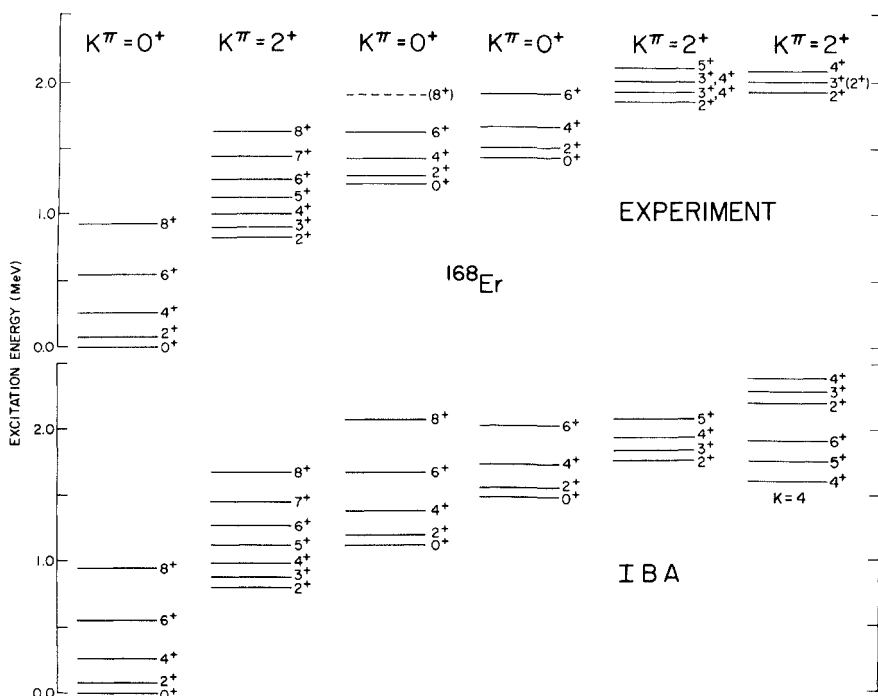


**Fig. 6.41.** Observed and calculated energies in  $^{168}\text{Er}$ . The  $J = 4^+, 5^+, 6^+$  levels of the  $K = 4$  band predicted near 1.6 MeV are not observed below 2 MeV (Warner, 1980).

**Table 6.13.** Relative  $B(E2)$  values from the  $\gamma$  band in  $^{168}\text{Er}$ 

$J_i$	$J_f K_f$	Exp	IBA (CQF)
2	0, 0	54.0	54
	2, 0	100	100
	4, 0	6.8	7.6
3	2, 0	2.6	2.6
	4, 0	1.7	1.8
	2, 2	100	100
4	2, 0	1.6	1.7
	4, 0	8.1	9.6
	6, 0	1.1	1.5
	2, 2	100	100
5	4, 0	2.9	3.5
	6, 0	3.6	4.4
	3, 2	100	100
	4, 2	122	95
6	4, 0	0.44	0.44
	6, 0	3.8	4.9
	8, 0	1.4	1.0
	4, 2	100	100
	5, 2	69	57
7	6, 0	0.7	1.9
	5, 2	100	100
	6, 2	59	36

Based on Warner, 1982.

predictions and their asymptotic approach to the Alaga rule value of 0.7 as  $N$  increases. Thus, the IBA automatically predicts a parabolic behavior for  $Z_\gamma$  against  $N$ , minimizing at midshell, that is nearly identical to the empirical pattern shown earlier in Fig. 6.15.

Of course, the agreement in energy for the higher bands in Fig. 6.41 is probably at least partially fortuitous since the empirical excitations seem to have some two-quasi-particle character. Also, the predicted  $K = 4$  band is not observed below 2 MeV. (It may be necessary to include  $g$  bosons in the IBA to account for this discrepancy.)

From all these results we hope that the power of the IBA as a simple yet general phenomenological model becomes apparent. In other approaches to collective nuclear structure, one must invoke different models (vibrator, rotor, etc.), in an ad hoc way to accommodate different structures. In the IBA, a single framework, embodied in the simple Hamiltonian of Eq. 6.51, encompasses all three limiting symmetries, and most intermediate situations as well. It does so simply through appropriate relative magnitudes of the coefficients  $\epsilon$ ,  $a_2$ ,  $a_0$ , or  $\chi$ , and by diagonalization of a small set of basis states. The “ad-

hocness" is still there, of course, now appearing in the choice of parameters, but the simplicity of the *framework* greatly facilitates calculations and helps us to understand transitional cases in a unified context.

Having dealt at some length with the IBA predictions in the CQF, it is useful to comment on the physical significance of  $\chi$ . Since the CQF has only one significant parameter, it is possible to compare IBA predictions as a function of  $\chi$  with geometrical model predictions as a function of  $\beta$  or  $\gamma$ . It has been shown that one can relate  $\beta$  and  $\chi$  by the equation

$$\beta_{IBA} = \frac{1}{2} \beta_0 \left[ -\sqrt{\frac{2}{7}} \chi \pm \sqrt{\left(\frac{2}{7}\right) \chi^2 + 4} \right] \quad (6.78)$$

where  $\beta_0$  is a normalization factor because the scale of  $\beta_{IBA}$  is undetermined. Thus we see that, as  $\chi$  varies from  $-\sqrt{7}/2 \rightarrow 0$ ,  $\beta_{IBA}$  goes from  $\sqrt{2} \beta_0 \rightarrow \beta_0$ —that is, both SU(3) and O(6) are deformed rotors, the latter slightly less so. The  $\beta - \chi$  correlation is relatively minor in importance. The essential structural evolution in the IBA is one of  $\chi$  with  $\gamma$ . This is easy to see by carefully comparing Figs. 6.19 and 6.42, in which the same three observables are plotted against  $\chi$  for the IBA and  $\gamma$  for the Davydov model. (The use of the latter as a point of comparison is convenient but not valid in the strict sense since the O(6) limit is  $\gamma$  soft, not rigid; however, the reader will recall our statement that most predictions of the Davydov model for fixed  $\gamma$  are nearly identical to those of a  $\gamma$  soft model with the same  $\gamma_{rms}$ .) These two figures show that each observable passes through the *same* set of values via a similar path. Simply by equating

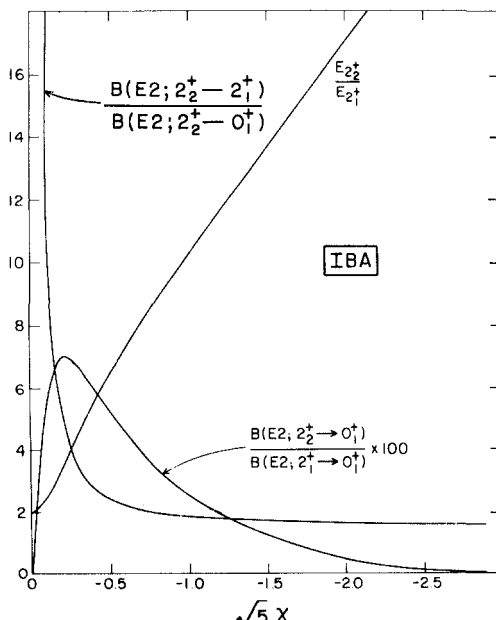


**Fig. 6.42.** Three observables, relating to axial asymmetry, as a function of  $\chi$  (for  $N = 16$ ) in the IBA (compare Fig. 6.19).

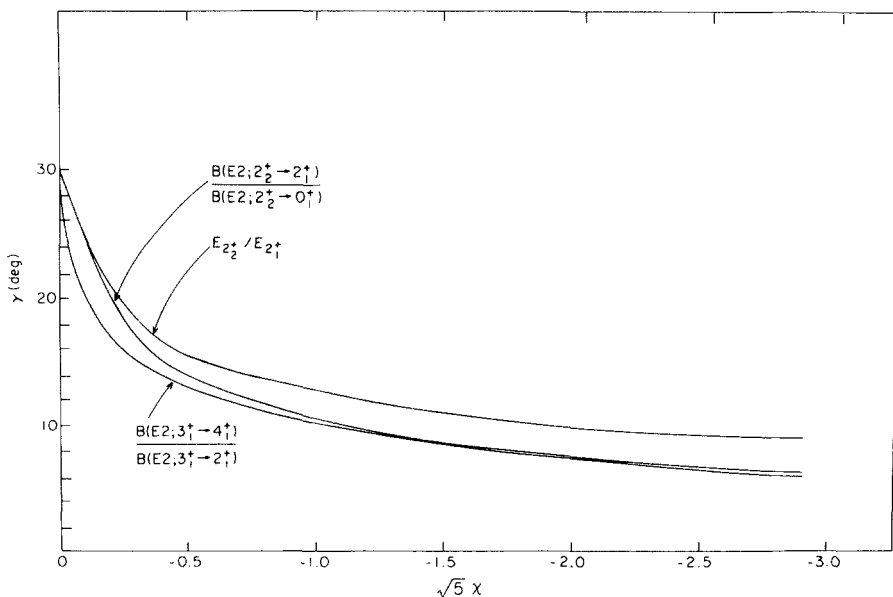


**Fig. 6.43.** Relation between the geometrical asymmetry  $\gamma$  and the IBA parameter  $\chi$  (Casten, 1984). For  $N = 16$  (the dependence on  $N$  is weak).

values of each observable, one can assign an effective  $\gamma$  to each  $\chi$  value. This  $\gamma$ - $\chi$  correlation is shown in Fig. 6.43. The fact that all three observables show the same correlation supports the validity of associating each  $\chi$  value with an asymmetry  $\gamma$ . The picture provided by this correlation is simple: increasing deviations of  $\chi$  from SU(3) toward O(6) correspond to increasing axial asymmetry and to larger and larger values of  $\gamma_{\text{rms}}$ . Since the IBA never introduces a minimum in  $V(\gamma)$ , this increase in  $\gamma_{\text{rms}}$  can *only* arise if the potential becomes increasingly flatter in  $\gamma$  as  $\chi \rightarrow 0$ . Figure 6.44 confirms this by showing the effective potential  $V(\gamma)$  for several  $\chi$  values. This figure shows one other interesting point. The reader may have noted in Fig. 6.43 that  $\gamma \neq 0^\circ$  for SU(3), even though this limit is supposed to be that of a symmetric rotor. Figure 6.44 shows the reason. Although the minimum in  $V(\gamma)$  occurs at  $\gamma = 0^\circ$ , the potential is not infinitely steep (for finite  $N$ ), and zero point motion leads to a finite  $\gamma_{\text{rms}}$ .

The body of research relating to the IBA in the last decade is enormous. We have only summarized a few highlights, emphasizing the symmetries of the IBA, transition regions, the role of finite boson number, some experimental tests of the model, and a geometrical understanding of it. We have completely ignored important topics such as the intrinsic state formalism, which allows many IBA results to be obtained analytically; the extension of the CQF to the  $SU(3) \rightarrow U(5)$  transition region by adding an  $\epsilon n_d$  to Eq. 6.76; the use of effective boson numbers, especially in regions where important subshell gaps occur that might alter the proper counting of valence nucleons; the  $N_p N_n$  parameterization of the IBA; and numerous extensions to the model.

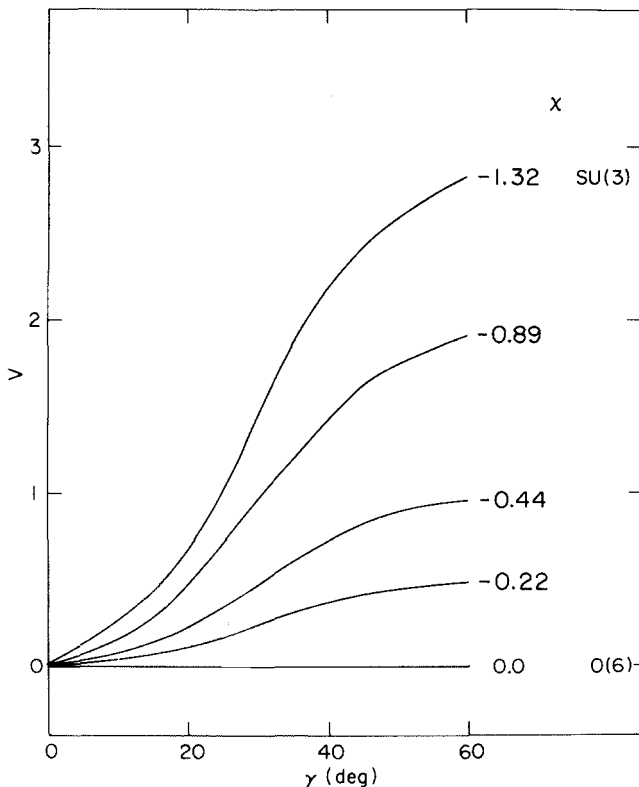


**Fig. 6.44.** Dependence of the IBA potential on  $\gamma$  for several  $\chi$  values (Casten, 1984, Ginocchio, 1980).

The two most important of these latter are the IBA-2, in which protons and neutrons are distinguished and treated separately, and the IBFM, which incorporates a single fermion coupled to the boson core so that odd A nuclei can be calculated. The IBA-2 has its own symmetries and has led to the recognition of an important new collective mode, the so-called M1 scissors mode, in which protons and neutrons oscillate (in angle) relative to each other (see Fig. 6.1). This mode, recently discussed by Richter and collaborators in the rare earth region, is now known to be widespread near 3 MeV excitation energy in deformed nuclei. Its existence and properties are closely connected with a new quantum number that arises in the IBA-2,  $F$ -spin, which describes the degree of proton-neutron symmetry. For many IBA-2 Hamiltonians,  $F$ -spin is a good quantum number. This classification leads to the concept of an  $F$ -spin multiplet—a group of nuclei, widely dispersed throughout a mass region but displaying similar level schemes.  $F$ -spin also facilitates the projection of complex IBA-2 calculations into simpler, equivalent IBA-1 cases. The development of boson models for both even and odd mass nuclei raises the possibility of treating both in a single unified framework. This leads to the concept of boson-fermi symmetries or even supersymmetries (often called SUSY's).

These are all extensive topics that merit their own discussion but that are well outside the scope of this book. Also beyond that ken are important

studies extending the basic model to incorporate  $g$  bosons. These efforts aim both to reduce the impact of “boson cutoffs” that lead to reduced  $B(E2)$  values between high-spin states and to account for classes of excitations (e.g.,  $K = 3$  and  $K = 4$  bands) that regularly appear among the low-lying intrinsic excitations of deformed nuclei. The incorporation of  $g$  bosons has followed two distinct paths, one in which a single  $g$  boson is introduced numerically and allowed to interact with the  $s - d$  bosons, and another in which a full complement of  $g$  bosons is incorporated group theoretically by expanding the parent group  $U(6)$  to  $U(15)$ .

Other extensions to the IBA involve the inclusion of two-quasi-particle excitations so that “backbending” phenomena (see Chapter 8) may be treated, the introduction of higher-order terms such as those cubic in  $s$  or  $d$  bosons (e.g.,  $(\mathbf{d}^\dagger \mathbf{d}^\dagger \mathbf{d}^\dagger)^c (\mathbf{d} \mathbf{d} \mathbf{d})^v$ ) that incorporate a  $\gamma$  dependence in the IBA potential, and the expansion of the model basis with  $p$  and  $f$  bosons so that negative parity states appear.

Finally, a most significant recent facet of the whole arena of algebraic modelling in nuclear structure is the development of sophisticated approaches that invoke symmetries in the Fermions directly. Some of these, like the IBA, emphasize fermion dynamical symmetries in the valence space. Others are even more general. They use techniques founded in symplectic group theory to incorporate all oscillator shells simultaneously, thereby affecting important renormalizations and offering the possibility to describe giant E2 resonances

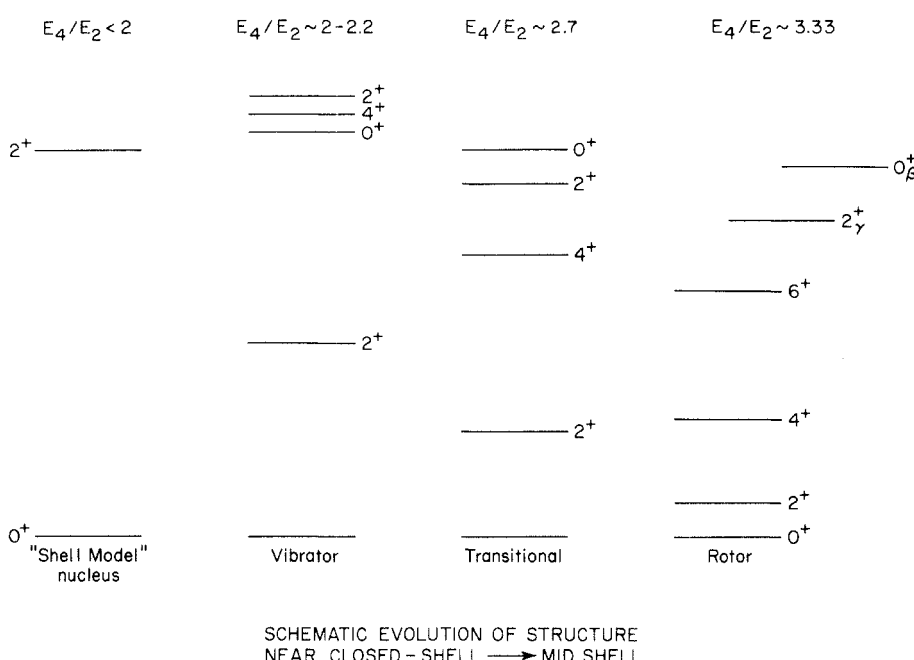


**Fig. 6.45.** An imaginary, but typical, sequence of level schemes and nuclear structure types from a near closed shell region to a well deformed midshell nucleus.

and low-lying collectivity without effective charges, in a single coherent algebraic framework. Though far beyond the scope of this book to describe, these more microscopic models are nonetheless active current research areas. For all this work the reader is referred to the recent literature.

### 6.7 The Development of Collectivity: Phenomenology and Microscopic Basis

We have seen that magic nuclei do not display low-lying collective behavior. Moreover, collectivity and a softness toward deformation go hand in hand as valence nucleons are added beyond closed shells. In midshell regions of medium and heavy nuclei, one invariably encounters a large concentration of deformed nuclei exhibiting rotational behavior and low-lying vibrational excitations of  $\beta$ ,  $\gamma$ , and octupole type.

A schematic view of such a structural evolution, typical in broad brush strokes of many regions, is shown in Fig. 6.45. The basic trend reflects the systematics of the Sm nuclei shown in Fig. 6.23. As long as neither type of nucleon is magic,  $E_{2_1^+}$  drops and  $E_{4_1^+}/E_{2_1^+}$  ranges from  $<2 \rightarrow 3.33$  as nucleons of either type are added. The structural sequence is shell model  $\rightarrow$  vibrator  $\rightarrow$  transitional  $\rightarrow$  rotor. In the transitional region,  $E_{4_1^+}/E_{2_1^+}$  usually jumps rapidly from  $<2.5$  to  $>3.0$ . Earlier in this chapter we discussed two kinds of transitions, one spherical-deformed, the other spherical- $\gamma$ -soft-deformed.  $E_{4_1^+}/E_{2_1^+}$  values near  $\sim 2.5$  can occur in either case, but in one case they imply softness to quadrupole deformation, in the other an extreme softness to axial asymmetry.

Despite the apparent simplicity of Fig. 6.45 and the concepts behind it, real nuclear systematics is usually much more complex. This is exemplified by Fig. 2.13, which shows the systematics of  $E_{2_1^+}$  in the  $A = 100$  region, and by Fig. 6.46 (left), which shows similar data for the energy ratio  $E_{4_1^+}/E_{2_1^+}$  in the  $A = 150$  region. While the general pattern of increased collectivity toward midshell can be discerned, these plots provide few obvious clues to simple understanding of

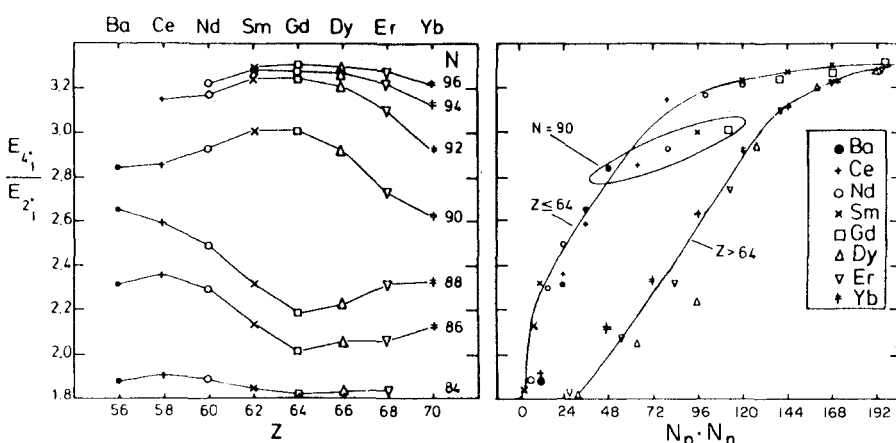


**Fig. 6.46.** Normal (left) and  $N_p - N_n$  (right) plots of  $E_{4_1^+}/E_{2_1^+}$  for the  $A = 150$  region (Casten, 1985a).

the structural behavior. One important clue, however, is provided in Figs. 2.6–2.8, which show the behavior of  $E_{2+}$  in a set of singly magic nuclei, the Sn isotopes, and in nuclei with *both* valence protons and neutrons. We have commented that the much lower values in the latter strongly suggests that it is the *valence proton-neutron interaction* that leads to softness. Earlier, we formalized this idea slightly by giving some qualitative arguments why the  $T = 0$  component of the p-n interaction can induce single nucleon configuration mixing, unlike its  $T = 1$  component, or the like-nucleon interaction, and why such mixing is tantamount to the development of nonspherical nuclear shapes. Here, we wish to illustrate and discuss a phenomenological approach that greatly simplifies the systematics of nuclear transition regions and provides some insights into the operation of the p-n interaction, and the development of collectivity and deformation. (Caveat lector: this is one of the pet ideas of the author who is, not surprisingly, rather favorably biased toward it.)

### The $N_p N_n$ Scheme

The approach is called the  $N_p N_n$  scheme, and is an attempt to parameterize nuclear data in such a way as to explicitly emphasize the valence p-n interaction. Suppose we make the assumption that the onset of collectivity, configuration mixing, and deformation in nuclei is simply due to the p-n interaction and, moreover, that this interaction is fairly long range, orbit independent, and relevant only for the *valence* protons and neutrons. Then, its strength will scale as the product,  $N_p N_n$ , of the number of valence protons times the number of valence neutrons.  $N_p$  and  $N_n$  are always counted to the nearest closed shells,

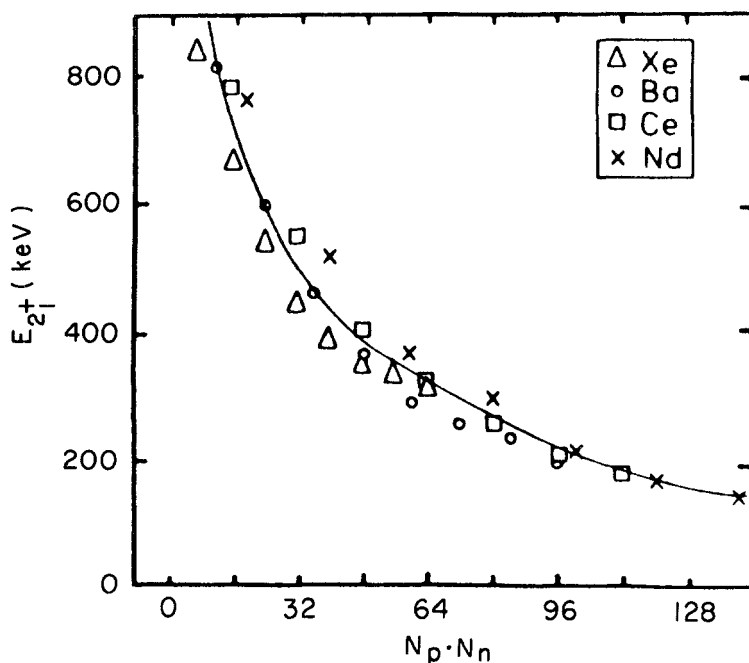
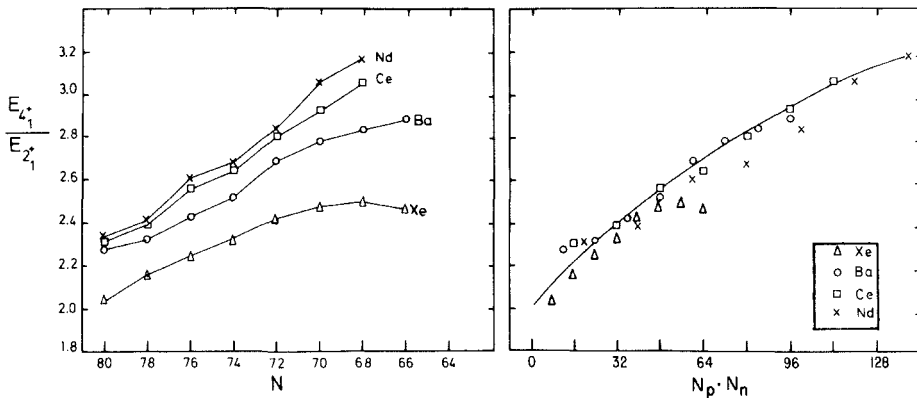


Fig. 6.47.  $N_p N_n$  plot of  $E_{2+}$  for the  $A = 130$  region (compare Fig. 2.14) (Casten, 1985a).



**Fig. 6.48.** Normal (left) and  $N_p \cdot N_n$  (right) plots of  $E_{4_1^+}/E_{2_1^+}$  for the  $A = 130$  region (Casten, 1985a).

whether these valence nucleons are particles or holes. It is important to understand that the valence p–n interaction embodied in the  $N_p \cdot N_n$  scheme is not the total p–n interaction, but the collectivity-and deformation-driving part of it (primarily the  $T = 0$  component). The  $T = 1$  component must be identical to the p–p and n–n  $T = 1$  forces, and as we have emphasized repeatedly, aside from the pairing interaction, these are repulsive on average and do not lead to configuration mixing, collectivity, and deformation. (The Sn nuclei in Fig. 2.6 are a classic example of this.)

To illustrate the  $N_p \cdot N_n$  scheme, the data shown for the  $A = 130$  region in Fig. 2.14 are replotted, in Fig. 6.47, in terms of  $N_p \cdot N_n$  instead of  $N$  or  $Z$  as is normally done. Figure 6.48 compares normal and  $N_p \cdot N_n$  plots for  $E_{4_1^+}/E_{2_1^+}$  in the same region.

It is evident that the  $N_p \cdot N_n$  plot substantially simplifies the systematics: the data that fell on several distinct curves before now coalesce so that they can be described by a single curve for a given mass region. If such behavior is general, the  $N_p \cdot N_n$  scheme offers a phenomenological tool to simplify and unify the treatment of nuclear systematics, and has a simple underlying microscopic basis.

However, applying the  $N_p \cdot N_n$  scheme to some other regions is less straightforward. If there are substantial subshell gaps in the single-particle level energies, the counting of  $N_p$  and  $N_n$  may be ambiguous. Moreover, the gaps themselves may also evolve, partly as a consequence of the p–n interaction itself. If the p–n interaction is expanded in multipoles, the monopole and quadrupole components generally dominate. The monopole component  $P_0(\cos \theta)$  is obviously constant as a function of the angles between the proton and neutron orbits, and is therefore independent of the total angular momentum  $J$  to which a pair of protons and neutrons are coupled. The monopole p–n interaction does depend on the relative radial behavior of the proton and neutron orbits, and therefore on which orbits are filling in a given mass region. Its effect is to shift the effective proton and neutron single-particle energies. As one proceeds through a pair of proton and neutron major

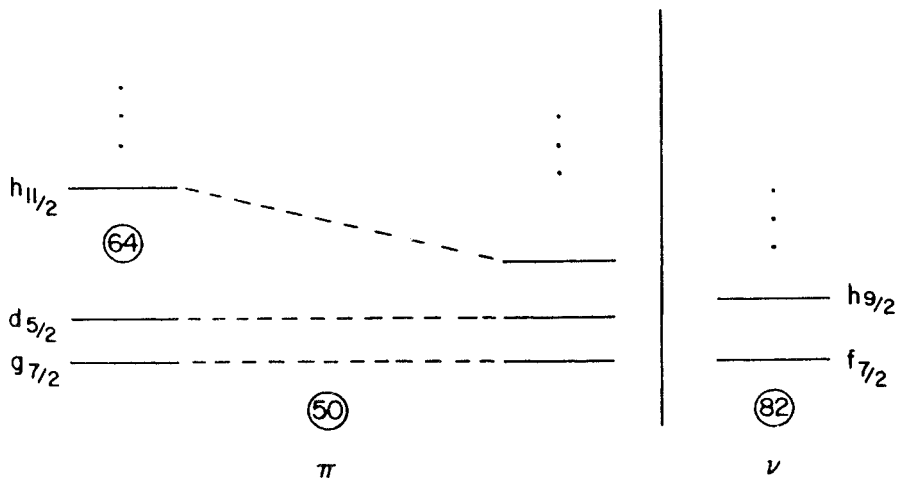


**Fig. 6.49.** Illustration of the eradication of a proton subshell gap at  $Z = 64$  as a function of neutron number due to the monopole p-n interaction.

shells, the specific behavior of the integrated monopole p-n interaction induces distinct patterns of shifts in the single-particle energies that can and do cause the appearance and disappearance of subshell gaps. Since the radial integral is largest for orbits with similar shell model quantum numbers (see Fig. 3.5), the largest effects in heavy nuclei generally occur when spin-orbit partner orbits, such as  $g_{9/2p}$  and  $g_{7/2n}$ , are filling. In such a situation, the single-particle energies of both these orbits are significantly lowered relative to their neighbors. The consequences can be rather dramatic and are now thought to be the underlying reason for the very sudden onsets of deformation near  $A = 100$  and  $A = 150$ . The idea is illustrated in Fig. 6.49 for the latter region. As neutrons begin to fill the  $h_{9/2}$  orbit near  $N = 90$ , the strong  $1h_{11/2p} - 1h_{9/2n}$

N = 88									
$2^+ 205$	$199$	$258$	$301$	$334$	$344$	$334$	$344$	$358$	
$0^+ 0$	$0^+ 0$	$0^+ 0$	$0^+ 0$	$0^+ 0$	$0^+ 0$	$0^+ 0$	$0^+ 0$	$0^+ 0$	
$^{142}_{54}\text{Xe}_{88}$	$^{144}_{56}\text{Ba}_{88}$	$^{146}_{58}\text{Ce}_{88}$	$^{148}_{60}\text{Nd}_{88}$	$^{150}_{62}\text{Sm}_{88}$	$^{152}_{64}\text{Gd}_{88}$	$^{154}_{66}\text{Dy}_{88}$	$^{156}_{68}\text{Er}_{88}$	$^{158}_{70}\text{Yb}_{88}$	
N = 90									
$2^+ 181$	$158$	$130$	$122$	$123$	$138$	$192$	$243$		
$0^+ 0$	$0^+ 0$	$0^+ 0$	$0^+ 0$	$0^+ 0$	$0^+ 0$	$0^+ 0$	$0^+ 0$	$0^+ 0$	
$^{144}_{54}\text{Xe}_{90}$	$^{146}_{56}\text{Ba}_{90}$	$^{148}_{58}\text{Ce}_{90}$	$^{150}_{60}\text{Nd}_{90}$	$^{152}_{62}\text{Sm}_{90}$	$^{154}_{64}\text{Gd}_{90}$	$^{156}_{66}\text{Dy}_{90}$	$^{158}_{68}\text{Er}_{90}$	$^{160}_{70}\text{Yb}_{90}$	

**Fig. 6.50.** Contrasting behavior of  $E_{2_1^+}$  for  $N = 88$  and  $N = 90$  isotones.

interaction causes the effective single-particle energy of the  $1h_{11/2}$  proton orbit to decrease and to obliterate the gap at  $Z = 64$ . Thus, for  $N < 90$ , the effective proton shell in this region is  $Z = 50 - 64$ , while for  $N \geq 90$ , the effective shell is the normal major shell  $Z = 50 - 82$ .

There is some very simple and beautiful empirical evidence for this concept from the energies of the first  $2^+$  states in the  $N = 88$  and  $N = 90$  isotones. These data are shown in Fig. 6.50. If the effective proton shell were the normal one from  $Z = 50 - 82$ , one would expect  $E_{2+}^*$  to decrease as the number of protons were increased past  $Z = 50$  until the near midshell region at  $Z = 66$ , after which  $E_{2+}^*$  should increase once again. This is precisely what happens for  $N = 90$ . Exactly the opposite behavior, however, characterizes the  $N = 88$  isotones. (The  $N = 84, 86$  isotones are similar to  $N = 88$ .) Without the concept of a significant subshell gap at  $Z = 64$  for these neutron numbers, such behavior would be completely incomprehensible. But if one assumes an effective proton shell  $Z = 50 - 64$  for  $N = 88$ , the midshell point is  $Z = 57$ , and one would now expect  $E_{2+}^*$  to increase for  $Z$  between 57 and 64. This is exactly the behavior observed.

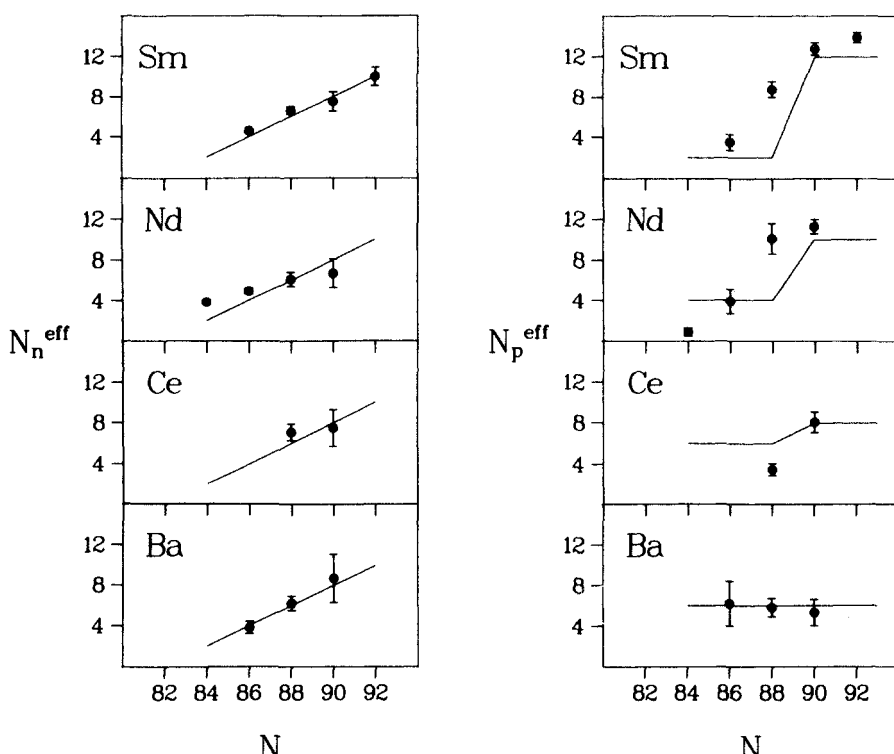


**Fig. 6.51.** Effective numbers of valence protons and neutrons in the  $A = 150$  transitional region empirically extracted from  $g(2^+_1)$  factors. The solid lines give the normal dependence of  $N_n^{eff}$  against  $N$  and the changes in  $N_p^{eff}$  against  $N$ , assuming the  $Z = 64$  gap disappears suddenly between  $N = 88$  and  $N = 90$  (Wolf, 1987).

Of course, the idea of an instantaneous disappearance of the  $Z = 64$  gap at  $N = 90$  is an unrealistically simple scenario. More likely, the dissipation of the gap is more gradual. Recently it has been shown that nuclear  $g$  factors for  $2_1^+$  states can be used to extract *effective* valence proton and neutron numbers. The details of this technique are beyond the scope of this book, but the results for  $N_{p\text{eff}}$  and  $N_{n\text{eff}}$  are shown in Fig. 6.51. They support the idea of a rapid but not instantaneous dissipation of a proton subshell gap as manifested by an increase in the effective value of  $N_p$  with neutron number for the Ce, Nd, and Sm nuclei. The solid lines in the figure show the abrupt dissipation scenario at  $N = 90$ .

A similar story characterizes the  $A = 100$  region. Indeed, it originated in that region with the pioneering microscopic calculations of Federman and Pittel; the concept involved is sometimes known as the Federman-Pittel mechanism. We have seen the effect for this region in Fig. 3.4 as a dramatic change in single-particle energies between  $^{40}\text{Zr}$  and  $^{50}\text{Sn}$ . The principal change, a lowering of the  $1g_{7/2}$  neutron orbit, is caused by the filling of the  $1g_{9/2}$  proton orbit between Zr and Sn. (Other, like-nucleon effects, arising from the filling of the neutron 50–82 shell, have a smaller impact since filling a given major shell is unlikely to alter much the ordering of the same orbits; they will tend to move in step.) In any case, the lowering of the  $1g_{7/2n}$  orbit lowers the  $1g_{9/2p}$  orbit in turn, obliterating the shell gap at  $Z = 38$  (or 40) and suddenly increasing the size of the proton shell from  $Z = 38\text{--}50$  to  $Z = 28\text{--}50$ . Nuclei such as Zr effectively go from  $N_p = 2$  to  $N_p = 10$ . Deformation promptly ensues. It is only because of a mechanism such as this that one can explain the precipitous drop in  $E_{2\dagger}$  for Zr (and Sr) at  $N = 60$  in Fig. 2.13.

This discussion provides a way to link the origin of deformation in terms of subshell evolution to the structure of intruder states discussed earlier in this chapter. There, we commented that intruder states appear as low-lying excitations in some nuclei (e.g., Sn, Pb) because they effectively correspond to an increase in the number of valence nucleons, and therefore, to an increase in the p–n interaction. On account of this, they are also more deformed than the normal states. How low the deformed intruder states go depends on two factors: the size of the energy gap to be overcome and the strength of the p–n interaction in the particular intruder orbits involved. Intruder excitations of the type we considered in the Cd nuclei, or in Pb, correspond to a large gap ( $Z = 50, 82$ ) and a moderate interaction. Suppose, however, that the gap is smaller and/or the interaction stronger. Then it becomes possible for the intruder energies to drop below those of the “normal” states and become the (now deformed) new ground state. In this view, the presence of excited intruders in some regions and the sudden onset of deformation in others are just two facets of a common mechanism. Such a model, discussed extensively by Heyde and co-workers in recent years, works and can account at least qualitatively for the Cd-Sn and Pb intruders. It also accounts for the spherical-deformed phase transition near  $A = 100$  (Sr, Zr) and  $A = 150$  (Ce, Nd, Sm, Gd), where the  $Z = 40, 64$  subshell gaps come into play.

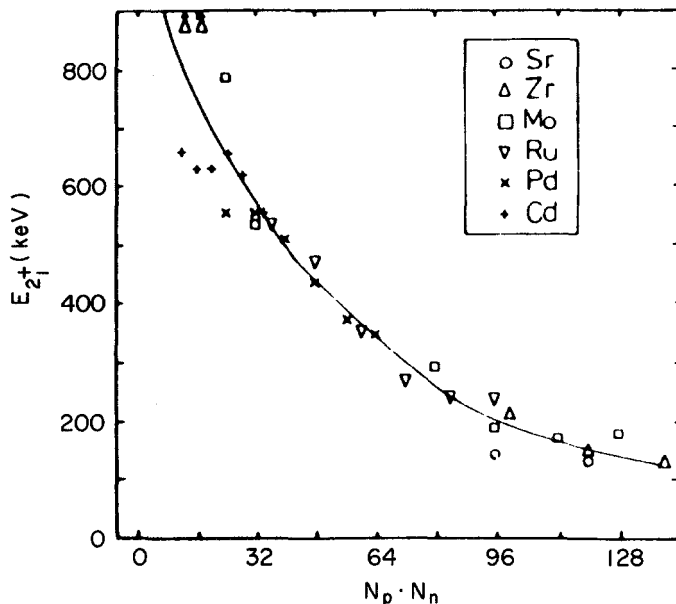
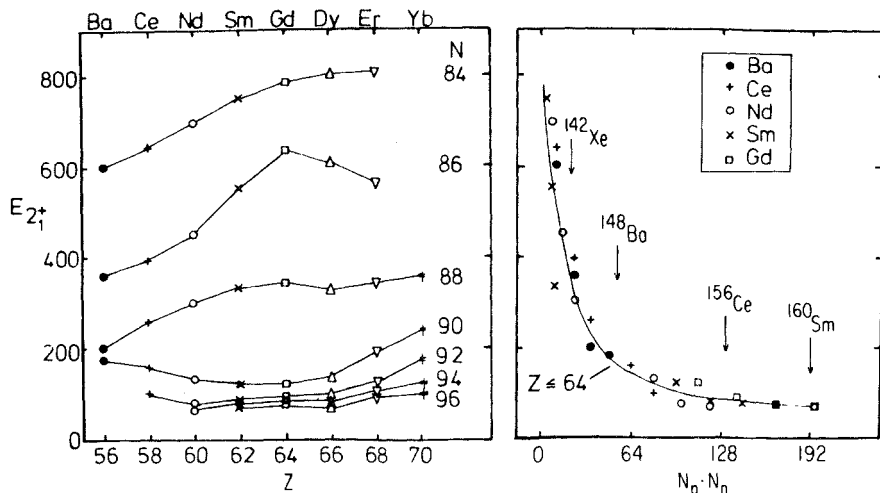


Fig. 6.52.  $N_p N_n$  plot of  $E_{2_1^+}$  for the  $A = 100$  region (compare Fig. 2.13) (Casten, 1985a).

The monopole p-n interaction effectively modifies the *valence space* for the protons and neutrons. This in turn affects the *numbers* of protons and neutrons on which the quadrupole p-n interaction may act. All this suggests that if one defines  $N_p$  and  $N_n$  based on the known evolution of these subshell gaps, then  $N_p N_n$  may again be a realistic first-order estimate of the integrated quadrupole p-n interaction strength. Figure 6.52 demonstrates this for  $E_{2_1^+}$  in the  $A = 100$  region. Compare Fig. 2.13, which shows the same data in a normal plot. On the right of Fig. 6.46, the  $N_p N_n$  plot of  $E_{4_1^+}/E_{2_1^+}$  for the  $A = 150$  region was included. In these figures the protons shells are taken to be  $Z = 38\text{--}50$  ( $50\text{--}64$ ) for  $N < 60$  ( $N < 90$ ) and  $Z = 28\text{--}50$  ( $50\text{--}82$ ) for  $N \geq 60$  ( $N \geq 90$ ). The effects are dramatic: the extremely complex systematics seen in normal plots against  $N$  or  $Z$  are instantly simplified and the data coalesce into single smooth curves in  $N_p N_n$  plots. The existence of two curves on the right in Fig. 6.46 is not surprising; they correspond to the two halves of the proton shell. The circled points at  $N = 90$ , which deviate from the smooth curve, demonstrate the imperfection of the assumption of an instantaneous change in proton shell structure at  $N = 90$ . Thus, the  $N_p N_n$  scheme is generalized to all transition regions in medium and heavy nuclei and provides a simple, yet powerful, guide to understanding and predicting the systematic behavior of nuclear properties.

It can also be used as a more reliable way of estimating the properties of unknown nuclei. The reason is that, whereas in traditional plots against  $N$  or  $Z$  such nuclei constitute *extrapolations* beyond the known ranges, the  $N_p N_n$  values of many unknown nuclei far off stability are actually *smaller* than those for known nuclei in the same region. The  $N_p N_n$  scheme converts the normal



**Fig. 6.53.** Normal (left) and  $N_p N_n$  (right) plots of  $E_{2+}$  for the  $A = 150$  region. In the  $N_p N_n$  plot, only the  $Z \leq 64$  points are shown. The arrows point to the  $N_p N_n$  values for the extremely neutron rich nuclei indicated. Predictions for  $E_{2+}$  (or other observables) for these nuclei are obtainable simply by reading off the appropriate curve at these  $N_p N_n$  values (Casten, 1986).

process of *extrapolation* into one of *interpolation*, which is inherently much more reliable. Figure 6.53 illustrates this, giving as well one more illustration of the simplification achieved by the  $N_p N_n$  scheme. The vertical arrows point to the locations of four unknown neutron-rich nuclei in the rare earth region whose  $N_p N_n$  values are considerably less than those for known nuclei. Since this plot was constructed,  $^{148}\text{Ba}$  has been studied and the predictions verified. Preliminary reports on another nucleus in this region,  $^{142}\text{Xe}$ , also show that the  $N_p N_n$  scheme provides a much more accurate structural guide.

In the same vein, one can use the  $N_p N_n$  scheme to parameterize collective model calculations. Normally, in phenomenological models such as geometric collective models or the IBA, the Hamiltonian contains a number of terms, each incorporating a free strength parameter. These must be estimated for each individual nucleus, and therefore, the calculation of extensive sets of nuclei can involve an enormous proliferation of parameters. If instead, the parameters are written as *functions* of  $N_p N_n$ , it is often possible to calculate sets of 50–100 nuclei with only 4–6 parameters. Moreover, for reasons that are obvious from the previous discussion, this process automatically give parameter estimates for unknown nuclei further from stability, so their predictions become interpolative.

Finally, the  $N_p N_n$  scheme has recently been applied to odd  $A$  nuclei by Bucurescu, Zamfir, and colleagues with intriguing results. Energy ratios based on different initial single-particle configurations probe the p–n interaction for different orbit combinations. Moreover,  $N_p N_n$  plots in odd nuclei provide a sensitive signature of the evolution of strongly coupled and decoupled band structures (see discussion of these in Chapter 8).

Thus far, we have discussed the  $N_p N_n$  scheme for a given region and have

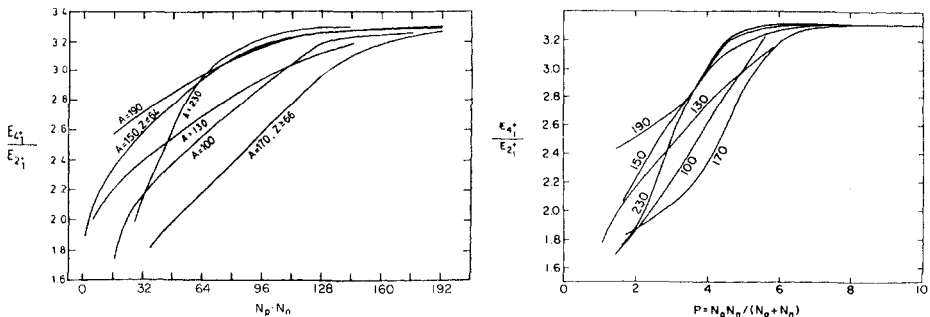


**Fig. 6.54.**  $N_p N_n$  (left) and  $P$ -factor (right) plots summarizing the systematics of  $E_{4+1}/E_{2+1}$  in six regions of medium and heavy nuclei (based on Casten, 1987).

noted its simplifying power. Further advantages of this approach are evident when one compares different regions. As we saw in Chapter 2, different regions appear to behave in entirely different fashion vis a vis the development of collectivity and deformation: one needs only to glance at Figs. 2.13 and 2.14 or Figs. 6.46 and 6.48 for a dramatic illustration of this. In contrast,  $N_p N_n$  plots are similar for essentially all regions of medium and heavy mass nuclei. Figure 6.54 (left) collects the smooth curves, drawn through  $N_p N_n$  plots, of the ratio  $E_{4+1}/E_{2+1}$  for six mass regions in heavy nuclei. What appeared earlier to be radically different behavior from one region to another becomes a set of nearly parallel curves in  $N_p N_n$ . The similarity in *structure* of these curves gives confidence that the  $N_p N_n$  scheme is a meaningful indicator. It also provides some confidence in extrapolating the curves for a new region once a few nuclei in that region are studied.

The other feature in Fig. 6.54 is that the curves for different regions are rather widely displaced: *changes* in structure are correlated with *changes* in  $N_p N_n$  throughout medium and heavy nuclei but the *absolute* value of  $N_p N_n$  provides little information. However, a slight modification of the  $N_p N_n$  scheme puts it on an absolute scale and provides further physical insight. To see this we consider the parameter

$$P = \frac{N_p N_n}{(N_p + N_n)} \quad (6.79)$$

$P$  can be viewed in several ways. It is simply a normalized value of  $N_p N_n$ . It is also a measure of the integrated strength of the valence p-n interaction compared to the valence pairing interaction that scales as the total number of valence nucleons. Finally, it is the average number of p-n interactions *per* valence nucleon. For this reason,  $P$  has been called a nucleonic “promiscuity factor.” If we now plot the same data used to obtain Fig. 6.54 (left) against  $P$ , we obtain the results shown on the right of that figure. Individually, the six curves show exactly the same behavior as their counterparts in the  $N_p N_n$  plot, but the different regions are coalesced into a narrow envelope, providing a

unifying framework for understanding the systematic behavior of nearly all medium and heavy mass nuclei and highlighting, even more than  $N_p N_n$ , the correlation between the p-n interaction and collectivity.

A slightly more detailed glance at the right-hand side of Fig. 6.54 reveals a fascinating point directly correlated with our understanding of the residual pairing and p-n interactions. If we take the value  $E_{4\pi}^+ / E_{2\pi}^+ \sim 3.0$  as a measure of the "transition point" from spherical and vibrational to deformed, we see that all the regions pass through this value in the narrow range of  $P$  values between 4 and 5. This value, denoted  $P_{\text{crit}}$ , gives a kind of "critical" value that acts as a signature for deformation. One can formulate a rule: nuclei with  $P < P_{\text{crit}} = 4-5$  will not be deformed, unlike nuclei with  $P > P_{\text{crit}}$ . Simple consideration of the formula for  $P$  refines this idea: a necessary condition for  $P > 4$  is that *both*  $N_p, N_n \geq 4$ , while a sufficient condition for  $P \geq 5$  is that *both*  $N_p, N_n \geq 10$ . Thus, no nucleus can be deformed unless there are at least four valence protons *and* four valence neutrons and a nucleus *must* be deformed if there are at least 10 valence nucleons of each type. Apparent exceptions to this rule such as the light Hg ( $Z = 80$ ) nuclei, which have two proton holes relative

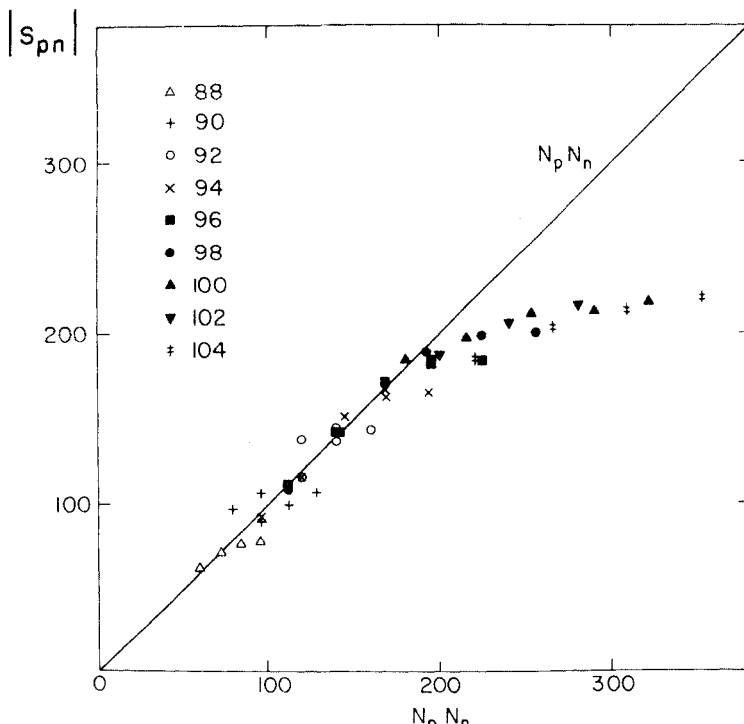


**Fig. 6.55.** Calculated  $|S_{pn}|$  values for the deformed rare earth nuclei, illustrating the saturation in quadrupole collectivity. Compare the behavior of empirical  $B(E2)$  values in Fig. 5.3 (Casten, 1988b). The legend gives the neutron number corresponding to each symbol.

to  $Z = 82$ , are indeed only apparent since the reason deformation sets in these nuclei is another example of the movement of single-particle energies of one type of nucleon as a function of the number of the other: as  $N$  decreases, the  $h_{9/2p}$  orbit from above  $Z = 82$  descends across the  $Z = 82$  gap and enters the shell below. The counting of  $N_p$  should therefore be based on some effective  $Z$  value between 82 and 92.

The value of  $P_{\text{crit}} \sim 4$  to 5 is interesting in itself. We know from the energy gap,  $2\Delta$ , in even-even nuclei that typical like-nucleon pairing interactions have strengths of  $V_{\text{pair}} \sim 1$  MeV. Similarly, p–n interactions are on the order of 200–300 keV (see Chapter 4). Thus,  $P$ , which gives the ratio of the number of p–n interactions to pairing interactions, equals 4–5 at precisely the point at which the *integrated* p–n interaction strength begins to dominate the pairing strength. This provides an appealing physical picture that simply states that softness to deformation and the phase transition to deformed shapes occur just when the deformation-driving p–n interaction begins to dominate the spherical-driving like-nucleon pairing interaction.

The  $N_p N_n$  scheme is based on the rather crude assumption that the p–n interaction is orbit independent. Since it is not, one might expect situations in which  $N_p N_n$  is not the best scaling parameter. In fact, we have already seen evidence for this: most observables are smooth against  $N_p N_n$  but they are not *linear* in  $N_p N_n$ . The valence p–n interaction increases with  $N_p N_n$ , but is not necessarily proportional to it. The most dramatic evidence for this occurs in the empirical behavior of  $B(E2:0_1^+ \rightarrow 2_1^+)$  values in deformed nuclei. These increase from the beginning of a shell through the transition region. But, instead of continuing this increase unabated until midshell, they saturate. This was illustrated earlier for rare earth nuclei in Figs. 2.16 and 5.3. The reader will recall from our discussion of the IBA that this  $B(E2:0_1^+ \rightarrow 2_1^+) \sim N^2$  both in SU(3) and in realistic symmetry breaking calculations for deformed nuclei. Thus, assuming constant boson effective charges  $e_B$ , such IBA calculations must disagree significantly with the data near midshell. These and other data suggest that, although some simplicity will be lost, it might be useful to have a more refined estimate of p–n strength than  $N_p N_n$ . This can be obtained very easily by a simple, explicit calculation of the integrated quadrupole p–n interaction among the valence nucleons. The result, called  $|S_{pn}|$ , is shown in Fig. 6.55. Clearly, instead of  $N_p N_n$ , one can use these calculated  $|S_{pn}|$  values to define effective  $(N_p N_n)_{\text{eff}}$  products and therefore effective values of  $N_p$  and  $N_n$  themselves. If these are then used to recalculate quantities such as  $B(E2:0_1^+ \rightarrow 2_1^+)$  values, the observed saturation is excellently reproduced.

If we anticipate our discussion of the Nilsson model in the next chapter, we can easily explain the behavior of  $|S_{pn}|$ . (Readers unfamiliar with the Nilsson model, please forgive this short digression: better yet, return to it after reading the next chapter.)  $|S_{pn}|$  is obtained simply by integrating (summing) the products of the individual proton and neutron quadrupole moments for each Nilsson orbit over all filled orbits up to a given  $N, Z$ . Downward sloping lines in the Nilsson diagram correspond to equatorial orbits, while flat or upward sloping lines represent more polar orbits. Thus, at the beginning of a shell,

when both protons and neutrons are filling the equatorial downward sloping orbits, there will be high overlap and significant contributions to the integrated quadrupole p-n interaction. Near midshell, however, some neutrons will enter flat or upward sloping orbits that will have lower overlap with the downward sloping proton orbits, and vice versa. These, and proton-neutron pairs in which both particles are in flat Nilsson orbits with zero quadrupole moments, will contribute little or nothing to further increases in the integrated quadrupole p-n interaction strength. This strength should therefore increase linearly with  $N_p N_n$  at the beginning of a shell and then saturate toward midshell.

One last point is relevant before ending this discussion—the concept of a p-n interaction scaling approximately with  $N_p N_n$  at the beginning of a shell and then saturating near midshell was originally proposed as a convenient ansatz in order to provide a simple phenomenological approach to the systematics of certain collective observables. Very recently, however, Zhang and co-workers have *empirically* extracted actual p-n interaction energies for the last proton and last neutron in a given nucleus and, by carrying out appropriate sums, obtained the total valence p-n interaction energies for a given nucleus. The results show exactly the initial linearity with  $N_p N_n$  and subsequent slower growth that we have been discussing. That they do not completely saturate highlights the fact that  $S_{pn}$  is just the quadrupole interaction. The total p-n interaction includes the always attractive monopole component whose strength is monotonic throughout a shell and so provides a continuously increasing “base” to the total  $T=0$  p-n strength.

We have seen that the  $N_p N_n$  scheme, and its siblings  $P$  and  $|S_{pn}|$  plots, provide a simple yet powerful way of correlating a vast amount of systematic data on the development of collectivity, phase transitions, and deformation in medium and heavy nuclei. These concepts have an appealing microscopic foundation in the deformation-driving  $T=0$  component of the valence p-n interaction and its competition with its opposite number, the spherical-driving like-nucleon pairing interaction. In this way, these ideas, albeit phenomenological, bring together a number of threads running throughout this book. Through this phenomenology, we are beginning to develop a unified, coherent view of the evolution of nuclear structure. This view emphasizes the importance of the p-n interaction, and its role both in modifying the underlying shell structure and in inducing correlations, configuration mixing and deformation. What is needed now is to graduate from phenomenology to a real microscopic theory of nuclear structure and its evolution that embodies these ideas.

Another key issue is to understand the relation between the obvious centrality of the p-n interaction and the equally obvious successes of collective models that make no *explicit* mention of this interaction. The resolution of this seeming paradox appears to be twofold. First, the p-n interaction determines the “mean field,” that is, the correlations and deformation of the ground state (or the base state of a family of states such as the intruders), upon which the collective excitations are then constructed. Secondly, the p-n interaction, through its monopole component, affects the detailed distribution and energies of the underlying single-particle states. As we have seen, this is critical to

the evolution of subshell gaps and therefore to the content of the valence space on which the quadrupole component acts. Moreover, these single-particle states are the fodder with which (see Chapter 9) the detailed microscopic structure (e.g., energies, collectivity) of the vibrational excitations is constructed. Thus, the p–n interaction implicitly enters collective models both in the equilibrium shapes they present and in the single-particle energies used in obtaining their predictions.

## THE DEFORMED SHELL MODEL OR NILSSON MODEL

The purpose of this chapter is to describe the basic single-particle model applicable to nearly all deformed nuclei—the Nilsson model. This model is surely one of the most successful nuclear models ever developed. It accounts for most of the observed features of single-particle levels in hundreds of deformed nuclei and is always the first model turned to when new experimental information on such levels is obtained. It also provides a microscopic basis for the existence of rotational and vibrational collective motion that is directly linked to the spherical shell model. It is also very easy to incorporate extensions, refinements, and corrections to it. Essentially a single-particle model, the Nilsson model has enjoyed particular success in the interpretation of single nucleon transfer reactions.

Even before discussing this model, we are faced with a conceptual difficulty arising from the nonspherical shape, or the separation of the motion of an individual nucleon around the nucleus from rotations of the nucleus itself in space. These motions can be very different. Imagine a nucleus with prolate quadrupole distortion and a single nucleon orbiting in an equatorial plane, as shown by orbit  $K_1$  in Fig. 7.1. Now imagine that this nucleus can rotate about an axis perpendicular to the symmetry axis. With rapid rotation about this axis, the time averaged shape of the core becomes oblate (disc-like). What

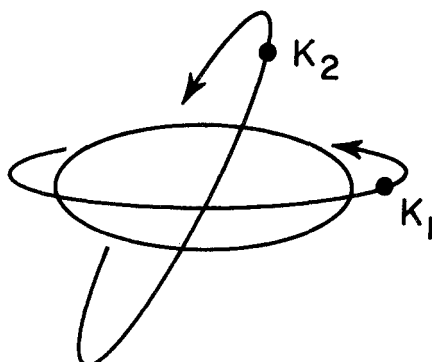


**Fig. 7.1.** Illustration of two single-particle orbits at different inclinations to a prolate deformed nucleus.

shape the orbit of the single nucleon takes then depends on the extent to which its motion is coupled to that of the core, that is, it depends on the separation of rotational and single-particle degrees of freedom. A rigorous separation is, in general, not possible. An approximate separation can be made, however, if the frequency of the nucleonic motion is much larger than the frequency of the nuclear rotation, in which case the individual nucleon executes many orbits during a single nuclear rotation, or, alternately phrased, the nucleus is essentially stationary during a single orbit of that nucleon.

This discussion is not only of formal interest, but alerts us to the possibility that the separability of these motions may be rather poor for extremely high rotational velocities. Modern experimental techniques have approached the limit where the characteristic frequencies for rotational and single nucleon motion are not distinct. It is then necessary to explicitly incorporate the effects of the rotation on the single-particle motion. Coriolis mixing is one such effect that we shall discuss at length, but there are others (relating to the underlying core shape, the effective single-particle energies, and so on) that are beyond the scope of this book. Mathematically, the separation of single-particle and rotational motion greatly simplifies calculations and is the principle reason why in a body-fixed frame of reference, one evaluates the single nucleon motion first and later superimposes the rotational motion. (Incidentally, the same basic type of problem applies to the spherical shell model, in which the “global” motion is linear motion of the center of mass, which is more easily distinguished.)

## 7.1 The Nilsson Model

We will discuss in considerable detail the quantitative properties of the Nilsson model and in particular the Nilsson energies and wave functions. First, however, we wish to proceed in a rather unconventional way in order to show that it is simple to “derive,” without detailed calculation, the entire Nilsson diagram and many of the prominent features of the Nilsson wave functions. The two necessary ingredients are simply a choice of deformed single-particle potential, such as a shell model potential with quadrupole deformation  $\beta$ , and the recognition that the nuclear force is short range and attractive.

Consider first, then, a valence nucleon in a single  $j$  orbit in such a prolate deformed potential (Fig. 7.1). It will have lower energy if its orbit lies closer to the rest of the nuclear matter than if it lies at larger distances from it. Clearly, then, the orbit labeled  $K_1$  will be lower in energy than  $K_2$ . The energy depends on the *orientation* with respect to the nuclear symmetry axis. This is contrary to the spherical shell model where there is no preferred direction in space. One can specify this orientation by the magnetic substate of the nucleon—that is, the projection of the total angular momentum on the symmetry axis as shown in Fig. 7.2. As in our earlier discussion of even-even nuclei, this quantity is usually denoted by the symbol  $K$ . (Technically,  $\Omega$  is used for the projection of the single-particle angular momentum on the symmetry axis and  $K$  for the projection of the total angular momentum. However, since the

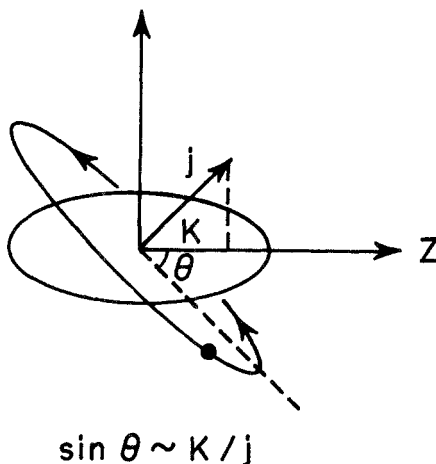


**Fig. 7.2.** Diagram defining the quantities  $j$ ,  $K$ , and  $\theta$  in the discussion of the Nilsson model.

rotational angular momentum for low-lying states of axially symmetric nuclei is perpendicular to the symmetry axis, it contributes nothing to  $K$  and therefore  $K = \Omega$  and is often substituted for it.) The low  $K$  values correspond to equatorial motion near the bulk of the nuclear matter for a prolate quadrupole distortion, and have lower energy.

One can easily go a step further. Consider the classical orbit angles corresponding to different  $K$  values. Suppose  $j = 13/2$  (e.g., the  $i_{13/2}$  orbit) with  $K = 1/2, \dots, 13/2$ . Classically, as illustrated in Fig. 7.2, we can approximate the angle of an orbital plane by  $\theta = \sin^{-1}(K/j)$ . These angles are given in Table 7.1. The interesting feature is that  $\theta$  changes slowly for low  $K$  values and rapidly for high  $K$  values. Therefore one expects that the difference in energy between low  $K$  values is rather slight and increases rapidly for the higher ones. With these simple considerations, we can now develop a limited region of a Nilsson diagram for a single  $j$ . This is shown in Fig. 7.3. The characteristic features are just as we have derived: for  $\beta > 0$ , the energy drops rapidly with  $\beta$  for low  $K$  values and rises rapidly for the higher  $K$  values and the separation of adjacent  $K$  values increases sharply with  $K$ . We shall see that the energies for small deformations depend on  $K^2$ .

The only additional step needed to construct the full Nilsson diagram of deformed single-particle energies as a function of  $\beta$  is to combine several  $j$  values. As discussed earlier, the characteristic feature of a deformed field is single-nucleon configuration mixing. Therefore, we must now superimpose this configuration *mixing* of different  $j$  values on the  $K$  splitting just considered.

**Table 7.1.** Classical orbit angles, relative to the nuclear equator, for  $j = 13/2$ .

$K$	1/2	3/2	5/2	7/2	9/2	11/2	13/2
$\theta(\text{deg})$	4.4	13.3	22.6	32.6	43.8	57.8	90
$\Delta\theta(\text{deg})$		8.9	9.3	10.0	11.2	14.0	32.2

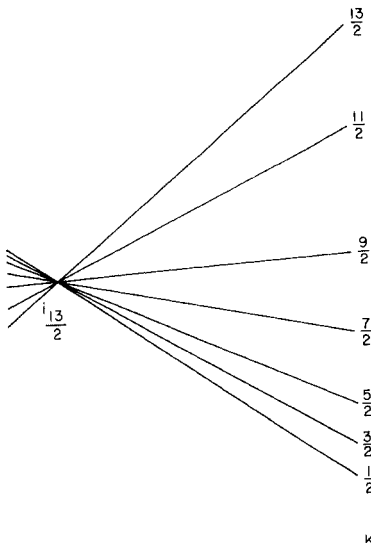


**Fig. 7.3.** Variation of single-particle energies of  $i_{13/2}$  orbits with different projections  $K$  (orientations  $\theta$ ) as a function of deformation ( $\beta > 0$ , prolate, to the right).

Recalling a fundamental rule of quantum mechanics that no two levels with the same quantum numbers may cross (an infinitesimal interaction will cause them to repel when they get sufficiently close) and noting that the only remaining good quantum number for these orbits is  $K$ , it then follows that no two lines in the Nilsson diagram corresponding to the same  $K$  value (and parity) cross. As two such lines approach each other they must repel (see Fig. 1.9). Thus, it is now possible to incorporate several  $j$  values into the Nilsson diagram and to extend it to realistic deformations where the energies of different orbits intermingle. This is shown in Fig. 7.4, which gives the Nilsson diagram for two different regions. Each line, representing a Nilsson state, starts out straight and is downward or upward sloping according to the angle of the orbit relative to the main mass of the nucleus. It only starts to curve when it approaches another level with the same  $K$  and parity. The entire structure of the diagram relies thus on only three factors:  $K$  splitting (resulting from the effects of a short-range nuclear interaction in a deformed field), level-level repulsion, and the input single-particle shell model energies.

The Nilsson wave functions are equally easy to deduce qualitatively, even though they are a complex result of a multistate diagonalization. (We ignore here the phases of the various terms in these wave functions, most of which can only be obtained by explicit diagonalization.) The interaction that leads to configuration mixing in Nilsson model is of quadrupole form. (We will discuss other deformed shapes later.) For very small quadrupole deformations  $\beta$ , the nuclear wave functions must be nearly pure in  $j$ ; as the deformation increases, the configuration mixing will increase.

The nondiagonal mixing matrix elements of the quadrupole interaction, not

surprisingly, tend to mix configurations that differ by two units in angular momentum and in which the nucleon spin orientation is not changed. For example, in the 50–82 shell, the  $d_{5/2}$  and  $s_{1/2}$  orbits have large matrix elements and mix substantially, even though they are slightly further separated than the  $d_{5/2}$  and  $d_{3/2}$  orbits. The  $g_{7/2}$  and  $d_{3/2}$  mix more than  $g_{7/2}$  and  $d_{5/2}$  do. Likewise, in the 82–126 shell, the quadrupole matrix element between the  $p_{3/2}$  and  $f_{7/2}$  orbits is strong. However, the closeness of the energies of the  $f_{7/2}$  and  $h_{9/2}$  orbits leads to substantial mixing, even though the matrix element is not favored. Therefore, combining a regard for the energy separations of different shell model orbits and the most important quadrupole mixing matrix elements, one can estimate the Nilsson wave functions, that is, the composition of the wave functions in terms of amplitudes for different  $j$  subshells.

Consider the example of the 82–126 neutron shell shown in Fig. 7.4. As  $\beta$  increases, the  $f_{7/2}$  and  $h_{9/2}$  orbits begin to mix. We recall that the angle of the orbital orientation depends primarily on the ratio  $K/j$  ( $\theta \approx \sin^{-1} K/j \approx K/j$  for

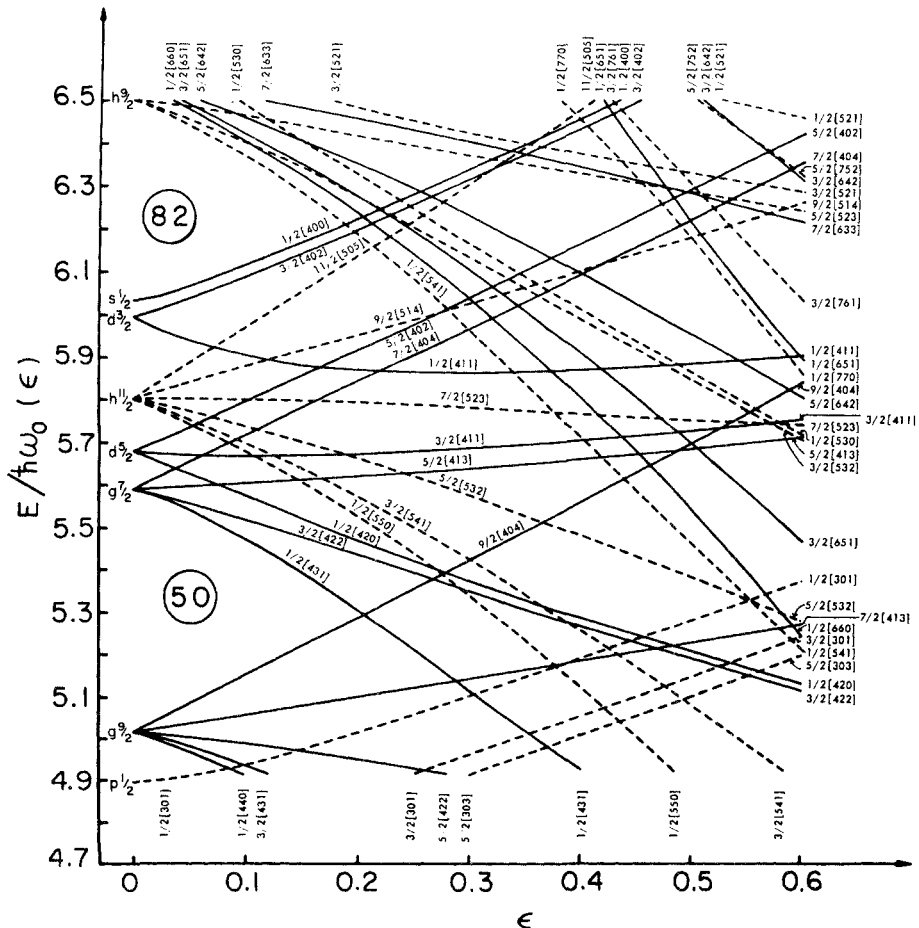


**Fig. 7.4. (a)** Nilsson diagram for the  $Z=50-82$  regions. The abscissa is the deformation parameter  $\epsilon$ , which is nearly the same as  $\beta$ . (Gustafson, 1967).

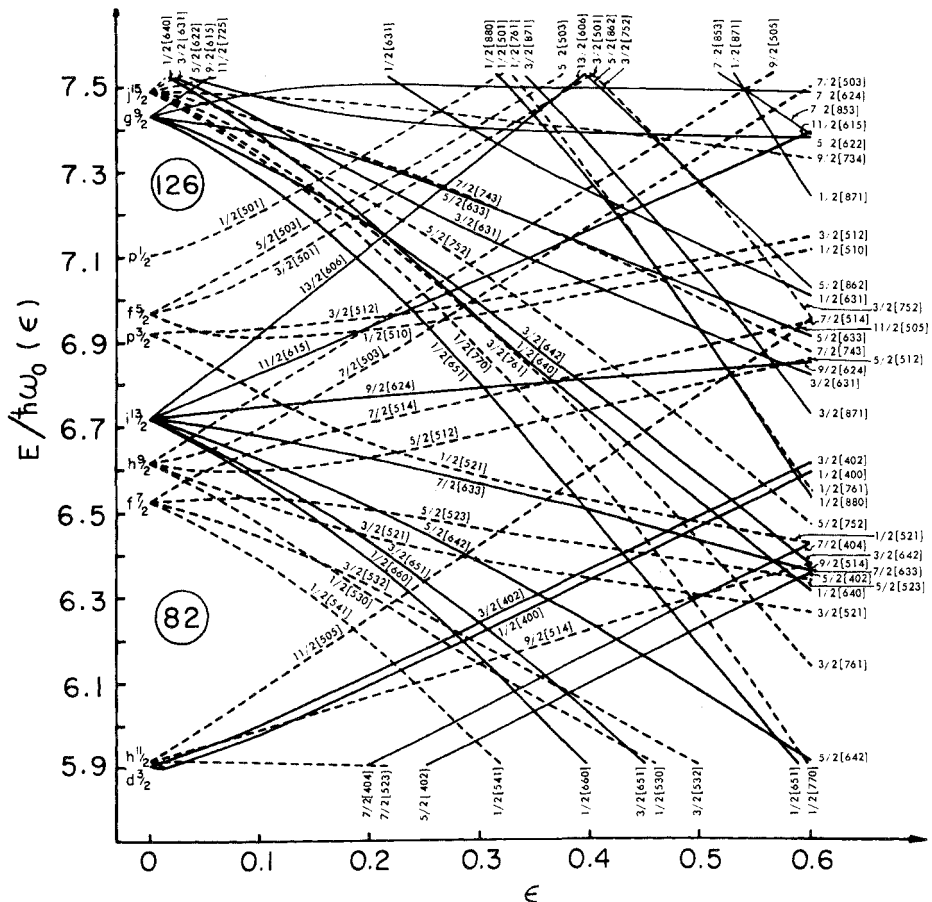


**Fig. 7.4. (b)** Nilsson diagram for the  $N = 82$ - $126$  regions. The abscissa is the deformation parameter  $\epsilon$ , which is nearly the same as  $\beta$ . (Gustafson, 1967).

small  $K$ ). Small angles can occur either because  $K$  is low, or for given  $K$ , because  $j$  is high. Thus, the energies of the  $K = 1/2$ ,  $3/2$ , and  $5/2$  orbits from the  $h_{9/2}$  shell decrease in energy faster with deformation than those from the  $f_{7/2}$  orbit. This difference in rate of decrease of the Nilsson energies with deformation can overcome the small spherical  $f_{7/2}$ - $h_{9/2}$  energy separation. The low  $K$   $f_{7/2}$  and  $h_{9/2}$  orbits therefore approach each other, mixing more and more. However, the two orbits cannot cross and so repel each other, leading to an *inflection point* at the value of  $\beta$  where they would have crossed. This effect is very clear for the  $K = 5/2$  and  $K = 7/2$ ,  $f_{7/2}$  and  $h_{9/2}$  orbits in Fig. 7.4.

An interesting feature of the Nilsson diagram is apparent if one looks at the energies past the “pseudo crossing.” Starting at large deformations and tracing back toward  $\beta = 0$  the energy of the lowest  $K = 5/2$  orbit is drawn as if it stems from the  $f_{7/2}$  shell. However, one sees that it actually points directly back to the  $h_{9/2}$  spherical energy. This reflects the fact that this orbit, for large deformations, is actually the continuation of the  $h_{9/2}$  shell. In effect, while the

energies do not cross, the wave functions do “exchange” principle wave function components near the inflection point.

In contrast to these examples, the  $K = 9/2$  orbit from the  $h_{9/2}$  shell is virtually straight since there is no other nearby (negative parity)  $j$  shell with a  $K = 9/2$  component. This reflects the general feature that the Nilsson wave functions for the highest  $K$  values in a given shell are very pure.

The extreme example of this, in the 82–126 shell, is the orbits stemming from the  $i_{13/2}$  shell. This shell, with  $l = 6$ , has positive parity and lies amidst a grouping of negative parity orbits. It has been brought down from the next major shell by the strong spin-orbit interaction in the shell model. Having opposite parity it cannot mix with any other orbits in the 82–126 shell. Therefore the wave functions of these *unique parity* Nilsson orbits are extremely pure, consisting almost solely of  $j = 13/2$  components even to rather large deformations. This special structure has many extremely important consequences. The simplicity of their wave functions makes a number of physical effects particularly simple to understand. Moreover, certain residual interactions such as Coriolis effects are both simple and particularly strong in these orbits. Finally, many of these same features make the states stemming from these orbits easily amenable to empirical study.

This discussion of the structure of the Nilsson diagram for a given major shell can be applied to any shell and the entire Nilsson diagram can be constructed. The only other point to note is that the higher the shell, the stronger the effects we have been considering will be, since a particle in a higher shell is at a larger radius, further outside the spherical nucleus, and therefore has more to gain energetically, upon deformation, if it is equatorial.

It should be evident by now that it is easy to write down not only the approximate energies but also estimates of the wave functions of almost any Nilsson orbit without detailed calculation. We shall give a couple of examples of this in a moment, but first it is convenient to define the Nilsson quantum numbers labeling each orbit. This is also instructive because it highlights the physical nature of the various orbits. A typical Nilsson orbit is labeled as follows:

$$K^\pi [N n_z \Lambda]$$

The first quantum numbers give the  $K$  value and parity. Inside the brackets the three quantum numbers are  $N$ , the principle quantum number of the major shell;  $n_z$ , the number of nodes in the wave function in the  $z$  direction ( $n_z$  is particularly critical for understanding the structure of the wave function); and  $\Lambda$ , the component of the orbital angular momentum along the  $z$ , or symmetry, axis. By definition,  $K = \Lambda + \Sigma = \Lambda \pm 1/2$ , where  $\Sigma$  is the projection of the intrinsic nucleon spin on the symmetry axis. Hence, one sometimes sees an alternate notation  $[N n_z \Lambda \uparrow]$  or  $[N n_z \Lambda \downarrow]$ , where the arrow replaces  $K$  and indicates whether the spin angular momentum aligns ( $\uparrow$ ) or antialigns ( $\downarrow$ ) with the orbital angular momentum. The two notations are equivalent, but using  $K$  is somewhat more convenient and common.

For the most common case of a prolate nucleus, equatorial orbits are nearest the nuclear matter and lie lowest. It is clear from Fig. 7.1 that these orbits are also those in which the nucleon wave function is most extended in

the  $z$  direction. Their wave functions have the largest number of nodes in the  $z$  direction and hence the largest values of  $n_z$ . We note also that there is a relation between the permissible values of  $n_z$  and  $\Lambda$  such that their sum must be even if  $N$  is even (positive parity) and odd if  $N$  is odd (negative parity).

We are now in a position to label all the Nilsson orbits in a given shell. There are two ways this can be approached, one by labeling the sequence of orbits from each spherical  $j$  shell and another in which all orbits of a given  $K$  value are labeled according to increasing energy. To make the labeling absolutely clear, we will illustrate both approaches (for a prolate nucleus). We start from the fact that the lowest-lying orbit has the highest possible  $n_z$ . Clearly the maximum value of  $n_z$  for a given principle quantum number  $N$  is  $n_z = N$ . The lowest orbit for a given  $N$  has  $K = 1/2$ , since this is the most equatorial orbit. Taking  $N = 5$  for illustration, noting that if  $K = 1/2$ ,  $\Lambda$  can only be 0 or 1, and that  $n_z + \Lambda$  must be odd since  $N$  is odd, the Nilsson quantum numbers for the lowest  $N = 5$  orbit must be

$$K^{\pi}[N n_z \Lambda] = 1/2^- [550]$$

This Nilsson labeling describes the  $K = 1/2$  orbit stemming from the  $h_{11/2}$   $j$  shell. Although most of the  $N = 5$  orbits occur in the 82–126 major shell, the  $h_{11/2}$  orbit is the one that is pushed down by the spin orbit interaction into the lower, predominantly  $N = 4$ , 50–82 shell. Continuing for the other orbits from the  $h_{11/2}$  shell, the next has  $K = 3/2$ . Since its orbital orientation is slightly more inclined away from the equatorial plane, it is less extended in the  $z$  direction and has the next lower  $n_z$  value. Its Nilsson quantum numbers are  $3/2^-$  [541]. Again, the  $\Lambda$  value is fixed by the requirements that  $n_z + \Lambda$  is odd and  $\Lambda = K \pm 1/2$ . The rest of the  $h_{11/2}$ -based orbits are then  $5/2^-$  [532],  $7/2^-$  [523],  $9/2^-$  [514],  $11/2^-$  [505].

The next  $N = 5$  orbits are in the 82–126 shell proper, and stem from the  $f_{7/2}$  parent (although their actual wave functions contain large  $h_{9/2}$  amplitudes). The  $K = 1/2$  orbit, having higher energy than the  $K = 1/2$  orbit from the  $h_{11/2}$  shell, must be less extended in the  $z$  direction and must have a lower  $n_z$ . Its Nilsson quantum numbers are then trivially,  $1/2^-$  [541]. The  $K = 3/2$  orbit is  $3/2^-$  [532]. One can continue filling the entire shell in this way, and it is easy to reproduce the labels shown in Fig. 7.4.

An alternative way is to proceed not by energy for a given parent  $j$  shell but by  $K$  value. For example, the sequence of  $K = 1/2$  orbits, starting with that from the  $h_{11/2}$  orbit, will be (recall that  $\Lambda = 0$  or 1)

$$1/2^-[550], 1/2^-[541], 1/2^-[530], 1/2^-[521], 1/2^-[510], \text{ and } 1/2^-[501]$$

The unique parity orbit in the 82–126 shell is the lowest  $N = 6$  orbit, and therefore its Nilsson quantum numbers must be  $1/2^+[660]$ ,  $3/2^+[651]$ , ...,  $13/2^+[606]$ .

Let us now consider the wave functions in more detail. These wave functions can be written in many forms. Because they involve single- $j$  configuration mixing, they can be expanded in a spherical basis. For many purposes the easiest and most physically transparent form is one that the previous discussion anticipated, an expansion in shell model orbits specified by their  $j$  values. Thus, we write

$$\psi_{\text{Nilss}} = \sum_i C_j^i \phi_j \quad (7.1)$$

where the  $\phi_i$  are solutions to the spherical independent particle model and the  $C_j$  are expansion coefficients. Using this language, it is easy to make at least crude estimates of the actual Nilsson wave functions. For example, for  $\beta = 0.23$  ( $\epsilon \approx 0.95$ ,  $\beta \approx 0.22$ ) the  $5/2-[523]$  orbit will have a wave function that is predominantly  $h_{9/2}$ , with the next largest component  $f_{7/2}$ . Crudely, we can estimate that  $\psi(5/2-[523]) \approx 0.5\phi_{11/2} + 0.8\phi_{9/2} + \dots$ . We emphasize that this is at best a guess as to the Nilsson wave functions and that the phases are arbitrary. We engaged in this exercise simply because it is useful to have at least *some*, albeit crude, a priori feeling for the structure of these wave functions. It will also remove some of the mystery from the actual Nilsson wave functions. To take another example, consider that the  $3/2-[532]$  orbit for a deformation of  $\beta \approx 0.23$  is just past the inflection point with the  $3/2-[521]$  orbit. Its wave function should be roughly equal admixtures of  $f_{7/2}$  and  $h_{9/2}$  components. In contrast, the wave function for the same orbit for a deformation of  $\beta \approx 0.05$  would be largely  $f_{7/2}$ .

The wave functions near the top of the 82–126 shell are particularly simple:  $\psi(1/2-[501])$  is dominated by a  $p_{1/2}$  component. Near midshell, the situation is somewhat more complicated since a given wave function will contain components from  $j$  shells both above and below it. A particularly nice example is the  $1/2-[521]$  orbit. Careful inspection of the Nilsson diagram shows that although it starts out from the  $p_{3/2}$  shell, it soon mixes with the  $K = 1/2$   $f_{5/2}$  orbit, undergoing a virtual crossing before  $\beta \approx 0.1$ . At this point its wave function is a very thorough mixture of  $\phi_{3/2}$  and  $\phi_{5/2}$  components. Continuing to larger deformations, at  $\beta \approx 0.2$  there is another inflection point due to interaction with a combination of the  $K = 1/2$  orbits from the  $f_{7/2}$  and  $h_{9/2}$  shells. Therefore, we might expect at  $\beta \approx 0.25$  that  $\psi(1/2-[521]) \approx C_{3/2}\phi_{3/2} + C_{5/2}\phi_{5/2} + C_{7/2}\phi_{7/2} + C_{9/2}\phi_{9/2}$  with all four  $C_j$  values substantial in magnitude.

As we anticipated, the unique parity orbits are extremely pure, and increasingly so as  $K$  increases. For example, the  $13/2^+[606]$  orbit *must* (assuming no  $N$  mixing) be pure  $j = 13/2$ , while  $\psi(1/2[660]) \approx 0.95\phi_{13/2} + 0.3\phi_{9/2} + \dots$  (These numbers are only rough estimates but do embody the physics and reflect the actual amplitudes from real calculations.) Note that the only other significant contribution besides  $i_{13/2}$  comes from the  $g_{9/2}$  orbit, which differs by two units of

**Table 7.2.** Nilsson wave functions ( $C_j$  coefficients) for some  $N = 5$  orbits

$K\pi[Nn_z\Lambda]$	$j$						
	1/2	3/2	5/2	7/2	9/2	11/2	
3/2-[532]		0.234	0.369	-0.560	-0.651	0.268	
5/2-[523]			0.237	-0.472	-0.826	-0.196	
7/2-[514]				0.323	0.938	0.128	
1/2-[521]	-0.510	0.345	0.473	0.431	0.444	0.120	
5/2-[512]				-0.023	0.836	-0.515	0.157
1/2-[510]	0.021	-0.676	0.586	-0.343	0.277	0.067	
3/2-[512]		0.379	0.815	0.283	0.327	0.063	
7/2-[503]					0.937	-0.336	0.099
9/2-[505]						0.998	0.071
1/2-[501]	-0.821	-0.361	-0.411	-0.122	-0.104	-0.019	

\* $\delta = 0.22$ ,  $\kappa = 0.0637$ ,  $\mu = 0.42$ .

angular momentum and has its spin and orbital components aligned in the same way as the  $i_{13\sigma}$ .

Table 7.2 gives examples of some actual Nilsson wave functions for a typical Nilsson potential ( $\delta = 0.22$ ,  $\beta \approx 0.23$ ). Inspection of the table shows that all our guesses as to the structure are semiquantitatively correct. Of course, fine details are beyond this discussion and some amplitudes are more difficult to intuit a priori.

It is worth pausing here to reflect on and to re-emphasize what we have done. Without any detailed calculation whatsoever, using only simple considerations of the attractive nature of the nuclear force and the nuclear shapes involved, we have essentially "derived" the entire Nilsson diagram, the Nilsson energies, and the asymptotic Nilsson quantum numbers. We have also discussed the basic structure of the wave functions.

At this point, however, we can obtain a deeper understanding of the Nilsson model and diagram and of the role of the quantum number,  $n_z$ , by a slightly more formal approach.

To begin, we consider the Nilsson Hamiltonian for a single-particle orbiting in a deformed potential and inspect two instructive limits, corresponding to small and large deformation. Actually there are many Nilsson-type Hamiltonians incorporating many variants of the single-particle deformed potential. Various authors have used deformed harmonic oscillator or modified harmonic oscillator potentials, Wood-Saxon potentials, and others. The differences reside primarily in details that do not concern us here so we will content ourselves with the modified harmonic oscillator originally used by Nilsson.

The Nilsson model is a shell model for a deformed nucleus. It provides a description of single particle motion in a nonspherical potential,  $V = V_0(r) + V_2(r) P_2(\cos\theta)$ . The original and basic form incorporated only quadrupole deformed axially symmetric shapes. An appropriate single-particle Hamiltonian for a nucleus with symmetry axis  $z$  is:

$$H = T + V \\ = \frac{\mathbf{p}^2}{2m} + \frac{1}{2} m [\omega_x(x^2 + y^2) + \omega_z z^2] + C \mathbf{l} \cdot \mathbf{s} + D \mathbf{l}^2 \quad (7.2)$$

where  $\omega_x$ ,  $\omega_y$ , and  $\omega_z$  are one-dimensional oscillator frequencies in the  $x$ ,  $y$ , and  $z$  directions. This Hamiltonian satisfies the eigenvalue equation  $H\psi_i = E_i\psi_i$ , where  $\psi_i$  is a Nilsson wave function written in the form  $\psi_i = \sum_j C_j \phi_j$ . The  $\mathbf{l}^2$  and  $\mathbf{l} \cdot \mathbf{s}$  terms ensure the proper order and energies of the single-particle levels in the spherical limit ( $\beta = 0$ ).

Although the form of the Hamiltonian in Eq. 7.2 is useful, it is also convenient to introduce an alternate version written directly in terms of a nuclear deformation parameter  $\delta \approx 3/2\sqrt{5/4\pi}$   $\beta \approx 0.95\beta$ . To do this, one writes the frequencies as

$$\begin{aligned} \omega_x^2 &= \omega_y^2 = \omega_0^2 \left(1 + \frac{2}{3}\delta\right) \\ \omega_z^2 &= \omega_0^2 \left(1 - \frac{4}{3}\delta\right) \end{aligned} \quad (7.3)$$

where  $\omega_0$  is the oscillator frequency ( $\hbar\omega_0 = 41A^{-1/3}$ ) in the spherical potential with  $\delta=0$ . It is assumed that the nuclear volume remains constant as a function of  $\omega_0$ . Therefore, one has the condition  $\omega_x \omega_y \omega_z$  constant or

$$\omega_0 = \left(1 - \frac{4}{3}\delta^2 - \frac{16}{27}\delta^3\right)^{-\frac{1}{6}} = \text{constant} \quad (7.4)$$

For positive deformations  $\delta$  or  $\beta > 0$  (prolate shapes),  $\omega_z$  decreases with increasing deformation while  $\omega_x$  and  $\omega_y$  increase. This is physically reasonable since an increasing prolate deformation elongates the nucleus in the  $z$  direction. This increases the “length” of a circumferential route and therefore lowers the frequency of orbiting in this direction. In contrast, the nucleus is “squeezed” in the  $x$  and  $y$  direction so the orbit frequencies can be larger for a given energy.

Inserting these definitions into Eq. 7.2 allows us to rewrite the Hamiltonian in terms of the operator  $\mathbf{r}^2 Y_{20}$  as follows

$$H = \frac{\mathbf{p}^2}{2m} + \frac{1}{2}m\omega_0^2\mathbf{r}^2 - m\omega_0^2\mathbf{r}^2\delta\frac{4}{3}\sqrt{\frac{\pi}{5}}Y_{20}(\theta, \phi) + C\mathbf{l} \cdot \mathbf{s} + D\mathbf{l}^2 \quad (7.5)$$

The two equivalent versions of the Nilsson Hamiltonian in Eqs. 7.2 and 7.5 allow us to understand the structure of the model in the limits of large and small deformations, respectively. Note that, in the literature the  $\mathbf{l} \cdot \mathbf{s}$  and  $\mathbf{l}^2$  terms are usually expressed in terms of parameters  $\kappa = C/2\hbar\omega_0$  and  $\mu = 2D/C$ .  $\kappa$  typically takes on values around 0.06 and  $\mu$  varies from 0 to  $\approx 0.7$ .

For small deformation,  $j$  is approximately a good quantum number. Equation 7.5 consists of a Hamiltonian for an isotropic oscillator with  $\mathbf{l}^2$  and  $\mathbf{l} \cdot \mathbf{s}$  terms plus a perturbation proportional to  $\delta \mathbf{r}^2 Y_{20}$ . The former part gives the spherical shell model energies and is spherically symmetric. The eigenstates of this Hamiltonian can be labeled by the quantum numbers  $Nlj$  and  $m$  of the spherical single-particle states. Treating the  $Y_{20}$  term as a perturbation, the shift in energies relative to  $\delta = 0$  is

$$\Delta E(Nljm) = -\frac{4}{3}\sqrt{\frac{\pi}{5}}m\omega_0^2\delta\langle Nljm | \mathbf{r}^2 Y_{20}(\theta, \phi) | Nljm \rangle \quad (7.6)$$

We can evaluate this by separating the radial and angular parts and using the relation for a harmonic oscillator potential that

$$\frac{1}{2}m\omega_0^2\langle Nljm | \mathbf{r}^2 | Nljm \rangle = \frac{1}{2}\hbar\omega_0\left(N + \frac{3}{2}\right) \quad (7.7)$$

Evaluating the matrix element of the spherical harmonic  $Y_{20}$  gives the final result for small  $\delta$

$$\Delta E(Nljm) = -\frac{2}{3}\hbar\omega_0\left(N + \frac{3}{2}\right)\delta\frac{[3K^2 - j(j+1)][\frac{3}{4} - j(j+1)]}{(2j-1)j(j+1)(2j+3)} \quad (7.8)$$

where we have replaced the projection  $m$  with  $K$ , the projection of the total angular momentum on the  $z$  axis.

This simple result has three facets that account for the structure of the Nilsson diagram for small deformations:

- There is a proportionality to  $\delta$ , the quadrupole deformation.
- The shifts display a dependence on  $K^2$ .
- They depend linearly on the oscillator quantum number  $N$ .

We have seen exactly these features in our intuitive derivation and in the Nilsson diagram, especially for unique parity orbits for which  $j$  is a good quantum number out to rather large deformations.

Another direct implication of Eq. 7.8 is that for  $\delta > 0$  there are more downward sloping than upward sloping orbits. For  $j > 1/2$ , the  $[3K^2 - j(j+1)]$  term is negative, giving downward sloping orbits (since  $3/4 - j(j+1)$  is negative) if

$$K < \sqrt{\frac{j(j+1)}{3}} \approx \frac{j}{1.8} = 0.65j \quad (7.9)$$

and upward sloping for  $K > 0.65j$ . For example, for  $j = 13/2$ , orbits with  $K = 1/2, 3/2, 5/2, 7/2$  should be downward sloping and  $K = 9/2, 11/2$ , and  $13/2$  upward sloping. This feature is indeed displayed by the exact numerical diagonalizations depicted in the Nilsson diagram of Fig. 7.4. Note the interesting physical correlation here. The angular orientation of an orbit to the symmetry axis is approximately given by  $\sin\theta \approx K/j$  and  $K/j \approx 0.65$  corresponds to  $\theta \approx 40^\circ$ . Inclinations greater than these are unfavored energetically by a prolate quadrupole deformation.

The dependence on  $N$  implies that the slopes of the energy levels in a Nilsson diagram are steeper for larger  $N$ . Thus, heavier nuclei are easier to deform than lighter ones. We commented implicitly on this  $N$  effect earlier and can now explain its physical origin a bit more precisely. A nucleon in a high oscillator shell will have a larger average radius [indeed, we just utilized the fact that the expectation value  $\langle \mathbf{r}^2 \rangle \propto (N + 3/2)$ ]. Therefore, as the nucleus deforms, the nuclear matter approaches this outer orbit. Since the nuclear force is attractive, the energy of a particle in this orbit decreases. The effect is obviously less for a particle in a lower oscillator shell that is already closer to (or inside) the bulk of the nucleus when it is spherical.

In the opposite limit of large deformation, the  $\mathbf{l} \cdot \mathbf{s}$  and  $\mathbf{l}^2$  terms in Eqs. 7.2 and 7.5 are negligible and the Hamiltonian simply reduces to an anisotropic harmonic oscillator whose form shows that the motion clearly separates into *independent* oscillations in the  $z$  direction and in the  $xy$  plane. Therefore the number of quanta in these directions,  $n_z$  and  $(n_x + n_y)$ , separately become good quantum numbers. The eigenvalues of the one dimensional harmonic oscillator with quanta  $n_i$  are simply  $\hbar\omega_i(n_i + 1/2)$ . This gives the familiar result for an isotropic three-dimensional harmonic oscillator that  $E \approx \hbar\omega(N + 3/2)$  where  $N = n_1 + n_2 + n_3$ . Thus, in the present case of *large*  $\delta$ , the eigenvalues of the anisotropic harmonic oscillator of Eq. 7.2 go asymptotically to

$$E(n_x, n_y, n_z) = \hbar\omega_x(N - n_z + 1) + \hbar\omega_z\left(n_z + \frac{1}{2}\right) \quad (7.10)$$

Since  $H$  is independent of the angle  $\phi$  around the  $z$  axis, the Hamiltonian corresponding to Eq. 7.10 is invariant with respect to rotations about the  $z$  axis. Therefore the  $z$ -projection of both the orbital and spin angular momenta of a

particle must be constants of the motion. As we have stated, these quantum numbers—the eigenvalues of the operators  $l_z$  and  $s_z$ —are commonly denoted by  $\Lambda$  and  $\Sigma$  while their sum, the projection of the total angular momentum on the symmetry axis, is indicated by  $K$ . The asymptotic energies  $E(n_x, n_y, n_z)$  can then be more conveniently expressed in terms of the quantum numbers  $K[Nn_z\Lambda]$  of the familiar Nilsson orbit notation.

Asymptotically, these energies are dependent on  $n_z$  and independent of  $\Lambda$ . The separation according to  $n_z$ , that is, according to the extent of the motion in the  $z$  direction or perpendicular to it, simply reflects the point made at the beginning of this chapter that, since the nuclear force is attractive, equatorial orbits will be favored and polar orbits unfavored in energy. The independence of  $\Lambda$  occurs for large  $\delta$  because the terms in  $\mathbf{l} \cdot \mathbf{s}$  and  $\mathbf{l}^2$  are negligible. Since  $K = \Lambda \pm \Sigma$ , this independence of  $\Lambda$  becomes an independence of  $K$  for large  $\delta$ . This is exactly opposite to the small deformation limit.

In general, a given value of  $n_z$  will have a number of degenerate states that can be specified by  $\Lambda$ , taking on the values  $(N-n_z), (N-n_z-2), (N-n_z-4), \dots 0$  or 1. For finite deformation where the  $\mathbf{l} \cdot \mathbf{s}$  and  $\mathbf{l}^2$  terms cannot be ignored, the eigenvalues will also split according to the value of  $\Lambda$  and, therefore, of  $K$ .

The asymptotic separation of the Nilsson diagram for large deformation according to  $n_z$  and the approximate independence of  $\Lambda$  or  $K$  are surprisingly little known, but can easily be seen in the Nilsson diagram for large deformations. As evident in Fig. 7.4 for large  $\epsilon$ , the lowest-lying orbits have  $n_z \approx N, N-1$ , while in midshell  $n_z = 1-2$  orbits predominate and near the end of a shell the  $n_z = 0$  and  $n_z = 1$  orbits are collected. The independence of  $\Lambda$  or  $K$  is illustrated nicely by the nearly degenerate and parallel orbits pairs  $7/2^-[503]$  and  $9/2^-[505]$ ,  $3/2^-[512]$  and  $1/2^-[510]$ , or  $3/2^+[422]$  and  $1/2^+[420]$ .

A nice empirical verification of the separability of the motion into components along and perpendicular to the symmetry axis comes from the properties of certain orbits differing by  $\pm 2$  in their principle quantum number  $N$ . In principle, the Nilsson Hamiltonian (specifically the  $\mathbf{l}^2$  and  $\mathbf{l} \cdot \mathbf{s}$  terms) can couple states with  $\Delta N = \pm 2$ , although these couplings are normally neglected since such states are separated by two oscillator shells ( $\approx 10$  MeV). For large deformations, however, the sensitivity of the energies to  $n_z$  leads to the phenomenon that steeply upsloping orbits from oscillator shell  $N$  may eventually cross steeply downsloping orbits from the  $N + 2$  shell. These orbits will have small and large values of  $n_z$ , respectively. An example of such  $\Delta N = 2$  orbit pairs are the  $3/2^+[402]$  and  $3/2^+[651]$  orbits. A priori, their mixing might be expected to be large in the near crossing region. However, that mixing has been empirically deduced from single nucleon transfer cross sections. The extracted interaction matrix elements are typically only  $\approx 50-100$  keV. Such small coupling matrix elements between states with very different distribution of quanta in the  $z$  and  $xy$  directions points to the approximate validity of the separation of motion in these two perpendicular directions. It is worth noting, however, that the presence of other deformation components, such as hexadecapole ( $\beta_4$ ) shapes, can greatly increase  $\Delta N = 2$  mixing.

To recapitulate some of the preceding points, we see two limiting situations of the Nilsson scheme. For small deformations  $\delta$ , the energies are approxi-

mately given by Eq. 7.8. They are linear in  $\delta$ ,  $j$  remains an approximately good quantum number (the configuration mixing is still small), and the orbits are separated principally by their  $K$  quantum numbers. For large deformations, the energies (Eq. 7.10) are again linear in  $\delta$  (recall that the  $\omega_i$  are linear in  $\delta$ ). The slopes, however, now depend on  $n_z$  and the energies separate according to the distribution of motion along and perpendicular to the  $z$  axis. For intermediate deformations, a transition between these two coupling schemes takes place.

## 7.2 Examples

Having discussed the Nilsson model both physically and formally, we can now turn to its application to odd mass deformed nuclei. Actually, this works in much the same way as the shell model for the single-particle excitations of spherical nuclei. The principle difference lies in the degeneracy of the orbits. In the shell model, an orbit  $j$  can contain  $2j + 1$  nucleons. In the Nilsson model, the degeneracy is broken according to the orbit orientation, or  $K$  value, and each Nilsson orbit can contain only two nucleons, corresponding to the two ways ( $\pm K$ ) in which the nucleon can orbit the nucleus (clockwise or counter-clockwise). Neglecting pairing for a moment, in a deformed region the Nilsson orbits are sequentially filled, two protons and neutrons to each, until the last odd nucleon is placed. This defines the ground state. Excited single-particle excitations can be obtained two ways, either by raising the last odd nucleon to a higher orbit, thereby changing its Nilsson quantum numbers, or by lifting a nucleon from one of the filled orbits to the last orbit, completing a pair of nucleons in the latter and leaving a hole below the Fermi surface. One therefore expects to have a sequence of intrinsic excitations whose energies and quantum numbers can be simply read off from the Nilsson diagram once the deformation is specified.

Here, in effect, is the major difference between the spherical shell model and the Nilsson model:  $N = 105$  corresponds to 21 holes relative to the magic number 126. A typical shell model calculation would diagonalize some residual interaction among 21 neutrons in the 82–126 shell and the complexity would be enormous. By switching to a deformed basis, the Nilsson model regains a “single-particle” picture, but with *deformed* single-particles orbits, each a relatively simple mixture of spherical  $j$  orbits. Multiparticle (or quasi-particle) excitations (the equivalent of seniority  $v \geq 3$  in the spherical shell model) only begin to appear near the pairing gap at 1.5–2.0 MeV. The deformed ansatz gives a remarkable simplification.

We recall and emphasize here that the Nilsson wave function is only a specification of the orbital motion of the nucleons in a body fixed coordinate system: the full specification of the wave function requires a consideration of the rotational behavior. This is absolutely crucial for an understanding of the structure of odd mass deformed nuclei and, indeed, for a deeper understanding of the Nilsson model itself, as well as its testing and application to real nuclei. We shall turn to the rotational motion shortly.

It is nevertheless useful at this point to indicate how well and simply the Nilsson model can be applied to deformed nuclei by way of a brief example or two. Consider the nucleus  $^{177}\text{Hf}$  with 72 protons and 105 neutrons. All the protons will be paired off to total angular momentum zero and, at least for the low-lying single-particle excitations, can be ignored. The same applies to the first 104 neutrons. Simple counting in the Nilsson scheme for  $\epsilon \approx 0.3$  shows that the 105th neutron will enter the  $7/2^-$ -[514] orbit. We therefore expect that the ground state of  $^{177}\text{Hf}$  will be  $7/2^-$ . (Actually, this is not so trivial: we have implicitly assumed that the lowest angular momentum will be equal to the  $K$  value for a given orbit. While this is generally true, it is not always the case, especially when strong Coriolis effects are present. This is a question that must be dealt with when we consider the rotational motion of an odd nucleus in more detail. For the moment we accept this assumption.) A low-lying excited state can clearly be formed by lifting the last neutron to the  $9/2^+$ -[624] orbit, giving a  $9/2^+$  state. Similarly, one of the two nucleons in the  $5/2^-$ -[512] orbit may be raised into the  $7/2^-$ -[514] orbit leaving a hole with spin  $5/2^-$ . Other low-lying excitations should correspond to the  $1/2^-$ -[521],  $7/2^-$ -[514], and  $7/2^-$ -[503] orbits at appropriate energies. A partial empirical level scheme for  $^{177}\text{Hf}$  is given in Fig. 7.5, showing the bandhead levels corresponding to each intrinsic Nilsson excitation. It corresponds rather well with our predictions. If we now go to  $^{179}\text{Hf}$ , we would expect the ground state to be  $9/2^+$ -[624] with the  $7/2^-$ -[514] an excited (hole) state. Moreover, all the excitations that were *above* the Fermi surface in  $^{177}\text{Hf}$  will now *decrease* in energy while those that were *below* the Fermi surface will *increase* in excitation energy. Comparisons of the two-level schemes in Fig. 7.5, which uses the convention that particle excitations are shown on the right and hole excitations on left, reveals exactly this behavior. In general, as one sequences through a series of isotopes (or isotones, if one is

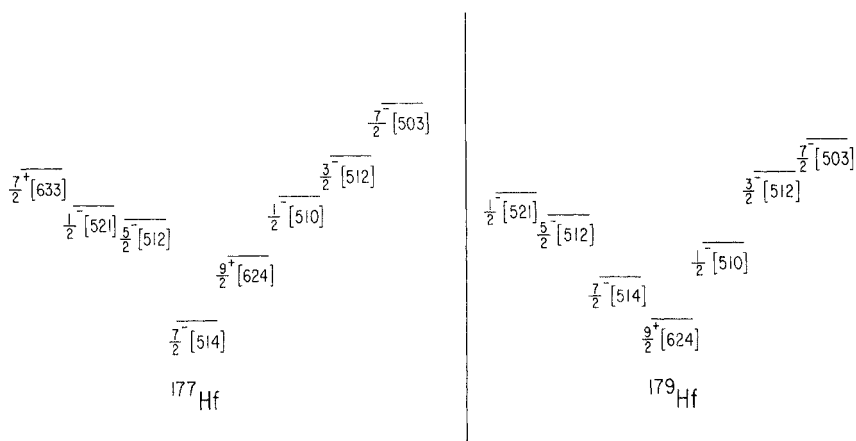


**Fig. 7.5.** Empirical bandheads of intrinsic Nilsson excitations in  $^{177}\text{Hf}$ ,  $^{179}\text{Hf}$ . Particle (hole) states are on the right (left).

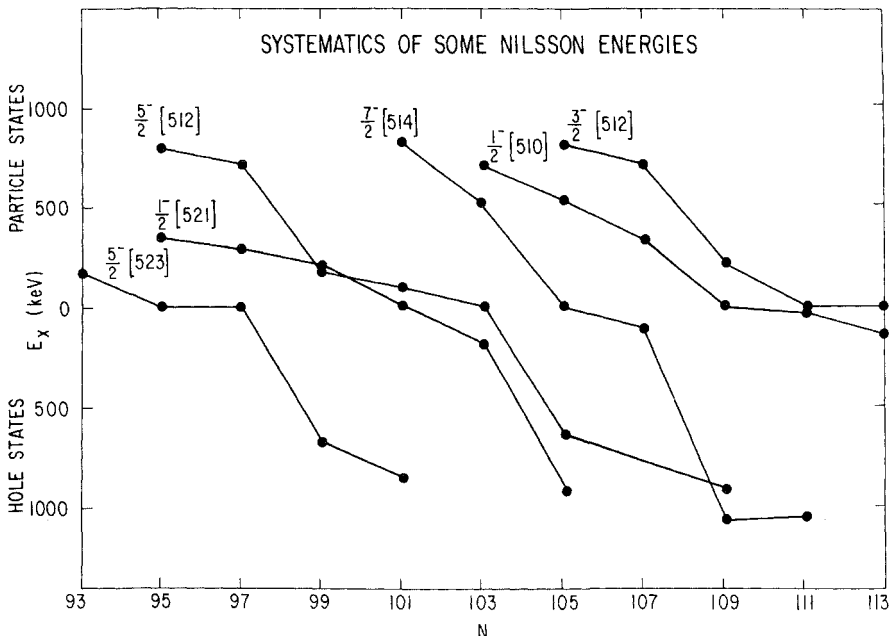


Fig. 7.6. Systematics of some Nilsson orbit excitation energies in the rare earth region. Hole states are given negative energies (extracted from Bunker, 1971).

dealing with odd proton nuclei), the energy of a given Nilsson orbit should descend along the right-hand side of the "V." At some point it should become the ground state, or at least occur very low in the spectrum, then increase in energy along the left arm of the "V." At least approximately, the behavior exemplified by the systematics in Fig. 7.6 (here hole energies are shown as negative values) is typically observed. Deviations from it can be due to changes in deformation across such a sequence (we have implicitly assumed a constant deformation), or to shifts in the relative positions of the Nilsson orbits from effects such as higher order deformation components (hexadecapole deformations), or to Coriolis effects.

A nearby nucleus that shows one such case is  $^{183}\text{W}$ , whose level scheme will be discussed at great length in the next chapter and is illustrated in Fig. 8.1. Simple counting would suggest that the ground state is  $7/2^-[503]$ , with low-lying  $1/2^-[510]$  and  $3/2^-[512]$  particle excitations. Yet, the empirical level scheme shows that the latter two orbits are near the ground state and the  $7/2^-[503]$  occurs at a few hundred keV excitation energy. An explanation of this will be given in Chapter 8.

We have seen that it is as easy in the Nilsson model as in the shell model to determine the expected order of single-particle excitations and their energies and to deduce, virtually by inspection, an anticipated level scheme. Though this seems a trivial exercise, one should not lose sight of the fact that by considering a deformed shell model potential, one is able to account instantly

for the low-lying levels of literally hundreds of deformed odd mass nuclei, ranging from  $A \approx 20$  to the actinides. There have been innumerable tests of this model over the last three decades and it has proved capable of correlating a vast amount of data, particularly when some rather simple refinements (primarily Coriolis mixing and hexadecapole deformations) are incorporated.

### 7.3 Prolate and Oblate Shapes

It is interesting to break the discussion at this point to discuss an extremely basic question that is seldom alluded to but is now easy to answer. It is an empirical fact that the vast majority of deformed nuclei are prolate rather than oblate in their ground states. The only candidates for oblate nuclei are those in which either  $N$  or  $Z$  is near the very end of a major shell (e.g., Hg). However, the Nilsson diagram can be applied equally on the oblate side.

Although we will not discuss it explicitly, the derivation of the model for oblate shapes should be self-evident by now. Here the “core” nucleus is disc shaped, and the lowest energy orbits will be polar with high  $K$  values. The sequence of levels will be more or less inverted relative to the prolate case. For example (see the sketch in Fig. 7.3), the  $i_{13/2}$  shell model state will again split into seven orbits in order of increasing energy  $K = 13/2, 11/2, 9/2, \dots, 1/2$ . For small  $|\beta|$ , the energies are again linear in  $K^2$ , and hence the spacings between different  $K$  levels are proportional to  $K$ .

Although the empirical preference for prolate shapes is well known, it is much less understood *why* it should be so. Years ago, this issue was discussed with some frequency, but since has been ignored without having received a satisfactory or at least well-known explanation. However, a simple understanding actually involves only two considerations, namely the specific *sequence* of single-particle spherical  $j$  shells and the relative *angular orientations* of different  $K$  orbits in the Nilsson model.

A casual inspection of the Nilsson diagram seems to show no preference for oblate or prolate shapes. Energy-favored downward sloping orbits appear on both sides. Furthermore, if we imagine a spherical closed shell nucleus with a single valence nucleon (see Fig. 3.1), the resulting disk-like orbital “ring” would appear to be oblate. There is no elongation along a symmetry axis but an orbital *plane* superimposed on the spherical core.

Why, therefore, are most nuclei, and in particular those at the beginning of major shells, prolate? Consider a single  $j$  shell such as  $i_{13/2}$ . We recall from an earlier discussion (see Table 7.1) that the orientations of the orbital planes change very little for low  $K$  values, but increase rapidly for higher  $K$ . Thus, while on the oblate side, a single  $K = 13/2$  orbit may descend as rapidly in energy as its  $K = 1/2$  partner on the prolate side, there are *several* prolate orbits that have comparable, strongly down sloping energies. In contrast, only a couple of orbits will be steeply down sloping on the oblate side. We saw before that the “switch” to up sloping should occur at  $K = 9/2$ . When several valence nucleons are present, as there must be for the nucleus to be deformed, a *summation* over their energies will favor a prolate deformation.

This is almost, but not quite, the desired explanation. One other ingredient is necessary. To see this, consider the sequence of spherical  $j$  values (see Fig. 3.2, or Fig. 7.4 for  $\beta = 0$ ). Suppose that, instead of this order, the lowest orbit had been  $p_{1/2}$ ,  $p_{3/2}$ , or even  $f_{7/2}$  instead of a higher  $j$  orbit. The preceding argument would then have had little weight. Upsloping orbits would soon be encountered for both prolate and oblate shapes. It is because the lowest orbits after a shell closure have relatively *high j*, with many  $K$  values, that a distinction between the oblate and prolate behavior can be made and a preference for prolate deformations can develop. Thus, the second key feature is the modification of the shell model potential to include components that favor lower energy for higher  $l$  and  $j$  orbits. The nearly universal preference for prolate shapes in nuclei stems from the specific radial shape of the shell model central potential that is intermediate between harmonic oscillator and square well, which favors large  $l$  values, and from the properties of the sine (the orbit inclinations as a function of  $K$ ). Once again, we have an example of how a very simple but physically intuitive appreciation of the structure of a given model leads to important results even without detailed calculation.

#### 7.4 Interplay of Nilsson Structure and Rotational Motion

We have discussed the structure of the Nilsson wave functions as linear combinations of single  $j$  shell model wave functions with expansion coefficients  $C$ , and have seen a number of examples of such wave functions. It cannot be emphasized too strongly that these are wave functions in the body-fixed system, that is, the nonrotating nucleus. In this system,  $j$  is clearly not a good quantum number. However, the nucleus exists in space and the total angular momentum  $J$  must be a constant of the motion. The projection of this angular momentum  $K$ , (and the expectation value  $\langle j \rangle$  of the single-particle angular momentum) on the nuclear symmetry axis are also good quantum numbers. The Nilsson wave function is known as an *intrinsic state* or a state of excitation of an isolated body, which in this case is the deformed nucleus. The real nuclear states are combinations of this intrinsic motion and a superimposed rotational motion of the core. Phrased another way, the Nilsson wave function does not possess a fixed angular momentum  $J$ ; rather, it can be projected onto states of many different angular momenta. It is because of this seemingly abstract idea that a particle in a given Nilsson orbit actually gives rise not to a single state in a deformed nucleus (as would be the case for a single shell model particle in a given orbit  $j$ ), but rather to a set of states comprising what is known as a *rotational band*.

A proper understanding of the interplay of this rotational motion and the intrinsic motion leads to a much deeper understanding of the wave functions for odd mass deformed nuclei, of the actual nature of the rotational motion involved, of the reasons why single nucleon transfer reactions are such powerful probes of Nilsson model wave functions, and of the effects of the Coriolis interaction.

The same approach used to obtain the first order rotational energy expres-

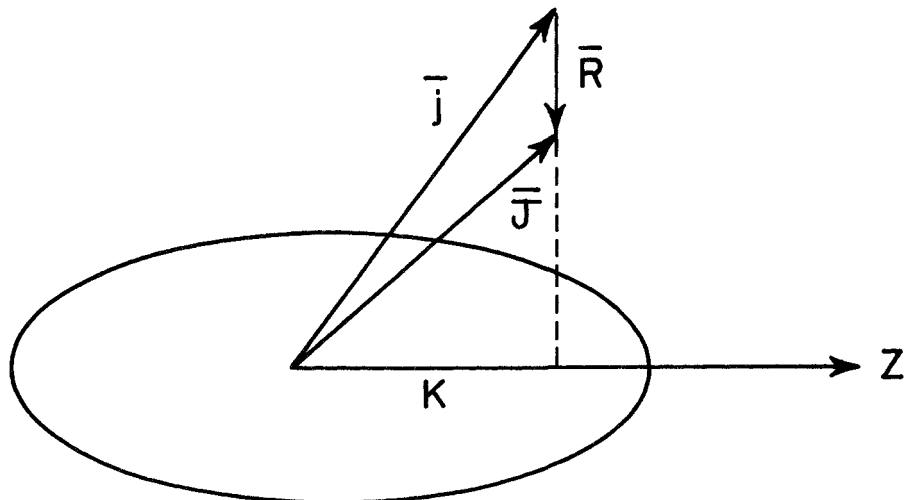


**Fig. 7.7.** Angular momentum diagram for an odd mass deformed nucleus. Note: this figure can be very misleading—see text and Fig. 7.9.

sion in even-even nuclei can also be used for odd mass nuclei. If the odd nucleon, considered for a moment to be in a single  $j$  orbit, does not polarize the even-even core, then the total angular momentum results from the vector sum of the core rotation and the odd particle angular momentum. This is illustrated in Fig. 7.7. We now start with the same rotational Hamiltonian as before and obtain, using the notation for the different angular momenta given in Fig. 7.7,

$$\mathbf{H} = \frac{\hbar^2}{2I} \mathbf{R}^2 = \frac{\hbar^2}{2I} (\mathbf{J} - \mathbf{j})^2 = \frac{\hbar^2}{2I} (\mathbf{J}^2 + \mathbf{j}^2 - 2\mathbf{J} \cdot \mathbf{j}) \quad (7.11)$$

We can convert this to a more useful form by defining the familiar raising and lowering operators

$$\begin{aligned} \mathbf{J}_{\pm} &= \mathbf{J}_1 \pm i\mathbf{J}_2 \\ \mathbf{j}_{\pm} &= \mathbf{j}_1 \pm i\mathbf{j}_2 \end{aligned} \quad (7.12)$$

Simple multiplication of these operators gives  $\mathbf{J}_+ \mathbf{j}_- + \mathbf{J}_- \mathbf{j}_+ = 2(\mathbf{J}_1 \mathbf{j}_1 + \mathbf{J}_2 \mathbf{j}_2)$ . Therefore

$$\mathbf{J} \cdot \mathbf{j} = \mathbf{J}_1 \mathbf{j}_1 + \mathbf{J}_2 \mathbf{j}_2 + \mathbf{J}_3 \mathbf{j}_3 = \frac{1}{2} (\mathbf{J}_+ \mathbf{j}_- + \mathbf{J}_- \mathbf{j}_+) + \mathbf{J}_3 \mathbf{j}_3$$

and hence

$$H = \frac{\hbar^2}{2I} [\mathbf{J}^2 + \mathbf{j}^2 - 2\mathbf{J}_3 \mathbf{j}_3 - (\mathbf{J}_+ \mathbf{j}_- + \mathbf{J}_- \mathbf{j}_+)]$$

Replacing these operators with their eigenvalues where possible and using the fact that, for low-lying states, both  $J_3$  and  $j_3$  have the same projection  $K$ , gives

$$E(J) = \frac{\hbar^2}{2I} [J(J+1) - 2K^2 + \langle \mathbf{j}^2 \rangle - (\mathbf{J}_+ \mathbf{j}_- + \mathbf{J}_- \mathbf{j}_+)] \quad (7.13)$$

or

$$E(J) = \frac{\hbar^2}{2I} [ J(J+1) - 2K^2 + \langle j^2 \rangle ] + V_{\text{Coriolis}} \quad (7.14)$$

where

$$V_{\text{Coriolis}} = -\frac{\hbar^2}{2I} (\mathbf{J}_+ \mathbf{j}_- + \mathbf{J}_- \mathbf{j}_+)$$

The first term on the right in Eq. 7.14 is identical to the rotational energy expression for an even-even nucleus. It is clear from Fig. 7.7 that this must be the case, since this figure would collapse to that of an even mass rotor if there were no single-particle angular momentum  $j$ . The other terms in Eq. 7.14 arise specifically from the presence of the odd particle and are intimately connected with the coupling between rotational and particle degrees of freedom. Even the resemblance of the first term to the symmetric top formula is fundamentally misleading. We shall see momentarily that the simple picture illustrated in Fig. 7.7 conceals some important physical effects, and that the rotational motion is not as simple as commonly believed, but an alternate picture that is nearly as simple will allow us to retrieve Eq. 7.14 in a transparent, elegant way that will disclose a much different understanding of rotational motion in odd mass nuclei.

The third and fourth terms in Eq. 7.14 involve the  $j$  structure of the deformed single-particle wave function (Nilsson wave function). Whatever value  $\langle j^2 \rangle$  takes, both it and  $K$  should be constant within a rotational band (neglecting band mixing). The last term is called the *Coriolis interaction* because its effects are very similar to the classical Coriolis force acting on any rotating macroscopic body. The Coriolis interaction has important consequences in both even and odd deformed nuclei and will be extensively discussed later. We will show then that, in first order, its effects on energies simply correspond to a change in the  $\hbar^2/2I$ .

To this order then, the energy levels of a given rotational band in an odd mass nucleus should behave as  $\hbar^2/2IJ(J+1)$ . In Fig. 7.8, we illustrate a number of examples of rotational bands in heavy nuclei and show that this simple formula works remarkably well. Also included in the figure are two examples where it clearly fails to provide even a reasonable first-order estimate. One of these involves a  $K = 1/2$  band ( $1/2^-$ -[521] in  $^{169}\text{Er}$ ) that we shall later see incorporates a special (diagonal) Coriolis interaction. The other is a “band” (“ $h_{11/2}$ ” in  $^{133}\text{La}$ ) that appears to be partly “upside down” (e.g.,  $E(11/2^-) \ll E(5/2^-)$ ,  $E(7/2^-)$ ) and unrelated to the kind of structure that we have been examining. It too involves especially strong Coriolis effects and will be discussed later. Here, we wish to raise, and resolve, an apparent paradox that arises from Fig. 7.7 (and that is intimately related to this type of inverted structure).

Equation 7.11 states that the total angular momentum results from the vector combination of the rotational angular momentum  $R$  and the particle angular momentum  $j$ , that is  $\mathbf{J} = \mathbf{R} + \mathbf{j}$ . The situation was sketched in Fig. 7.7, which is a simplification since the Nilsson wave function contains, in general, a linear combination of functions of different  $j$ . That is not the point. Consider,

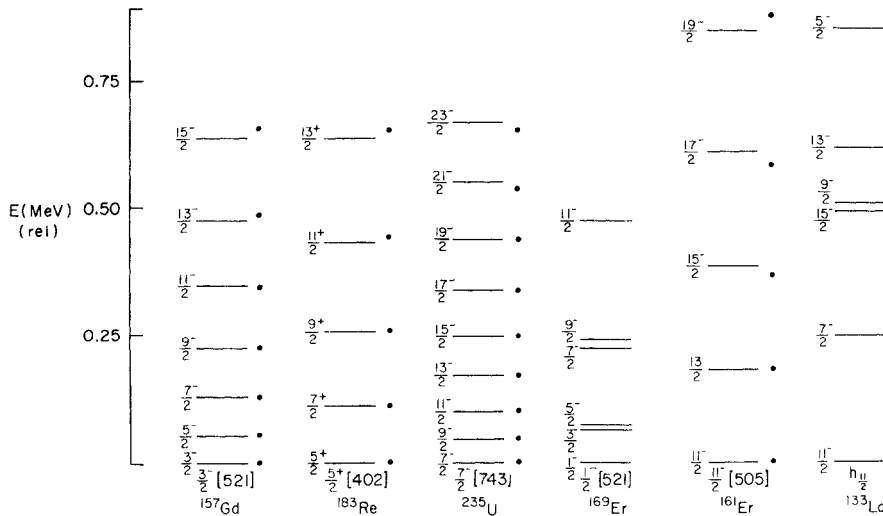
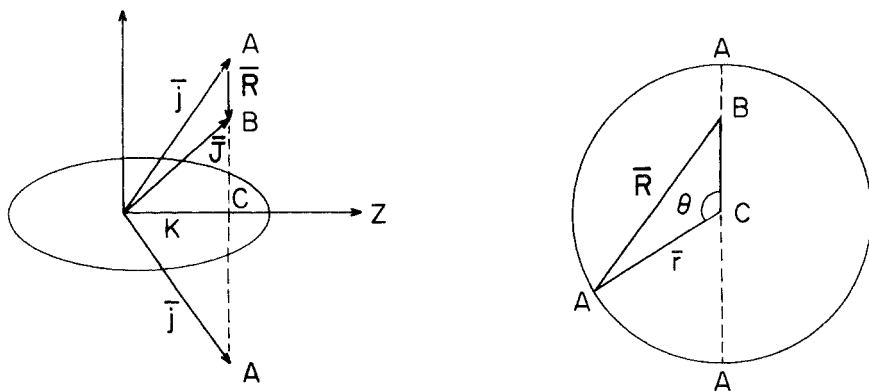


**Fig. 7.8.** Rotational bands in some deformed odd-mass nuclei. The dots give the rotational energy predictions from Eq. 7.14 after normalization to the first two levels. Dots for the energies of the  $K = 1/2, 1/2^- [521]$  band in  $^{169}\text{Er}$  are omitted since they require a “decoupling parameter” term (to be discussed in Chapter 8). As discussed later in the text, the rightmost “band” is so Coriolis mixed that no single Nilsson label is possible.

for simplicity, the one case in which a single  $j$  value does nearly characterize the Nilsson wave functions—the unique parity orbits. To be specific, let us take a Nilsson wave function such as that for the  $1/2^+[660]$  orbit from the  $i_{13/2}$  neutron shell in the rare earth region. (For convenience we neglect Coriolis mixing.) Now, we have seen examples of rotational bands with spins  $J = K, K + 1, K + 2, \dots$  whose energies vary approximately as  $J(J + 1)$ , or in this case, a sequence with  $J = 1/2, 3/2, 5/2, 7/2, \dots$ . The common view (Fig. 7.7) of this band as consisting of a single particle in the  $1/2^+[660]$  orbit coupled to a sequence of successively faster core rotations is seriously in error. To see this, recall that we have taken a simple case where the Nilsson wave function consists of only one  $j$  value,  $j = 13/2$ . This is therefore the *only* single-particle angular momentum in the system. This in turn implies that any *total* angular momentum *other* than  $J = 13/2$  *must* incorporate angular momentum from another source. That source can only be the rotational motion. Thus, as in Fig. 7.7, one can imagine a  $J = 17/2$  state obtained by coupling a  $j = 13/2$  single-particle angular momentum to a core rotational angular momentum  $R = 2$ . Similarly,  $J = 9/2, 5/2$  states could be formed by the antiparallel coupling of  $j = 13/2$  and  $R = 2, R = 4$ , respectively. The only energies in the system are the Nilsson energy, which is constant (independent of  $J$ ), and the rotational energy,  $\hbar^2/2I \mathbf{R}^2$ . Hence, the  $J = 9/2$  state (with  $R = 2$ ) should have higher energy than the  $J = 13/2$  state (with  $R = 0$ ). The  $J = 5/2$  and  $1/2$  states should be expected still higher. Moreover, the energy difference  $E(9/2) - E(13/2)$  should equal  $E_{R=2} - E_{R=0}$ , or in other words,  $E_{2+}$  of the neighboring even-even core nucleus;  $E(5/2) - E(13/2)$  should equal  $E_{4+}$ , and so on. This picture leads to “upside down” rotational bands with the

lower spin states lying higher than the state with  $J = j$ . Such band structures do indeed exist (as we noted in discussing the right-most band in Fig. 7.8). They have recently become highly interesting as a particular manifestation of important Coriolis effects in high-spin states. However, they are not the normally observed situation and are certainly not consistent with most of the empirical rotational bands shown in Fig. 7.8. Clearly, there is something wrong with this picture.

A clue to a more accurate understanding of the rotational motion begins by recalling that we are dealing with an axially symmetric deformed nucleus. This means that *any* orientation of the angular momentum vector  $\mathbf{j}$  with respect to the symmetry axis  $z$  that maintains a projection  $K$  is indistinguishable from any other orientation and therefore is equally likely: the angular momentum vector  $\mathbf{j}$  is free to precess around the  $z$  axis. Figure 7.7 showed only one *particular* orientation of this angular momentum vector—that corresponding to the smallest possible value of  $|R|$ , since  $\mathbf{j}$  and  $\mathbf{R}$  are aligned. In contrast, imagine that the angular momentum  $\mathbf{j}$  were rotated 180° to that shown in the figure so that it lay in the plane of the page but pointed downward, below the  $z$  axis. This situation is depicted on the left in Fig. 7.9. The amount of core rotation required to produce a final total angular momentum  $\mathbf{J}$  would clearly be much larger. If we extend this idea to other angles of the angular momentum vector  $\mathbf{j}$ , then, as  $\mathbf{j}$  precesses,  $\mathbf{R}$  will point in a continually varying direction and  $|R|$  will take on a constantly changing series of values.



### ROTATIONAL MOTION IN ODD A NUCLEI

**Fig. 7.9.** (Left) Angular momentum diagram for an odd-mass deformed nucleus. This is a more rigorous version of Fig. 7.7 that incorporates important refinements. (Right) Path (circle) followed by the tip of the  $\mathbf{j}$  vector with time as it precesses about the  $z$  axis (point C). This is an "end view" of the time dependence of the diagram on the left. I am grateful to D. D. Warner for this figure.

Consider again our example of a  $j = 13/2$  particle in a  $K = 1/2$  orbit. For  $J = 1/2$ ,  $J$  points nearly along the  $z$  axis, and  $|R|$  remains roughly constant in magnitude, although not in direction, as  $\mathbf{j}$  precesses, at a value  $|R| \approx 6$ . On the other hand, for  $J = 13/2$ ,  $|R|$  takes on values ranging from 0 to 12 as  $\mathbf{j}$  precesses. Since the rotational Hamiltonian,  $\hbar^2/2I\mathbf{R}^2$ , is quadratic in  $\mathbf{R}$ , large  $|R|$  values carry more weight than small ones. Therefore, a situation in which  $|R|$  varies smoothly from 0 to 12 will have, on average, higher energy than one in which  $|R|$  is approximately constant at a value  $|R| = 6$ , and the  $J = 13/2$  state will require more (rotational) energy than the  $J = 1/2$  level.

This analysis can be made more quantitative by viewing the nucleus end on. This situation is depicted in the side and end views in Fig. 7.9. Point  $C$  is along the symmetry axis at a distance  $K$  from the origin. Point  $B$  is the terminus of the fixed total angular momentum vector  $\mathbf{J}$ , and point  $A$  marks that of the single-particle angular momentum  $\mathbf{j}$ . The circle in the end view shows the path followed by the angular momentum vector  $\mathbf{j}$  as it precesses about the symmetry axis  $z$ . We can now calculate the expectation value of  $\mathbf{R}^2$  by allowing  $\mathbf{j}$  to rotate about the point  $C$  at a radius  $r$ . From simple trigonometry

$$\mathbf{R}^2 = r^2 + (BC)^2 + 2r(BC)\cos\theta \quad (7.15)$$

Integrating this expression over of  $\theta$  gives

$$R^2_{\text{ave}} = r^2 + (BC)^2$$

but

$$r^2 = (AC)^2 = j^2 - K^2$$

and

$$(BC)^2 = J^2 - K^2$$

Thus

$$R^2_{\text{ave}} = j^2 - K^2 + J^2 - K^2 \quad (7.16)$$

or, taking the quantum mechanical expectation values

$$R(R+1) = J(J+1) + j(j+1) - 2K^2 \quad (7.17)$$

This is *exactly the same* as Eq. 7.14 except for the Coriolis term that has not been included since we have assumed that  $K$  is constant and, as we shall see, the Coriolis interaction inherently mixes different  $K$  values. (Since we assumed a single- $j$  wave function,  $\langle \mathbf{j}^2 \rangle$  has become  $j(j+1)$ .) Note that the assumption of constant  $K$  is equivalent to the assumption that the particle angular momentum vector  $\mathbf{j}$  precesses exactly about the  $z$  axis. We shall shortly encounter a special, though not uncommon, situation in which precession is about an axis perpendicular to the  $z$  axis: clearly in such a situation it will be  $K$ , not  $R$ , that changes continuously. This then will bring us back to the picture in Fig. 7.7, which leads to “inverted” rotational sequences.

We therefore see that the derivation of Eq. 7.14 for the eigenvalues in a rotational band built on a given Nilsson orbit was correct, even though the

simple picture that is commonly used to illustrate this situation, Fig. 7.7, is too simplistic. The more accurate view shown in Fig. 7.9 gives the same formula in a trivial manner. It has been a constant emphasis in this book that most results in nuclear structure physics can be derived, at least semi-quantitatively, by very simple, often intuitive, analyses. This example warns us that such an approach cannot be careless handwaving, but must accurately reflect the correct underlying physics.

The most important conclusion from the present analysis is the recognition that the rotational motion in a deformed odd mass nucleus is far from simple. Not only does the *magnitude* of the rotational angular momentum  $|R|$  vary with time but its *direction* in space also changes. In the  $J = 1/2$  state, for example, the nucleus at times rotates clockwise about the  $y$  axis, at other times counter clockwise about this axis, and at still other times about a continuously varying axis in the  $xy$  plane. The rate of rotation is relatively constant corresponding to  $|R| = 6$ . In the  $J = 13/2$  state, on the other hand, the nucleus is at times stationary ( $R = 0$ ) while at others it rotates at frequencies varying from values corresponding to  $R = 0$  to those for  $|R| \approx 12$ ! We can see that the *rotational* motion is really a complex, time dependent, variation that includes not only a true rotational component but also a kind of tumbling motion. The fact that the principle term in Eq. 7.14 (i.e., the term that depends on  $J$ , the others being constant) has the same form as in the symmetric top or in the rotational energy expression for an even-even nucleus, is really almost an accidental result of the particular combination of the precessing single-particle motion and the varying core rotational motion needed to produce a constant total momentum  $J^*$ .

For typical (nonunique parity) Nilsson wave functions, several  $j$  values commonly appear and the “rotational” motion is even more complex. From the formal standpoint, one need not worry about this since, as we saw in deriving Eq. 7.14, as long as the proper vector character of the angular momenta are taken into account the correct results always emerge.

There is one other important point implicit to this discussion. It should be clear by now that while many values of  $|R|$  contribute to the wave function for a state of spin  $J$  in a rotational band built on a given Nilsson orbit, the special value  $R = 0$  can *only* occur if the Nilsson wave function  $\psi_{Nils}$  contains an amplitude  $\phi_j$ —that is, *only* if it contains an amplitude for the single nucleon in the orbit with  $j = J$ . For any other  $j$  value, the state with total angular momentum  $J$  can be constructed only by incorporating some rotational motion. As we shall see, this has important consequences for single nucleon transfer reactions. We recall that for a given oscillator shell  $N$ ,  $j_{\max} = N + 1/2$  (e.g.,  $j_{\max} = 11/2$  for  $N = 5$ ). It is thus clear that *all* states with  $J > N + 1/2$  *must* have  $R \neq 0$ .

Having discussed the basic Nilsson model and the basic rotational motion in odd mass deformed nuclei, we turn in the next chapter to a detailed discussion of specific tests of and refinements to the model, with emphasis on the crucial and pervasive effects of Coriolis coupling.

\*The author is grateful to D. D. Warner, with whom this analysis was worked out.

## NILSSON MODEL: APPLICATIONS AND REFINEMENTS

### **8.1 Single Nucleon Transfer Reactions**

The description of odd mass deformed nuclei in terms of Nilsson orbits and their configuration-mixed nonspherical wave functions has been an extremely successful model for over three decades. One of its most appealing features is that it is extremely easy to test empirically and to measure the detailed shell model ( $j$ ) composition of individual Nilsson wave functions. As we shall see momentarily, single nucleon transfer reactions provide a direct and specific measure of each successive component in the Nilsson wave functions. This remarkable property stems from a particularly simple feature of the interplay of rotational and single-particle motion in producing final states of given total angular momentum  $J$ .

Although we shall defer our discussion of experimental probes of nuclear structure to a later chapter, an exception will be made for single nucleon transfer reactions leading to deformed odd mass nuclei, because they are so intimately linked with the basic structure of the Nilsson model itself. The underlying reason stems from a point about the rotational motion brought out at the end of the previous chapter. Since  $\mathbf{J} = \mathbf{R} + \mathbf{j}$ , a component with  $R = 0$  in a state of spin  $J$  can *only* occur if the Nilsson wave function  $\psi = \sum C_j \phi_j$  contains an amplitude for the single-particle angular momentum  $j = J$ . If we could somehow sample the  $R = 0$  components of a sequence of states in a rotational band, we would be sampling the successive  $C_j$  amplitudes in the Nilsson wave function for the underlying intrinsic state. Single nucleon transfer reactions do just that.

We will pursue this point in a moment, but first it is interesting to consider how and under what conditions such reactions occur, as well as some of the experimental considerations applicable to them. We shall do this for the ( $d, p$ ) reaction, but the same reasoning applies to other light-ion single nucleon transfer reactions such as ( $d, t$ ), ( $^3\text{He}, \alpha$ ), ( $\alpha, t$ ), and so on. First, consider a schematic diagram of such a reaction as was shown in Fig. 3.3. An incident nucleon, in this example a deuteron, passes near a target nucleus. As it experiences the nuclear force (we neglect Coulomb effects) several things may occur. The deuteron may simply scatter from the nucleus elastically or inelastically (producing excited states). It could be absorbed by the target nucleus producing a nucleus  $A' = A + 2$  in a highly excited “compound” nuclear state. It could attract one nucleon, such as a neutron, from the target nucleus

and emerge from the collision as a triton, leaving behind a residual nucleus with  $A' = A - 1$ . This is a (d, t) reaction. Or, a neutron could be stripped off and enter an orbit around the target nucleus, producing a final nucleus with mass  $A' = A + 1$ , a (d, p) reaction. These reactions can be experimentally selected by detecting the outgoing particle and identifying it. This can be done with a number of different techniques we will not discuss here. Some utilize the different magnetic rigidities of the outgoing particles. Others exploit the dependence on the mass and charge of the ratio of the energy loss  $\Delta E$  in a thin detector to the total energy.

In any case, we assume we have identified an outgoing proton, thereby "tagging" a (d, p) reaction event. This reaction is not necessarily a single step process. It could be accompanied by inelastic scattering or Coulomb excitation. Or it could be the result of a compound nuclear reaction in which the deuteron was first fully absorbed. To select appropriate experimental conditions to favor a simple single step process, we consider some of the parameters describing the reaction process of Fig. 3.3. If the closest distance of the incident projectile from the target nucleus is large, the interaction is weak, and stripping occurs with low probability. When scattering occurs it will not be at large angles. Two-step processes involve a product of such single-step amplitudes, and will be negligible. For a close collision (distance of closest approach), the nuclear interaction and hence the scattering angle are much greater. The probability of a single event occurring is much larger but so is that for multistep processes. The optimum situation of large, direct, reaction cross sections but small multistep amplitudes occurs for an intermediate angle corresponding to a "grazing" collision. This discussion is highly qualitative since quantum mechanical interference effects lead to significant oscillations of  $\sigma(d, p)$  with  $\theta$ . Nonetheless, for targets with  $A > 100$  and typical incident deuteron energies  $E_d \approx 10-15$  MeV, most (d, p) experiments emphasize detection at angles  $40^\circ \leq \theta \leq 125^\circ$ . Similar considerations apply for heavier projectiles, except that, for a given bombarding energy per nucleon, the heavier projectile brings in more angular momentum and is more likely to excite final states involving larger angular momentum transfer.

With this brief digression finished, we turn to consider the nuclear structure information obtainable from single-step reactions such as (d, p). We consider the population of members of a rotational band built on some Nilsson orbit in a deformed odd mass final nucleus. Since the reaction is single step, sequential processes, such as transfer followed by inelastic scattering, are eliminated by the choice of experimental conditions. Indeed, by definition—the *only* thing that can occur is that a single nucleon can be transferred to a given, quantized, empty valence orbit (Nilsson wave function  $\psi_{\text{Nils}}$ ). In particular, the process *cannot* induce any *rotation* of the target nucleus. Since no rotational notion can be imparted, it follows that the probability of populating a state with a given total angular momentum  $J$  must be proportional to the probability,  $C_{j=j}^2$ , for a shell model single-particle wave function  $\phi_{j=j}$  in the Nilsson wave function. Thus, even though the *intrinsic* wave function for *each* state in the rotational band is identical, the (d, p) cross section for populating each

successive state successively samples a specific component of the Nilsson wave function. The cross sections for populating the  $J = K, K + 1, K + 2, K + 3, \dots$  states directly give  $C_{\kappa}^2, C_{\kappa+1}^2, C_{\kappa+2}^2, C_{\kappa+3}^2$  in  $\psi_{\text{Nil}}^{\text{N}}$ . Since the sequence of  $C$  values is characteristic of each specific Nilsson wave function, the pattern of cross sections is an identifying signature of a particular orbit and is commonly called a fingerprint pattern. Much of the study of Nilsson orbits in heavy nuclei is grounded in this basic property of single nucleon transfer sections.

Note the interesting point brought out in the last chapter that since  $j_{\max} = N + 1/2$  for a given shell, single-step single-nucleon transfer reactions can *never* populate states with  $J > N + 1/2$ . All components in the wave functions of such states must have  $R \neq 0$ . If such states are populated, it is immediate evidence either for multistep processes or for wave function admixtures from higher major shells (e.g.,  $\Delta N = 2$  mixing that can be induced by large hexadecapole deformation components).

The formal expression for the single nucleon transfer cross section to a specific state of spin  $j$  of a rotational band in a deformed nucleus built on a Nilsson orbit  $i$ , is given by

$$\frac{d\sigma_i(j)}{d\Omega} = N \phi_i^{DW}(\theta) C_j^2 P_i^2 \quad (8.1)$$

where we have included a pairing factor denoted by  $P_i^2$ , which we shall discuss in a moment. (The quantity  $(C_j P)^2$  is analogous to the spectroscopic factor (see chapters 2 and 3) for spherical nuclei.) This formula is extremely well known and has been extensively used for two decades in probing the structure of Nilsson wave functions; strangely, its simple origins described earlier are often only vaguely understood, and the power of (d, p), (d, t), and other single-particle reactions in elucidating Nilsson structure often seems almost magical.

Before discussing this equation in relation to the empirically deduced structure of various Nilsson orbits in typical deformed nuclei, we must add a few more comments on the other factors appearing in it. In a formal derivation of Eq. 8.1, there must occur an integral linking the initial and final states

$$\langle \phi_p \psi_{\text{Nil}}(A+1) | \phi_d \psi_{e-e}(A) \rangle$$

giving the overlap of the initial deuteron-( $A$ )-nucleon even-even target system with the final proton-( $A + 1$ ) nucleon odd mass system. This matrix element involves the internal structure of the incoming and outgoing projectiles and the degree to which the final nucleus looks like the target plus a neutron in a specific orbit. It is usually assumed for simplicity that the latter point is satisfied:  $\langle \psi_{\text{Nil}}(A+1) | \phi_n \psi_{e-e}(A) \rangle^2$  is unity. This is really just the single-step process assumption. The former aspect concerning the projectile/ejectile structure is absorbed into the arbitrary normalization constant  $N$  in Eq. 8.1.

The reaction process also depends on kinematic effects ( $E_d$ ,  $\theta$ , etc.). These kinematic factors are included in the function  $\phi_i(\theta)$ , which can be calculated by standard DWBA techniques. Typically,  $\phi_i(\theta)$  has a diffractive oscillatory pattern that is a function of  $\theta$ . The specific extent and locations of maxima and minima are functions of the transferred angular momentum  $l$ . Starting from an

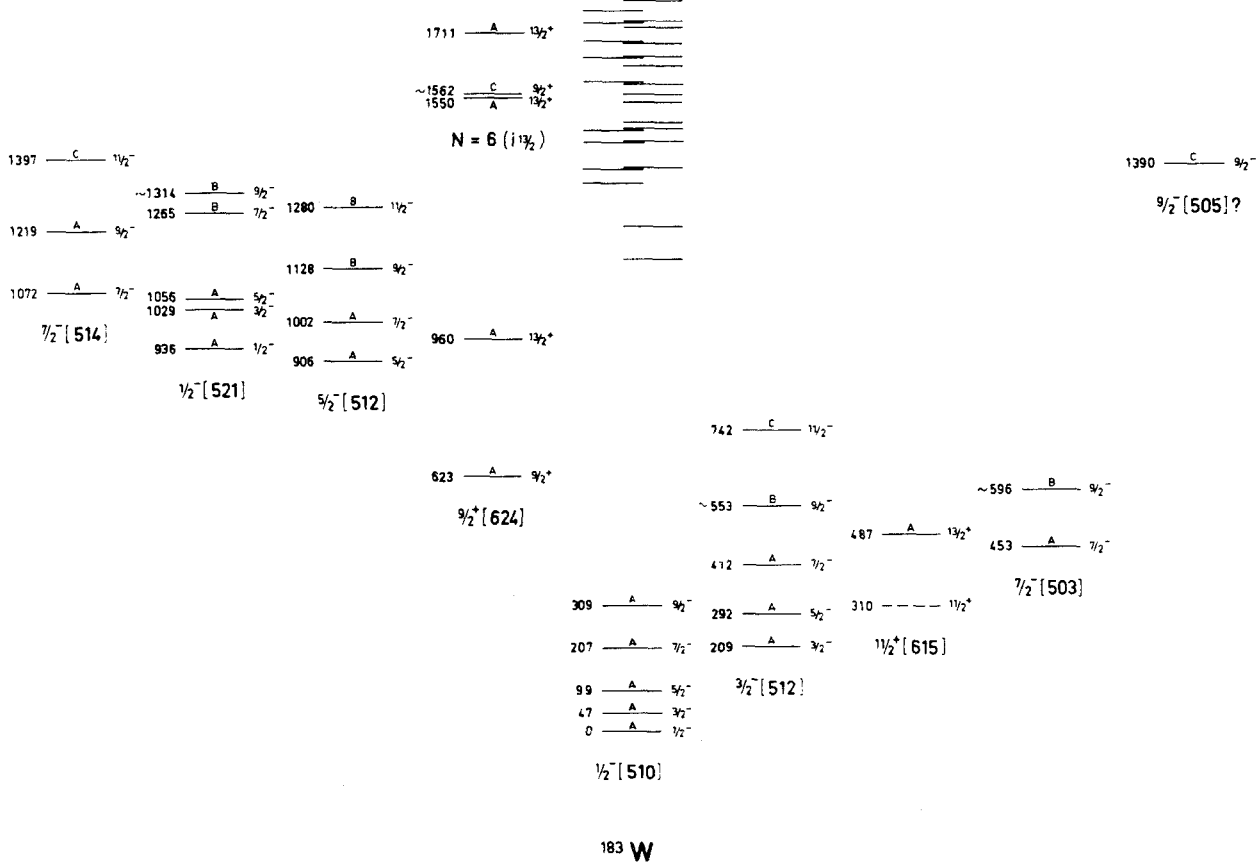


Fig. 8.1. Level scheme for  $^{183}\text{W}$ . Levels without Nilsson assignments are given at top center (Casten, 1972). Particle (hole) excitations are on the right (left).

even-even nucleus, the final angular momentum  $J = j = l \pm 1/2$  and the final state parity is  $\pi = (-1)^l$ . In principle, a measurement of the angular distribution of the outgoing particles can provide information on the  $J^\pi$  values of various final states. In practice, this information is somewhat unreliable in deformed nuclei, and measurements are typically made at only two or three angles: the ratio of the cross sections at these angles provides at least a qualitative guide to the transferred orbital angular momentum  $l$ . On account of the centrifugal barrier, it should not be surprising that, for low-energy, light projectiles, the population of higher  $l$  values is inhibited: the cross sections decrease with increasing  $l$  (and therefore  $J$ ). Generally, it turns out that the angular distributions for small  $l$  values are somewhat forward peaked, while those for large  $l$  transfers are backward peaked. Therefore, a ratio such as  $\sigma(125^\circ)/\sigma(60^\circ)$  increases with transferred orbital angular momentum  $l$ . The cross sections  $\phi_i(\theta)$  also have a dependence on the reaction  $Q$  value (the difference in incoming and outgoing projectile energies). The  $Q$  value is easily deduced from the known nucleon separation energies. For example, for a (d, p) reaction

$$Q(d, p) = E_d - E_p = S(n) - E_x - B.E.(d)$$

where B.E.(d) is the deuteron binding energy 2.23 MeV. Since  $S(n) \approx 5-8$  MeV in heavy nuclei,  $Q(d, p)$  is typically positive for low  $E_x$  and decreases as  $E_x$  increases.

As noted, the use of reactions that carry more momentum into the system such as ( $^3\text{He}$ ,  $\alpha$ ), favors high  $l$  transfers. Therefore, the ratio of populations of a given state in ( $\alpha$ ,  $^3\text{He}$ ) and (d, p),  $\sigma(\alpha, ^3\text{He})/\sigma(d, p)$ , can also serve as a "meter" for the transferred angular momentum  $l$ . Indeed, at back angles, it singles out the highest  $jl$  values accessible (e.g.,  $j = 13/2$  in the odd neutron rare earth nuclei: see the following discussion (Fig. 8.9)).

The factor  $P^2$  is  $U^2$  for a stripping reaction such as (d, p), and  $V^2$  for a pickup reaction such as (d, t). It represents the probability that the single nucleon orbit involved is initially either empty or filled, respectively. It is reasonable that this factor is present. In a (d, p) or (d, t) reaction, a given orbit can be populated only to the extent that it is initially empty or full, respectively. Thus (d, p) tends to populate orbits above the Fermi surface, while (d, t) populates orbits below the Fermi surface most intensely.

Now we can turn to the extraction of specific nuclear structure information from these reactions. It is easiest to show this using a specific example. Consider the final nucleus  $^{183}\text{W}$  whose level scheme is shown in Fig. 8.1 with the states arranged according to Nilsson assignment and rotational band in the same format as in Fig. 7.5 for  $^{177,179}\text{Hf}$ . Figure 8.2 shows (d, p) and (d, t) spectra leading to  $^{183}\text{W}$ , while Table 8.1 summarizes the measured cross sections (at 90°) for those negative parity states that were assigned to specific Nilsson states. Table 8.2 gives similar information for  $^{185}\text{W}$ . We assume that the "kinematic" factors  $N\phi_i(\theta)$  are known so that the cross sections may be used to extract empirical values of  $C_i P_i$  for the  $i$ th band.

Look at Fig. 8.2, bearing in mind the strong  $l$  dependence of the DWBA

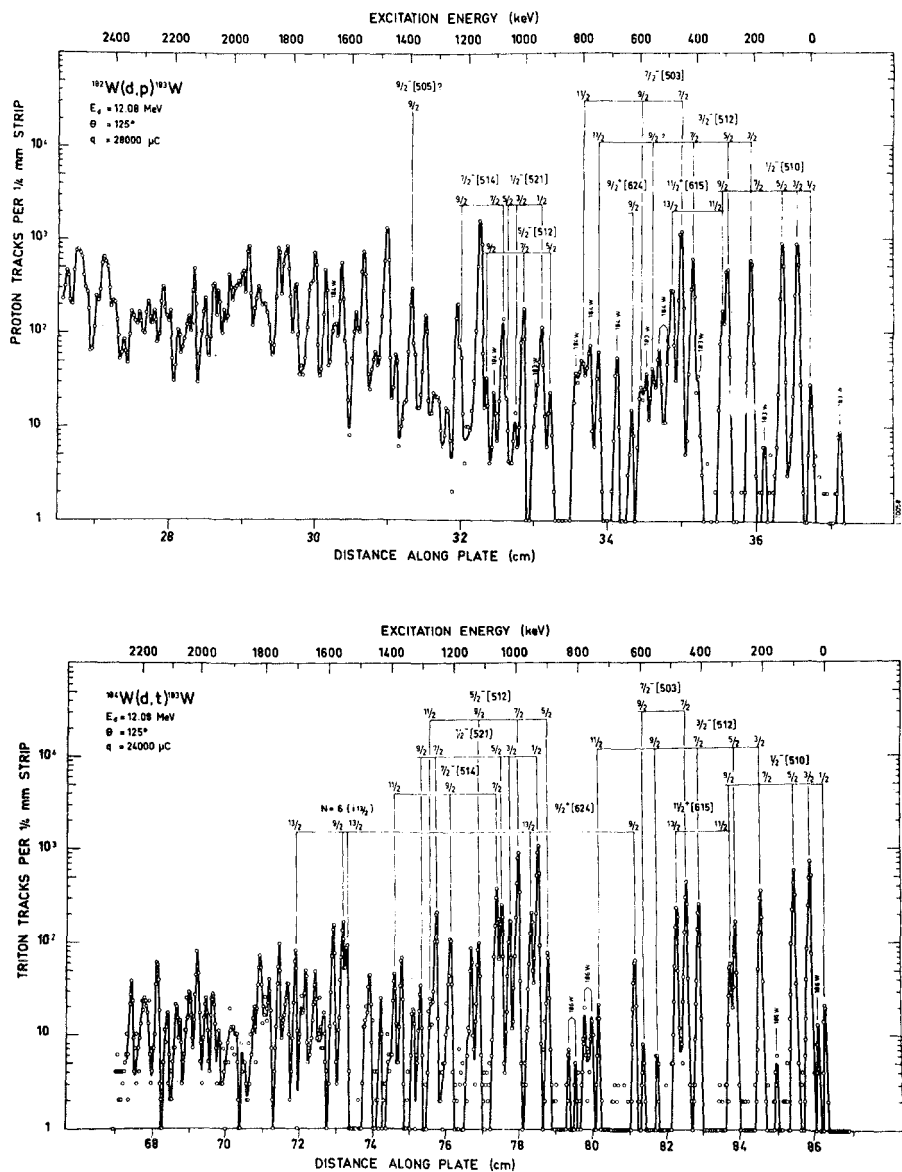


Fig. 8.2. (d, p) and (d, t) spectra leading to  $^{183}\text{W}$ . The peaks are labeled by the Nilsson assignments (Casten, 1972).

cross sections. Typically  $\sigma(\text{d}, \text{p})$  drops by an order of magnitude as  $l$  changes from  $l=1$  to  $l=5$ . Thus, large cross sections may not imply large  $C_i^2 P_i$  values and vice versa.

Extracting the  $C_i^j$  coefficients and the structure of each band now only requires an estimate of the pairing factors  $U_i$  or  $V_i$ . The simplest way to do this

**Table 8.1** Comparison of unperturbed, Coriolis coupled and experimental cross sections in  $^{183}\text{W}$  ( $\theta = 90^\circ$ )\*

State	$\sigma(d,p) \mu\text{b/sr}$			$\sigma(d,t) \mu\text{b/sr}$		
	Unper-turbed	Per-turbed	Experi-mental	Unper-turbed	Per-turbed	Experi-mental
9/2 9/2-[505]	64	65	25	1.8	1.2	
7/2 7/2-[503]	357	364	284	38	48	72
9/2	7.0	8.0	$\approx 3$	0.6	1.3	$\approx 1$
3/2 3/2-[512]	138	208	131	29	60	58
5/2	249	184	96	48	34	35
7/2	30	48	87	5.8	17	44
9/2	6.0	3.9	4	1.0	1.0	<1
11/2	0.2	0.4	4	0.0	0.1	1
1/2 1/2-[510]	0.3	0.4	8	0.2	0.6	5
3/2	334	269	264	195	179	150
5/2	98	163	202	53	65	103
7/2	33	18	11	18	15	14
9/2	3.3	5.5	11	1.6	1.6	7
5/2 5/2-[512]	0.0	0.0	6	0.2	0.2	19
7/2	17	7.9	29	269	217	237
9/2	1.2	1.2	3	14	25	18
11/2	0.1	0.0		1.3	0.8	4
1/2 1/2-[521]	25	15	15	280	280	364
3/2	7.0	2.8	3	128	114	54
5/2	5.1	4.3		86	87	66
7/2	4.3	1.8		71	64	69
9/2	0.7	0.6		10	10	8
7/2 7/2-[514]	2.0	3.8	16	40	81	91
9/2	2.6	3.0	3	45	35	29
11/2	0.0	0.1	<4	0.8	1.3	15

\*Casten, 1972.

is to assume a Fermi energy, and the simplest assumption here is to assume that it coincides with the energy of the Nilsson orbit that forms the ground state in the odd mass nucleus. For a reasonable choice of the gap parameter  $\Delta$  (typically 0.75–1 MeV), it is easy to solve the quasi-particle Eq. 5.23, to obtain  $U$  and  $V$  as a function of excitation energy. However, the Fermi energy need not coincide exactly with any specific Nilsson orbit. For example, in  $^{183}\text{W}$  the ground state is the 1/2-[510] orbit (see Fig. 7.4) and the 3/2-[512] orbit occurs at an excitation energy of approximately 200 keV, while in  $^{185}\text{W}$  the order is reversed but the two bands occur within  $\approx 20$  keV each other. If the deformation has not changed, one cannot account for this asymmetric situation by placing the Fermi surface at, say, the position of the 1/2-[510] orbit in  $^{183}\text{W}$  and at the 3/2-[512] orbit in  $^{185}\text{W}$ . Given the separation of these two orbits in the Nilsson diagram,  $\approx 150$  keV, it is clear that in  $^{185}\text{W}$ , the Fermi surface must be approximately centered between these two orbits, producing (see Fig. 5.7) low excitation energies for both. Since the  $U$  and  $V$  factors change rapidly near the Fermi surface, such fine details of the Fermi surface location can have significant effects on single nucleon transfer cross sections for low lying orbits.

**Table 8.2.** Comparison of unperturbed, Coriolis coupled, and experimental cross sections in  $^{185}\text{W}$  ( $\theta = 90^\circ$ )\*

State	$\sigma(d,p) \mu\text{b}/\text{sr}$			$\sigma(d,t) \mu\text{b}/\text{sr}$		
	Unper-turbed	Per-turbed	Experi-mental	Unper-turbed	Per-turbed	Experi-mental
9/2 9/2-[505]	66	62	25	3.3	3.9	10
7/2 7/2-[503]	334	341	316	58	72	154
9/2	6.4	10		1.0	2.1	$\approx 3$
11/2	0.5	0.5	$\approx 6$	0.1	0.2	1
3/2 3/2-[512]	107	30	5	59	1.7	1
5/2	195	247	301	97	173	207
7/2	23	7.2	11	12	1.0	1
9/2	4.7	6.5	11	2.1	4.5	11
11/2	0.2	0.1		0.1	0.0	$\approx 0.4$
1/2 1/2-[510]	0.2	0.2	4	0.3	0.9	3
3/3	180	262	357	343	423	308
5/2	53	0.3	$\approx 4$	92	14	11
7/2	18	37	104	32	55	99
9/2	1.8	0.0		2.7	0.1	$\approx 1$
11/2	0.1	0.2	5	0.2	0.4	4
5/2 5/2-[512]	0.0	0.0	$<3$	0.2	0.2	14
7/2	17	7.7	32	268	208	206
9/2	1.2	1.1		14.1	24	$\approx 20$
1/2 1/2-[521]	14	14	$<62$	281	280	$\approx 266$
3/2	6.4	2.8		129	107	$\approx 43$
5/2	4.7	3.8		86	89	$\approx 20$
7/2	3.9	1.6		72	60	$\approx 25$
9/2	0.5	0.6		10	10	11
7/2 7/2-[514]	2.1	4.1	15	40	86	80
9/2	2.7	1.2		45	34	19

\*Casten, 1972.

A more empirical way to extract  $U$  and  $V$  factors is from the ratio of  $(d, p)$  and  $(d, t)$  cross sections to the same state in an odd mass nucleus of mass  $A$ . This procedure is slightly inconsistent, since the  $U^2$  factors refer to the emptiness of Nilsson orbits in the target nucleus  $A$  in the  $(d, p)$  reaction while the  $V^2$  factors relevant to  $(d, t)$  refer to the orbit occupancies in its  $A + 2$  target nucleus. Nevertheless, this technique is widely used and is adequate for essentially all cases of practical importance.

We could now extract *empirical*  $C_j$  values from the measured  $(d, p)$  and  $(d, t)$  cross sections. For technical reasons, it is easiest and most common to use *theoretical* sets of  $C_j$  coefficients to calculate theoretical cross sections and to compare these with the measurements.

By identifying appropriate sequences of cross sections, the states in an odd mass nucleus may be sorted into rotational bands whose Nilsson wave functions can be identified. Such assignments are made in Tables 8.1 and 8.2 for  $^{183}$ ,  $^{185}\text{W}$ , and the theoretical and experimental cross sections are compared. In

Fig. 8.2, the deduced  $J$  values and Nilsson quantum numbers are indicated above the corresponding peaks.

Careful inspection shows very different patterns for the different rotational bands, justifying the term *fingerprint patterns*. For example, the  $1/2^-$ -[510] band has a very small cross section to the  $1/2^-$  state, large cross sections to the  $3/2^-$  and  $5/2^-$  levels, and smaller cross sections thereafter. The  $7/2^-$ -[503] band has a large cross section only for the  $7/2^-$  state. For the positive parity levels, essentially only the  $13/2^+$  states are populated. (Note that we have not attached specific Nilsson quantum numbers to some of the latter levels. The reason will be clear after we have discussed the strong Coriolis mixing between these bands.) The  $U^2$  and  $V^2$  dependence in Eq. 8.1 is also evident in Fig. 8.2. For the low-lying bands where  $U^2$  and  $V^2$  are roughly comparable, the same states were populated in both (d, p) and (d, t), whereas at higher energies, the levels separate according to whether they are populated in stripping ( $U^2$ ) or pick up ( $V^2$ ). For example, the  $1/2$   $1/2^-$  [521] and  $7/2$   $5/2^-$  [512] hole states are stronger than the ground band states in (d, t), but much weaker in (d, p).

Tables 8.1 and 8.2 are well worth careful inspection. Although there are small differences in detail, especially for weaker states, the characteristic fingerprint patterns are often observed experimentally. Examples are the  $5/2^-$ -[512] and  $1/2^-$ -[510] bands in  $^{183}\text{W}$  and the  $7/2^-$ -[503] band in  $^{185}\text{W}$ . Indeed, these fingerprint patterns are often the technique used to identify the specific Nilsson orbits in the first place. The reader should not minimize the impressive successes of such a simple model, many of whose predictions can be anticipated without calculation despite the presence of perhaps dozens of valence nucleons.

Nevertheless, while qualitative *patterns* emulate the data, the detailed predictions often disagree substantially with the experimental results. Examples are the  $5/2$   $3/2^-$ -[512],  $5/2$   $1/2^-$ -[510],  $3/2$   $1/2^-$ -[521], and  $7/2$   $7/2^-$ -[514] states in both nuclei. There are differences of nearly an order of magnitude in the cross sections for populating certain corresponding states in the two nuclei. For example, in (d, p) in  $^{183}\text{W}$ , the  $5/2$   $1/2^-$ -[510] state is strongly populated while the  $5/2$   $3/2^-$ -[512] state is weak; in  $^{185}\text{W}$ , it is just the opposite.

Both of these phenomena are striking manifestations of the importance of the Coriolis interaction in odd mass nuclei. As we shall see, we can greatly improve the predicted cross sections if we take this residual interaction into account. The importance of the Coriolis interaction goes far beyond the question of sorting out difficulties with single nucleon transfer reactions. It is especially important for high-spin states in both odd and even mass nuclei, and has been shown to lead to a new coupling scheme—the so-called rotation aligned coupling scheme characterized by “decoupled” bands in many nuclei, and by the backbending phenomenon. It is in fact difficult to overestimate its significance in understanding odd mass deformed nuclei. We turn now to a systematic treatment of the Coriolis interaction with emphasis on its physical origin, its principal effects, and a simplified discussion of some easy ways to estimate its effects by inspection.

## 8.2 The Coriolis Interaction in Deformed Nuclei

The origin of the Coriolis interaction has already been seen in Eq. 7.13, where the rotational energy expression for a single-particle coupled to a deformed rotor contains a term  $-\hbar^2/2I (\mathbf{J}_\pm \cdot \mathbf{j}_\pm + \mathbf{J}_\pm \cdot \mathbf{j}_\pm)$  where  $\mathbf{J}_\pm$  acts on the total angular momentum and  $\mathbf{j}_\pm$  on the particle angular momentum. This term is an interaction between the rotational and single-particle motion and has physical effects similar to that of the Coriolis force on a classic rotating body. The simple properties of operators such as  $\mathbf{J}_\pm, \mathbf{j}_\pm$  are discussed in any standard quantum mechanics text. They serve as raising and lowering operators for the  $z$  projections,  $K$  and  $\Omega$ , of the total and single-particle angular momenta. Their matrix elements are (equating  $K$  and  $\Omega$  and calling both  $K$ ):

$$\langle K | \mathbf{J}_\pm | K \pm 1 \rangle = \sqrt{(J \mp K)(J + K + 1)} \quad (8.2)$$

$$\langle K | \mathbf{j}_\pm | K \pm 1 \rangle = \sqrt{(j \mp K)(j + K + 1)} \quad (8.3)$$

Note that both  $\mathbf{J}_+$  and  $\mathbf{j}_-$  decrease  $K$  while both  $\mathbf{J}_-$  and  $\mathbf{j}_+$  increase  $K$ .

The physical nature of the Coriolis interaction is easy to see. It is analogous to the classic effect that occurs in any rotating body. Consider the analogy of a projectile traveling northward from the equator on the earth's surface, illustrated in Fig. 8.3. A projectile launched at the equator initially travels eastward at a rate given by the rotational speed of the earth at the equator. Since the earth's circumference at higher latitudes is less, an observer at a northern latitude has a smaller rotational velocity. To this observer, the

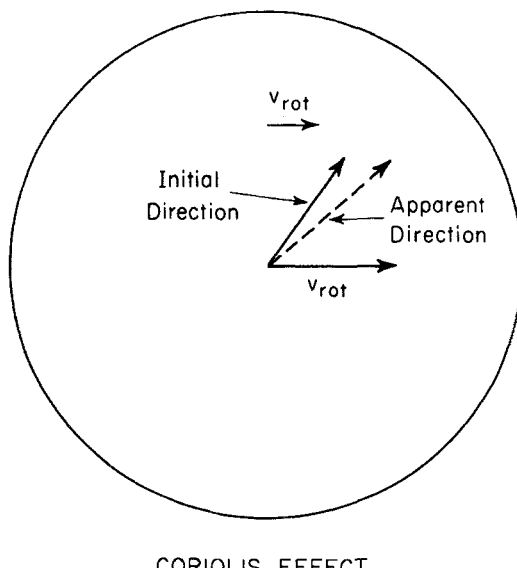


**Fig. 8.3.** Coriolis effect in a rotating system resulting from the dependence of rotational velocities on "latitude."

projectile that was fired directly northward will appear to be deflected toward the east. This is the Coriolis effect, and while it is sometimes called a fictitious or apparent force, it has real physical effects. (It accounts for the fact that river banks tend to be eroded more on the right (facing downstream) side in the northern hemisphere.) We see from this illustration that the Coriolis interaction effectively tilts the orbit relative to the equator. If we now picture the orientation of the angular momentum vector perpendicular to the orbit instead of the orbit itself, the Coriolis effect is equivalent to a change in its projection onto the equator. Thus it is understandable that, in the nuclear case, the Coriolis interaction alters the projection of the angular momentum  $K$  on the symmetry axis, *admixing* different  $K$  values. Another way of looking at this that will be useful later is to recall that  $K$  is only a good quantum number if the nuclear potential is axially symmetric. Therefore, the Coriolis interaction effectively introduces small amounts of axial asymmetry as it mixes  $K$  values.

We now evaluate the Coriolis matrix element explicitly. We consider two intrinsic Nilsson states characterized by  $K$  and  $K+1$ . Since  $J$  is a good quantum number, we can replace  $\mathbf{J}_\pm$  with its eigenvalue. This cannot be done with  $\mathbf{j}_\pm$  because of the configuration ( $j$ ) mixing in Nilsson wave functions, although it can be done approximately for the unique parity orbits where one  $j$  value dominates. Noting that only one of the two terms in  $\mathbf{J}_+ \mathbf{j}_- + \mathbf{J}_- \mathbf{j}_+$  gives a nonvanishing result, we get

$$\langle \psi_{JK} | V_{\text{Cor}} | \psi_{JK+1} \rangle = \frac{-\hbar^2}{2I} \sqrt{(J-K)(J+K+1)} \langle K | j_- | K+1 \rangle (U_1 U_2 + V_1 V_2) \quad (8.4)$$

where the symbols  $K, K+1$  in the  $\mathbf{j}_-$  matrix element are a shorthand for the two Nilsson wave functions and the effects of pairing are included in the factor  $(U_1 U_2 + V_1 V_2)$ . The pairing factor has the general effect of *reducing* the Coriolis matrix elements since its maximum value is unity. The reduction is least for orbits in similar positions relative to the Fermi surface (then  $U_1 \approx U_2$  and  $V_1 \approx V_2$ , hence  $(U_1 U_2 + V_1 V_2) \approx U_1^2 + V_1^2 = 1$ ). It is least for orbits laying on far opposite sides (then  $U_1 \approx V_2$  and  $U_2 \approx V_1$ , so  $(U_1 U_2 + V_1 V_2) \approx (U_1 V_1 + U_2 V_2)$  and one factor in each term is small). For diagonal Coriolis matrix elements, the factor is obviously unity.

For a single  $j$  shell, the  $\mathbf{j}_-$  matrix element is

$$\langle jK | j_- | jK+1 \rangle = \sqrt{(j-K)(j+K+1)} \quad (8.5)$$

This is approximately correct for unique parity orbits. For an arbitrary Nilsson wave function, terms like this occur for each  $j$ , so that, in general,

$$\langle jK | j_- | jK+1 \rangle = \sum_j C_j^K C_j^{K+1} \sqrt{(j-K)(j+K+1)} \quad (8.6)$$

where the  $C_j^K$  and  $C_j^{K+1}$  coefficients are those describing the specific Nilsson wave functions. An interesting limiting case occurs for  $J, j \gg K$ , if  $j$  is approximately a good quantum number. This applies for low  $K$  orbits from the high-spin unique parity states or for high spin, low  $K$  states generally if  $\beta$  is small (little configuration mixing). Then Eqs. 8.4 and 8.6 give

$$V_{\text{Cor}} = \frac{-\hbar^2}{2I} J j \quad (8.7)$$

This is a general upper limit on the strength of the Coriolis interaction. For typical inertial parameters (say 15 keV for rare earth nuclei) and say,  $J, j \approx 11/2$ , this attains  $\approx 400$  keV! Typical spacings between Nilsson orbits are  $\approx 150$  keV. Coriolis mixing is not necessarily a minor perturbation!

Since the Coriolis matrix elements change  $K$  by  $\Delta K = \pm 1$ , it is generally a nondiagonal interaction. However, it has an important *diagonal* matrix element that contributes to certain rotational energies. For  $K = 1/2$ , the symmetrization of the wave function gives rise to terms with  $K = \pm 1/2$ , allowing a diagonal  $\Delta K = 1$  contribution to the energies from the cross terms. Substituting Eqs 8.4 and 8.6 in Eq. 7.14, we get for the rotational energies for  $K = 1/2$  bands including Coriolis mixing

$$E_{\text{rot}}(J) = \frac{-\hbar^2}{2I} \left[ J(J+1) + \delta_{K \frac{1}{2}} a (-1)^{J+\frac{1}{2}} \left( J + \frac{1}{2} \right) \right] \quad (8.8)$$

where  $a$  is the well-known decoupling parameter given by substituting  $K = -1/2$  in Eq. 8.6

$$a = \sum_j (-1)^{j-\frac{1}{2}} \left( j + \frac{1}{2} \right) C_j^2 \quad (8.9)$$

The two phase factors in Eqs. 8.8 and 8.9 come from the symmetrization of the wave functions (e.g., Eq. 6.10). The phase factor in Eq. 8.8,  $(-1)^{J+1/2}$ , means that the contribution to the rotational energies from the Coriolis interaction *alternates* in sign with  $J$ .

It is clear from Eq. 8.9 that  $a$  can be either positive or negative. The behavior of  $E(J)$  in Eq. 8.8 as a function of  $a$  is shown in Fig. 8.4. If  $a < 0$ , states with spins  $3/2, 7/2, 11/2, \dots$  are lowered in energy while the alternate spin states are raised. For  $a > 0$ , the opposite situation occurs. On account of the factor  $(J + 1/2)$  the effect grows with spin. On account of the factor  $(j + 1/2)$  the effect, on average, increases for heavy nuclei ( $j_{\text{ave}} \propto N$ ). For  $|a| = 1$ , Eq. 8.8 shows that the levels occur in degenerate pairs. If  $a = -1$ , the  $J = 3/2$  state coincides with the  $J = 1/2$  level. Similarly, the  $(5/2, 7/2)$  and  $(9/2, 11/2)$  pairs are degenerate. If  $a = +1$ , the degenerate pairs are  $(3/2, 5/2), (7/2, 9/2), \dots$ . For  $|a| > 1$ , the level order within a rotational band is no longer monotonic in spin. Clearly, the typical rotational spacings can be so severely perturbed as to obscure the normal  $J(J+1)$  spacings and even the ordering of different spin states. As we shall see, these effects propagate via nondiagonal Coriolis mixing, and affect many bands with  $K \neq 1/2$ . We can now understand one of the anomalous rotational spacings and sequences in Fig. 7.8, specifically that for the  $1/2^-$ -[521] band. This is a  $K = 1/2$  band with its decoupling parameter close to unity.

For an arbitrary Nilsson wave function, many terms can appear in Eq. 8.9 for  $a$ . Frequently these terms (each carrying a phase) largely cancel and the resultant  $a$  values are rather small, typically less than unity. However, very large  $a$  values can be obtained if the wave function is dominated by few terms with high  $j$  values. The classic example of this is the unique parity orbits for

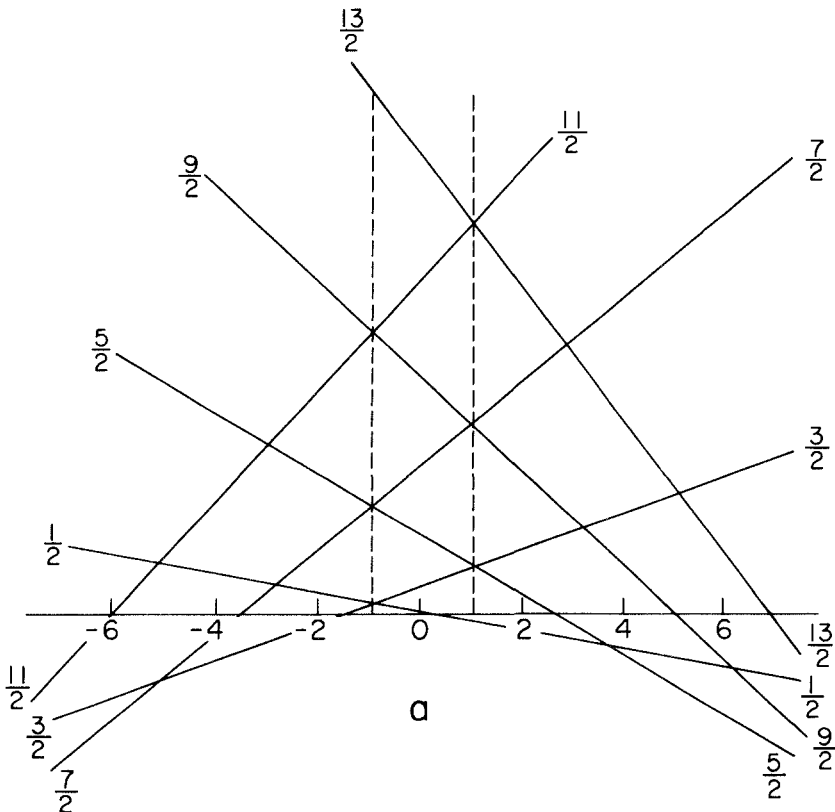


**Fig. 8.4.** Dependence of rotational energies ( $J$ ) on the decoupling parameter  $a$ . The dashed lines are for  $|a| = 1$  (based on Preston, 1975).

which  $\langle j \rangle \approx N + 1/2$  (e.g.,  $j = 13/2$  in the  $N = 6$  shell), and the wave functions are nearly pure in  $j$ . For these special orbits, Eq. 8.9 gives  $a \approx (-1)^N(N + 1)$ . For example,  $a \approx 7$  for the  $1/2^+[660]$  orbit. This enormous value so perturbs the normal spacing that the  $13/2^+$  level is among the lowest-lying levels in the rotational band. For  $\hbar^2/2I = 15$  keV, the decoupling term is  $\approx -750$  keV! In general, the sign of  $a$  is always such that the  $J = N + 1/2$  level (e.g.,  $J = 13/2$  for the  $i_{13/2}$  shell) is lowered.

The reader may recall an apparent paradox in the order and spacing of rotational energies in odd mass nuclei that was discussed in Chapter 7. The simplest view led to the notion that rotational bands should be “upside down.” We showed that the “normal” order was regained when the precession of  $j$  around the symmetry axis was considered. We also pointed out that in some cases an “upside down” pattern does in fact occur. We have just encountered that case where large Coriolis effects in unique parity orbits upset the monotonic order of rotational energies with  $J$ . Having gone to great lengths to explain away this paradox in Chapter 7, why does it now appear in the data? In

other words, what happened to the precession argument? As we shall see later, the physical difference here is that  $K$  is no longer a good quantum number ( $\pm 1/2$  values are admixed), so the precession need not be about the symmetry axis: the Coriolis force, by mixing  $K$  values, forces the angular momentum vector to switch back and forth (precess) about the *rotation* axis instead. Thus,  $\mathbf{j}$  and  $\mathbf{R}$  are nearly parallel or antiparallel, so now  $J = 13/2$  does correspond to  $|R| \approx 0$ ,  $J = 9$  to  $|R| \approx 2$ , and so on.

One often reads that  $a$  is called the *decoupling parameter* because it represents a decoupling of the rotational and single-particle motion. It is now easy to see why this name is appropriate. For  $a = +1$ , the energy differences of the  $1/2, 5/2, 9/2, \dots$  states are exactly the same as those between the  $0^+, 2^+, 4^+, \dots$  states of the even-even core: the odd particle acts like a spectator to the rotation. Moreover, it is clear from the comment just made that changes in core rotation have little effect on the orientation of  $\mathbf{J} = (\mathbf{R} + \mathbf{j})$  when  $a$  is large (i.e., when  $|j|$  is large,  $K/j$  is small, so  $\sin\theta = K/j$  is small, and  $\mathbf{J}$  is nearly aligned along the rotation axis). Extrapolating to very large  $a$  values in Fig. 8.4 shows that the  $J = 13/2$  state will lie lowest, followed by the  $9/2$  level ( $13/2 - 2$ ), and then by the  $5/2$  level ( $13/2 - 4$ ). The alternate spin levels are much higher. Thus the rotational energies of alternate  $J$  values (with  $|J-j|$  even) are nearly parabolic in  $|J-j|$  where  $j$  is the dominant  $j$  of the unique parity orbit. Sequential states differ mainly in  $R$ : the rotational motion is effectively decoupled from that of the odd particle. We shall encounter a related but even more dramatic effect later as a consequence of the nondiagonal Coriolis interaction.

Turning now to these nondiagonal Coriolis effects, there are two significant observable effects. One concerns rotational energies and stems from a propagation of the highly perturbed level order in the  $K = 1/2$  band to higher  $K$  bands via successive  $\Delta K = 1$  Coriolis mixings. Precisely because of the large decoupling parameters, this is most important for unique parity states and, as we shall see, accounts for their importance in high-spin studies where the  $(J+1/2)$  factor in Eq. 8.8 becomes crucial. The other effect occurs in “normal” rotational bands (especially in their impact on single nucleon transfer cross sections). We shall discuss this first.

Consider the admixture of two bands as shown in Fig. 8.5. Recalling our discussion in Chapter 1 of two-state mixing and the fact that the Coriolis mixing increases with  $J$ , the perturbed energies will behave as illustrated. It is easy to show that, to first order, the effect of the Coriolis interaction is to decrease the effective inertial parameter,  $\hbar^2/2I$ , for the lower band and to increase it for the higher band.

Equation 1.6 gives the energy shifts of the two interacting states relative to the unperturbed spacing for a given spin  $J$

$$\frac{\Delta E_s}{\Delta E_u} = \frac{1}{2} \left[ \sqrt{1 + \frac{4V^2}{\Delta E_u^2}} - 1 \right] \approx \frac{V^2}{\Delta E_u^2}$$

where the last step assumes small mixing (Eq. 1.12). Thus  $\Delta E_s \propto V^2_{Cor}$ . Isolating the spin dependence Eq. 8.4 gives

$$\Delta E_s \propto \frac{\hbar^2}{2I} (J-K)(J+K+1)$$

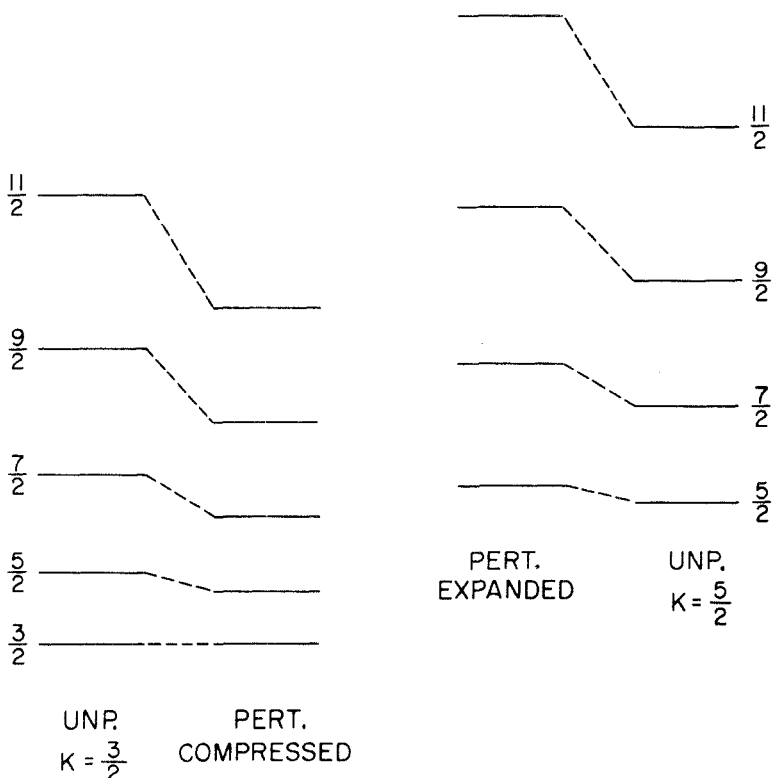


**Fig. 8.5.** Illustration of the changes in effective rotational parameters,  $\hbar^2/2I$ , resulting from two-state Coriolis mixing.

or

$$\Delta E_s \propto -\frac{\hbar^2}{2I} [J(J+1) - K(K+1)] \quad (8.10)$$

which is just the rotational energy expression ( $J, K$  dependent parts). The Coriolis interaction merely alters the effective rotational spacings. The lower band is compressed, the upper one expanded. This simple result breaks down for very large or multistate mixing, but even in these cases gives a useful framework.

In general, there can be many low-lying Nilsson bands with assorted  $K$  values; thus a realistic Coriolis mixing calculation will be a multistate diagonalization. The admixed wave functions can be written

$$\psi(J) = \sum_i \alpha_i \phi_{\text{Nil}}^i(J) \quad (8.11)$$

where the  $\alpha_i$  are the mixing amplitudes that depend on  $J$ .

In this way, for example, a predominantly  $K = 3/2$  band may contain admixtures of  $K = 7/2$  through the intermediary of  $K = 5/2$ . We shall see later that this is especially important for the unique parity case. Although such mixing can be rather complicated, one can almost always estimate the effects of a full multistate diagonalization rather accurately by carrying out a sequence of two-state mixing calculations. We shall see examples of this shortly.

At this stage it is important to discuss the actual magnitudes of the Coriolis mixing matrix elements. The quantities  $\hbar^2/2I$ ,  $(J-K)(J+K+1)$ , and the  $U$ ,  $V$  factors are easy to estimate, as we have done. They are dependent on the orbits involved but not on their detailed structure (Nilsson wave functions). However,  $\langle \psi_{\text{Nil}}(K) | j_- | \psi_{\text{Nil}}(K+1) \rangle$  depends explicitly on the structure of the states included, as evident in Eq. 8.6.

As with the decoupling parameter, the nondiagonal  $j_-$  matrix elements for the unique parity orbits are both large and particularly simple to calculate, since one  $j$  term in Eq. 8.6 dominates. For example, for  $\beta \approx 0.23$  and typical Nilsson parameters  $\kappa$  and  $\mu$ , the Coriolis matrix element of  $j_-$  connecting the  $1/2^+[660]$  and  $3/2^+[651]$  Nilsson orbits is  $\approx 6.6$ . If we had assumed the wave functions consisted only of the  $j = 13/2$  component, Eq. 8.6 gives  $\langle K | j_- | K+1 \rangle \approx N + 1$ , which is the maximum possible value for any matrix element of  $j_-$  in a given shell. Thus, to a good approximation, the unique parity Coriolis matrix elements can be estimated using the single  $j$  approximation, and moreover, they have very nearly the maximum possible values.

Table 8.3 provides a number of other examples of off-diagonal  $j_-$  matrix elements in the  $N = 5$  shell. The reader may easily derive these numbers by applying Eq. 8.6, using the wave functions given earlier in Table 7.2. Inspection of Table 8.3 reveals two global features. First, Coriolis matrix elements for nonunique parity orbits are considerably smaller. Second, their relative values can differ by more than an order of magnitude.

In considering a given level scheme and attempting to determine whether Coriolis mixing effects will be important, it is often useful to be able to estimate, without calculation, the approximate magnitude for Coriolis matrix elements. A very simple rule allows one to do this. For nonunique parity orbits, Coriolis matrix elements divide roughly into two classes, allowed and nonallowed. The allowed matrix elements are those in which both  $n_z$  and  $\Lambda$

**Table 8.3.** Theoretiral valus  $\langle K | j_- | K+1 \rangle^*$

9/2-[505]	7/2-[503]	3/2-[512]	1/2-[510]	5/2-[512]	1/2-[521]	7/2-[514]
9/2-[505]	-0.973					2.847
7/2-[503]	-0.973			2.858		
3/2-[512]			0.951	0.045	2.546	
1/2-[510]			0.951		-2.541	
5/2-[512]		2.858	0.045			-1.151
1/2-[521]			2.546	-2.541		
7/2-[514]	2.847				-1.151	

\*The Nilsson model parameters are  $\delta = 0.2$ ,  $\kappa = 0.0637$ ,  $\mu = 0.42$ .

change by one unit, but their sum remains constant ( $\Delta n_z = -\Delta \Lambda$ ). (The unique parity case is, of course, in this class.) Examples from the table are the matrix elements between the  $3/2^-$ -[512] and  $1/2^-$ -[521] orbits or between the  $7/2^-$ -[514] and  $9/2^-$ -[505] orbits. Such allowed  $j_z$  matrix elements are typically on the order of  $N/2 - N/3$ . All of the others are nonallowed matrix elements and are typically  $< 1$ . Examples of these are the matrix elements between  $7/2^-$ -[514] and  $5/2^-$ -[512] or  $1/2^-$ -[510] and  $3/2^-$ -[512].

It is important to note that Coriolis mixing between orbits in the latter class is not always negligible, especially if they have the same  $n_z$  values. As we have seen, the Nilsson diagram separates approximately according to  $n_z$  values for large deformations. Therefore, it can often occur that two orbits with identical  $n_z$  values differing in  $K$  by  $\Delta K = \pm 1$  lay very close to each other. Their Coriolis mixing can be large even with a small matrix element. A classic example of this occurs for the  $1/2^-$ -[510] and  $3/2^-$ -[512] orbits in  $^{183,185}\text{W}$ . We shall discuss this case in some detail momentarily.

Having dealt with typical values of the  $j_z$  matrix elements, it is useful to develop a feeling for the absolute magnitudes of the full Coriolis matrix elements in Eq. 8.4. For well-deformed nuclei,  $\hbar^2/2I \approx E_{2_1^+}/6$  where  $E_{2_1^+}$  is given by a neighboring even-even nucleus. For rare earth nuclei,  $\hbar^2/2I \approx 14-18$  keV, while for the actinides,  $\hbar^2/2I \approx 7$  keV. The matrix elements of  $\mathbf{J}_\pm$  given by the square root factor are typically 2-3 for moderate spin states, although they can become very large for high spins. Finally, as noted, the pairing factor becomes very small for high-lying orbits on opposite sides of the Fermi surface, while for orbits near the Fermi surface, or for those on the same side, this factor is typically between 0.7 and 1.0. Thus, typical nonunique parity *allowed* Coriolis matrix elements in the rare earth region are roughly  $V_{\text{Cor}} \approx (16)(3)(1)(0.8) \approx 40$  keV. This estimate is only accurate to a factor of 2-3. *Nonallowed* Coriolis matrix elements will, of course, be less.

For unique parity orbits, the  $j_z$  matrix elements are  $\sim N$ . In addition, the *observed* states are typically of rather high  $J$ , since single nucleon transfer reactions preferentially populate the  $J = N + 1/2$  states for which  $C_J \approx 1$  and heavy ion reactions tend to feed the high-spin unique parity levels. Taking  $\sqrt{(J-K)(J+K+1)} \approx N$ , the Coriolis matrix elements linking unique parity orbits can be extremely large, typically reaching  $V_{\text{Cor}}(\text{unique parity}) \approx 16(6)(6)(0.8) \approx 400$  keV. Such matrix elements mixing states often only a couple of hundred keV apart have enormous structural effects.

From extensive experience with Coriolis mixing calculations, it has been found that the *actual empirical* matrix elements are generally about 20-50% lower than these theoretical estimates. This conclusion emerges from comparisons of extensive data on level energies and single nucleon transfer cross sections in many deformed nuclei. We will not detail this evidence here, but one example of it is trivially evident in Fig. 8.1, which shows that the  $7/2^-$  states of the  $7/2^-$ -[514] and  $5/2^-$ -[512] bands in  $^{183}\text{W}$  are separated by only 70 keV. If we consider this an isolated two-state system (an approximation good enough for the present purposes although not for detailed calculations) and recall that such states can never be closer than twice their mixing matrix element, then the

Coriolis matrix element between these two states must be  $\leq 35$  keV. Since both bands are hole excitations, the pairing factor is near unity. Using  $\hbar^2/2I = 18$  keV ( $E_{2_1^+}(^{184}\text{W}) = 111$  keV) and the  $j_z$  matrix element from Table 8.3 gives a predicted Coriolis matrix element of 55 keV. The maximum matrix element allowed empirically is only 65% of this. Other similar examples abound.

Despite this attenuation, Coriolis mixing effects, especially among unique parity orbits, represent a substantial perturbation to the rotational picture and can seldom be ignored. One final point to emphasize before considering some actual calculations is that in weakly deformed and transitional nuclei, Coriolis matrix elements are far larger than in well-deformed nuclei because of the smaller moments of inertia. Matrix elements between unique parity orbits may reach an MeV or more, and under certain circumstances may even lead to a new coupling scheme, the so-called rotation aligned scheme we shall discuss later.

As an example of multistate Coriolis mixing, let us consider the level scheme of  $^{183}\text{W}$  shown in Fig. 8.1. In principle, a full calculation cannot neglect the unseen bands that occur at higher energies, but in practice, one assumes that their effects are small (at least for nonunique parity orbits). We will see one way to estimate whether such an assumption is grossly violated. Under this assumption, the Coriolis mixing among the negative parity bands involves diagonalizing matrices of varying size,  $2 \times 2$  for  $J = 1/2$ , up to  $6 \times 6$  for  $J = 11/2$ . For the positive (unique) parity states, the strength of the Coriolis mixing precludes safely ignoring unseen bands and therefore one usually carries out a full  $7 \times 7$  diagonalization.

We consider first the negative parity states. We note the empirical result (from ratios of (d, p) to (d, t) cross sections) that the Fermi surface is slightly below the  $1/2-[510]$  orbit. For simplicity we ignore the  $9/2-[505]$  band. (In any case, it can only affect  $J = 9/2$  states.) From our earlier discussion, we anticipate that the principle mixing effects will occur between the  $1/2-[521]-3/2-[512]$  and  $5/2-[512]-7/2-[503]$  pairs. That this is not quite true highlights the other factors that must be taken into account in practical situations. Although the matrix element connecting the  $1/2-[510]$  and  $3/2-[512]$  orbits is rather small ( $\approx 1$ ), they lay so close to each other that the mixing is substantial. Likewise, the “forbidden” matrix element between the  $5/2-[512]$  and the  $7/2-[514]$  orbits ( $\approx 1.1$ ), strongly admixes these close-lying bands. In contrast, despite the large  $j_z$  matrix element between the  $5/2-[512]$  hole orbit and the particle excitation  $7/2-[503]$ , the pairing factor substantially reduces the overall matrix element. The one exception to the simple rule given above for estimating Coriolis matrix elements among these bands occurs for the  $1/2-[510]$  and  $1/2-[521]$  pair: the supposedly forbidden  $j_z$  matrix element has a value  $\approx 2.5$ . Although these bands are nearly an MeV apart, the coupling between them is nonnegligible. Thus, the principle Coriolis admixtures will be between the  $1/2-[510]$  and  $3/2-[512]$  bands, the  $5/2-[512]$  and  $7/2-[514]$  bands, and the  $1/2-[510]$  and  $1/2-[521]$  bands. Second-order mixtures of, say, the  $1/2-[510]$  into the  $5/2-[512]$  band, will be very small. Thus, a rather good simulation of the full diagonalization should be obtainable by considering sequential two-state mixing of the

**Table 8.4.** Calculated mixing amplitudes ( $\alpha_i \times 100$ ) for the  $7/2^-$  states in  $^{183,185}\text{W}$ 

$K\pi[Nn_z\Lambda]$	$A$	$E_x$	$7/2^-[503]$	$3/2^-[512]$	$1/2^-[510]$	$5/2^-[512]$	$1/2^-[521]$	$7/2^-[514]$
$7/2^-[503]$	185	244	+100	—	—	+5	—	—
	183	453	+100	—	—	+5	—	—
$3/2^-[512]$	185	174	—	+91	+42	—	+2	—
	183	412	—	-96	+26	—	-8	—
$1/2^-[510]$	185	334	—	-41	+90	—	-11	—
	183	207	—	+27	+96	—	-5	—
$5/2^-[512]$	185	986	-5	—	—	+98	—	-19
	183	1002	-5	—	—	+98	—	-17
$1/2^-[521]$	185	1335	—	+6	-9	—	-99	—
	183	1265	—	-6	-7	—	-100	—
$7/2^-[514]$	185	1058	+1	—	—	-19	—	-98
	183	1072	+1	—	—	-17	—	-99

\*Casten, 1972.

preceding three pairs. As an example, consider the  $7/2^-$  states with a Coriolis attenuation factor 0.7. With  $\hbar^2/2I = 18$  keV and a pairing factor of 0.9, we obtain  $\approx 41$  keV for the full  $1/2^-[510]-3/2^-[512]$  Coriolis matrix element. The final spacing of the  $7/2^-1/2^-[510]$  and  $7/2^-3/2^-[512]$  states is 205 keV. Working backwards in Fig. 1.7, we see that  $R$  must be rather large and therefore the energy shift induced in each state by the mixing is a small fraction ( $\approx 0.05$ ) of their unperturbed spacing. Reducing the full separation by 10% to estimate the unperturbed splitting gives  $R \approx 3.8$ . Another application of Fig. 1.7 or Eq. 1.8 gives the admixed wave functions as  $\psi$  ("7/2 1/2-[510]") =  $(0.97)$  7/2 1/2-[510] +  $(0.24)$  7/2 3/2-[512] and the orthogonal combination. For the  $7/2^-1/2^-[510]-7/2^-1/2^-[521]$  mixing we take a pairing factor of 0.6, giving the full Coriolis matrix element of  $\approx 88$  keV.  $\Delta E_{\text{final}} = 1058$  keV, so we can use the final spacings to obtain  $R \approx 12$ . The admixed wave functions are  $\psi$  ("7/2 1/2-[510]") =  $(0.99)$  7/2 1/2-[510] +  $(0.08)$  7/2 1/2-[521] and the orthogonal combination. Finally, for  $7/2^-3/2^-[512]$  and  $7/2^-1/2^-[521]$ , the pairing factor is  $\approx 0.5$ . Calculations again give  $R \approx 12$ , and final wave functions of  $\psi$  ("7/2 3/2-[512]") =  $(0.99)$  7/2 3/2-[512] +  $(0.08)$  7/2 1/2-[521], and the orthogonal combination. In all three cases the signs of the amplitudes are arbitrary.

We can test these estimates by reference to the detailed wave functions resulting from a full diagonalization given in Table 8.4. The three admixtures just calculated are  $1/2^-[510]-3/2^-[512] = 0.24$ ,  $1/2^-[510]-1/2^-[521] = 0.08$ , and  $3/2^-[512]-1/2^-[521] = 0.08$ . The exact calculations give 0.26, 0.05 and 0.08!

We can also estimate the energy shifts. Using the same  $R$  values we get the following results (in keV):

$$7/2^-1/2^-[510]: -12.0(3/2^-[512]) - 7.2(1/2^-[521]) = -19.2 \text{ keV}$$

$$7/2^-3/2^-[512]: +12.0(1/2^-[510]) - 5.8(1/2^-[521]) = +6.2 \text{ keV}$$

$$7/2^-1/2^-[521]: +7.2(1/2^-[510]) + 5.8(3/2^-[512]) = +13.0 \text{ keV}$$

where the orbits in parenthesis give the mixing partner that induced each shift. Again, these estimates are close to the results of an exact calculation.

With these shifts, and similar ones for other  $J$  values, the  $1/2-[510]$  band is compressed and the  $1/2-[521]$  and  $3/2-[512]$  bands are expanded, reflecting the derivation in Eq. 8.10 that, to first order, Coriolis induced energy shifts can be absorbed into changes in  $\hbar^2/2I$ . Indeed, one clue to the presence of Coriolis effects in empirical level schemes is unequal *empirical*  $\hbar^2/2I$  values (i.e., after mixing), with larger magnitudes for the higher-lying (expanded) bands and smaller values for the lower (compressed) states. A measure of the adequacy of a calculation is whether the *input* (unperturbed)  $\hbar^2/2I$  values are substantially closer: they should be if the deformation is the same for all excited states and small microscopic “blocking” effects are neglected.

### 8.3 Coriolis Mixing and Single Nucleon Transfer Cross Sections

Strong Coriolis effects are at the heart of most current research in high-spin states, and thus occupy a crucial role in modern nuclear structure physics. They were first studied extensively in single nucleon transfer reactions, however, and, although such work is not so common nowadays, it is an appropriate starting point for our discussion since the effects of Coriolis mixing are so dramatic and also easy to understand physically in this context.

While the energy shifts previously discussed may seem rather small and perhaps easily negligible, such an impression is misleading because even small admixtures can have large effects on single nucleon transfer cross sections. The expression for the cross section to a state of spin  $J$  in a given band in the presence of Coriolis mixing is an obvious generalization of Eq. 8.1 given by

$$\frac{d\sigma}{d\Omega}(J) = 2N\phi_l(\theta) \left[ \sum_i \alpha_i C_j^i P_i \right]^2 \quad (8.12)$$

where the  $\alpha_i$ 's are the Coriolis mixing amplitudes and the sum is over the admixed bands. Note that the sum is coherent, thus magnifying the effects. Simple manipulations also show that the total cross section is conserved for each spin  $J$ : that which is lost by some states must be gained by others.

Before considering the example of  $^{183}\text{W}$  in detail, it is useful to emphasize how small mixing amplitudes can have significant effects. For simplicity, assume a two-state mixing of bands with identical  $C_i$  coefficients and pairing factors for some spin  $J$ . Then, if the mixing amplitude of each band in the other is 0.22 (meaning that the amplitude for the “parent” state is still 0.975), this gives a 50% increase in the cross section of one state and a 50% decrease in the other [ $\sigma_1 \propto (1.22)^2$ ,  $\sigma_2 \propto (0.78)^2$ ]. The two cross sections that would have been equal without mixing now differ by a factor of three!

Another feature is evident from Eq. 8.12. If two admixed states have very *different* unperturbed  $C_i$  values for some  $J$ , the state with the larger  $C_i$  value will be relatively unaffected while that with the smaller may be drastically altered. Indeed, much of the resultant cross section may easily come from the small admixture rather than from the parent orbit itself. To be specific, suppose the two bands have equal pairing factors, that  $C_1^1 = 0.2$  and  $C_2^1 = 0.8$ ,

and that the mutual mixing amplitudes are  $\pm 0.22$ . Then, assuming that the phases are such that the cross section for the state of spin  $J$  in band 1 is increased, the ratio of perturbed to unperturbed cross sections is  $\approx 3.5$  for band 1 [ $(0.2 + 0.22(0.8))^2$ ] and  $\approx 0.9$  for band 2 [ $(0.8 - 0.22(0.2))^2$ ]. This is another example (bandmixing in even nuclei was the first) of how relatively small mixing interactions and amplitudes can lead to drastic effects on certain observables, especially when one of the unperturbed transition rates is small or forbidden. If the phases were reversed (which would happen if the *unperturbed* positions of the two bands were *exchanged*), the same analysis shows that despite the small mixing, the cross section for band 1 would essentially vanish while that for band 2 would increase only by about 6%. Finally, if one  $C_j$  coefficient is nearly zero, the cross section will come only from the mixing. It will therefore be independent of the signs of the mixing amplitudes and will always be increased by the mixing.

Simple application of Eq. 8.12 to the mixing amplitudes such as those given in Table 8.4 for the  $7/2^-$  states of the negative parity bands in  $^{183}\text{W}$  gives the cross sections labeled "perturbed" in Table 8.1. The point of this section is highlighted by the enormous differences between perturbed and unperturbed

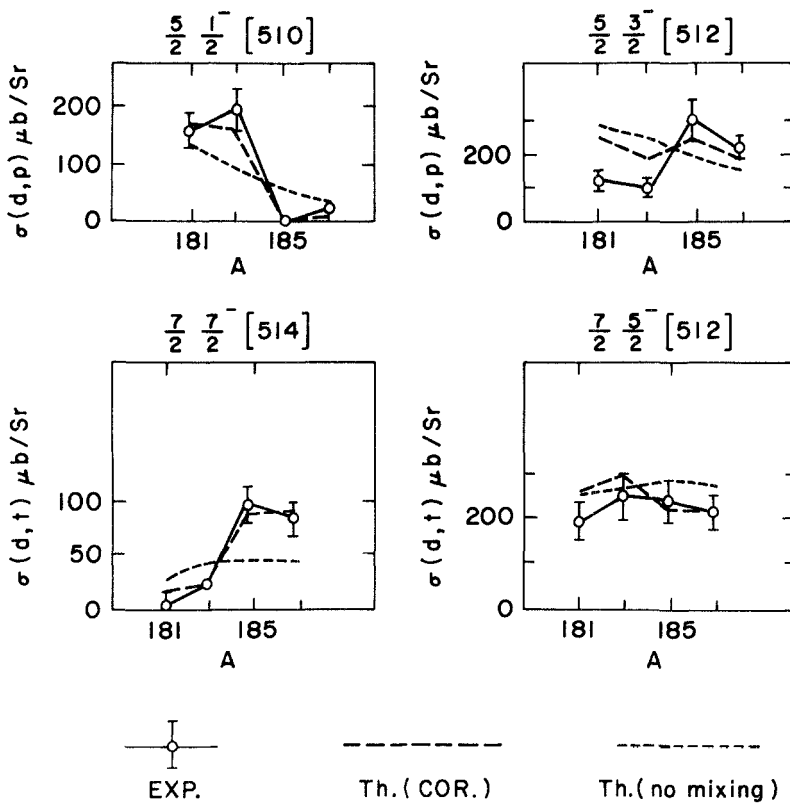


**Fig. 8.6.** Systematics of experimental, unmixed, and Coriolis coupled ( $d, p$ ) and ( $d, t$ ) cross sections in W isotopes.

cross sections even in cases where the mixing amplitudes of Table 8.4 are small. For example, because of its small value of  $C_{1/2}$ , nearly all the cross section to the  $1/2\ 1/2-[510]$  state stems from weak mixing with the  $1/2\ 1/2-[521]$  state. The cross sections for the  $3/2^-$  levels of the  $1/2-[510]$  and  $3/2-[512]$  bands are significantly shifted by the mixing. The same applies to the  $J = 5/2$  and  $7/2$  states of these bands and to the  $7/2$  states of the  $5/2-[512]$  and  $7/2-[514]$  bands. Table 8.2 shows similar Coriolis mixing results in  $^{185}\text{W}$ .

Figure 8.6 shows the systematics of some empirical and Coriolis calculated cross sections across the odd mass W isotopes. It includes a comparison with the unmixed cross sections. The latter are constant except for small, smooth changes in the pairing factor  $P^2$ , in Eq. 8.1. The figure highlights the changes in single nucleon transfer cross sections brought about by the Coriolis interaction as well as the dramatic shifts that can occur from one isotope to another. This is particularly evident for the  $1/2-[510]$  and  $3/2-[512]$  bands in  $^{183}\text{W}$  and  $^{185}\text{W}$ . An understanding of this is obvious from our discussion of two-state mixing in Chapter 1. As we have stated before, these two bands have interchanged positions (energies) in these two nuclei. In  $^{183}\text{W}$ , the  $1/2-[510]$  band is the lower, ground state orbital, while the  $3/2-[512]$  band is the first excited intrinsic excitation. In  $^{185}\text{W}$ , the  $3/2-[512]$  orbital forms the ground state and the  $1/2-[510]$  band is close, lying just above it. Therefore, the *signs* of the mixing amplitudes are inverted between  $^{185}\text{W}$  and  $^{183}\text{W}$ . In the familiar terminology of first-order perturbation theory, the sign of the energy denominator has changed from one nucleus to the other. Therefore, for those states where the two unperturbed Nilsson wave functions have comparable  $C$  coefficients, cross sections that were increased in  $^{183}\text{W}$  will be decreased in  $^{185}\text{W}$  and vice versa. For cases where the  $C$  coefficient in one is negligible, the cross section to that state will increase relative to the unmixed case in both nuclei. Another example of inversion concerns the  $7/2-[514]$  and  $5/2-[512]$  bands, in which the  $7/2^-$  levels interchange positions between  $^{181}\text{W}$  and  $^{183}\text{W}$ . Figure 8.6 shows the dramatic effect on the weaker cross section.

Before turning to the positive parity levels, it is worth re-emphasizing the extremely large effects involved here. Empirical fingerprint patterns automatically incorporate the effects of Coriolis mixing and can differ from those predicted by the Nilsson model by sufficiently large quantities as to completely obscure the identification of the bands if Coriolis mixing is not taken into account. Moreover, the mistakes that one would make would not even necessarily be the same in neighboring nuclei, and the systematics of the Nilsson orbits deduced could be completely wrong.

### Unique Parity States

We now consider the unique parity orbits. Here, the Coriolis mixing becomes at once much stronger but also somewhat simpler to interpret. The reason is that, for practical purposes, only the  $J = N + 1/2$  ( $J = 13/2$  for the odd neutron rare earth nuclei) state is important because of the utter dominance of the  $C_{j=N+1/2}$  coefficients in the Nilsson wave functions for these orbits. Moreover, the Coriolis matrix elements are all very similar and only directly link adjacent

orbits stemming from the same  $j$  shell (although second-order ( $\Delta K = 2$ ) mixing is significant).

Before discussing practical calculations, let us take a schematic model. Assume the Fermi surface lies below the whole group of unique parity orbits in some nucleus. The order of their excitation energies is  $K = 1/2, 3/2, \dots, (N+1/2)$ .

PROPAGATION OF DECOUPLING  
via CORIOLIS MIXING

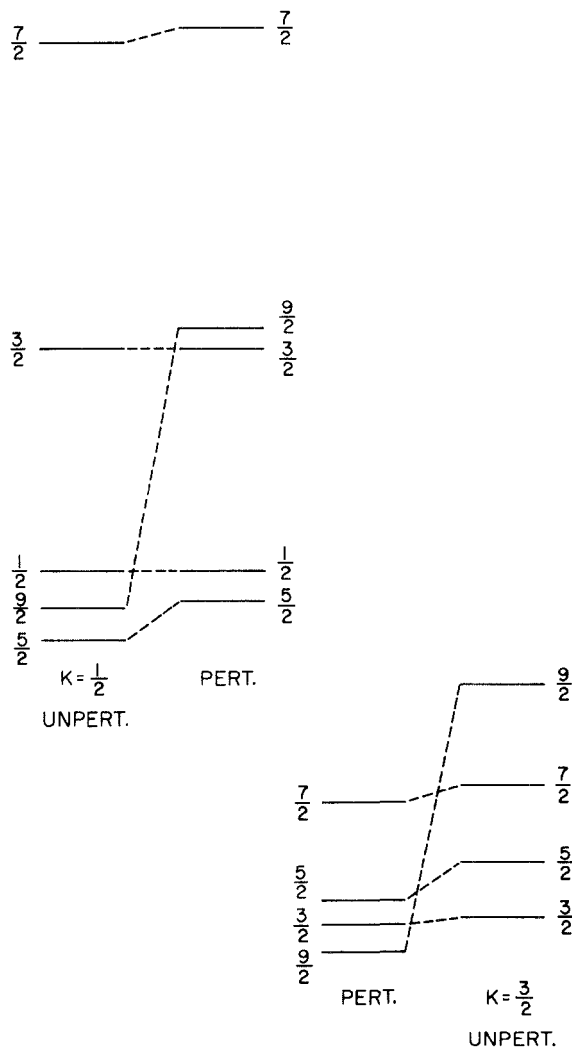


**Fig. 8.7.** Illustration of how the irregular rotational spacings in strongly decoupled  $K = 1/2$  bands can propagate to  $K \neq 1/2$  bands via Coriolis mixing.

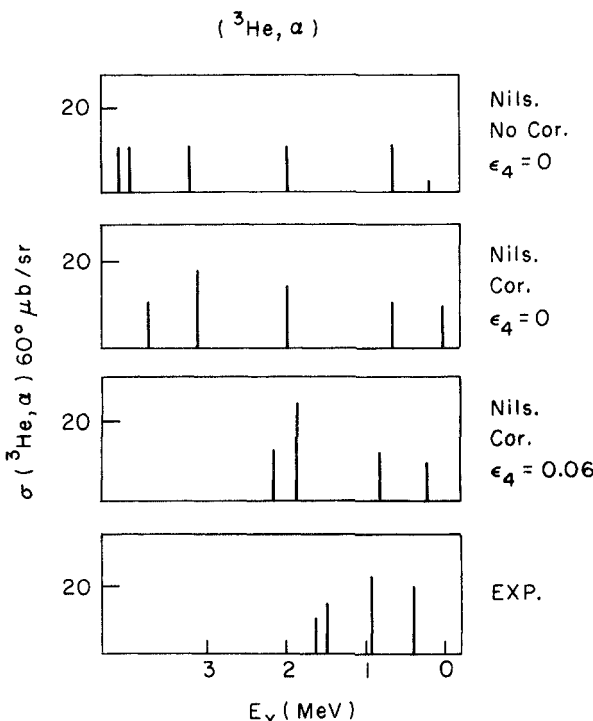


Fig. 8.8.  $(^3\text{He}, \alpha)$  cross sections for  $^{183}\text{W}$  (based on Kleinheinz, 1973).

Each mixes with the  $K + 1$  and  $K - 1$  member of the series. We thus have a situation analogous to one discussed in Chapter 1, in which equally spaced states each mix with adjacent levels. One general result is that lowest band will be pushed much lower. Moreover, given the increase of the Coriolis matrix elements with  $J$ , it will be severely compressed, and its wave functions will be a complex mixture of several components with all wave function components in phase.

The principle difference between this schematic situation and the real one arises because of the large decoupling parameter for the  $K = 1/2$  band. For  $N = 6$ , this has the effect of greatly lowering the  $13/2^+, 9/2^+, 5/2^+, 1/2^+$  states and raising the  $11/2^+, 7/2^+, 3/2^+, \dots$  states of that band prior to mixing. Consider now the effect of Coriolis mixing on the nearby  $K = 3/2$  band. The situation is illustrated in Fig. 8.7. The reordering of energies in the  $K = 1/2$  band because of the large diagonal Coriolis effect (decoupling parameter) causes the unperturbed spacings between the  $3/2, 7/2$ , and  $11/2$  states of the two bands to be much larger than between the  $5/2, 9/2$ , and  $13/2$  states. Therefore, in the lower-lying  $K = 3/2$  band, the  $5/2, 9/2, \dots$  group is shifted down substantially more than the  $3/2, 7/2, \dots$  group. The perturbed energies of the  $K = 3/2$  band take on an alternating pattern as well, relative to a pure  $J(J+1)$  rotational spacing, and appear as if the  $K = 3/2$  band had a decoupling parameter of the same sign and slightly smaller magnitude than the  $K = 1/2$  band. When the  $K = 3/2$  band in

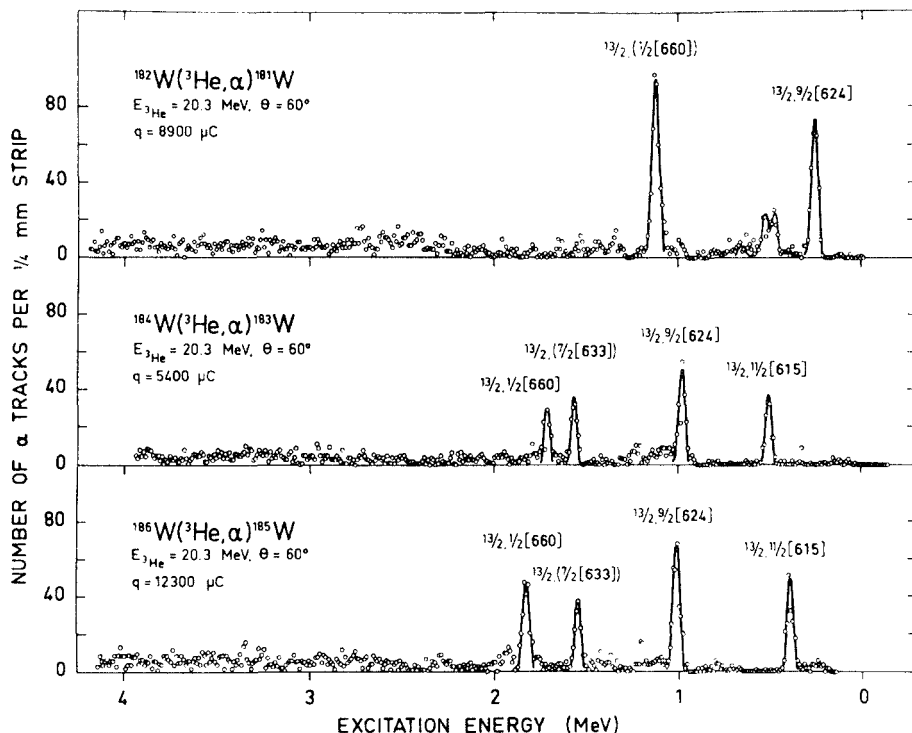


Fig. 8.9. ( $^3\text{He}, \alpha$ ) spectra in W isotopes (Kleinheinz, 1973).

turn mixes with the  $K = 5/2$  band, this "signature" is passed on in a somewhat reduced form. In effect, the Coriolis mixing "propagates" the decoupling parameter throughout the entire sequence of unique parity orbitals.

If the Fermi surface is below the  $K = 1/2$  orbit, the effect is reversed. The  $K = 1/2$  band lies *below* the  $K = 3/2$  band and therefore the closest lying pairs are the  $3/2$ ,  $7/2$ , and  $11/2$  states. Also the propagation is severely damped by the pairing factor as one goes from hole states to particle states. In the W isotopes that we have been considering, the Fermi surface is near the  $9/2^+[624]$  and  $11/2^+[615]$  orbits, and the effect of the  $K = 1/2$  band is negligible. (This is linked with a point we will make shortly, that strong diagonal Coriolis matrix elements are most effective in inducing a rotation aligned coupling scheme when the Fermi surface lies near the low  $K$  orbits.) In W, the primary observable mixing among the unique parity orbitals should be in the  $K = 5/2$ ,  $7/2$ ,  $9/2$ , and  $11/2$  orbits. As contrasted with the normal parity states, here the matrix elements and spacings are comparable and a two-state mixing calculation is hopelessly crude. The results for  $^{183}\text{W}$  of an explicit calculation of the single nucleon transfer strengths ( $C_{j=13/2}$  coefficients) to  $13/2^+$  states is shown in the top two panels of Fig. 8.8. Since the  $j$  matrix elements arise almost solely from the  $j = 13/2$  term in Eq. 8.6, and since the  $C_{j=13/2}$  coefficients all have the same sign, the phases of the resulting wave functions are such that in any two-

state mixing of these orbits, the cross section to the *lower* state is increased while that to the higher is decreased. This persists in the multistate extension, and the net effect is to transfer cross section from the higher-lying bands to the lower ones. This is the point alluded to in the schematic model at the beginning of this discussion. We now compare this calculation with the empirical situation.

In  $^{183}\text{W}$ , the lowest-lying unique parity orbit is  $11/2^+[615]$ . The  $9/2^+[624]$  and  $7/2^+[633]$  orbits are hole excitations. An ideal reaction to study these unique parity orbits is the ( $^3\text{He}, \alpha$ ) reaction, which preferentially excites higher-spin hole levels. In the rare earth region it can almost be used as a “ $J = 13/2^+$  meter.” Typical ( $^3\text{He}, \alpha$ ) spectra, for  $^{181-185}\text{W}$ , are shown in Fig. 8.9. Comparison with the ( $d, t$ ) reaction in Fig. 8.2 vividly illustrates the selectivity. In the absence of Coriolis mixing, the ( $^3\text{He}, \alpha$ ) reaction to  $13/2^+$  states in  $^{183}\text{W}$  should look like that shown schematically at the top of Fig. 8.8, in which there are five nearly equally strong peaks. (That for the  $K = 11/2^+$  is weaker than the others due to the smaller  $V^2$  factor and the peak from the  $13/2^+[606]$  orbit is absent since  $V \approx 0$ .) In contrast, the data show only four peaks but with the same total cross section expected for the six unperturbed states. This illustrates both the shifting and the descent of strength just discussed. (The empirical ( $^3\text{He}, \alpha$ ) spectrum (Fig. 8.9) for  $^{181}\text{W}$  shows this effect even more; only two peaks consume nearly all the  $13/2^+$  strength.) The bottom-most panel of Fig. 8.8 summarizes the empirical  $C_{j=13/2}$  coefficients in bar graph form for  $^{183}\text{W}$ .

The second panel of Fig. 8.8 includes Coriolis mixing, and is somewhat better than the unmixed calculations shown in the top panel. Further improvement requires, as we shall now see, the introduction of hexadecapole deformations. The study of such shape components offers us an ideal situation to apply the same kind of intuitive approach we used for the Nilsson model itself.

### Hexadecapole Deformations and Unique Parity States

Although quadrupole distortions dominate heavy nuclei, hexadecapole effects are not at all negligible and, as we shall see, frequently have major impact. It is by now well known that most heavy deformed nuclei have either positive or negative hexadecapole deformations superimposed on their quadrupole distortions. Figure 6.10 illustrated the effect of hexadecapole deformations on the nuclear shape for both signs of  $\epsilon_4$ . For  $\epsilon_4 > 0$ , the nucleus takes on a so-called pin cushion or barrel shape, while for  $\epsilon_4 < 0$ , it is “clover leafed.” Remarkably, we can now understand, without calculation, the origin of the shape components, their expected systematics, and their effects on Nilsson energies, on Coriolis mixing, and on single nucleon transfer cross sections. To illustrate the usefulness of this approach, we shall carry out the following discussion without any formal derivations. We will then compare our understanding with the results of actual calculations.

It is obvious that creating a positive ( $\epsilon_4 > 0$ ) hexadecapole shape requires the occupation of orbits situated at large radii relative to the bulk of the nuclear matter in orientations roughly  $45^\circ$  to the equatorial plane, so that the “corners” of the mass distributions will be filled in. In a given shell, the orbits

with the largest radii are the unique parity orbits since they stem from the next higher oscillator shell. From the relation  $\sin\theta \sim K/j$ , we see that  $\theta = 45^\circ$  corresponds to  $K/j \sim 0.7$ . For the  $i_{13/2}$  neutron orbit in the rare earth region, this gives  $K \sim 9/2$ . Thus, the largest contributions to an increasing positive hexadecapole deformation in this region occurs when the  $9/2^+$  [624] orbit is filling near the Fermi surface. Simple counting in the Nilsson scheme shows that this occurs around  $A \sim 180$ .

At the other extreme, analogous reasoning shows that negative  $\epsilon_4$  values are favored when very low or very high  $K i_{13/2}$  orbits are filling. The former occur near the beginning of the deformed region at neutron number  $N \sim 92$ . The latter occur near the end of the shell and serve to reduce the positive  $\epsilon_4$  values for  $A > 180$ . The expected  $\epsilon_4$  systematics should therefore consist of large negative values at the beginning of the deformed region that decrease in absolute value with mass, cross zero, turn positive, and maximize around the W isotopes, followed by a rather rapid decrease towards zero as the  $^{208}\text{Pb}$  closed shell is approached. This is *exactly* the systematics observed empirically, as shown in Fig. 8.10.

[A technical point is worth mentioning here. In this discussion, we have used  $\epsilon_4$  as the deformation parameter. Figure 8.10 is expressed in terms of  $\beta_4$ . In Nilsson's original paper, the principle discussion was carried out in terms of deformations  $\beta_2$  and  $\beta_4$ . The disadvantage of these parameters when discussing  $\Delta N = 2$  mixing and hexadecapole deformations is that, even for  $\beta_4 = 0$ , there will be finite  $\Delta N = 2$  mixing. In contrast, the  $\epsilon$  representation discussed in an appendix to Nilsson's original article, was *designed* so that  $\Delta N = 2$  mixing vanishes when  $\epsilon_4 = 0$ . The relation between  $\epsilon_2$ ,  $\epsilon_4$  and  $\beta_2$ ,  $\beta_4$  is complex and coupled. Either set of deformation parameters may be converted into the other by the use of Fig. 9 of the article by S. G. Nilsson et al (1969). However,

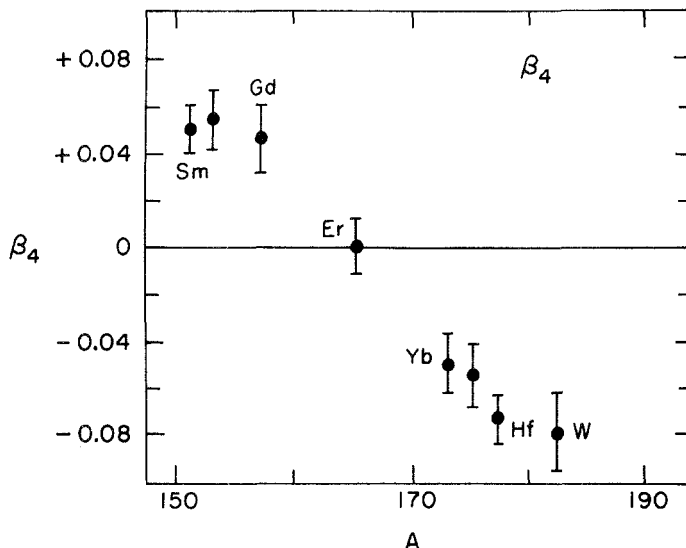


Fig. 8.10. Systematics of  $\beta_4$  in the rare earth nuclei.

one should note that there is a mistake in this figure and that its proper use requires the reversal in the sign of  $\epsilon_4$ . Very crudely,  $\epsilon_4 \sim -\beta_4$ .]

We can go one step further. Since the orbit inclination  $\theta$  changes slowly for low  $K$ , there will be more low-angled orbits ( $\theta < 45^\circ$ ) than orbits near  $45^\circ$ . Therefore, negative  $\epsilon_4$  deformations should predominate and the “crossing point” to positive values should occur past midshell. This is also seen in Fig. 8.10.

The principle effect of hexadecapole deformations on the Nilsson wave functions is to admix components with  $\Delta N = \pm 2$ . Thus, the  $N = 6 i_{13/2}$  Nilsson orbits will now contain some components from the  $N = 4, 8$  shells, and the  $N = 5$  normal parity orbits will contain contributions from  $N = 3, 7$ . Normally, this  $\Delta N = 2$  mixing is minuscule because of the large energy separation of oscillator shells. However, inspection of the characteristic form of the Nilsson diagram (downsloping early, upsloping late), shows that there are a few isolated regions where steeply downsloping unique parity orbits from one shell (e.g.,  $i_{13/2}$ ) intersect upsloping orbits from the next lower shell (here,  $N = 4$ ). If the nuclei in such regions have large  $\epsilon_4$ , then substantial  $\Delta N = 2$  mixing can occur. An example of such interacting orbits was discussed earlier in Chapter 7 in the context of a comment on the relative purity of the  $n_z$  quantum number at large deformations.

Thus far we have discussed the origin of hexadecapole deformations, their systematics, and their relatively minor effects on Nilsson wave functions. It remains to discuss their enormous impact on Coriolis mixing and single nucleon transfer cross sections. This impact arises mostly from the effect of  $\epsilon_4$  on Nilsson energies of orbits that can Coriolis mix. It is easy to see what the main effects will be. Consider, for example, a large positive  $\epsilon_4$  and the  $i_{13/2}$  orbits. It is obvious that both equatorial ( $K = 1/2, 3/2, 5/2$ ) and polar ( $K = 13/2$  and perhaps  $11/2$ ) orbits will be, on average, further from the nuclear matter than for  $\epsilon_4 = 0$ , and therefore their energies will increase. The mid- $K$  orbits ( $K = 7/2, 9/2$ ) will be closer to the nuclear matter and their energies will decrease. Hence the overall effect will be a *compression* of the energy separations from  $K = 1/2$  to  $7/2$  or  $9/2$ . Moreover, this compression will become more extreme as  $\epsilon_4$  increases. In fact one can imagine sufficiently large  $\epsilon_4$  values that some of these  $K$  orbits may actually cross and interchange their relative positions. Figure 8.11 shows an explicit calculation of the  $i_{13/2}$  energies for fixed  $\epsilon_2$  as a function of  $\epsilon_4$ . All these features appear. There is a compression, and even a crossing, near  $\epsilon_4 \sim 0.1$ . The envelop of the energies can easily be compressed by a factor of two and, therefore, the already large Coriolis mixing among the unique parity orbits will increase still further (the Coriolis matrix elements themselves will not substantially change).

Recall from our discussion of cross sections to  $13^+/2$  states in the W isotopes that Coriolis mixing calculations produce some improvement in the predictions, but that significant discrepancies remain. The mixing casts some cross section from higher lying levels into the lower ones. With the increased Coriolis mixing that now occurs with a large positive  $\epsilon_4$ , this effect will be exaggerated, as shown in the third panel in Fig. 8.8, where we see much better agreement with the empirical cross sections.

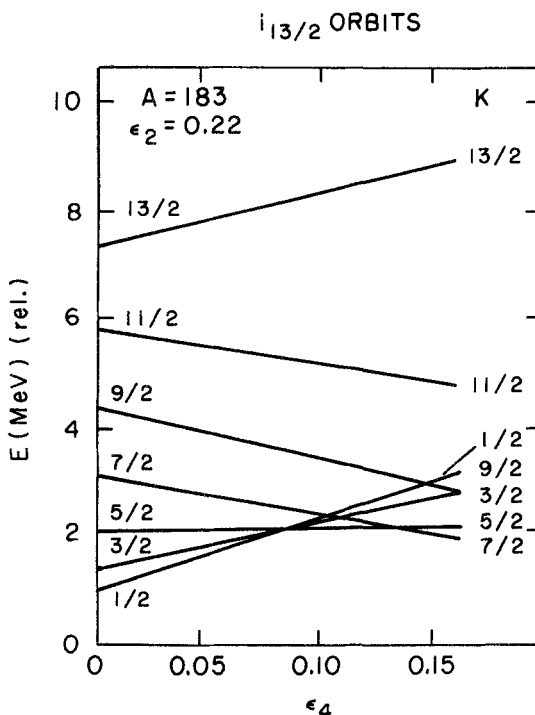


**Fig. 8.11.** Effect of hexadecapole deformations on  $i_{13/2}$  Nilsson energies.

One of the beauties of the Nilsson model is its easy extendibility. We see here an excellent example where the basic model predictions are in strong disagreement with the data but where simple and physically reasonable refinements easily remove most of the discrepancies, and thereby show both the usefulness of the model as a starting point and also the absolutely crucial need to incorporate certain of these extensions. The particular case we have been considering is historically interesting as well: the large changes in  $i_{13/2}$  energies, Coriolis mixing, and  $(^3\text{He}, \alpha)$  cross sections as  $\epsilon_4$  varies from 0 to 0.06 provided the first definitive evidence for large hexadecapole deformations in the odd W isotopes. Another interesting point is that while  $\epsilon_4$  values of zero and 0.06 can be easily distinguished in this way, the approximate constancy of the envelope of  $K = 1/2$  to  $7/2$  orbits from  $\epsilon_4 = 0.06$ –0.16 precludes a further refinement in the actual  $\epsilon_4$  values.

There is one other consequence of large hexadecapole deformations that should be mentioned. We have been discussing permanent or static hexadecapole shape components. However, it is also possible that the nuclear potential energy surface may be “soft” in  $\epsilon_4$ , and that this will lead to hexadecapole vibrations, just as softness in  $\beta$  and  $\gamma$  leads to  $\beta$  and  $\gamma$  vibrations. It is not surprising that the heavy even-even rare earth nuclei, especially the Os isotopes, display rather low-lying ( $\sim 1$  MeV)  $K = 4$  bands that have been interpreted in terms of hexadecapole vibrations by Baker and co-workers. Of

course, such  $K = 4$  intrinsic excitations can also be thought of as double  $\gamma$  vibrations: the particular states in the Os isotopes appear to be mixtures of both modes, and interestingly, their  $\gamma$  decay seems to pick up the two-phonon character while their single nucleon transfer cross sections reveal the hexadecapole aspect. This is a nice illustration of how a complementarity of experimental approaches can highlight different features of nuclear excitations.

#### 8.4 Coriolis Effects at Higher Spins

Our rather brief treatment of the unique parity orbits does not even begin to hint at their importance in modern nuclear structure physics, especially at high spin. Indeed, the unique parity states are the most thoroughly studied of high-spin levels and are nearly always used as the first testing ground for new theoretical ideas. Some of the reasons for this should be obvious from the preceding discussion. Primary is the purity of the unique parity states in  $j$ , resulting from the shell model spin orbit interaction that separates them from other levels of the same parity by nearly the distance between major shells. Their properties can be calculated with extremely high reliability and more simply than most other states. Second, since Coriolis effects are crucial to most of the physics at high spins, the fact that these states form an isolated but strongly admixed set enhances the ease with which one may spot the influence of extra degrees of freedom. Colloquially speaking, these states “close under the Coriolis interaction.”

Another key feature of the unique parity states is that Coriolis effects are largest amongst the low  $K$  orbitals, both because the matrix elements are themselves slightly larger and also because the energy separations are smallest. Noting that these are precisely the orbits whose angular momenta are aligned most nearly parallel to the nuclear rotation axis (their orbital motion is most nearly equatorial), we have three factors contributing to the development of the so-called rotation aligned scheme to which we have alluded and to which we now turn.

##### Rotation aligned coupling

This coupling scheme, illustrated in Fig. 8.12, was originally introduced to account for apparently anomalous rotational spacings in certain orbits in odd mass nuclei (see extreme right in Fig. 7.8). Figure 8.12 shows angular momentum diagrams for the cases of large and small  $K$ . We assume for simplicity that the Nilsson wave functions can be approximated by a single  $j$  value. We can write the total Hamiltonian as  $\mathbf{H} = \mathbf{H}_{\text{Nil}} + \mathbf{H}_{\text{rot}}$ . The Nilsson energy of a single nucleon can be represented by  $\mathbf{H}_{\text{Nil}} = \epsilon_j + \Delta E(jK)$  where the  $\epsilon_j$  are the spherical single particle energies and the  $\Delta E$  are the shifts due to the deformed potential. Writing Eq. 7.8 for  $\Delta E(jK)$  as a constant plus a  $K$ -dependent term, we have  $E_{\text{Nil}} \approx \epsilon_j + \text{const} + C\delta K^2$ , and hence (neglecting the constant term)

$$\begin{aligned} H &= \epsilon_j + \frac{\hbar^2}{2I} [J(J+1) - 2K^2 + \langle \mathbf{j}^2 \rangle] + \mathbf{V}_{\text{Cor}} + C\delta K^2 \\ &= \epsilon_j + \frac{\hbar^2}{2I} [J(J+1) + j(j+1)] + \left( C\delta - \frac{2\hbar^2}{2I} \right) K^2 + \mathbf{V}_{\text{Cor}} \end{aligned} \quad (8.13)$$

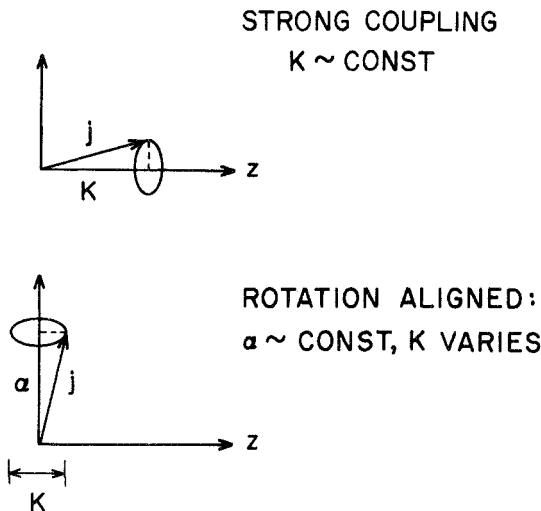


**Fig. 8.12.** Diagram for strong coupling and rotation aligned or decoupled level schemes (based on Stephens, 1975).

This is the Nilsson energy of the odd particle plus the total rotational energy. At the top of Fig. 8.12  $K$  is large and the  $K^2$  term dominates the  $\mathbf{V}_{\text{Cor}}$  term. Since the coefficient of  $K^2$  is linear in  $\delta$  and since the inertial parameter,  $\hbar^2/2I$ , decreases with increasing deformation, this is a situation that is valid for large deformation and/or large  $K$ . The dominance of the  $K^2$  term implies that  $K$  is a good quantum number (the  $K$  mixing terms are relatively small) and one has the so-called deformation aligned or strong coupling scheme we have been discussing. Coriolis mixing effects are a small (but important) perturbation that causes the angle of the vector  $j$  to “wobble” slightly as it precesses about the  $z$  axis.

However, there are situations in which this coupling scheme does not occur. An obvious one is for high spins for which  $\mathbf{V}_{\text{Cor}} \propto J$ ; when this term dominates the  $K^2$  term, the solutions must be approximate eigenfunctions of  $\mathbf{V}_{\text{Cor}}$  that correspond to a new coupling scheme in which  $K$  specifically is *not* a good quantum number. One then has the situation illustrated in the lower part of Fig. 8.12, where the particle angular momentum vector,  $j$ , precesses about an axis perpendicular to the symmetry axis (i.e., about the rotation axis). Clearly,  $K$  will vary significantly and include negative values. It is now the alignment along the rotation axis, commonly called  $\alpha$ , that is the good projection quantum number. This coupling scheme will be realized when

$$\left( C \delta - \frac{2\hbar^2}{2I} \right) K^2 \ll \mathbf{V}_{\text{Cor}} \quad (8.14)$$

that is, especially for low  $K$  values. This is physically plausible since  $j$  already points nearly along the rotation axis. Clearly, if  $K$  is large, an enormous Coriolis interaction (extremely high  $J$  values) would be required to enforce precession about the rotation axis, whereas for low  $K$ , such precession can

occur at relatively low spins. Inspection of Eq. 8.14 shows that the rotation aligned scheme can also be realized for low  $J$  if the coefficient of  $K^2$  vanishes. Since  $\hbar^2/2I \sim 1/\delta$ , it is clearly possible to choose a  $\delta$  value that satisfies this cancellation requirement. For the  $A \approx 130$  region, numerical estimates give  $\delta \approx 0.17$  ( $\beta \approx 0.18$ ). This is a rather moderate deformation and accounts for the fact that the rotation aligned scheme often manifests itself in transitional, moderately deformed prolate nuclei early in a shell (where the low  $K$  orbits are filling). For larger deformations, the inertial parameter  $\hbar^2/2I$  drops rapidly while the Nilsson energies further split and the Coriolis effects decrease below a critical value. In most well-deformed nuclei we see normal (strongly coupled) rotational behavior.

The energies in the rotation aligned scheme are very easy to visualize. The total angular momentum points essentially along the rotation axis and is composed of the particle angular momentum  $\mathbf{j}$  plus a core rotation  $\mathbf{R}$ . Thus, from Eq. 8.13

$$E_{\text{rot}}(J) \approx \frac{2\hbar^2}{2I} [J(J+1) + j(j+1) + \mathbf{V}_{\text{Cor}}]$$

For high spin unique parity states, low  $K$  values and moderate deformations,  $J, j \gg K$  and  $j$  is nearly a good quantum number. Moreover, in the rotation aligned scheme,  $|j| \approx |\alpha|$ . Therefore, using Eq. 8.7 and neglecting terms independent of  $J$ , we have

$$E_{\text{rot}}(J) \approx \frac{2\hbar^2}{2I} [J(J+1) - 2J\alpha] = \frac{2\hbar^2}{2I} [(J-\alpha)(J-\alpha+1) - \alpha^2] \quad (8.15)$$

This equation is simply that for a rotor of spin  $(J-a)$ . But  $|(J-a)| \approx |R|$ , the *core* rotational angular momentum! So the energies do *not* behave like those of a rotor with spin  $J$ , but rather like those of the *rotational core*. Moreover, the lowest energies occur for the highest alignments,  $\alpha$ . The reader may recall that when we derived Eq. 7.17, we set the problem up as the solution to why rotational bands were not upside down, and why for example, the core angular momenta  $R$  were not 0, 2, 4... for states with  $J = 13/2$  and  $(9/2, 17/2), (5/2, 21/2), \dots$ , respectively. The solution involved recognizing the *variation* of  $|R|$  values that occurs when the particle angular momentum vector precesses around the symmetry axis. We alluded to the possibility that rotational bands with core rotational spacings did indeed exist in certain circumstances. We now see those circumstances—when the precession is no longer about the symmetry axis but rather about the rotation axis—so that  $R$  is nearly a constant of the motion.

To understand the implications of Eq. 8.15, let us take as an example a situation of maximum alignment for the rare earth nuclei where the unique parity orbit has  $j = 13/2$ . We take  $\alpha = 13/2$ . The energy difference  $E_{17/2} - E_{13/2}$  is given by the energy difference between  $R = 2$  and  $R = 0$ , that is, by the energy of the first  $2^+$  state in the even-even core nucleus or  $6(\hbar^2/2I)$ . This is completely different from the strongly coupled case in which  $E_{17/2} - E_{13/2} = \hbar^2/2I [17/2(19/2) - 13/2(15/2)] = 64 (\hbar^2/2I)$ . This difference is enormous, as is the energy saving if the rotation aligned scheme is applicable. It was precisely

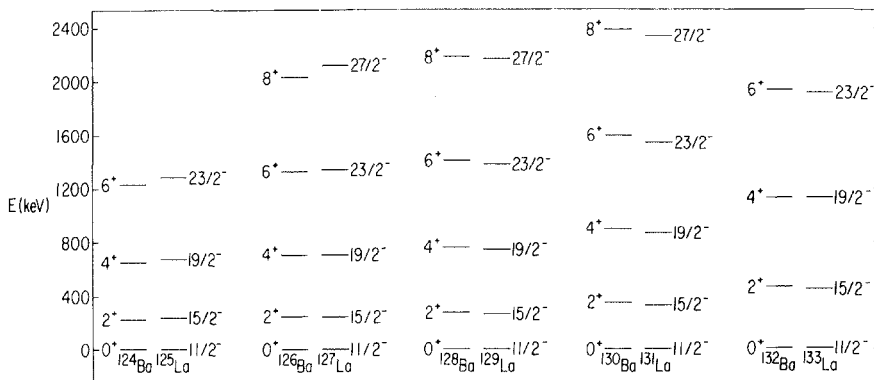


**Fig. 8.13.** Comparison of rotational spacings in Ba and La nuclei. This is the classic example of decoupled band structure (based on Stephens, 1975).

the observation of such spin and energy sequences in moderately deformed odd mass nuclei, such as the La isotopes, with energy spacings nearly *identical* to those of the adjacent even-even Ba nuclei, that inspired the development of the rotation aligned scheme. The remarkable La–Ba comparison is shown in Fig. 8.13. The similarity of spacings in the odd and even mass nuclei is striking, extending even to the way they track with neutron number.

The sequence of  $R = 0, 2, 4, 6, \dots$  values leads in turn to low-lying rotational states that differ in spin by two units (the alternate spin states are higher in energy). This is another difference from the strongly coupled case of “normal” rotational sequences  $J = K, K + 1, K + 2, K + 3, \dots$

Note that it is also possible for  $\mathbf{R}$  and  $\mathbf{j}$  to be *antialigned*, producing total spin values  $J < j$ . Thus, the state with  $J = 9/2$  also corresponds to a core angular momentum  $R = 2$  and will have an identical energy to that for the  $J = 17/2$  level. Since the energies follow an  $R(R+1)$  rule, and since states with spins  $J = j \pm R$  have identical energies, it follows that a plot of  $E(J)$  vs.  $J$  will be a parabola whose minimum is at or near  $J = j$ . It is possible, of course, that the alignment along the rotation axis does not attain its maximum value. For example, if  $\alpha = 11/2$ , one can still apply Eq. 8.15. In this case the lowest aligned state, with  $R = 0$ , will have  $J = 11/2$ . States with  $J = 7/2$  and  $J = 15/2$  will occur higher with  $R = 2$ . This sequence of states also forms a parabola, but one lying slightly higher than for the case of maximum alignment. Continuing this process, sequences of parabolas will occur: each succeeding one corresponds to the next lower  $\alpha$  value. The states along the lowest parabola are called the *favored* states and may be either *favored aligned* or *favored antialigned*. Those on the higher parabolas are called *unfavored* states and may also be aligned or antialigned.

In a sense, this picture resembles that of a weak coupling model. There is, however, a qualitative difference. If the coupling of a particle with angular momentum  $\mathbf{j}$  to a core state  $\mathbf{R}$  is weak, all states with  $(j - R) \leq J \leq (j + R)$  will form a nearly degenerate multiplet since  $\mathbf{j}$  and  $\mathbf{R}$  can have any relative orientations. Here, however, only the energies of the favored states approxi-

mate those of a weak coupling model. The other, unfavored states are pushed considerably higher.

Of course the exact solution for the rotation aligned scheme can be obtained by explicit diagonalization of the Nilsson particle-plus-rotor Hamiltonian. An example taken from Stephens is shown in Fig. 8.14, for the case where the unique parity orbit is the  $h_{11/2}$  and the Fermi surface is below the  $K = 1/2$  orbit. (Note that in all of the preceding discussion of the  $i_{13/2}$  orbits, the only relevant property of the unique parity orbits was the purity in  $j$ , and therefore nearly identical effects result for any other unique parity orbits simply by substituting a different  $j$ . For example, if the unique parity orbit is  $h_{11/2}$  rather than  $i_{13/2}$ , the lowest spin state will be  $J = 11/2$  and the favored aligned states will have spins  $J = 11/2, 15/2, 19/2, \dots$ . This makes for a very generally applicable scheme with close correlations from mass region to mass region.) In Fig. 8.14, the favored aligned states are given by the thick lines, the others as thin lines. The characteristic feature of the decoupled band emerges clearly on the prolate side, whereas on the oblate side, the Fermi surface is near the high  $K$  orbits, so the lowest states form a normal strongly coupled band. For the rotation aligned scheme, the favored aligned energies remain remarkably close to those of the core energies (which can be seen at  $\beta = 0$ ) even out to relatively large deformations.

This brief summary of rotational alignment shows that it can be a rather widely applicable phenomenon, occurring especially in moderately deformed nuclei, where Coriolis effects are strong and deformation effects still rather weak, whenever the Fermi surface is near the low  $K$  unique parity Nilsson orbits. The rotation aligned scheme relies on the notion that it is energetically

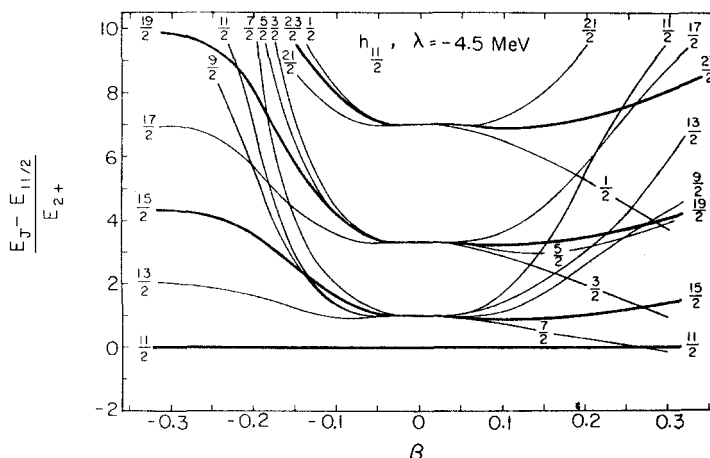


**Fig. 8.14.** Behavior of particle-rotor level energies with  $\beta$  for unique parity levels including Coriolis mixing. The Fermi surface is below the entire  $h_{11/2}$  set of orbits. Note the strongly coupled pattern ( $\Delta J = 1, J(J+1)$  spacings) on the left and the decoupled pattern ( $\Delta J = 2, E_{\min}$  for  $J = 11/2$ , compressed (core) rotational spacings) on the right (Stephens, 1975).

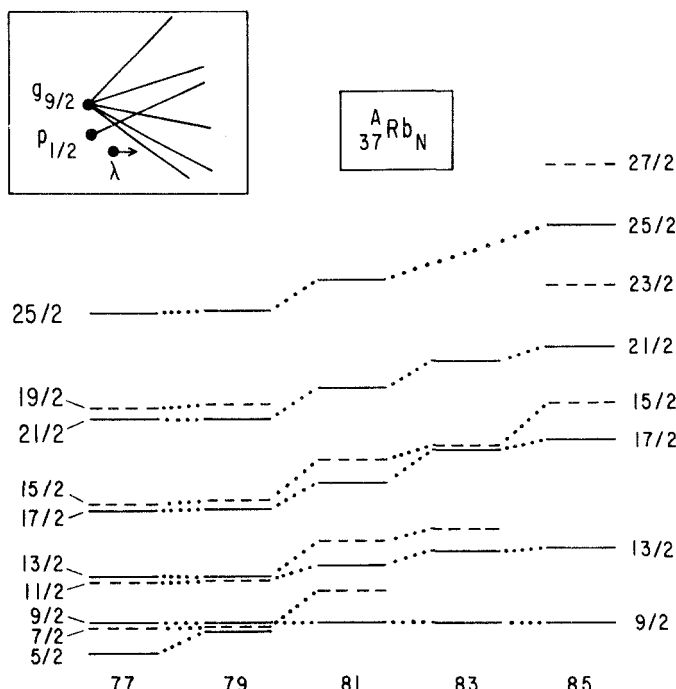


**Fig. 8.15.** Empirical proton unique parity ( $\pi = +, g_{9/2}$ ) levels of odd mass Rb isotopes. The isotopes span a strongly coupled (deformed) toward decoupled (weakly deformed) transition. The inset indicates the proton orbits and the movement of the proton Fermi surface (with *decreasing*  $N$ ). Solid levels are favored states (dashed are unfavored) in the rotational aligned picture (based on Tabor, 1989).

easier to achieve a given spin by combining a particle angular momentum aligned nearly along the rotation axis with a small amount of core rotation than it is to couple a particle angular momentum aligned elsewhere with a large core rotation.

If we inspect a sequence of nuclei, it is possible to observe smooth transitions from rotation aligned behavior when the Fermi surface is near the low  $K$  unique parity orbits early in a shell (moderate deformation) to strongly coupled as the Fermi surface rises. The odd  $Z$  Rb isotopes, shown in Fig. 8.15, provide a nice example. The low  $N$  isotopes are reasonably well deformed: a transition toward smaller deformations takes place as  $N$  increases. The proton Fermi surface is just below the entire  $g_{9/2}$  unique parity shell. Near  $^{85}\text{Rb}$ , a fine decoupled structure exists: the low-lying levels form a  $\Delta J = 2$  sequence, starting at  $J = 9/2$ , that is, a fully aligned ( $\alpha = 9/2$ ) configuration. The alternate spins are shifted quite high. (Incidentally, in modern parlance this splitting of favored and unfavored states is known as “signature splitting”.) As  $N$  decreases, the deformation increases, simultaneously reducing the Coriolis strength among the  $g_{9/2}$  proton orbits and lowering the  $K = 1/2, 3/2$  orbit energies so that the Fermi energy moves into this group (see inset): a transition to a strongly

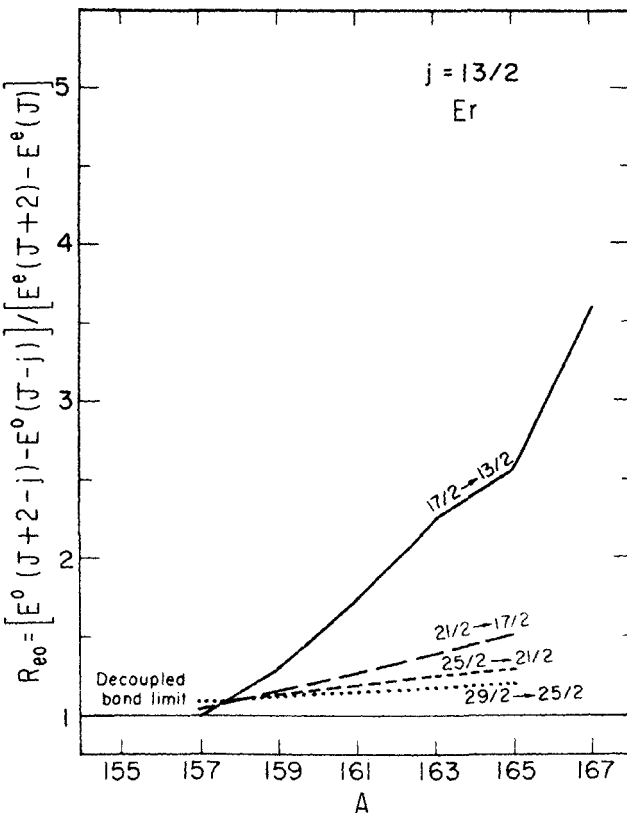


**Fig. 8.16.** Plot of  $R_{eo}$  (see text) against  $A$  for several energy differences in the Er nuclei (based on Stephens, 1975).

coupled scheme ensues. By  $^{77}\text{Rb}$ , a nearly monotonic  $\Delta J = 1$  sequence appears although a fully developed rotational pattern has yet to emerge.

Another beautiful example of such a transition from a decoupled toward a strongly coupled scheme occurs in the neutron deficient, near-stable Er isotopes. Stephens displays this transition in a way that highlights a couple of important points. Consider a state of spin  $J$  in an odd mass nucleus. If the state is fully aligned ( $\alpha = j$ ), then the core rotational angular momentum  $|R| = |J - j|$  and the energy difference in the odd mass nucleus  $E(J) - E(j) = (\hbar^2/2I)|J - j|^2 = E_{eo}(|J - j|)$  of the neighboring even-even nuclei. If the strongly coupled limit applies, these rotational energy differences in the odd mass nucleus will be much larger than those in the even-even nucleus for states with  $J > j$ :  $E(J) - E(j) = (\hbar^2/2I)[J(J + 1) - j(j + 1)]$ . Figure 8.16 shows the data for the lowest band based on the  $i_{13/2}$  orbital in the odd mass Er isotopes. The ordinate is the ratio  $R_{eo}$  of the energy difference  $E^o(J + 2) - E^o(j)$  of two states in each odd mass nucleus divided by the energy difference  $E^e(J + 2 - j) - E^e(J - j)$  taken from the data for the neighboring even-even nucleus. If the

odd mass nucleus has full rotation alignment ( $\alpha = 13/2$ ), then  $R_{eo} \approx 1$  independent of spin.

If the rotational band in the odd mass nucleus is strongly coupled, the larger spacings will lead to  $R_{eo} \gg 1$ . Empirically, near  $^{157}\text{Er}$   $R_{eo} \approx 1$ , but a clear transition toward a strongly coupled limit is observed with increasing neutron number. This is caused both by an increase in deformation, which reduces the strength of the Coriolis interaction ( $V_{cor} \propto \hbar^2/2I$ ), and by an increase in the Fermi surface from near the low  $K$  unique parity orbits toward the mid- $K$  orbits. In addition, we note that the transition proceeds much more slowly for higher spins. The energy spacing  $E_{29/2} - E_{25/2}$  remains very close to the rotation aligned limit. This is simply because, as we have noted several times, the Coriolis interaction increases with  $J$  for high spin states and therefore the rotation aligned coupling scheme persists longer.

One last point, of some interest in terms of testing this picture of rotation alignment and favored and unfavored states, concerns the relative role of high- and low-spin levels. The entire picture described so far assumes a simple axially symmetric rotational core and its coupling to the odd particle motion. It entirely neglects any effects due to rotation-vibration coupling, axially asymmetry, mixing with quasi-particle states, and so on. If one considers the rather general situation of a fixed number of valence nucleons spanning a specific set of single-particle states it is clear that, while there are many ways of constructing low and intermediate spin states from different combinations of the single-particle angular momenta, there is only one way of constructing the highest spin level—by aligning all these individual particle angular momenta along the same direction in space. Therefore, *any* model for this highest spin state has the same structure, independent of the assumptions of the model. For other high-spin (but not the highest-spin) states there will, in general, be only a few ways of constructing them and different models may present somewhat different, but mostly likely not very different, predictions. For low-spin states, however, different models with different interactions may have entirely different effects on specific subsets of states. Their energies and structure may differ markedly from one model to another. Although the beauty of and evidence for rotation aligned behavior is most dramatic in the high-spin states, perhaps the most sensitive tests of such models occur in the low-spin, unfavored, antialigned levels. Study of such levels may provide evidence for other degrees of freedom of some importance.

We should briefly apply our understanding of Coriolis effects to even-even nuclei. This will provide a simple understanding of the widespread phenomena of backbending. Consider a specific two-quasi-particle state with both particles in a low  $K$  unique parity orbit paired to  $J^\pi = 0^+$  and with the Fermi surface below all the unique parity orbits. Neglect for a moment the interaction between the two particles. Since the particles are in the lowest unique parity orbits, their energies are greatly lowered due to the strong Coriolis interaction with particles in higher  $K$  orbits. This is analogous to the situation discussed in Chapter 1 of a set of equally spaced states with equal matrix elements connecting adjacent levels. The lowest level is pushed down and becomes a collective (strongly admixed) combination of amplitudes. From the

size of the unique parity Coriolis mixing matrix elements, we have seen that this energy lowering can be substantial. The tendency will be for each particle to align its angular momentum with the rotation axis. Since the Coriolis interaction grows with spin, it may well be that at some  $J$  value it becomes energetically favorable to form a state, not from a core angular momentum

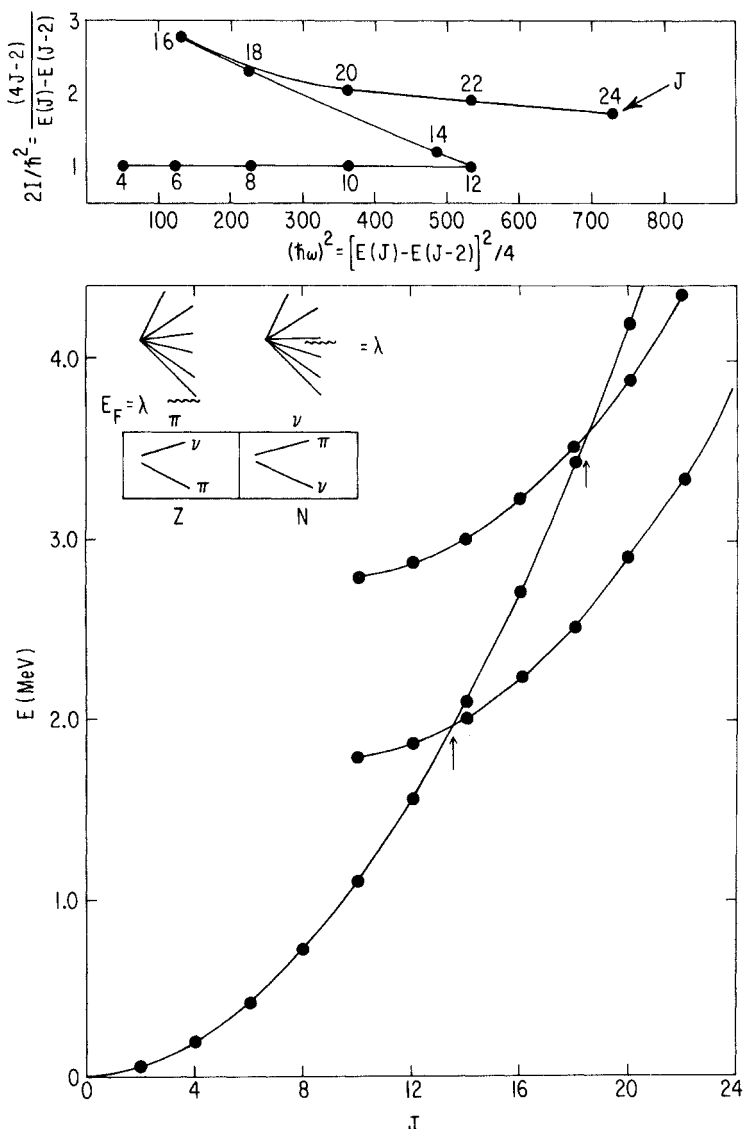


**Fig. 8.17.** Illustration of the idea of crossing bands and frequencies in a plot of  $E(J)$  against  $J$  (lower part) leading to the backbending phenomenon (top). The insets give an example, appropriate to the Ce region, of how one can understand the systematics of proton ( $\pi$ ) and neutron ( $\nu$ ) crossing frequencies (sketched in the small boxes) against  $Z$  and  $N$  (based on Wyss, 1989).

$R = J$  superimposed on a spin  $0^+$  pairing condensate, but rather by breaking the pair of particles in a high  $j$  orbit so that their spins couple to  $(2j - 1)$  ( $2j$  is forbidden by the Pauli principle) and coupling this angular momentum nearly parallel to a much lower core rotational angular momentum of  $R \approx J - (2j - 1)$ . The lower energy required because of the lower expenditure of core rotational energy more than compensates for the energy lost in breaking the pair of particles.

In such a case, a plot of the yrast energies against  $J$  will increase parabolically until this transition or critical angular momentum ( $J_{\text{crit}}$ ), where the sudden drop in required  $R$  values leads to a smaller energy jump to the next higher angular momentum. This is illustrated in Fig. 8.17 (lower), where  $J_{\text{crit}} = 14$ . The figure also shows the continuation of the “decoupled pair” band below the critical angular momentum. That is, the configuration in which the angular momenta of the two particles are aligned nearly along the rotation axis also exists below spin  $J$ : it is just not yrast. The “crossing” spin is simply that point where this rotation aligned band begins to be favored energetically. This spin depends on the deformation and the location of the Fermi surface relative to the low  $K$  unique parity orbits. It therefore varies with  $N$  or  $Z$ .

Despite the radically altered structure at  $J_{\text{crit}}$ , the deviation from  $J(J + 1)$  behavior is often difficult to detect in this kind of plot. A more convenient presentation has become standard, which is to plot the inverse of the inertial parameter,  $2I/\hbar^2$ , defined for each particular spin as we will describe shortly, against a quantity proportional to the square of the energy difference between adjacent rotational energy states. In an ideal rotational band,  $E(J) - E(J - 2) = (\hbar^2/2I) [J(J + 1) - (J - 2)(J - 1)] = \hbar^2/2I (4J - 2)$ . Thus the quantity  $(4J - 2)/(E(J) - E(J - 2))$  should be constant. If the moment of inertia increases slightly with  $J$ , due, for example, to centrifugal stretching effects, then  $2I/\hbar^2$  may increase gradually with  $J$  but, in any case,  $2I/\hbar^2$  is empirically defined as  $(4J - 2)/(E(J) - E(J - 2))$ . One then plots  $2I/\hbar^2$  against the abscissa  $(E(J) - E(J - 2))^2/4$ , which is 1/4 the square of the energy difference between these two levels and is called  $(\hbar\omega)^2$ . (When plots like this are done for an odd mass nucleus,  $J$  is redefined as  $J - j$ , where  $j$  is the spin of the unique parity orbit and is taken to be a good quantum number.)

Note that both ordinate and abscissa in such a plot are trivially obtained (without ever knowing the actual excitation energies) simply from the observed  $\gamma$ -ray transition energies between adjacent rotational levels. At low spins, each successive transition energy increases and  $2I/\hbar^2$  is more or less constant (ideal rotational behavior) or slightly increasing. This gives a horizontal or slightly rising line. At the crossing point, as is evident from Fig. 8.17, the level energy increases by a smaller amount than would have been expected; that is, the transition energy  $(\hbar\omega)$  increases less than expected, or may decrease, while  $2I/\hbar^2 \propto 1/(E(J) - E(J - 2))$  increases. A plot of  $2I/\hbar^2$  against  $(\hbar\omega)^2$  will exhibit an upbend or perhaps a backbend at the crossing frequency. After this spin, a normal rotational pattern, but with much lower  $R$  values and hence smaller spacings, is re-established with a different “scale factor”  $2I/\hbar^2$ . The upper part of Fig. 8.17 shows such a “backbending” plot for the yrast states (first crossing

only), and aptly reflects the origin of the name backbending. The smaller energy spacing between the  $J = 12$  and  $J = 14$  states in the lower part becomes the sharp backbend in the upper part. The concept of crossing frequency now replaces that of  $J_{\text{crit}}$ .

One can view the reason for the upbend or backbend in two equivalent ways, both based on the rotational energy expression  $(\hbar^2/2I) R(R+1)$ . In one, the  $R$  values are effectively lower, as we have described. This is the view in terms of a new aligned coupling scheme in which  $R$  suddenly decreases to take advantage of the angular momentum gained from the aligned particle. The other view is phrased directly in terms of Coriolis coupling in that the coupling causes a substantial lowering of the states of the two-quasi-particle aligned band. This lowering is larger for higher spins so that, at some spin, they cross the "normal" levels. (Of course, there can be other origins for backbending behavior, such as shape changes of nucleus as a whole: we do not discuss these here.)

In a realistic situation, there will be an interaction between the ground band and the decoupled band near the critical or crossing frequency. Just below  $J_{\text{crit}}$ , the decoupled band is higher. Its interaction with a ground band will lower the energies of the latter, effectively increasing  $2I/\hbar^2$ , while simultaneously reducing the transition energies. This causes a slight upbend for  $J < J_{\text{crit}}$ ; mixing smooths out the sharply angled ideal pattern. The net effect is to lead to an S shaped curve where the sharpness of the backbending or upbending depends on the strength of the interaction between the two bands.

The data for many nuclei have now been accumulated and backbending is a widespread phenomenon. As expected, it is typically observed when the Fermi surface is near the low  $K$  orbits of the unique parity orbit. It tends to disappear with increasing mass for a given sequence of isotopes as the Fermi surface rises toward the higher  $K$  orbits.

How this works in practice can be illustrated by the example in Fig. 8.17. The lower part, discussed earlier, shows a normal plot of  $E(J)$  vs.  $J$  and depicts two crossings occurring at different  $E, J$  and crossing frequencies ( $\hbar\omega$ ). The insets show typical Nilsson diagrams for proton and neutron unique parity orbits and indicate where the Fermi energies ( $E_F$ ) are in this example. We can now understand the expected systematics of backbending in this region. As  $Z$  increases,  $E_F^\pi$  (proton Fermi energy) increases. Moreover, the deformation  $\beta$  increases as deformation driving orbits are filled. For both reasons, the energy required to occupy the low  $K$  unique parity orbits decreases. Hence, the proton crossing (labeled  $\pi$  in the inset) occurs at lower energy and angular momentum and hence lower  $\hbar\omega$ . As  $N$  increases, the deformation decreases as polar orbits are encountered. Hence the *proton* crossing frequency increases with  $N$  as the energies of the proton unique parity orbits rise. The *neutron* crossing frequencies have an opposite behavior. They decrease with increasing  $N$  (decreasing  $\beta$ ) since the energy separation to the low  $K$  orbits decreases, but increase with  $Z$  because the deformation increases. These ideas are sketched in the figure as crossing frequencies for protons and neutrons. While the arguments are qualitative, they are borne out both experimentally and theo-

retically in a cranked shell model calculation in a region such as the neutron deficient Xe–Ba–Ce nuclei, to which this example applies.

There is no reason why there should not be backbending in odd nuclei, and this has indeed been observed. Again, the study of such states has become a major “industry” in itself and cannot be described in any detail here. There is one particular point deserving mention, however: the use of backbending studies in odd mass nuclei to identify the nature of the *specific* particles producing the backbend in the neighboring even–even nuclei. So far, we have made little mention of whether or not the unique parity orbits involved are the proton or neutron orbits. In the rare earth region, backbending can be caused, for example, either by aligning two protons in an  $h_{11/2}$  orbit or two neutrons in an  $i_{13/2}$  orbit. It is difficult to distinguish these two from the backbending plot in the even nucleus itself. However, the odd nucleus can be used to resolve this ambiguity with the technique known as *odd particle blocking*. The basic idea is extremely simple. Consider an even–even nucleus in which the backbending is caused by alignment of two *neutron* quasi-particles in a specific low  $K$  unique parity orbit. Now consider the rotational states in the neighboring odd proton nucleus where the odd *proton* is in a low  $K$  unique parity orbit. As the spin

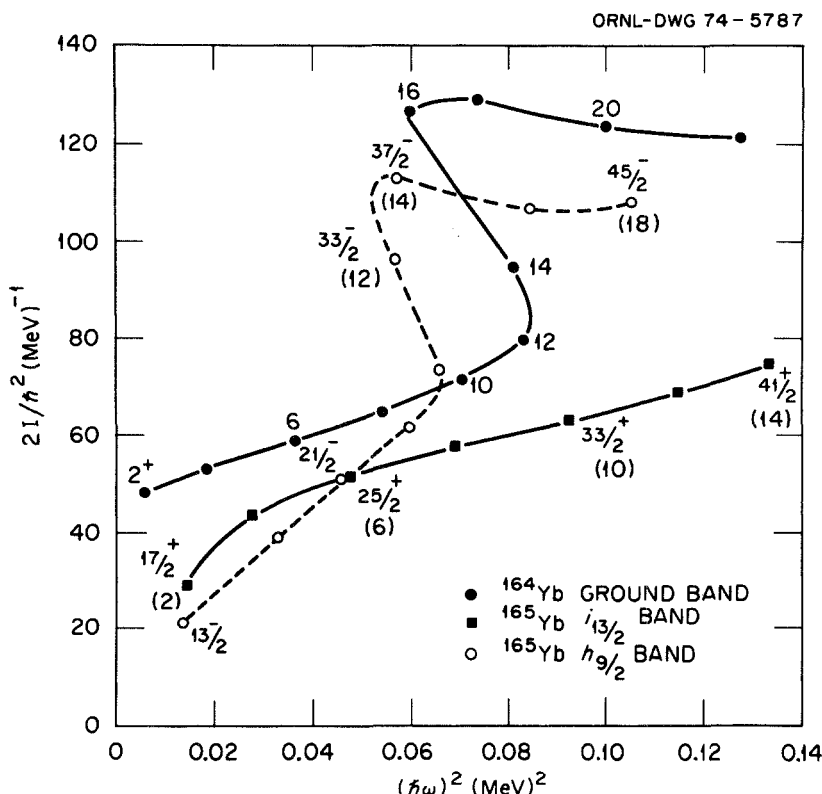


Fig. 8.18. Example of the odd particle blocking technique for intrinsic excitations in  $^{164-165}\text{Yb}$  (Riedinger, 1974).

increases, there is no reason why two low  $K$  neutron quasi-particles cannot align. Therefore backbending should ensue, and at approximately the same frequency as in the neighboring even-even nucleus. On the other hand, if one considers a rotational band built on the same unique parity low  $K$  orbit in the neighboring odd *neutron* nucleus, the alignment of two neutrons in that orbit will be blocked by the prior occupation by the last odd neutron. There should be no backbend, or at least a greatly reduced effect. If this is observed, one deduces that the backbend in the even-even nucleus results from neutron alignment. This technique has been exploited in many nuclei and an example is given in Fig. 8.18. Here we see a case where backbending occurs in the even nuclei  $^{164}\text{Yb}$ . In the neighboring odd nucleus  $^{165}\text{Yb}$ , the band based on the  $h_{9/2}$  orbit also backbends, but not that based on the  $i_{13/2}$  orbit. Thus one deduces that the backbending in  $^{164}\text{Yb}$  nuclei is caused by the  $i_{13/2}$  neutrons and not  $h_{9/2}$  neutrons, at least at this transition frequency.

The study of high-spin states, backbending, and related phenomena in heavy nuclei has become a major area of activity in the last decade and an enormous literature has developed. It is not our purpose here to summarize either it or the many refinements and improvements that have been made to this simple picture. Our aim is rather to provide some insight into the "traditional" background. Suffice it to say that much more sophisticated calculations are now standard, involving a "cranked" or rotated shell model that quantitatively accounts for the transformation from the body-fixed Nilsson scheme to the actual rotating system in the laboratory. Some of these calculations include the effects of axial asymmetry or hexadecapole deformations as well.

Empirically, double and even triple backbending has also been observed at higher transition frequencies. This has been interpreted in terms of the successive alignment of first one pair of particles along the rotation axis and then a second pair and sometimes even a third. Note that this reduces the overall pairing strength. At very high rotation, the alignment of all pairs can lead to a situation of complete pairing collapse. The study of unpaired intrinsic states is a currently active field.

Another phenomenon which has recently attracted much attention is that of *superdeformation*. This refers to a state at much larger than normal quadrupole distortion, typically  $\beta \sim 0.6$ . It has now been widely observed at spins  $J \sim 40\text{--}60$  in many rare earth nuclei and, possibly, at lower spins in the Hg region. Its explanation involves steeply downsloping Nilsson orbits, stemming from the second oscillator shell above the valence one, that descend, with increasing  $\beta$ , into the low-lying spectrum. Their occupation tends to stabilize very large deformations.

Clearly, as ever higher spins are sought and attained, increasing sophistication in data acquisition and analysis is required and a remarkable richness of phenomena unfolds. From all this has developed a deeper understanding of rotational particle coupling, nuclear shapes and potential energy surfaces, the phenomena of superdeformation and pairing collapse, and so on. The reader is referred to a fascinating literature.

## 9

## MICROSCOPIC TREATMENT OF COLLECTIVE VIBRATIONS

Although there are many microscopic approaches to deriving the structure, energies, and systematics of collective states from the shell model, there is one that has been widely used for nearly three decades, is still commonly encountered, and is easily adaptable to higher-order treatments. Moreover, it clearly shows the basic microscopic physics that must be at the heart of any approach. The technique referred to appears in two forms, the *Tamm-Dancoff Approximation* (TDA) and the *Random Phase Approximation* (RPA). Doubtless, the reader who is at all versed in nuclear structure physics has encountered calculations carried out in the RPA or references to such techniques. Except to the practitioners of this art unfortunately, the phrases TDA and RPA tend to elicit fear and mystery. Those sections of theoretical papers describing such calculations are frequently glossed over, and the reader quickly leaps to tables or figures of the results. This is unfortunate for two reasons. First, these sections often contain important information on the input physics (e.g., single-particle energies, interaction strengths, etc.). Second, these techniques are actually rather easy to understand if they are presented in a simplified form that illustrates the essential physics rather than in an abstract formalism designed to cover every generalization. In the next few pages we shall present a simple derivation and discussion of the basic ideas involved, and then illustrate the techniques with a particular calculation for rare earth nuclei. As the reader will see, the end result will not only be a set of predictions for comparison with experiment but a deeper understanding of the microscopic nature of many aspects of collective behavior as well as of a very useful, but often obscure, tool. It will then be easy to make predictions of the basic structure of particular collective states without detailed or complex calculations. Simply by visual inspection of a Nilsson diagram, we will be able to predict the energy behavior of collective vibrations (e.g.,  $\gamma$  or octupole), the systematics of their collective properties (e.g.,  $B(E2)$  or  $B(E3)$  values), and even such details as whether they should be seen in single nucleon transfer reactions. In short, a simple understanding of the basic ideas behind the microscopic structure of collective states will give us the ability to anticipate, without calculation, many results of detailed RPA or TDA calculations.

The following derivation, inspired by Lane, may seem rather formal and abstract, but it is in fact easy to follow and leads to some very simple, powerful, and useful results.

## 9.1 Structure of Collective Vibrations

To start, we denote the ground state wave function of a many-body system by  $\Psi_0$ .  $\Psi_0$  is an eigenfunction of a Hamiltonian,  $\mathbf{H}$ , such that

$$\mathbf{H}\Psi_0 = E_0\Psi_0 \quad (9.1)$$

We call  $\Psi_0$  the vacuum state and will see exactly what this means later.

Consider now an arbitrary operator  $\mathbf{O}_\alpha^\dagger$  that acts on  $\Psi_0$ , giving a new wave function  $\Psi_\alpha$

$$\Psi_\alpha = \mathbf{O}_\alpha^\dagger \Psi_0 \quad (9.2)$$

Now, *suppose*, and this is the key point on which all else depends, that  $\mathbf{O}_\alpha^\dagger$  happens to satisfy the operator relation

$$[\mathbf{H}, \mathbf{O}_\alpha^\dagger] \equiv (\mathbf{H}\mathbf{O}_\alpha^\dagger - \mathbf{O}_\alpha^\dagger\mathbf{H}) = \omega_\alpha \mathbf{O}_\alpha^\dagger \quad (9.3)$$

Although we have yet to specify what form  $\mathbf{O}_\alpha^\dagger$  must have for Eq. 9.3 to be obeyed, or what  $\omega_\alpha$  is, let us center our attention for the moment on the implications of this equation. Writing out Eq. 9.3 explicitly and acting on  $\Psi_0$ , we have

$$\mathbf{H}\mathbf{O}_\alpha^\dagger \Psi_0 - \mathbf{O}_\alpha^\dagger \mathbf{H} \Psi_0 = \omega_\alpha \mathbf{O}_\alpha^\dagger \Psi_0$$

Using Eq. 9.2, this is

$$\mathbf{H}\Psi_\alpha - \mathbf{O}_\alpha^\dagger \mathbf{H} \Psi_0 = \omega_\alpha \Psi_\alpha$$

Using Eq. 9.1, we have

$$\mathbf{H}\Psi_\alpha - \mathbf{O}_\alpha^\dagger E_0 \Psi_0 = \omega_\alpha \Psi_\alpha$$

or, since  $E_0$  is a number, not an operator,

$$\mathbf{H}\Psi_\alpha - E_0 \mathbf{O}_\alpha^\dagger \Psi_0 = \omega_\alpha \Psi_\alpha$$

Using Eq. 9.2 again, we obtain

$$\mathbf{H}\Psi_0 - E_0 \Psi_\alpha = \omega_\alpha \Psi_\alpha$$

or, finally

$$\mathbf{H}\Psi_\alpha = (\omega_\alpha + E_0)\Psi_\alpha \quad (9.4)$$

Thus,  $\Psi_\alpha$ , the result of acting on  $\Psi_0$  with  $\mathbf{O}_\alpha^\dagger$

- a) is *also* an eigenfunction of  $H$ , and
- b) has an excitation energy  $\omega_\alpha$  with respect to the ground state  $E_0$ .

Thus,  $\mathbf{O}_\alpha^\dagger$  is a *creation operator for the excitation*  $\alpha$ . This basic idea, plus some simplifying assumptions about the structure of  $\mathbf{O}_\alpha^\dagger$ , is the basis for the TDA and RPA.

To proceed, we obviously need to find operators  $\mathbf{O}_\alpha^\dagger$  that satisfy Eq. 9.3. Alternatively, we can ask what the *condition* is such that Eq. 9.3 is satisfied. To see this, let us expand  $\mathbf{O}_\alpha^\dagger$  in another set of arbitrary operators that form a complete set:

$$\mathbf{O}_\alpha^\dagger = \sum_r X_{\alpha r} \mathbf{O}_r \quad (9.5)$$

That is, the wave function for excitation  $\alpha$  is

$$\Psi_\alpha = \left( \sum_r X_{\alpha r} \mathbf{O}_r \right) \Psi_0 \quad (9.6)$$

This is basically a definition of the expansion coefficients  $X_{\alpha r}$ . Using Eq. 9.5 in Eq. 9.3 gives

$$\left[ \mathbf{H}, \sum_s X_{\alpha s} \mathbf{O}_s \right] = \omega_\alpha \sum_r X_{\alpha r} \mathbf{O}_r,$$

where, to avoid confusion, we use different subscripts in the independent summations on the two sides. Since the  $X$  coefficients are just numbers, we have

$$\sum_s X_{\alpha s} [\mathbf{H}, \mathbf{O}_s] = \omega_\alpha \sum_r X_{\alpha r} \mathbf{O}_r, \quad (9.7)$$

Now, we *define* a set of coefficients,  $M_{rs}$ , by the relation

$$[\mathbf{H}, \mathbf{O}_s] = \sum_r M_{rs} \mathbf{O}_r, \quad (9.8)$$

and substitute this into Eq. 9.7:

$$\sum_s X_{\alpha s} \sum_r M_{rs} \mathbf{O}_r = \omega_\alpha \sum_r X_{\alpha r} \mathbf{O}_r,$$

or,

$$\sum_{s,r} M_{rs} X_{\alpha s} \mathbf{O}_r = \omega_\alpha \sum_r X_{\alpha r} \mathbf{O}_r, \quad (9.9)$$

This, however, is just a matrix equation that must be satisfied for each  $r$  and can be written

$$\mathbf{M} \mathbf{X}_\alpha = \omega_\alpha \mathbf{X}_\alpha \quad (9.10)$$

where  $\mathbf{M}$  is the matrix whose elements are  $M_{rs}$  and  $\mathbf{X}_\alpha$  is a column vector with elements  $X_{\alpha r}$ .

Thus, Eq. 9.4 and the condition on the  $\mathbf{O}_\alpha^\dagger$ , Eq. 9.3, follow if Eq. 9.9 holds. Alternatively, if Eq. 9.9 is true, then defining the  $\mathbf{O}_\alpha^\dagger$  by Eq. 9.5, we find that Eqs. 9.3 and 9.4 are obeyed.

At this point, it is probably not clear why we have indulged in this process of piling definition upon definition. The aim was to produce Eq. 9.9. The reason, and the *practical* use of all this is as follows.

The basic idea of the TDA and RPA (or higher-order approximations) is

- a) to make assumptions about the operators  $\mathbf{O}_r$  defined in Eq. 9.5
- b) to then use the definition given in Eq. 9.8 to solve for  $M$  (that is for the elements  $M_{rs}$ )
- c) to then use these  $M_{rs}$ 's in Eq. 9.9 to solve for the  $X_{\alpha r}$ 's.

By Eq. 9.5 we then know the *detailed structure* of the operators  $\mathbf{O}_\alpha^\dagger$  that create the excitation  $\Psi_\alpha^\dagger$ ! If this seems amazing and magical, good. If it seems abstract and artificial, be patient.

To remove a little of the magic (but hopefully not the awe), let us consider two simple assumptions for the  $\mathbf{O}_\alpha$ 's and see what results. Suppose the  $\mathbf{O}_\alpha$ 's have the schematic form:

$$\text{i) } \mathbf{O}_\alpha^\dagger \approx \mathbf{A}_r^\dagger \quad (9.11)$$

$\mathbf{O}_\alpha$  creates a particle-hole excitation by raising one nucleon to orbit  $r$

$$\text{ii) } \mathbf{O}_\alpha^\dagger \approx \mathbf{A}_r^\dagger + \mathbf{A}_j \quad (9.12)$$

$\mathbf{O}_\alpha$  creates and destroys a particle-hole excitation, denoted, for the moment, simply by  $j$ . Later, when it becomes necessary to specify both orbits involved in excitation “ $j$ ,” we will expand the notation.

Approximation or assumption (i) is called the TDA and (ii) is called the RPA. Before proceeding, we use the general forms of (i) and (ii) to understand the meaning of the TDA and RPA.

We need only to recall that  $\Psi_0$  is the *ground state*. That is, any destruction operator acting on  $\Psi_0$  must give zero:

$$\mathbf{O}_\alpha \Psi_0 = 0 \quad (9.13)$$

For the TDA (assumption (i)), this is equivalent to

$$\mathbf{O}_\alpha \Psi_0 = \sum_r X_{\alpha r} \mathbf{A}_r \Psi_0 = 0$$

This will hold if  $\mathbf{A}_r \Psi_0 = 0$  for all  $r$ . Therefore, this  $\Psi_0$  has no particle-hole excitations  $r$ . If it had any,  $\mathbf{A}_r$  could destroy one, giving a nonzero wave function that did not contain a particle in that orbit. Thus,  $\Psi_0$  must be a closed shell nucleus. Alternatively phrased,  $\Psi_0$  has no built in correlations. The TDA therefore corresponds to creating excitations from a very simple, uncorrelated, uncollective ground state.

Assumption (ii), the RPA, on the other hand, means that we define  $\mathbf{O}_\alpha^\dagger$  in terms of Eq. 9.5 by

$$\mathbf{O}_\alpha^\dagger = \sum_r (X_{\alpha r} \mathbf{A}_r^\dagger + Y_{\alpha r} \mathbf{A}_r)$$

where, for convenience, we have separated those arbitrary operators “ $\mathbf{O}_\alpha$ ” that are particle-hole creation operators (denoted  $\mathbf{A}_r^\dagger$ ) from those that are particle-hole destruction operators (denoted  $\mathbf{A}_r$ ). Thus, we have

$$\mathbf{O}_\alpha \Psi_0 = \left( \sum_r X_{\alpha r} \mathbf{A}_r^\dagger + Y_{\alpha r} \mathbf{A}_r \right) \Psi_0 = 0$$

But by definition,  $\Psi_0$  is the ground state, implying that

$$\mathbf{A}_r^\dagger \Psi_0 = 0 \quad (9.14)$$

for those  $r$  for which  $Y_{\alpha r} \neq 0$ . But  $\mathbf{A}_r^\dagger$  creates a particle-hole excitation  $r$ . Equation 9.14 holds then if  $\Psi_0$  already contains such a particle-hole excitation so that  $\mathbf{A}_r^\dagger$  is “blocked.” Equation 9.13 can also be satisfied by cancellations of several terms ( $X_{\alpha r}$  and  $Y_{\alpha r}$  terms), which again implies the existence of particle-hole excitations in  $\Psi_0$ . Thus, although  $\Psi_0$  is itself the ground state

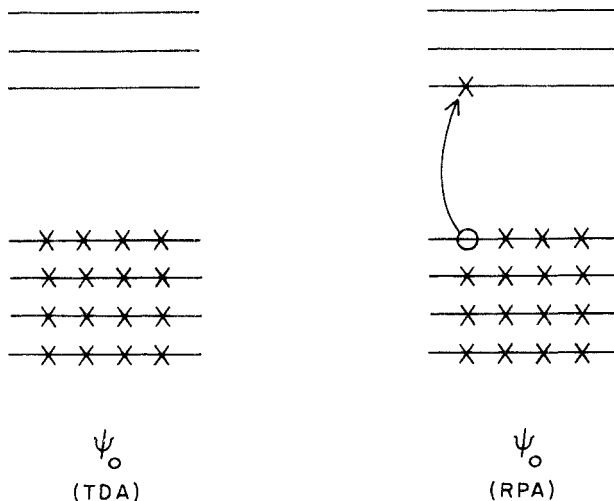


**Fig. 9.1.** Highly schematic illustration of the difference between the TDA and RPA approximations to the microscopic structure of collective excitations.

wave function, it already has some built in excitations (or correlations, or collectivity). We illustrate the TDA and RPA in a very schematic way in Fig. 9.1. We expect that the RPA will be a somewhat more realistic or better approximation, at least for nonclosed shell (or subshell) nuclei.

Now, let us use the approximations (i) and (ii) to see how they allow us to solve for  $\mathbf{M}$ , and hence for  $\mathbf{O}_\alpha^\dagger$ ,  $\Psi_\alpha$ , and  $\omega_\alpha$ . If we do this, we will then know both the *microscopic structure* of the excitation  $\alpha$  directly in terms of the occupation of the single-particle shell model orbits and the excitation energy of this excitation!

For simplicity, we consider the TDA, approximation (i). Then, Eq. 9.8 is

$$[\mathbf{H}, \mathbf{A}_s^\dagger] = \sum_r M_{rs} \mathbf{A}_r^\dagger \quad (9.15)$$

Multiplying by  $\mathbf{A}_i$  on the left, writing out the commutator, and taking the matrix element of Eq. 9.15 for state  $\Psi_0$ , gives

$$\langle \Psi_0 | \mathbf{A}_i \mathbf{H} \mathbf{A}_s^\dagger | \Psi_0 \rangle - \langle \Psi_0 | \mathbf{A}_i \mathbf{A}_s^\dagger \mathbf{H} | \Psi_0 \rangle = \left\langle \Psi_0 \left| \mathbf{A}_i \sum_r M_{rs} \mathbf{A}_r^\dagger \right| \Psi_0 \right\rangle$$

Recalling that  $\mathbf{A}_s^\dagger$  and  $\mathbf{A}_s$  simply create and destroy particles in orbit  $s$ , and abbreviating wave functions  $\Psi_s \equiv \mathbf{A}_s^\dagger \Psi_0$  by  $s$ , (and similarly for  $i$ ), we have

$$\langle i | \mathbf{H} | s \rangle - \langle \Psi_0 | \mathbf{A}_i \mathbf{A}_s^\dagger \mathbf{H} | \Psi_0 \rangle = \sum_r M_{rs} \langle \Psi_0 | \mathbf{A}_i \mathbf{A}_r^\dagger | \Psi_0 \rangle \quad (9.16)$$

where we also used the fact that the quantities  $M_{rs}$  are just numbers.

Now, the right side of Eq. 9.16 vanishes unless  $r = i$  (since for  $r \neq i$  it contains the factor  $\langle \Psi_0 | \mathbf{A}_i \mathbf{A}_r^\dagger | \Psi_0 \rangle = \langle \Psi_0 | \mathbf{A}_i | \Psi_0 \rangle$ , which vanishes by orthogonality since  $\Psi_0$  has no particle in orbit  $i$  to be destroyed). For  $r = i$ , we have on the right side,  $\langle \Psi_0 | M_{is} \mathbf{A}_i \mathbf{A}_i^\dagger | \Psi_0 \rangle = M_{is}$ . So

$$\langle i | \mathbf{H} | s \rangle - \langle \Psi_0 | \mathbf{A}_i \mathbf{A}_s^\dagger \mathbf{H} | \Psi_0 \rangle = M_{is}$$

But the second term on the left,  $\langle \Psi_0 | \mathbf{A}_i \mathbf{A}_s^\dagger \mathbf{H} | \Psi_0 \rangle = \langle \Psi_0 | \mathbf{A}_i \mathbf{A}_s^\dagger E_0 | \Psi_0 \rangle$ , also vanishes unless  $i = s$ , in which case it is given by the ground state energy  $E_0$ . Thus, we have the simple result

$$M_{is} = \langle i | \mathbf{H} | s \rangle - E_0 \delta_{is} = \langle i | \mathbf{H} | s \rangle \quad (9.17)$$

since we can choose to set  $E_0 = 0$ . The particle-hole (or quasi-particle) energies contained in  $\mathbf{H}$  are energy differences between empty and filled orbits. We call these energies  $\Delta\epsilon$ . In the RPA, a similar derivation yields a slightly more complicated result that the reader can easily work out using analogous arguments.

This result, Eq. 9.17, simply states that the matrix elements  $M_{is}$  of the matrix  $\mathbf{M}$  that, via Eq. 9.9, give the coefficients (vectors)  $X_\alpha$  and the energy  $\omega_\alpha$  defining the excitation  $\alpha$ , are equal to matrix elements of the Hamiltonian between states  $i$  and  $s$ . In order to calculate this explicitly, we need only to make some choices for  $\mathbf{H} = \Delta\epsilon + \mathbf{V}$ . Starting from a shell model or Nilsson model that gives the particle-hole energies  $\Delta\epsilon_i$ , we need only specify the interaction  $\mathbf{V}$ . Suppose we make the reasonable assumption that  $\mathbf{V}$  is a quadrupole interaction. Then,

$$\langle i | \mathbf{V} | j \rangle \equiv C Q_i Q_j \quad (9.18)$$

where the  $Q$ 's are proportional to the transition quadrupole matrix element from the ground state to a particle-hole state with the particle in orbit  $i$  or  $j$ . That is,  $Q_i$  means  $\langle i | \mathbf{Q}_i | \Psi_0 \rangle = \langle i | \mathbf{r}^2 \mathbf{Y}_2 | \Psi_0 \rangle$ .  $C$  is the strength of the interaction. For an attractive interaction,  $C < 0$ . To keep the notation simple, recall that we have specified each particle-hole excitation by a single subscript. Technically this is incomplete; each such excitation involves elevating a particle to some empty orbit and vacating a filled one. As long as no confusion results, we shall keep to this notation but the reader should keep in mind that each  $\Delta\epsilon_i$  involves a pair of orbits and the energy difference between them.

Substituting Eq. 9.18 in Eq. 9.9 and using Eq. 9.17, we have

$$\sum_{s,r} \langle r | \mathbf{H} | s \rangle X_{\alpha s} \mathbf{O}_r = \omega_\alpha \sum_r X_{\alpha r} \mathbf{O}_r$$

or

$$\sum_{s,r} [\Delta\epsilon_r \delta_{rs} + \langle r | \mathbf{V} | s \rangle] X_{\alpha s} \mathbf{O}_r = \omega_\alpha \sum_r X_{\alpha r} \mathbf{O}_r$$

or

$$\sum_r \Delta\epsilon_r X_{\alpha r} \mathbf{O}_r + C \sum_{s,r} Q_s Q_r X_{\alpha s} \mathbf{O}_r = \omega_\alpha \sum_r X_{\alpha r} \mathbf{O}_r$$

This must be satisfied for all  $r$ , so

$$\Delta\epsilon_r X_{\alpha r} + C \sum_s Q_s Q_r X_{\alpha s} = \omega_\alpha X_{\alpha r}$$

or

$$(\epsilon_r - \omega_\alpha) X_{\alpha r} = -C \sum_s Q_s Q_r X_{\alpha s}$$

or, finally, we get the expansion coefficients or amplitudes for the wave function  $\Psi_\alpha$  of Eq. 9.6

$$X_{\alpha r} = \frac{C Q_r \sum_s Q_s X_{\alpha s}}{\omega_\alpha - \Delta \epsilon_r} \quad (9.19)_{\text{TDA}}$$

To find the eigenvalues  $\omega_\alpha$ , we multiply Eq. 9.19 by  $Q_s$  and sum over  $r$ , obtaining

$$\sum_r X_{\alpha r} Q_r = C \sum_r \left( \frac{Q_r^2 \sum_s Q_s X_{\alpha s}}{\omega_\alpha - \Delta \epsilon_r} \right)$$

But  $\sum_r X_{\alpha r} Q_r$  on the left is identical to  $\sum_s X_{\alpha s} Q_s$  on the right, so cancelling these, we have

$$\frac{1}{C} = \sum_r \frac{Q_r^2}{\omega_\alpha - \Delta \epsilon_r} \quad (9.20)_{\text{TDA}}$$

which is the desired result. Note that the wave functions specified by the  $X_\alpha$  and the energy  $\omega_\alpha$  are now written in terms of completely known quantities: single-particle energies and single-particle transition quadrupole moments. Given a single-particle model (shell, Nilsson, etc.), they are easily calculable. Indeed, we shall see shortly that, using these results, we can for example virtually "derive"  $\gamma$  vibrational wave functions by inspection of the Nilsson diagram without detailed calculations.

We emphasize that in Eq. 9.19, the quantity  $\sum_s Q_s X_{\alpha s}$  is just a number, so that

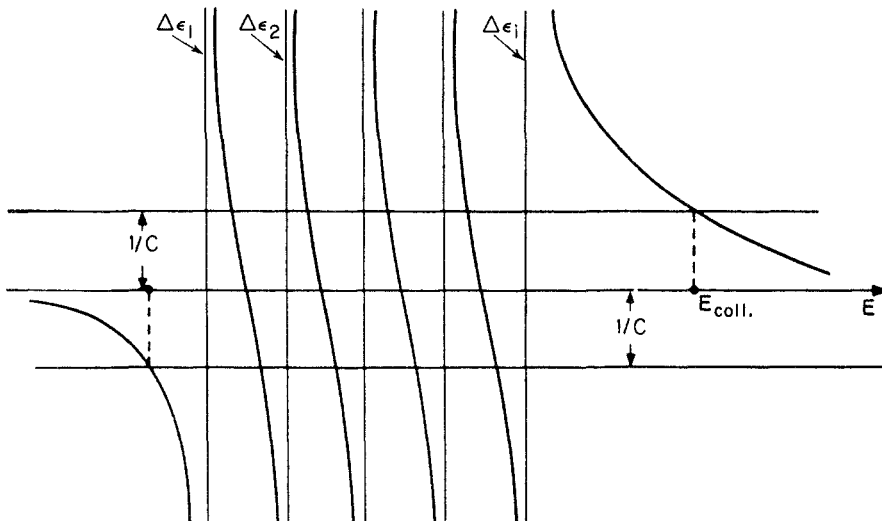


**Fig. 9.2.** Illustration of the solution to Eq. 9.20<sub>TDA</sub>. The energies  $\omega_\alpha$  correspond to those points where the vertical curves cross the "1/C" lines. The lowest (rightmost) solution is the collective one (Ring, 1980).

the coefficients of the vibrational wave functions for the excitation  $\alpha$  are simply proportional to  $Q_r/(\Delta\epsilon_r - \omega_\alpha)$ . This fundamental result is of great importance.

Recall that the  $Q_r$  are the quadrupole transition matrix elements connecting the ground state with a particular ( $r$ th) particle-hole excitation. Thus the amplitude for particle-hole excitation  $r$  in the vibrational wave function is proportional to the matrix element for a quadrupole transition to this particle-hole excitation and is inversely proportional to the difference between the particle-hole energy,  $\Delta\epsilon_r$ , and the vibrational energy,  $\omega_\alpha$ . Particle-hole excitations that require energies close to  $\omega_\alpha$  and have large quadrupole matrix elements are strongly favored.

The eigenvalue Eq. 9.20 has several possible solutions that are labeled  $\alpha$ . These correspond to those energies  $\omega_\alpha$  such that the right-hand side takes on the value  $1/C$ . These solutions are illustrated in Fig. 9.2. One solution always appears significantly lowered in energy. This is the *collective vibration*.

It is easy to see this if we take a highly simplified example. Suppose there are  $N$  identical particle-hole energies  $\Delta\epsilon$  and that the  $Q_r$  values are also all equal. Then the lowest solution has the wave function amplitudes

$$X_{\alpha r} = a Q_r$$

where  $a$  is just a constant. By normalization of this  $N$ -component wave function, we have  $a = (1/\sqrt{N}Q_r)$ . This means that the wave function consists of a sum of *equal* amplitudes for all particle-hole excitations, with all amplitudes *in phase*. This is exactly the formal definition of a *coherent* or *correlated wave function*, which has many comparable amplitudes contributing with the same sign. To see how this collectivity manifests itself, let us calculate an E2 (or quadrupole) transition rate from the vibration  $\alpha$  to the ground state:

$$\begin{aligned} \langle \Psi_\alpha | | \mathbf{r}^2 \mathbf{Y}_2 | | \Psi_0 \rangle &= \sum_{r=1}^N \left\langle \frac{1}{\sqrt{N}} Q_r \Psi_r | | \mathbf{r}^2 \mathbf{Y}_2 | | \Psi_0 \right\rangle \\ &= \frac{N Q_r}{\sqrt{N}} = \sqrt{N} Q_r \end{aligned}$$

Hence,

$$B(E2 : \Psi_{vib\ \alpha} \rightarrow \Psi_0) \propto \langle \Psi_\alpha | | \mathbf{r}^2 \mathbf{Y}_2 | | \Psi_0 \rangle^2 = N Q_r^2$$

which is  $N$  times the single-particle  $B(E2)$  value. Since this exhausts the total strength, it follows that no other solution has any strength. Of course, this is an extreme simplification, but it does demonstrate what is meant by collectivity and coherence and how they arise from this microscopic formalism.

Finally, the eigenvalue for the collective solution in this degenerate case is given from Eq. 9.20 by setting all  $(\omega_\alpha - \Delta\epsilon_r)$  constant, giving

$$E_{vib\ \alpha} = \omega_\alpha = \Delta\epsilon_r + C \sum_{r=1}^N Q_r^2 = \Delta\epsilon_r + NCQ_r^2 \quad (9.21)$$

The vibrational energy is lowered (recall that  $C < 0$  for an attractive residual interaction), relative to the (common) particle-hole energy by the large amount

$NCQ^2$  This leads to an alternate viewpoint on the structure and origin of the vibrational wave functions since they are identical to those we obtained in Chapter 1 for the mixing of a set of degenerate levels. The lowest wave function (see Eq. 1.13) was a sum of equal amplitudes for all basis states: this state was lowered by an amount proportional to the number of admixed states while all of the others were raised in energy.

Before closing this discussion and looking at applications of these ideas, it is worth recapitulating the key ingredients that lead to the results obtained:

- We discussed a simple but abstract operator formalism leading to the essential Eqs. 9.3, 9.4, 9.5, and 9.8. Equations 9.3 and 9.4 show the properties of the excitation  $\alpha$  whose structure we are interested in. Equation 9.5 defines the creation operators  $\mathbf{O}_\alpha^\dagger$  and Eq. 9.9, with the definitions of Eq. 9.8, gives a means for solving for the coefficients  $X_\alpha$  that define the wave function  $\Psi_\alpha$  of Eq. 9.6, and for the energies  $\omega_\alpha$ .
- We made simple choices for the form of the various operators  $\mathbf{O}_\alpha^\dagger$ . These correspond to the TDA ( $\mathbf{O}_\alpha^\dagger$  contains only particle-hole creation operators) and the RPA ( $\mathbf{O}_\alpha^\dagger$  contains both particle-hole creation and destruction operators).
- We made a simple choice for the residual interaction  $V$ . This step is often called a *schematic model*. Doing this allowed us to calculate the  $X_\alpha$ 's, hence the  $\mathbf{O}_\alpha^\dagger$ 's, and hence the structure and energy ( $\omega_\alpha$ ) of the vibrational state  $\Psi_\alpha$ .

The TDA represents the gross approximation that the ground state is a pure, undisturbed, closed shell nucleus. This is generally not realistic and the use of the RPA to incorporate ground state correlations is more common. We therefore present (without derivation) the eigenvalue results analogous to Eq. 9.20<sub>TDA</sub>, for the RPA:

$$\frac{1}{C} = \sum_r Q_r^2 \left[ \frac{1}{\omega_\alpha - \Delta \epsilon_r} - \frac{1}{\omega_\alpha + \Delta \epsilon_r} \right]$$

or

$$\frac{1}{C} = 2 \sum_r Q_r^2 \frac{\Delta \epsilon_r}{\omega_\alpha^2 - \Delta \epsilon_r^2} \quad (9.20)_{RPA}$$

This is similar to the TDA expression except for the more complicated factor multiplying the  $Q_r^2$ . Note that, in the degenerate case (all  $\Delta \epsilon_r$  equal) this gives

$$\omega_\alpha^2 - \Delta \epsilon_r^2 = 2 C \Delta \epsilon_r \sum_r Q_r^2$$

or

$$\omega_\alpha = \left( \Delta \epsilon_r^2 + 2 C \Delta \epsilon_r \sum_r Q_r^2 \right)^{\frac{1}{2}}$$

or, if all the  $Q_r$  are equal,

$$\omega_\alpha = \left( \Delta \epsilon_r^2 + 2 C \Delta \epsilon_r N Q_r^2 \right)^{\frac{1}{2}}$$

Using Eq. 9.20<sub>TDA</sub> and labeling the energies  $\omega_\alpha$  as  $\omega_\alpha^{TDA}$  or  $\omega_\alpha^{RPA}$ , we have

$$\begin{aligned}\omega_{\alpha}^{\text{RPA}} &= \left[ (\omega_{\alpha}^{\text{TDA}})^2 - C^2 \left( \sum_r Q_r^2 \right)^2 \right]^{\frac{1}{2}} \\ &= \left[ (\omega_{\alpha}^{\text{TDA}})^2 - (CNQ_r^2)^2 \right]^{\frac{1}{2}}\end{aligned}$$

if all the  $Q_r$  are equal. This shows that  $\omega_{\alpha}^{\text{RPA}}$  is always less than  $\omega_{\alpha}^{\text{TDA}}$ . The RPA leads to greater collectivity.

We close this section by noting that the discussion has been phrased in terms of spherical single-particle-hole energies  $\epsilon_i$  and single-particle quadrupole moments (or other moments for other choices of  $V$ , such as octupole moments). However, as hinted at a couple of times, the single-particle energies can be Nilsson energies equally well, and the  $\mathbf{A}_i^\dagger$ 's and  $\mathbf{A}_i$ 's can be creation and destruction operators for Nilsson orbits. Then  $\Psi_0$  is the ground state of the deformed nucleus. A related point concerns our choice for  $V$  in our example of a schematic model in Eq. 9.18. It seems to ignore the short-range parts of the residual (nonsingle particle) interaction such as the pairing interaction. However, the whole formalism is identical if the pairing interaction is incorporated into the definition of the single-particle or Nilsson energies by defining these as quasi-particle energies instead of single-particle energies. Then the TDA or RPA can give the structure of vibrations in deformed nuclei in terms of amplitudes for *specific Nilsson quasi-particle excitations*. We thus see how a rather formidable looking formalism leads simply and elegantly to an easy way of deducing the particle (or quasi-particle) composition of specific collective vibrations. This is one answer to the apparent dichotomy that we noted earlier between the independent particle picture of the nucleus and the existence of collective excitations and correlations. The key element, of course, is in a sense inserted a priori by defining the operators  $\mathbf{O}_{\alpha}^\dagger$  as linear combinations of single-particle (or two-quasi-particle) operators and by simplifying the interaction  $V$ . Ultimately, the method is tested by its agreement with experiment. This test has been passed many times, making the result a useful, elegant, and powerful approach to the microscopic structure of collective vibrations.

## 9.2 Examples: Vibrations in Deformed Nuclei

The formalism just developed is ideally suited for understanding the microscopic structure of vibrations in spherical nuclei. Indeed, calculations for nuclei such as Pb or Sn were among its first applications. Since these nuclei are singly magic, the simpler TDA is a reasonable approximation and is frequently used. Pioneer applications of this formalism to such cases were made by Kisslinger and Sorenson and are described in many texts. We will turn instead to the application of these ideas to deformed nuclei.

Departing from singly magic nuclei, the p-n interaction rapidly induces configuration mixing that obscures shell structure. The onset of deformation affects the single-particle energies, as we have seen in the Nilsson scheme. So for  $\beta = 0.3$ , any remnants of the 50, 82, or 126 shell gaps almost totally

disappear. Excitations involving orbits from the shells below or above the valence shell must be incorporated in realistic calculations, and the RPA becomes a necessary refinement.

Even higher-order forms of the operator  $\mathbf{O}_\alpha^\dagger$  are sometimes applied and are often called *higher RPA* (HRPA) for obvious reasons. Other approaches such as that of Kumar and Baranger or the more recent refinement, the dynamic deformation theory, may be used. The full sweep of many-body theory encompasses many varied and complementary approaches.

One of the most interesting, informative, and physically transparent applications of the RPA is to the  $\gamma$  bands in deformed nuclei. The relevant calculations were carried out by Bès and co-workers in the early 1960s and remain the standard for the microscopic structure of these modes.

The basis states here are naturally the Nilsson orbits. Pairing must be included via a BCS calculation, so that, for the ground state, there is a distribution of occupation amplitudes over several orbits near the Fermi energy  $\lambda$ . This can be seen quantitatively in a modification to Eq. 9.20<sub>RPA</sub>. For this discussion, we must specifically label both orbits involved in the quasi-particle excitation as we must specify occupation amplitudes for each. Replacing the particle-hole energy  $\Delta\epsilon$ , with  $E_i + E_j$ , where the  $E$ 's are quasi-particle energies defined by

$$E_i = \sqrt{(\epsilon_i - \lambda)^2 + \Delta^2}$$

we have, for the energies  $\omega_\alpha$ , the equation

$$\frac{1}{C} = \frac{\sum_{ij} Q_{ij}^2 (E_i + E_j)(U_i V_j + U_j V_i)^2}{\omega_\alpha^2 - (E_i + E_j)^2} \quad (9.22)$$

where  $Q_{ij}$  now means  $\langle i | \mathbf{r}^2 \mathbf{Y}_{2\pm2} | j \rangle$ . The wave functions are now linear combinations of two-quasi-particle excitations rather than single-particle-hole excitations, but the physical idea is identical. Note that in Eq. 9.22,  $E_i$  changes more slowly than  $\epsilon_i$  when  $(\epsilon_i - \lambda) < \Delta$ . Therefore, a wider range of  $\epsilon_i$  values and orbits can contribute. Also, the pairing factor favors pairs of quasi-particle excitations on opposite sides of the Fermi surface; as an analogue to particle-hole excitations, this is not surprising.

The matrix elements of  $\mathbf{r}^2 \mathbf{Y}_{2\pm2}$  that determine the important  $\gamma$ -vibrational amplitudes are easily deduced by writing  $\mathbf{r}^2 \mathbf{Y}_{2\pm2}$  in Cartesian coordinates as

$$\mathbf{r}^2 \mathbf{Y}_{2\pm2} \approx (\mathbf{x} \pm i\mathbf{y})^2 \quad (9.23)$$

This is a field (operator) that does not change  $n_z$  (there is no effect in the  $z$ -direction) but that changes  $\Lambda$  by  $\pm 2$ . (For a table giving the structure of all the low multipole operators in Cartesian form, see Mottelson and Nilsson, 1959). Another practical selection rule is that the sum  $n_z + n_x + n_y = N$  should be conserved; otherwise the matrix element would involve Nilsson wave functions  $[Nn_z \Lambda]$  and  $[N'n'_z \Lambda']$  with  $N' = N \pm 2$ . Such states are far apart (about 10 MeV). Thus, the important components of the  $\gamma$ -vibration will be two-quasi-particle excitations involving a Nilsson orbit within about 2 MeV of the Fermi

surface differing by  $\Delta K = \pm 2$ ,  $\Delta \Lambda = \pm 2$  ( $N, n_z$  unchanged) from another near the Fermi surface.

Since both  $K$  and  $\Lambda$  change by the same amount, the projection  $\Sigma$  of the intrinsic nucleon angular momentum will not change ( $\Delta \Sigma = 0$ ). In considering which orbits satisfy this rule, recall that the ground state consists of a correlated wave function  $\Psi_0 = X_1\phi_1 + X_2\phi_2 + \dots$ , each of whose components describes two particles in the same Nilsson orbit but with opposite  $K$  values so that the resultant  $K = 0$ . Since  $K = \Lambda \pm \Sigma$ , there two nucleons also have equal and opposite  $\Lambda$  values ( $\pm \Lambda$ ). Hence,  $r^2 Y_{2z2}$  will also have matrix elements satisfying the above rule that connect orbits such as [1/2 521] and 3/2[521], since the  $\Lambda = \pm 1$ ,  $K = \pm 1/2$ , and  $K = \mp 3/2$  components differ by  $\Delta \Lambda$  and  $\Delta K = 2$ , respectively.

Let us now apply these ideas to a couple of examples. Consider  $^{184}\text{W}$ . The ground states of  $^{183},^{185}\text{W}$  are 1/2-[510] and 3/2-[512]. This approximately locates the neutron Fermi energy in the Nilsson diagram (see Figs. 8.1 and 7.4). Then we deduce by inspection that the important neutron components of the  $\gamma$  vibration in  $^{184}\text{W}$  are two-quasi-particle states of the form

$$\frac{1}{2}^- [510] \otimes \frac{3}{2}^- [512], \frac{1}{2}^- [510] \otimes \frac{5}{2}^- [512]$$

and

$$\frac{3}{2}^- [512] \otimes \frac{7}{2}^- [514] \quad (9.24)$$

The analogous proton amplitudes can be similarly deduced. To see how well this estimate works, we show the detailed results of RPA calculations in Table 9.1, from which it is evident that we have indeed identified the most important two-quasi-particle components.

**Table 9.1.** Principle neutron two-quasi-particle amplitudes ( $\times 100$ ) for the  $\gamma$ -vibration in several rare earth nuclei\*

Two-quasi-particle states	$^{154}\text{Gd}$	$^{160}\text{Dy}$	$^{164}\text{Dy}$	$^{170}\text{Er}$	$^{174}\text{Yb}$	$^{178}\text{Hf}$	$^{184}\text{W}$	$^{186}\text{W}$
11/2-[505] $\otimes$ 7/2-[514]	—	—	—	7	7	—	—	—
11/2-[505] $\otimes$ 7/2-[503]	11	12	15	25	26	21	11	8
9/2-[514] $\otimes$ 5/2-[523]	9	7	—	—	—	—	—	—
9/2-[514] $\otimes$ 5/2-[512]	25	23	21	20	14	—	—	—
9/2-[505] $\otimes$ 5/2-[503]	—	—	—	—	—	—	11	16
7/2-[523] $\otimes$ 3/2-[521]	19	12	—	—	—	—	—	—
7/2-[514] $\otimes$ 3/2-[512]	—	—	—	17	35	48	34	26
7/2-[503] $\otimes$ 3/2-[501]	—	—	—	—	—	7	20	26
5/2-[523] $\otimes$ 1/2-[541]	9	—	—	—	—	—	—	—
5/2-[523] $\otimes$ 1/2-[521]	20	36	51	29	14	8	—	—
5/2-[512] $\otimes$ 3/2-[521]	—	—	—	9	7	—	—	—
5/2-[512] $\otimes$ 1/2-[510]	—	—	9	31	56	56	32	24
3/2-[532] $\otimes$ 1/2-[530]	24	8	—	—	—	—	—	—
3/2-[521] $\otimes$ 1/2-[541]	9	—	—	—	—	—	—	—
3/2-[521] $\otimes$ 1/2-[521]	27	45	46	25	13	8	—	—
3/2-[512] $\otimes$ 1/2-[510]	—	—	—	8	13	22	66	70

\*Bès, 1965. The table only includes amplitudes from the  $N = 5$  shell.

As a second case, consider  $^{68}_{\text{Er}}{}^{170}\text{Er}_{102}$ . Here the principle neutron two-quasi-particle components of the  $\gamma$ -vibration would be expected to be

$$\begin{aligned} & \frac{1}{2}^- [521] \otimes \frac{5}{2}^- [523] \\ & \frac{1}{2}^- [521] \otimes \frac{3}{2}^- [521] \\ & \frac{1}{2}^- [510] \otimes \frac{5}{2}^- [512] \\ & \frac{3}{2}^- [512] \otimes \frac{7}{2}^- [514] \\ & \frac{7}{2}^- [503] \otimes \frac{11}{2}^- [505] \end{aligned} \quad (9.25)$$

Comparison with Table 9.1 again shows that these comprise most of the main neutron components of the  $\gamma$ -vibration in  $^{170}\text{Er}$ . Perusal of this table shows how various two-quasi-particle amplitudes systematically grow and decay across the region as the Fermi surface rises, and how different amplitudes are favored by the energy denominator and pairing factors in Eqs. 9.20<sub>RPA</sub> and 9.22.

It is sometimes possible to test such predictions using single nucleon transfer reactions. Since the  $^{183}\text{W}$  target ground state is the  $1/2^-$ -[510] orbit, the (d, p) reaction can only populate two-quasi-particle states in  $^{184}\text{W}$  of the specific form  $1/2^-$ [510]  $\otimes \psi_{\text{Nils}}$ . Moreover, they will contribute proportionally to  $U^2$ , the emptiness of  $\psi_{\text{Nils}}$  in  $^{183}\text{W}$ . In  $^{183}\text{W}$ , therefore, the hole state  $5/2^-$ [512] component should not contribute significantly to  $\sigma(d, p)$ , for the  $\gamma$ -vibration, while neutron transfer involving the  $3/2^-$ [512] orbit should. (Of course, in  $^{182}\text{W}$  the  $\gamma$ -vibration must have similar structure. Hence,  $5/2^-$ [512] transfer will be important for the  $^{183}\text{W}(d, t)^{182}\text{W}$  cross section.) In any case, the (d, p) cross section to the various spin states of the  $\gamma$  rotational band in  $^{184}\text{W}$  will be determined primarily by the  $C_j$  coefficients for the  $3/2^-$ [512] orbit.

The explicit expression for  $\sigma(d, p)$  into an even-even nucleus is not quite as simple as given in Chapter 8 for an odd-mass final nucleus, since each state of spin  $J$  can be constructed by coupling a component ( $j_1$ ) of the  $1/2^-$ [510] orbit with one  $j_2$  from the  $3/2^-$ [512] orbit. In general, several  $j_1, j_2$  pairs can lead to the same  $J$ . Their relative contributions are given by Clebsch-Gordon coefficients. The population of a two-quasi-particle state in an even-even nucleus in (d, p) is thus given by a generalization of Eq. 8.1

$$\sigma(d, p)_{e-e} = 2N \left[ \sum_{l_1 l_2} \phi_l(j_1 K_1 j_2 K_2 | J K \rangle C_{j_2}) \right]^2 U_2^2 \quad (9.26)$$

where the  $\phi_l$  are DWBA cross sections ( $l = j \pm 1/2$ ). It can easily happen that several  $l$  values contribute to this expression for a given final state. In the case of  $^{184}\text{W}$ , for example, the  $J^\pi = 2^+$ , state can arise by coupling the target  $j = 1/2^-$  state with  $j = 3/2^-$  or  $j = 5/2^-$  components of the  $3/2^-$ [512] wave function; these proceed by  $l = 1$  and  $l = 3$  transfer, respectively. For a higher spin target such as  $^{167}\text{Er}$  ( $7/2^+$ ), there are even more possibilities. A  $4^-$  level can be formed by

coupling the  $7/2^+$  ground state with  $j_z = 1/2, 3/2, 5/2, 7/2, 9/2, 11/2$  (the upper limit here is provided not by angular momentum conservation but by the available orbits in the  $N = 5$  shell where  $j_{\max} = 11/2$ ). This involves six contributions, with  $l = 1, 1, 3, 3, 5, 5$ , respectively.

Thus, generally the “fingerprint patterns” in even-even nuclei will be somewhat “washed out” and less orbit sensitive than in odd nuclei. Nevertheless, the (d, p) data for population of the  $\gamma$ -band in  $^{184}\text{W}$  does have a pattern very close to that predicted for the transfer of a  $3/2^-$ [512] neutron Nilsson orbit, and the corresponding (d, t) data in  $^{182}\text{W}$  confirms the presence of the  $5/2^-$ [512] orbit in the  $\gamma$ -vibration there. Note that not only can the important orbits be identified in this way, but their amplitudes in the  $\gamma$ -vibration may be deduced (approximately) by comparing, for example, the cross sections into the even-even nucleus to those for transfer of the same orbit into the neighboring odd  $A$  nucleus. In this way, even the detailed structure of RPA calculations are confirmed, at least for a couple of important amplitudes. Other amplitudes, such as  $3/2^-$ [512]  $\otimes$   $7/2^-$ [514] cannot be directly tested.

In a few special cases it is possible to test for amplitudes involving a non-target-ground state orbit. As an example,  $^{185}\text{W}$  has a ground state  $3/2^-$ [512] and a low-lying  $1/2^-$ [510] excited state. If  $^{185}\text{W}$  were stable, permitting the relevant (d, t) reaction to  $^{184}\text{W}$ , it would be possible to study the  $1/2^-$ [510]  $\otimes$   $5/2^-$ [512] component in the  $^{184}\text{W}$   $\gamma$ -vibration, because the ( $3/2^-$ ) ground state of  $^{185}\text{W}$  has a strong Coriolis admixture of the  $3/2$   $1/2^-$ [510] state. (The case starting with  $^{183}\text{W}$  is not the same, even though here too the  $1/2$ [510] and  $3/2^-$ [512] orbits are admixed, since the  $1/2^-$  $^{183}\text{W}$  ground state cannot contain a  $3/2$   $3/2^-$ [512] admixture.) In the  $^{185}\text{W}$ (d, t) $^{184}\text{W}$  case, the  $\gamma$  band would be primarily populated by a coherent combination of the components  $3/2^-$ [512]  $\otimes$   $7/2$ [514] and  $1/2^-$ [510]  $\otimes$   $5/2$ [512].

To return to our discussion of the structure of collective excitations, we see how an understanding of the basic formalism and philosophy of the RPA allows us to understand and even anticipate the detailed microscopic structure of excitations such as the  $\gamma$  vibrations of deformed nuclei. A little further thought reveals five additional basic features of these excitations.

First, the unique parity orbit is generally unimportant in the  $\gamma$  vibration, since this vibration has positive parity and therefore both quasi-particles have to be in a unique parity orbit. But, from the sequence of asymptotic Nilsson quantum numbers, we see that any pair with  $\Delta K = 2$  also has  $\Delta n_z = 2$ , and therefore will not be connected by a  $r^2 Y_{2z2}$  operator.

Second, since the important orbits are those within a certain distance of the Fermi surface, the  $\gamma$  vibrational wave functions will not change radically from one nucleus to the next or even over a small region. This is almost a requirement of a collective mode. We can go even further and predict how the structure will vary. From our discussion of the relevant (large) matrix elements and of the role of the energy denominator, it is clear that a given Nilsson orbit will, for some mass  $A$ , be high above the Fermi surface and will contribute little. As  $A$  ( $N$  or  $Z$  really) increases, this Nilsson orbit will drop closer to the Fermi surface and gain importance. Later, it will become a hole state and begin

decreasing in amplitude as it recedes further from the Fermi energy. Thus, for most two-quasi-particle excitations, a plot of their contributions against  $N$  or  $Z$  (whichever is relevant) will be bell shaped. Inspection of Table 9.1 shows that, for most orbits, this is precisely the observed behavior. Amplitudes for two-quasi-particle states such as  $9/2^-[514]$  and  $5/2^-[512]$  containing an excitation from the  $h_{11/2}$  orbit from the next lower major shell peak early in the deformed region. The  $5/2^-[523] \otimes 1/2^-[521]$  component increases into the deformed region and attains its maximum amplitude near  $N = 98$  ( $^{164}\text{Dy}$ ), but contributes little for  $N > 104$ . Finally, the  $7/2^-[514] \otimes 3/2^-[512]$  combination is negligible until rather late in the shell, but becomes strong near  $N = 108$  and again drops off in importance near  $N = 112$ .

Third, we note that for any given nucleus, the number of significant components is surprisingly low, typically three to five for neutrons and slightly fewer for protons (since the protons are filling the lower shell with fewer orbits). Thus the word "collective" must be taken in context. One should not imagine 50 to 100 nucleons or amplitudes significantly involved in this or other collective excitations.

Fourth, one should address the question of how the collectivity (as measured, for example, by large  $B(E2:\gamma \rightarrow g)$  values) arises if only a few orbits contribute strongly. This is especially so since "single-particle"  $B(E2)$  values in odd-mass deformed nuclei (i.e.,  $B(E2)$  values where one particle changes its Nilsson orbit) are much smaller than in "shell model" nuclei. The former are typically  $10^{-3}$  to  $10^{-4}$  s.p.u., since the shell model strength is fragmented by configuration mixing in deformed nuclei. Yet  $B(E2:\gamma \rightarrow g)$  values are typically  $\approx 10$  s.p.u. This can only arise then as a specific effect of coherence: the dominant contributions to these  $E2$  matrix elements must add in phase.

This can be understood (at least qualitatively) by expressing the structure of the vibration in an equivalent but, in a sense, inverted picture that we alluded to briefly earlier. Instead of conceiving the vibration as built up of components that arise by operating with  $r^2 Y_{2+2}$  on the orbits near the Fermi surface, imagine a set of closely spaced two-quasi-particle states at some excitation energy (e.g., 2 to 3 MeV) that mix by an appropriate interaction (that need not be specified). Then, by the arguments concerning two- and multistate mixing in Chapter 1, one level will be pushed down and its wave function will have the most coherent admixture of amplitudes. More specifically, if one starts with the idealized case of a set of degenerate levels with equal mixing matrix elements, the lowest state after mixing is described by a thoroughly mixed wave function (see Eq. 1.13) with all amplitudes identical and with the *same phase*. For the still schematic case of nondegenerate but equally spaced initial states that mix with equal matrix elements, a similar result is obtained. For the more realistic case of more or less random initial spacings but roughly comparable  $r^2 Y_{2+2}$  matrix elements (since otherwise the orbits in question would not be important in the  $\gamma$  vibration), the same qualitative feature persists. Sample diagonalizations show this. In particular, the lowest state always has its various wave function amplitudes in phase. Thus the  $B(E2:\gamma \rightarrow g)$

values will have the maximum possible collectivity consistent with this set of orbits and matrix elements.

This leads to the fifth feature—the energy systematics of the  $\gamma$ vibration—which we can again deduce qualitatively without explicit calculation. We need only refer once again to the aforementioned mixing calculations and recall that (taking for simplicity the case of  $N$  degenerate levels mixing with each other with equal matrix elements) *one state* is pushed down well below all others and that its energy lowering is  $(N - 1)V$ , where  $V$  is the mixing matrix element. Thus the  $\gamma$  vibration will be lower when there are more contributing (mixing) states. This occurs precisely when there is an abundance of Nilsson orbits near the Fermi surface with identical  $n_z$  values so that many large  $\mathbf{r}^2 \mathbf{Y}_{2,2}$  matrix elements with  $\Delta n_z = 0, \Delta \Lambda = \pm 2$  contribute.

It was shown in our earlier discussion of the Nilsson model that at the beginning of a shell, the steepest downsloping orbits have high  $n_z$  (for prolate nuclei). Since these orbit energies are so strongly correlated with the extent of the wave function in the  $z$  direction, even neighboring orbits will have different  $n_z$  values. This makes it difficult to find nearby orbit pairs with  $\Delta \Lambda = \pm 2$  and  $\Delta n_z = 0$ . Near the top of a shell, the large changes in orbit angles for different  $K$  values means that there will be fewer orbits and that they will be further apart on average. Thus, both cases only permit a few important  $\gamma$ -vibrational amplitudes. Just before midshell, however, one encounters a region where orbits with various  $n_z$  and  $\Lambda$  values congregate so that there will be more contributing  $\Delta n_z = 0, \Delta \Lambda = \pm 2$  orbit pairs, hence greater collectivity and a lower  $\gamma$ -band energy. This qualitative behavior is sketched in Fig. 9.3 (which also includes actual values calculated by Bès). These may be compared with the observed systematics shown earlier in Fig. 2.17. The similarity of both observed and calculated patterns to our simplified estimates is remarkable. (The sharp drop empirically observed in  $E_\gamma$  near  $A = 190$  is beyond this approach since it involves the onset of  $\gamma$ -softness and large  $\gamma_{\text{rms}}$  values even in the ground state.)

It is worth noting that this systematics stems from the *specific detailed microscopic* structure of the  $\gamma$  vibration. It is not simply a handwaving statement that vibrations will be lowest, and be most collective, at midshell where there are the most valence nucleons. Few of the valence nucleons actually participate. Moreover, other excitations, such as the  $\beta$  vibration (see the following), have radically different systematics.

Similar arguments can be applied to other vibrational modes such as octupole (or hexadecapole vibrations). For example, for  $K = 0^-$  octupole vibrations, the relevant operator is  $\mathbf{Y}_{3,0}$  and hence  $\Delta n_z = \pm 3, \Delta \Lambda = \pm 0$  amplitudes are critical. Being of negative parity, octupole vibrations need two orbits of opposite parity. Thus, they *must* involve the unique parity orbit, and therefore, there will not generally be as many available two-quasi-particle states that can contribute. Octupole vibrations thus tend to be rather high-lying and not very collective. They should lie lowest early in the deformed region where there are a number of  $\Delta n_z = \pm 3, \Delta K = 0$  combinations involving excitations from the high  $j$  normal parity orbits into the unique parity orbits.

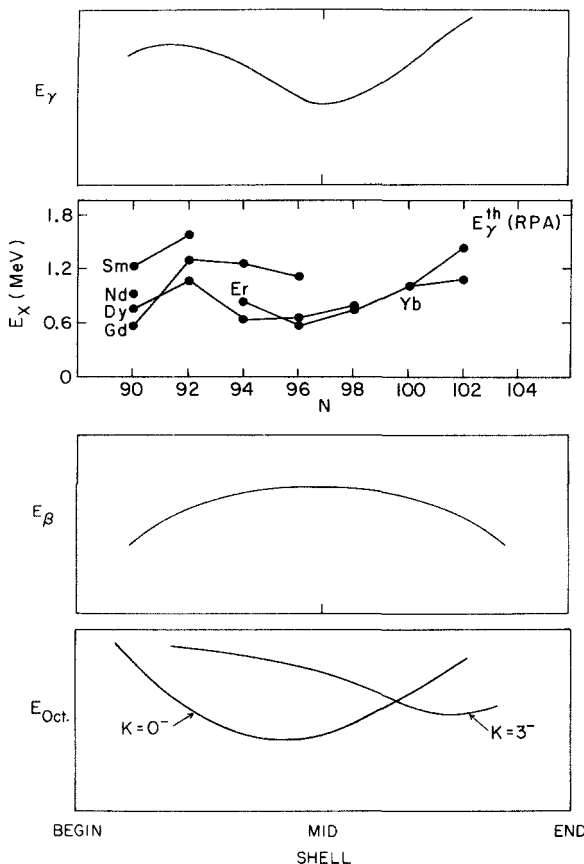


**Fig. 9.3.** Qualitative estimate of the systematics of  $\gamma$ ,  $\beta$ , and octupole vibrations across a shell. The second panel shows the actual calculations for a  $\gamma$ vibration from Bès (1965).

For neutrons in the rare earth region, for example, amplitudes such as  $1/2^-[530] \otimes 1/2^+[660]$ ,  $3/2^-[521] \otimes 3/2^+[651]$ , and  $5/2^-[512] \otimes 5/2^+[642]$  can contribute. As the shell fills, the low  $K$  unique parity orbits, whose participation is essential, begin to fill in the ground state, effectively blocking the collectivity. Thus  $K = 0, 3^-$  excitations should rise in energy. Late in the shell, the normal parity orbits are all low  $K$ , while the nearest unique parity ones are high  $K$ . Hence  $K = 0^-$  octupole excitations are inhibited. Now, however,  $K = 3^-$  octupole vibrations, with amplitudes satisfying  $\Delta n_z = 0$ ,  $\Delta \Lambda = \pm 3$  such as  $11/2^+[615] \otimes 5/2^-[512]$  or  $9/2^+[624] \otimes 3/2^-[521]$ , begin to increase in collectivity and drop in energy. Thus one expects the qualitative systematics shown in Fig. 9.3, where the  $K$  sequence of successive octupole excitations in a given nucleus is seen to change from  $K = 0^- - 3^-$  to  $K = 3^- - 0^-$  as a major shell fills. This inversion of  $K$  ordering across a shell is verified in detailed calculations by Neergaard and Vogel and confirmed by experimental systematics. It is interesting that this inversion arises from the interplay of the quadrupole (Nilsson

diagram structure) and octupole ( $\mathbf{Y}_{3\pm K}$  operators) modes. As a consequence, the locus of the lowest  $J^\pi = 3^-$  excitation (regardless of its  $K$  value) will have an undulating character. First the  $K = 0^-$  excitation drops. Then it rises, and the  $K = 3^-$  excitation drops in energy.

It is instructive to apply similar arguments to the  $\beta$  vibration. Here one encounters a different situation because of the  $K = 0$  requirement, for which the relevant operator is  $\mathbf{r}^2 \mathbf{Y}_{20}$ . This has large matrix elements only between Nilsson orbits with  $\Delta N = \pm 2$ ,  $\Delta n_z = +2$ ,  $\Delta \Lambda = 0$ . However, any  $\Delta N = 2$  matrix elements will naturally be small because of the large energy denominators. It is not surprising then that  $\beta$  vibrations are generally less collective than  $\gamma$  vibrations.

The collectivity that characterizes these states must arise from a completely different origin. It occurs as a consequence of pairing correlations according to an idea outlined in Chapter 1. The pairing interaction smooths out the Fermi surface, leading to a gradual falloff in occupation amplitudes for Nilsson orbits around the Fermi energy. Thus, the ground state consists of a linear combination of two-quasi-particle components, each with  $K = 0$  and with the two particles coupled antiparallel in the same Nilsson orbit. We then need to evaluate the matrix elements of  $\mathbf{r}^2 \mathbf{Y}_{20}$  not between two-quasi-particle (Nilsson) states but between two different linear combinations of pair wave functions. For simplicity, consider a case of just two orbits,  $a$  and  $b$ , mixed by the pairing interaction, and let the ground state and an excited  $K = 0$  state be orthogonal admixtures:

$$\psi_{g.s.} = a \phi_a + b \phi_b$$

$$\psi_{0_\beta^+} = -b \phi_a + a \phi_b$$

The calculation of  $\langle \psi_{0_\beta^+} | \mathbf{r}^2 \mathbf{Y}_{20} | \psi_{g.s.} \rangle$  is just a special case of the general result discussed in Chapter 1.<sup>18</sup> We have now

$$\begin{aligned} \langle \psi_{0_\beta^+} | \mathbf{r}^2 \mathbf{Y}_{20} | \phi_{g.s.} \rangle &= a b [\langle \phi_b | \mathbf{r}^2 \mathbf{Y}_{20} | \phi_b \rangle - \langle \phi_a | \mathbf{r}^2 \mathbf{Y}_{20} | \phi_a \rangle] \\ &\quad + (a^2 - b^2) \langle \phi_a | \mathbf{r}^2 \mathbf{Y}_{20} | \phi_b \rangle \end{aligned} \quad (9.27)$$

The last term vanishes since  $\mathbf{Y}_{2,0}$  cannot change the orbits of both particles. The first two matrix elements are just the quadrupole moments of two particles in orbits  $b$  and  $a$ , respectively. Thus,

$$\langle \psi_{0_\beta^+} | \mathbf{r}^2 \mathbf{Y}_{20} | \phi_{g.s.} \rangle = a b [Q_b - Q_a] \quad (9.28)$$

and this is small unless the orbits  $a$  and  $b$  have very different quadrupole moments.

As we have discussed, the orientation of a Nilsson orbit (and hence its quadrupole moment) is closely linked to its up- or downsloping character. For prolate nuclei, downsloping orbits are equatorial and have prolate quadrupole moments, while upsloping orbits are oblate. So  $\beta$  vibrations should be relatively collective and low-lying only in regions of the Nilsson diagram where orbits with very different slopes lie near each other. Inspection of Fig. 7.4

shows that at the beginning and end of major shells, regions of strongly up- and downsloping orbits approach each other from different shells. (The fact that they have different  $N$  values is inconsequential, since the allowed  $\mathbf{r}^2\mathbf{Y}_{20}$  matrix elements in Eqs. 9.27 and 9.28 are diagonal: they do not connect the two orbits involved.) Near midshell, there are virtually no such orbit combinations. Thus,  $\beta$  vibrations should be low in energy at the start and end of a shell and should peak (and have the lowest collectivity) near midshell. This is illustrated in Fig. 9.3 and can be compared to the empirical situation in Fig. 2.17. The qualitative agreement is reasonable.

The brief discussion of the TDA and RPA formalism in this chapter, and its application to some of the most important low-lying vibrations in medium and heavy nuclei is meant only as an introduction to the field. In practical calculations there are numerous subtleties (e.g., detailed choices of single-particle energies) and sophistications (e.g., higher-order operators,  $\mathbf{O}_y$ , than in Eqs. 9.11 and 9.12, or other related approaches involving self-consistent many-body theory). Nevertheless, the underlying physics is always similar to that outlined here. It is hoped that the present discussion will have removed some of the mystery from such calculations and indicated how simple arguments, based on the *form* (operator) for each type of vibration and the available single-particle orbits, can lead to reasonable deductions of the principle wave function components, their mass dependence, collectivity, and energy systematics.

*This page intentionally left blank*

PART IV  
EXPERIMENTAL TECHNIQUES

*This page intentionally left blank*

# 10

## A FEW SELECTED EXPERIMENTAL TECHNIQUES

The extraction of nuclear structure information from experimental observations has been implicit in much of the foregoing discussion. On numerous occasions we used the energies of certain levels, transition rates, ratios of energies, or ratios of transition rates to glean an idea of the underlying structure.

In this chapter we will briefly outline the key ideas characterizing a few experimental techniques that illustrate the rich variety of experimental tools available to elucidate nuclear structure. In no sense will the discussion be complete either for any specific technique or as a summary of all possible tools available. The choice of technique to be described is largely arbitrary, dictated in part by the information each provides, but especially by the author's experience.

We have already used single nucleon transfer reactions, such as (d, p) or (d, t), to help gain a detailed understanding of the behavior of odd-mass deformed nuclei. The use of stripping and pickup reactions to study near-closed-shell spherical nuclei actually came first. It was in such work that the concept of *spectroscopic factor* was first developed (the analogous quantity for deformed nuclei is  $C^2$ , or  $C^2 U^2$ ). We will not dwell further on these techniques, but will turn instead to a few others to show a variety of empirical approaches to nuclear structure.

The basic data needed to probe nuclear structure is extremely varied. They include nuclear masses and binding energies, level energies and  $J^\pi$  values, reaction cross sections, relative and absolute  $\gamma$ -ray transition rates, electric and magnetic moments (especially quadrupole moments),  $\beta$  decay rates, nuclear radii, and so on. Here, we will illustrate the experimental side of nuclear structure physics by brief, mostly qualitative, discussions of Coulomb excitation, "complete" spectroscopy, with emphasis on average resonance capture (ARC), and heavy ion reactions, in particular (H.I.,  $xn\gamma$ ). In each case the discussion will be elementary, aimed at introducing the basic ideas and approaches, the type of physics they provide, and the advantages and limitations of each technique. No attempt will be made to encompass the highly evolved sophistication in their current use.

### 10.1 Coulomb Excitation

This technique has, since its introduction in the 1950s, provided perhaps the most abundant source of detailed information on absolute  $\gamma$ -ray transition

probabilities, especially  $B(E2)$  values and nuclear quadrupole moments. It has thereby provided perhaps the most solid evidence for the presence, evolution, and variety of collective behavior exhibited by atomic nuclei. Without demeaning the important role of inelastic scattering techniques and direct lifetime measurements, the most salient data demonstrating the collective vibrational and rotational character of heavy nuclei certainly comes from Coulomb excitation studies. In particular, the data for the plot of  $B(E2:2_1^+ \rightarrow 0_1^+)$  values in Fig. 2.16, which so vividly pointed to collective effects away from closed shells, came predominantly from Coulomb excitation, as do nearly all of the absolute E2 transition rates connecting  $\gamma$  and ground bands in heavy nuclei shown in Fig. 2.18.

The basic aim of Coulomb excitation is to provide a well understood means of exciting atomic nuclei in a controlled manner—via a tractable, nonnuclear interaction—so that nuclear matrix elements themselves can be extracted from the data. As its name implies, Coulomb excitation involves the process of nuclear excitation solely by the electromagnetic field between an incident projectile and a target nucleus. By bombarding a target nucleus of atomic number  $Z_2$  with a projectile of atomic number  $Z_1$ , at an energy sufficiently below the repulsive Coulomb barrier between these two positively charged objects, one ensures that the projectile does not enter the target nucleus, and indeed, that its distance of closest approach is sufficiently far away that the effects of the nuclear force are negligible. (We will briefly mention a variant of this technique later where the latter condition is relaxed so as to exploit certain quantum mechanical Coulomb–nuclear interference effects.) The electromagnetic field is well understood and the process of Coulomb excitation can be calculated explicitly. The principle computational tool for this is the so-called deBoer-Winther computer code, developed in the late 1960s, which revolutionized the modern use of the Coulomb excitation techniques by allowing a simple and sufficiently accurate treatment of the complex multiple excitations that occur when the incident projectile is itself a heavy ion.

The Coulomb excitation formalism has been lucidly described in great detail in the classic paper by Alder, Bohr, Huus, Mottelson, and Winter. There is no need to repeat their derivations and formalisms here. In fact, nearly all of the key features, parameter dependencies, experimental arrangements and constraints, possibilities, and limitations of the technique can be understood and derived by a simple discussion of a few key ingredients. The main points are illustrated in Fig. 10.1, which shows two possible trajectories for a projectile (of energy  $E_p$ ) incident in the vicinity of a typical target nucleus. The figure defines a few basic quantities of importance in understanding the reaction. We start by recalling that the Coulomb interaction is given by

$$V_{\text{Coul}}(r_{12}) = \frac{Z_1 Z_2 e^2}{r_{12}}$$

where  $Z_1$  and  $Z_2$  are the projectile and target atomic numbers, and  $r_{12}$  is the time-dependent distance between target and projectile. Clearly, the probability for exciting the nucleus by this Coulomb field is related to the magnitude of  $V(r_{12})$  along the hyperbolic collision trajectory. The crucial ingredients are

## COULOMB EXCITATION

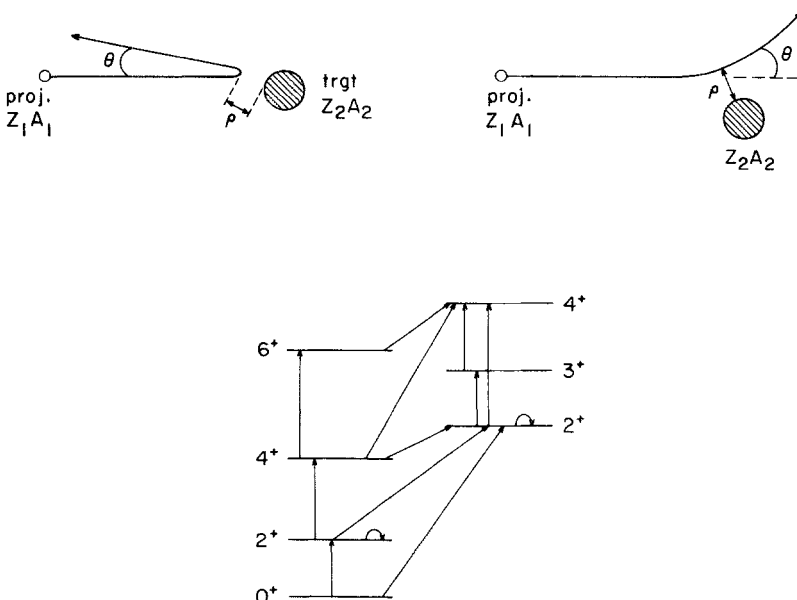


**Fig. 10.1.** (Top) Diagram of some important parameters in the Coulomb excitation process. (Bottom) Some E2 matrix elements involved in multiple Coulomb excitation.

then the product  $Z_1 Z_2$  and the sequence of values taken by  $r_{12}$ . Since most of the excitation will take place when the Coulomb field is strongest, the most important physical parameter is  $\rho$ , commonly called the *distance of closest approach*.

Clearly, the scattering angle  $\theta$  is closely connected with  $\rho$ : smaller values of  $\rho$  during the collision lead to greater Coulomb interaction strengths and therefore larger scattering angles. Conversely, the smallest distance of closest approach,  $\rho_{\min}$ , will be obtained when  $\theta \approx 180^\circ$ , and is given by

$$\rho_{\min} = \frac{2 Z_1 Z_2 e^2}{m_0 v^2}$$

where  $m$  is the reduced mass of the projectile and target.

The essence of Coulomb excitation can then be summarized as follows: for a given target nucleus, the excitation probabilities depend on  $E_p$ ,  $Z_1$ , and  $\theta$ . For a given  $\rho$ ,  $\theta$ , they will be largest for projectiles of highest atomic number ( $Z_1$ ). For a given projectile, they will be largest for the maximum energy  $E_p$  (and therefore the minimum value of  $\rho$ ), provided that  $E_p$  is well below the Coulomb barrier. In practice, projectile energies up to approximately 80% of the Coulomb barrier are used. Interestingly, Coulomb excitation has been of such importance in nuclear physics that the desirability of exploiting this dependence on  $Z_1$  and  $E_p$  in the form of higher-energy heavy-ion projectiles helped

motivate the development of more powerful Tandem Van de Graaff accelerators in the 1960s.

To further understand the Coulomb excitation process and the design of Coulomb excitation experiments, let us consider the collision process in more detail. A projectile passes near a target nucleus, and during the course of the encounter, boosts this nucleus to an excited state. In the simplest such encounter, the projectile continues along its hyperbolic path and exits the region of the target nucleus at an angle  $\theta$ . The excited target nucleus subsequently decays, nearly always by  $\gamma$ -ray emission, to lower-lying levels.

A common simplification in the treatment of Coulomb excitation data, known as the semiclassical approximation, assumes that the excitation of the target nucleus has negligible effect on the hyperbolic orbit of the projectile. In most cases, this is reasonable, since typical excitation energies produced in Coulomb excitation are less than 1 MeV, whereas typical projectiles are massive heavy ions such as  $^{16}\text{O}$ ,  $^{32}\text{S}$ , and heavier species, with energies ranging upwards of 50 MeV. The validity of this approximation is embodied in the parameter  $\eta$  defined as:

$$\eta = \frac{Z_1 Z_2 e^2}{\hbar v} \approx \frac{Z_1 Z_2 A_1^{1/2}}{6.32 E_p^{1/2} (\text{MeV})}$$

The semiclassical approximation is valid if  $\eta \gg 1$ . This condition is satisfied for most cases of practical interest. For example, for 60 MeV  $^{16}\text{O}$  ions incident on  $^{150}\text{Sm}$ ,  $\eta = 40.5$ .

Another important concept in the Coulomb excitation process is the excitation energy  $\Delta E$  imparted to the target. For a given projectile,  $E_p$ ,  $\theta$ ,  $\rho_{\min}$ , it is not surprising that the cross section drops rapidly with increasing  $\Delta E$ . This dependence is embodied in the parameter  $\xi$  defined as the difference in incoming and outgoing  $\eta$  values,  $\eta_i$ ,  $\eta_f$ . For small  $\Delta E$  ( $\Delta E/E_p \ll 1$ )

$$\xi = \frac{Z_1 Z_2 A_1^{1/2} \Delta E}{12.65 E_p^{3/2}} = \frac{\eta_f \Delta E}{2 E_p} \ll \eta$$

Since  $\Delta E/E_p$  is typically  $\approx 10^{-2}$ ,  $\xi$  typically ranges from 0 to 1.

The cross section for single step E2 Coulomb excitation can then be written

$$\frac{d\sigma}{d\theta} = \frac{Z_1^2 e^2}{\hbar v \rho^2} B(E2:i \rightarrow f) df(\theta, \xi)$$

where  $df(\theta, \xi)$  arises from an integral over the orbit of the projectile along the classical trajectory. This expression embodies our previous comments. The cross section increases as the distance of closest approach of the projectile decreases, or as its charge increases. It also increases with increasing  $E_p$ : the  $1/v$  factor is more than compensated by large  $df(\theta, \xi)$  values for small  $\xi$  (large  $E_p$ ) as we will discuss next. The  $df(\theta, \xi)$  factor contains a  $\sin^4 \theta/2$  dependence representing the underlying classical Rutherford scattering. (Often, Coulomb excitation yields are given as a ratio to Rutherford scattering, removing this strong dependence.) More importantly,  $df(\theta, \xi)$  decreases exponentially with  $\xi$ . For large  $\eta$ , the integral of  $df(\theta, \xi)$  over  $\theta$  drops by a factor of 3 as  $\xi$  goes

from 0 to 0.5 and by a factor of 10 as  $\xi$  goes from 0.5 to 1.0. In our example of 60 MeV  $^{16}\text{O}$  ions on  $^{150}\text{Sm}$ , these three  $\xi$  values correspond to excitation energies of 0, 1.5, and 3.0 MeV, respectively. Clearly, Coulomb excitation is a tool for exciting low-lying states!

The preceding discussion implicitly assumed a single-step Coulomb excitation process. There is no inherent reason, however, why multiple excitations cannot occur during the collision process. Such multiple Coulomb excitation is actually very common with heavy ion projectiles. The idea is illustrated in Fig. 10.1 (bottom). It is convenient to view this as a sequential process in which the target is excited first to one level, then subsequently to another. However, recognizing the extremely short collision times involved ( $\approx 10^{-22}$  seconds) the uncertainty principle  $\Delta t \Delta E > \hbar$  implies a large uncertainty in the system energy during the collision. This permits the process of "virtual" excitation over short time periods during which the conservation of energy is not required. Since the probability of direct Coulomb excitation decreases exponentially with excitation energy while virtual excitation decreases roughly linearly, it turns out that the virtual excitation process is dominant in most multiple Coulomb excitation situations. While high-lying states can be virtually excited during the collisions, the range of final excitation energies produced is governed by an exponential behavior. Nevertheless, the presence of virtual excitation both offers an opportunity to excite levels not otherwise accessible and imposes a complexity on the resulting analysis because the extraction of nuclear matrix elements from Coulomb excitation data ultimately involves solving a set of simultaneous equations that involve all matrix elements (and their generally unknown relative signs) that connect all levels involved, virtually or otherwise, in the excitation process.

The solution of these equations can be greatly facilitated by certain experimental tactics. One of these is based on the recognition that the only direction fixed in space in a Coulomb excitation collision is that provided by the incident beam direction. By conservation of momentum, those excitation processes in which the projectile is scattered backwards at  $180^\circ$  can involve no transverse momentum transfer to the target nucleus and, therefore, only the  $m = 0$  magnetic substates of the final nuclear levels are excited. This immediately reduces the number of simultaneous equations to be solved by a factor on the order of  $(2J+1)^2$ , where  $J$  is the average spin of the levels excited in the target nucleus.

This quantum mechanical constraint can be imposed experimentally by detecting the de-excitation  $\gamma$ -rays in coincidence with back scattered projectiles. Excitation of  $m \neq 0$  substates increases slowly for  $\theta < 180^\circ$ , so that in practice, one measures the backscattered particles at angle, ranging from  $160^\circ$  to  $175^\circ$ . This technique uses annular detectors in which the incident beam passes through a central hole and the backscattered particles are recorded in the back angle annulus. Coincidence with backscattered particles has another advantage: it preferentially selects those collisions with high excitation probabilities ( $\rho$  small), thereby enhancing yields and leading to increased multiple excitation so that  $B(E2)$  values for higher-lying states can be measured.

There is another aspect of the fact that the incident beam defines a direction in space. De-excitation  $\gamma$ -rays have a particular angular distribution. In principle, one should measure the yields at a series of angles and integrate over angle. However, since virtually all Coulomb excitation proceeds by E2 excitation (these are the strongest matrix elements connecting low-lying states), any angular distribution involved can only include Legendre polynomials  $P_l(\cos\theta)$  of order 0, 2, and 4. Moreover, the coefficient of the quartic term is small in most cases. Therefore, many Coulomb excitation experiments are performed with the  $\gamma$ -ray detectors situated at  $55^\circ$  relative to the beam axis since, at this angle,  $P_2$  also vanishes, making the yields nearly identical to those obtained by integrating over all angles.

Another simplification exploits the  $Z_1$  and  $E_{\text{proj}}$  dependence of Coulomb excitation cross sections by carrying out a sequence of experiments starting with light, low-energy projectiles. Typically, in even-even nuclei, Coulomb excitation by protons or  $\alpha$ -particles excites only the first level or the first couple of levels. It is easy to extract the nuclear matrix elements for these. Indeed, it was in the early days of Coulomb excitation, when only these projectiles were available, that many  $B(E2; 2^+_1 \rightarrow 0^+_1)$  values were first determined. With these matrix elements in hand, a second experiment is performed, using a heavier, and/or more energetic, projectile to excite the next set of levels. This process continues until all of the matrix elements are deduced sequentially. Most Coulomb excitation studies of heavy nuclei have been carried out in this manner. In recent years, however, the development of sophisticated search algorithms in conjunction with the deBoer-Winther code has led to the possibility of simultaneously fitting an extensive set of Coulomb excitation measurements made with high energy, heavy ion projectiles to extract a reasonably unique and consistent set of matrix elements.

Thus far we have discussed experiments in which the presence of Coulomb excitation is indicated by the observation of de-excitation  $\gamma$ -rays. This is the most common approach. It is hampered, however, by a built in ambiguity: one does not generally know what fraction of each level's population (which is deduced from the number of detected  $\gamma$ -rays de-exciting that level) resulted from direct excitations and from the decay of higher-lying levels. The detection of the outgoing, scattered projectile gives the number of excitations of each level directly. Although the energy resolution of typical particle detectors, or the poor efficiency of high resolution magnetic spectrometers, hampers the use of this technique, it is often a valuable tool. It also leads to an alternative to the preceding step-by-step approach to unravelling the E2 matrix elements. In the traditional approach just described, this is achieved by choosing the experimental conditions ( $Z_1$  and  $E_p$ ) so that  $\rho_{\min}$  attains different values sequentially, the smallest corresponding to the most complex excitation processes. From Fig. 10.1 it is clear that this can also be obtained with a *single* projectile and fixed energy, simply by varying the angle  $\theta$  at which the scattered projectile is detected. With the use of multiple particle detectors positioned at different scattering angles, such a program can be carried out in a single experiment, thus saving valuable running time and assuring identical experimental conditions for each angle measured. The cost is that, for most angles, the full set of magnetic substates must be included in the calculation.

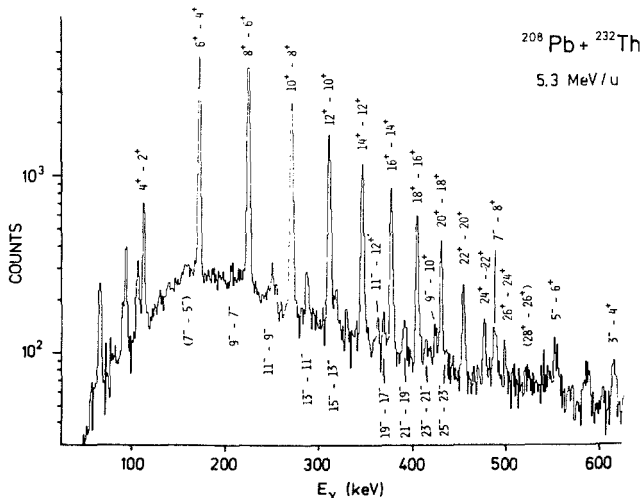
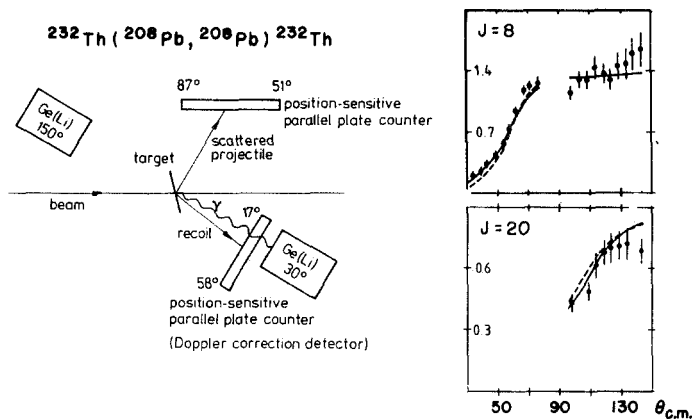
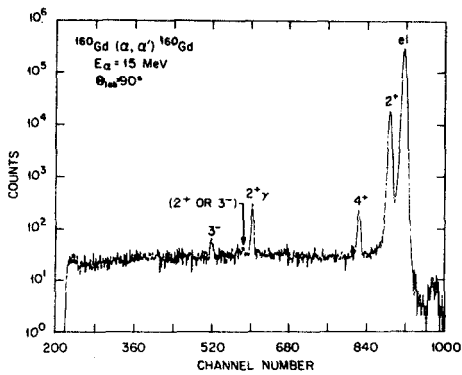


**Fig. 10.2.** Data from two Coulomb excitation experiments. (Top)  $\alpha$ -induced excitation of  $^{160}\text{Gd}$  (Ronningen, 1977). (Bottom) Excitation of  $^{232}\text{Th}$  by  $^{208}\text{Pb}$  ions (Ower, 1982). The diagram shows the experimental arrangement (see text). The spectrum at bottom illustrates the relative yields of different  $\gamma$ -rays while the boxes at the right give the population of two spin states as a function of  $\theta$ . Note that the higher spin level is not seen at forward angles and is also much weaker at back angles although, as expected, its yield increases faster with  $\theta$  than the  $J = 8$  level.

A final criterion that controls the choice of many of the projectiles used in Coulomb excitation is that one generally wants to avoid projectile excitation itself. Figure 10.1 is drawn in the laboratory system, but in the center of mass system, it is impossible to distinguish projectile and target. One therefore usually chooses projectiles that have very high-lying first excited states, generally magic or doubly magic nuclei such as  $\alpha$  particles,  $^{16}\text{O}$  or  $^{208}\text{Pb}$ . Sometimes it is more convenient to reverse the kinematic conditions and use the nucleus conceptually considered to be the target as a projectile. This is useful when the appropriate projectiles are not available, but it is also used, by choice, because of the different scattering angles then obtained in the laboratory system. For example, by using a Pb projectile on a Mg target, all yields will be in the forward direction. In some cases such reversed kinematics can be advantageous.

To obtain a concrete feeling for Coulomb excitation spectra, it is useful to inspect the two examples shown in Fig. 10.2. The top one nicely illustrates low energy,  $\alpha$  induced, Coulomb excitation with detection of the inelastically scattered projectiles. The strongest peak corresponds to elastic scattering. The  $2^+$  and  $4^+$  members of the ground band are also strong. The excitation probabilities fall off very rapidly as more excitation steps are required and the  $6^+, 8^+, \dots$  states are not seen. Weaker, higher-lying peaks correspond to the vibrational levels,  $2^+$ , and  $3^-$ . The former is much stronger because there are two excitation routes and because it involves E2 rather than E3 excitation. Also note that Coulomb excitation is almost always limited to natural parity states [ $\pi = (-1)^l$  such as  $0^+, 2^+, 4^+, 3^-$ , but not  $1^+$  or  $3^+$ ] simply because of the angular momentum conservation rules. This is rigorous in a single-step process and nearly always characterizes multiple Coulomb excitation yields also.

The lower part of Fig. 10.2 shows the experimental set up for  $^{208}\text{Pb}$  induced Coulomb excitation of  $^{232}\text{Th}$ . Such massive projectiles impart considerable recoil to the target leading to Doppler shifts in the  $\gamma$ -ray energies that depend on the angle of recoil. The "Doppler" detector tags a specific angle. The typical Ge(Li)  $\gamma$ -ray spectrum shown demonstrates the ability to populate high ground band and even side band states ( $\pi = -$ , here). (The  $2^+ \rightarrow 0^+$  and  $4^+ \rightarrow 2^+$   $\gamma$ -ray transitions are actually the strongest in this reaction; their weakness in the spectrum is due to the fact they are highly converted.) Figure 10.2 includes typical yields as a function of the angle of the scattered projectile. Note the strong increase with  $\theta$  corresponding to smaller impact parameters  $\rho$ .

To understand multiple excitation more thoroughly, let us consider the excitation of the  $2^+$  band in Fig. 10.1. Even for relatively light projectiles there are two possible excitation routes, a direct one from the ground state and a double excitation via the  $2^+_1$  state. In typical experimental conditions in which backscattered particles are selected, the probability of exciting the  $2^+_1$  state may well be greater than 50 percent per detected backscattered particle. In rotational nuclei, the Coulomb excitation matrix elements,  $\langle 2^+_1 | E2 | 2^+ \rangle$  and  $\langle 2^+_1 | E2 | 0^+ \rangle$ , are simply related by Clebsch-Gordon coefficients. The latter is slightly larger. However, it also involves a larger  $\Delta E$  than the step linking the

$2^+_1$  and  $2^+_\gamma$  levels. Therefore, in typical deformed nuclei, these two excitation routes,  $0^+_1 \rightarrow 2^+_1 \rightarrow 2^+_\gamma$  and  $0^+_1 \rightarrow 2^+_\gamma$ , may well be comparable. Since they interfere coherently, and since that interference may be either constructive or destructive, depending on the relative signs of the matrix elements, the net yield of the  $2^+_\gamma$  level can vary from almost vanishing to several times the yield obtained for the direct route alone. The measurement of the excitation probabilities for this level can then directly yield even the signs of these nuclear matrix elements. This is especially true if the measurements are done at several different beam energies, since the individual excitation routes have a different dependence on beam energy. The signs of such matrix elements can provide critical tests of certain nuclear models.

A second application of the multiple excitation process involves the recognition that one kind of two-step excitation involves not an excitation from one level to another, but a change from one magnetic substate of a single level to another magnetic substate. This is also depicted in Fig. 10.1 for a couple of states. Recalling that each step in a Coulomb excitation process involves a matrix element connecting the initial and final levels, it is clear that this step will involve the quadrupole moment,  $\langle 2^+_1 | E2 | 2^+_1 \rangle$ , of the level. If one measures the  $B(E2:0^+_1 \rightarrow 2^+_1)$  value sufficiently accurately (typically within one percent), it is possible to extract the  $2^+_1$  quadrupole moment, including its sign. In a few cases this technique, known as the reorientation effect, has even been applied to the measurement of quadrupole moments of higher excited states such as the  $2^+_\gamma$  level.

There are other ways of obtaining the same information, such as the use of Coulomb-nuclear interference effects, which we will discuss in a moment, as well as muonic atom studies. While there has not always been agreement between the quadrupole moments extracted from these different approaches, the use of Coulomb excitation remains a standard technique.

Some nuclei are now known to display not only quadrupole but hexadecapole deformations— $\beta_4$  or  $\epsilon_4$  shape components—as well. These were discussed in connection with the Coriolis mixing of unique parity levels in odd mass nuclei in Chapter 8. Typical hexadecapole shapes were shown in Fig. 6.10. Such shape components are also of interest in evaluating the role of g bosons in the IBA (see Chapter 6). Once again, if the E2 matrix elements are all well determined from previous Coulomb excitation experiments, the discrepancies in the yields of certain states, for example the  $4^+$  level, can be attributed to direct E4 excitation and the relevant E4 transition moments determined. It is largely from such data that the systematics (Fig. 8.10) of hexadecapole deformations throughout deformed nuclei, both in the rare earth and actinide regions, has been mapped out.

Occasionally it is useful to bridge the gap between Coulomb excitation and nuclear inelastic scattering by using projectile energies close to the Coulomb barrier. In this technique, the scattering cross sections contain both Coulomb and nuclear amplitudes, and more importantly, an interference term between them. It has been shown that this interference term is very sensitive to the magnitude of the quadrupole moment of, for example, the  $2^+_1$  state. This is

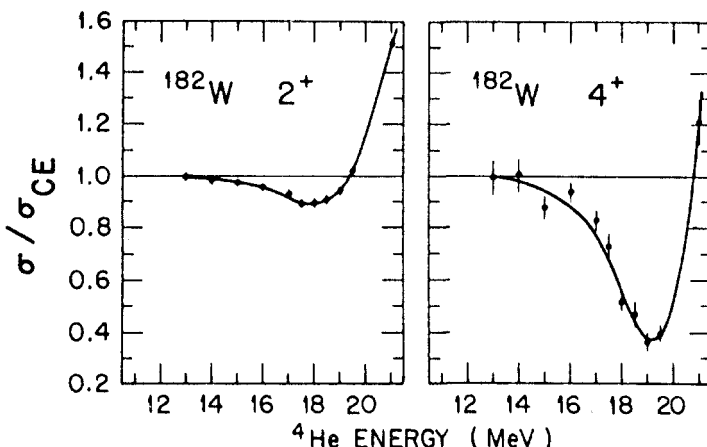


**Fig. 10.3.** Coulomb/nuclear interference effects in  $\alpha$ scattering near the Coulomb barrier (Bemis, 1973).

illustrated in Fig. 10.3, which shows the excitation cross sections for the  $2^+_1$  and  $4^+_1$  levels divided by the pure Coulomb excitation cross sections. Deviations from unity represent the effect of the Coulomb/nuclear interference. This technique has been applied to many nuclei, in particular those in the W region. The measured yields can also give hexadecapole shape components because of the large interference effects for  $4^+$  levels.

Until recently, Coulomb excitation experiments were carried out almost exclusively below or at the Coulomb barrier. The reasoning was that interference with direct or compound nuclear reactions would obscure the simplicity of the technique. However, the increase of Coulomb excitation amplitudes with projectile energy is not vitiated by competition with other processes. And higher incident energies can provide access to higher-lying excitations. This point has recently been exploited in very high-energy Coulomb excitation studies of collective states, such as giant resonances (single or multiple) where other excitation amplitudes are small. A technique thought by some to have already witnessed its greatest popularity is thus being rejuvenated.

## 10.2 Spectroscopically Complete Techniques

### $(n, \gamma)$

The  $(n, \gamma)$  reaction has been used for several decades to elucidate nuclear structure. It has some severe limitations and some powerful advantages. Its primary attribute is *nonselectivity*, which makes it complementary to selective processes such as Coulomb excitation or transfer reactions. In certain forms, such as *average resonance capture* (ARC), the  $(n, \gamma)$  reaction is actually designed to be *completely* nonselective and to provide an *a priori* guarantee of disclosing *all* states in certain spins and excitation energy ranges. The basic idea of the  $(n, \gamma)$  reaction can be seen in Fig. 10.4 (left). An incident low-energy

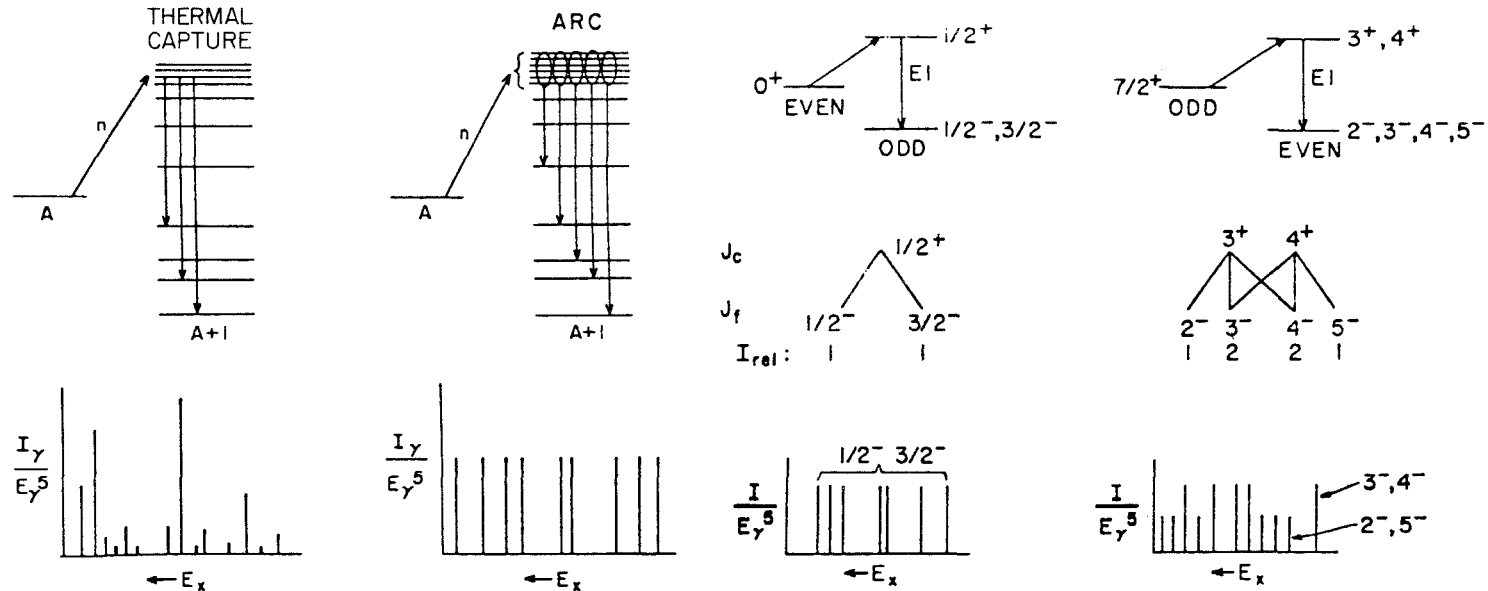


Fig. 10.4. (Left) Schematic illustration of the difference between thermal neutron capture and ARC. (Right) Examples of the spin values and relative averaged intensities available in the ARC process on even- and odd-mass targets.

neutron impinges on a target nucleus (of mass  $A$ ) and is captured, forming a compound nucleus of mass  $A+1$  at an excitation energy (neglecting recoil)  $E_c = S(n) + E_n$  where  $S(n)$  is the neutron separation energy. This rather high-lying, low-spin compound nuclear capture state is extremely complex and its decay, governed by that complexity, is largely statistical. The capture state de-excites either by relatively high-energy "primary" transitions that directly feed low-lying states or by a myriad of different cascade routes passing through the high density of levels that occur between  $\approx 2$  MeV and the neutron binding energy. In either case, low-lying levels are finally populated: they decay by discrete "secondary" transitions. With few exceptions, the distribution of primary transition intensities can be described statistically in terms of a so-called Porter-Thomas distribution with one degree of freedom. This is a broad distribution, characterized by a most probable intensity of zero. Thus, while each primary transition immediately discloses a specific low-lying level, little or no nuclear structure information can be deduced, and moreover, many primary transitions will be too weak to be observed. Owing to the multipole decomposition of the radiation field, the dominant primary transitions are nearly always  $E1$  in nature.  $M1$  transitions are nearly an order of magnitude weaker and other multipolarities are almost never observed. Therefore, primary transitions can be useful in immediately giving certain spin parity limitations.

Most neutron capture experiments are carried out at thermal neutron energy ( $E_n \approx 0.025$  eV), where  $s$  wave capture is totally dominant. For most nuclei,  $S(n) = 5$  to  $8$  MeV, and the level density is extraordinarily high so that level spacings of capture states are typically in the few eV range. If one of these levels happens to coincide with  $E_c$ , the thermal capture cross section will be very large. Usually, however, it will be much smaller, arising from a sum over the tails of several nearby levels. This difficulty can sometimes be avoided by "tuning" the neutron energy (e.g., by Bragg diffraction) to a "resonance" so that  $E_c$  coincides with a level of appropriate spin. Since level energies at capture state energies are statistically distributed, such a process usually selects a particular isotope as well, thus eliminating the need for enriched targets. On the other hand, such epithermal neutron fluxes are normally orders of magnitude weaker than at thermal energies.

The obvious disadvantage of either thermal or resonant energy neutron capture is the enormously wide distribution of primary transition intensities and the fact that, in general, no nuclear structure information is obtainable from them other than pinpointing the existence and energies of specific levels and giving certain limitations on their spins. A technique developed in the early 1970s and utilized frequently in the last decade is an extension of resonance neutron capture that avoids many of its disadvantages while having the unique property of providing the possibility of an *a priori* guarantee of observing all levels in certain spin and excitation energy ranges. This is the so-called average resonance capture (ARC) process. The idea is extremely simple, as is illustrated in Fig. 10.4 (left). Suppose one carries out a sequence of resonance capture experiments with steadily increasing neutron energies,

sequentially populating, say, 50 to 100 individual resonances, and then sums all the spectra so obtained. The statistical Porter Thomas distributions of each resonance would then be nearly completely averaged out and all states of a given final spin would be populated with nearly the same summed intensity. Such an approach, although conceptually appealing, is clearly tedious and time consuming. An alternative that achieves the same end automatically is to use a beam of neutrons that has been rendered specifically *non*-monoenergetic. This can be achieved by passing a reactor neutron beam through certain filter materials, notably scandium and  $^{56}\text{Fe}$ , which have minima in their neutron scattering cross sections near 2 keV and 24 keV, respectively. Having passed through such materials, a reactor neutron beam will have an energy centered around 2 or 24 keV with a FWHM (typically 1 to 2 keV) determined by the thickness of the filter material. The FWHM must be sufficiently broad so that a large number ( $N_r$ ) of resonances are simultaneously populated, but not so broad that it degrades the energy resolution of the primary  $\gamma$ -ray transitions following capture. The width of these lines is a convolution of the detector (usually Ge) resolution (typically  $\approx$  5 to 6 keV at 6 MeV) with the energy width of the incident neutron beam.

To illustrate the process more concretely, consider a typical deformed even-even target nucleus. Since the ground state is  $0^+$  and 2 keV neutrons are predominantly *s* wave, the capture state will be  $J = 1/2^+$ . For nuclei such as  $^{155}\text{Sm}$ ,  $^{167}\text{Er}$ ,  $^{183}\text{W}$ , the level spacing of  $1/2^+$  states at 1 MeV is  $\approx$  10 eV. Therefore, a 2 keV neutron beam with 1 keV FWHM will populate  $\approx$  100 resonances. The fluctuations in the combined Porter Thomas distribution go approximately as  $2/\sqrt{N_r}$ . Therefore, instead of orders of magnitude variations in primary transition intensities, the fluctuations in the ARC spectrum intensities will be  $\pm 2/\sqrt{100} = \pm 20\%$ . (Actually, this variance refers to the reduced intensities, defined as  $I/E^5$ , since it is necessary to remove a secular energy dependence.) If we consider just E1 primary transitions (they dominate M1 transitions by a factor of  $\approx$  6), the final states will be  $1/2^-$ ,  $3/2^-$  (Fig. 10.4, right).

When the target is odd mass, there are two possible capture state spins. Each will decay by E1 (and weaker M1, which we ignore) primary transitions. In the simplest approximation, neglecting a spin dependence of the level density near the neutron separation energy, both of these spins contribute equally. Thus, as illustrated in Fig. 10.4 (right), the relative reduced intensities will fall into two groups differing by a factor of  $\approx$  2. An ARC spectrum was shown for  $^{196}\text{Pt}$  in Fig. 5.8. The  $^{195}\text{Pt}$  target has  $J^\pi = 1/2^-$ , so that the (*s*-wave) capture state is  $J_c = 0^-, 1^-$ . Decay of the  $1^-$  levels by E1 transitions lead to  $0^+$ ,  $1^+$ , and  $2^+$  states. The  $0^-$  level only feeds  $1^+$  levels. Final states with  $J^\pi = 1^+$  should thus be twice as intense as  $0^+$ ,  $2^+$  levels. Of course, as we have seen in many models, low-lying  $1^+$  states are very rare. So, in practice, we expect rather uniform intensities. The good averaging in Fig. 5.8 is immediately apparent, especially when contrasted with typical intensity fluctuations of one to two orders of magnitude in thermal capture experiments.

The preceding examples correspond to 2 keV ARC measurements where *s* wave capture still dominates. At 24 keV, both *s* and *p* wave components are

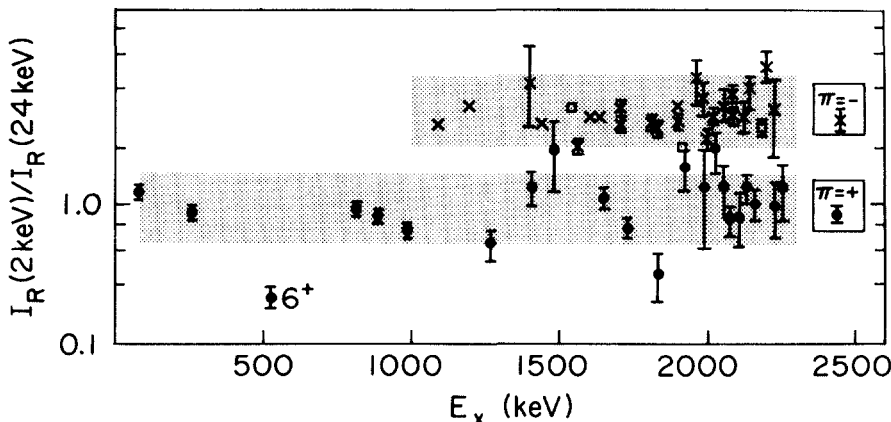
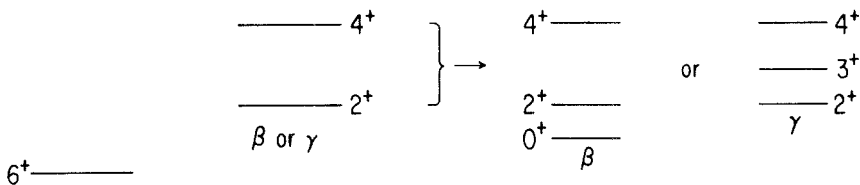


**Fig. 10.5.** Ratio of reduced primary intensities in ARC at 2 and 24 keV in  $^{168}\text{Er}$ , for states of known parity (Davidson, 1981).

roughly comparable and a wider range of final  $J^\pi$  values becomes accessible. The ratio of reduced ARC intensities at 2 and 24 keV provides a nearly ideal parity meter for the final states. An example is shown in Fig. 10.5.

The limitation on excitation energies accessible in ARC stems from two sources. First, with increasing  $E_x$ , the level density increases, which may make it impossible to resolve individual levels. At first this is not a serious problem since an unresolved pair of levels appears in the spectrum as a single peak of twice the area and is therefore readily identified. At higher excitation energies, however, and especially in odd-odd nuclei, the probability of missed levels rapidly increases. Second, and more importantly, the secular decrease of the observed reduced intensities  $I_\gamma$  (recall, it is the quantity  $I_\gamma/E_\gamma$  <sup>5</sup> that is constant) eventually leads to a point at which they can no longer be safely detected above the background.

It is important to realize the consequences of the ARC-based *guarantee of completeness*. It is not simply a question of finding an additional level or two beyond that obtainable with other techniques. Its most profound importance lies not so much in finding all levels (of certain  $J^\pi$  and  $E_x$  ranges), but in *knowing* that one has found all levels. This rather subtle point is best discussed by two illustrative examples. Consider the imaginary level scheme shown on the top in Fig. 10.6 and suppose that the ARC process populates levels with spins  $2^+$ ,  $3^+$ ,  $4^+$  via E1 primary transitions. The figure clearly depicts a deformed rotational nucleus with an excited vibrational band containing at least  $2^+$  and  $4^+$  levels. However, the figure is ambiguous as to whether this is a  $\gamma$  band with an undetected  $3^+$  state or a  $\beta$  band with undetected  $0^+$  state. Even though  $0^+$  states are not accessible to the ARC process in our example, this question can be unambiguously decided. If the ARC data discloses a  $3^+$  level between the  $2^+$  and  $4^+$  states, then the band is clearly a  $\gamma$  vibrational excitation. Equally certain, if no such  $3^+$  level is detected, there must be an undetected lower-lying  $0^+$  level below the  $2^+$  state. (Only  $K^\pi = 0^+$  bands have a spin sequence  $0^+, 2^+$ ,



$4^+$  —————

$2^+$  —————  
 $0^+$  —————  
g

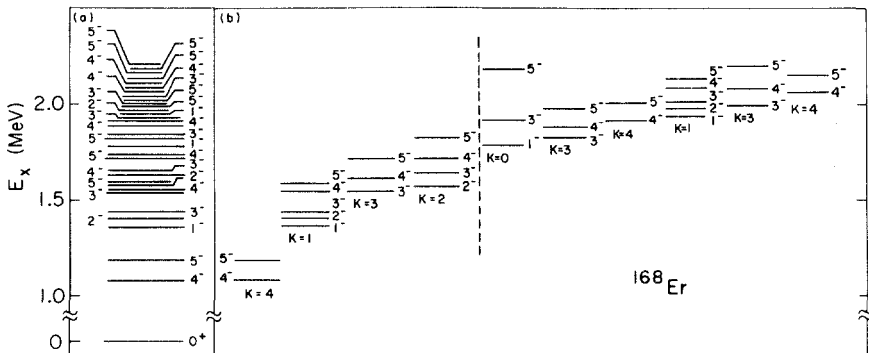


**Fig. 10.6.** Examples of “completeness” arguments using ARC. (Bottom left) All  $\pi = -$  levels in  $^{168}\text{Er}$ ; (Bottom right) Arrangement into rotational bands. The numbers of bands of each  $K$  value above  $\sim 1700$  keV (right of dashed line) are discussed in the text.

$4^+, \dots)$  In this case, an ARC experiment identifies a particular vibrational structure and points to an unobserved lower lying level simply by the nonobservation of *another* level. This process of obtaining information by nonobservation is unique to completely nonselective processes.

Another common situation concerns levels with several existing  $J^\pi$  possibilities, say  $1/2^-$ ,  $3/2^-$ ,  $5/2^-$ , in an odd mass nucleus. ARC at 2 keV (*s*-wave) will populate only (and all)  $1/2^-$  and  $3/2^-$  levels. Therefore, if the level in question is undetected, its spin can unambiguously be assigned as  $5/2^-$ . Again, one has an example of spin assignment by nonobservation.

The completeness inherent in the ARC technique can also provide important nuclear *structure* information, even though the process itself gives no direct information on nuclear matrix elements. An example concerns the higher-lying negative parity states in the well-deformed nucleus  $^{168}\text{Er}$ . Here, the lowest negative parity states were already known and assigned to rota-

**Table 10.1.**  $^{168}\text{Er}$ . Numbers of negative-parity states and deduced rotational band structures†

Number of observed states	$J^\pi$				
	1 <sup>-</sup> 2	2 <sup>-</sup> 1	3 <sup>-</sup> 4	4 <sup>-</sup> 5	5 <sup>-</sup> 6
Unique allocation of these to rotational bands					
one $K^\pi = 0^-$ band	1	—	1	—	1
one $K^\pi = 1^-$ band	1	1	1	1	1
two $K^\pi = 3^-$ bands	—	—	2	2	2
two $K^\pi = 4^-$ bands	—	—	—	2	2

†The tabulation includes all negative-parity levels with spins from 1<sup>-</sup> to 5<sup>-</sup> above 1780 keV not already allocated to rotational bands with band-heads below 1570 keV.

\*Davidson, 1981

tional bands. Between 1400 and 2000 keV, an ARC measurement disclosed the set of negative parity states shown on the left in the lower part of Fig. 10.6. The  $^{167}\text{Er}$  ground state is  $7/2^+$ , so the capture spins are  $3^+, 4^+$ ; therefore E1(M1) primary transitions following  $s$  and  $p$  wave ARC populate all 1<sup>-</sup>–5<sup>-</sup> levels (up to 2 MeV) and distinguish the 2<sup>-</sup>, 5<sup>-</sup> group from 3<sup>-</sup>, 4<sup>-</sup> states from the factor of two difference in reduced intensities. Combined with other data, a full set of unambiguous  $J^\pi$  assignments was made, but no structural information about these states was known. However, given just the *knowledge* that this set of negative parity states is complete, one can not only deduce the number of rotational bands present, but their precise  $K$  values and the number of levels of spin 0<sup>-</sup>, without having observed them. The idea is illustrated in Table 10.1. The top gives the number of levels of each  $J$ . The key point is that the number of 5<sup>-</sup> levels is one greater than the number of 4<sup>-</sup> states. There are only two ways to produce a 5<sup>-</sup> state without an accompanying 4<sup>-</sup> level, either in a  $K^\pi = 0^-$  band with levels 1<sup>-</sup>, 3<sup>-</sup>, 5<sup>-</sup>, or in a  $K^\pi = 5^-$  band with levels 5<sup>-</sup>, 6<sup>-</sup>, 7<sup>-</sup>, .... It is easy to rule out the latter. There are two 1<sup>-</sup> levels and only one 2<sup>-</sup> level. Again, the only way this can occur is if there is a  $K^\pi = 0^-$  band. Thus there cannot be a  $K^\pi = 5^-$  band. Having established that there is one  $K = 0^-$  band, we have accounted for one 1<sup>-</sup>, one 3<sup>-</sup>, and one 5<sup>-</sup> state. Since there are two 1<sup>-</sup> levels and only one  $K^\pi = 0^-$  band, the other 1<sup>-</sup> state must be the bandhead of a  $K^\pi = 1^-$  band. This accounts for one each of the 1<sup>-</sup>, 2<sup>-</sup>, 3<sup>-</sup>, 4<sup>-</sup>, and 5<sup>-</sup> levels, and thereby exhausts the 1<sup>-</sup> and 2<sup>-</sup> levels but leaves two 3<sup>-</sup> levels unaccounted for. Each of these must be  $K^\pi = 3^-$  bandheads that account for two additional 4<sup>-</sup> and 5<sup>-</sup> levels. There are still two levels of each of these spins unaccounted for, and thus there must also be two  $K^\pi = 4^-$  bands.

This now accounts for all of the states disclosed in the ARC measurement. We have deduced the exact number of negative parity rotational bands and their  $K$  values, and the fact that there is only one 0<sup>-</sup> band and no  $K = 5$  bands below 2 MeV in  $^{168}\text{Er}$ . And we have deduced all this without assigning a single state to a single rotational band, attempting to fit any of them into specific rotational energy patterns, or inspecting their  $\gamma$ -ray decay. The key was the *knowledge* that the set of levels was complete. Some other experiment that

disclosed the same set of levels without providing this knowledge could not have led to the same analysis.

### Completeness with $(\alpha, xny)$ Reactions and Extremely High Resolution $\gamma$ -ray Spectroscopy

Other techniques besides ARC can provide near guarantees of completeness. Examples that have been well documented are the  $(n, n')$  reaction, the  $(\alpha, xny)$  reaction, and the  $(n, \gamma)$  reaction where one detects the low-energy, secondary transitions. In all these cases the completeness is virtually assured, although the method by which this occurs does not provide a specific guarantee. In each of these reactions, the  $\gamma$ -ray cascade from the initial formation state passes through so many routes down to the lower-lying levels that the population of the latter is effectively averaged out. Then, if one detects the secondary  $\gamma$ -rays connecting these states and fits these  $\gamma$ -rays into a level scheme using the Ritz combination principle, perhaps accompanied by information from  $\gamma$ - $\gamma$  coincidence data, one is nearly assured of locating all levels. This has been demonstrated in many important experiments. However, note that there is a conceptual difference between these cases and the ARC situation. In the latter, the levels are populated directly and the measurement itself discloses their existence. In these other cases, the existence of specific low-lying levels must be deduced indirectly by building a level scheme through Ritz combinations. It is possible to miss a state in this process if, for example, it decays solely by one  $\gamma$ -ray to the ground state and is not observed to be fed by a discrete transition from above. There would then be neither identifying coincidence relations nor Ritz combinations. Nevertheless, such a case is rare, and these reactions have been used to obtain essentially complete level schemes.

The uniformity of population is exemplified by the  $^{123}\text{Te}(\alpha, ny)^{126}\text{Xe}$  reaction in Fig. 10.7, where the final level populations from side-feeding  $\gamma$ -rays are plotted against  $E_\alpha$  for  $J_{\text{final}} = 4$  and 6. The smooth behavior and the clear correlations with excitation energy demonstrates the unlikelihood of missing a particular level. Moreover, the excitation functions show a difference in shape for the two  $J_{\text{final}}$  values. Such a dependence is systematic and allows one to assign final state spins. A typical level scheme from  $(\alpha, ny)$  is shown in Fig. 10.8. The richness is readily apparent, as is the wide range of spins accessible. In comparison with  $(n, \gamma)$  and the (Heavy ion,  $xny$ ) reactions to be discussed,  $(\alpha, xny)$  occupies an intermediate niche with a wider spin range than  $(n, \gamma)$  and access to more states of a given spin than heavy ion reactions.

We have mentioned the study of secondary  $\gamma$ -rays with the  $(n, \gamma)$  reaction. Such experiments encompass all the standard techniques of  $\gamma$ -ray spectroscopy including the measurement of  $\gamma$ -ray energies and intensities, coincidence relations, and angular correlations, as well as the associated studies of conversion electrons. Coincidence studies are very important in deducing nuclear level schemes. They provide keys to the relative order and placement of specific  $\gamma$ -rays that complement those provided by energy sums alone. Conversion electron studies are important in providing multipolarity information on particular transitions. Angular correlation studies of successive cascade  $\gamma$

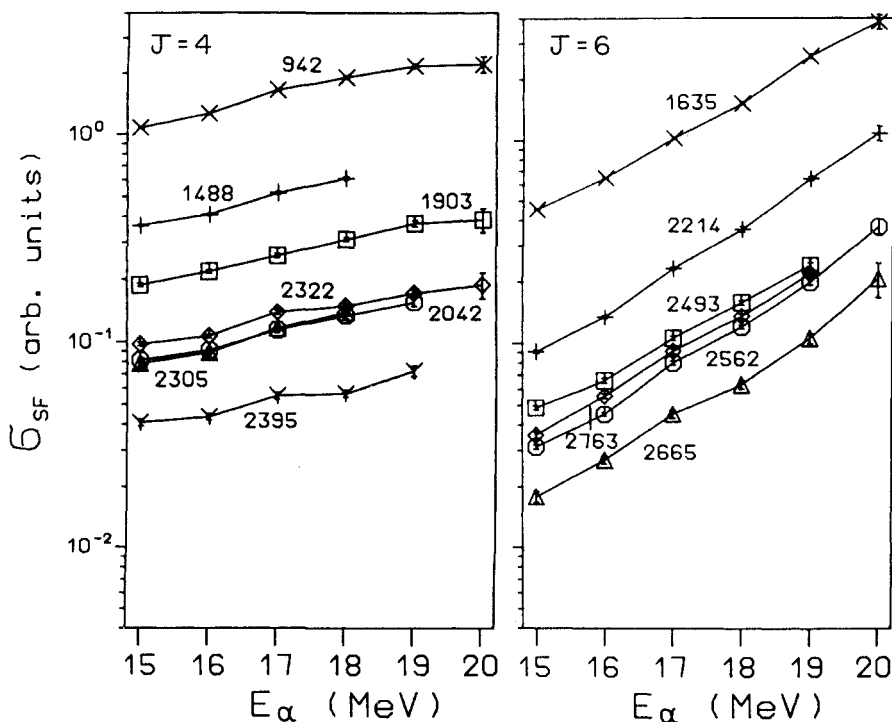
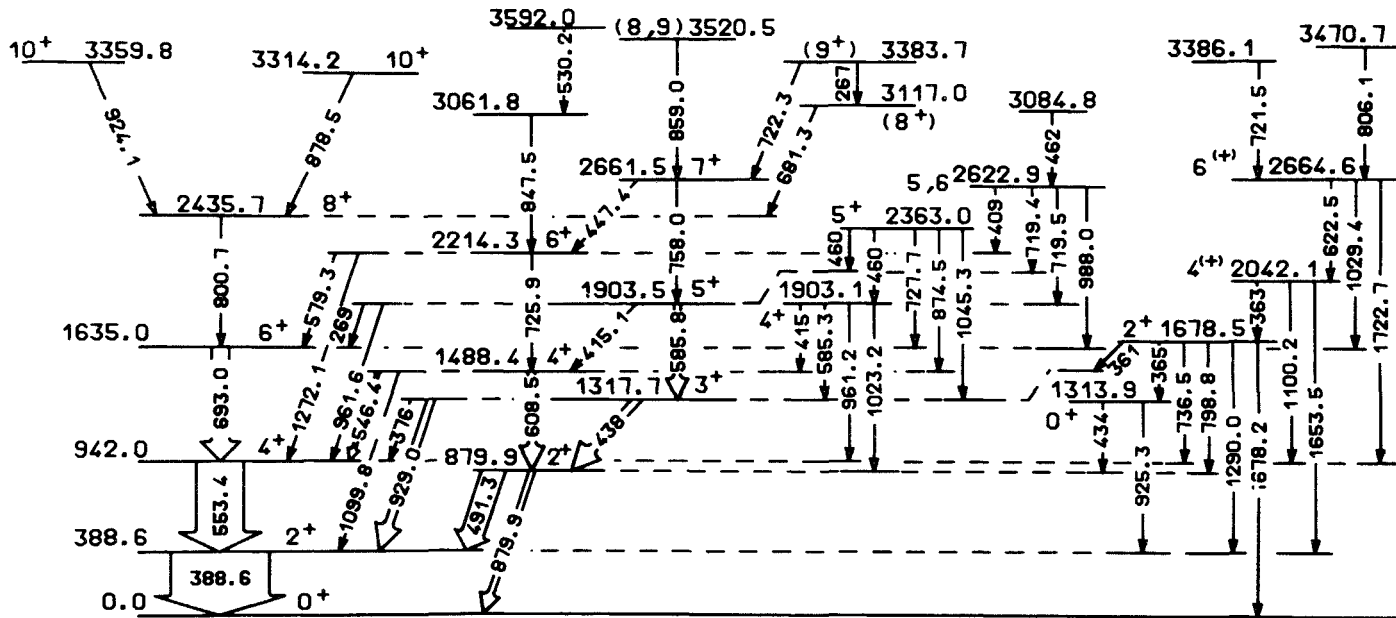


**Fig. 10.7.** Excitation functions for  $J = 4$  and  $J = 6$  states in the reaction  $^{123}\text{Te}(\alpha, n\gamma)^{126}\text{Xe}$  (Lieberz 1989). The yields  $\sigma_{SF}$  are for “side-feeding” transitions that exclude discrete feeding. Note the nearly monotonic behavior against  $E_\alpha$  (labeled for each line in keV) and the dependence of the slopes on  $J$ .

rays also provide information on level spins, but they are seldom as unambiguous as conversion electron measurements.

We will illustrate some of these techniques by focusing on the exceptional capabilities of two instruments at the Institut Laue Langevin in Grenoble, namely the electron magnetic spectrometer, BILL, and the  $\gamma$ -ray spectrometer, GAMS. Both are characterized by very high resolution and reasonable efficiency. BILL achieves this by magnetic focussing, while GAMS measures  $\gamma$ -ray energies by diffracting the  $\gamma$ -rays at precisely measured angles. Solid state Ge  $\gamma$ -ray detectors normally have resolutions ranging from  $\approx 800$  eV at 100 keV to  $\approx 1.5$  keV at  $\approx 800$  keV. The corresponding numbers for the GAMS spectrometers in normal operation are  $\approx 50$  eV and  $\approx 400$  eV. The corresponding  $\gamma$ -ray energy precision is typically 50 to 200 eV for Ge detection and 1 to 20 eV for GAMS. A portion of a typical GAMS spectrum is shown in Fig. 10.9. The primary impact of such resolution is not the higher level energy precision that, in any case, far exceeds the predictive capabilities of modern nuclear models. It is rather in the avoidance of accidental energy combinations (“Ritz combinations”) that can lead to incorrect  $\gamma$ -ray placements and, thereby, incorrectly deduced structure information.

Consider an example of a typical deformed nucleus in which 250  $\gamma$ -rays are



$$^{126}_{54} \times e$$

Fig. 10.8. Typical level scheme from the  $(\alpha, n\gamma)$  reaction (positive parity levels only). (Lieberz, 1989).

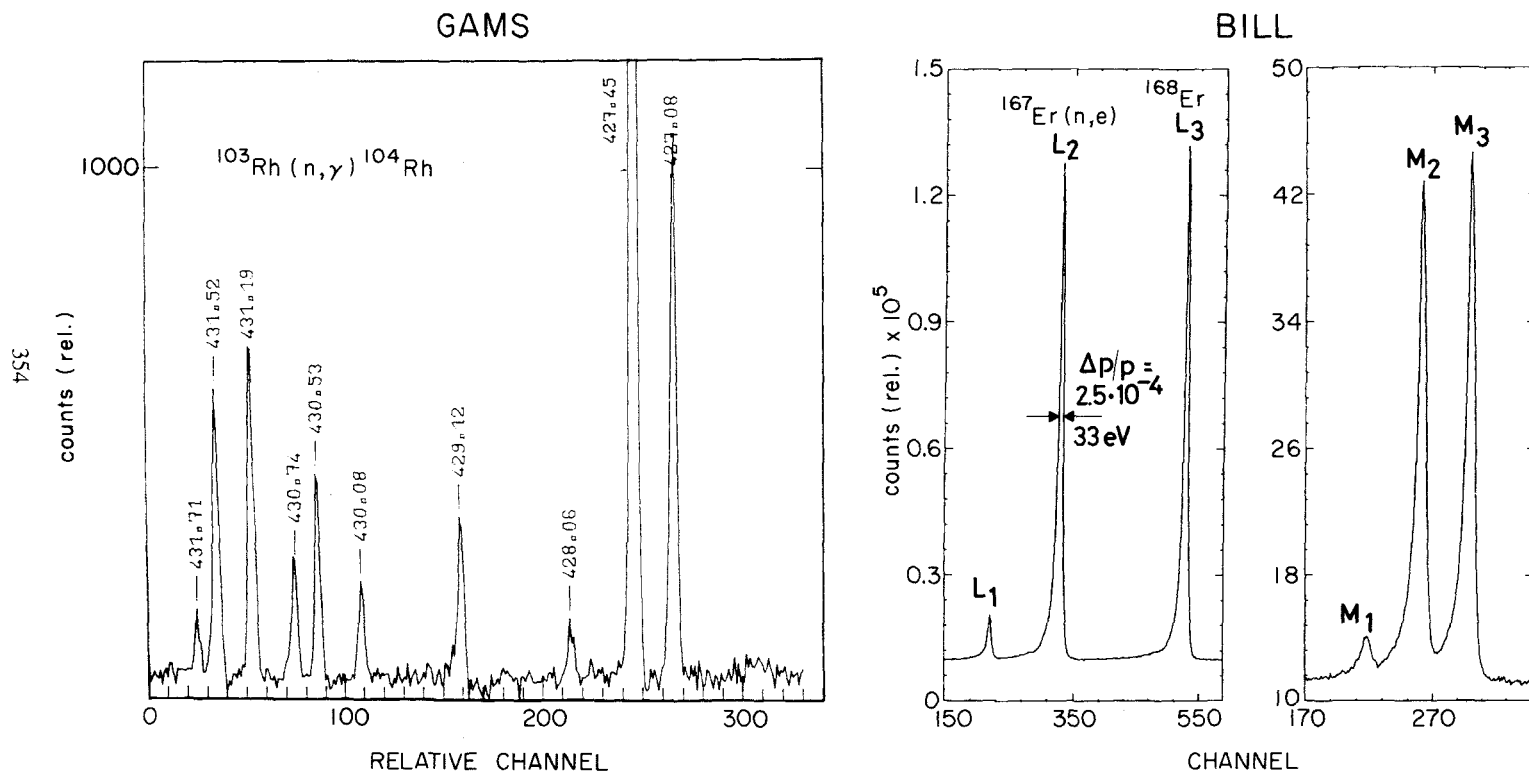


**Fig. 10.9.** Examples of GAMS and BILL data. Note the remarkable resolution and energy precision of GAMS and the sensitivity to transition multipolarities resulting from the resolution of  $L$  and  $M$  lines with the BILL spectrometer. From Krusche, 1989 (GAMS) and based on data discussed in Gelletly, 1981 (BILL).

observed with energies up to 1 MeV. If each  $\gamma$ -ray has an energy precision of  $\pm 0.1$  keV, then crudely, this set of transitions "blocks out" a total energy window of 50 keV or about 5 percent of the total. Roughly speaking, this is the percentage of transitions that might be involved in incorrect Ritz combinations. If a typical level has four de-excitation  $\gamma$ -rays, then one in every two to three levels will have a mistakenly placed  $\gamma$ -ray either feeding or de-exciting it. Clearly, this can lead to incorrect spin assignments, and certainly to incorrectly assessed nuclear structure information. In contrast, with GAMS, the probability of an accidental, incorrect Ritz combination would be 1/4 to 1/2 percent, or in other words, perhaps one  $\gamma$ -ray in the entire level scheme would be misplaced.

The advantages of GAMS are actually more important than this example illustrates. Its resolution, though energy dependent, is particularly good for the low-energy  $\gamma$ -rays (below  $\approx 300$  keV) that often provide the most crucial nuclear structure information. They occur in competition with higher energy transitions that are kinematically favored (transition rates are proportional to  $B(E2) \times E_\gamma^5$ ). The observation of a low energy transition therefore nearly always signals the presence of crucial collective matrix elements that overcome the phase space hindrance.

One of the most powerful methods for assignment of electromagnetic transition multipolarities is the use of conversion electron process. A level de-exciting by electromagnetic radiation may occasionally knock out an atomic electron rather than emit a  $\gamma$ -ray. The probability of this is highly correlated with the energy of the transition, its multipolarity, and the particular electron shell involved. Conversion electron emission probabilities are normally expressed in terms of so-called conversion coefficients, which are the ratios of

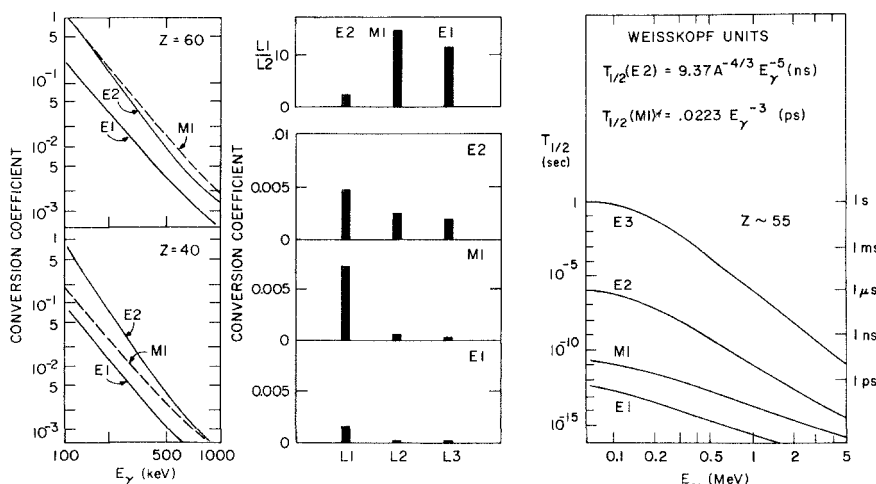


**Fig. 10.10.**  $K$  conversion coefficients and  $L$  subshell ratios for E1, E2, and M1 transitions. Lifetimes for transitions of "single-particle" strength (including conversion) as a function of transition energy are also shown (right).

the probability of emission of an electron from a given shell ( $K, L, M, N, \dots$ ) compared to that of the associated  $\gamma$ -ray. Figure 10.10 (left) illustrates the  $K$  conversion coefficients for two  $Z$  values and E1, M1, and E2 multipolarities. When  $L$  shell electrons are emitted there are several possible transitions, the so-called  $L$  subshell electron lines, each corresponding to a particular energy difference between electronic orbits in the atom. The energies of these lines depend on the particular element and grow rapidly with  $Z$ : in heavy nuclei near  $A \approx 150$  binding energies are  $\approx 60$  keV for the  $K$  shell and  $\approx 10$  to 12 keV for the  $L$  subshells. The separation of the  $L_1:L_2:L_3$  lines is  $\approx 1$  to 2 keV. Transition multipolarities can be deduced from  $K$  conversion coefficients if the relative  $\gamma$  and electron intensity scales are known. However, the safest and most sensitive method is the ratio of  $L$  subshell electron lines, which avoids all recourse to  $\gamma$ -ray intensities. Figure 10.10 indicates the very different E1, M1, and E2  $L$  subshell patterns for a 200 keV transition in a nucleus with  $Z = 70$ . (The figure also includes, for convenient reference, the single-particle lifetimes for M1, E1, and E2 transitions for  $\gamma$ -rays below  $\approx 5$  MeV for  $Z = 55$ .) Unfortunately, solid state electron detectors are incapable of resolving most  $L$  subshell energy differences and can be used only for the measurement of  $K$  shell electron intensities, or perhaps, the  $K$  to total  $L$  shell ratios. In contrast, the BILL double focusing spectrometer can easily separate  $L$  subshell transitions, and frequently, the  $M$  subshells as well. Furthermore, its efficiency allows one to observe some  $N$  and  $O$  lines. A portion of a BILL spectrum is included in Fig. 10.9.

### 10.3 Heavy Ion Compound Reactions and High Spin States

All of the techniques discussed so far deal essentially with low spin states. In the last fifteen years, however, a large fraction of nuclear structure studies has centered on high spin states, and an incredible richness of phenomena, barely touched on in this hook, has been uncovered. We will give just the briefest introduction to some of the many approaches to this field.

A projectile incident upon a target nucleus carries an orbital angular momentum of  $\mathbf{l} = \mathbf{r} \times \mathbf{p}$ . The study of high-spin states, which necessarily involves the transfer of large amounts of angular momentum to a target nucleus, will clearly benefit from the use of heavy ion projectiles. An early example of this approach was the pioneering  $(\alpha, xny)$  studies of Lark and Morinaga in the 1960s. They were able to populate the ground state rotational bands of many even-even deformed nuclei up to the  $6^+$  and  $8^+$  levels. These early studies provided important information on rotational structure, supplying impetus, for example, to develop higher-order terms in the rotational energy expansion (see Chapter 6). A natural outgrowth of these studies was the use of true heavy ion projectiles;  $^{12}\text{C}$ ,  $^{16}\text{O}$  at first, and subsequently, nearly all nuclear species up to and including  $^{208}\text{Pb}$  and U. In the last couple of years, evidence for discrete levels up to spins of  $60\hbar$  and beyond have been detected and have led to the discovery of the phenomenon known as superdeformation.

Figure 10.11 illustrates the basic population ideas behind a  $(\text{H.I.}, xny)$  reac-

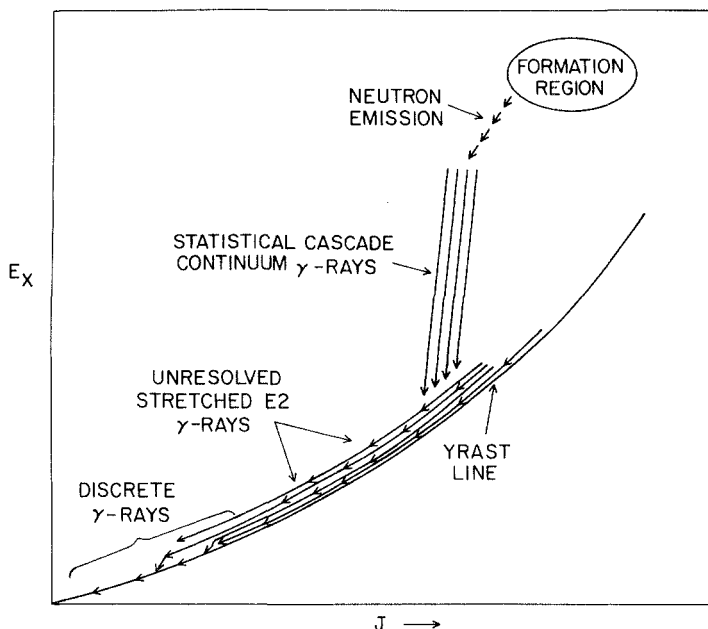


**Fig. 10.11.** Schematic idea of the flow of population and the de-excitation mechanisms in (heavy ion,  $xn\gamma$ ) reactions.

tion. An incident heavy ion impinges on and is captured by a target nucleus, forming a compound nucleus. This state is formed at extremely high spin and excitation energy. It is invariably particle unstable. The first step in the return to a quiescent state is the emission of a number of evaporation neutrons. This process is favored over  $\gamma$  ray emission both because it involves the strong rather than the electromagnetic interaction and also because the more massive neutrons provide a more efficient way of removing angular momentum for a given energy emission. (Recall our discussion in Chapter 1 of the difficulties inherent in high multipolarity  $\gamma$  ray emission.)

This process exaggerates one of the key features of (H.I.,  $xn\gamma$ ) reactions—they lead to extremely neutron deficient nuclei. They do so primarily because most heavy ion projectiles (such as  $^{16}\text{O}$  or  $^{32}\text{S}$ ) have nearly equal numbers of protons and neutrons. When added to a heavy target nucleus, a compound nucleus with a relative deficiency of neutrons is produced. This occurs because the valley of stability in heavy nuclei proceeds, on an average, by adding more neutrons than protons. The additional evaporation of several neutrons from the initial compound nuclear state increases the neutron deficiency. Thus, (H.I.,  $xn\gamma$ ) reactions are useful both for studying high-spin states and gaining access to nuclei not otherwise observable.

Neutron emission, which proceeds along a path slanted toward the origin in Fig. 10.11, terminates when the nucleus eventually reaches an excitation energy that no longer permits particle emission. The only recourse is  $\gamma$  ray

decay that can carry off considerable energy but relatively little angular momentum. It therefore proceeds along nearly vertical de-excitation paths. Given the high complexity of the compound state just prior to  $\gamma$ -ray emission, there are a myriad of possible routes and the decay is characterized by a nearly statistical "rain cloud" pattern.

There have been many studies in recent years of the average properties of the statistical continuum of  $\gamma$  rays including measurements of their average multipolarities, average energies, and so on. We will not delve into this here. The net result is that, finally, states relatively near the yrast levels are reached. At this point the de-excitation path must closely follow the yrast line. The de-excitation converts to the emission of a sequence of E2  $\gamma$ -ray transitions feeding down any of several nearly parallel rotational bands in the yrast

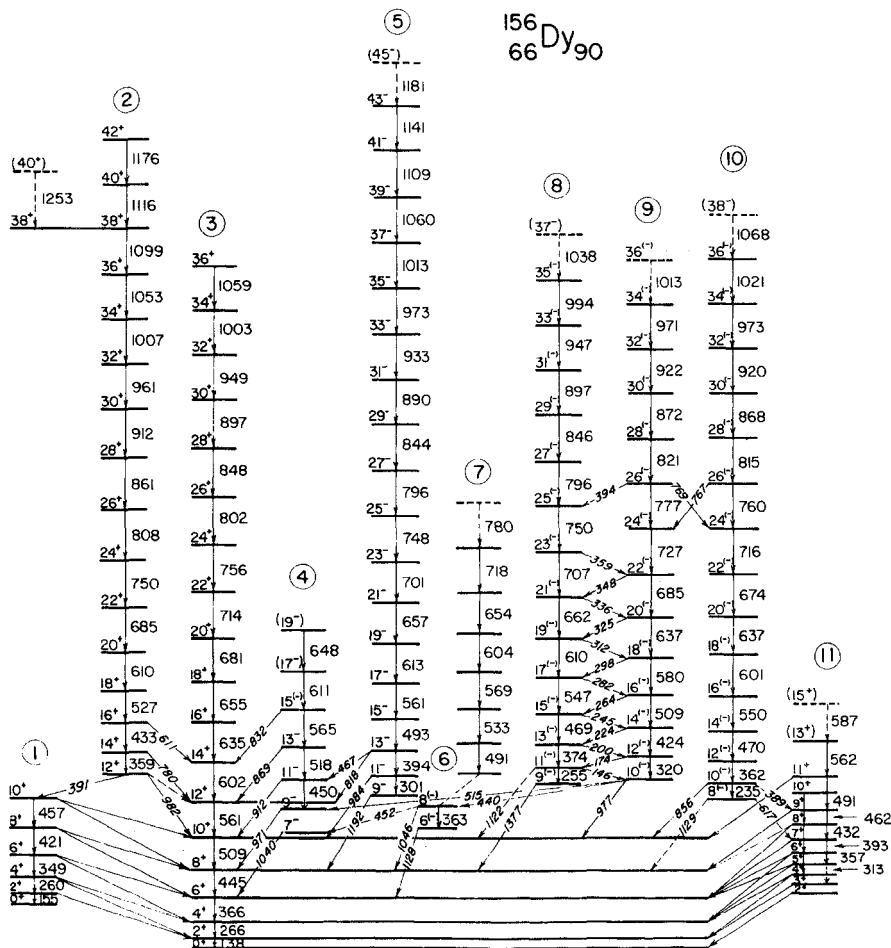


Fig. 10.12. Typical (H.I.,  $xn\gamma$ )-based level scheme (Riley, 1988).

region. Eventually, the de-excitation of these "side bands" terminates at or near their bandheads and the intensity feeds into the yrast sequence itself. From here on all the decay proceeds simply by stretched E2 transitions in the ground state band.

Experimentally, the techniques for the study of (H.I.,  $xn\gamma$ ) reactions clearly center around the detection and placement of the discrete  $\gamma$ -ray lines that de-excite the various high-spin levels, as well as the characterization of average properties of the continuum lines. In a way, the situation is exactly complementary to the ( $n, \gamma$ ) reaction. In heavy ion reactions, the discrete levels observed are "cold," that is, among the lowest-lying states of those spins energetically possible. The reaction discloses states over an extremely wide spin range. In ( $n, \gamma$ ), on the other hand, "hot" excited states are formed, extending several MeV above the yrast sequence and encompassing a variety of excitations, but always with spins within a few units of the target spin.

A typical level scheme observed in a (H.I.,  $xn\gamma$ ) reaction is shown in Fig. 10.12. One notes the separation of the levels into sequences of quasi-rotational bands extending over extremely large ranges of spin. Even though these bands may mix with one another, the decay, as we have noted, is preferentially down the rotational band sequences rather than to high spin yrast states. We saw in Chapter 6 why the decay remains within each band as long as the mixing is not very spin dependent.

Except in the case of superdeformation, most of these rotational bands are characterized by similar inertial parameters,  $\hbar^2/2I$ , and similar nuclear shapes. Since they also involve similar spins, there will be many  $\gamma$ -ray transitions of nearly comparable energies. This poses a serious experimental problem. It is only with the development of multifold coincidence techniques in the last years that this process has reached the stage of experimental sophistication required to produce level schemes such as those in Fig. 10.12. The typical experimental arrangement consists of a target surrounded by a large array of  $\gamma$ -ray detectors, usually Ge detectors flanked by anti-Compton shields designed to enhance the photopeak efficiency and discriminate against Compton effects. Such arrays are commonly called "balls" and may involve upwards of 50 to 100 detectors, more in some proposed versions.

The procedure is to set up an electronic demand for two-, three-, or fourfold coincidences as a prerequisite for triggering the recording of an event. This allows one to select specific cascades and different spin regimes. The details are well beyond the scope of this book, but an indication of the differences in "fold" spectra is shown in Fig. 10.13. There is clearly a great advantage, in terms of spectral "cleanliness," in arrays that are large enough to provide sufficient solid angle to permit efficient multifold triggers.

We have already described some of the interesting results from heavy ion reactions, namely the phenomenon of backbending and quasi-particle alignment in conjunction with our discussion of the Coriolis interaction. Recently, a particularly intriguing phenomena has been discovered: superdeformation in which rotational sequences are observed with moments of inertia indicating deformation values of near  $\beta \approx 0.5-0.6$ . This was first observed in 1986, and in

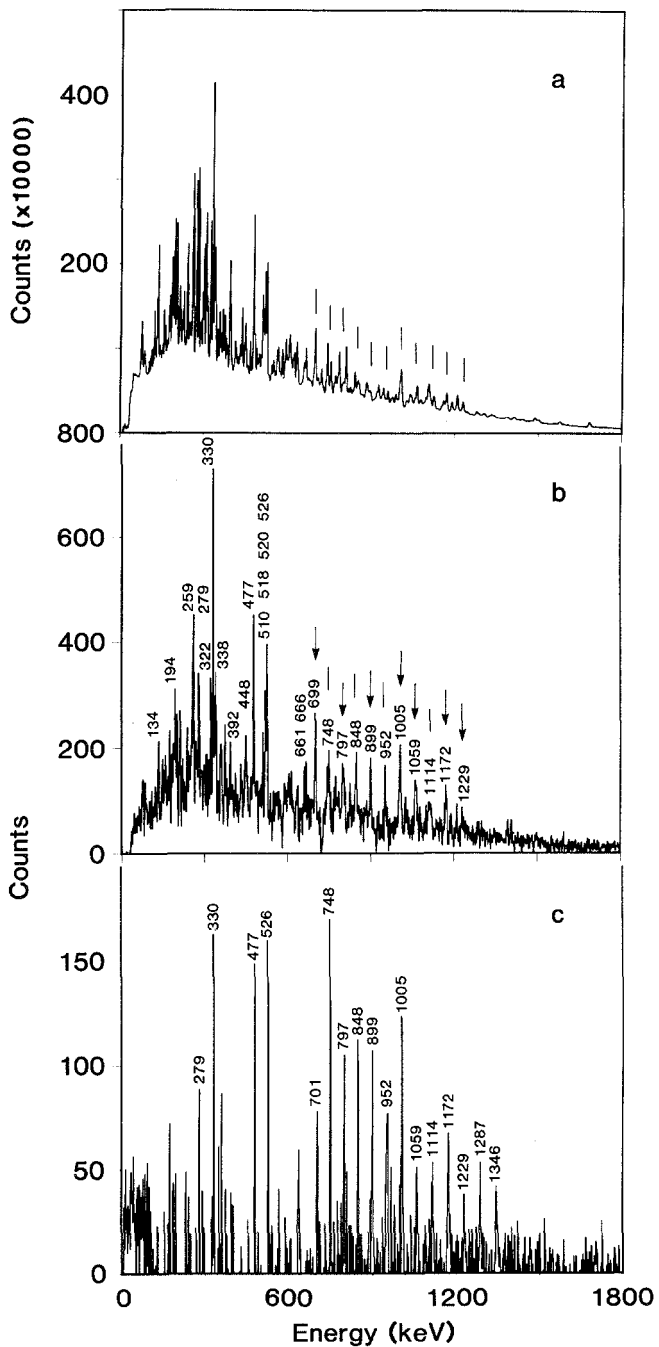


**Fig. 10.13.** Example of the advantages of multifold coincidence gating. Data from the reaction  $^{124}\text{Sn}(^{29}\text{Si}, xn\gamma)^{148}\text{Gd}$ . Each successive (lower) spectrum incorporates an additional coincidence requirement (Deleplanque, 1988). (Top) "Singles"; (Middle) Single coincidence gate; (Bottom) double gated. The lines remaining in this spectrum are mostly from the superdeformed band.

the short time since, numerous other superdeformed sequences have been found. At first, only high spin levels were associated with such structure. Recently, in the Hg region, superdeformed states with  $J \sim 10$  have been assigned.

Initial interpretations of the superdeformed states involve the concept of energy gaps in the Nilsson diagram at large deformations caused by the presence of strongly downsloping Nilsson orbits from the  $N' = N+2$  oscillator shell. These deformed "shell gaps" act in a similar way to spherical shell gaps and lend greater stability to those nuclei whose Fermi surface is near the gap. The detailed characterization of superdeformed levels and the correct prediction of their systematics offers a challenge to modern theories, both of high spin states and of the behavior of single particle levels well above the Fermi surface. Critical to such predictions has been the development of sophisticated "cranked" shell model calculations that properly account for the effects of extremely fast rotational motion, along with the incorporation of specific corrections for shell structure not included by simply specifying the deformation parameters. The effects of the monopole proton-neutron interaction may well be important in a detailed understanding of some of the latter effects.

#### 10.4 Heavy Ion Transfer Reactions

Another experimental technique for nuclear structure studies involving heavy ions that has been used in the last decade, albeit to a lesser extent, involves heavy ion transfer reactions. The basic idea of the reaction is illustrated in Fig. 10.14. As opposed to the compound nuclear formation that is characteristic of (H.I.,  $xn\gamma$ ) reactions, heavy ion transfer reactions are essentially direct. Imagine an incident heavy ion passing rather far from a potential target nucleus (region I). There will be little interaction. The orbit of the projectile will be only slightly changed and the probability for particle transfer will be very small. If, on the other hand, the projectile nucleus passes very close to the target nucleus (region III), it will likely be absorbed, forming a compound nucleus, with minuscule probability that an ejectile similar to the incident projectile will be emitted. The effective cross section for one or two nucleon transfer will likewise be very small. Hence, there is an "impact parameter

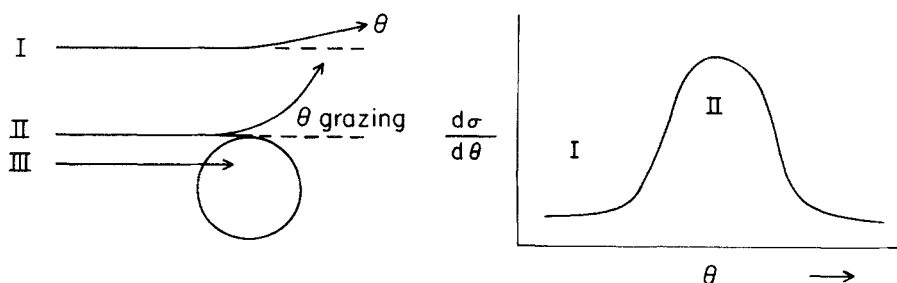


**Fig. 10.14.** Illustration of three trajectories, and the associated angular distribution, for a heavy ion transfer reaction.

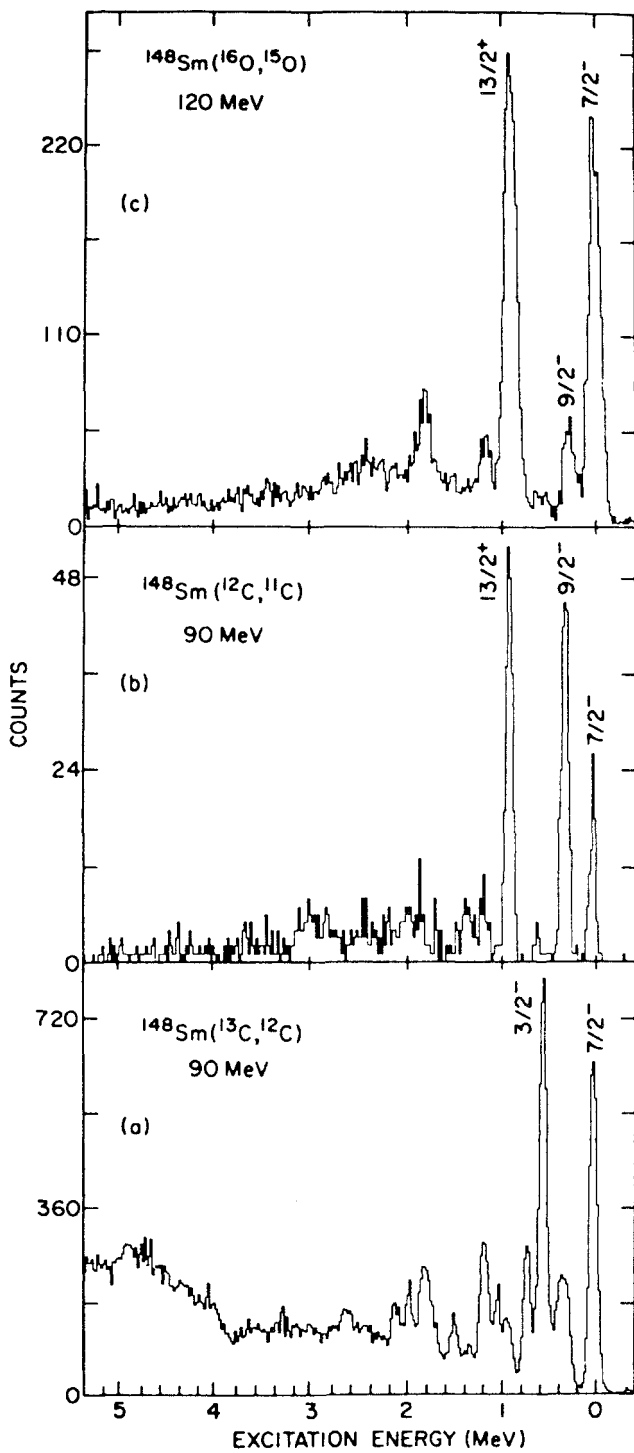


Fig. 10.15. Spectra for three heavy ion single neutron transfer reactions leading to  $^{149}\text{Sm}$  (Bond, 1983).

window," in which the transfer cross section maximizes, corresponding to a "grazing" collision (region II). Thus the expected angular distribution is the so-called "bell shaped curve" shown in Fig. 10.14.

Such one and two nucleon heavy ion transfer data have mostly been exploited to study the reaction mechanism. But they can also be used in some interesting ways to preferentially populate, and therefore identify, selected high-spin states. This selectivity, especially when combined with coincidence  $\gamma$ -ray detection, overcomes the inherently poorer energy resolution of heavy ion reactions. The idea is to exploit the possibility of high angular momentum transfer and the differences in the orbits of the transferred nucleon for different incident projectiles. Figure 10.15 shows some characteristic results.

As opposed to (H.I.,  $xn$ ) compound nuclear reactions in which the incident projectile is absorbed along with all its angular momentum, heavy ion transfer reactions only deposit large amounts of angular momentum if the incident and outgoing energies and orbital angular momenta ( $\mathbf{l} = \mathbf{r} \times \mathbf{p}$ ) are quite different. The ( $^{13}\text{C}$ ,  $^{12}\text{C}$ ) reaction, with a  $Q$  value near zero, is similar to (d, p), populating low and medium spin states (lowest panel of Fig. 10.15). In contrast,  $Q$  values for the ( $^{16}\text{O}$ ,  $^{15}\text{O}$ ) and ( $^{12}\text{C}$ ,  $^{11}\text{C}$ ) reactions are highly negative (the projectiles are tightly bound), so under appropriate kinematic conditions ( $E_p$ ,  $\theta_{\text{scat}}$ ), large  $l$  transfers are favored (top two panels).

There is more to it than this. In  $^{12}\text{C}$ , the last neutron occupies a  $p_{1/2}$  orbit while it fills a  $p_{3/2}$  orbit in  $^{16}\text{O}$ . This leads to very different selectivity for  $J = l - 1/2$  and  $J = l + 1/2$  final states in the two reactions as we see in the figure: in the middle, the  $9/2^-$  ( $h_{9/2}, j = l - 1/2$ ) state is comparable in strength to the  $13/2^+$  ( $i_{13/2}, j = l + 1/2$ ) and the  $7/2^-$  level ( $f_{7/2}, j = l + 1/2$ ) is weaker than either. In contrast, in the top panel, the  $J = l + 1/2$  transfers ( $13/2^+$ ,  $7/2^+$ ) are strongly favored over the  $J = l - 1/2$  ( $9/2^-$ ). This spin-orbit selectivity also leads to interesting polarization phenomena. Studies of a number of nuclei ( $^{144}\text{Nd}$ ,  $^{149}\text{Sm}$ , several Er isotopes, etc.) have exploited this technique.

In this short introduction to some of the experimental techniques of nuclear structure physics we have, of necessity, been forced to be selective, giving only a few illustrative examples of the rich possibilities that exist. Completely untouched on, for example, are:  $\beta$  decay and the study of the spectroscopy of fission product nuclei, which in conjunction with powerful modern isotope separators, provides access to hundreds of extremely neutron rich nuclei on the opposite side of stability to that accessible in heavy ion reactions; inelastic scattering (except as touched on briefly in the discussion of Coulomb/nuclear interference effects); the study of nuclear radii and isotope and isomer shifts with laser-based techniques; the study of magnetic moments using integral and differential perturbed angular correlation techniques; and the use of photon induced nuclear excitations to study both giant resonances and the recently discovered isovector collective M1 scissors mode. The reader is simply referred to the literature to pursue these or other topics as his or her interests dictate. Hopefully the structural background provided by this book will facilitate such an adventure.

*This page intentionally left blank*

## REFERENCES

This list includes two categories of references. One consists of those specifically cited in the text (for example, as the source for figures or tables). (The author apologizes for the disproportionate and semi-obscene number of citations of his own work here. This reflects both the fact that the topics covered in the book tend to be those that I am interested in and may have worked on, and a degree of laziness in choosing illustrative figures from my own papers rather than searching the literature for the better ones.) The other category gives a few classic articles and other excellent works, often textbooks, review articles, or compilations, which are suggested for additional study. All of these are recommended. Papers that the author has personally found to be continually and particularly helpful, some indispensable reference works, and a few others are marked with an asterisk. No attempt is made to provide a complete reference list for ideas and data discussed in this book. This list is for the benefit of the reader, not for the recognition of earlier accomplishments. That is the task of appropriate review articles. References are cited in the text by first author only, with date of publication.

- Alaga, G., Alder, K., Bohr, A., and Mottelson, B.R. (1955). Mat. Fys. Medd. Dan. Vid. Selsk. 29, No. 9.
- \*Alder, A., Bohr, B., Huus, T., Mottelson, B.R., and Winter, A. (1956). Rev. Mod. Phys. 28, 432.
- Alder, K. and Winther, A. (1966). *Coulomb Excitation* (Academic Press, New York).
- Aprahamian, A., Brenner, D.S., Casten, R.F., Gill, R.L., and Piotrowski, A. (1987). Phys. Rev. Lett. 59, 535.
- Aprahamian, A., Brenner, D.S., Casten, R.F., Gill, R.L., Piotrowski, A., and Heyde, K. (1984). Phys. Lett. 140B, 22.
- Arenas Peris, G.E. and Federman, P. (1988). Phys. Rev. C38, 493.
- Arima, A., Harvey, M., and Shimizu, K. (1969). Phys. Lett. 30B, 517.
- \*Arima, A. and Iachello, F. (1976). Ann. Phys. (N.Y.) 99, 253.
- \*Arima, A. and Iachello, F. (1978a). Ann. Phys. (N.Y.) 111, 201.
- \*Arima, A. and Iachello, F. (1979). Ann. Phys. (N.Y.) 123, 468.
- Arima, A. and Iachello, F. (1978b). Phys. Rev. Lett. 40, 385.
- Arima, A., Otsuka, T., Iachello, F., and Talmi, I. (1977). Phys. Lett. 66B, 205.
- Arvieu, R. and Moszkowski, S. A. (1966). Phys. Rev. 145, 830.
- \*Baranger, M. (1960). Phys. Rev. 120, 957.
- Barrett, B.R. and Kirson, M. W. (1970). Nucl. Phys. A148, 145.
- Bemis, C. E., Jr., Stelson, P. H., McGowan, F. K., Milner, W.T., Ford, J.L.C., Jr., Robinson, R.L., and Tuttle, W. (1973). Phys. Rev. C8, 1934.
- Bengtsson, T., Ragnarsson, I., and Aberg, S. (1988). Phys. Lett. 208B, 39.
- \*Bès, D.R., Federman, P., Maqueda, E., and Zuker, A. (1965). Nucl. Phys. 65, 1.
- Bès, D.R. (1961). Mat. Fys. Medd. Dan. Vid. Selsk. 33, No. 2.
- Bès, D.R. (1963). Nucl. Phys. 49, 544.
- Bès, D.R. and Sorensen, R. A. (1969). Adv. in Nucl. Phys. 2, 129.
- Bohle, D., Richter, A., Steffen, W., Dieperink, A.E.L., Lo Iudice, N., Palumbo, F., and Scholten, O. (1984). Phys. Lett. 137B, 27.

- \*Bohr, A. and Mottelson (1969, 1975). Nuclear Structure. Vols. I and II, Benjamin, New York.
- Bohr, A. and Mottelson (1953). Mat. Fys. Medd. Dan. Vid. Selsk. 24, No. 16.
- Bond, P.D. (1983). Comments Nucl. Part. Phys. 11, 231.
- Braun-Munzinger, P. (1984). Editor, Nuclear Physics with Heavy Ions, Nucl. Sci. Res. Conf. Series, Vol. 6, Harwood Academic, New York.
- Brink, D.M., de Toledo Piza, R., and Kerman, A.K. (1965). Phys. Lett. 19, 413.
- Bromley, D.A., Gove, H.E., Paul, E.B., Litherland, A.E., and Almqvist, E. (1957). Can. J. Phys. 35, 1042.
- Brown, G.E. and Bosterli, M. (1959). Phys. Rev. Lett. 3, 472.
- \*Brussaard, P.J. and Glaudemans, P.W.M. (1977). *Shell Model Applications in Nuclear Spectroscopy*, North Holland, Amsterdam.
- Bucurescu, D. G., Cata, G., Cutoiu, D., Dragelescu, E., Ivascu, M., Zamfir, N. V., Gizon, A., and Gizon, J. (1989). Phys. Lett. 229B, 321.
- Bunker, M. and Reich, C. W. (1971). Rev. Mod. Phys. 43, 348.
- \*Castaños, O. and Draayer, J. P. (1989). Nucl. Phys. A491, 349.
- \*Casten, R. F. (1985a). Nucl. Phys. A443, 1.
- Casten, R. F. (1986). Phys. Rev. C33, 1819.
- Casten, R. F., Aprahamian, A., and Warner, D.D. (1984). Phys. Rev. C29, 356.
- Casten, R. F., Brenner, D.S., and Haustein, P.E. (1987). Phys. Rev. Lett. 58, 658.
- Casten, R. F., von Brentano, P., and Haque, A.M.I. (1985b). Phys. Rev. C31, 1991.
- Casten, R. F. and Cizewski, J.A. (1978). Nucl. Phys. A309, 477.
- Casten, R. F., Frank, A., Moshinsky, M., and Pittel, S. (1988). (Editors), *Contemporary Topics in Nuclear Structure Physics*, World Scientific, Singapore.
- Casten, R. F., Heyde, K., and Wolf, A. (1988b). Phys. Lett. 208B, 33.
- Casten, R. F., Kleinheinz, P., Daly, P.J., and Elbek, B. (1972). Mat. Fys. Medd. Dan. Vid. Selsk., 38, No. 13.
- \*Casten, R. F., Warner, D.D., Brenner, D.S., and Gill, R.L. (1981). Phys. Rev. Lett. 47, 1433.
- Casten, R. F., Warner, D.D., and Aprahamian, A. (1983). Phys. Rev. C28, 894.
- \*Casten, R. F. and Warner, D.D. (1988a). Rev. Mod. Phys. 60, 389.
- Casten, R. F., Warner, D.D., Stelts, M.L., and Davidson, W.F. (1980). Phys. Rev. Lett. 45, 1077.
- Cizewski, J. A., Casten, R.F., Smith, G.J., Stelts, M.L., Kane, W.R., Borner, H.G., and Davidson, W.F. (1978). Phys. Rev. Lett. 40, 167.
- Cizewski, J.A., Casten, R.F., Smith, G.J., MacPhail, M.R., Stelts, M.L., Kane, W.R., Borner, H.G., and Davidson, W.F. (1979). Nucl. Phys. A323, 349.
- Cohen, B.L. and Price, R.E. (1961). Phys. Rev. 121, 1441.
- Cottle, P. D., and Bromley, D. A. (1987). Phys. Rev. C35, 1891.
- Davidson, W.F., Warner, D.D., Casten, R.F., Schreckenbach, K., Borner, H.G., Simic, J., Bogdanovic, M., Koicki, S., Gelletly, W., Orr, G.B., and Stelts, M.L. (1981). J. Phys. G7, 455.
- Davydov, A.S. and Filippov, G.F. (1958). Nucl. Phys. 8, 237.
- Deleplanque, M.A. and Diamond, R.M. (1988). GAMMASPHERE Proposal.
- de Shalit, A. and Goldhaber, M. (1953). Phys. Rev. C92, 1211.
- \*de Shalit, A. and Feshbach, H. (1974). *Theoretical Nuclear Physics, Vol. I, Nuclear Structure*, Wiley, New York.
- \*de Shalit, A. and Talmi, I. (1963). *Nuclear Shell Theory*, Academic Press, New York.
- \*Dobaczewski, J., Nazarewicz, W., Skalski, J., and Werner, T. (1988). Phys. Rev. Lett. 60, 2254.
- Eisberg, R. and Resnick, R. (1974). *Quantum Physics*, Wiley, New York.
- Eisenberg, J.M. and Greiner, W. (1970). *Nuclear Models, Vol. 1, Excitation Mechanisms of the Nucleus, Vol. 2, and Microscopic Theory of the Nucleus, Vol. 3*, North Holland, Amsterdam.
- Endt, P.M. and Van der Leun, C. (1978). Nucl. Phys. A310, 1.

- Elliott, J.P. (1958). Proc. Roy. Soc. A245, 128 and 562.
- Elliott, J.P. and Harvey, M. (1963). Proc. Roy. Soc. A272, 557.
- Fallieros, S. and Ferrell, R. (1959). Phys. Rev. 116, 660.
- \*Federman, P. and Pittel, S. (1977, 1978). Phys. Lett. 69B, 385 and 77B, 29.
- \*Gallagher, C.J. (1964). In *Selected Topics in Nuclear Spectroscopy* (ed. B.J. Verhaar), North Holland, Amsterdam.
- Garrett, J.D. (1984). Nucl. Phys. A421, 313c.
- Garrett, J.D., Nyberg, J., Yu, C. H., Espino, J. M., and Godfrey, M.J. (1988). In *Contemporary Topics in Nuclear Structure Physics*, p. 699 (volume referenced elsewhere in this listing).
- Gelletly, W. and Schreckenbach, K. (1981). Private communication.
- Ginocchio, J. N. and Kirson, M. W. (1980). Nucl. Phys. A380, 31.
- Gneus, G. and Greiner, W. (1971). Nucl. Phys. A171, 449.
- Gustafson, C., Lamm, I.L., Nilsson, B., and Nilsson, S.G. (1967). Ark. Fysik 36, 613.
- Hager, R.S. and Seltzer, E.C. (1968). Nucl. Data A4, 1.
- Haxel, O., Jensen, J.H.D., and Suess, H.E. (1950). Z. Phys. 128, 295.
- Hecht, K. (1964). In *Selected Topics in Nuclear Spectroscopy* (ed. P.J. Verhaar), North Holland, Amsterdam.
- \*Heyde, K. (1990). *The Nuclear Shell Model*. Springer Series in Nuclear and Particle Physics, Springer-Verlag, Berlin.
- Heyde, K. (1989). Int. J. Mod. Physics A4, 2063.
- Heyde, K., Jolie, J., Moreau, J., Ryckebusch, J., Waroquier, M., Van Duppen, P., Huyse, M., and Wood, J.L. (1987). Nucl. Phys. A466, 189.
- Heyde, K. and Sau, J. (1986). Phys. Rev. C33, 1050.
- \*Heyde, K., Van Isacker, P., Casten, R.F., and Wood, J.L. (1985b). Phys. Lett. 155B, 303.
- \*Heyde, K., Van Isacker, P., Waroquier, M., Wood, J. L., and Meyer, R. A. (1983). Phys. Rep. 102, 291.
- Holmberg, P. and Lipas, P.O. (1968). Nucl. Phys. A117, 552.
- \*Hornyak, W.F. (1975). *Nuclear Structure*, Academic Press, New York.
- Iachello, F. and Scholten, O. (1979). Phys. Rev. Lett. 43, 679.
- Iachello, F. and Talmi, I. (1987). Rev. Mod. Phys. 59, 339.
- Janssen, D.R., Jolos, R. V., and Donau, F. (1974). Nucl. Phys. A224, 93.
- Kerman, A.K. (1959). In *Nuclear Reactions, Vol. 1* (eds. P. M. Endt and M. Demuer), North Holland, Amsterdam.
- \*Kisslinger, L.S. and Sorensen, R. A. (1960). Mat. Fys. Medd. Dan. Vid. Selsk 32, No. 9.
- Kleinheinz, P., Casten, R.F., and Nilsson, B. (1973). Nucl. Phys. A203, 539.
- Krusche, B., Börner, H., Takruri, F., Robinson, S., Michaelson, S., and MacMahon, D. (1989). Private communication.
- Kumar, K. and Baranger, M. (1968). Nucl. Phys. A122, 273.
- Kumar, K. (1982). In *Contemporary Research Topics in Nuclear Physics* (eds. D.H. Feng, M. Vallieres, M.W. Guidry, and L.L. Riedinger), Plenum, New York.
- Kuo, T.T.S. and Brown, G.E. (1966). Nucl. Phys. 85, 40.
- \*Lane, A.M. (1964). *Nuclear Theory*, Benjamin New York.
- Leander, G.A., Dudek, J., Nazarewicz, W., Nix, J.R., and Quentin, Ph. (1984). Phys. Rev. C30, 416.
- \*Lederer, C.M. and Shirley, S. (1977). *Table of Isotopes, 7th Edition*, Wiley, New York.
- Lieberz, W., Dewald, A., Wirowski, R., Zell, K. O., and von Brentano, P., to be published.
- Lipas, P.O. (1962). Nucl. Phys. 39, 468.
- Ma, W.C., Quader, M.A., Emling, H., Khoo, T.L., Ahmad, I., Daly, P.J., Dichter, B. K., Drigert, M., Garg, U., Grabowski, Z.M., Holzmann, R., Janssens, R.V. F., Piiparinen, M., Trzaska, W.H., Wang, T.F. (1988). Phys. Rev. Lett. 61, 46.
- Mampe, W., Schreckenbach, K., Jeuch, P., Maier, B.P.K., Braumandl, F., Larysz, J., and von Egidy, T., 1978. Nucl. Instr. and Meth. 154, 127.
- Mayer, M. G. (1950). Phys. Rev. 78, 16.

- \*Molinari, A., Johnson, M. B., Bethe, H.A., and Alberico, W. M. (1975). Nucl. Phys. A239, 45.
- Mottelson, B.R. and Nilsson, S. G. (1959). Mat. Fys. Skr. Dan. Vid. Selsk., 1, No. 8.
- Nagai, Y., Styczen, J., Piiparinne, M., Kleinheinz, P., Bazzacco, D., von Brentano, P., Zell, K. O., and Blomqvist, J. (1981). Phys. Rev. Lett. 57, 1259.
- \*Nathan, O., and Nilsson, S. G. (1965). In *Alpha, Beta, and Gamma Ray Spectroscopy*, Vol. 1 (ed. K. Siegbahn), North Holland, Amsterdam.
- Neergaard, K. and Vogel, P. (1970). Nucl. Phys. A145, 33.
- \*Nilsson, S. G. (1955). Dan. Mat. Fys. Medd. 29, No. 16.
- Nilsson, S. G. and Prior, O. (1961). Mat. Fys. Medd. Dan. Vid. Selsk 32, No. 16.
- Nilsson, S. G., Tsang, C. F., Sobiczewski, A., Szymanski, Z., Wycech, S., Gustafson, C., Lamm, I.L., Moller, P., and Nilsson, B. (1969). Nucl. Phys. A131, 1.
- Ower, H., Elze, Th. W., Idzko, J., Stelzer, K., Grosse, E., Emeling, H., Fuchs, P., Schwalm, D., Wollersheim, H. J., Kaffrell, N., and Trautmann, N. (1982). Nucl. Phys. A388, 421.
- Paar, V. (1979). Nucl. Phys. A331, 16.
- Preston, M.A. and Bhaduri, R. K. (1975). *Structure of the Nucleus*, Addison-Wesley, Reading, MA.
- Preston, M.A. and Kiang, D. (1963). Can. J. Phys. 41, 742.
- \*Raman, S., Malarkey, C.H., Milner, W.T., Nestor, C.W., Jr., and Stelson, P.H. (1987). At. Data and Nucl. Data Tables, 36, 1.
- Ratna Raju, R.D., Draayer, J.P., and Hecht, K. T. (1973). Nucl. Phys. A202, 433.
- \*Riedinger, L.L., Johnson, N.R., and Hamilton, J.H. (1969). Phys. Rev. 179, 1214.
- Riedinger, L.L., Smith, G.J., Stelson, P.H., Eichler, E., Hagemann, G.B., Hensley, D.C., Johnson, N.R., Robinson, R.L., and Sayer, R. O. (1974). Phys. Rev. Lett. 33, 1346.
- Riley, M.A., Simpson, J., Sharpey-Schafer, J.F., Cresswell, J.R., Cranmer-Gordon, H.W., Forsyth, P.D., Howe, D., Nelson, A.H., Nolan, P.J., Smith, P.J., Ward, N.J., Lisle, J.C., Paul, E., and Walker, P.M. (1988). Nucl. Phys. A486, 456.
- Ring, P. and Schuck, P. (1980). *The Nuclear Many-Body Problem*, Springer, New York.
- Ronningen, R.M., Hamilton, J.H., Ramayya, A.V., Varnell, L., Garcia Bermudez, G., Lange, J., Lourens, W., Riedinger, L.L., Robinson, R.L., Stelson, P.H., and Ford, J.L.C., Jr. (1977). Phys. Rev. C15, 1671.
- \*Sakai, M. (1984). At. Data and Nucl. Data Tables 31, 399.
- Scharff-Goldhaber, G. and Wenner, J. (1955). Phys. Rev. 98, 212.
- Scholten, O., Iachello, F., and Arima, A. (1978). Ann. Phys. (N.Y.) 115, 325.
- Sheline, R. K. (1960). Rev. Mod. Phys. 32, 1.
- \*Schiffer, J.P. (1971). Ann. Phys. (N.Y.) 66, 798.
- \*Schiffer, J.P. and True, W. W. (1976). Rev. Mod. Phys. 48, 191.
- \*Stephens, F.S. (1975). Rev. Mod. Phys. 47, 43.
- Stephens, F.S. and Simon, R.S. (1972). Nucl. Phys. A183, 257.
- Tabor, S.L., Cottle, P.D., Gross, C.J., Huttmeier, U.J., Moore, E. F., and Nazarewicz, W. (1989). Phys. Rev. C39, 1359.
- \*Talme, I. (1962). Rev. Mod. Phys. 34, 704.
- Twin, P., Nyako, B.M., Nelson, A. H., Simpson, J., Bentley, M.A., Cranmer-Gordon, H. W., Forsyth, P.D., Howe, D., Morhtar, A. R., Morrison, J.D., Sharpey-Schafer, J.F., and Sletten, G. (1986). Phys. Rev. Lett. 57, 811.
- Van Duppen, P., Coenen, E., Deneffe, K., Huyse, M., and Wood, J.L. (1985). Phys. Lett. 154B, 354.
- Van Maldeghem, J., Heyde, K., and Sau, J. (1985). Phys. Rev. C32, 1067.
- Warner, D.D., Casten, R.F., and Davidson, W.F. (1980). Phys. Rev. Lett. 45, 1761.
- Warner, D.D. (1984). Phys. Rev. Lett. 52, 259.
- Warner, D.D. and Casten, R.F. (1982). Phys. Rev. Lett. 48, 1385.
- \*Warner, D.D. and Casten, R.F. (1983). Phys. Rev. C28, 1798.
- Waroquier, M. and Heyde, K. (1971). Nucl. Phys. A164, 113.

- \*Wilets, L. and Jean, M. (1956). Phys. Rev. C102, 788.
- \*Wilkinson, D. (1983). Editor, *Collective Bands in Nuclei, Vol. 9, Progress in Particle and Nuclear Physics*, Pergamon Press, New York.
- Wirowski, R., Yan, J., Dewald, A., Gelberg, A., Lieberz, W., Schmittgen, K.P., von der Werth, A., and von Brentano, P. (1988). Z. Phys. A239, 509.
- Wolf, A. and Casten, R.F. (1987). Phys. Rev. C36, 851.
- Wu, C.L., Feng, D.H., Chen, X.G., Chen, J.Q., and Guidry, M.W. (1986). Phys. Lett. 168B, 313.
- Wyss, R., Granderath, A., Lieberz, W., Bengtsson, R., von Brentano, P., Dewald, A., Gelberg, A., Gizon, A., Gizon, J., Harissopoulos, S., Johnson, A., Nazarewicz, W., Nyberg, J., and Schiffer, K. Nucl. Phys., to be published.
- Zamfir, V., Casten, R.F., and von Brentano, P. (1989). Phys. Lett. 226B, 11.
- Zhang, J.-Y., Casten, R.F., and Brenner, D.S. (1989). Phys. Lett. 227B, 1.

*This page intentionally left blank*

## INDEX

This listing gives the locations of principal discussions of various ideas and topics. Occasionally, casual references to an idea or technique (e.g., parenthetical comments in the text) are not listed. Also, themes running throughout the text, sometimes implicitly, such as the attractive nature of the nuclear force, the Pauli principle, two-state mixing, the nuclear potential, collectivity, and so on are only cited where they are explicitly the principal topic. Ideas, nuclei, and so on that are the subject of figures are cited by the page numbers where those figures are discussed rather than where the figures themselves occur. Greek letters and words are alphabetized according to their latin spelling and acronyms (e.g., RPA, GAMS, CFP's) are generally given according to the way they are commonly thought of: thus, CFP's are listed under "coefficients..." while GAMS is given according to the letters themselves. Such decisions are often quite arbitrary.

- Alaga rules, 172–183, 212–214, 228–230
- algebraic models, 3, 197–235
- ( $\alpha, xy$ ), 351
- ARC, 346–351
- axial asymmetry, 168, 175–197, 221–234
- backbending (see decoupled bands, rotation alignment), 233, 307–313
- bandmixing, 175–183, 228–234
- bell-shaped angular distributions, 361–363
- B(E2) values, 41, 42, 118, 121, 126, 151–154, 159–161, 170–183, 189–193, 206, 207, 211, 212, 217, 221–233, 244, 245, 327, 336
- $\beta$ -decay, 29
- $\beta$ -vibrations, 26, 36, 43, 168, 169, 230, 328–331
- BILL, 352–356
- binding energies, 7, 10, 29, 126, 127
- Casimir operators, 202
- central potentials, 49–52
- charge independence, 12, 15
- charge symmetry, 8
- closed shells, 31, 49, 58, 68
- CFP's, 111–115, 149–154
- coherence, 23–25
- collective models, 3, 34, 141–331
- collectivity, 23, 24, 130, 320–322, 327
- completeness (spectroscopic), 344, 348–351
- configuration mixing, 141–145, 249–252
- conversion coefficients, 355, 356
- Coriolis coupling, 24, 175, 265, 266, 279–312, 326
- and backbending, 307–312
- decoupling parameter, 282–284
- hexadecapole deformation, 296–300
- high spin states, 280–282, 287, 290, 300–313
- off diagonal mixing, 280–312
- rotation alignment, 267, 268, 294, 295, 300–313
- unique parity states, 292–300
- correlations (in ground state), 316, 320

- Coulomb excitation, 29, 335–344  
 Coulomb force, 56, 57  
 Coulomb-nuclear interference, 343, 344  
 cranked shell model, 312, 361  
 crossing frequency, 309, 310  
 cubic terms (in IBA), 220, 233
- Davydov model, 168, 187–191  
 decoupled bands, 266, 279, 283, 284  
 deformation, 141–145, 156–331  
     and configuration mixing, 141–145  
     intruder states, 156–161  
     m-shell distributions, 143–145  
     pairing, 101–103, 131  
     p–n interaction, 126, 141–145,  
         156–161, 233–246  
     p–p, n–n interactions, 126, 141–145,  
         156–161  
 degenerate model (*see* RPA, TDA),  
     320–322  
 δ-function residual interaction (*see*  
     residual interactions), 69–104,  
     128–131  
 detector arrays, 359  
 deuteron, 9, 14, 26  
 dynamic deformation theory, 323  
 dynamical symmetry, 199, 202–235  
 energy, staggering in  $\gamma$ -band, 194, 195  
 even–even nuclei, 69–108, 141–246  
 experimental techniques, 29, 59, 60, 64,  
     136, 137, 271–279, 288–299,  
     335–363
- Federman-Pittel mechanism, 236–239  
 fermion symmetry models, 233  
 finite boson number effects, 206–209,  
     212, 218, 224, 227–231, 244, 245  
 folds (coincidence), 359  
 f-spin (and multiplets), 232  
 $\gamma$ -vibrations, 36, 43, 166–169, 175–183,  
     194, 195, 228–231, 323–326  
 $\gamma$ -ray multipolarities, 29  
 GAMS, 226, 227, 352–355  
 gap (pairing), 80–85, 93, 132–137  
 gap parameter ( $\Delta$ ), 133  
 g-boson, 233  
 generator (group), 202, 203  
 geometric interpretation of residual  
     interactions, 76, 85–92, 96–103
- geometric models, 34, 145–331  
 g factors, 238, 239  
 giant resonances, 146, 147, 232  
 group theory (IBA), 199, 202–214
- harmonic oscillator potential, 47, 50, 58  
 harmonic vibrator model, 42, 145–161  
 heavy ion fusion reactions, 29, 183, 351,  
     356–361  
 heavy ion transfer reactions, 361–363  
     and spin sensitivity, 363  
 hexadecapole deformation, 296–300, 344
- IBA, 143, 197–235  
     and Alaga rules, 212–214, 228–230  
     assumptions, 198, 199  
     backbending, 233  
     bandmixing, 228–230  
     collective models, 197, 198, 206–216,  
         220, 223, 226, 231  
     CQF, 217, 224–231  
     dynamical symmetries, 199, 202–235  
         U(5), 205–208, 215, 217–220  
         O(6), 205, 215–220  
         SU(3), 205, 208–215  
     extensions to s-d IBA-1, 232, 233  
     finite boson number, 206–209, 212,  
         218, 224, 227–231, 244, 245  
      $\gamma$ -softness, 205, 215–221, 230–233  
     group structure, 199, 202–221  
     NpNn, 231  
     symmetry triangle, 221–231  
     transition regions, 221–231  
     triaxiality, 220, 230, 231, 233  
     intruder states, 156–161, 239, 243–245  
     irreducible representations, 202  
     isospin, 12, 68, 69, 81–83, 141–145
- $j^2$ -configurations, 67–108  
 $j^n$ -configurations, 104, 109–137  
 $j_1 j_2$ -configurations, 67–108  
 $jj$  coupling, 74
- K quantum number, definition, 165, 166  
 K mixing (*see* Coriolis coupling),  
     175–183, 191, 228–234
- $l^2$ -potential, 53, 263, 264  
 like-nucleon interaction, 10, 15, 34,  
     59–62, 126, 127, 141–145, 156–161

- Lipas formula, 185–186  
 $LS-jj$  coupling, 74
- magic numbers, 8, 31, 48, 52  
Mikhailov plots, 178–181  
and IBA, 228–230
- mirror nuclei, 7, 10  
valence mirror nuclei, 127
- models  
algebraic, 3, 197–235  
collective, geometric, 3, 34, 141–331  
microscopic (RPA, TDA) 3, 24, 142, 143, 313–331  
Nilsson, 3, 33, 37, 247–312, 323–326  
shell, 31, 33, 47–137
- moment of inertia, 131, 132, 164
- $m$ -scheme, 109–111, 146, 147
- $m$ -state distribution and deformation, 143–145
- $m$ -state localization, 72, 90, 96
- multiparticle systems (shell model), 109–137
- multipole decomposition of residual interactions, 59, 94–104, 236–240  
and limits on multipole order, 95–98
- monopole interaction, 61, 98–100, 236–240
- pairing, 94, 100, 104
- quadrupole interaction, 94, 99–103
- repulsion of like nucleons, 99
- repulsive effects of attractive interactions, 99
- multiphonon states, 148–156, 159–161, 169, 170
- multipolarities, 40
- multistate mixing, 17, 22–25, 271–312, 319–322, 327–330  
and Coriolis coupling, 271–312
- ( $n, \gamma$ ), 344–356
- $n$ -hole configurations, 106, 107, 125
- Nilsson model, 3, 33, 37, 145, 244, 245, 247–312, 319, 323–326  
and asymptotic quantum numbers, 253–256
- Coriolis coupling, 265, 266, 279, 280–312
- decoupled bands, 266, 279, 283, 284
- $K$  splitting, 249, 250
- large deformation limit, 258–260
- Nilsson diagram, 250–260  
Nilsson Hamiltonian, 256–269  
orbit angle, 249–250  
rotational motion, 264–270  
single nucleon transfer, 271–279, 288, 290–299
- small deformation limit, 257–260
- unique parity orbits, 252, 253
- U-, V-factors, 273, 279
- $N_p N_n$  scheme (valence p–n interaction), 231, 235–246  
and collective models, 246
- effective valence nucleon numbers, 238, 239, 244
- intruder states, 239, 243
- monopole p–n interaction, 236–240
- nuclei far from stability, 240, 241
- odd  $A$  nuclei, 241
- parametrization of collective models, 241
- P-factor, 242–246
- $S_{pn}$ , 244, 245
- saturation of collectivity, 244, 245
- subshell gaps, 236–240, 244
- unified view of phase transitions, 245, 246
- ( $n, n'\gamma$ ), 351
- nuclear force, 4, 6–17, 57
- nuclear size, 3, 6
- nuclei  
Ba, 34, 220, 303  
Bi, 64, 66, 84, 92  
Ca, 31, 62–66, 125, 126  
Cd, 34, 35, 146, 156–160, 207, 239  
Cl, 84, 85, 95, 107  
Dy, 36, 66, 191, 359  
Er, 36, 105, 174, 178, 179, 191, 266, 306, 307, 325, 328, 349, 350  
Gd, 174, 266, 342  
Hf, 174, 191, 212–214, 261  
Hg, 243, 244  
K, 107  
La, 266, 303  
Nb, 62, 65  
Nd, 127–130, 363  
Os, 191, 299, 300  
Pb, 22, 32, 33, 64, 78, 105, 158, 239, 322  
Po, 33, 78  
Pt, 136, 137, 191, 218–220  
Rb, 305, 306

- R**e, 266  
**R**u, 35, 161  
**S**b, 64, 101  
**S**c, 44, 62, 101  
**S**m, 191, 363  
**S**n, 33, 64, 66, 105, 146, 177, 239  
**S**r, 239  
**T**e, 33–35, 78, 146, 160  
**T**i, 114  
**T**h, 342  
**U**, 266  
**V**, 114, 115  
**W**, 36, 91, 262, 275–279, 288–299, 325  
**X**e, 34, 146, 220, 351  
**Y**b, 33, 37, 66, 184, 212–214, 312  
**Z**r, 62, 65, 66, 239  
nuclei far from stability, 240
- oblate shape, 263, 264  
octupole vibrations, 36, 169, 328–330  
odd A nuclei, 247–312  
odd particle blocking, 311, 312  
orbit dependence of nuclear forces, 61, 236–239, 244, 245  
**O(6)**, 193, 196, 205, 214–221
- pairing, 15, 76, 84, 93, 94, 100–104, 130–137, 323  
and deformation, 131, 132  
 $\delta$ -function interaction, 76, 93, 94, 100, 130, 131  
ground state spin, 131  
moment of inertia, 131, 132  
Nilsson orbits, 132  
off-diagonal matrix elements, 93, 132, 135, 136  
pairing gap, 80, 93, 132–137  
pairing property of residual interactions, 15, 104  
parabolic rule, 101–103  
quasi-particles, 132–136  
RPA, 323  
separation energies, 131  
transformation of energy zero, 134  
pairing plus quadrupole (PPQ) model, 94  
parabolic rule, 99–103  
parity, 54, 55  
particle-hole spectra, 105, 107
- particle versus hole matrix elements, 106–108, 125  
Pauli principle, 5, 14–17, 34, 46, 47, 56, 57, 68, 69, 72–104, 109–111, 130, 144, 145  
and allowed  $J$  values, 68, 69  
independent particle motion, 47, 57  
*m*-scheme, 109–111  
pairing, 130  
residual interactions, 72–104, 130  
valley of stability, 56  
P-factor, 235–246  
p–f bosons, 233  
phase transitions, 196, 197, 221–231, 235–246  
phonon model, 145–161, 169–170  
potentials, 47  
proton, neutron distinguishability, 81–83  
p–n interaction, 10, 14–16, 34, 59–62, 81–85, 88–92, 95, 98–103, 127, 141–145, 156–161, 233–246, 322  
and configuration mixing, 127, 141–145, 322  
deformation, 127, 141–145, 156–161  
isospin formalism, 81–84  
like-nucleon interactions, 10–15, 34, 59–62  
mass dependence, 92  
orbit dependence, 61, 236, 237, 244, 245  
pairing, 243  
parabolic rule, 99–103  
separation energies, 14, 15, 84  
strength of, 92, 244, 245  
probe size, 95, 96  
prolate, oblate shapes, 163, 263–264
- quadrupole deformation, 161–246  
quadrupole interaction, 94–104  
quadrupole moments, 9, 14, 26, 107, 164, 171  
quadrupole vibrations (spherical nuclei), 147–161  
quasi-particles, 132–136, 323
- range of nuclear force, 4, 10, 15–17, 96–103  
and multipole order, 96–98  
repulsive aspect of like nucleon interaction, 29, 30, 80–84, 99, 126

- residual interactions, 15, 59, 61, 67–137  
 and binding energies, 126, 127  
 $\delta$ -function interaction, 69–104  
 even tensors, 117, 121–124  
 geometric interpretation, 76, 85–92,  
 96–103  
 multipole decomposition, 59, 94–104  
 odd tensors, 70, 95, 104, 116–120,  
 123–130  
 off-diagonal matrix elements, 108  
 pairing force, 15, 76, 93, 94, 100, 104,  
 130–137  
 repulsive effects of attractive interactions, 99  
 repulsion of like nucleons, 29, 30, 84,  
 99, 126  
 seniority, 70, 104, 116–130  
 separation of radial and angular parts,  
 71, 83, 95  
 sensitivity to orbit, 61, 236–239  
 surface  $\delta$ -interaction, 125, 129  
 Ritz combinations, 351  
 rotation alignment, 267, 268, 294,  
 300–313  
 and Fermi surface, 300–310  
 weak coupling, 303, 304  
 rotational energies, 183–186, 264–270  
 rotational motion, 36, 38, 165, 166,  
 264–270  
 rotation-vibration coupling, 175–183  
 RPA, 142, 146, 196, 313–331  
 and collectivity, 320–322, 327  
 degenerate model, 320–322  
 $\gamma$ -vibration, 323–326  
 HRPA, 323  
 Nilsson model, 319, 323–326  
 schematic model, 318–322  
 TDA, 313–331
- $S_{pn}$ , 245  
 saturation of collectivity, 244, 245  
 scissors mode, 147, 232  
 s, d bosons (*see* IBA), 198  
 second quantization, 148  
 selection rules, 151, 160, 161, 170–183,  
 189–193, 206, 207, 211, 212,  
 217–221  
 seniority, 70, 104, 155–130  
 and conservation of, 117  
 constancy of energies, 119
- even tensors, 116–130  
 odd tensors, 116–130  
 pairing property, 118  
 separation of rotational and particle motions, 247, 248  
 separation energies, 7, 13, 14, 29, 30, 131  
 shapes of nuclei, 29  
 shell model, 31, 33, 44–137  
 shell structure, 50–56  
 single-particle energies, 50–54, 58–62,  
 98–100, 130  
 single-particle transfer reactions, 29, 59,  
 60, 64, 271–279, 288, 290–299, 326,  
 335  
 spectroscopic completeness, 348–351  
 spherical-deformed transition regions,  
 141–145, 196, 197, 221–231,  
 233–245  
 spin-orbit potential, 54–56, 263, 264  
 square well potential, 47  
 subshell gaps, 236–240, 361  
 surface  $\delta$ -interaction, 125, 129  
 SU(3), 205, 207–214  
 superdeformation, 312, 359, 361  
 symmetry triangle, 221–231  
 symplectic models, 233, 334  
 systematics, 28–43, 115–130, 164,  
 176–181, 221–231, 233–246, 262,  
 326–331
- T=0 p–n interaction, 81–93, 141–145, 236  
 T=1 interaction, 81–93, 141–145, 236  
 Talmi-Glaubman rule, 105  
 TDA (*see* RPA), 143, 146, 313–331  
 transition rates and two-state mixing (*see*  
*also* B(E2) values, selection  
 rules), 25–27, 29  
 transition regions, 141–145, 196, 197,  
 221–231, 235–246  
 two-state mixing, 5, 17–27, 137, 181–183,  
 187, 230, 250–253, 280–312,  
 327–330  
 and Coriolis coupling, 280–312  
 level repulsion, 22  
 multistate mixing, 17, 22–25, 327–330  
 strong mixing limit, 20, 21  
 weak mixing limit, 21, 22
- U-factors, 133, 273–279  
 U(5), 205–207, 217–221

- valence particles, 33  
valley of stability, 29, 30, 56  
V-factors, 133, 273–279  
vibrational model, 42, 145–161  
and B(E2) values, 42, 151–154,  
159–161  
energies 147–150, 154–161  
multiphonon states, 147–161  
vibrational motion, 26, 36, 43  
vibrations of deformed nuclei, 166–168,  
230–231, 323–331  
VMI, 185  
weak coupling and rotational alignment,  
303, 304  
weakness of nuclear force, 14, 15, 57  
Wilets-Jean model, 168, 187–193  
yrast states, 357–361  
 $z_\beta, z_{\beta\gamma}, z_\gamma$ , 176–181